

Lecture Notes

Design of Flexible Pavements

Prof. dr. ir. A.A.A. Molenaar
Nootdorp, July 2018
a.a.a.molenaar@hotmail.com
tel: +31 6 26171739 or +31 15 3108305

Table of contents

Preface	5
1. Introduction	8
2. Major defect types in flexible pavements	10
2.1 Cracking	10
2.2 Deformations	13
2.3 Desintegration and wear	15
3. Early design systems, the CBR method	15
4. AASHTO empirical design method	18
5. Development of mechanistic empirical design methods	29
5.1 Introduction	29
5.2 Stresses in a homogeneous half space	31
5.3 Stresses in two-layer systems	34
5.4 Stresses in three-layer systems	45
5.5 Stresses due to horizontal loads	51
5.6 Stresses in multilayer systems, available computer programs	55
6. Axle loads, wheel loads and contact pressures	76
6.1 Axle loads	76
6.2 Wheel loads	81
6.3 Contact pressures	82
7. Climatic data	91
7.1 Introduction	91
7.2 Temperature	91
7.3 Moisture	96
8. Asphalt mixtures	104
8.1 Introduction	104
8.2 Mixture stiffness	105
8.2.1 Mixture stiffness determined by means of testing	105
8.2.2 Mixture stiffness determined with nomographs and equations	112
8.3 Bitumen stiffness	116
8.3.1 Composition of bitumen	116
8.3.2 Characterizing bitumen by means of Pen, $T_{R\&B}$ and PI	119
8.3.3 Bitumen stiffness nomograph	121
8.3.4 Measuring bitumen stiffness by means of the Dynamic Shear Rheometer DSR	124
8.3.5 Bitumen stiffness and chemical composition	128
8.3.6 Bitumen stiffness and aging	130
8.4 Mixture stiffness at high temperatures, long loading times and high confining pressures	134
8.5 Poisson's ratio of asphalt mixtures	137
8.6 Fatigue resistance	138
8.6.1 Strain signals in pavements	139
8.6.2 Tensile strains and cracking caused by permanent deformation	141
8.6.3 Stress and strain signals in fatigue tests	144
8.6.4 Discussion on differences between laboratory and field conditions and their consequences for pavement design	151
8.6.5 Discussion on the differences between the various fatigue tests and potential size effects	152
8.6.6 Fatigue based on dissipated energy	156
8.6.7 Some practical aspects with respect to 2 and 4 point bending tests as well as UCT and indirect tension tests	161
8.6.8 Tests on slabs and beam on elastic foundation (BOEF) tests	165
8.6.9 Which test should we preferably use?	174

8.6.10 Equations and nomographs to predict fatigue relationships	175
8.7 Healing	181
8.8 Adhesive cracking	189
8.9 Aging related cracking	195
8.10 Permanent deformation in asphalt mixtures	196
9. Granular materials	205
9.1 Introduction	205
9.2 Estimation of the resilient characteristics of unbound base materials and sands	205
9.3 Estimation of the resilient characteristics of Dutch sands and unbound base materials made of recycled concrete and masonry	213
9.4 Estimation of the stiffness of granular materials by means of graphs and tables	219
9.5 Resilient modulus of granular materials determined with the repeated load CBR test	223
9.6 Estimation of the failure characteristics of unbound materials	231
9.7 Allowable stress and strain conditions in granular materials, permanent deformation models	234
10. Base courses showing self cementation	238
11. Stabilized base courses	244
11.1 Introduction	244
11.2 Cement stabilized base and sub-base courses	245
11.2.1 Cement treated sands	245
11.2.2 Cement stabilized granular layers	247
11.2.3 Cement treated RAP and recycled crushed concrete – masonry mixtures	251
12. Subgrade soils	256
12.1 Introduction	256
12.2 Models to predict the resilient modulus of soils	256
12.3 Estimation of the subgrade modulus using empirical equations	259
12.4 Allowable subgrade strain	261
12.5 Prediction of subgrade deformation	262
13. Lime treated soils	263
13.1 Introduction	263
13.2 Example of the effects of lime	264
13.3 Mechanical properties of lime stabilizations	267
14. Factors affecting pavement design and performance	271
14.1 Introduction	271
14.2 Lateral wander	272
14.3 Effect of limited pavement width	274
14.4 Design considerations when using cemented bases and sub-bases	276
14.5 Design considerations when using bases and sub-bases of blast furnace slags	276
15. Design aspects not related to thickness design	281
15.1 Introduction	281
15.2 Shrinkage cracking	282
15.3 Reflection cracking	284
15.3.1 Introduction	284
15.3.2 Measuring crack activity	287
15.3.3 Analysis tools for predicting propagation of reflection cracks	289
15.3.4 Construction techniques to counter reflection crack problems	297
15.4 Top - down cracking and lack of bond between layers	310
15.4.1 Introduction	310

15.4.2 Stresses at the pavement surface due to the complex pressure distributions in the tire – pavement contact area	314
15.4.3 Field studies on top - down cracking	321
15.4.4 Other types of surface cracking	324
15.4.5 Conclusions on top – down (surface) cracking	324
15.5 Raveling and bleeding	324
15.5.1 Introduction	324
15.5.2 Bleeding	326
15.5.3 Raveling	327
15.6 Skid resistance	343
15.7 Noise and noise reducing pavement surfaces	357
15.8 Road roughness	381
16 Thickness design systems	395
16.1 Introduction	395
16.2 How accurate are our pavement performance predictions?	395
16.3 Pavement design systems	403
16.3.1 SHELL pavement design system	404
16.3.2 FPS21	407
16.3.3 KENLAYER	407
16.3.4 AASHTO MEPD	417
16.3.5 3D-MOVE	420
16.3.6 French design method	423
16.3.7 Dutch design method	433
16.3.8 South African design catalogue TRH14	440
16.3.9 Highway Design Model (HDM)	441
17. Do we build what we have designed?	452
18. Measuring material properties, how many tests do we need	462
19. Probabilistic approach to pavement design	465
20. Relation between contract type, types of specifications and pavement design	474
20.1 Traditional contracts and recipe type specifications	475
20.2 Performance related specifications and contracts	476
20.3 Design, build, finance and maintain contracts	479
21. Closure	482
References	483
Appendices	
Appendix A: Factors influencing the accuracy of fatigue performance predictions	490
Appendix B: Quality control procedure for flexible pavements in case of innovative contracts as used in the Netherlands for main roads	503

Preface

The booklet in front of you is the completely revised 2007 version of the "LECTURE NOTES on the DESIGN OF FLEXIBLE PAVEMENTS" which I prepared for the MSc program at the faculty of Civil Engineering and Geo Sciences of the Delft University of Technology.

The reason why I revised the 2007 notes, 6 years after I retired in 2012, is a quite simple one. I feel honored and blessed to be still invited to teach class on this subject at the University of Stellenbosch in South Africa and at the Technical University in Wuhan, China. For these classes I regularly update my presentations using a.o. the results and findings of the 20 PhD students who graduated under my supervision at the Delft University after 2007, and of PhD students who graduated with prof. Scarpas in Delft and prof. Jenkins in Stellenbosch. I also included in those presentations, as good as possible, important developments published in journals and books etc. I wrote "as good as possible", and I did this by purpose since it is almost impossible to study in detail the overwhelming amount of material on each and every topic in pavement engineering that is coming available nowadays by means of journals, conference proceedings, reports etc.

From experience I know that students need more than copies of power point presentations and a long list of references; they also need an up to date reader which gives an as good as possible overview on the topic and which can be used as a basic source of information. It was clear to me that the 2007 version of the notes could not fulfill that purpose anylonger. Of course I could use one or more of the excellent text books which are available on the topic but also these get outdated rather quickly and on top of that they are too expensive for most students.

Because of all this I decided to rewrite to 2007 notes and make them available for free to everybody who is interested in the topic.

Compared to the 2007 notes I made the following revisions.

- I rewrote completely the topic on asphalt mixtures.
- Furthermore I made extensive revisions in the chapter on granular materials by adding information on how to predict the resilient modulus of those materials from physical parameters like gradation, moisture content etc. Information on this was taken from the AASHTO MEPD reports.
- Those AASHTO reports were also used to revise the part on estimating the resilient modulus of soils.
- With respect to stabilized base courses extensive information was added on cement treated mixtures of recycled crushed concrete – masonry mixtures.
- The part on the mechanical characteristics of lime treated soils has also been revised somewhat.
- New in the chapter on factors influencing pavement design and performance is the part on bases and sub-bases made of blast furnace slags.
- Entirely new is chapter 15 dealing with "Design aspects not related to thickness design". In this chapter we discuss shrinkage cracking, reflection cracking, top – down cracking, raveling and bleeding, skid resistance, traffic noise and noise reducing surface layers and road roughness. I added this chapter to show students that designing a flexible pavement is much more than designing its thickness. All the items discussed in this chapter are not part of any design system but nevertheless have a big impact on the service provided to the road user and also have a big effect on maintenance needs. All these items should not be "forgotten" when designing a pavement.
- Chapter 16 is revised by discussing more design systems than was done in the 2007 notes.
- I added a new short chapter 17 on "Do we build what we have designed?" I decided to add this chapter in order to make students aware of the fact that because of all kind of construction related issues, the layer characteristics of the pavement as built might very

- well not be what was assumed when making the design analyses; therefore pavements might very well perform quite differently from what was expected.
- Furthermore chapter 18 is added which contains a short discussion on the number of measurements we need to make to get a reliable value for e.g. the tensile strength of a material. This chapter was added to show students that it is not that easy to pinpoint a certain value to a certain material characteristic especially when the variability is rather high. This implies that we have to live with uncertainties.
 - Also new is chapter 19 on "Probabilistic approach to pavement design". I consider this to be an important chapter because it informs the student how we can take into account variations and uncertainties with respect to developments in traffic, climate changes, model errors and with large variations in material characteristics, mixture properties, layer thickness etc. Because of this, pavement performance predictions can never be accurate and precise and instead of predicting the amount of cracking after so many years we should much more focus on what is the chance of having a certain amount of cracking after X years and which are the most important factors affecting this.
 - The last new chapter is chapter 20 which is on "Contract types, specifications, quality control and pavement design".

As one will notice, the reference list contains a large number of PhD theses that were produced at the Delft University of Technology. These theses can be downloaded via <https://repository.tudelft.nl> or via my website <https://molenaarfiles.stackstorage.com>. The user name is *molenaarfiles* and the password is *Molenaar2016*. Here one can find a folder "PhD theses" which contains all theses produced by students who graduated under my supervision as well as some other theses. Under the folder "MSc theses" the reports can be found of students who got their MSc under my supervision.

I have done my best to mention in the references all sources and their authors from which I used some information but I am aware of the fact that I did not give credit to everybody whose information I used. I hope they will accept my apologies for these omissions.

Although this booklet is close to 500 pages, which is about 300 pages more than the 2007 version, it is certainly not a booklet on "everything you wanted to know about flexible pavements". Many important subjects were only briefly discussed and in not enough detail. Some important topics were even not discussed at all such as:

- hot and cold recycling of asphalt mixtures,
- half warm mixtures,
- foamed bitumen mixtures,
- seal coats,
- construction techniques etc.

After long deliberations I decided not to include these topics because I felt it would be better to refer to references such as the ones listed hereunder where these topics are extensively discussed.

- WIRTGEN manuals on Cold Milling and Cold Recycling (see website WIRTGEN),
- MS-4 The Asphalt Handbook from the Asphalt Institute (pdf can be downloaded from the web),
- Hot Mix Asphalt Material, Mixture Design and Construction (see website NCAT)
-

It might very well be that some experts and colleagues might not agree (at all) with what I have written down. If this is the case I warmly invite them to send me an email with their comments and criticism since that will help me in improving these notes.

In spite of these shortcomings I nevertheless hope that this booklet will be useful for many pavement engineering students.

Finally I like to mention that this booklet is part of a series of three, the two other ones are:

- Cohesive and non-cohesive soils and unbound granular materials for bases and sub-bases in roads. January 2015
- Structural evaluation and strengthening of flexible pavements using deflection measurements and visual condition surveys. March 2015.

Both can be found in the website mentioned above being <https://molenaarfiles.stackstorage.com>

I have given great care to the preparation of these notes; some errors however can never be avoided. It is therefore greatly appreciated if you inform me about any typing errors and other errors you may have found.

Prof. dr. ir. André A. A. Molenaar

1. Introduction

These lecture notes are dealing with the design of flexible pavements. One should realize that designing a pavement implies much more than designing its thickness. The design should also involve measures and techniques to guarantee for a sufficient long period of time the smoothness, skid resistance and reduced noise production. Designing a pavement doesn't only imply "taking care" for traffic induced stresses and strains, also environmental effects like effects of temperature and moisture should be taken into account.

Stress and strain analyses are nevertheless important parts of the design process but before we start with a discussion on stress and strain analyses in pavements, we better ask ourselves "what is a flexible pavement" or "what do we define as being a flexible pavement". In these notes all pavements which are not considered to be a cement concrete pavement or a concrete block (small element) pavement are considered to be a flexible pavement. This implies that also pavements with a relatively stiff cement treated subbase or base are classified as a flexible pavement.

Some examples of what is considered to be a flexible pavement are given in figure 1.

In the South African structures, the bearing capacity of the pavement is provided by the unbound base and subbase (structure I) or by the unbound base and cement treated subbase (structure II). The asphalt top layer provides a smooth riding surface and skid resistance. These structures have been successfully used in South Africa for moderately (structure I) and heavily loaded (structure II) roads. The "secrets" of the success of these pavements are the high quality, abundantly available, crushed materials used for the base and subbase and the high levels of compaction achieved. Furthermore the minimum CBR required for the subgrade is 15%. When that is not reached, improvement of the subgrade should take place. The cement treated subbase as used in structure II not only provides a good working platform for the construction and compaction of the unbound base but also influences the stress conditions in the pavement such that relatively high horizontal confining stresses develop in the unbound base. As we know from the lectures on unbound materials (CT4850), unbound materials become stiffer and stronger when the degree of confinement increases.

Structure III is an example of a heavily loaded highway pavement structure in the Netherlands. One will notice the striking difference between structure II which is used for heavily loaded pavements in South Africa and structure III that is used in the Netherlands for these purposes. The reasons for these differences are quite simple being that the conditions in the Netherlands are completely different from those in South Africa. There are e.g. no quarries in the Netherlands that can provide good quality crushed materials; these have to be imported from other countries. Limitations in space and strict environmental requirements require to recycle as much as possible materials that come available from demolishing old buildings and structures and old asphalt that comes available from road reconstruction projects. Since it has been shown that good quality base courses can be built of mixtures of crushed concrete and crushed masonry, extensive use is made of unbound base courses made of these recycled materials. A porous asphalt concrete top layer (void content > 20%) is used for noise reducing purposes. The thickness of the entire pavement structure is quite significant for two reasons. The first one is because the bearing capacity of the subgrade is quite often not more than 2% (this is in densely populated western part of the country) which necessitates the construction of a rather thick sand subbase. The second reason for the large thickness is that the road authorities don't want to have pavement maintenance because of lack of bearing capacity. Such maintenance activities involve major reconstruction which cause, given the very high traffic intensities, great hinder to the road user which is not considered to be acceptable. For that reason pavement structures are built such that maintenance is limited to repair or replacement of the top layer (porous asphalt concrete).

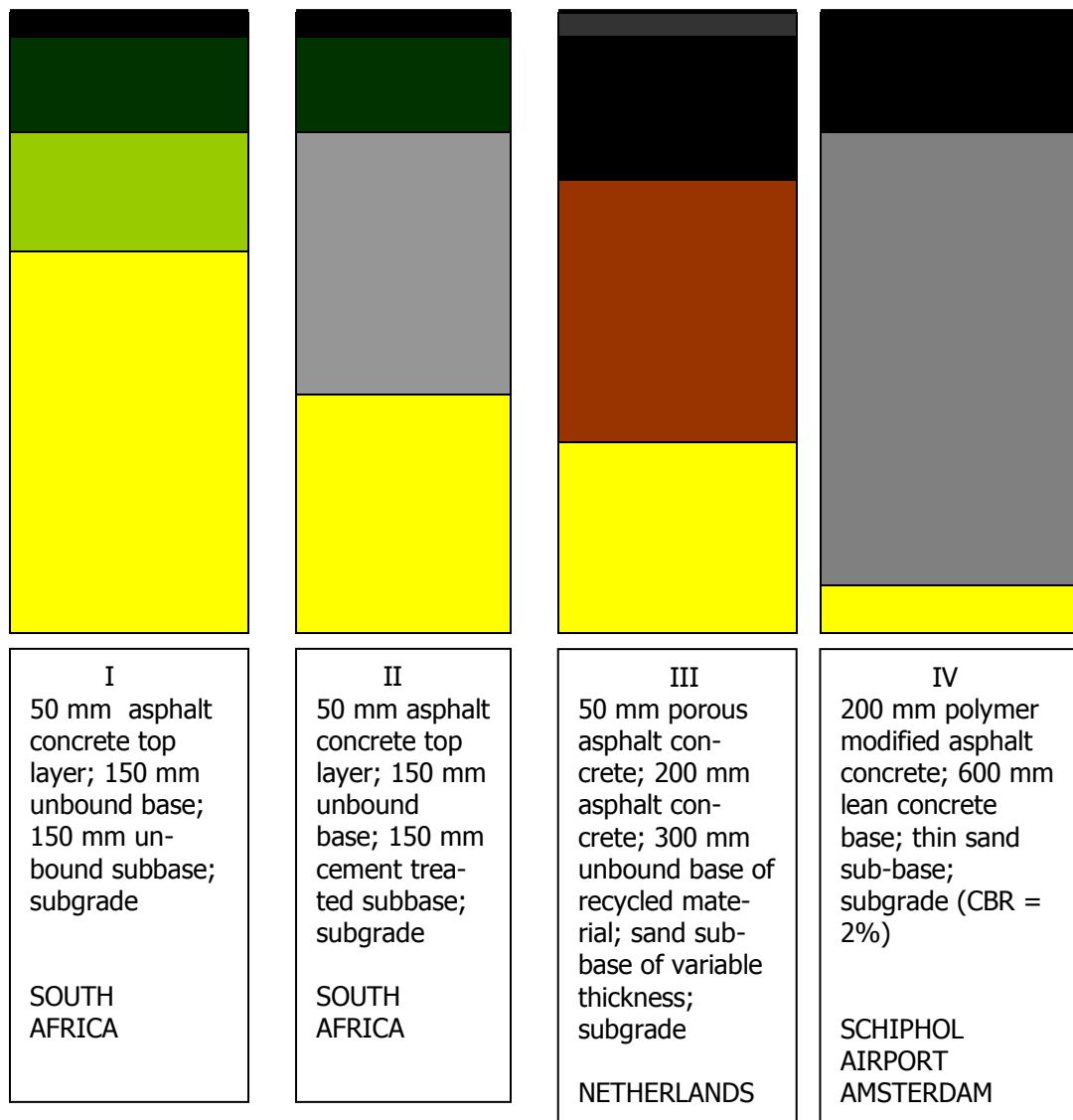


Figure 1: Different types of flexible pavement structures.

With respect to compaction of the unbound base it should be noted that it would be very hard to achieve the same results in the Netherlands as in South Africa. In South Africa the excellent compaction is achieved by soaking the base material and using a high compaction effort. The excessive amount of water used easily disappears because of the high evaporation rates. The recycled materials used for base courses in the Netherlands contain a significant amount of soft material (masonry) which is likely to crush if the compaction effort is too heavy. Furthermore the excessive amount of water used for compaction will not disappear easily because of the much lower evaporation rates. Using the South African way of compacting granular base and subbase courses in the Netherlands will therefore not lead to similar good results.

Structure IV is the structure used for the runways and taxiways of Amsterdam's Schiphol Airport. The airport is situated in a polder with poor subgrade conditions ($\text{CBR} \approx 2\%$). Combined with the airport's philosophy to maximize the use of the runway and taxiway system and minimize the need for maintenance, this results in rather thick pavement structures. A total thickness of 200

mm polymer modified asphalt concrete is used to reduce the risk for reflective cracking. For that reason the lean concrete base is also pre-cracked.

From the discussion given above it becomes clear that the type of pavement structure to be selected depends on the available materials, climatic conditions, maintenance philosophy etc. From the examples given above it also becomes clear that one has to be careful in just copying designs which seem to be effective and successful in other countries. One always has to consider the local conditions which influence the choice of a particular pavement type.

2. Major defect types in flexible pavements

Pavements are designed such that they provide a safe and comfortable driving surface to the public. Of course they should be designed and constructed in such a way that they provide this surface for a long period of time at the lowest possible costs. This implies that the thickness design and the material selection should be such that some major defect types are under control meaning that they don't appear too early and that they can be repaired easily if they appear. Major defect types that can be observed on flexible pavements are:

- cracking,
- deformations,
- disintegration and wear.

A short description of these defect types and their causes is given hereafter. Later in these notes it will be described how these defect types are taken care of in pavement design.

2.1 Cracking

Cracks in pavements occur because of different reasons. They might be traffic load associated or might develop because of thermal movements or some other reason. Figure 2 e.g. shows a combination of wheel track alligator cracking and longitudinal cracking. These cracks are most likely wheel load associated.



Figure 2: Longitudinal and alligator cracking in the wheel paths



Figure 3: Cracking observed on a narrow polder road in the Netherlands.

Since they only appear in the right hand wheel track close to the edge of the pavement. This is an indication that the cracks are most probably due to edge load conditions resulting in higher stresses in the wheel track near the pavement edge than those that occur in the wheel track close to the center line. Because of this specific loading condition, cracks might have been initiated at the top of the pavement.

Figure 3 is a picture of a cracked surface of a rather narrow pavement. If vehicles have to pass each other, the outer wheels have to travel through the verge. From the edge damage that is observed one can conclude that this is regularly the case. The base material which is visible in the verge seems to be a stiff and hard material. This is an indication that some kind of slag that shows self cementing properties was used as base material. Further indications of the fact that such a base material has been used can be found from the fact that the pavement surface is smooth; no rutting is observed. The extensive cracking of the pavement surface might be a combination of shrinkage cracks that have developed in the base. It is however also very well possible that the adhesion between the asphalt layer and the base is rather poor. If this is the case then high tensile strains will develop at the bottom of the asphalt layer causing this layer to crack.



Figure 4: Low temperature cracking observed on a highway in Minnesota.

Figure 4 is a typical example of low temperature cracking. In areas with cold winters, this type of cracking is quite often the dominating cracking type. Due to the very cold weather, the asphalt concrete wants to shrink. In principle this is not possible and tensile stresses develop as a result of the drop in temperature. The magnitude of the tensile stress depends on the rate of cooling and the type of asphalt mixture; especially the rheological properties of the bituminous binder are of importance. If the tensile stresses are becoming too high, the pavement will crack at its weakest point. Further cooling down of the pavement results in additional cracking and existing cracks will open. It is obvious that crack spacing and crack width are interrelated. A large crack spacing results in wide cracks and vice versa. Low temperature cracking can be the result of a single cooling down cycle but also can be the result of repeated cooling down cycles (low temperature fatigue).

Figure 5 is an example of temperature related block cracking. The pavement of course not only shrinks in the longitudinal direction but also in the transversal direction. In that case the friction between the asphalt layer and the base is of importance. If that is high, high tensile stresses might occur in the transversal direction causing longitudinal cracks. Combined with the crack pattern shown in figure 4, this results in block cracking.



Figure 5: Low temperature associated block cracking observed on a highway in Minnesota.

As mentioned before, low temperature cracking can be the major cause of maintenance and traffic associated cracking is only of secondary importance in such cases. However, when heavy wheel loads are passing a crack like the one shown in figure 4, high tensile stresses will develop at the crack edge simply because of the fact that there is no load transfer. This problem might increase during the spring when moisture enters the crack and weakens the supporting layers. All this means that although traffic associated cracking is not the main problem, traffic can cause accelerated damage development near cracks.

A type of cracking that has many similarities with low temperature cracking is reflective cracking. In that particular case, a crack or joint in the layer underneath the asphalt layer tends to propagate through the asphalt layer. The problem often occurs in pavements with a cement treated base or in overlaid jointed concrete pavements (figure 6). Reflective cracking can even occur in new pavements when the cemented base shrinks due to hardening. Shrinkage cracks that develop in the base can easily reflect through the asphalt top layer especially if this layer is thin. If however the cement treated base is pre-cracked or if shrinkage joints have been made, the problem of reflective cracking can be minimized.

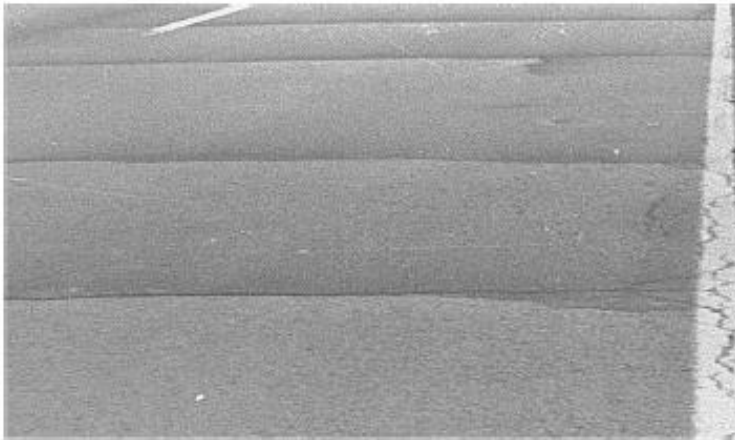


Figure 6: Example of reflective cracking in an overlaid jointed concrete pavement.

In these lecture notes we will concentrate on traffic induced cracking as well as reflective cracking. Low temperature is not considered because it is not really an issue in the Netherlands with its moderate climate.

Of course cracks can develop for many other reasons than traffic and environmental effects. One example of such "another reason" is given in figure 7 which shows severe cracking in the emergency lane due to the widening of the embankment next to that lane. Due to the widening, excessive shear stresses developed in the existing embankment resulting in the development of a shear plane leading to severe longitudinal cracking not only in the emergency lane but also in the slow lane (this lane is already repaired as the picture shows). The problem was aggravated by



the fact that a significant height difference occurred across the longitudinal crack resulting in very dangerous driving conditions for motor cyclists. This type of cracking is clearly due to a soil mechanics problem and therefore is beyond the scope of these lecture notes.

Figure 7: Severe longitudinal cracking due to shear failure in the existing embankment as a result of widening the road (extended embankment is on the right hand side).

2.2 Deformations

Deformations in pavements can be divided in longitudinal and transverse deformations. Longitudinal deformations can further be divided in short, medium and long wave deformations. Short wave deformations are of the order of a few centimeters and are mainly caused by surface irregularities such as raveling (this will be discussed later). Medium wave deformations are in the order of a few decimeters and usually are caused by imperfections in the pavement structure itself. Long wave deformations are in the order of meters and are caused by settlements, swelling soils, frost heave etc. Although they cause major annoyance, long wave deformations are, because of their origin, outside the scope of these lecture notes.



Figure 8: Roughness due to severe cracking.

Therefore we will restrict ourselves to short and medium wave length longitudinal deformations, also called unevenness or roughness.

Figure 8 shows a severely cracked farm to market road in Ohio. Due to the extensive amount of cracking, the pavement has become rather rough. It is quite clear from the picture that cracking has not only resulted in longitudinal but also transverse deformations. It is a typical example of medium wavelength roughness.

Figure 9 shows a pavement in Zimbabwe. Lack of maintenance has resulted in potholes which obviously result in a large decrease of driving comfort. Even dangerous situations might occur when driving at night. The reason for the potholes is that pavement has cracked severely, comparable to a condition shown in figure 8, and at given moment small pieces of the surface layer have been driven out. Erosion of the potholes due to rain and wind results in depressions of significant size and depth.



Figure 9: Roughness due to potholes as a result of severe cracking.



Figure 10: Longitudinal deformations due to settlements.



Figure 11: Rutting in an asphalt pavement.



Figure 12: Unevenness due to “buckling” of the base made of blast furnace slag.

Figure 10 was taken on a provincial road close to the Delft University in the Netherlands. The long wave longitudinal unevenness that can be observed is clearly the result of settlements. Please note that the settlements also have caused deformations in the transverse direction.

Next to longitudinal deformations, transversal deformations can occur. These can be the result of movement of the subsoil (settlements, swell, frost heave), but they also might be the result of traffic. The best known transversal deformation type due to traffic is rutting or permanent deformation that occurs in the wheel paths. A typical example of rutting is shown in figure 11. Rutting can develop in the asphalt layer(s) or in the unbound base, subbase or subgrade. Rutting can be the result of a densification process or as a result of shear failure. The rutting shown in figure 11 is clearly caused by shear failure in the asphalt layer. Shear failure can be recognized by the ridges that have developed next to the depression. Furthermore one can state that the narrower the depression the higher the layer is located in the structure where the shear failure has developed. The same is true for corrugations or washboard formation that is quite often observed near traffic lights or on unsurfaced roads.

Figure 12 shows a type of longitudinal unevenness that is quite often observed on pavements with a base course made of blast furnace slags. Because of the chemical reactions that take place, the material wants to expand resulting into compressive stresses that at a given moment become higher than the compressive strength of the material. Buckling of the base course is then the result leading to ridges which negatively influence driving comfort and which might have a negative effect on traffic safety because of loss of cargo from trucks.

2.3 Desintegration and wear

Raveling, bleeding and pothole formation can be rated as signs of disintegration and wear. Pothole formation has already been discussed in the previous section so we will concentrate ourselves in this section on raveling and bleeding.

Bleeding is a defect type that can be recognized as black, “fatty” looking spots on the pavement surface. It is an indication of overfilling of the voids in the aggregate skeleton with bituminous mortar. It is an indication that the mixture is not well designed. Due to the high bitumen content, the mixture suffers probably from lack of stability at higher temperatures and high traffic loads might squeeze out the bituminous mortar. Another reason might be that because of the low void content, there is not enough space for the bituminous mortar when it expands with increasing temperatures. In any case, the result is the same being a black, shiny surface with hardly any macro or micro texture and thus a low skid resistance.

Raveling is the loss of aggregate from the surface layer. It can occur on any type of asphalt mixture but especially open graded mixtures like porous asphalt concrete (void content > 20%) are sensitive for this damage type (figure 13). Raveling develops because of cohesive failure in the bituminous mortar or adhesive failure in the interface between aggregate and bituminous mortar.

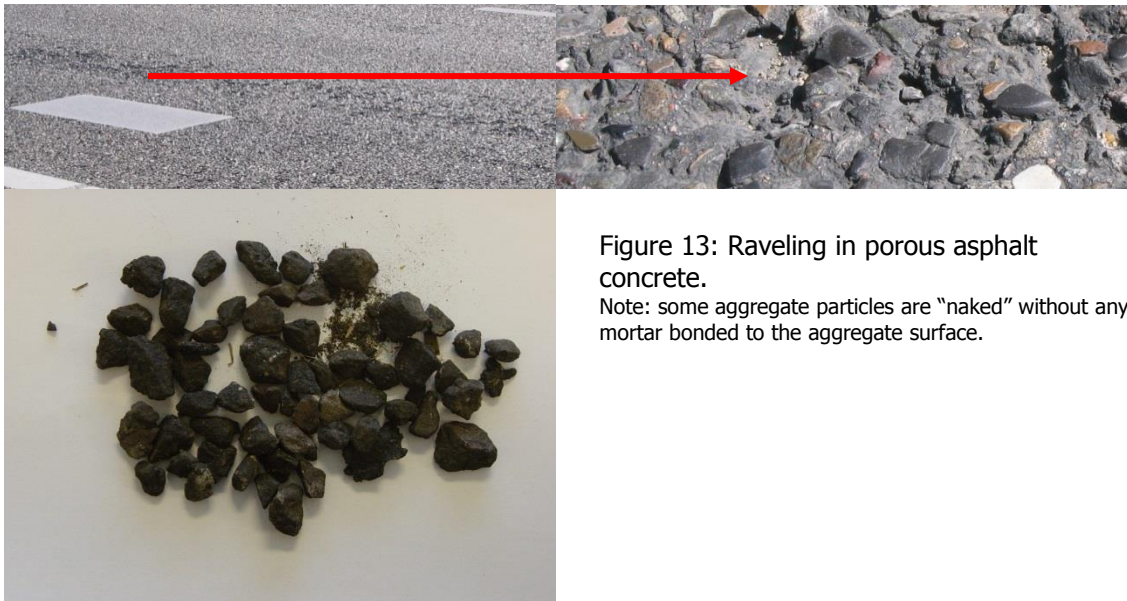


Figure 13: Raveling in porous asphalt concrete.

Note: some aggregate particles are “naked” without any mortar bonded to the aggregate surface.

Raveling provides a rough pavement surface resulting in an increased noise level. Furthermore the loose aggregate particles might result in windscreen damage. If raveling occurs on pavements with a thin asphalt surfacing, like the one shown in figure 9, then it is the first step to pothole formation.

3. Early design systems, the CBR method

Until now we have discussed damage types that can occur on flexible pavements. Before we start discussing the mechanistic empirical design systems that are developed, some information on the early design systems is given. Some knowledge on these systems is necessary because they are still used in several parts of the world and because it gives an understanding on how and why design systems developed to the mechanistic empirical systems used nowadays. Figure 14 is an

example of the problems one encountered in the early years of motorization. In those days most roads were earth or gravel roads and the strength of the pavement solely depended on the shear strength of the materials used.



Figure 14: Pavement problem in the early years of motorization.

One has to realize that nowadays about 65% of the global road network still consists of earth and gravel roads. Problems as shown in figure 14 therefore still quite often occur as is shown in figure 15.



Figure 15: Timber truck completely stuck on an earth road due to too high contact pressures and a too low shear resistance of the pavement material.

In both cases it is clear that the stresses induced in the pavement are higher than the allowable ones resulting in shear failure of the pavement surface and resulting in the fact that in both cases the vehicle got "stuck in the mud". The question now is why a light vehicle, such as shown in figure 14, suffered from the same problems as the heavy vehicle shown in figure 15. This has to do with the fact that the contact pressures caused by the light vehicle shown in figure 14 are of the same order of magnitude as the contact pressures caused by the heavy vehicle shown in figure 15. The lesson we learn from this is that it is not really the weight of the vehicle that is of importance or the number of axles but the contact pressure distribution under the tires. This distribution not only depends on the wheel load but also on the area over which the wheel load is distributed. This depends to a very large extent on the tire pressure. In the old days, solid tires were initially used and when pneumatic tires were introduced, high tire pressures had to be used because of the size of the tire (see figure 14). This resulted in small contact areas and high contact pressures. All this means that the contact pressure due to the vehicle shown in figure 14 could very well be the same as the contact pressure due to the vehicle shown in figure 15. Therefore similar types of surface defects can be expected.

The other reason why both vehicles run into problems is the lack of bearing capacity of the pavement material. On both pictures we notice an excessive amount of water and from our

lectures in soil mechanics we know that an excessive amount of water results in a low shear resistance especially in case of soils which contain a high amount of fine grained materials. We all know that the undrained shear strength of a saturated clay or silt is very low. In that case the cohesion is low and the angle of internal friction is about zero.

From this example it is clear that knowledge on the pressures applied to the pavement and the strength of the materials used is essential in order to be able to design pavements that can sustain millions of load repetitions.

The early design systems were, not surprisingly, based on determining the required thickness of good quality layers on top of the subgrade to prevent shear failure to occur in the subgrade. Of course the required thickness was dependent on the shear resistance of the subgrade and the amount of traffic. Furthermore the quality of the covering layers had to be such that shear failure didn't occur in these layers. This was the basis for the CBR thickness design method which is schematically shown in figure 16.

In the CBR design charts, the traffic load was characterized by means of a number of commercial vehicles per day and the shear resistance of the materials was characterized by means of their CBR value. The charts were used in the following way. First of all the number of commercial vehicles had to be determined. When this number was known, the appropriate curve had to be selected. Next the CBR value of the subgrade needed to be determined and the required layer thickness on top of the subgrade could be estimated by means of figure 16; this will be illustrated by means of an example. If e.g. the subgrade CBR is equal to α %, then the total thickness on top of the subgrade of a better quality material should be H_1 . If the CBR of the base material (for reasons of simplicity no subbase is applied in this case) is equal to β , then the thickness of a better quality material (better than the base material) on top of the base should be H_2 . In most cases such a material would be asphalt concrete so H_2 would be equal to the required asphalt thickness. The thickness of the base is then $H_1 - H_2$.

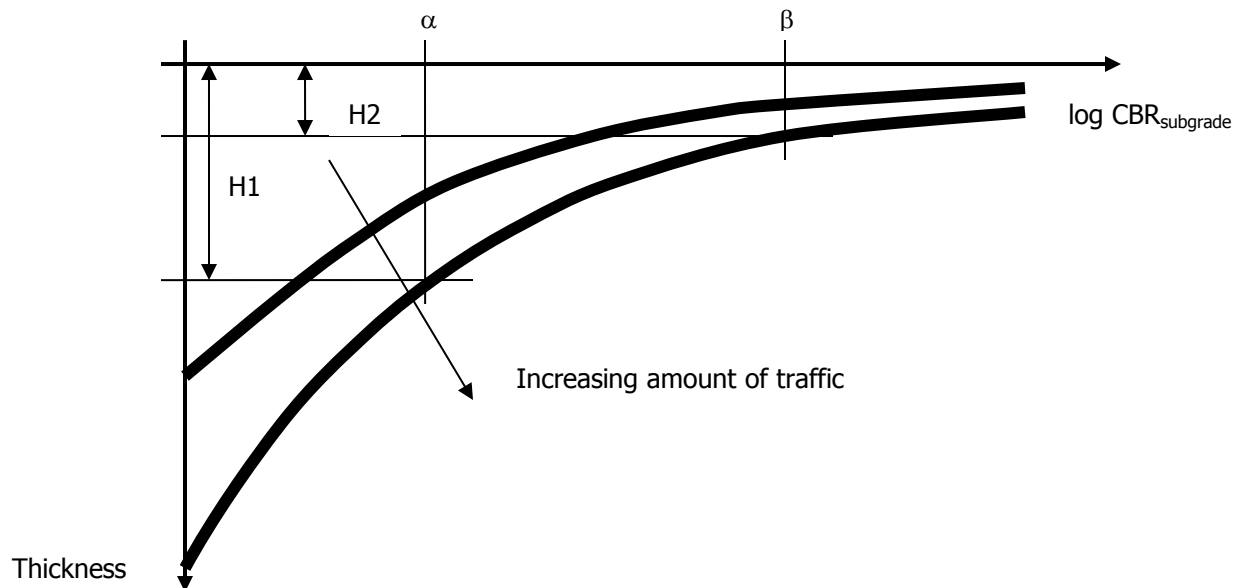


Figure 16: Principle of the CBR design charts.

The minimum asphalt thickness to be applied was 50 mm. The CBR values of the unbound materials used in the pavement structure is determined by means of the CBR test which is schematically shown in figure 17. Although the test has been described in detail in the part I of

the lecture notes on cohesive and non-cohesive soils and unbound materials, a summary of the basics of the test will be given here.

In the CBR test a plunger is pushed into the soil sample with a specific displacement rate and the load that is needed to obtain that displacement rate is monitored. The load – displacement curve that is obtained in this way is compared to the load – displacement curve of a reference material and the CBR is calculated as shown in figure 18.

The CBR design method results in thin asphalt layers which are mainly needed to provide a smooth driving surface and sufficient skid resistance.

4. AASHTO empirical design method

In the late 1950's, it was understood that, with the rapid increase in number and weight of the vehicles, these simple systems were not good enough anymore for the design of pavements and a strong need for improved methods developed. For that reason the American State Highway and Transportation Officials (AASHTO) launched a large research program that had to result in a better understanding of pavement performance in general and in a system that would allow durable and economical feasible pavement structures to be designed. For that reason a number of flexible and rigid pavement test sections were built which were subjected to a variety of traffic loads. This test is known as the AASHTO Road Test, the results of which, e.g. the load equivalency concept, are still used today.

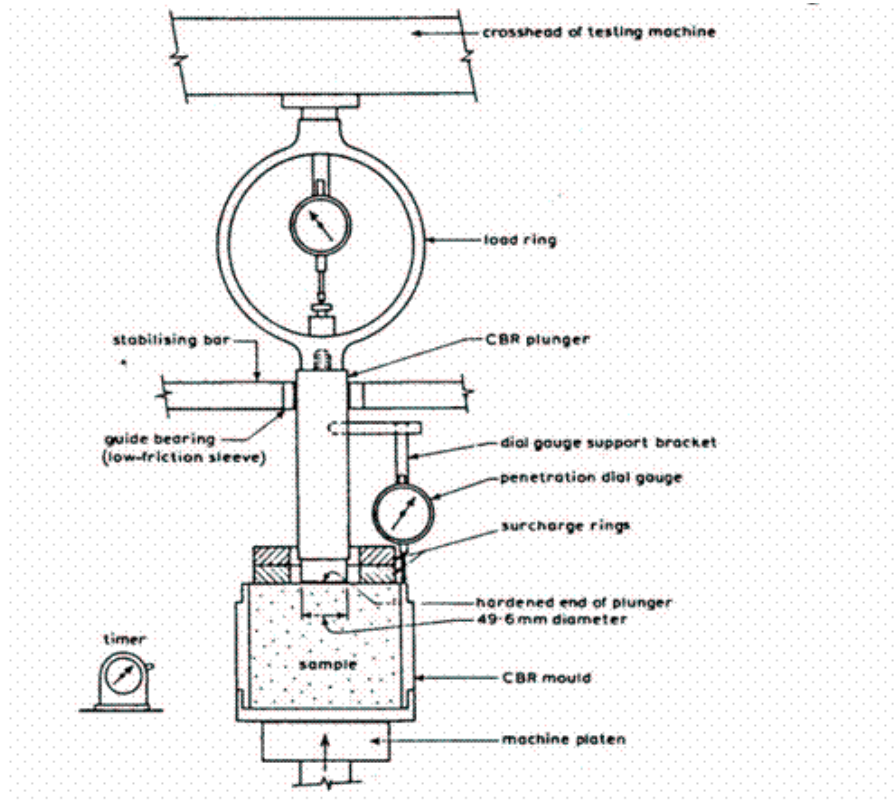


Figure 17: Principle of the CBR test.

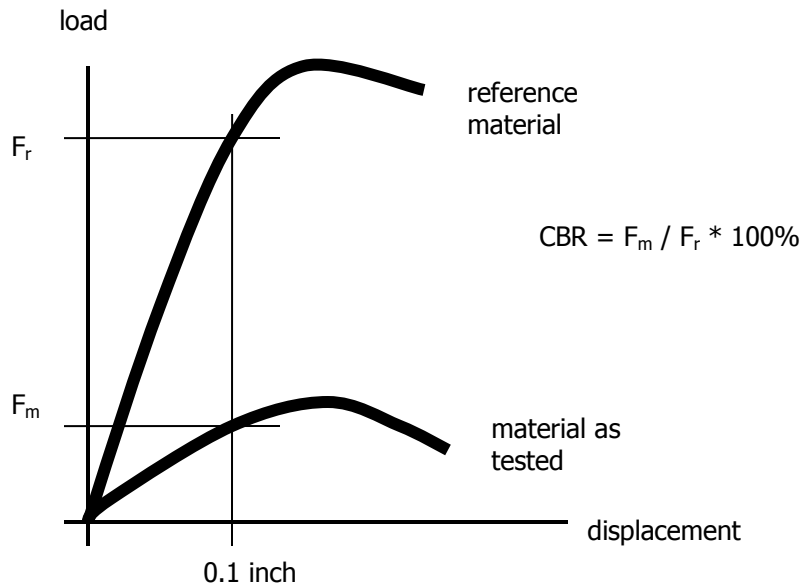


Figure 18: Assessment of the CBR value.

It is beyond the scope of these lecture notes to discuss the Road Test in detail. The interested reader is referred to reference [1].

We will limit ourselves to a short description of the Interim Design Guide published in the early 1980's [2]. It is important to understand the principles of this guide since it is still being used in many places all around the world.

One of the most important concepts that was developed during the test was the present serviceability index (PSI). This index is a number that reflects the "service" that is given by the pavement to the road user. The index was developed by correlating the physical condition of the various test sections in terms of the amount of cracking, rutting and unevenness to the ratings given by a panel of road users to the "service" provided by the pavement to the user. This latter rating was a number ranging from 5, being very good, to 0, being very poor. For main roads a PSI level of 2.5 was considered to be minimum acceptable level. The PSI is calculated as follows:

$$PSI = 5.03 - 1.91 \log (1 + SV) - 1.38 RD^2 - 0.01 \sqrt{ C + P }$$

Where: PSI = serviceability index,
SV = slope variance, a measure of the unevenness of the pavement surface,
C + P = percentage of cracked and patched pavement surface,
RD = rut depth.

As one could expect, the unevenness of the pavement has a significant effect on the PSI value; it dominates all the other factors. Detailed analyses of the data however showed that the amount of cracking and the slope variance correlate well with each other [119].

The pavement design method that was developed using the results of the AASHO Road Test involves the calculation of the so called structural number in relation to the allowable drop in PSI and the number of load repetitions after which this drop in PSI is allowed to occur. The structural number SN is calculated using:

$$SN = a_1 D_1 + a_2 D_2 + a_3 D_3$$

Where: a_i = structural coefficient of layer i [-],
 D_i = thickness of layer i [inch],
 i = 1 is the asphalt layer, 2 = base, 3 = subbase.

Other factors that are taken into account are the effective resilient modulus of the subgrade. Furthermore the method allows to design pavements with a certain level of reliability. Also the variation that occurs in the prediction of the occurring number of load repetitions as well as the variation that occurs in the layer thickness, structural layer coefficient and subgrade modulus can be taken into account by means of the overall standard deviation.

The design chart is shown in figure 19.

The subgrade modulus might vary during the year due to seasonal variations. One therefore has to determine the effective roadbed resilient modulus which is determined using the chart given in figure 20. Figure 20 is used as follows: one first determines the modulus which is to be used in each month (please note that it is also possible to define the subgrade modulus each half month). Then the relative damage is determined using the scale at the right hand part of the figure. Next the sum of the damage factors is determined and divided by 12 (or 24 if the damage factor is defined per half month). This value is then used to determine the effective roadbed or subgrade modulus. An example of how to use the chart is given in table 1.

Month	Roadbed soil modulus [psi]	Relative damage u_f
January	20,000	0.01
February	20,000	0.01
March	2,500	1.51
April	4,000	0.51
May	4,000	0.51
June	7,000	0.13
July	7,000	0.13
August	7,000	0.13
September	7,000	0.13
October	7,000	0.13
November	4,000	0.51
December	20,000	0.01
Average u_f		$3.72 / 12 = 0.31$

Table 1: Calculation of the mean relative damage factor for the estimation of the effective subgrade modulus.

Since the mean relative damage factor = 0.31, we determine from figure 20 that the mean effective roadbed (or subgrade) modulus is 5,000 psi.

NOMOGRAPH SOLVES:

$$\log_{10} W_{18} = Z_R \cdot S_o + 9.36 \cdot \log_{10} (SN+1) - 0.20 + \frac{\log_{10} \left[\frac{\Delta PSI}{4.2 - 1.5} \right]}{0.40 + \frac{1094}{(SN+1)^{5.19}}} + 2.32 \cdot \log_{10} M_R - 8.07$$

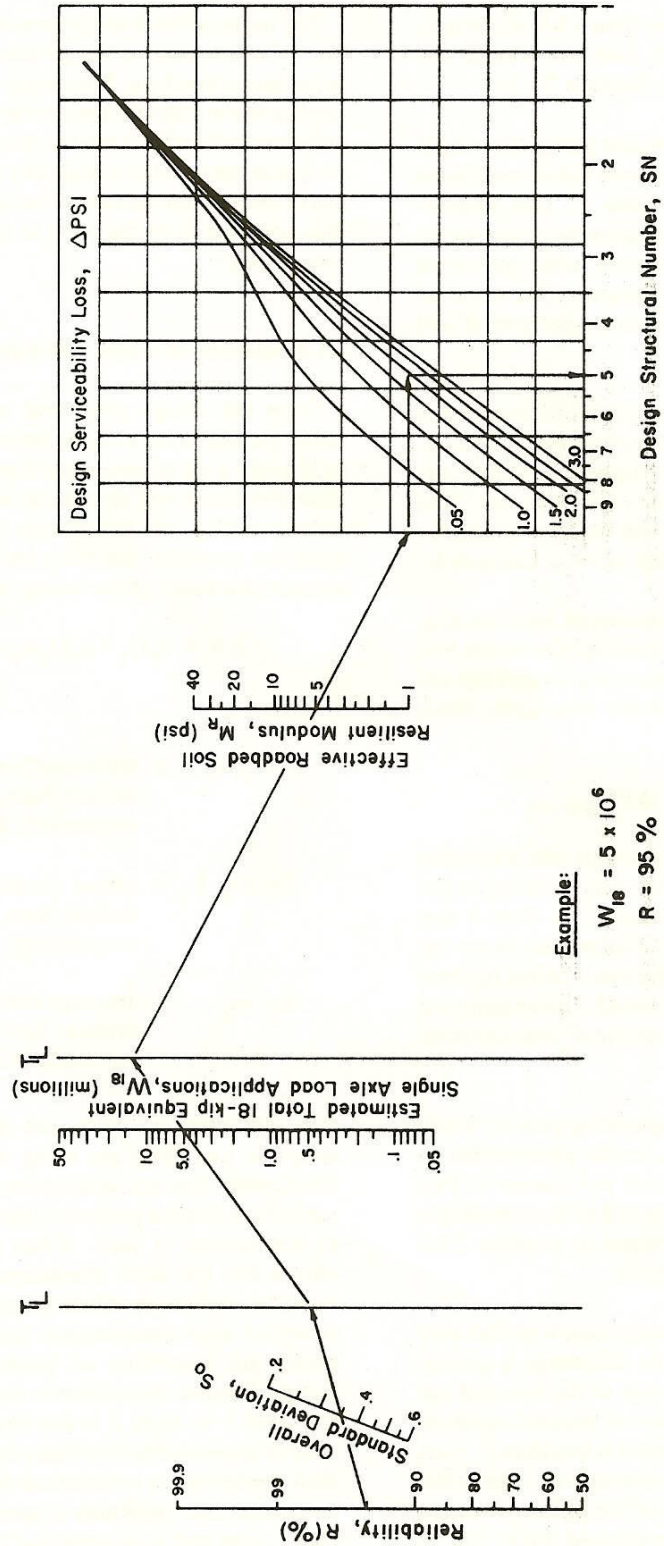


Figure 19: AASHTO design chart for flexible pavements based on using mean values for each input.

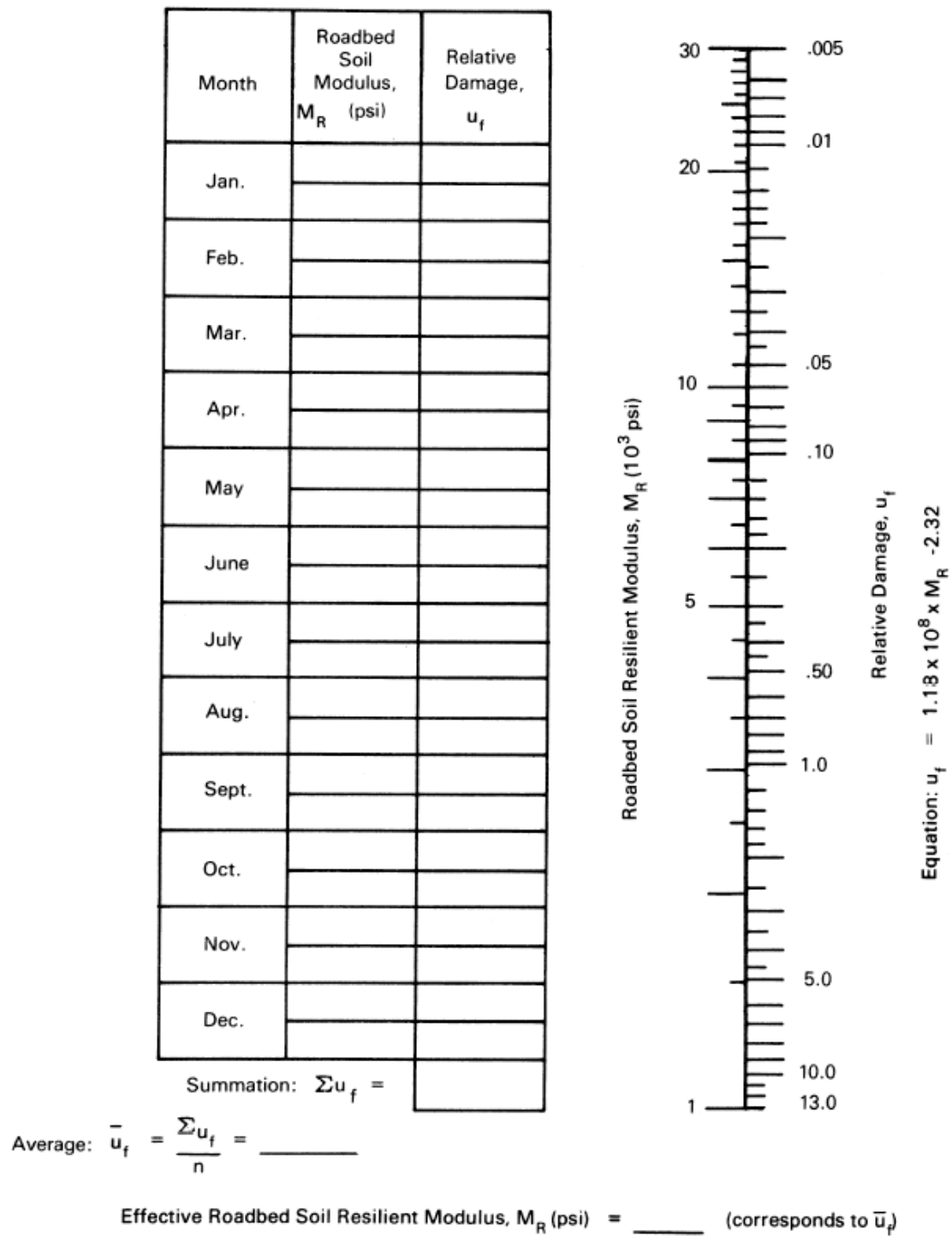


Figure 20: Chart to determine the effective roadbed (subgrade) modulus.

Charts to determine the structural layer coefficients for asphalt concrete, base and subbase are given in figures 21, 22 and 23.

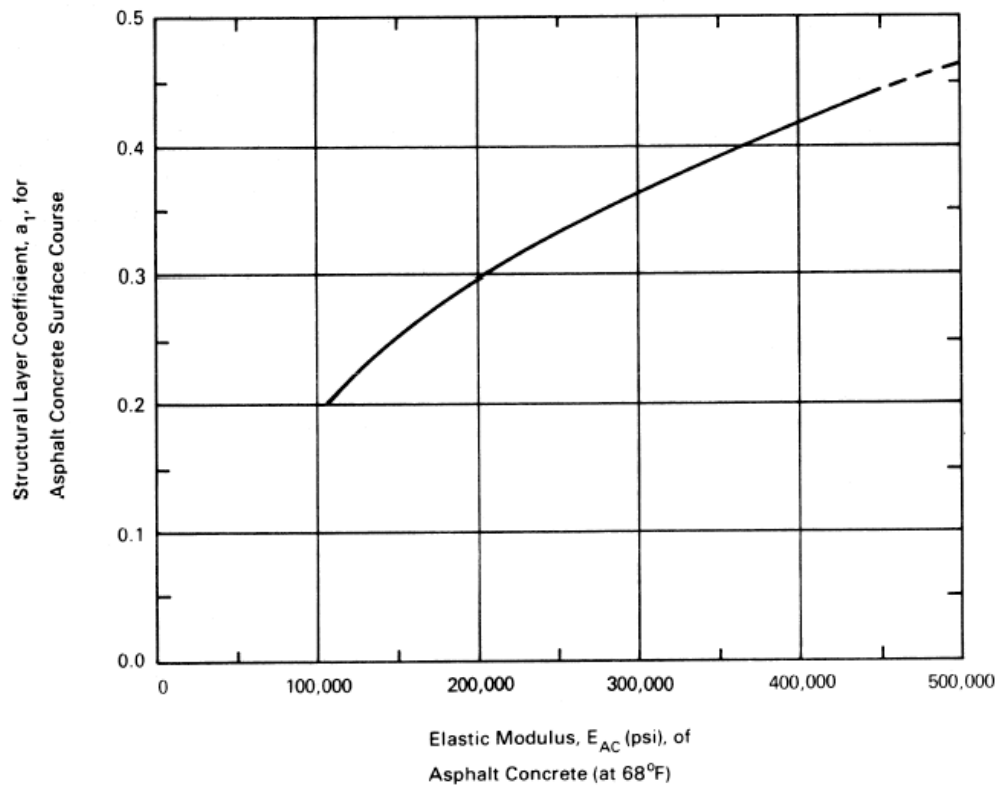


Figure 21: Chart for determining the structural layer coefficient for asphalt; please note that the asphalt modulus is at 68 °F (20 °C).

The charts given in figures 22 and 23 are based on the following equations:

For the base: $a_2 = 0.249 \log E_{BS} - 0.977$

For the subbase: $a_3 = 0.227 \log E_{SB} - 0.839$

Both the resilient modulus of the base, E_{BS} , and the subbase, E_{SB} , are stress dependent following

$$E = k_1 \theta^{k_2}$$

Where: E = modulus [psi],
 θ = sum of the principal stresses [psi] (see table 2).
 k_1, k_2 = material constants (see table 3).

The sum of the principal stresses in the base and subbase depends of course on the thickness and stiffness of the layers placed on top of them as well as on the magnitude of the load. Suggested values for θ are presented in table 2.

As one will notice from table 3, the material constants k_1 and k_2 are dependent on the moisture condition of the material (dry, damp, wet) as well as the quality of the material (indicated by the range in values).

Asphalt concrete thickness [inch]	Roadbed resilient modulus [psi]		
	3000	7500	15000
< 2	20	25	30
2 – 4	10	15	20
4 – 6	5	10	15
> 6	5	5	5

Table 2: Estimated values for θ in the base and subbase.

(a) Base		
Moisture Condition	k_1^*	k_2^*
Dry	6,000 - 10,000	0.5 - 0.7
Damp	4,000 - 6,000	0.5 - 0.7
Wet	2,000 - 4,000	0.5 - 0.7

(b) Subbase		
Dry	6,000 - 8,000	0.4 - 0.6
Damp	4,000 - 6,000	0.4 - 0.6
Wet	1,500 - 4,000	0.4 - 0.6

Table 3: Values for k_1 and k_2 for base and subbase materials.

Also charts have been provided for cement treated bases and bituminous treated base courses. These charts are shown in figures 24 and 25.

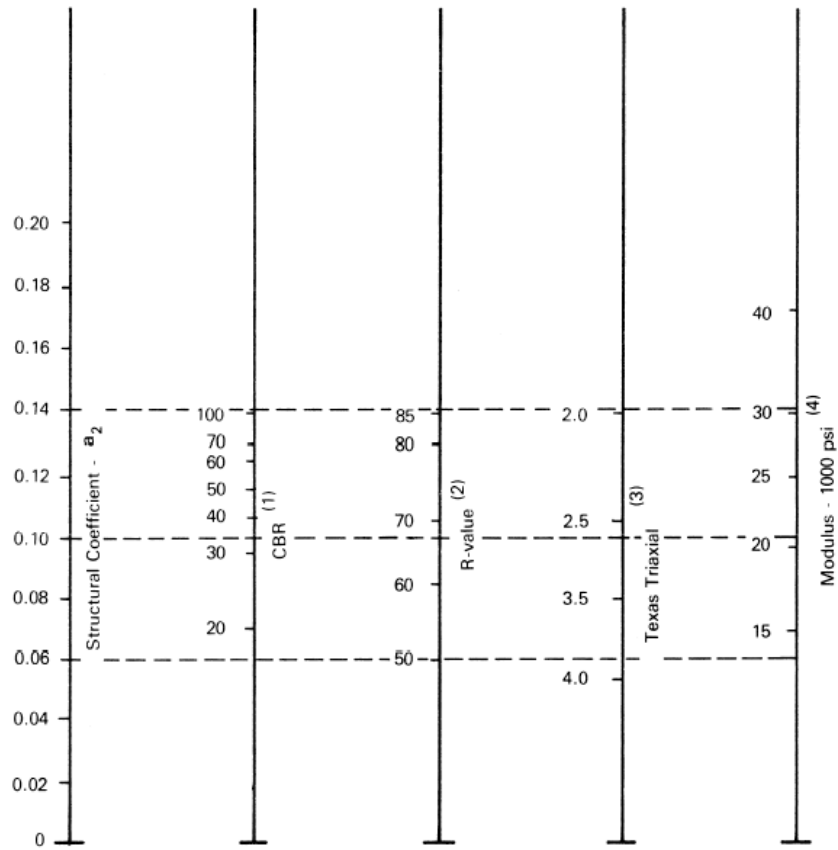
The traffic load is expressed as number of equivalent 18 kip (82 kN) single axles. To get this number the following equation is used.

$$N_{eq} = \sum_{i=1}^{i=n} (L_i / 82)^4$$

Where: N_{eq} = number of equivalent 18 kip (82 kN) single axles,
 n = number of axle load classes,
 L_i = axle load of axle load class i .

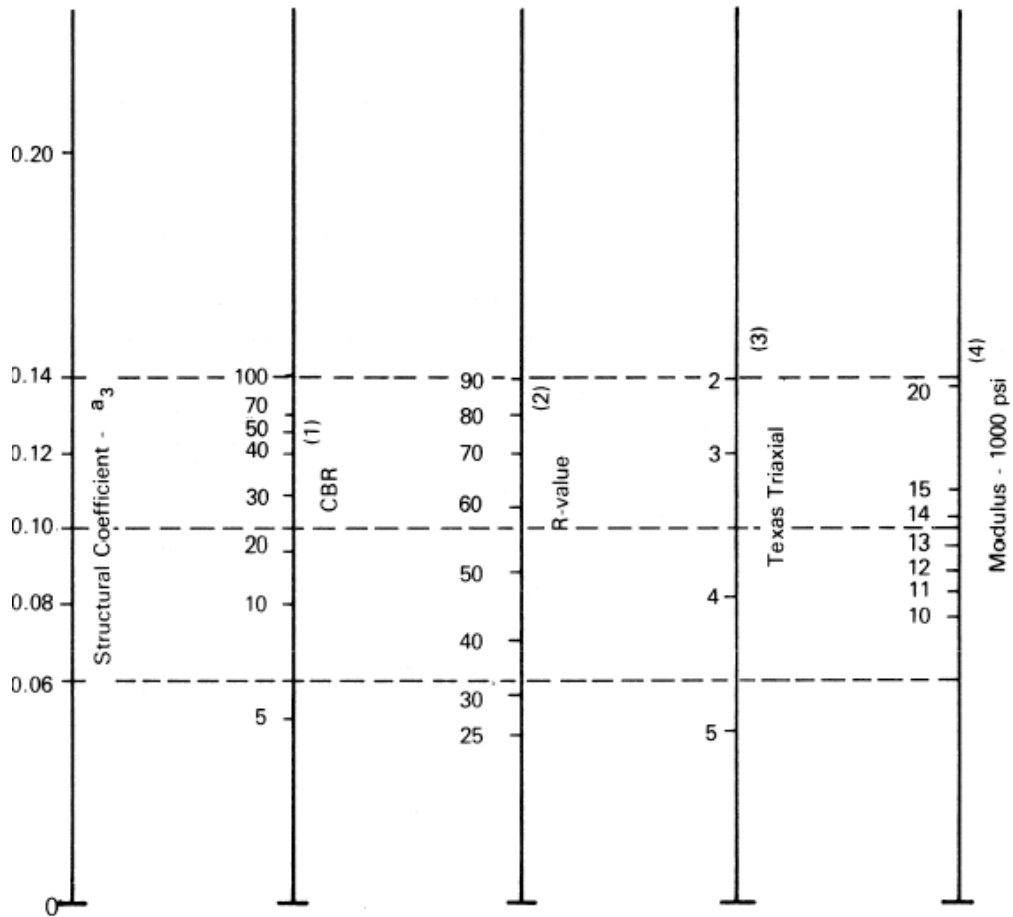
The reliability level to be used depends on the importance of the road. Freeways and very important highways are to be designed with a high level of reliability (90% and higher) because of the fact that traffic delays due to maintenance because of premature failure is considered not to be acceptable. Roads of minor importance can be designed with a much lower reliability level. Low volume roads e.g. can be designed with a reliability level of 60 – 70%.

The overall standard deviation is much more difficult to estimate. It appeared that this value was 0.45 for the asphalt pavements of the AASHO Road Test. Because production and laying techniques have significantly be improved since then, a lower value could be adopted. Since it is difficult to estimate a proper value, use of the 0.45 value is still suggested.



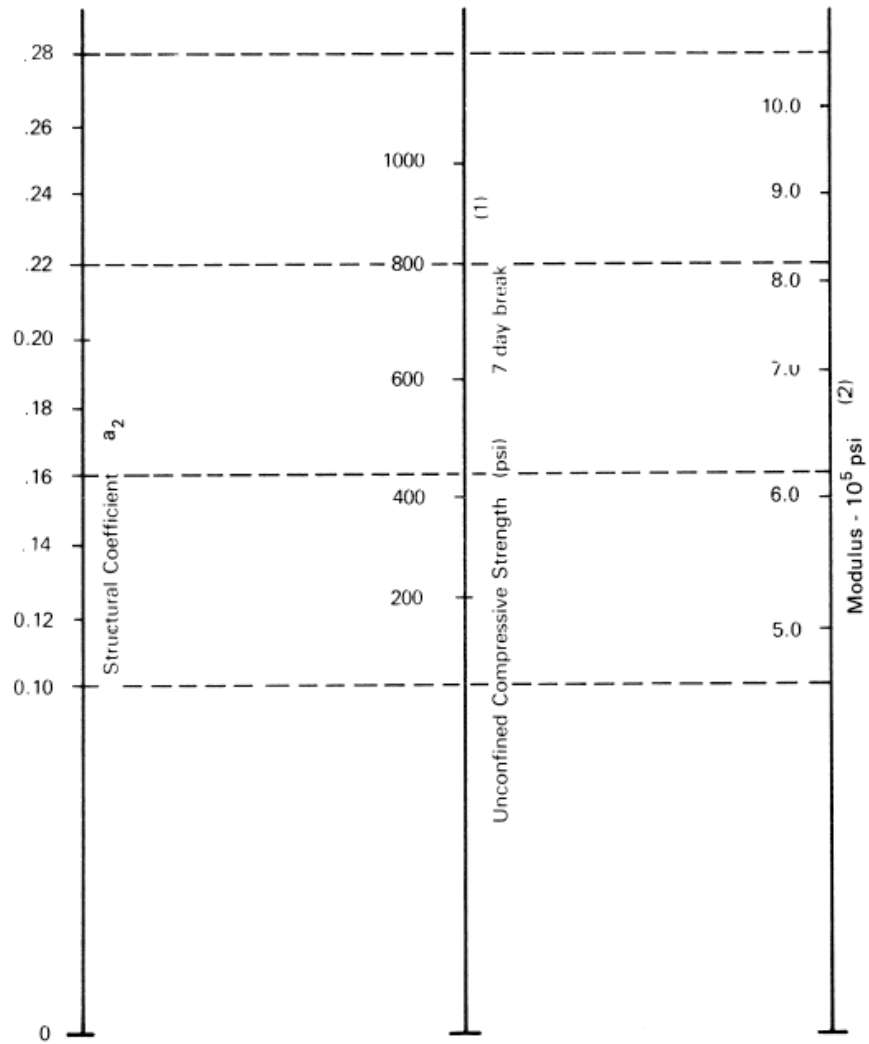
- (1) Scale derived by averaging correlations obtained from Illinois.
 (2) Scale derived by averaging correlations obtained from California, New Mexico and Wyoming.
 (3) Scale derived by averaging correlations obtained from Texas.
 (4) Scale derived on NCHRP project (3).

Figure 22: Chart to estimate the structural layer coefficient for granular base courses.



- (1) Scale derived from correlations from Illinois.
- (2) Scale derived from correlations obtained from The Asphalt Institute, California, New Mexico and Wyoming.
- (3) Scale derived from correlations obtained from Texas.
- (4) Scale derived on NCHRP project (3).

Figure 23: Chart to estimate the structural layer coefficient for granular subbases.



- (1) Scale derived by averaging correlations from Illinois, Louisiana and Texas.
 (2) Scale derived on NCHRP project (3).

Figure 24: Chart to estimate the structural layer coefficient of cement treated base layers.

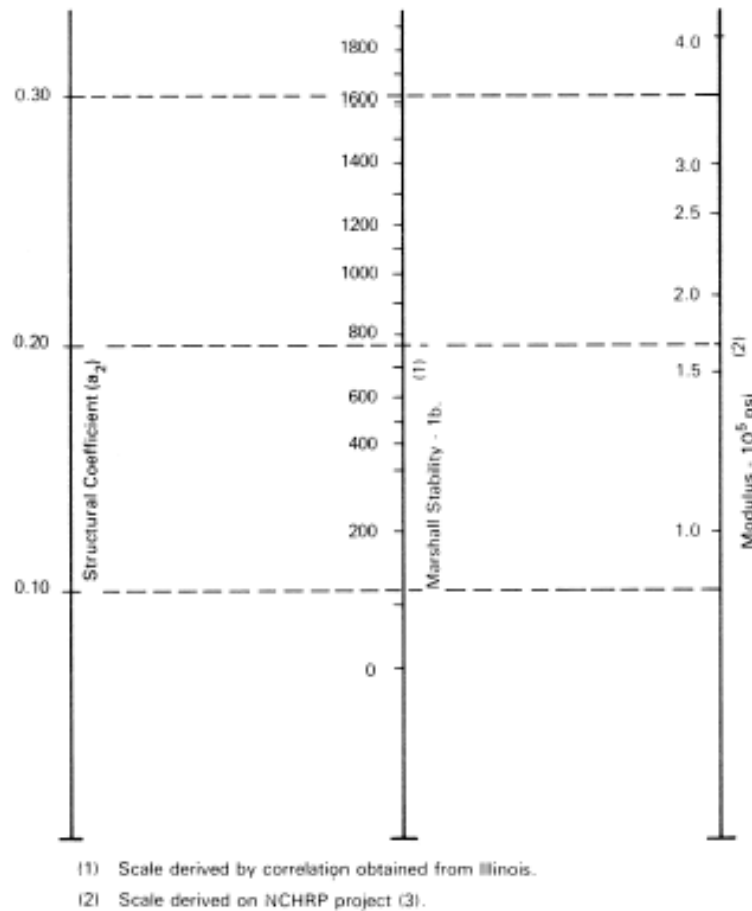


Figure 25: Chart to estimate the structural layer coefficient for bituminous treated base courses.

Drainage is a very important feature of pavement structures. Insufficient drainage might result in moisture conditions close to saturation. As we have seen in table 3, such conditions result in significant lower values for k_1 implying that the modulus of the unbound base and subbase can be 3 times lower in wet conditions than when they are dry. In order to be able to take care for improper drainage, it is suggested to multiply the structural layer coefficients with a drainage factor (m_i) following:

$$SN = a_1 D_1 + m_2 a_2 D_2 + m_3 a_3 D_3$$

Recommended m values are given in table 4.

It should be noted that the selection of the actual layer thicknesses has to follow a certain procedure. First of all one should determine the SN of the entire structure. Following the example in figure 20, we determine that the required $SN = 5$. Then we determine the required SN_1 on top of the base. Assuming a modulus of 30000 psi for the base ($a_2 = 0.14$) we determine that $SN_1 = 2.6$ and we determine the required asphalt thickness (assuming $a_1 = 0.4$) as $D_1 = SN_1 / a_1 = 2.6 / 0.4 = 6.5$ inch. If we assume that the modulus of the subbase is 15000 psi ($a_3 = 0.11$), we

determine in the same way the required thickness on top of the subbase as $SN_2 = 3.4$ The required base thickness is $D_2 = (SN_2 - SN_1) / a_2 = (3.4 - 2.6) / 0.14 = 5.8$ inch. Furthermore we calculate the thickness of the subbase as $D_3 = (SN - SN_2) / a_3 = (5 - 3.4) / 0.11 = 14.6$ inch.

Quality of Drainage	Percent of Time Pavement Structure is Exposed to Moisture Levels Approaching Saturation			
	Less Than 1%	1 - 5%	5 - 25%	Greater Than 25%
Excellent	1.40 - 1.35	1.35 - 1.30	1.30 - 1.20	1.20
Good	1.35 - 1.25	1.25 - 1.15	1.15 - 1.00	1.00
Fair	1.25 - 1.15	1.15 - 1.05	1.00 - 0.80	0.80
Poor	1.15 - 1.05	1.05 - 0.80	0.80 - 0.60	0.60
Very Poor	1.05 - 0.95	0.95 - 0.75	0.75 - 0.40	0.40

Table 4: Drainage factor m.

5. Development of mechanistic empirical design methods

5.1 Introduction

Although the AASHTO design method was a major step forward it still had the drawback of being highly empirical. The method is in fact is nothing less than a set of regression equations which are valid for the specific conditions (climate, traffic, materials etc.) of the Road Test. This implies that it is a bit risky to use the method in tropical countries where the conditions are completely different. Fortunately, road constructions are forgiving structures implying that the method at least results in an initial design that can be refined to meet local conditions.

The fact that the AASHTO method cannot be directly used for conditions for which it hasn't been developed became very apparent when attempts were made to use it in developing countries. The main problem was the PSI concept; it appeared e.g. that a pavement in the developed world with a low PSI implying that immediate maintenance was needed, was still a pavement with an acceptable quality in developing countries. This clearly indicated the need to have performance criteria and design methods that would fit the needs and circumstances in developing countries. All this resulted in the development of the Highway Design Model [3], a design system that is fully suited for those conditions. A short discussion about this model is given in chapter 16.3.7.

Another problem with the Guide is that it provides no information with respect to maintenance that is needed from a preservation point of view. The PSI value e.g. is strongly dependent on pavement roughness and damage types like cracking and rutting don't seem to have a large influence on the PSI. However control of cracking and rutting is important from a preservation point of view and in order to be able to make estimates on such maintenance needs, knowledge on stresses and strains and strength of materials is essential. Furthermore, if such information is not available, then it is almost impossible to evaluate the potential benefits of new types of materials and structures with which no experience has been obtained yet.

Given these drawbacks, one realized immediately after the Road Test that mechanistic based design tools were needed to support the AASHTO Guide designs. For that reason, much work has been done in the 1960's on the analysis of stresses and strains in layered pavement systems [6,

7, 8, 9] and on the characterization of the stiffness, fatigue and permanent deformation characteristics of bound and unbound pavement materials. The work done on the analysis of stresses and strains in pavements is all based on early developments by Boussinesq [4] and Burmister [5]. References [10, 11 and 12] are excellent sources with respect to research on pavement modeling and material characterization done in those days and should be on the reading list of any student in pavement engineering. It is remarkable to see that much of the material presented then still is of high value today.

Since then, much progress has been made and the reader is referred e.g. to the proceedings of the conferences organized by the International Society of Asphalt Pavements, the proceedings of the Association of Asphalt Pavement Technologists, the Research Records of the Transportation Research Board, the proceedings of RILEM conferences on asphalt materials, the proceedings of the International Conferences on the Bearing Capacity of Roads and Airfields, the Mairepav conferences and those of many other international conferences to get informed about these developments.

Given the possibilities we have nowadays with respect to material testing, characterization and modeling, it is possible to model pavements structures as accurate as possible using non linear elasto-visco-plastic models and using advanced finite element techniques that allow damage initiation and progression to be taken into account as well as the effects of stress re-distribution as a result of that. Also such methods allow the effects of joints, cracks and other geometry related issues to be taken into account. Furthermore these methods also allow to analyze the effects of moving loads which implies that inertia and damping effects can be taken into account.

The question however is to what extent such advanced methods should be used for solving day to day problems. This is a relevant question because advanced pavement design methods involve advanced testing and analyses techniques which require specific hardware and skills. Furthermore pavement design is to some extent still an empirical effort because many input parameters cannot be predicted with sufficient accuracy on before hand. Examples of such input parameters are climate, traffic and the quality of the materials as laid and the variation therein. All this means that although advanced methods provide a much better insight in why pavements behave like they do, one should realize that even with the most advanced methods one only can achieve a *good estimate* of e.g. pavement performance. Obtaining an *accurate prediction* is still impossible. Because of this, practice is very much interested in design methods which are, on one hand, based on sound theoretical principles but, on the other hand, are very user friendly and require only a limited amount of testing in order to save money and time.

One should realize that the need to use accurate modeling is influenced to a very large extent by the type of contracts used for road construction projects. In recipe type contracts, the contractor is only responsible for producing and laying mixtures in the way as prescribed by the client. In this case the contractor is neither responsible for the mixture design nor the design of the pavement structure; these are the responsibilities of the client. This immediately implies that the clients in this case will choose "proven" designs and materials, in other words he will rely on experience, and the contractor has no incentive to spend much effort and resources in advanced material research and pavement design methods. If however contractors are made more responsible for what they make, meaning that contractors take over from the authorities the responsibility for the performance of the road over a certain period of time, then they are much more willing to use more advanced ways of material testing and pavement design. More on this topic can be found in chapter 19.

The purpose of these lecture notes is not to provide an overall picture of existing mechanistic empirical design methods. The goal of these notes is to provide an introduction into pavement design using the analytical methods and material characterization procedures as they are

common practice nowadays in the Netherlands and elsewhere. This implies that we will concentrate in these notes on the use of multi layer linear elastic systems and the material characterization needed to use these systems. Also attention will be paid to how to deal with pavement design in case the main body of the structure consists of unbound materials which exhibit a stress dependent behaviour. Also the characterization of lime and cement treated layers will be discussed.

5.2 Stresses in a homogeneous half space

Although pavement structures are layered structures, we start with a discussion of the stresses in a homogeneous half space. Solutions for this were first provided by Boussinesq at the end of the 1800's. Originally Boussinesq developed his equations for a point load but later on the equations were extended for circular wheel loads. The stresses under the center of the wheel load can be calculated using:

$$\sigma_z = p \left[-1 + \frac{z^3}{(a^2 + z^2)^{3/2}} \right]$$

$$\sigma_r = \sigma_t = \left[-(1 + 2\nu) + \frac{2 \cdot z \cdot (1 + \nu)}{\sqrt{(a^2 + z^2)}} - \left\{ \frac{z}{\sqrt{(a^2 + z^2)}} \right\}^3 \right] \cdot \frac{p}{2}$$

$$w = \frac{2 \cdot p \cdot a \cdot (1 - \nu^2)}{E}$$

Where:

σ_z	= vertical stress,
σ_r	= radial stress,
σ_t	= tangential stress,
ν	= Poisson's ratio,
E	= elastic modulus,
a	= radius of the loading area,
p	= contact pressure,
z	= depth below the surface.

Please note that the cylindrical coordinate system is used for the formulation of the stresses (see figure 26).

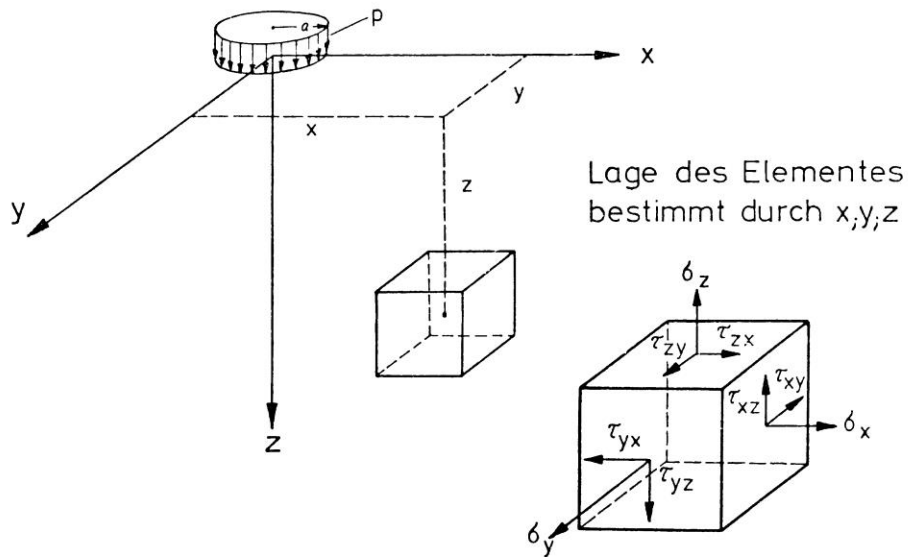
This is not the place to give the derivations that resulted in the equations given above. The interested reader is referred to [4, 6].

In figure 27 some graphical solutions are provided for the Boussinesq equations.

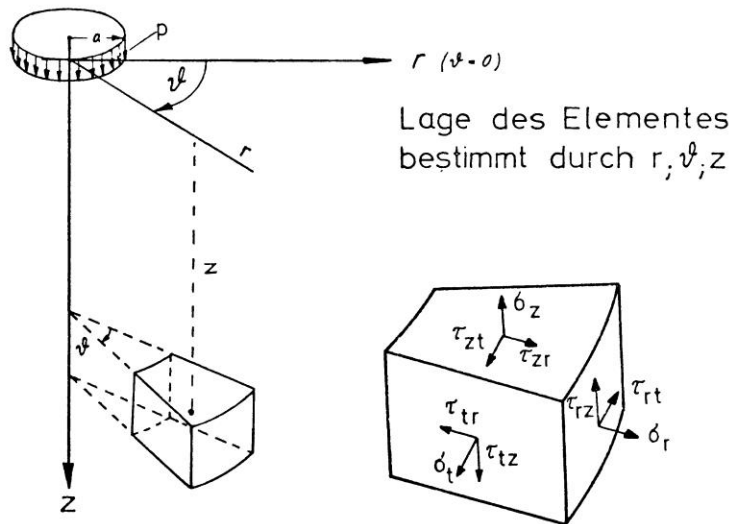
The Boussinesq equations are useful to estimate stresses in e.g. earth roads where the road structure is built by using the natural available material. One can e.g. derive the Mohr's circles from the calculated stresses and then one can determine whether the stresses that occur are close to the Mohr – Coulomb failure line, implying early failure, or not.

Many of these earth roads however are layered systems simply because the top 200 mm or so have different characteristics than the original material simply because of compaction that is applied etc. The higher stiffness of this top layer results in a better spreading of the load. This is schematically shown in figure 28.

1. Im kartesischen Koordinatensystem



2. Im zylindrischen Koordinatensystem



positive Spannungen bedeuten Zug

negative Spannungen bedeuten Druck

Der Kontaktdruck p wird als Druckspannung negativ eingesetzt

Figure 26: Cartesian and cylindrical coordinate system.

Note: Spannungen = stresses, Zug = tension, Druck = compression, p = compressive stress and therefore negative

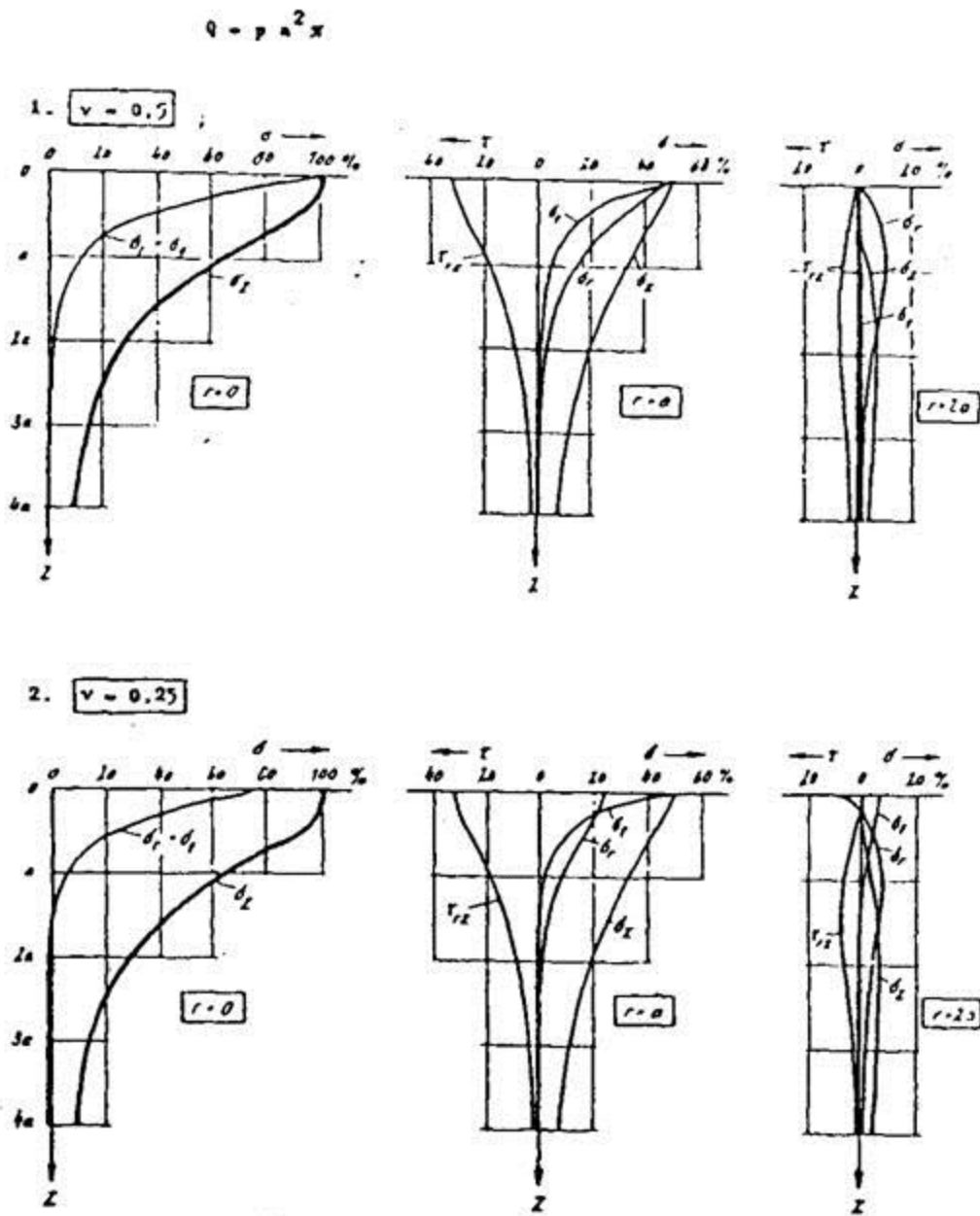


Figure 27: Graphical solutions for Boussinesq's equations.

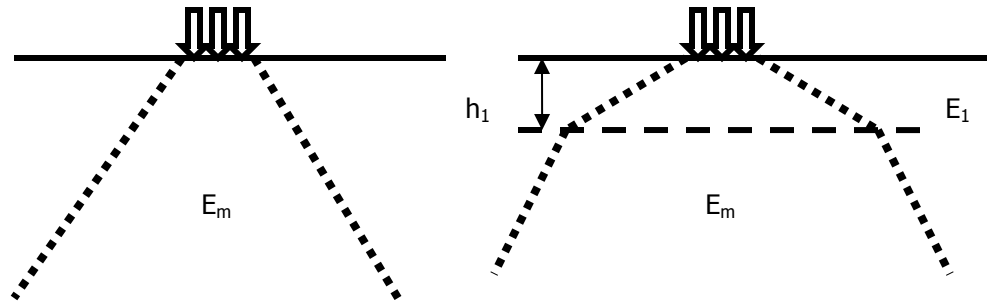


Figure 28: Effect of applying a stiffer top layer on the spreading of the load.

In order to be able to calculate stresses in such two layered systems, Odemark's equivalency theory [13] is of help. The idea behind Odemark's theory is that the vertical stresses at the interface between the top layer with stiffness E_1 and thickness h_1 and the half space with stiffness E_m are the same as the stresses in a half space at an equivalent depth h_{eq} with stiffness E_m . This principle is shown in figure 29.

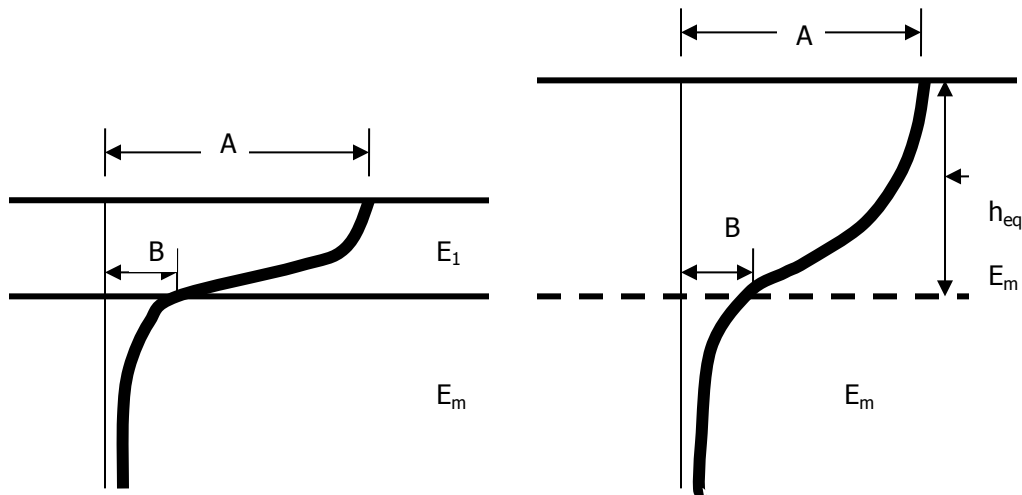


Figure 29: Principle of Odemark's equivalency theory.

The figure on the left hand side shows the distribution of the vertical stresses in a two layer system. On the right hand side the equivalent h_{eq} is shown resulting in the same vertical stress (B) at the interface between the top layer and the underlying half space.

Odemark showed that the equivalent layer thickness can be calculated using:

$$h_{eq} = n h_1 (E_1 / E_m)^{0.33}$$

If Poisson's ratio of the top layer equals Poisson's ratio of the half space, then $n = 0.9$.

The question of course is how well this Odemark/Boussinesq approach allows accurate predictions of the vertical stresses in pavements to be made. As is shown in figure 30 [14], this approach seems to be fairly effective in case one is dealing with pavements having unbound bases and subbases.

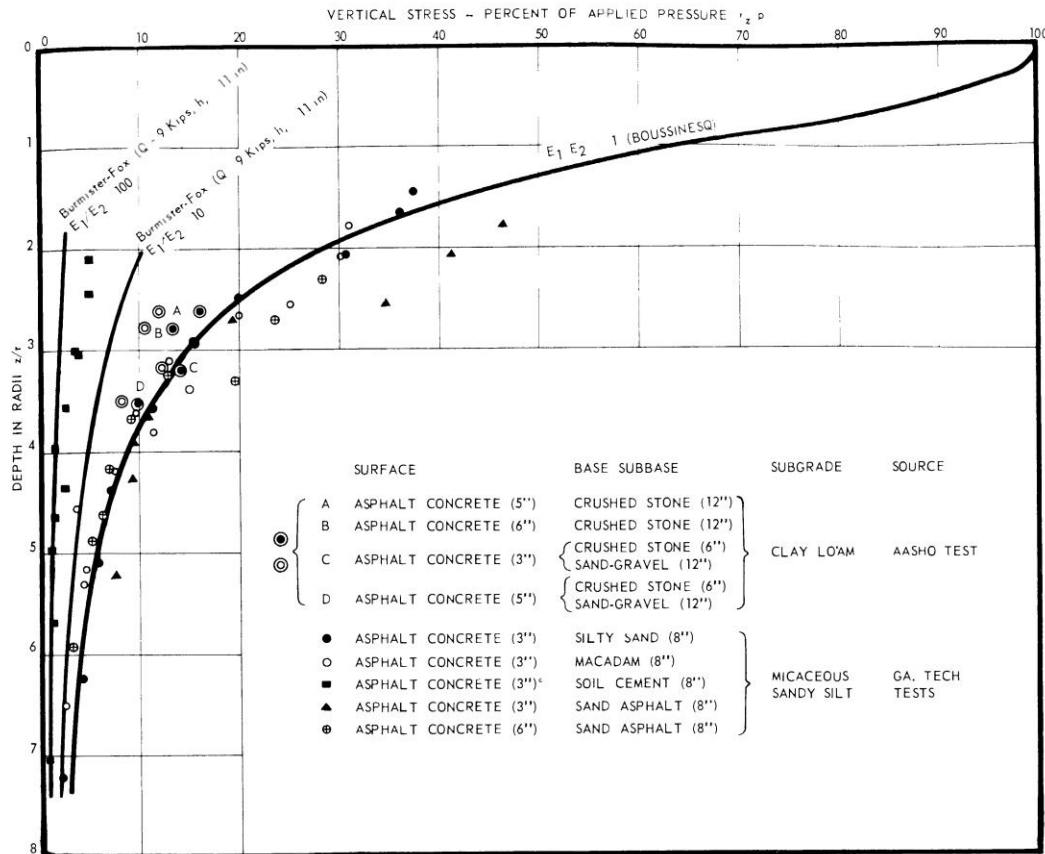


Figure 30: Comparison of measured and calculated vertical stresses in pavements.

Let us illustrate the procedure by means of an example. We want to know the stresses in a homogeneous half space (modulus 100 MPa) that is loaded with a wheel load of 50 kN. Since the contact pressure is known to be 700 kPa, we can calculate the radius of the loading area following:

$$\pi p a^2 = Q$$

Where:

- p = contact pressure,
- a = radius of the contact area,
- Q = wheel load.

In this way we calculate $a = 150$ mm. If we assume Poisson's ratio to be 0.25, then we can derive from figure 27 that the vertical stress under the centre of the load at a depth of 150 mm ($z = a$) is to 60% of p being 420 kPa. Assume that this stress is too high and that a layer is placed on top of the half space having a modulus of 300 MPa and a thickness of 150 mm. The equivalent layer thickness of this layer is:

$$h_{eq} = 0.9 h_1 (E_1 / E_m)^{0.33} = 0.9 * 150 * (300 / 100)^{0.33} = 194 \text{ mm}$$

We can now calculate the vertical stress using the same Boussinesq chart but this time the depth at which we have to determine the stress is $194 + 150 = 344$ mm which is at a depth of $z = 2.3$ a.

From figure 27 we notice that now the vertical stress is equal to approximately 20% of p being 140 kPa.

5.3 Stresses in two-layer systems

If the stresses in the subgrade due to a wheel load are too high, a stiff top is needed to reduce these stresses. Such a system, a stiffer layer on top of a softer half space, is called a two layer system. It could represent e.g. a full depth asphalt pavement on top of a sand subgrade.

Burmister [5] was the first one who provided solutions for stresses in a two layer system. Again, it is beyond the scope of these lecture notes to provide a detailed discussions on the mathematical background. Here only attention will be paid to the results of those mathematical analyses and how they can be used in practice.

Figure 31 shows the effect of a stiff top layer on the distribution of the vertical stresses in a two layer system. First of all we notice that the distribution of the vertical stress is bell shaped. Furthermore we notice that the magnitude of the vertical stress is very much influenced by the stiffness of the top layer. The width of the stress bell however is much less influenced by the stiffness of the top layer.

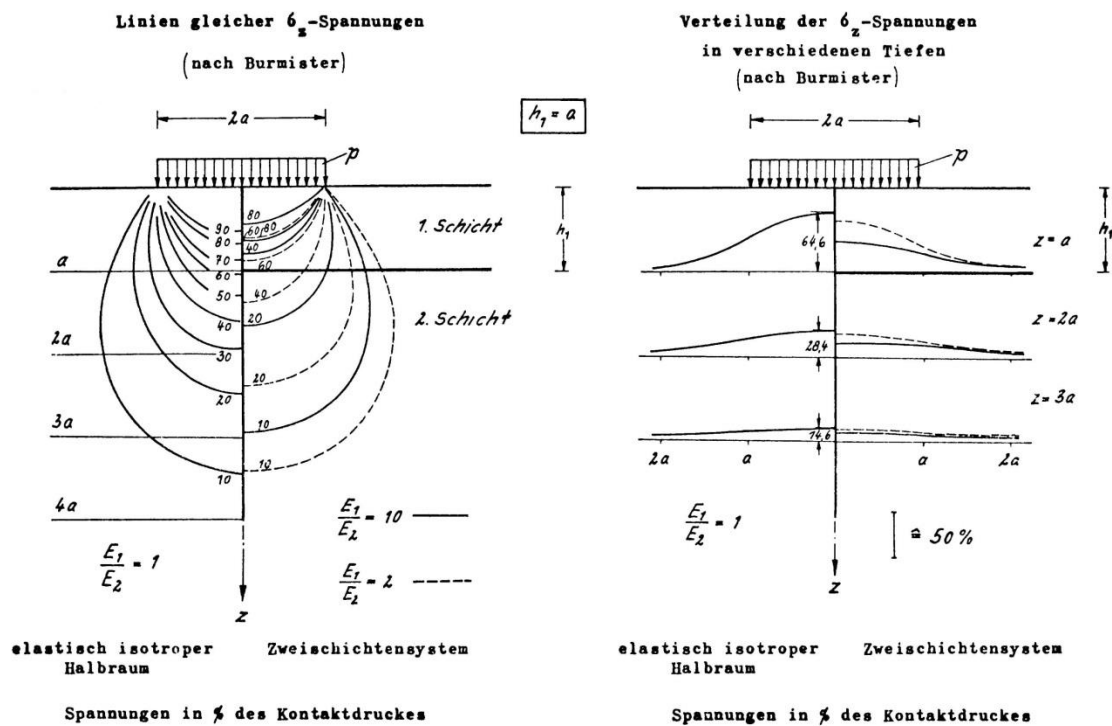


Figure 31: Distribution of the vertical stress in a one and two-layer system.

A stiff top layer not only provides protection to the second layer, also tensile stresses at the bottom of the top layer develop in case the top layer is a bound layer. These stresses are due to bending of the bound top layer. This implies that for two layer systems we are dealing with two design parameters being the horizontal tensile stress at the bottom of the top layer and the vertical compressive stress at the top of the second layer (figure 32).

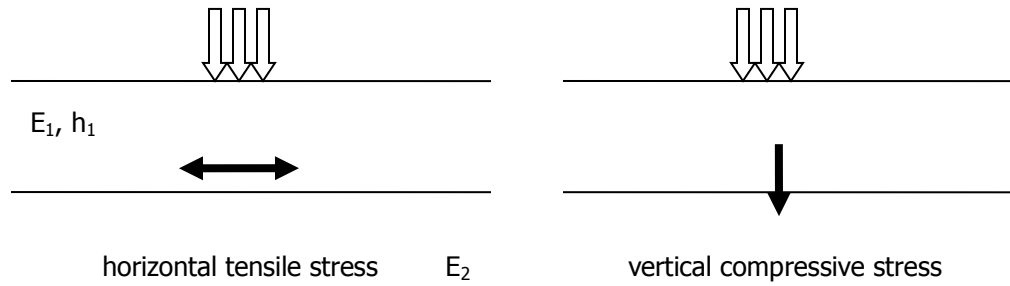


Figure 32: Design criteria in a two layer pavement system.

If the horizontal tensile stress at the bottom of the top layer is too high, it will be the cause for cracking of the top layer. If the vertical compressive stress at the top of the bottom layer is too high, excessive deformation will develop in that layer.

Figure 33 shows the distribution of the horizontal and vertical stresses in a two layer system under the centre of the load in relation to the ratio E_1 / E_2 and for $h = a$. Please note that Poisson's ratio is 0.25 for both layers.

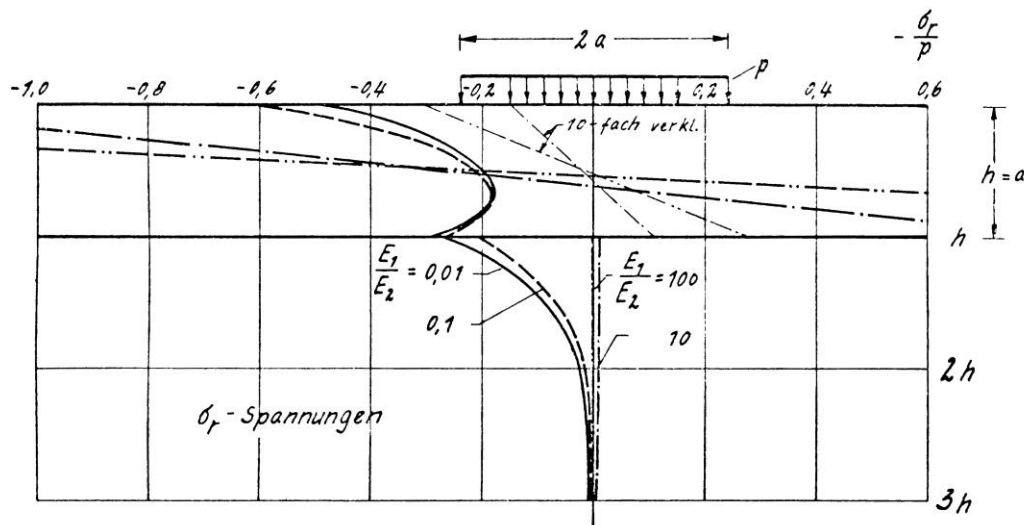


Figure 33a: Distribution of the horizontal stresses in a two layer system under the centre of a circular load (Poisson's ratio equals 0.25).

Note: 10 fach verkleinert = 10 times reduced

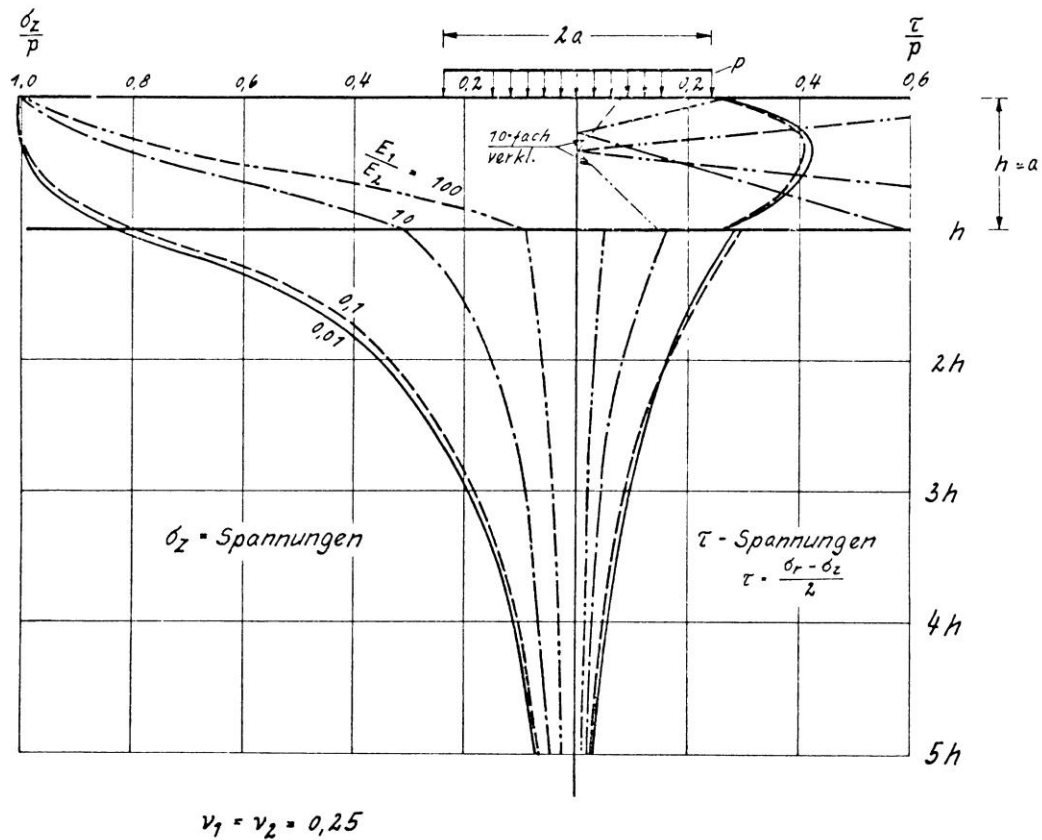


Figure 33b: Distribution of the vertical stresses in a two layer system under the centre of a circular load.

From the figure 33a one can observe that significant horizontal stresses (compressive at the top and tensile at the bottom) develop in the top layer. When $E_1 / E_2 = 10$, a tensile stress equal to the contact pressure p develops while this value becomes $2.7 * p$ when $E_1 / E_2 = 100$. One also observes that at those modulus ratio's the tensile stresses in the second layer can almost be neglected. Another interesting aspect is that the neutral axis is almost in the middle of the top layer for modulus ratio's of 10 and higher.

Figure 33b shows that a stiff top layer greatly reduces the vertical stresses in the bottom layer. As we have seen in figure 27, the stress at a depth of $z = a$ is 60% of the contact pressure in case of a half space. Figure 33b shows that if the modulus ratio is 10, the vertical stress at $z = a$ is 30% of the contact pressure and when the modular ratio is 100, the vertical stress at $z = a$ is only 10% of the contact pressure.

Let us go back for a moment to Odemark's equivalency theory. We have noticed that in a half space, the vertical stress at a depth of $z = a$ under the centre of the load equals 60% of the contact pressure. If we assume that the top part of that half space is replaced over a depth of a by a material that has a 10 times higher modulus, than the equivalent layer thickness of that layer equals:

$$h_{eq} = 0.9 * a * (10)^{0.33} = 1.92 * a$$

From figure 27 we can determine that the vertical stress at that depth equals approximately 30% of p . This is in excellent agreement with the result obtained from figure 33b. This is considered to be proof of the validity of Odemark's approach.

Until now no attention has been paid to the conditions at the interface. From our structural design classes we know that it makes quite a difference whether layers are perfectly glued to each other and there is no slip (full friction) between the layers or whether the layers can freely move over each without any friction (full slip). The effect of those two interface conditions on the stresses at the bottom of the top layer are shown in figure 34.

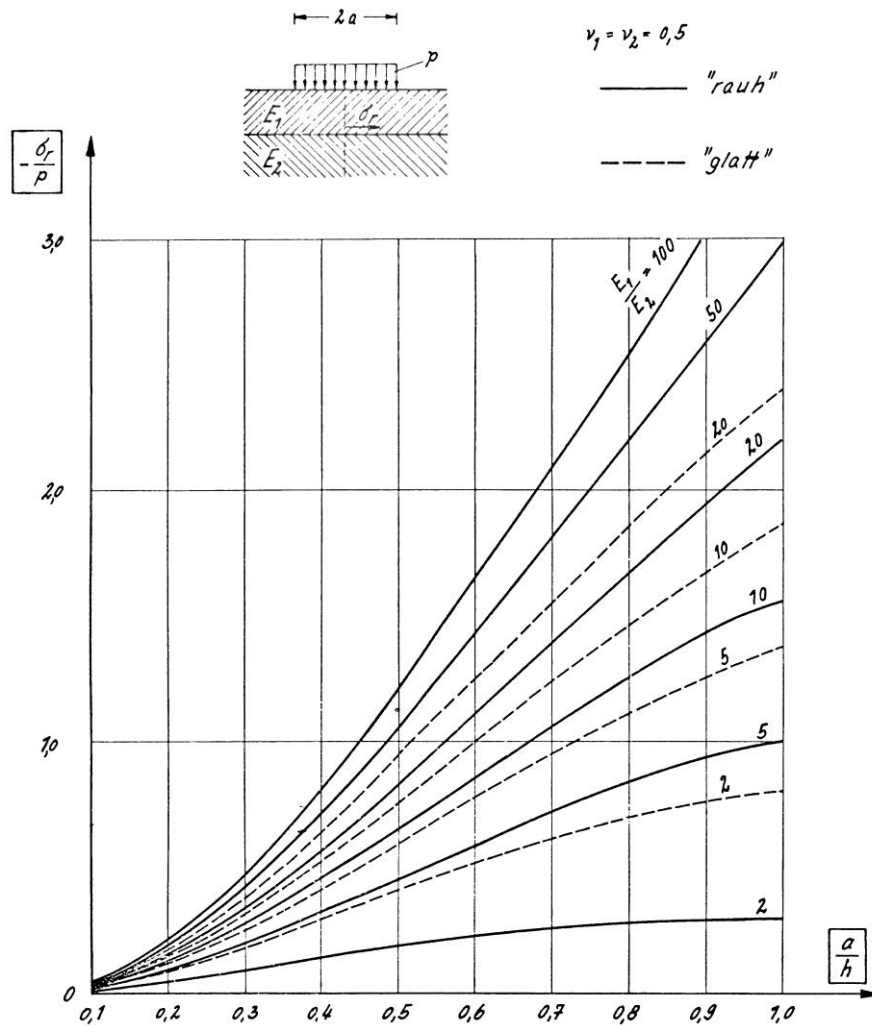


Figure 34a: Influence of friction on the radial stresses at the bottom of the top layer under the wheel centre (please note that Poisson's ratio is 0.5).

Note: *rauh* = full friction, *glatt* = full slip

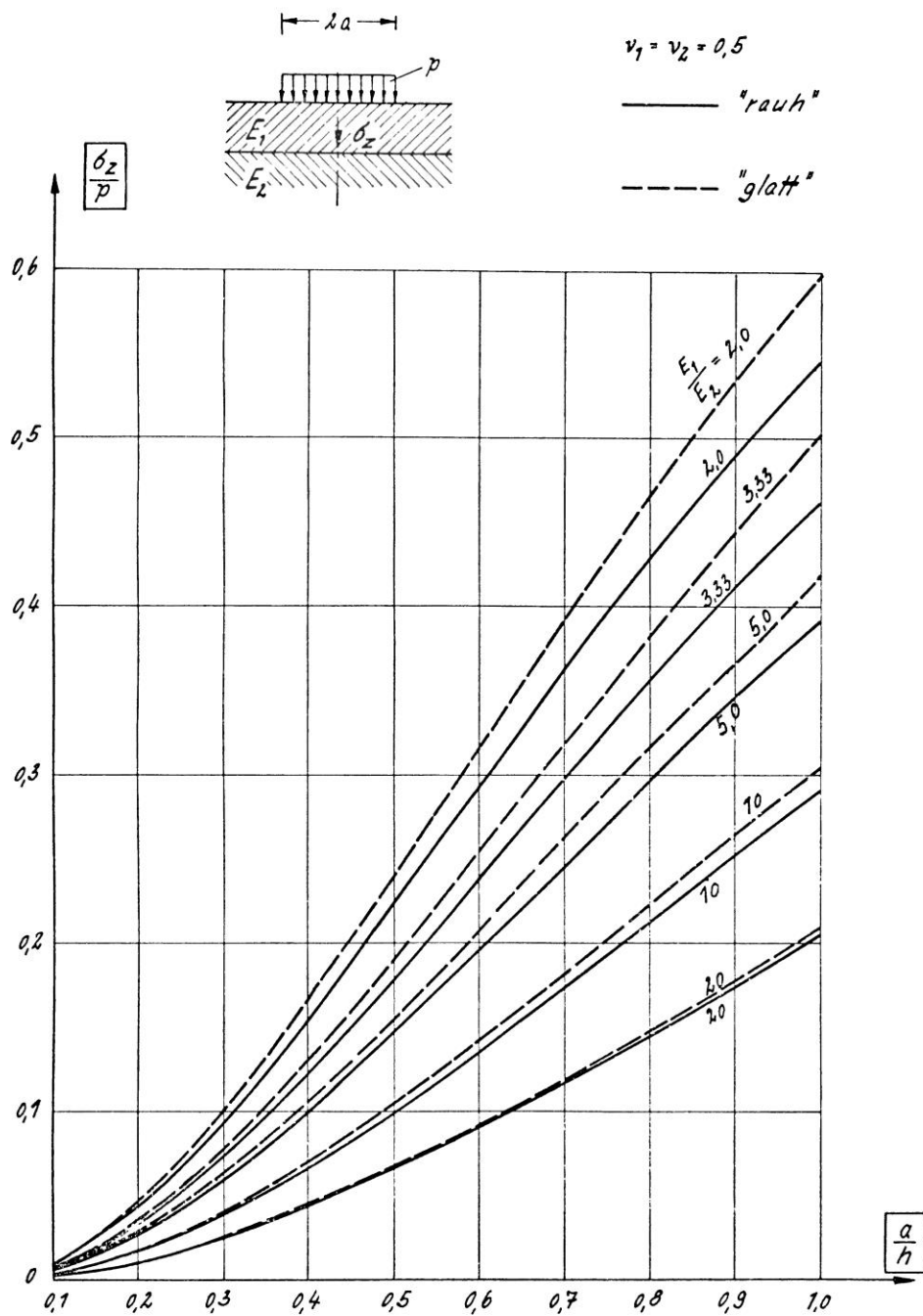


Figure 34b: Influence of friction on the vertical stress at the top of bottom layer under the wheel centre (please note that Poisson's ratio is 0.5).

As one will observe, the presence of friction has a significant influence on the radial (horizontal) stress at the bottom of the top layer especially at low values for the ratio E_1 / E_2 . We also note that the influence on the vertical stress is much smaller.

If there is full friction or full bond at the interface, the following conditions are satisfied.

a. The vertical stress just below and above the interface are equal because of equilibrium, so:

$$\sigma_z \text{ bottom, top layer} = \sigma_z \text{ top, bottom layer}$$

b. The horizontal displacements just above and below the interface are the same because of full friction, so:

$$u_r \text{ bottom, top layer} = u_r \text{ top, bottom layer}$$

c. The vertical displacements just above and below the interface are the same because of continuity, so:

$$u_z \text{ bottom, top layer} = u_z \text{ top, bottom layer}$$

In case of full slip, only conditions a. and c. are satisfied.

Another important factor is Poisson's ratio. Since measurements needed to determine Poisson's ratio are somewhat complicated, values for this parameter are usually estimated from information available from literature. The question then is to what extent wrong estimates influence the magnitude of the stresses. Information on this can be found in figure 35. Figure 35a e.g. shows that the influence of Poisson's ratio on the radial stress at the bottom of the asphalt layer is quite significant. This also means that it will have a significant influence on the radial strain. As one can see from figure 35b, the influence of Poisson's ratio on the vertical stress at the top of the bottom layer is limited.

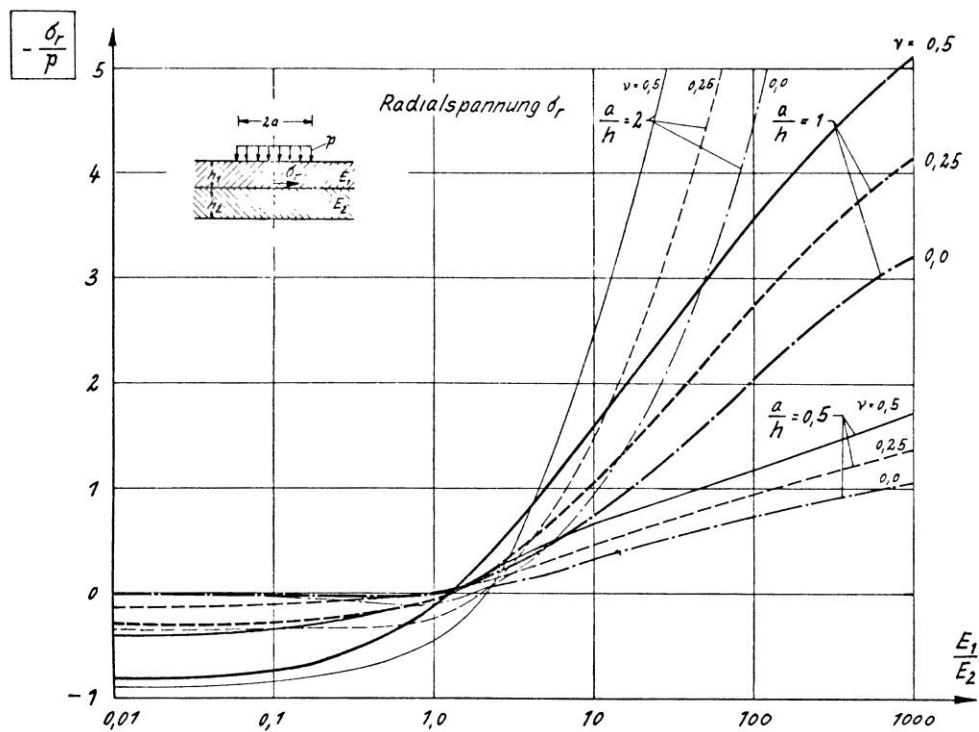


Figure 35a: Influence of Poisson's ratio on the radial stress at the bottom of the top layer.

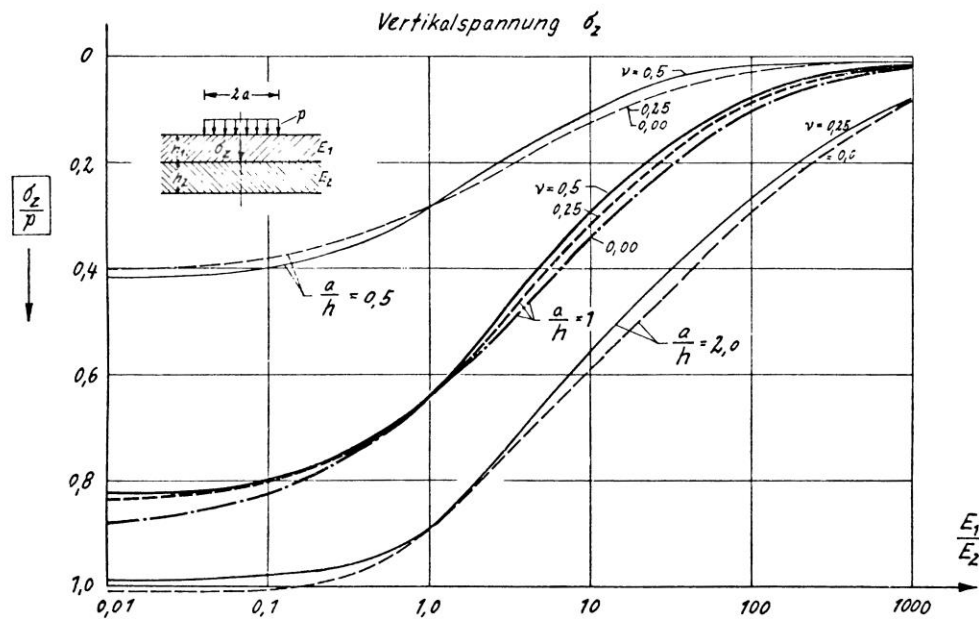


Figure 35b: Influence of Poisson's ratio on the vertical stress at the top of the bottom layer.

By means of the figures available we now can estimate the stresses and strains in two layer pavements. This will be illustrated by means of the following example.

Assume we have a two layer structure consisting of a 150 mm thick asphalt layer on top of a sand subgrade. The elastic modulus of the asphalt layer is 5000 MPa while the modulus of the sand layer is 100 MPa. A 50 kN wheel load is applied on the pavement. The contact pressure 700 kPa which results in a radius of the circular contact area of 150 mm. Poisson's ratio for both the asphalt and the sand layer equals 0.35. We want to know the stresses and strains in the locations indicated below.

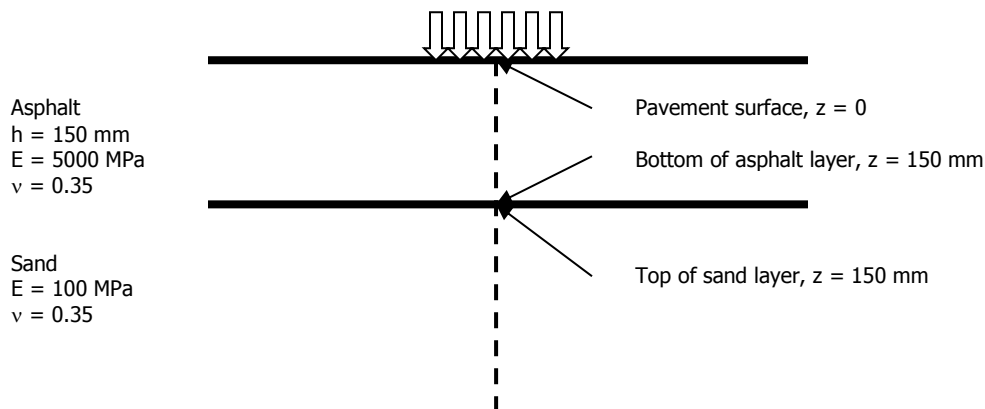


Figure 36: Two layer pavement example problem.

Let us start with the calculation of the stresses and strains at the bottom of the asphalt layer. Since both layers have a Poisson ratio of 0.35, we have to use figure 35 and interpolate between the lines for $v = 0.25$ and $v = 0.5$. Since $E_1 / E_2 = 50$ and $a / h = 1$ we read from the graphs

shown in figure 37 that $-\sigma_r / p = 2.7$ and $\sigma_z / p = 0.15$. Since the contact pressure is a compressive stress and we decided to express compression by means of the minus sign (-), we calculate $\sigma_r = \sigma_t = 1890$ kPa and $\sigma_z = -105$ kPa.

Please note that under the centre of the load centre there is not only a horizontal radial stress σ_r , but also a horizontal tangential stress σ_t (see also figure 26). These stresses are acting perpendicular to each other and because the load centre is in the axis of symmetry, the tangential stress is equal to the radial stress.

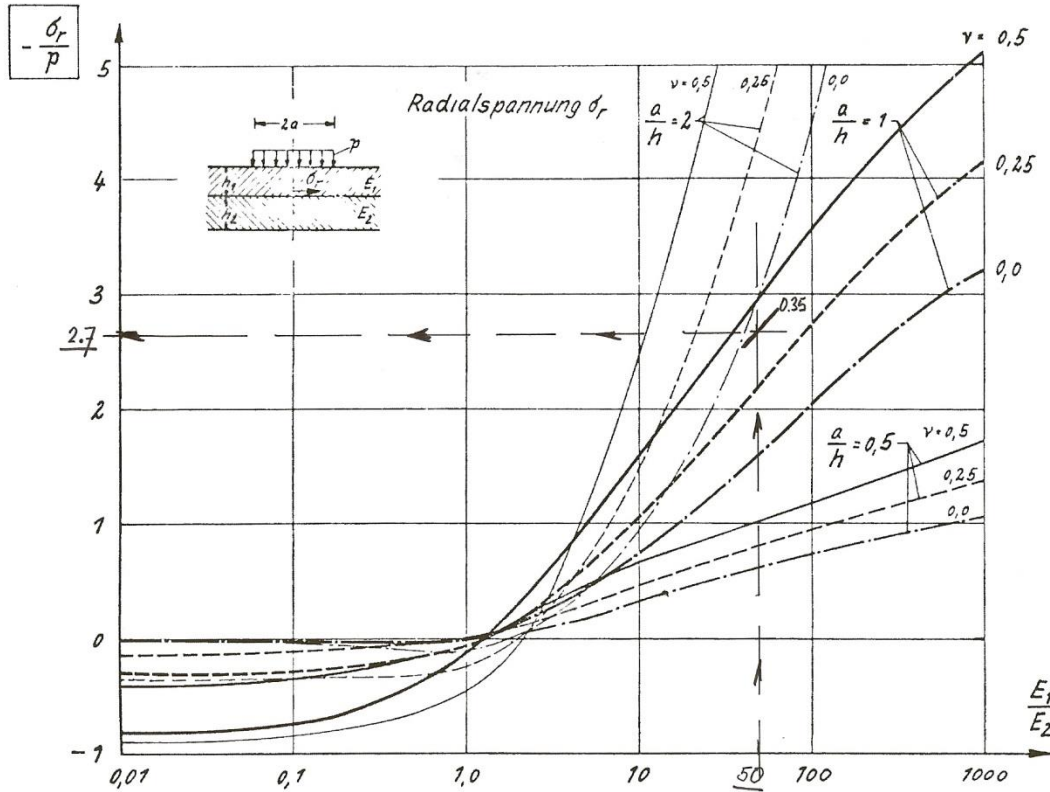


Figure 37a: Estimation of the horizontal stress at the bottom of the asphalt layer.

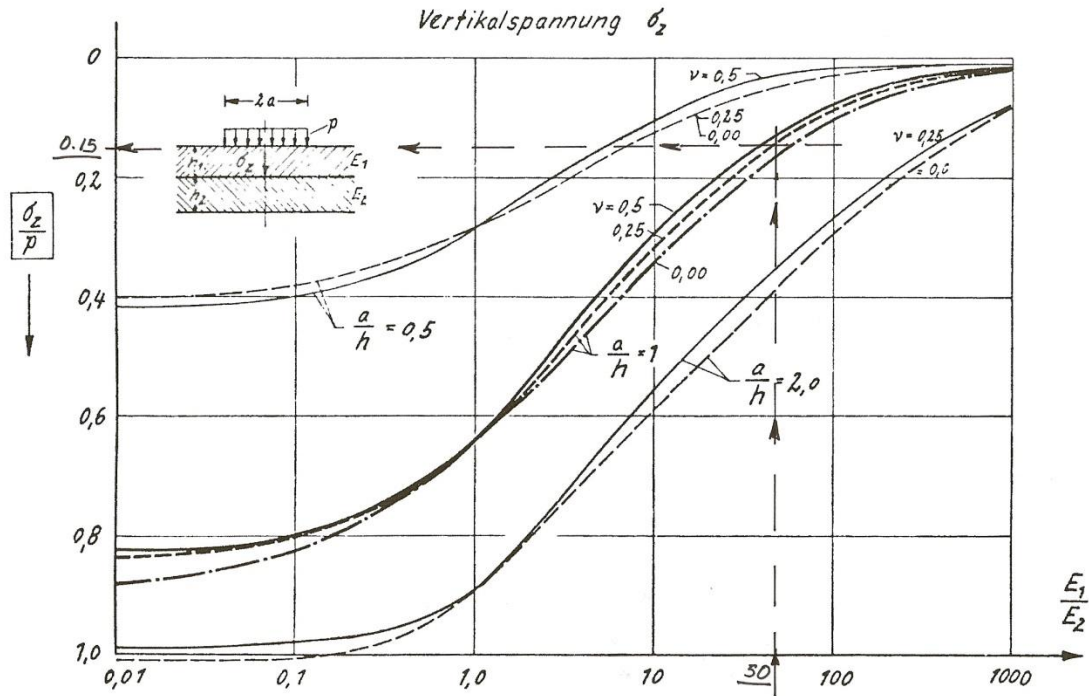


Figure 37b: Estimation of the vertical stress at the top of the subgrade.

The strains are calculated as follows:

$$\varepsilon_r = \varepsilon_t = (\sigma_r - \nu \sigma_t - \nu \sigma_z) / E = (1890 - 0.35 * 1890 - 0.35 * -105) / 5000000 = 2.53 * 10^{-4}$$

$$\varepsilon_z = (\sigma_z - \nu \sigma_r - \nu \sigma_t) / E = (-105 - 0.35 * 1890 - 0.35 * 1890) / 5000000 = -2.86 * 10^{-4}$$

Please note that the units used for the stresses and elastic modulus is kPa. This implies that the value of 5000000 is used for the modulus (originally it was given in MPa).

Let us now consider the stresses and strains at the top of the asphalt layer. We notice that figure 35 is not of help anymore because that figure only gives information about the stresses at the bottom of the asphalt layer. We know however that, for reasons of equilibrium, the vertical stress at the top of the asphalt layer is equal to the contact pressure, so $\sigma_z = -700$ kPa. There are no graphs available to estimate the horizontal stress at the top of the asphalt layer for $\nu = 0.35$, but we can make a reasonable estimate of those stresses. From figure 35 we determine that the tensile stress at the bottom of the asphalt layer is $-2.2 * p$ if $\nu = 0.25$. If we insert that value in figure 33, then we can determine that the radial stress at the top of the pavement equals $2.5 * p$ (see figure 38).

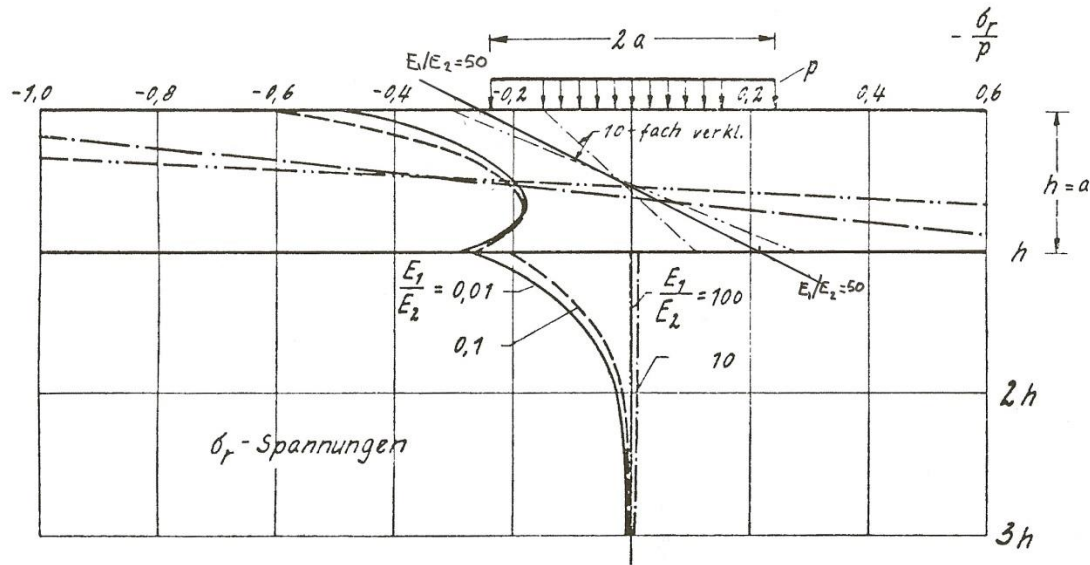


Figure 38: Estimation of the horizontal stress at the top of the asphalt layer.

Going back to figure 35a we notice that the radial stresses at the bottom of the asphalt layer are $2.7 * p / 2.2 * p = 1.23$ times higher when $\nu = 0.35$ instead of 0.25. Therefore we estimated the radial compressive stress at the top of the asphalt layer to be $1.27 * 2.5 * p = -2223 \text{ kPa}$ (the - sign is because p is compressive).

Using these values we calculate:

$$\varepsilon_r = \varepsilon_t = (\sigma_r - \nu\sigma_t - \nu\sigma_z) / E = (-2223 - 0.35 * -2223 - 0.35 * -700) / 5000000 = -2.4 * 10^{-4}$$

$$\varepsilon_z = (\sigma_z - \nu\sigma_r - \nu\sigma_t) / E = (-700 - 0.35 * -2223 - 0.35 * -2223) / 5000000 = 1.71 * 10^{-4}$$

This later value implies that a vertical tensile strain develops at the top of the asphalt layer!

Finally we will discuss the stresses and strains at the top of the subgrade.

Because of equilibrium, the vertical stress at the top of the subgrade is equal to the vertical stress at the bottom of the asphalt layer being -105 kPa. Also in this case we have no graphs available to estimate the horizontal stresses at the top of the subgrade. Nevertheless figure 33a is showing that the radial stress at the top of the subgrade is very small and almost zero for $E_1 / E_2 = 100$. For that reason we assume that at the top of the subgrade $\sigma_r = \sigma_t = 0$.

Using these values we calculate:

$$\varepsilon_r = \varepsilon_t = (\sigma_r - \nu\sigma_t - \nu\sigma_z) / E = (0 - 0 - 0.35 * -105) / 100000 = 3.68 * 10^{-4}$$

$$\varepsilon_z = (\sigma_z - \nu\sigma_r - \nu\sigma_t) / E = (-105 - 0 - 0) / 100000 = -1.05 * 10^{-3}$$

5.4 Stresses in three-layer systems

The calculation of the stresses and strains in three layer systems is based on the same principles as used for two layer systems. It is however much more complicated to derive tables [7] and charts [8] that allow the stresses at various points in the pavement to be estimated and as we will see from the given examples, those charts are not very user friendly.

Figure 39 shows the stresses and locations in a three layer system for which tables and graphs have been developed. Note that a Poisson's ratio of 0.5 was used for all layers.

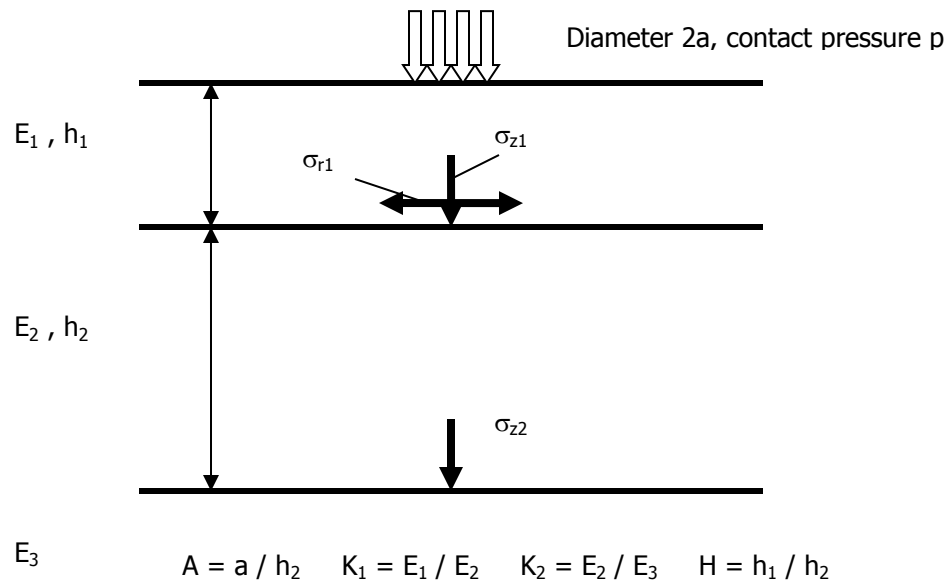


Figure 39: Locations in a three layer system for which tables and graphs to estimate stresses have been developed.

In developing these tables and graphs [7], [8], the following parameters have been used.

$$A = a / h_2; H = h_1 / h_2; K_1 = E_1 / E_2; K_2 = E_2 / E_3$$

Figures 40, 41 and 42 show the graphs for the estimation of resp. σ_{zz1} , σ_{zz2} , and σ_{rr1} for $K_1 = 20$ and $K_2 = 2$.

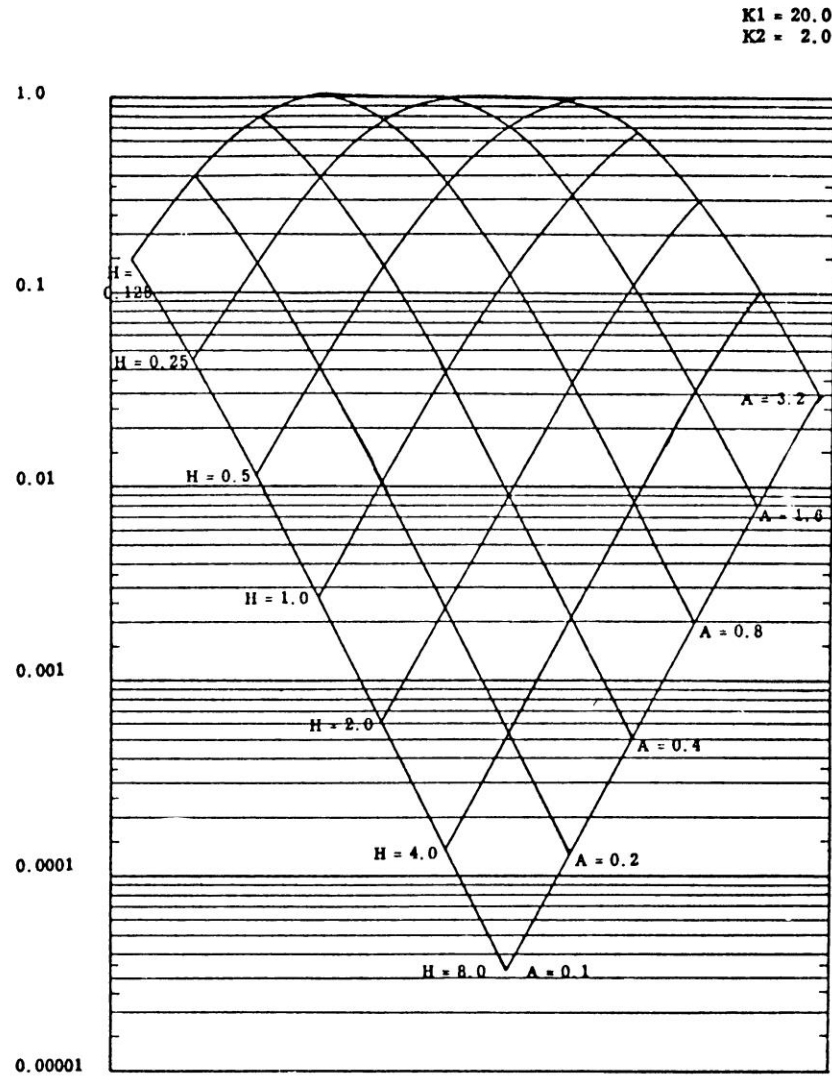


Figure 40: Chart to estimate σ_{zz1} (vertical stress at the top layer – base interface) in a three layer system.

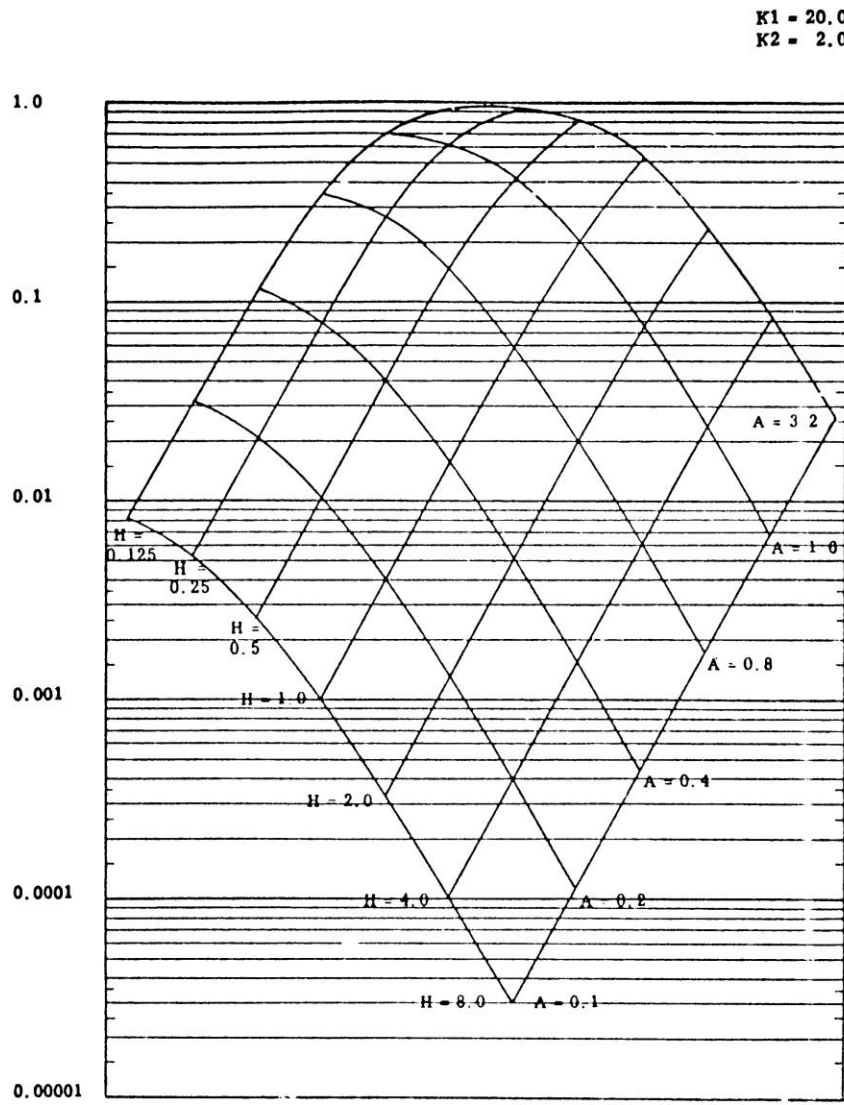


Figure 41: Chart to estimate σ_{zz2} (vertical stress at the base – subgrade interface) in a three layer system.

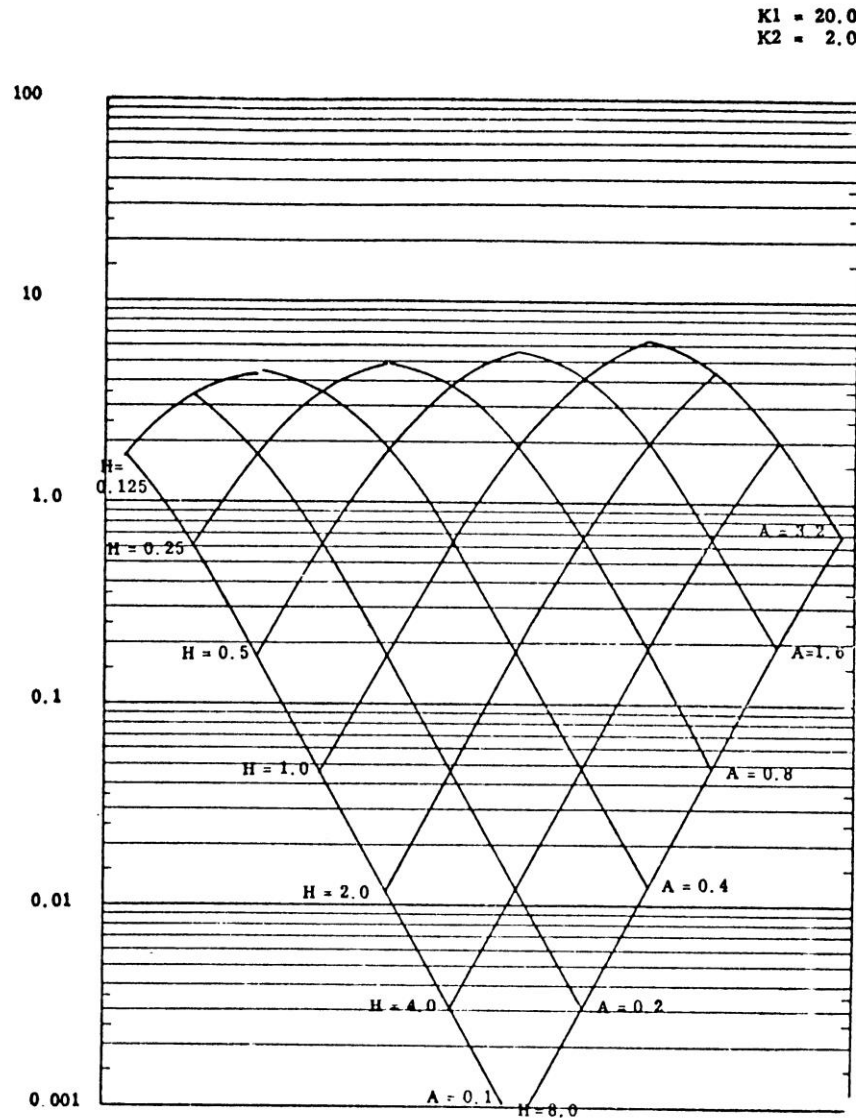


Figure 42: Chart to estimate σ_{rr1} (horizontal stress at the bottom of the top layer at the top layer – base interface) in a three layer system.

The use of the charts is illustrated by means of an example. Let us assume we have a three layer system consisting of 100 mm of asphalt ($E = 6000$ MPa) that is placed on a 300 mm thick base ($E = 300$ MPa) on a subgrade with a stiffness with $E = 150$ MPa. The magnitude of the load is 50 kN and the radius of the loaded area is 150 mm. This implies that the contact pressure is 700 kPa. This input means that $K_1 = 20$, $K_2 = 2$, $A = 2$ and $H = 0.33$. We want to know the horizontal stress at the bottom of the asphalt layer. Using figure 42 in the way as illustrated in figure 43, we derive that the horizontal stress factor is approximately 7 which results in $\sigma_{rr1} = 7 * 700 = 4900$ kPa.

K1 = 20.0
K2 = 2.0

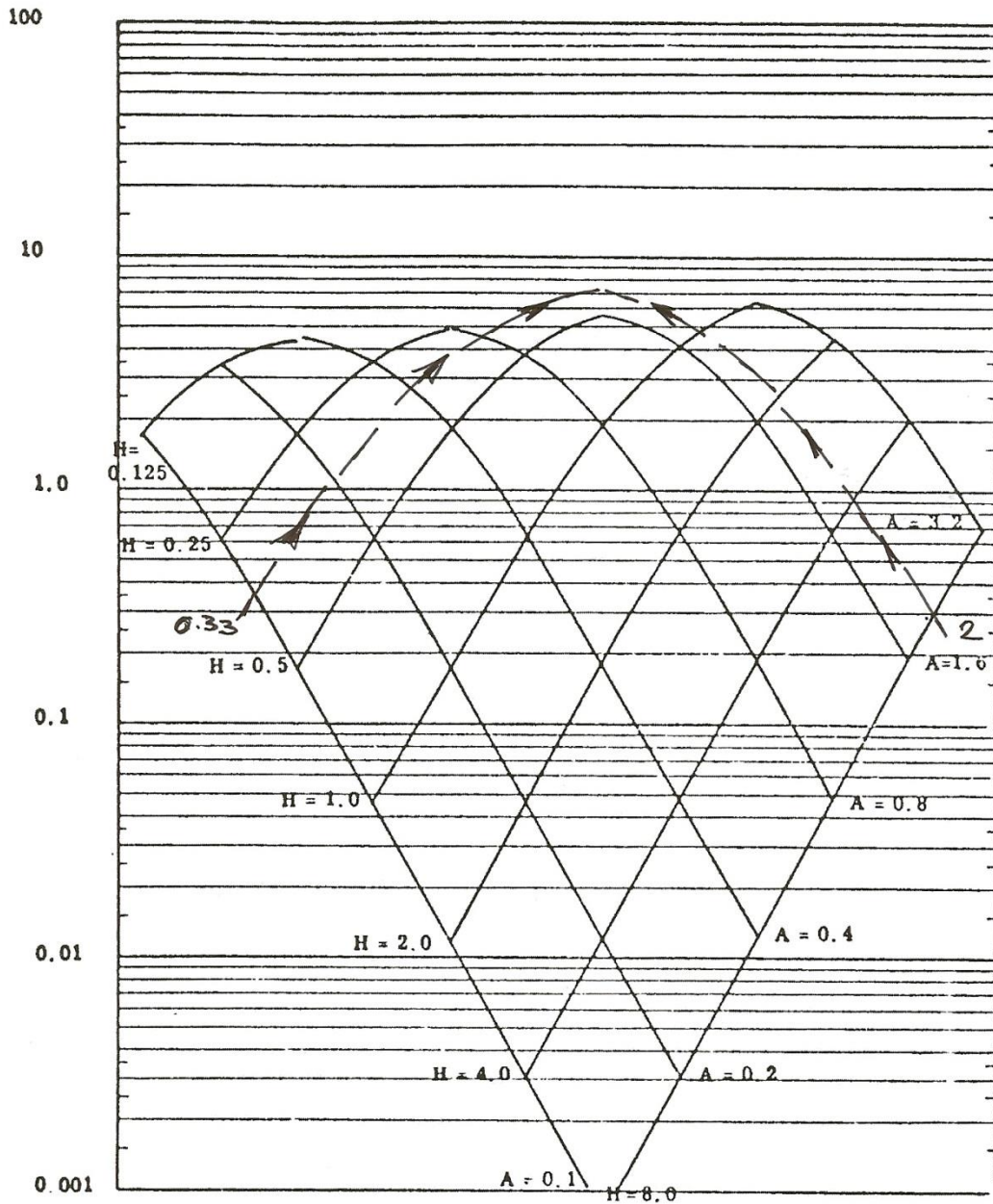


Figure 43: Example of the estimation of σ_{rr1} .

It is obvious that the determination of the stresses in this way is a quite time consuming approach especially since most of the time interpolations have to be made between the different charts. Furthermore the charts are only valid for Poisson's ratio equals 0.5 and most materials have a different value for this parameter. Therefore use of one of the many computer programs that are available nowadays is highly recommended. It should however been noted that in [15] a

graph has been presented that allows the tensile strain at the bottom of the asphalt top layer in a three layer system to be estimated. This chart is shown in figure 44.

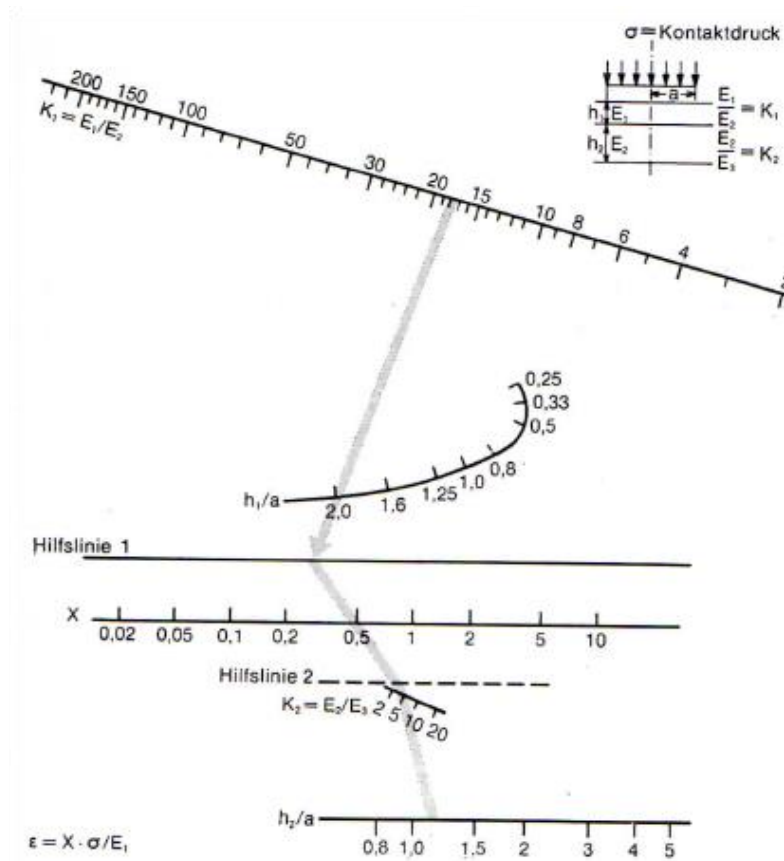


Figure 44: Chart to estimate the tensile strain at the bottom of the asphalt layer in a three layer system [15].

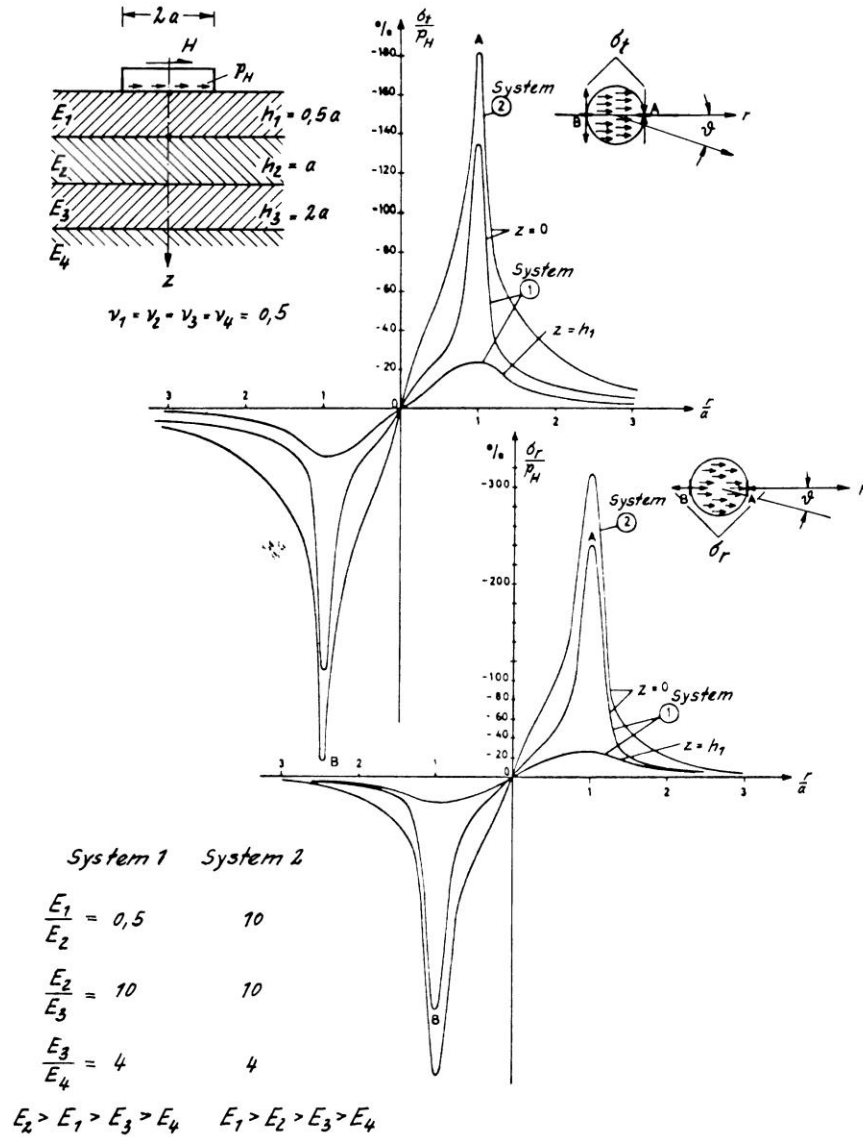
The chart is used in the following way. From $K_1 = E_1 / E_2$ and h_1 / a a point on the first "Hilfslinie" is determined. From $K_2 = E_2 / E_3$ and h_2 / a a point on the second "Hilfslinie" is determined. Then a line is drawn connecting these two points and the value of "x" is determined. The tensile strain at the bottom of the asphalt layer equals $\varepsilon = x \cdot \sigma / E_1$

5.5 Stresses due to horizontal loads

It is obvious that in reality not only vertical stresses are applied on the pavement surface. Also horizontal shear stresses are present, acting in the longitudinal and transverse direction. These shear stresses are due to traction forces, braking, cornering etc. They occur under free rolling as well as driven tires. As we will see in the next chapter, the real stress conditions in the contact area are indeed very complex. Several researchers have studied the effect of such shear forces and early work on this topic is done by Verstraeten [16] and Wardle and Gerrard [17]. Given the limited computational power in those days, they had to apply rigorous simplifications of the real stress conditions. Nevertheless, a good idea of the effect of these shear stresses can be obtained from their work. Figures 45, 46 and 47 are taken from the work presented by Verstraeten.

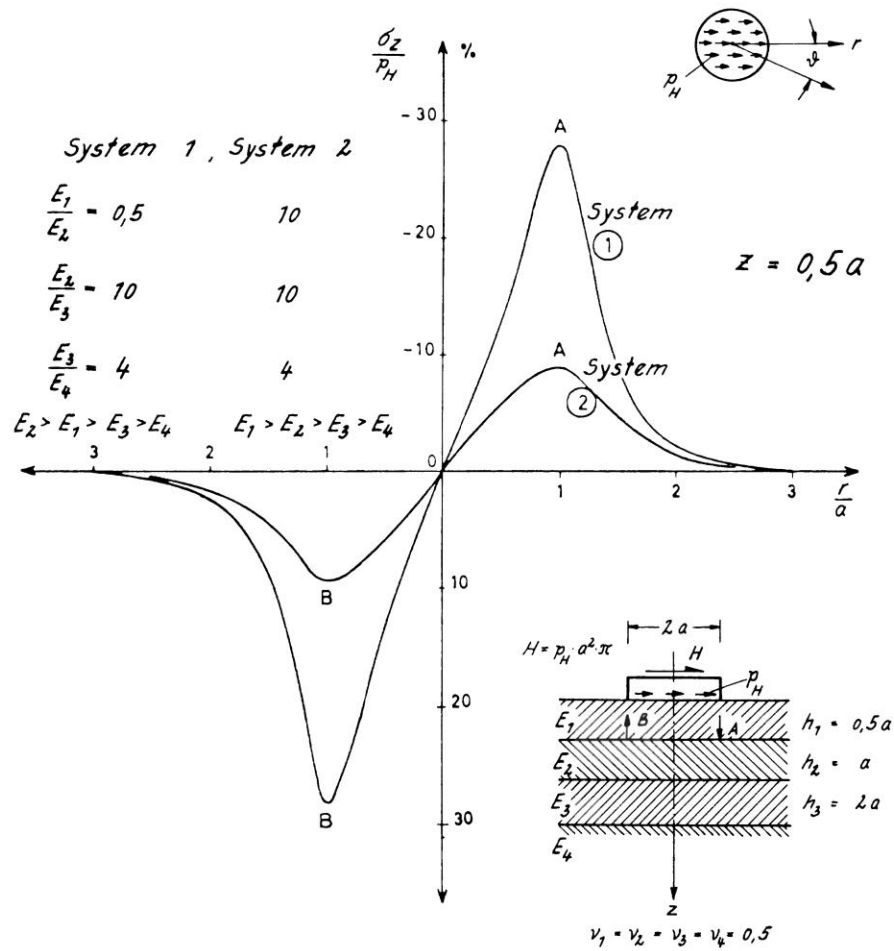
The figures show that depending on the applied shear force, significant radial and tangential stresses can develop at the pavement surface. Furthermore the figures show that the ratio of

stiffness of the top layer over the stiffness of the second layer has a large effect on the magnitude of these stresses.



Die Spannungen sind für $\varphi = 0, \pi$ dargestellt.
Für andere Werte von φ müssen diese mit $\cos \varphi$ multipliziert werden

Figure 45: Radial and tangential stresses in a pavement system due to a uniformly distributed, unidirectional, shear load.



Die Spannungen sind für $\vartheta = 0, \pi$ dargestellt. Für andere Werte von ϑ müssen diese mit $\cos \vartheta$ multipliziert werden

Figure 46: Vertical stresses in a pavement system due to a uniformly distributed, unidirectional shear load.

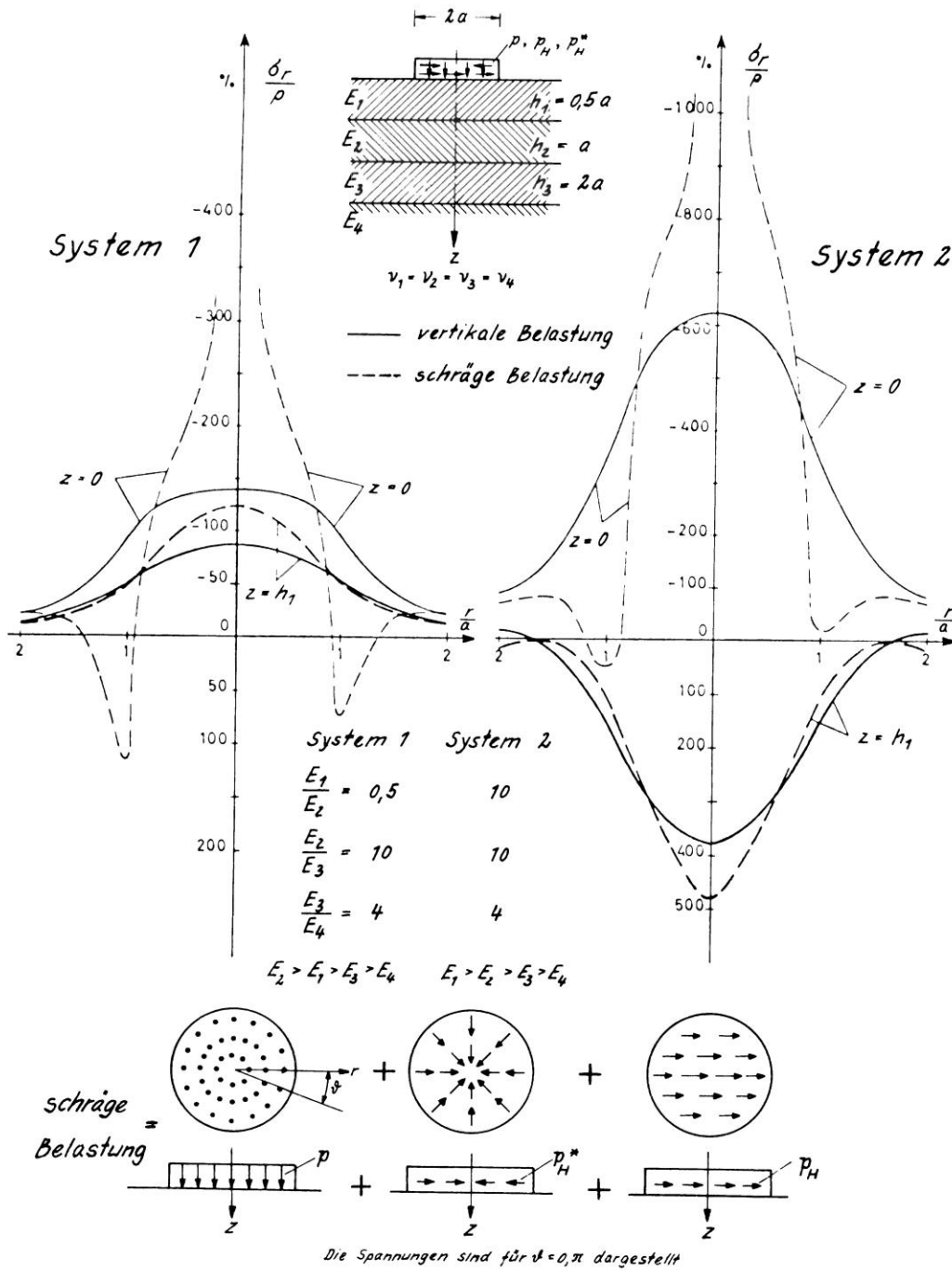


Figure 47: Radial stresses in a pavement system due to a combination of vertical stresses and uniformly distributed, unidirectional and multidirectional, shear forces.
Note: vertikaler Belastung = vertical load, schiefe Belastung = shear load

5.6 Stresses in multilayer systems, available computer programs

As has been mentioned in the previous section, it is strongly recommended to use a multilayer computer program for the analysis of stresses and strains in three layer systems. This becomes a necessity in case the number of layers is 4 or more. Charts for the assessment of stresses in a four layer systems even don't exist.

Many computer programs have been developed in time and it is almost impossible to give a complete picture of the available programs. Well known programs are BISAR, KENLAYER, CIRCLY, MePADS and WESLEA. BISAR and WESLEA only allow linear elastic materials to be taken into account. CIRCLY on the other hand allows taking into account anisotropic behavior of materials. Many of these programs have been incorporated in design systems such as the Shell Pavement Design System, OIA (developed in the Netherlands), MePADS (developed in South Africa). KENLAYER is an interesting system because it allows taking into account the stress dependent behaviour of unbound granular materials and soils and it allows the asphalt concrete to be modelled as a linear visco-elastic material. RUBICON, a program developed in South Africa, is a finite element based program that also allows to take into account the stress dependent behavior of granular materials. Furthermore this program allows probabilistic analyses to be made. A quite advanced program is 3D-Move which allows asphalt concrete to be modelled as a linear elastic and linear visco-elastic material. It furthermore allows complex contact stress distributions to be taken into account as well as the effect of dynamic wheel loads. It also allows performance predictions to be made in terms of development of the amount of cracking and permanent deformation in relation to the applied number of load repetitions. Another advanced pavement design program is the one developed for the American State Highway and Transportation Officials (AASHTO). This program allows predictions to be made on cracking, rutting and roughness progression as a function of the number of load repetitions and climate. Further details will be given in chapter 16 "Design Systems".

Many of these programs can be found on the internet and can be retrieved for free (e.g. the design programs developed for the Federal Aviation Agency FAA in the USA) while other software packages have to be purchased. It is beyond the scope of these lecture notes to discuss all the available programs in detail. In this part of the lecture notes we only discuss the output that is generated by the computer program BISAR developed by SHELL which calculates the stresses and strains in the pavement system due to traffic loads. These principles should be well understood before one is going to use the advanced design systems.

It is generally accepted that the BISAR program can be taken as the reference to which all other programs can be compared. This is because of the high mathematical stability of the BISAR program. Quite some programs have minor flaws of which the user should be aware before using them. To check whether these flaws exist the stresses, strains and displacements have to be calculated in a number of points of the pavement structure (see figure 48).

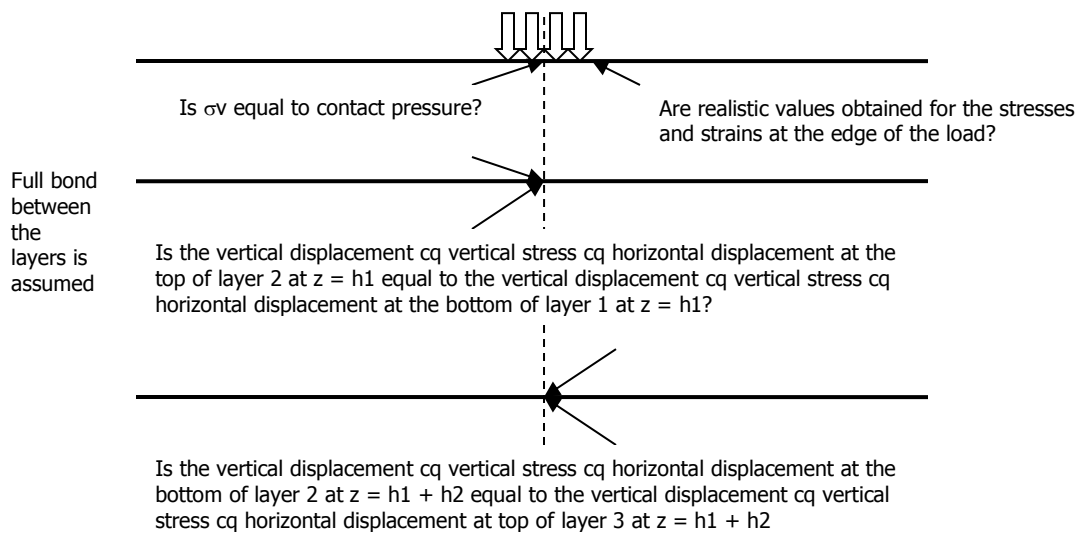


Figure 48: Locations in the pavement where consistency checks can be made.

Some programs do not fulfill the requirements set for the interface between layers 1 and 2 and/or the interfaces between layers 2 and 3. These programs often also not fulfill the equilibrium requirement at the pavement surface under the centre of the load. Other programs generate unrealistic results at the edge of the load. The problems at the interfaces and under the centre of the load at the pavement surface can easily be overcome by not requiring output at those interfaces but at locations that are e.g. 1 mm above or below the interface.

Almost all programs generate comparable results if stresses and strains are required at other locations in the pavement.

Although most of the problems mentioned above can be overcome quite easily, one must be aware of the fact that some programs have difficulties in generating realistic results for pavements with a thin asphalt layer that has a low modulus on top on a thick stiff (high modulus) base layer (so if $h_1 / h_2 < 1$ and $E_1 / E_2 < 1$).

It should be noted that the BISAR program passes all these requirements.

Let us now return to the output that is generated by these computer programs and let us explain the output that is generated by BISAR for two example problems.

The two problems that are analyzed are schematically shown in figure 49.

In the first example, only the vertical load is applied while in the second example the vertical and horizontal load is applied. The horizontal load acts in the x-direction and simulates a braking force. The stresses and strains are calculated for the locations which are defined with their x, y and z coordinates. The locations for which the stresses and strains are calculated are shown in table 5.

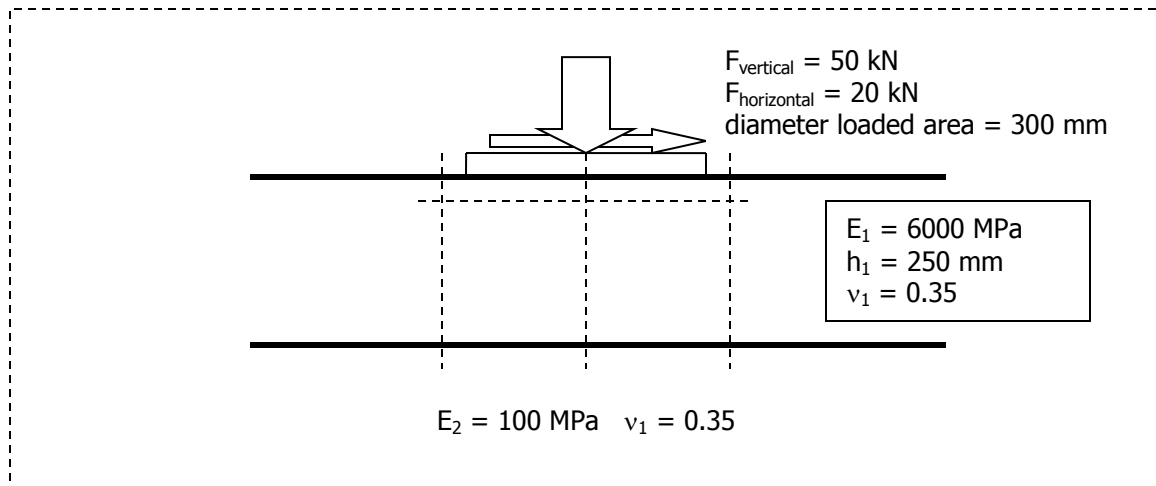


Figure 49a: Example problem.

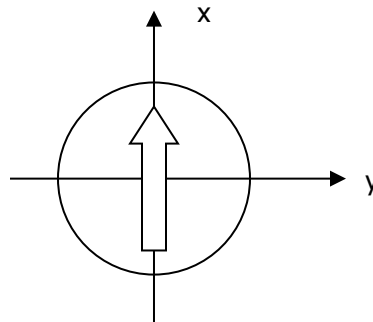


Figure 49b: Coordinate system and direction of the shear force as used in the example problem.

Load	Sheet	Layer	X [mm]	y [mm]	z [mm]
Vertical force only	2	1	0	0	0
	3	1	152	0	0
	4	1	152	0	10
	5	1	0	0	250
	6	2	0	0	250
Vertical and horizontal force	8	1	-152	0	0
	9	1	0	0	0
	10	1	152	0	0
	11	1	-152	0	10
	12	1	0	0	10
	13	1	152	0	10
	14	1	0	0	250
	15	2	0	0	250

Table 5: Locations where results are obtained.

Note: The sheet number refers to the handwritten numbers written on the output pages given in figure 50.

Please note that at the pavement surface and at a depth of 10 mm, the results are requested just outside the loaded area and at the load center. This is done to determine the effect of the shear forces. In figure 50 all the calculation results are given while the main results are summarized in table 6.

The sheets with the calculation results are pretty much self-explaining. The coordinates of the location at which the stresses and strains are requested are given in the top of the page. Then detailed information is given on the normal stresses and strains acting in the XX, YY and ZZ direction as well as on the shear stresses and strains in the YZ, XZ, and XY direction.

All this information is summarized in terms of principal stresses and strains as well as the directions in which these principal stresses and strains are acting (defined as "x comp., y comp., z comp."). The "minimax" principal stress and strain are usually called σ_2 and ε_2 . In table 6 a summary is given of these principal stresses and strains.

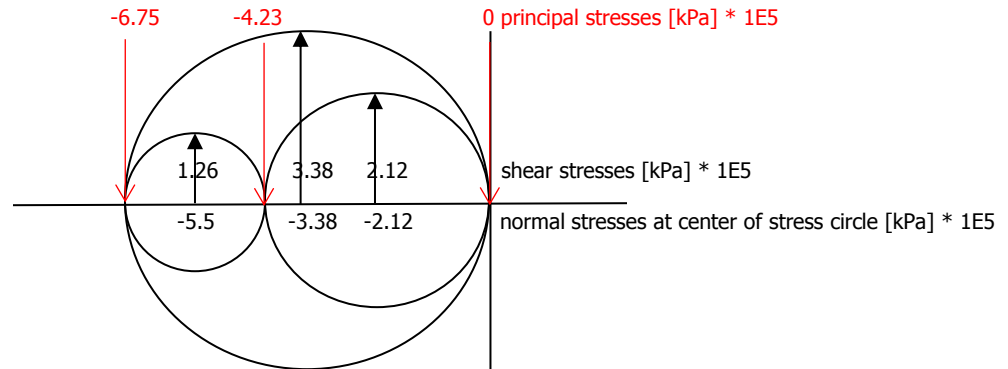
Furthermore three rows are given with the maximum, minimax, and minimum normal stress; these are the principal stresses. Then there are three rows which show the maximum, minimax and minimum stress together with shear stresses. These combinations of normal and shear stresses indicate the center of each of the three stress circles. As an example the stress circles derived from figure 50c are shown below.

Maximum stress $\sigma_1 = 0$, Minimax $\sigma_2 = -4.23 \text{ E5}$, Minimum $\sigma_3 = -6.76 \text{ E5}$ [σ], [τ] = [Pa]

Center of the stress circles with the radius (= shear stress)

Max: $\sigma = -3.38 \text{ E5}$ and $\tau = 3.38 \text{ E5}$, Minimax: $\sigma = -2.12 \text{ E5}$ and $\tau = 2.12 \text{ E5}$,

Minimum: $\sigma = -5.50 \text{ E5}$ and $\tau = 1.26 \text{ E5}$



Sheet nr.	σ_1 [Pa]	σ_2 [Pa]	σ_3 [Pa]	ε_1	ε_2	ε_3
2	-7.074E+05	-1.251E+06	-1.251E-6	2.800E-05	-9.421E-05	-9.241E-05
3	0	-4.231E+05	-6.758E+05	6.410E-05	-3.110E-05	-8.975E-05
4	-1.630E+05	-7.555E+05	-8.132E+05	6.434E-05	-6.897E-05	-8.195E-05
5	9.046E+05	9.046E+05	-3.547E+04	1.001E-04	1.001E-04	-1.115E-04
6	-3.705E+03	-3.705E+03	-3.547E+04	1.001E-04	1.001E-04	-3.288E-04
8	4.618E+05	0	-4.179E+05	1.013E-04	-2.565E-06	-9.658E-05
9	-5.867E+05	-1.251E+06	1.371E+06	5.514E-05	-9.421E-05	-1.213E-04
10	0	-9.337E+05	-1.308E+06	1.308E-04	-7.932E-05	-1.635E-04
11	-9.085E+04	-2.962E+05	-6.034E+05	3.733E-05	-8.874E-06	-7.798E-05
12	-5.887E+05	-1.122E+06	-1.239E+06	3.985E-05	-8.034E-05	-1.067E-04
13	-2.154E+05	-9.076E+05	-1.350E+06	9.578E-05	-5.996E-05	-1.595E-04
14	9.046E+05	9.046E+05	-3.547E+04	1.001E-04	1.001E-04	-1.115E-04
15	-3.694E+03	-3.705E+03	-3.548E+04	1.002E-04	1.002E-04	-3.289E-04

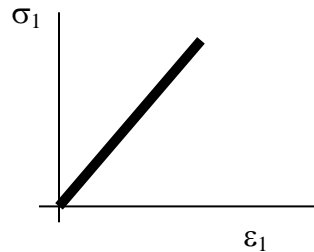
Table 6: Results of the example problems in terms of principal stresses and strains.

Furthermore the output shows the strain energy and the strain energy of distortion. The strain energy is composed of two distinct forms being volume changes and distortion (change in shape). Normal strains cause a change in volume while shear strains cause distortion. The total strain energy (U_{total}) is the sum of distortion energy ($U_{\text{distortion}}$) and volume energy (U_{volume}).

$$U_{\text{total}} = U_{\text{distortion}} + U_{\text{volume}}$$

For uni-axial loading, the strain energy per unit volume is the area under the stress – strain curve and equals

$$U_{\text{total}} = \sigma_1 \varepsilon_1 / 2$$



For a general 3D situation we calculate U_{total} using

$$U_{\text{total}} = (\sigma_1 \varepsilon_1 + \sigma_2 \varepsilon_2 + \sigma_3 \varepsilon_3) / 2$$

Since $\varepsilon_1 = [\sigma_1 - \mu (\sigma_2 + \sigma_3)] / E$ etc. U_{total} becomes

$$U_{\text{total}} = \{1/2E\} \{\sigma_1^2 + \sigma_2^2 + \sigma_3^2 - 2\mu (\sigma_2 \sigma_3 + \sigma_1 \sigma_3 + \sigma_1 \sigma_2)\}$$

We know that the first stress invariant (I_1), also called the hydrostatic stress (σ_{hyd}), is calculated using:

$$\sigma_{\text{hyd}} = (\sigma_1 + \sigma_2 + \sigma_3) / 3$$

If we only would have hydrostatic stresses, then we would only have volume change and U_{total} would be equal to U_{volume} . In that case

$$U_{\text{volume}} = \{3(1 - 2\mu) / 2E\} \sigma_{\text{hyd}}^2 = \{(1 - 2\mu) / 6E\} \{\sigma_1^2 + \sigma_2^2 + \sigma_3^2 + 2\sigma_2 \sigma_3 + 2\sigma_1 \sigma_2 + 2\sigma_1 \sigma_3\}$$

Since $U_{\text{distortion}} = U_{\text{total}} - U_{\text{volume}}$ we find

$$U_{\text{distortion}} = \{(1 + \mu) / 3E\} [(\sigma_1 - \sigma_2)^2 + (\sigma_2 - \sigma_3)^2 + (\sigma_3 - \sigma_1)^2] / 2]$$

As we will see later on $U_{\text{distortion}}$ can be used for fatigue analyses.

On sheets nr 1 and nr 7 of figure 50, we recognize the input. Please note on sheet 7 that the angle of the shear load is taken from the x-axis. Since the horizontal load is acting in the positive x-direction the shear direction equals 0° (the angle equals 180° if the shear load is acting in the negative x-direction). If the shear force was acting in the positive y-direction, the shear direction had to be 90° .



BISAR 3.0 - Detailed Report
(untitled)
System 1: (untitled)

Layer Number	Thickness (m)	Young's Modulus (Pa)	Poisson's Ratio	Shear Spring Compliance (m ² /N)
1	0,250	6,000E+09	0,35	0,000E+00
2		1,000E+08	0,35	

1.

Load Number	Normal Stress (Pa)	Shear Stress (Pa)	Radius of Loaded Area (m)	X (m)	Load - Position Y (m)	Shear Direction (°)
1	7,074E+05	0,000E+00	1,500E-01	0,000E+00	0,000E+00	0,000E+00

Figure 50a: Input for BISAR calculation; vertical load only.



BISAR 3.0 - Detailed Report
(untitled)
System 1: (untitled)

Position Number: 1 Layer Number: 1 X Coord (m): 0,000E+00 Y Coord (m): 0,000E+00 Z Coord (m): 0,000E+00

Load No.	Distance to Load Axis (m)	Theta (°)	Displacements (m)			Stresses (Pa)						Strains					
			Radial	Tangential	Vertical	Radial	Tangential	Vertical	Rad/Tang.	Rad/Vert.	Tang/Vert.	Radial	Tangential	Vertical	Rad/Tang.	Rad/Vert.	Tang/Vert.
1	0,000E+00	0,000E+00	0,000E+00	0,000E+00	3,092E-04	-1,251E+06	-1,251E+06	-7,074E+05	0,000E+00	0,000E+00	0,000E+00	-9,421E-05	-9,421E-05	2,800E-05	0,000E+00	0,000E+00	0,000E+00

Total Stresses (Pa) **XX:** -1,251E+06 **YY:** -1,251E+06 **ZZ:** -7,074E+05 **YZ:** 0,000E+00 **XZ:** 0,000E+00 **XY:** 0,000E+00
Total Strains **XX:** -9,421E-05 **YY:** -9,421E-05 **ZZ:** 2,800E-05 **YZ:** 0,000E+00 **XZ:** 0,000E+00 **XY:** 0,000E+00
Total Displacements (m) **UX:** 0,000E+00 **UY:** 0,000E+00 **UZ:** 3,092E-04

Principal Values and Directions of Total Stresses and Strains

	Normal		Shear		X	Y	Z
	Stress (Pa)	Strain	Stress (Pa)	Strain	Comp.	Comp.	Comp.
Maximum:	-7,074E+05	2,800E-05			0,0000	0,0000	1,0000
Minimum:	-1,251E+06	-9,421E-05			1,0000	0,0000	0,0000
Maximum:	-1,251E+06	-9,421E-05	2,716E+05	6,110E-05	0,0000	-0,7071	0,7071
Minimum:	-9,789E+05	2,716E+05	6,110E-05	0,0000	0,7071	0,0000	0,7071
Maximum:	-9,789E+05	2,716E+05	6,110E-05	0,0000	-0,7071	0,0000	0,7071
Minimum:	-1,251E+06	-9,421E-05	0,000E+00	0,000E+00	0,7071	-0,7071	0,0000

Strain Energy (J): 1,079E+02 **Strain Energy of Distortion (J):** 2,213E+01

Figure 50b: Output of BISAR calculation.



BISAR 3.0 - Detailed Report

(untitled)

System 1: (untitled)

Position Number: 2 Layer Number: 1 X Coord (m): 1,520E-01 Y Coord (m): 0,000E+00 Z Coord (m): 0,000E+00

Load No.	Distance to Load Axis (m)	Theta (°)	Displacements (m)			Stresses (Pa)						Strains					
			Radial	Tangential	Vertical	Radial	Tangential	Vertical	Rad/Tang.	Rad/Vert.	Tang/Vert.	Radial	Tangential	Vertical	Rad/Tang.	Rad/Vert.	Tang/Vert.
1	1,520E-01	0,000E+00	-1,337E-05	0,000E+00	2,892E-04	-4,231E-05	-6,758E-05	0,000E+00	0,000E+00	0,000E+00	0,000E+00	-3,110E-05	-8,795E-05	6,410E-05	0,000E+00	0,000E+00	0,000E+00

Total Stresses (Pa) XX: -4,231E+05 YY: -6,758E+05 ZZ: 0,000E+00 YZ: 0,000E+00 XY: 0,000E+00
Total Strains XX: -3,110E-05 YY: -8,795E-05 ZZ: 6,410E-05 YZ: 0,000E+00 XY: 0,000E+00
Total Displacements (m) UX: -1,337E-05 UY: 0,000E+00 UZ: 2,892E-04

Principal Values and Directions of Total Stresses and Strains

	Normal Stress (Pa)		Normal Strain		Shear Stress (Pa)		Shear Strain		X Comp.		Y Comp.		Z Comp.	
	Maximum:	0,000E+00	6,410E-05	6,410E-05	Maximum:	0,0000	1,0000	1,0000	0,0000	0,0000	0,0000	0,0000	0,0000	0,0000
	Minimum:	-4,231E+05	-3,110E-05	-3,110E-05										
	Minimum:	-6,758E+05	-8,795E-05	-8,795E-05										
	Maximum:	-3,379E+05	3,379E+05	7,603E-05										
	Minimum:	-2,116E+05	2,116E+05	4,760E-05										
	Minimum:	-5,495E+05	1,264E+05	2,843E-05										

Strain Energy (J): 3,630E+01 Strain Energy of Distortion (J): 2,623E+01

3.1

Figure 50c: Output of BISAR calculation (continued).



BISAR 3.0 - Detailed Report
(untitled)
System 1: (untitled)

Position Number: 3			Layer Number: 1			X Coord (m): 1,520E-01			Y Coord (m): 0,000E+00			Z Coord (m): 1,000E-02		
Load No.	Distance to Load Axis (m)	Theta (°)	Displacements (m)			Stresses (Pa)			Strains			Stresses (Pa)		
			Radial	Tangential	Vertical	Radial	Tangential	Vertical	Rad./Tang.	Rad./Vert.	Tang./Vert.	Radial	Tangential	Vertical
1	1.520E-01	0.000E+00	-1.048E-05	0.000E+00	2.898E-04	-7.182E+05	-7.555E+05	-2.580E+05	-2.296E+05	0.000E+00	0.000E+00	-6.058E-05	-6.897E-05	4.297E-05

Total Stresses (Pa) XX: -7,182E+05 YY: -7,555E+05 ZZ: -2,580E+05 YZ: 0,000E+00 XZ: -2,296E+05 XY: 0,000E+00
Total Strains XX: -6,058E-05 YY: -6,897E-05 ZZ: 4,297E-05 YZ: 0,000E+00 XZ: -5,167E-05 XY: 0,000E+00
Total Displacements (m) UX: -1,048E-05 UY: 0,000E+00 UZ: 2,898E-04

Principal Values and Directions of Total Stresses and Strains

	Normal		Shear		X	Y	Z
	Stress (Pa)	Strain	Stress (Pa)	Strain	Comp.	Comp.	Comp.
Maximum:	-1,630E+05	6,434E-05			-0,3822	0,0000	0,9241
Minimum:	-7,555E-05	-6,897E-05			0,0000	1,0000	0,0000
Maximum:	-8,132E+05	-8,195E-05	3,251E+05	7,315E-05	0,9241	0,0000	0,3822
Minimum:	-4,881E+05				-0,9237	0,0000	0,3832
Maximum:	-4,592E+05	2,962E+05	6,666E-05	-0,2703	0,3832	0,9237	0,6534
Minimum:	-7,843E+05	2,885E+04	6,490E-06	-0,6534	-0,2703	0,7071	0,6534

Strain Energy (J): 5,413E+01 Strain Energy of Distortion (J): 2,914E-01

4.

Figure 50d: Output of BISAR calculation (continued).



BISAR 3.0 - Detailed Report
(untitled)
System 1: (untitled)

Position Number: 4		Layer Number: 1		X Coord (m): 0,000E+00		Y Coord (m): 0,000E+00		Z Coord (m): 2,500E-01		
Load Distance to No. Load Axis (m)	Theta (°)	Displacements (m)			Stresses (Pa)			Strains		
		Radial	Tangential	Vertical	Radial	Tangential	Vertical	Rad/Tang.	Rad/Vert.	Tang/Vert.
1	0,000E+00	0,000E+00	0,000E+00	2,957E-04	9,046E+05	9,046E+05	-3,547E+04	0,000E+00	0,000E+00	0,000E+00

Total Stresses (Pa) XX: 9,046E+05 YY: 9,046E+05 ZZ: -3,547E+04 YZ: 0,000E+00 XZ: 0,000E+00 XY: 0,000E+00
Total Strains XX: 1,001E-04 YY: 1,001E-04 ZZ: -1,115E-04 YZ: 0,000E+00 XZ: 0,000E+00 XY: 0,000E+00
Total Displacements (m) UX: 0,000E+00 UY: 0,000E+00 UZ: 2,957E-04

Principal Values and Directions of Total Stresses and Strains

	Normal		Normal		Shear		Shear		X		Y		Z	
	Stress (Pa)	Strain	Stress (Pa)	Strain	Stress (Pa)	Strain	Stress (Pa)	Strain	Comp.	Dir.	Comp.	Dir.	Comp.	Dir.
Maximum:	9,046E+05	1,001E-04	9,046E+05	1,001E-04					1,0000		0,0000		0,0000	
Minimum:	9,046E+05	1,001E-04	9,046E+05	1,001E-04					0,0000		0,0000		0,0000	
Maximum:	-3,547E+04	-1,115E-04	-3,547E+04	-1,115E-04					0,0000		0,0000		0,0000	
Minimum:	-3,547E+04	-1,115E-04	-3,547E+04	-1,115E-04					0,0000		0,0000		0,0000	
Maximum:	4,346E+05		4,346E+05						0,7071		0,0000		0,7071	
Minimum:	4,346E+05		4,346E+05						0,7071		0,0000		0,7071	
Maximum:	4,346E+05		4,346E+05						0,7071		0,0000		0,7071	
Minimum:	4,346E+05		4,346E+05						0,7071		0,0000		0,7071	
Maximum:	9,046E+05		9,046E+05						0,7071		0,0000		0,7071	
Minimum:	9,046E+05		9,046E+05						0,7071		0,0000		0,7071	

Strain Energy (J): 9,251E+01 Strain Energy of Distortion (J): 6,629E+01

5.

Figure 50e: Output of BISAR calculation (continued).



BISAR 3.0 - Detailed Report

(untitled)

System 1: (untitled)

Position Number: 5 Layer Number: 2 X Coord (m): 0,000E+00 Y Coord (m): 0,000E+00 Z Coord (m): 2,500E-01

Load No.	Distance to Load Axis (m)	Theta (°)	Displacements (m)			Stresses (Pa)						Strains					
			Radial	Tangential	Vertical	Radial	Tangential	Vertical	Rad/Tang.	Rad/Vert.	Tang/Vert.	Radial	Tangential	Vertical	Rad/Tang.	Rad/Vert.	Tang/Vert.
1	0.000E+00	0.000E+00	0.000E+00	0.000E+00	2.957E-04	-3.705E+03	-3.705E+03	-3.547E+04	0.000E+00	0.000E+00	0.000E+00	1.001E-04	1.001E-04	-3.288E-04	0.000E+00	0.000E+00	0.000E+00

Total Stresses (Pa) XX: -3.705E+03 YY: -3.705E+03 ZZ: -3.547E+04 YZ: 0.000E+00 XZ: 0.000E+00 XY: 0.000E+00
Total Strains XX: 1.001E-04 YY: 1.001E-04 ZZ: -3.288E-04 YZ: 0.000E+00 XZ: 0.000E+00 XY: 0.000E+00
Total Displacements (m) UX: 0.000E+00 UY: 0.000E+00 UZ: 2.957E-04

Principal Values and Directions of Total Stresses and Strains

	Normal		Shear		X	Y	Z
	Stress (Pa)	Strain	Stress (Pa)	Strain	Comp.	Comp.	Comp.
Maximum:	-3.705E+03	1.001E-04			0.0000	1.0000	0.0000
Minimum:	-3.705E+03	1.001E-04			1.0000	0.0000	0.0000
Maximum:	-3.547E+04	-3.288E-04	1.588E+04	2.144E-04	0.0000	0.0000	1.0000
Minimum:	-1.959E+04		2.144E-04	0.7071	0.0000	0.7071	-0.7071
Maximum:	-1.959E+04		1.588E+04	2.144E-04	0.7071	0.0000	-0.7071
Minimum:	-1.959E+04		3.223E-02	4.329E-10	0.7071	0.0000	0.7071
Maximum:	-3.705E+03				-0.7071	0.7071	0.0000
Minimum:	-3.705E+03				0.7071	0.7071	0.0000

Strain Energy (J): 5.461E+00 Strain Energy of Distortion (J): 4.541E+00

Figure 50f: Output of BISAR calculation (continued).



BISAR 3.0 - Detailed Report

(untitled)

System 1: (untitled)

Layer Number	Thickness (m)	Young's Modulus (Pa)	Poisson's Ratio	Shear Spring Compliance (m ² /N)
1	0,250	6,000E+09	0,35	0,000E+00
2		1,000E+08	0,35	

7.

Load Number	Normal Stress (Pa)	Shear Stress (Pa)	Radius of Loaded Area (m)	X (m)	Y (m)	Shear Direction (°)
1	7,074E+05	2,829E+05	1,500E-01	0,000E+00	0,000E+00	0,000E+00

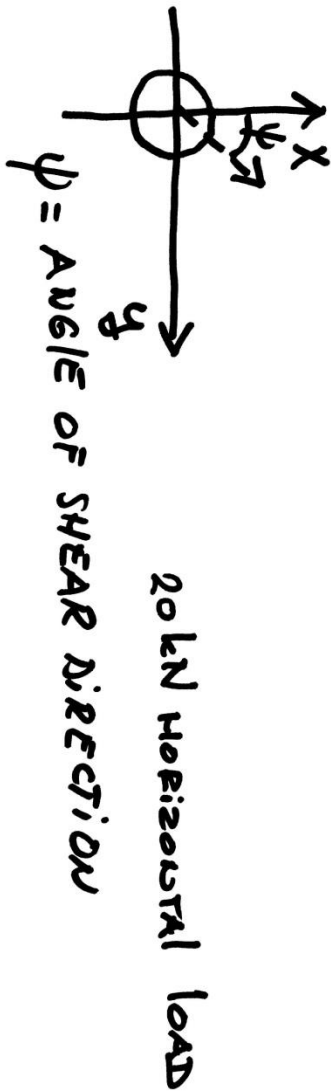
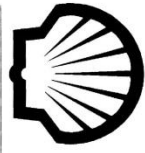


Figure 50g: Input for BISAR calculation; vertical and shear load.



BISAR 3.0 - Detailed Report

(untitled)

System 1: (untitled)

Position Number: 1 Layer Number: 1 X Coord (m): -1.520E-01 Y Coord (m): 0.000E+00 Z Coord (m): 0.000E+00

Load No.	Distance to Load Axis (m)	Theta (°)	Displacements (m)			Stresses (Pa)						Strains		
			Radial	Tangential	Vertical	Radial	Tangential	Vertical	Rad/Tang.	Rad/Vert.	Tang/Vert.	Radial	Tangential	Vertical
1	1.520E-01	1.800E+02	-3.901E-05	2.127E-12	2.839E-04	4.618E+05	-4.179E+05	0.000E+00	3.354E-03	0.000E+00	0.000E+00	1.013E-04	-9.659E-05	-2.564E-06

Total Stresses (Pa) XX: 4.618E+05 YY: -4.179E+05 ZZ: 0.000E+00 XZ: 0.000E+00 XY: 3.354E-03
Total Strains XX: 1.013E-04 YY: -9.658E-05 ZZ: -2.565E-06 XZ: 0.000E+00 XY: 7.546E-13
Total Displacements (m) UX: 3.901E-05 UY: -2.127E-12 UZ: 2.839E-04

Principal Values and Directions of Total Stresses and Strains

	Normal Stress (Pa)		Normal Strain		Shear Stress (Pa)		Shear Strain		X Comp.		Y Comp.		Z Comp.	
	Maximum:	4.618E+05	1.013E-04	-2.565E-06	Maximum:	4.398E+05	9.897E-05	0.7071	0.0000	0.0000	0.0000	0.0000	0.0000	0.0000
	Minimum:	0.000E+00	-9.658E-05	4.398E+05	Minimum:	2.309E+05	5.196E-05	0.7071	0.0000	0.0000	0.0000	0.0000	0.0000	0.0000
	Maximum:	-4.179E+05	-2.127E-12	2.839E-04	Maximum:	2.089E+05	4.701E-05	0.7071	0.0000	0.0000	0.0000	0.0000	0.0000	0.0000
	Minimum:	2.309E+05	5.196E-05	0.7071	Minimum:	-2.089E+05	-4.701E-05	0.7071	0.0000	0.0000	0.0000	0.0000	0.0000	0.0000

Strain Energy (J): 4.358E+01 Strain Energy of Distortion (J): 4.357E+01

8.

Figure 50h: Output of BISAR calculation.



BISAR 3.0 - Detailed Report
(untitled)
System 1: (untitled)

Position Number: 2 Layer Number: 1 X Coord (m): 0,000E+00 Y Coord (m): 0,000E+00 Z Coord (m): 0,000E+00

Load No.	Distance to Load Axis (m)	Theta (°)	Displacements (m)			Stresses (Pa)						Strains		
			Radial	Tangential	Vertical	Radial	Tangential	Vertical	Rad./Tang.	Rad./Vert.	Tang./Vert.	Radial	Tangential	Vertical
1	0.000E+00	0.000E+00	3,156E-05	0.000E+00	3,092E-04	-1,251E+06	-1,251E+06	-7,074E-05	0.000E+00	-2,829E-05	0.000E+00	-9,421E-05	-9,421E-05	2,800E-05

Total Stresses (Pa)
XX: -1,251E+06 YY: -1,251E+06 ZZ: -7,074E+05 YZ: 0,000E+00 XZ: -2,829E+05 XY: 0,000E+00
Total Strains
XX: -9,421E-05 YY: -9,421E-05 ZZ: 2,800E-05 YZ: 0,000E+00 XZ: -6,366E-05 XY: 0,000E+00
Total Displacements (m)
UX: 3,156E-05 UY: 0,000E+00 UZ: 3,092E-04

Principal Values and Directions of Total Stresses and Strains

	Normal Stress (Pa)		Normal Strain		Shear Stress (Pa)		Shear Strain		X		Y		Z	
	Maximum:	-5,867E+05	5,514E-05	-9,421E-05					Comp.	0,3921	Comp.	0,0000	Comp.	0,9199
	Minimum:	-1,251E+06	-9,421E-05						0,0000		1,0000		0,0000	
	Maximum:	-1,371E+06	-1,213E-04						0,9199	0,0000	0,0000	0,3921	0,3732	0,9278
	Minimum:	-9,789E+05							-0,9278	0,0000	0,0000	-0,7071	0,6505	0,2773
	Maximum:	-9,186E+05							-0,2773	0,6505	0,7071	-0,7071	0,6505	0,2773
	Minimum:	-1,311E+06							0,6505	0,7071	0,7071	-0,2773	0,2773	

Strain Energy (J): 1,259E+02 Strain Energy of Distortion (J): 4,014E+01

9.

Figure 50i: Output of BISAR calculation (continued).



BISAR 3.0 - Detailed Report

(untitled)

System 1: (untitled)

Position Number: 3 Layer Number: 1 X Coord (m): 1,520E-01 Y Coord (m): 0,000E+00 Z Coord (m): 0,000E+00

Load No.	Distance to Load Axis (m)	Theta (°)	Displacements (m)			Stresses (Pa)						Strains		
			Radial	Tangential	Vertical	Radial	Tangential	Vertical	Rad/Tang.	Rad/Vert.	Tang/Vert.	Radial	Tangential	Vertical
1	1,520E-01	0,000E+00	1,228E-05	0,000E+00	2,946E-04	-1,308E+06	-9,337E+05	0,000E+00	0,000E+00	0,000E+00	0,000E+00	-1,635E-04	-7,932E-05	1,308E-04

Total Stresses (Pa) XX: -1,308E+06 YY: -9,337E+05 ZZ: 0,000E+00 YZ: 0,000E+00 XZ: 0,000E+00 XY: 0,000E+00
Total Strains XX: -1,635E-04 YY: -7,932E-05 ZZ: 1,308E-04 YZ: 0,000E+00 XZ: 0,000E+00 XY: 0,000E+00
Total Displacements (m) UX: 1,228E-05 UY: 0,000E+00 UZ: 2,946E-04

Principal Values and Directions of Total Stresses and Strains

	Normal		Shear		X Comp.	Y Comp.	Z Comp.
	Stress (Pa)	Strain	Stress (Pa)	Strain			
Maximum:	0,000E+00	1,308E-04			0,0000	0,0000	1,0000
Minimum:	-9,337E+05	-7,932E-05			0,0000	0,0000	0,0000
Maximum:	-1,308E+06	-1,635E-04	6,540E+05	1,472E-04	-0,7071	0,0000	0,7071
Minimum:	-6,540E+05				0,7071	0,0000	0,7071
Minimum:	-4,669E+05		4,669E+05	1,050E-04	-0,7071	-0,7071	0,7071
Minimum:	-1,121E+06		1,871E+05	4,211E-05	-0,7071	0,7071	0,7071

Strain Energy (J): 1,440E+02 Strain Energy of Distortion (J): 1,021E+02

10.

Figure 50j: Output of BISAR calculation (continued).



BISAR 3.0 - Detailed Report
(untitled)
System 1: (untitled)

Position Number: 4 Layer Number: 1 X Coord (m): -1,520E-01 Y Coord (m): 0,000E+00 Z Coord (m): 1,000E-02

Load No.	Distance to Axis (m)	Theta (°)	Displacements (m)			Stresses (Pa)			Strains		
			Radial	Tangential	Vertical	Radial	Tangential	Vertical	Rad./Tang.	Rad./Vert.	Tang./Vert.
1	1,520E-01	1,800E+02	-3,548E-05	2,066E-12	2,841E-04	-2,144E+05	-6,034E+05	-1,727E-05	3,501E-03	-1,005E-05	1,706E-03

Total Stresses (Pa) **XX:** -2,144E+05 **YY:** -6,034E+05 **ZZ:** -1,727E+05 **YZ:** -1,706E-03 **XZ:** 1,005E+05 **XY:** 3,501E-03
Total Strains **XX:** 9,537E-06 **YY:** -7,798E-05 **ZZ:** 1,892E-05 **YZ:** -3,838E-13 **XZ:** 2,262E-05 **XY:** 7,876E-13
Total Displacements (m) **UX:** 3,548E-05 **UY:** -2,066E-12 **UZ:** 2,841E-04

Principal Values and Directions of Total Stresses and Strains

	Normal		Normal		Shear		Shear		X		Y		Z	
	Stress (Pa)	Strain	Stress (Pa)	Strain	Stress (Pa)	Strain	Comp.	Comp.	Comp.	Comp.	Comp.	Comp.	Comp.	Comp.
Maximum:	-9,085E+04	3,733E-05	-8,874E-06	-7,798E-05	2,563E+05	5,766E-05	0,6312	0,0000	0,7756	0,0000	-0,6312	0,0000	0,5484	0,0000
Minimum:	-2,962E+05	-8,874E-06	-6,034E+05	-7,798E-05	2,563E+05	5,766E-05	0,7756	0,0000	0,5484	0,0000	-0,6312	0,0000	0,5484	0,0000
Maximum:	-3,471E+05	2,563E+05	5,766E-05	0,4463	0,4463	0,4463	0,4463	0,7071	-0,7071	0,7071	-0,7071	0,7071	-0,4463	0,5484
Minimum:	-4,498E+05	1,536E+05	3,455E-05	0,5484	0,5484	0,5484	0,5484	0,7071	-0,7071	0,7071	-0,7071	0,7071	-0,4463	0,5484
Minimum:	-1,935E+05	1,027E+05	2,310E-05	-0,1021	0,9948	0,9948	0,9948	0,0000	0,0000	0,0000	0,0000	0,0000	0,9948	0,1021

Strain Energy (J): 2,314E+01 **Strain Energy of Distortion (J):** 1,497E+01

Figure 50k: Output of BISAR calculation (continued).



BISAR 3.0 - Detailed Report
(untitled)
System 1: (untitled)

Position Number: 5 Layer Number: 1 X Coord (m): 0,000E+00 Y Coord (m): 0,000E+00 Z Coord (m): 1,000E-02

Load No.	Distance to Load Axis (m)	Theta (°)	Displacements (m)			Stresses (Pa)			Strains		
			Radial	Tangential	Vertical	Radial	Tangential	Vertical	Rad./Tang.	Rad./Vert.	Tang./Vert.
1	0,000E+00	0,000E+00	2,998E-05	0,000E+00	3,094E-04	-1,122E-06	-1,122E+06	-7,058E-05	0,000E+00	-2,498E-05	0,000E+00

Total Stresses (Pa) XX: -1,122E+06 YY: -1,122E+06 ZZ: -7,058E+05 YZ: 0,000E+00 XZ: -2,498E+05 XY: 0,000E+00
Total Strains XX: -8,034E-05 YY: -8,034E-05 ZZ: 1,323E-05 YZ: 0,000E+00 XZ: -5,621E-05 XY: 0,000E+00
Total Displacements (m) UX: 2,998E-05 UY: 0,000E+00 UZ: 3,094E-04

Principal Values and Directions of Total Stresses and Strains

	Normal		Normal		Shear		X		Y		Z	
	Stress (Pa)	Strain	Stress (Pa)	Strain	Stress (Pa)	Strain	Comp.	Dir.	Comp.	Dir.	Comp.	Dir.
Maximum:	-5,887E+05	3,958E-05	-8,034E-05	-1,067E-04	3,250E+05	7,313E-05	-0,4244	0,0000	0,9055	0,0000	0,4244	0,0000
Minimum:	-1,122E+06	-8,034E-05	-1,239E+06	-9,137E+05	2,665E+05	5,996E-05	0,9055	0,0000	-0,3001	0,7071	-0,3001	0,6403
Maximum:	-1,239E+06	-1,067E-04	-9,137E+05	3,250E+05	5,996E-05	7,313E-05	-0,3001	0,7071	0,9055	0,0000	0,4244	0,0000
Minimum:	-8,552E+05	2,665E+05	-1,180E+06	-9,137E+05	5,996E-05	7,313E-05	0,6403	0,3001	-0,3001	0,7071	0,4244	0,0000
Maximum:	-1,180E+06	-9,137E+05	-8,552E+05	2,665E+05	5,996E-05	7,313E-05	0,4244	0,0000	-0,3001	0,7071	0,9055	0,0000
Minimum:	-9,137E+05	3,250E+05	-1,239E+06	-1,067E-04	-1,180E+06	-9,137E+05	0,9055	0,0000	0,4244	0,0000	0,3001	0,6403

Strain Energy (J): 9,949E+01 **Strain Energy of Distortion (J):** 2,701E+01

12.

Figure 50l: Output of BISAR calculation (continued).



BISAR 3.0 - Detailed Report
(untitled)
System 1: (untitled)

Position Number: 6 Layer Number: 1 X Coord (m): 1,520E-01 Y Coord (m): 0,000E+00 Z Coord (m): 1,000E-02

Load Distance to No. Load Axis (m)	Theta (°)	Displacements (m)			Stresses (Pa)						Strains		
		Radial	Tangential	Vertical	Radial	Tangential	Vertical	Rad./Tang.	Rad./Vert.	Tang./Vert.	Radial	Tangential	Vertical
1	1,520E-01	0,000E+00	1,451E-05	2,956E-04	-1,222E-06	-9,076E+05	-3,432E+05	0,000E+00	-3,587E+05	0,000E+00	-1,307E-04	-5,996E-05	6,702E-05

Total Stresses (Pa)	XX: -1,222E+06	YY: -9,076E+05	ZZ: -3,432E+05	YZ: 0,000E+00	XZ: -3,587E+05	XY: 0,000E+00
Total Strains	XX: -1,307E-04	YY: -5,996E-05	ZZ: 6,702E-05	YZ: 0,000E+00	XZ: -8,072E-05	XY: 0,000E+00
Total Displacements (m)	UX: 1,451E-05	UY: 0,000E+00	UZ: 2,956E-04			

Principal Values and Directions of Total Stresses and Strains

	Normal Stress (Pa)	Normal Strain	Shear Stress (Pa)	Shear Strain	X Comp.	Y Comp.	Z Comp.
Maximum:	-2.154E+05	9.578E-05			-0.3357	0.0000	0.9420
Minimum:	-9.076E+05	-5.996E-05			0.0000	1.0000	0.0000
Maximum:	-1.350E+06	-1.595E-04			0.9420	0.0000	0.3357
Minimum:			5.672E+05	1.276E-04	-0.9035	0.0000	0.4287
Maximum:	-7.826E+05				0.4287	0.0000	0.9035
Minimum:			3.461E+05	7.787E-05	-0.2374	-0.7071	0.6661
Maximum:	-5.615E+05				-0.2374	0.7071	0.6661
Minimum:			2.211E+05	4.975E-05	-0.6661	0.7071	0.2374
Maximum:	-1.129E+06				0.6661	0.7071	0.2374

Strain Energy (J): 1,245E+02 Strain Energy of Distortion (J): 7,356E+01

Figure 50m: Output of BISAR calculation (continued).



BISAR 3.0 - Detailed Report

(untitled)

System 1: (untitled)

Position Number: 7 Layer Number: 1 X Coord (m): 0,000E+00 Y Coord (m): 0,000E+00 Z Coord (m): 2,500E-01

Load No.	Distance to Axis (m)	Theta (°)	Displacements (m)			Stresses (Pa)						Strains					
			Radial	Tangential	Vertical	Radial	Tangential	Vertical	Rad/Tang.	Rad/Vert.	Tang/Vert.	Radial	Tangential	Vertical	Rad/Tang.	Rad/Vert.	Tang/Vert.
1	0,000E+00	0,000E+00	1,408E-05	0,000E+00	2,957E-04	9,046E-05	9,046E+05	-3,547E-04	0,000E+00	5,943E-02	0,000E+00	1,001E-04	1,001E-04	-1,115E-04	0,000E+00	1,337E-07	0,000E+00

Total Stresses (Pa) XX: 9,046E+05 YY: 9,046E+05 ZZ: -3,547E+04 YZ: 0,000E+00 XZ: 5,943E+02 XY: 0,000E+00
Total Strains XX: 1,001E-04 YY: 1,001E-04 ZZ: -1,115E-04 YZ: 0,000E+00 XZ: 1,337E-07 XY: 0,000E+00
Total Displacements (m) UX: 1,408E-05 UY: 0,000E+00 UZ: 2,957E-04

Principal Values and Directions of Total Stresses and Strains

	Normal		Normal		Shear		Shear		X		Y		Z	
	Stress (Pa)	Strain	Stress (Pa)	Strain	Stress (Pa)	Strain	Comp.	Comp.	Comp.	Comp.	Comp.	Comp.	Comp.	Comp.
Maximum:	9,046E+05	1,001E-04					1,0000	0,0000	0,0006	0,0000	0,0000	0,0000	0,0006	0,0000
Minimum:	9,046E+05	1,001E-04					0,0000	1,0000	0,0000	0,0000	0,0000	0,0000	0,0000	1,0000
Minimum:	-3,547E+04	-1,115E-04					-0,0006	0,0000	0,0000	0,0000	0,0000	0,0000	-0,7067	0,7076
Maximum:	4,346E+05		4,701E+05		1,058E-04		0,7067	0,0000	0,0000	0,0000	0,0000	0,0000	-0,7067	0,7076
Minimum:	4,346E+05		4,701E+05		1,058E-04		0,7071	0,0004	0,7071	0,7071	0,7071	0,7071	-0,7071	0,7071
Minimum:	9,046E+05		1,875E-01		4,366E-11		0,7071	-0,7071	0,7071	-0,7071	0,7071	0,0004	0,0004	0,0004

Strain Energy (J): 9,251E+01 Strain Energy of Distortion (J): 6,629E+01

14.

Figure 50n: Output of BISAR calculation (continued).



BISAR 3.0 - Detailed Report

(untitled)

System 1: (untitled)

Position Number: 8 Layer Number: 2 X Coord (m): 0,000E+00 Y Coord (m): 0,000E+00 Z Coord (m): 2,500E-01

Load No.	Distance to Load Axis (m)	Theta (°)	Displacements (m)			Stresses (Pa)						Strains		
			Radial	Tangential	Vertical	Radial	Tangential	Vertical	Rad/Tang.	Rad/Vert.	Tang/Vert.	Radial	Tangential	Vertical
1	0,000E+00	0,000E+00	1,408E-05	0,000E+00	2,957E-04	-3,705E+03	-3,705E+03	-3,547E+04	0,000E+00	5,959E+02	0,000E+00	1,001E-04	1,001E-04	-3,288E-04

Total Stresses (Pa) XX: -3,705E+03 YY: -3,705E+03 ZZ: -3,547E+04 YZ: 0,000E+00
Total Strains XX: 1,001E-04 YY: 1,001E-04 ZZ: -3,288E-04 XZ: 5,959E+02 XY: 0,000E+00
Total Displacements (m) UX: 1,408E-05 UY: 0,000E+00 UZ: 2,957E-04

Principal Values and Directions of Total Stresses and Strains

	Normal Stress (Pa)		Normal Strain		Shear Stress (Pa)		Shear Strain		X			Y			Z		
	Maximum:	-3,694E+03	1,002E-04	1,002E-04					Comp.	0,9998	0,0187	Comp.	0,0000	0,0000	Comp.	0,0000	0,0000
	Minimum:	-3,705E+03	1,001E-04	1,001E-04						0,0000	1,0000		0,0000	0,0000		0,9998	0,0000
	Maximum:	-3,548E+04	-3,289E-04		1,589E+04	2,146E-04			0,7202	0,6937	0,0000	0,0000	0,0000	-0,6937	-0,7202	-0,7070	-0,7070
	Minimum:	-1,959E+04			1,589E+04	2,145E-04			0,0133	-0,0133	0,7071	0,7071	0,7071	-0,7071	0,7070	0,0133	0,0133
	Minimum:	-3,699E+03			5,554E+00	7,498E-08			0,7070	0,7070	-0,7071	0,7071	0,7071	-0,7071	0,0133		

Strain Energy (J): 5,465E+00 Strain Energy of Distortion (J): 4,546E+00

15.

Figure 50o: Output of BISAR calculation (continued).

When the results of sheet 5 (vertical load, bottom of the asphalt layer) are compared with those of sheet 14 (vertical load + shear load, bottom of the asphalt layer), we observe that those are exactly the same. This implies that the effect of the shear force is not “visible” at a depth of 250 mm. The same is true if we compare the results of sheets 6 and 15.

The effect of the shear force is clearly visible when the results of sheet 3 (vertical load, location just outside loaded area at pavement surface) are compared with those obtained of sheets 8 and 9 (vertical load + shear load, location just outside loaded area at pavement surface). In case of only a vertical load, $\sigma_{xx} = -0.423$ MPa (sheet 3). In case of a vertical and a horizontal load $\sigma_{xx} = -1.308$ MPa (sheet 10) or $\sigma_{xx} = 0.462$ MPa (sheet 8). As one will observe, the applied braking force results in significant compressive horizontal stresses in front of the load in the direction of travel (x-direction) and a significant tensile stress at the back of the load. The principal strain at the pavement surface just behind the braking load (sheet 8) is slightly larger than the principal strain at the bottom of the asphalt layer (both are acting in the XX direction).

Although it is common practice in pavement engineering to ONLY take into account the maximum tensile stress or strain, the other two principal stresses/strains can of course not be neglected. How the other two principal stresses/strains should be taken into account in the design analysis will be discussed extensively in appendix C.

If we make a comparison of the stress conditions based on the energy of distortion, which does take into account the 3D stress/strain conditions, then we notice that the $U_{\text{distortion}}$ is the highest at the pavement surface just in front of the braking wheel. The 2nd highest $U_{\text{distortion}}$ is found at the same location, 10 mm below the surface. The 3rd highest $U_{\text{distortion}}$ is found at the bottom of the asphalt layer under the center of the wheel load. This value in case of braking forces is the same as without braking forces; it is approximately 65% of the $U_{\text{distortion}}$ at the pavement surface in front of the braking wheel.

Comparison of the results given in sheet 8 with those given in sheet 11 and comparison of the results given in sheet 10 with those given in sheet 13 show how the stresses and strains decrease with depth.

From this analysis it becomes clear that proper modeling of the contact stresses is very important in order to be able to analyze surface defects. Normally we ignore in our analyses the effect of the shear stresses that act at the pavement surface. These shear stresses are not only due to braking but they also occur under the driven wheels as well as the free rolling wheels. Under the free rolling tires they are caused by the fact that the tire wants to expand because of the vertical load but this is hindered by the friction between tire and pavement surface. Under the driven wheels/tires extra shear forces develop because of traction forces.

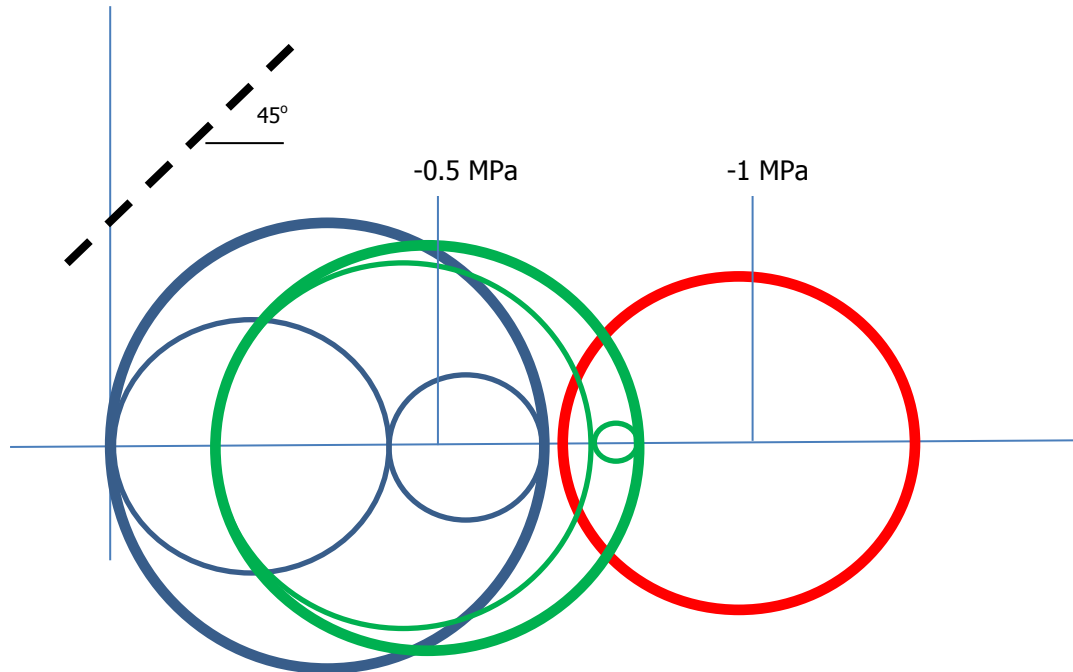
Furthermore the results show that although pavement thickness design is usually based on the tensile stresses/strains at the bottom of the asphalt layer, more critical conditions could occur in other locations in the pavement. Shell researchers [29] have e.g. shown that the maximum horizontal strain does not occur at the bottom of the asphalt layer if:

$$C = h_1 * E_2 / E_1 > 133 \text{ mm}$$

If h_1 (the top layer) ≤ 200 mm then the maximum tensile strain will occur in the lower half of the top layer and if $h_1 > 200$ mm then the maximum strain will occur in the upper half of the top layer.

Although thickness design analyses are mostly using the maximum tensile strain as design criterion, we should also have a look into the shear stress conditions and Mohr’s circles in other locations. As an example the stress circles in three locations at and close to the surface are shown hereafter. The red circle represents the stress conditions under the center of the load at the pavement surface when we only take into account a vertical load (Fig 50b), the blue circles show the stress conditions at the pavement surface 2 mm outside the loaded area (Fig 50c) and the red circles show the stress conditions 2 mm outside the loaded area at a depth of 10 mm from the surface. Since the angle of internal friction for asphalt concretes is around 45°, Mohr –

Coulomb's failure criterion (indicated with the dashed line) is much closer to the circles representing the stress condition at the edge of the tire print than to the circle representing the stress conditions under the center of the wheel. This implies that permanent deformation and shear failure will initiate at the edge of the contact area and not under the center of the wheel. This will be discussed in more detail in the section on permanent deformation in asphalt mixtures.



6. Axle loads, wheel loads and contact pressures

6.1 Axle loads

In order to be able to design a pavement structure, knowledge on the magnitude of the traffic loads is essential. Axle load measurements are therefore made to determine the number and weight of the axles passing over the pavement. Axle load measurements can be made in different ways varying between the up to date system shown in figure 51, to the much more simple system shown in figure 52.

The system as shown in figure 51 uses piezoelectric and coax cables to measure the axle load and other features of the truck. Such features include the speed of the truck as well as its registration number. Other items are the distance between the axles, the total length of the vehicle and a classification is made of the type of truck. This example shows amongst other things that the heaviest axle load is the tandem axle of the truck. The second axle from the front end of the truck was carrying a load of 223 kN (22.3 tons) while the third axle from the front carried 210 kN (21 tons). Comparing these values with the axle load regulations that prevail in the Netherlands (table 7), shows that the tandem axle is severely overloaded.

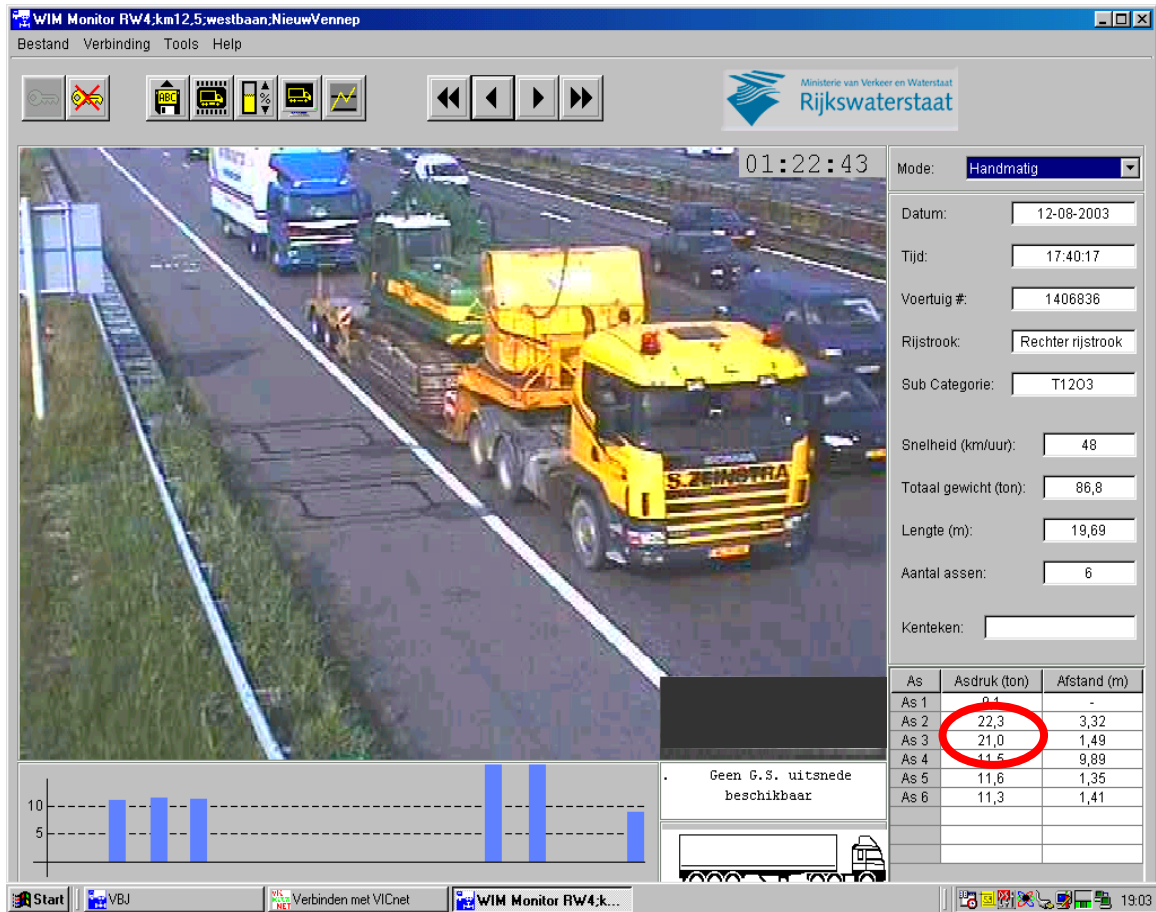


Figure 51: Example of a modern axle load survey unit as used in the Netherlands.

Maximum axle load driven axles (no restrictions with respect to suspension system, tires and steering)	115 kN
Maximum axle load non driven axles	100 kN
Maximum axle load tandem axles	
Axle distance < 1.0 m	100 kN
1.0 m ≤ axle distance < 1.3 m	160 kN
1.3 m ≤ axle distance < 1.8 m without air suspension system	180 kN
1.3 m ≤ axle distance < 1.8 m with air suspension system	190 kN
Maximum axle load triple axles	
Axle distance < 1.3 m	210 kN
1.3 m ≤ axle distance < 1.8 m without air suspension system	240 kN
1.3 m ≤ axle distance < 1.8 m with air suspension system	270 kN

Table 7: Axle load regulations in the Netherlands.



Figure 52: Simple axle load unit as used for surveys in Ghana

Figure 52 shows the axle load unit that was used in Ghana during an axle load survey program sponsored by the European Union [18]. The unit consisted of 4 Haenni WL 103 scales which were arranged in such a way that first the outer wheels of an axle were weighed and after that the total axle weight. This measurement procedure allowed to determine whether or not all the wheels of an axle were carrying the same load.

Table 8 shows the axle load distributions as they are used in the Netherlands as input for the thickness design of concrete pavements [19].

Axle load group (kN)	Average wheel load P (kN)	Axle load frequency distribution (%) for different types of road						
		heavily loaded motorway	normally loaded motorway	heavily loaded provincial road	normally loaded provincial road	municipal main road	rural road	public transport bus lane
20-40	15	20.16	14.84	26.62	24.84	8.67	49.38	-
40-60	25	30.56	29.54	32.22	32.45	40.71	25.97	-
60-80	35	26.06	30.22	18.92	21.36	25.97	13.66	-
80-100	45	12.54	13.49	9.46	11.12	13.66	8.05	-
100-120	55	6.51	7.91	6.50	6.48	8.05	2.18	100
120-140	65	2.71	3.31	4.29	2.70	2.18	0.38	-
140-160	75	1.00	0.59	1.64	0.83	0.38	0.38	-
160-180	85	0.31	0.09	0.26	0.19	0.38	0.00	-
180-200	95	0.12	0.01	0.06	0.03	0.00	0.00	-
200-220	105	0.03	0.01	0.03	0.00	0.00	0.00	-
Av. nr. of axles per heavy vehicle		3.5	3.5	3.5	3.5	3.5	3.1	2.5

Table 8: Axle load distributions as used in the Netherlands for the design of concrete pavements.

Table 8 is also suggested for use for the design of flexible pavements.

Table 9 shows the results of the axle load survey in Ghana as reported in [18].

Axle load	Axle 1	Axle 2	Axle 3	Axle 4	Axle 5	Axle 6
10	1	0	0	0	0	0
20	5	0	0	0	0	0
30	42	3	3	1	0	0
40	110	8	8	7	3	0
50	144	11	13	12	4	0
60	222	33	39	23	4	0
70	123	56	40	27	4	0
80	80	77	63	44	5	0
90	35	68	78	32	4	0
100	21	81	70	48	3	0
110	4	81	49	30	4	0
120	0	86	59	28	9	1
130	0	57	24	19	0	0
140	0	46	39	25	7	0
150	0	41	14	19	4	1
160	0	39	6	4	1	0
170	0	41	5	2	1	0
180	0	28	2	2	2	0
190	0	13	1	5	2	0
200	0	9	0	0	2	0
210	0	5	0	0	0	0
220	0	2	0	0	0	0
230	0	2	0	0	0	0
240	0	1	0	0	0	0
axle load summary [kN]						
max	112,5	236,5	189,0	191,5	203,5	153,5
avg	59,97	116,08	99,08	101,25	108,96	135,5
sa	16,77	38,06	28,43	31,75	43,10	25,46
tire pressure [kPa]						
max	1050	1015	980	980	945	840
avg	756	798	805	819	826	840
sa	105	77	63	56	49	0

Table 9: Results of axle load surveys in Ghana.

The results were obtained by means of axle load surveys carried out on different roads. In total 787 trucks were surveyed. The trucks had either 2, 3, 4, 5 or 6 axles. The axle loads, including the number 1 steering axle, are reported in table 9. The table also shows the maximum axle load measured, as well as the average axle load and the standard deviation. Given the fact that the allowable was 100 kN, it is quite clear that severe overloading occurred. This is a problem in many countries.

The table also shows interesting information with respect to the tire pressures. Normally tires should operate at an inflation pressure of around 700 kPa. The table shows that the mean tire pressure was indeed close to this value but also that some very exotic values occurred. These high tire pressures certainly result in high contact stresses and in accelerated pavement damage.

Table 10 shows results of axle load measurements as performed in Yemen [20]. Again one notices the large amount of very heavy, overloaded, vehicles.

Vehicle type	Axle	Axle load range [kN]		
		Min.	Max.	Average
Heavy busses (1%) vehicle weight	1	30	58	46
	2	49	107	84
		82	164	130
2 axle medium truck (34%) vehicle weight	1	33	63	47
	2	75	144	115
		115	191	162
2 axle heavy truck (30%) vehicle weight	1	33	99	70
	2	98	243	170
		145	343	240
3 axle truck (30%) vehicle weight	1	42	109	74
	2	67	226	153
	3	76	240	161
		187	553	388
4 axle truck (3%) vehicle weight	1	45	79	60
	2	80	202	134
	3	80	180	133
	4	92	193	136
		227	595	395
5 axle truck (2%) vehicle weight	1	44	89	67
	2	52	161	110
	3	52	169	109
	4	68	204	142
	5	70	201	151
		327	736	577

Table 10: Axle loads for the Hodeidah – Sanaa road [20].

Note: the percentages given are the percentages of occurring.

Table 11 is another example of overloading conditions. The results presented in that table are from axle load surveys done on the Jing-Zhu freeway in the Hubei province, China [21]. The table not only shows a significant amount of overloading (legal load limit is 100 kN) but also clearly indicates that the overload problem rapidly increased during the 1995 – 1998 period.

From the information given so far, it is clear that an as good as possible estimation of the axle load distribution is essential. Overloading seems to be a problem in many countries and one should realize that especially the heavy, overloaded vehicles are causing most of the pavement damage.

At this moment it is appropriate to recall the concept of load equivalency. This concept implies that one determines the damaging effect of a particular axle load relative to a standard axle load. The equivalent number of load repetitions is calculated using:

$$N_{eq} = (L/L_{ref})^m N_L$$

Where: N_{eq} = number of equivalent passages of the axle load considered,
 L = axle load to be considered,
 L_{ref} = reference axle load,
 N_L = number of repetitions of the axle considered,
 m = damage factor.

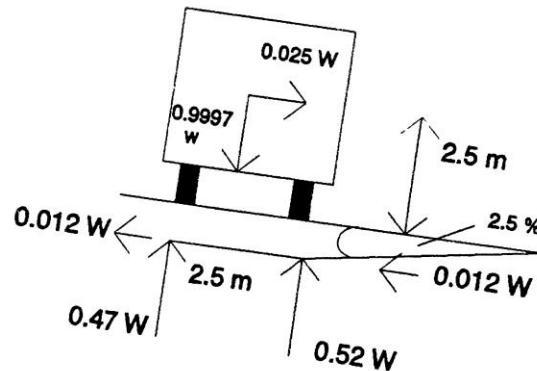
The equation implies that if the reference axle equals 100 kN and assuming $m = 4$, a 200 kN axle produces 16 times more damage than the reference axle does. It should be noted that the value of m depends on which damage type is considered. If one wants to know the damaging effect of various axle loads relative to each other in terms of fatigue of the asphalt layer, then $3 < m < 6$. If the effect on fatigue in a cement treated layer has to be considered, then $7 < m < 10$. If the effect on the loss of serviceability needs to be considered then $m = 4$.

Year	Axle load (kN)													
	< 60		60-100		100-130		130-150		150-180		>180		total	
	no.	%	no.	%	no.	%	no.	%	no.	%	no.	%	no.	%
1995	893	25.86	811	23.49	811	23.49	420	12.16	352	10.19	166	4.81	3453	100
1996	899	20.26	1027	23.15	1026	23.14	665	14.99	557	12.55	263	5.93	4437	100
1997	981	18.74	1218	23.26	1217	23.24	815	15.57	682	13.02	322	6.15	5235	100
1998	1078	17.66	1193	19.54	1192	19.52	1183	19.38	991	16.23	468	7.67	6105	100

Table 11: Axle loads on the Jing-Zhu freeway in China.

6.2 Wheel loads

One would expect that the wheel load is equal to the axle load divided by the number of wheels on the axle. This however is not true. Figure 53 e.g. shows that chamber of the pavement surface results in an unequal sharing of the axle load over both wheel groups of the axle.



W = Weight of the vehicle

Figure 53: Chamber of the roads results in unequal sharing.

The wheel group on the verge side of the road carries 52% of the load while the wheel group near the centre line of the road carries 47%. Wheel load measurements as carried out in Ghana [18] showed however that quite often the axle load was far from equally distributed over the wheels of the axle; some examples are shown in figure 54. The legal axle load limit at the time of the measurements was 100 kN. This implies that the heaviest axle load of 236.5 kN would

result in $(236.5 / 100)^4 \approx 31$ times more damage than the legal axle load. If we assume that the legal axle has 2 dual wheel sets, implying 4 wheel loads of 25 kN each, then the highest wheel load of 90 kN would result in $(90 / 25)^4 \approx 168$ more damage than the 25 kN load. All this implies that we should determine the occurring wheel loads rather than the occurring axle loads.

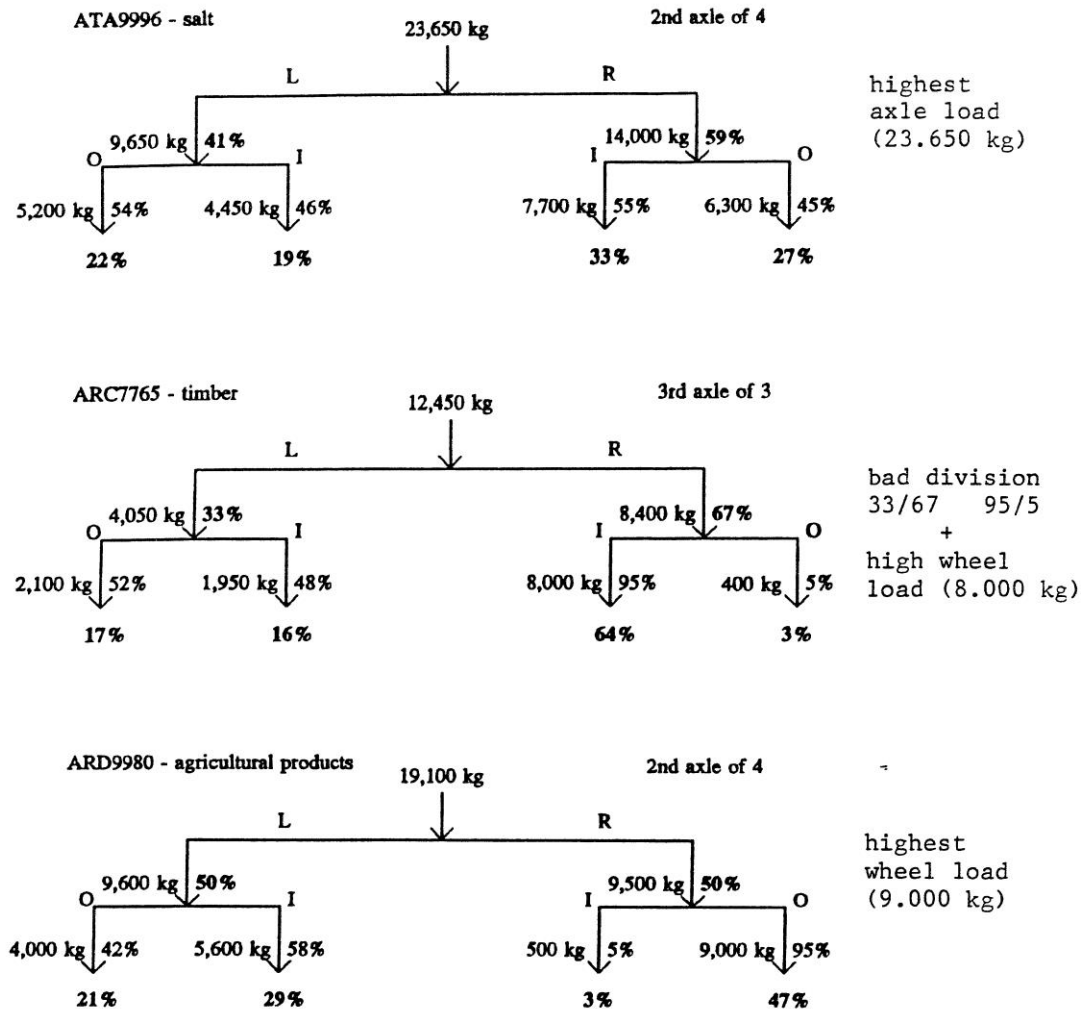


Figure 54: Examples of unequal sharing of the axle load over the wheels.

6.3 Contact pressures

As mentioned before, knowledge on axle and wheel loads is important but even more so is knowledge on the contact pressures. Wheel loads come in different sizes and shapes, some of them are shown in figure 55, and each of them produces a different contact pressure distribution.



Figure 55: Different tire types.

The well known dual tire configuration is shown on the left of figure 55; it is used all over the world for the driven and towed axles. Normally these tires have an inflation pressure of around 700 kPa. The steering axle of a truck always has a single tire, having the same dimensions as one of the dual tires. In western Europe however, most of the towed axles are equipped nowadays with a so called wide base or super single tire. This tire is shown on the far right of the picture. Normally the tire has an inflation pressure of 800 – 850 kPa. Use of super singles is reducing the total rolling resistance and does therefore reduce the fuel consumption. The super single tire cannot be used on the drive axle. Next to the super single tire, the super super single tire (50 cm width) is shown. This tire was developed for being used under the driven axle of trucks thereby replacing the dual wheel configuration. In between the super super single and the dual wheel is a small size dual wheel. This tire is not very much used yet. The idea behind it was that a smaller size tire would allow lowering the loading platform resulting in a larger loading capacity.

In order to avoid excessive wear to the tire, the tire pressure should be selected in relation to the tire load. The following relationships can be used for this.

The pressure used in the tires for dual wheels (1 axle has a dual wheel set on either side of the axle; total nr. of wheels = 4) can be estimated from:

$$p = 0.35 + 0.0035 L$$

Where: p = tyre pressure [MPa],
 L = axle load [kN].

The pressure in the super single tyres (1 axle has one wheel on either side of the axle; total nr. of wheels = 2) can be estimated using:

$$p = 0.42 + 0.0038 L$$

The units in this equation are the same as used in the previous equation.

The consequences of less optimal combinations of tire load and tire pressure are shown in figure 56. This figure shows that when the tire pressure is too low, the tire walls are carrying most of the load. This can result in rather high contact pressures at the edge of the. The combination of a 50 kN load with a 520 kPa pressure results in contact pressures under the wall of the tire of approximately 900 kPa. On the other hand, if the tire load is low and the tire pressure high, the contact pressure distribution becomes more or less parabolic with the peak value at the centre of the tire. From the results shown in figure 56 it is obvious that too high or too low tire pressures relative to the tire load will result in excessive damage to the tire but also to the pavement surface.

The reader should pay attention to a small detail of figure 56. One can observe that the contact area is not a circle but a rectangle. Furthermore one will observe that when the load increases, the length of the rectangle (driving direction) increases but the width of the rectangle remains the same.

Figure 57 [23] shows in much more detail the contact pressure distributions under a super single tire. One clearly recognizes the location of the ribs of the tire. Next to that one will notice the lateral shear forces that develop under the tire as a result of the fact that the tire ribs cannot expand freely due to the friction generated by the pavement surface. It will be quite clear that these complex stress distributions should be taken into account when surface defects like raveling and rutting in the top layer need to be modeled. For the analysis of stresses and strains at a greater depth (more than 50 mm), modeling of the contact stresses can be significantly simplified. In such cases it is sufficient to assume a circular contact area with a homogeneously distributed contact pressure. It is common practice to assume that the contact pressure is equal to the tire pressure. One should realize however that this is a gross oversimplification of reality and leads to an underestimation of the stresses and strains in the top part of the pavement. This assumption should therefore only be applied if no other information is available.

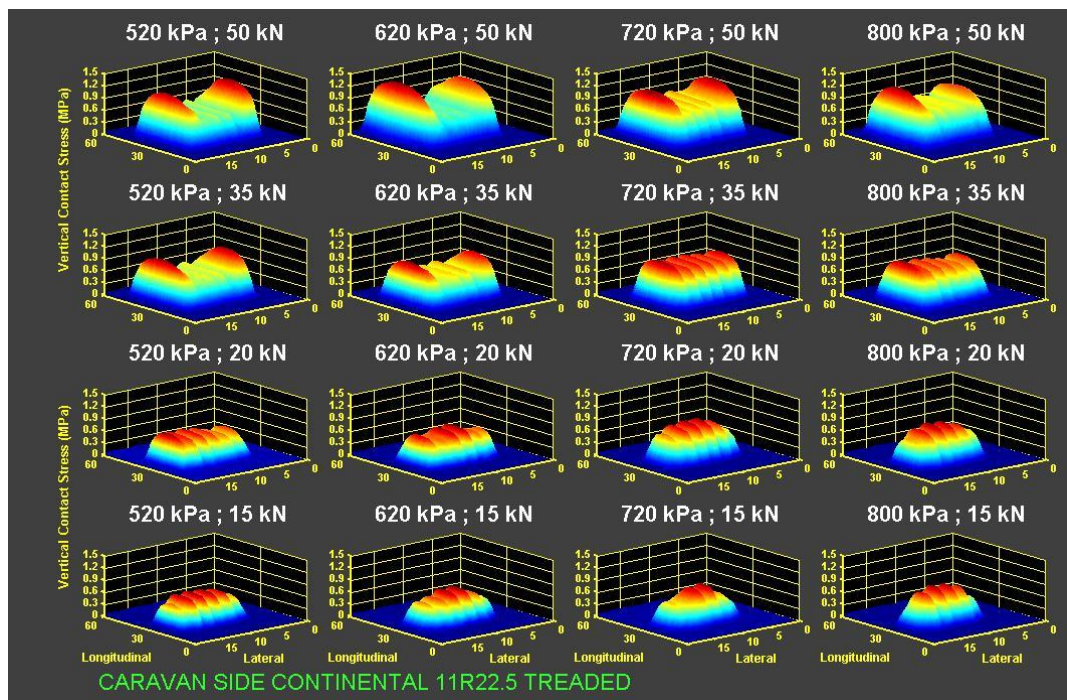


Figure 56: Vertical contact pressure distributions in relation to tire load and tire pressure.

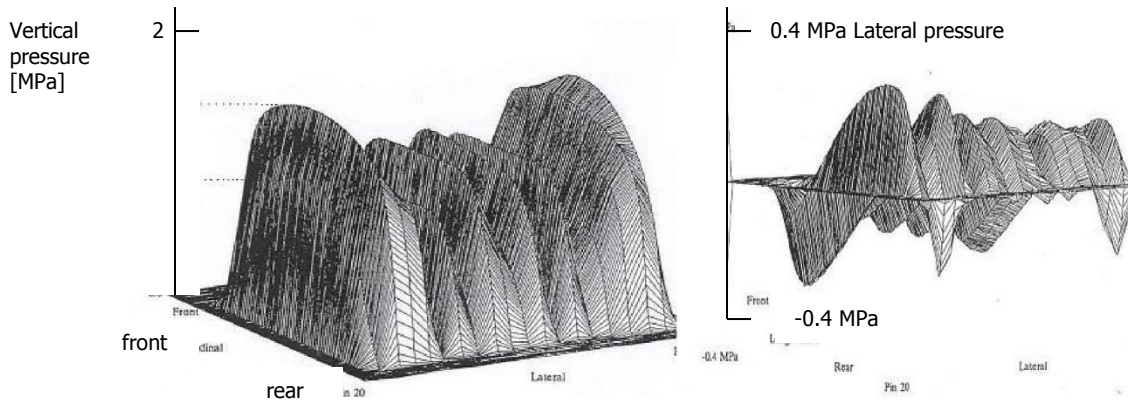


Figure 57: Vertical contact pressure distribution (left) and lateral contact pressure distribution (right) under a super single tire.

If one assumes that the contact pressure is equal to the tire pressure, then the radius of the circular contact area is calculated from:

$$\pi r^2 p = F$$

Where: r = radius of the contact area,
 p = contact pressure = tire pressure,
 F = wheel load.

There is however also a different method to calculate the radius of the contact area. This method is used in the design of concrete pavements. Knowing that the contact area is a rectangle in reality, an equivalent radius is calculated using:

$$a = b \sqrt{(0.0028 * F + 51)}$$

Where: b = parameter dependent on the type of tire (table 11)
 F = average wheel load (N) of the axle load group

Type of tire	Width of rectangular contact area(s) (mm)	Value of parameter b	Frequency distribution (%)	
			roads	public transport bus lanes
Single tire	200	9.2	39	50
Dual tire	200	12.4	38	50
Super single tire	300	8.7	23	0
Super super single tire	400	9.1	0	0

Table 11: Value of parameter b for different tire types.

It should be noted that the contact pressure calculated from the wheel load and the equivalent radius of the loading area is higher than the tire pressure.

A number of attempts have been made to model the contact pressure distributions under a tire. De Beer e.a. [22] have done a significant amount of work, but also the work done by

Groenendijk [23] and Fernando e.a. [24] should be recognized. Based on a large number of measurements, Fernando e.a. [24] developed the computer program Tireview that allows the 3D contact pressure distributions to be calculated for a number of tires, depending on the tire load and tire pressure. They also calculated to what extent these distributions should really be taken into account meaning: at which depth is a simplified contact pressure distribution acceptable. Similar work has been done by Groenendijk [23], Myers [25] and Blab [26] and also the work done by Wardle and Gerrard [17] on this topic as well as early work done by Verstraeten [16] should be mentioned.

The results of these studies will be summarized briefly hereafter and guidance for preparing input for multi layer analyses will be given.

Based on a large number of measurements, Fernando e.a. [24] concluded that for different radial tires used in dual wheel configurations, the contact area could be calculated as follows.

Tire type	Equation to predict contact area A
215/75R17.5	$A = 36.9172 + 0.0059 T_L - 0.1965 T_P$
11R24.5	$A = 41.9417 + 0.0087 T_L - 0.2228 T_P$
11R22.5	$A = 54.4740 + 0.0066 T_L - 0.4258 T_P$
295/75R22.5	$A = 173.2141 + 0.0061 T_L - 3.1981 T_P + 0.0164 T_P^2$
A	Predicted contact area [in ²]
T _L	Tire load [lbs]
T _P	Tire inflation pressure [psi]

Table 12: Contact area for different tire types.

Fernando proposes to calculate an equivalent contact pressure, p_e , by dividing the wheel load by the predicted contact area.

$$p_e = T_L / A$$

The effective radius of the contact area, r_e , is calculated following:

$$r_e = \sqrt{A / \pi}$$

Fernando showed that this way of calculating the contact pressure and contact area had a significant effect on the magnitude of the stresses calculated in the top 50 mm of the pavement when compared with the stresses and strains calculated using the traditional approach where the contact pressure is assumed to be equal to the tire pressure. At a greater depth the differences between the two approaches became insignificant.

Groenendijk [23] analyzed in his study the contact pressure distributions under super single tires. Just like Fernando he used the South African VRSPTA device (figure 58) to perform the contact pressure measurements. Figures 59, 60 and 61 show some typical results.

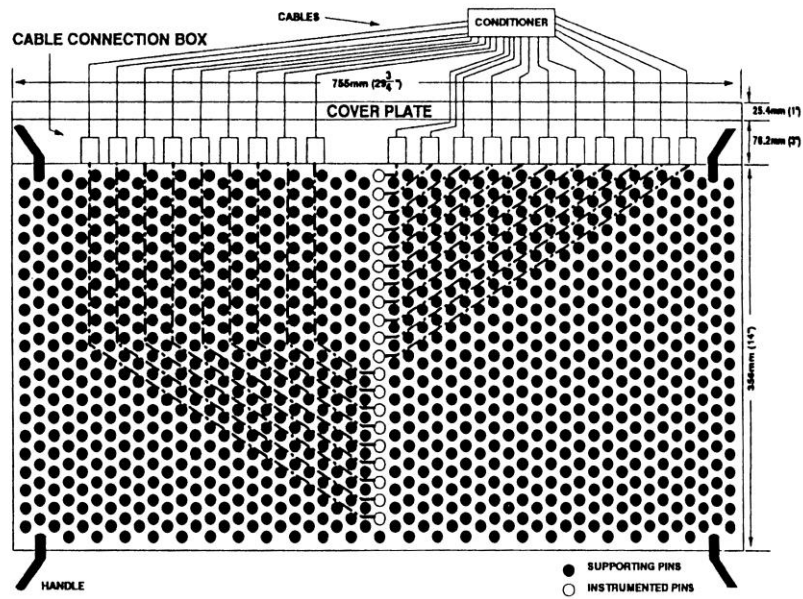


Figure 58: South African VRSPTA used for contact pressure measurements.

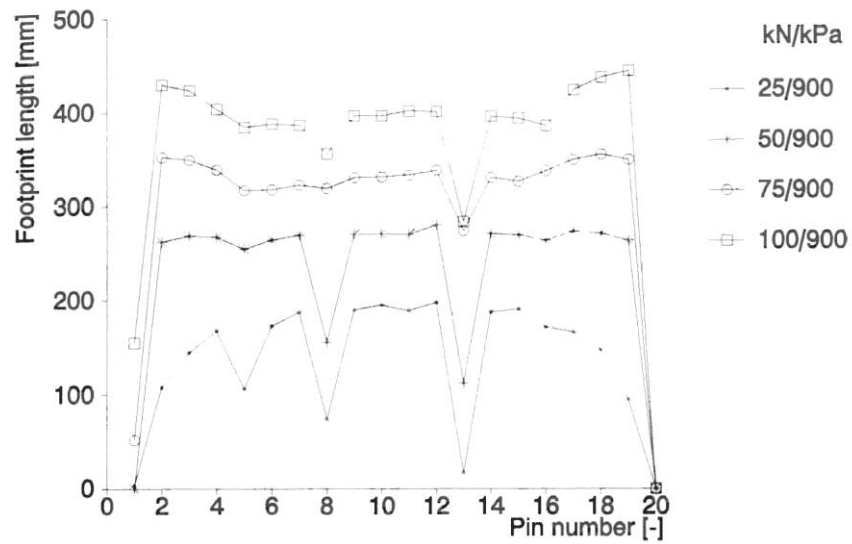


Figure 59: Foot print length of a new super single tire (R164BZ) in relation to the applied wheel load.

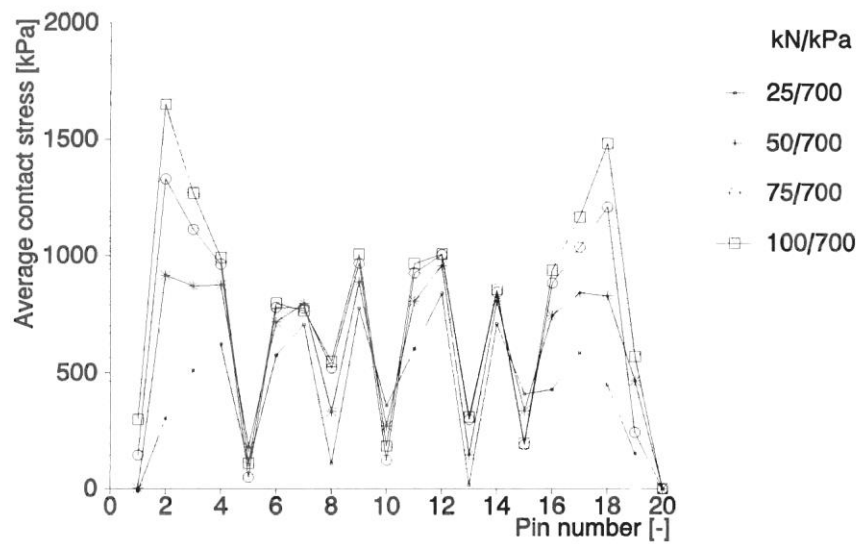


Figure 60: Variation of the vertical stresses along the width of the tire (new R164BZ) in relation to the applied wheel load.

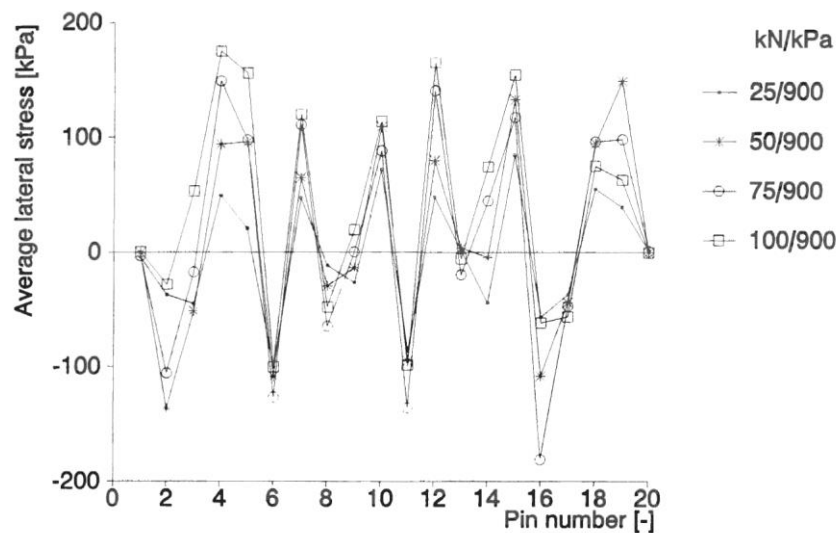


Figure 61: Variation of the transverse shear stresses along the width of the tire (new R164BZ) in relation to the applied wheel load.

Figures 62 and 63 show the longitudinal and transversal shear stress distributions as modeled by Groenendijk using the results of the contact pressure measurements.

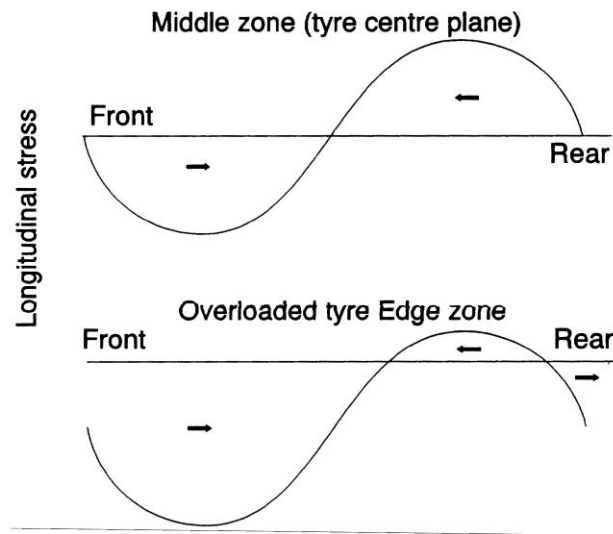


Figure 62: Modeled distribution of the longitudinal shear stresses.

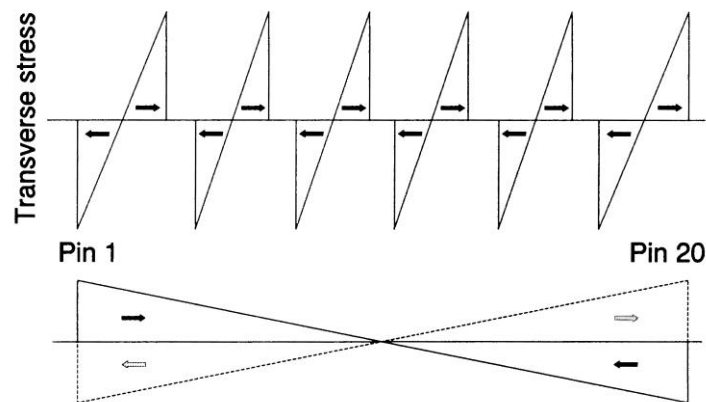


Figure 63: Modeled distribution of the transverse shear stresses. Top due to compression of the tread ribs. Bottom: due to overloading/underinflation (solid) or underloading/overinflation (dotted).

From these figures we observe that the width of the foot print is almost independent of the wheel load, only the length of the foot print changes with changing loading conditions. Furthermore similar trends are observed with respect to the vertical contact pressure as shown in figures 56 and 57, being high stresses at the edge of the tire if the tire pressure is too low with respect to the wheel load and high stress in the centre of the tire when the tire is over-inflated. Furthermore a zigzag pattern is observed for the lateral shear stresses. From his data, Groenendijk proposed the following equations to predict the length of the contact area and the vertical stresses and longitudinal and transversal shear stresses.

$$\begin{aligned}
Z_{len} &= 115 + 5.70 F - 3.11 \cdot 10^{-3} F p \\
Z_{aveMi} &= 422 - 1.2 F + 4.60 \cdot 10^{-3} F p + 0.322 p + 8.60 v \\
Z_{aveEd} &= 85.5 + 9.25 F + 0.290 p + 12.9 v \\
X_{maxMi} &= 10.3 + 2.56 F - 1.15 \cdot 10^{-3} F p + 2.50 v \\
X_{maxEd} &= 29.6 + 2.12 F - 1.19 \cdot 10^{-3} F p + 1.96 v \\
X_{minMi} &= -30.4 - 1.55 F - 8.68 \cdot 10^{-4} F p - 2.02 v \\
X_{minEd} &= 18.0 - 3.61 F + 1.12 \cdot 10^{-3} F p + 0.0394 p - 3.21 v \\
Y_{ampl} &= (114 - 0.682 F + 2.05 \cdot 10^{-3} F p) / 2
\end{aligned}$$

Where: Z_{len} = tire foot print length [mm],
 Z_{aveMi} = average vertical contact stress over the middle 60% of the tire width [kPa],
 Z_{aveEd} = average vertical contact stress over the edge 2 * 20% of the tire width [kPa],
 X_{maxMi} = maximum longitudinal shear stress averaged over the middle zone,
 X_{maxEd} = id averaged over the edge zone,
 X_{minMi} = minimum longitudinal shear stress averaged over the middle zone,
 X_{minEd} = id averaged over the edge zone
 Y_{ampl} = amplitude of the lateral shear stress zigzag pattern over the tire width [kPa],
 F = wheel load [kN],
 p = tire pressure [kPa],
 v = speed [m/s] (effect only studied for speeds up to 4 m/s !!!)

It should be noted that the contact stresses calculated using the equations given above are those acting under the tire ribs. They should not be smeared out over the entire tire footprint including the grooves! The 2 edges having a width of 20% of the entire width and don't have grooves. In the middle part there are 5 grooves cq 4 ribs.

It will be clear that such a complex contact pressure distribution can only be properly taken into account by means of a finite element program. Also a multi layer program can be used but in that case a large number of circular loads must be used to simulate the real load.

All in all it is quite clear that an as accurate as possible modeling of the load conditions is needed in order to be able to make realistic assessments of surface damage types like raveling, surface cracking and rutting in the wearing course. Therefore some suggestions to model the load are given in table 13. This table is based on the following assumptions.

Assume a super single load of 750 kN with a tire pressure of 850 kPa. Using Groenendijk's equations we obtain the following values for the size of the loaded area, the vertical pressure and lateral shear stresses.

$$\begin{aligned}
Z_{len} &= 344 \text{ mm} \\
Z_{aveMi} &= 898 \text{ kPa} \\
Z_{aveEd} &= 1026 \text{ kPa} \\
Y_{ampl} &= 193 \text{ kPa}
\end{aligned}$$

A close observation of the load model presented in table 13 shows that it is not that easy to match the real contact distribution by means of a combination of circular loads. Better representations of the actual load conditions are possible if more circles are used.

Outer strip 60 mm wide	Centre strip 180 mm wide	Outer strip 60 mm wide
Length 344 mm	Length 344 mm	Length 344 mm
Area 20640 mm ² Total load 21.175 kN	Area including grooves 61920 mm ² , total load 32.65 kN Area excluding grooves approximately 48000 mm ² Meaning approximately 12000 mm ² per rib	Area 20640 mm ² Total load 21.175 kN
Model outer strip by 6 circles	Model each rib by 6 circles	Model outer strip by 6 circles
Radius 33 mm	Radius 22 mm	Radius 33 mm
Vertical uniformly distributed pressure 1026 kPa	Vertical uniformly distributed pressure 898 kPa	Vertical uniformly distributed pressure 1026 kPa

Table 13: Suggestion to model the vertical contact pressure distribution under a super single tire (F = 75 kN, p = 850 kPa).

Note: suggestions for the longitudinal and transversal shear stress distributions are not made because of the relatively low values of these stresses.

For thickness design purposes the following approach is recommended. Determine the contact area for the tire considered using the equations provided by Fernando for tires used in dual wheel configurations and the equation provided by Groenendijk for super single tires. Calculate the effective contact pressure and the effective radius of the loading area following the procedure suggested by Fernando.

For analyses of surface damage like raveling, rutting and surface cracking an as detailed as possible modeling of the actual loading conditions should be used. The data provided by Groenendijk [23] and Myers [25] give useful guidance in doing so.

7. Climatic data

7.1 Introduction

Temperature has a significant effect on the stiffness as well as the fatigue and permanent deformation resistance of asphalt mixtures. It is therefore quite obvious that accurate knowledge of the temperature distribution in the pavement should be available in order to allow realistic analyses of the stresses and strains in asphalt pavements to be made. Furthermore moisture has a significant effect on the stiffness and strength characteristics of unbound materials and soils. In this chapter, information will therefore be given on how values for these important input parameters can be obtained.

7.2 Temperature

The temperature distribution in the pavement layers can vary significantly during the day and during the seasons of the year. Figure 64 [27] e.g. shows the temperature distribution during a hot spring and a hot summer day. One should realize that the surface temperatures can easily be 5 °C higher than the temperatures measured at 10 mm below the pavement surface. Figure 65 [27] shows the temperature gradient that exists over the asphalt layer thickness in case of the hot summer day shown in figure 64.

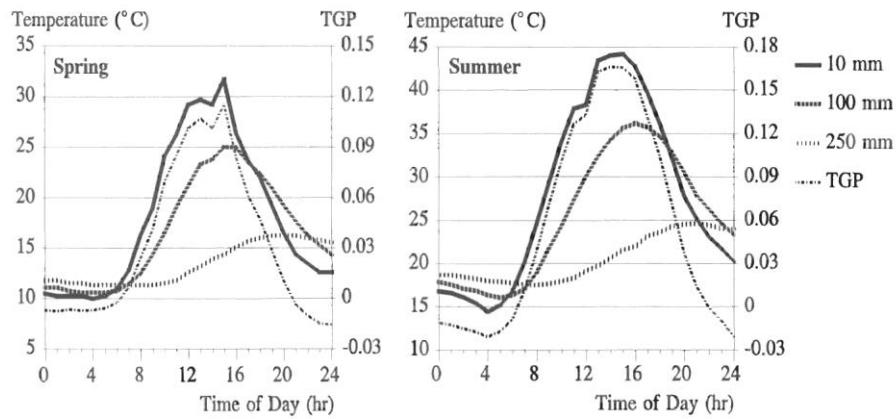


Figure 64: Temperature variations during the day over a the thickness of the asphalt pavement.

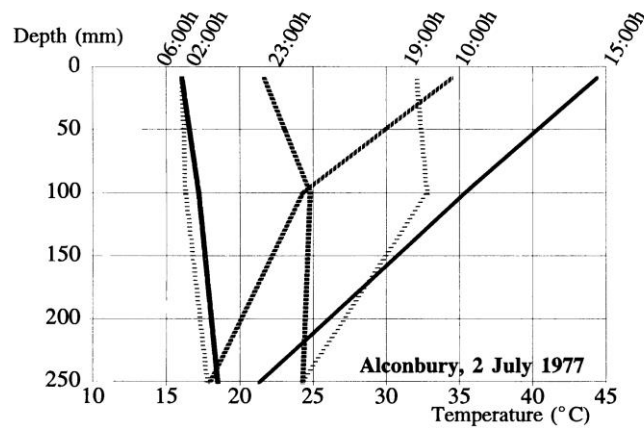


Figure 65: Temperature gradient in an asphalt pavement on a hot summer day.

From these figures it is clear that assuming a constant temperature over the thickness of the asphalt layer is far from reality unless one is dealing with thin asphalt layers. Furthermore the total asphalt thickness is commonly made of different types of asphalt mixtures, especially in case the total thickness is larger than 100 mm, which implies that even when the temperature is constant over the entire thickness, different stiffness values will be found for the different layers of which the total asphalt thickness is made of.

Van Gurp [27] in his thesis presents a method to deal with temperature variations over the total asphalt thickness. He divided the total thickness into three sub-layers (figure 66) and defined an equivalent asphalt thickness, $h_{1,eq}$ in the way as described in figure 67. This equivalent thickness has a modulus value equal to the modulus of the third sub-layer.

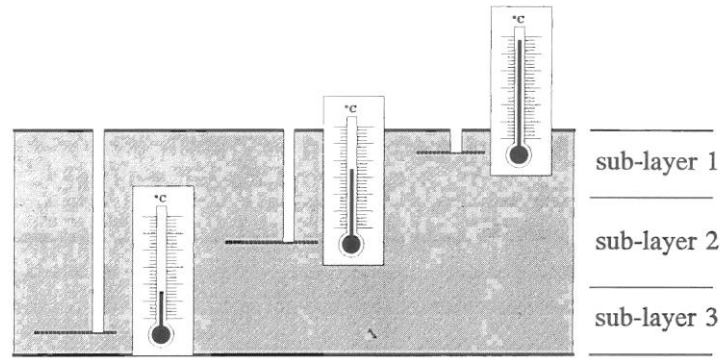


Figure 66: Dividing the total asphalt thickness in sub-layers.

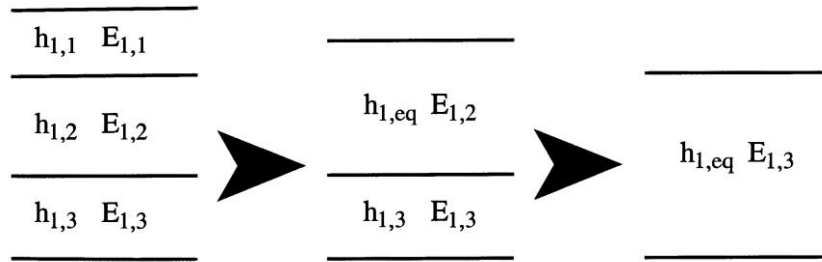


Figure 67: Calculation of the equivalent asphalt thickness $h_{1,eq}$.

The equivalent asphalt thickness is calculated as follows.

$$h_{1,eq} = (h_1 / 4) * [(n_1^2 n_2^2 + 64 n_1 n_2^2 + 110 n_1 n_2 + 16 n_2^2 + 64 n_2 + 1) / (n_1 n_2 + 2 n_2 + 1)]^{0.33}$$

Where: $h_{1,eq}$ = equivalent total asphalt thickness with stiffness $E_{1,3}$,
 n_1 = $E_{1,1} / E_{1,2}$,
 n_2 = $E_{1,2} / E_{1,3}$.

This equation is valid under the assumption that $h_{1,1} = 1/4 h_1$ and $h_{1,3} = 1/4 h_1$ and that the temperature is uniformly distributed over each of the sub-layers. The mean temperature of each sub-layer is used to calculate the modulus of that sublayer.

In order to be able to take into account the effects of temperature gradients, Van Gurp also defined a thermal gradient parameter (TGP) being:

$$TGP = 1 - h_{1,eq} / h_1$$

TGP takes a positive value when the top part of the total asphalt thickness is softer than the bottom part. Depending on TGP, a correction on the tensile strain calculated at the bottom of the asphalt layer, should be applied following:

$$\varepsilon_{r,corr} = \varepsilon_{r,uncorr} * (1 - TGP)$$

Where: $\varepsilon_{r,corr}$ = asphalt strain corrected for thermal gradients,

$\epsilon_{r,uncorr}$ = asphalt strain uncorrected for thermal gradients,
TGP = thermal gradient parameter, see figure 68.

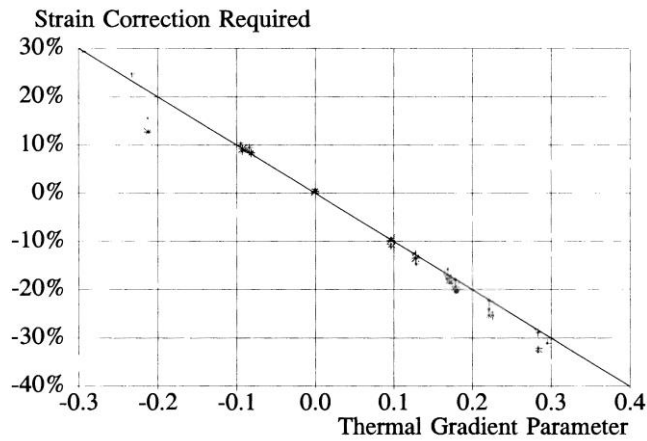


Figure 68: TGP vs strain correction required.

The procedure to use all this is as follows:

- calculate $h_{1,eq}$
- calculate the tensile strain $\epsilon_{r,uncorr}$ at the bottom of $h_{1,eq}$
- calculate TGP,
- calculate $\epsilon_{r,corr}$.

Van Gurp also presented a method to predict the asphalt temperature at a depth from the pavement surface of 1/3 of the total asphalt thickness. This equation is:

$$T = 8.77 + 0.649 T_0 + (2.20 + 0.044 T_0) \sin \{2\pi (hr - 14) / 24\} + \log (h_1 / 100) [-0.503 T_0 + 0.786 T_5 + 4.79 \sin \{2\pi (hr - 18) / 24\}]$$

Where: T = temperature at a depth of 1/3 h_1 from the pavement surface,
 T_0 = pavement surface temperature [$^{\circ}\text{C}$],
 T_5 = prior mean five days air temperature [$^{\circ}\text{C}$],
 h_1 = thickness of the asphalt layer [mm],
hr = time of the day in 24 hour system.

It is clear that the determination of the temperature to be adopted in the pavement design analysis can be a rather cumbersome task especially if large variations in temperature occur during the day and during the year. For that reason several simplification procedures have been developed and the one prepared for the Shell Pavement Design Manual [28] will be briefly described here-after.

Based on a large number of calculations, Shell researchers [29] concluded that it is possible to define a weighted mean annual air temperature (w-MAAT) such that the damage that accumulates over one year is the same as by taking into account varying temperature conditions over a year. In order to do so, a weighing factor has to be determined (figure 69 and table 14) using the mean monthly air temperature (MMAT) as input. When the weighing factor is known, the weighted mean annual air temperature can be determined. The procedure is explained by means of an example.

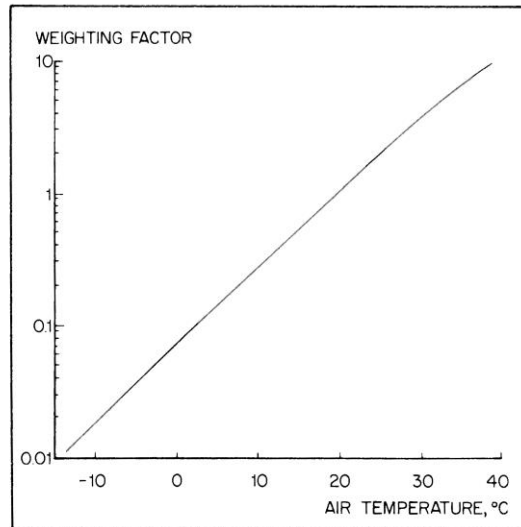


Figure 69: Temperature weighing chart.

Month	Mean monthly air temperature MMAT [$^{\circ}\text{C}$]	Weighing factor from figure 68
January	8	0.21
February	8	0.21
March	12	0.36
April	16	0.62
May	19	0.93
June	22	1.40
July	26	2.35
August	28	3.00
September	22	1.40
October	19	0.93
November	12	0.36
December	6	0.16
	Total of weighting factors	11.93
	Average weighting factor = total / 12	≈ 1
	Weighted mean annual air temperature w-MAAT determined from figure 68	$\approx 20^{\circ}\text{C}$

Table 14: Example how to calculate the weighted mean annual air temperature.

When the weighted mean annual air temperature is known, the effective asphalt temperature is estimated using figure 70.

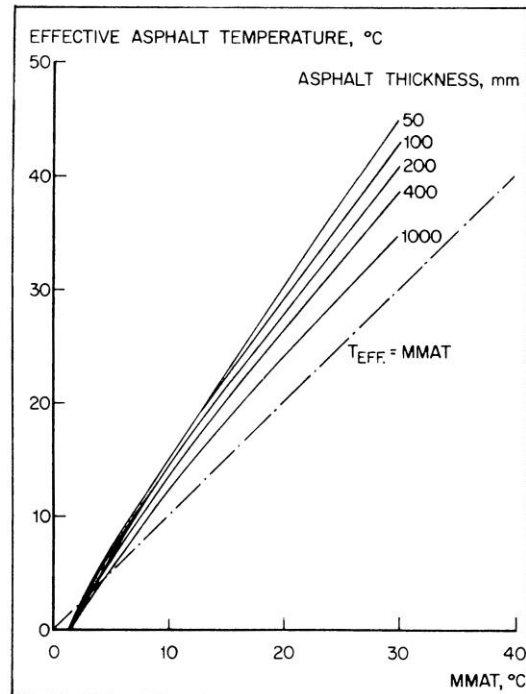


Figure 70: Effective asphalt temperature as a function of MMAT (also w-MAAT can be used) and the asphalt layer thickness.

It should be noted that the Shell procedure described here can be used for the thickness design of asphalt pavements but not for permanent deformation analyses. In those case one should take into account the real temperature distributions.

7.3 Moisture

Moisture has a large effect on the stiffness and bearing capacity of soils and unbound materials and for that reason it is important to qualify and quantify these effects. If no evaporation occurs and there are no changes in the groundwater level, the moisture conditions can be estimated from the suction characteristics of the soil. Figure 71 shows these characteristics for a number of soils.

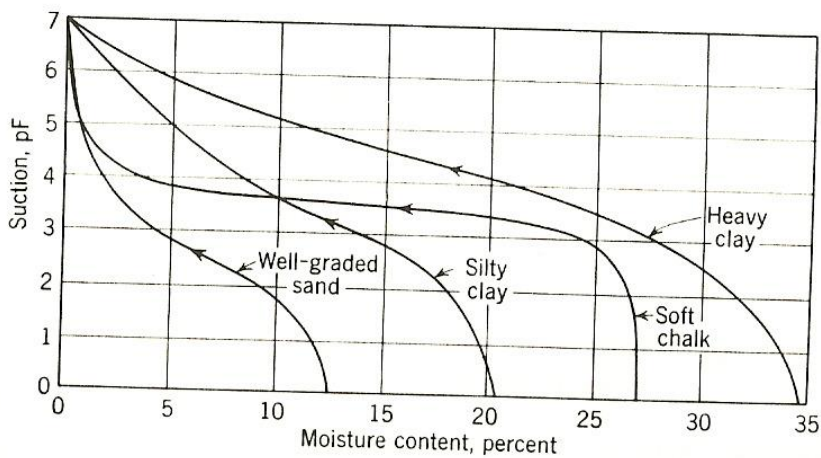


Figure 71: Suction characteristics of various soils.

In figure 71, the suction is given as the \log^{10} of cm of water column. This means that at a $pF = 2$, meaning a suction of 100 cm of water column, the moisture content in a well graded sand is about 8% while in the heavy clay it is 32%. This implies that at a height of 100 cm above groundwater level the moisture content in the sand equals 8% and 32% in the clay. It will be clear from the discussion so far that the pF curve provides very important information for estimating the moisture content above the groundwater level. From the figure it becomes clear that if evaporation is prevented and the groundwater level is 10m below the ground level, the moisture content near the surface of a heavy clay is still 27% (10 m above groundwater level = 1000 cm above groundwater level, read the graph at $pF = 3$). All this means that in this case a rather stable moisture profile develops above the groundwater level.

In case we have a 5m thick well graded sand on top of a heavy clay and the groundwater level would be 10m below the surface, then the moisture content at the top of the sand layer would be 4% (read moisture content at $pF = 3$). At 5m below the surface, the moisture content at the top of the clay would be 28% and at the bottom of the sand layer 5.5 (read pF curves at $pF = \log 500 = 2.7$).

Of course the moisture profile is more complex in reality because of drying or wetting of the top part of the soil. This is schematically shown in figure 72.

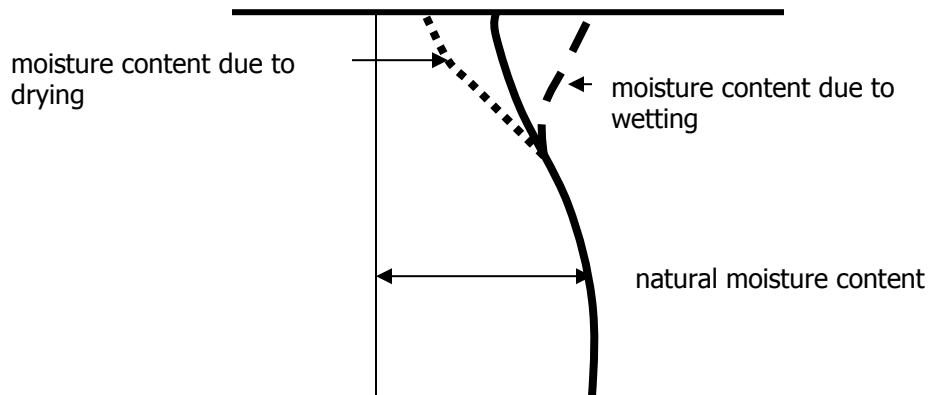


Figure 72: Moisture content variations due to drying and wetting.

Similar conditions occur in the pavement shown in figure 73

Figure 73 nicely shows that the zone of moisture variation, and so the zone of variation in bearing capacity and stiffness, can coincide with the area in which the outer wheels of trucks and lorries are loading the pavement. Especially during the wet period this can give rise to significant pavement problems because in that period the bearing capacity of the soil will be low (because of wetting) at locations where the stresses due to traffic are the highest. Also in the dry season this can create problems especially when the subgrade shrinks due to moisture loss. Shrinkage near the pavement edge can result in longitudinal cracks in the pavement near the pavement edge.

It has however been shown that moisture variations are almost negligible at a distance of approximately 1.2 m from the pavement edge. This implies that if a paved shoulder is applied having a width of 1.2 m or more, the zone that is influenced by the traffic loads doesn't coincide with the zone subjected to seasonal moisture variations.

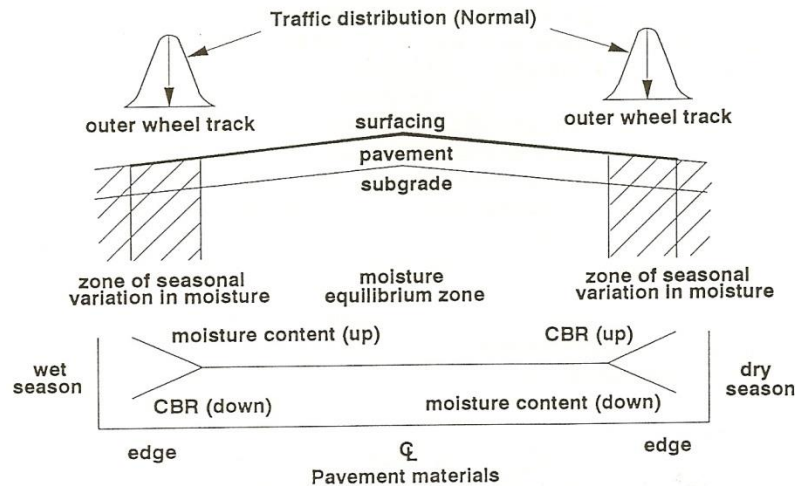


Figure 73: Variation in moisture content occur near the pavement edge.

A typical example of pavement damage that occurs due to drying of the soil is shown in figure 74.

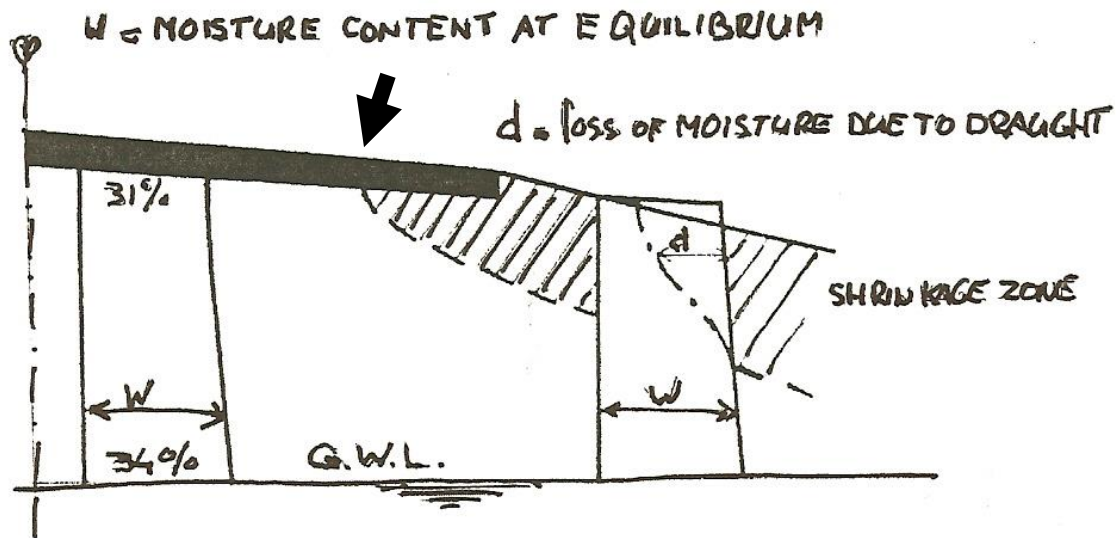


Figure 74: Due to an extended dry period, the subgrade under the pavement edge started to shrink resulting in significant cracking at location of the arrow.

Figure 74 was made when making a study of extensive longitudinal cracking in the verge and in the pavement near the edge observed in several roads in Surinam after an extended period of draught.

Figure 75 shows the changes that occurred in the groundwater level near a polder road with a peat subgrade in the Netherlands after a relatively hot and dry summer. The draught problem became severe because of the presence of willows near the pavement edge. These types of trees are "heavy drinkers" and lowered the groundwater level even further resulting in excessive shrinkage and cracks in the pavement.

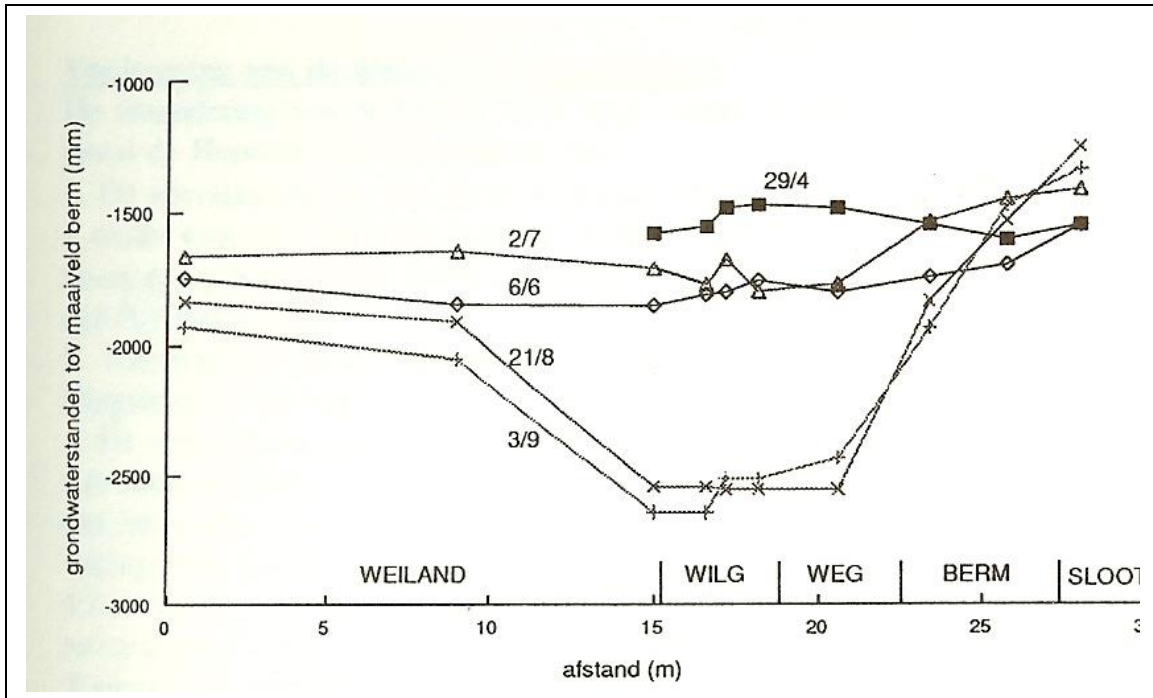


Figure 75: Changes in the transverse profile of a polder road due to shrinkage of the peat subgrade due to moisture loss in a hot and dry summer and the presence of poplars and willows.

Note: 1. the numbers on the lines give the dates (day/month),
 2. weiland = grass land, wilg = willow, weg = road, berm = verge, sloot = ditch,
 3 vertical axis shows depth of ground water level measured from the top of the pavement.

Although it is clear that suction curves are extremely useful for the determination of moisture profiles, those curves are not readily available. Determination of soil suction in the laboratory is a time consuming test that has to be performed with great precision. If such curves are not available, soil suction of fine grained soils may be estimated by means of the equations given below which were reported by Saxton e.a. [30].

$$\psi = 100 A \theta^B$$

Where: ψ = water potential or matrix suction [kPa],

θ = volumetric moisture content [m^3 / m^3],

For $10 < \psi < 1500$ kPa

A = $\exp [-4.396 - 0.0715 C - 4.880 \cdot 10^{-4} S^2 - 4.285 \cdot 10^{-5} S^2 C]$

B = $-3.140 - 2.22 \cdot 10^{-3} C^2 - 3.484 \cdot 10^{-5} S^2 - 3.848 \cdot 10^{-5} S^2 C$

S = percentage sand being all particles between 2 mm and 50 μm ,

C = percentage clay being all particles smaller than 2 μm .

For the Mechanistic Empirical Design System developed for AASHTO a set of equations was developed to determine the relationship between suction "h" in psi and the volumetric water content θ_w . These equations, taken from [31], are presented below.

Keep in mind that the *volumetric* moisture content is needed as input. This means that the optimum moisture content which is obtained from the moisture – density relationship determined with the Proctor test (which is a mass %) needs to be translated from a moisture content by mass into a volumetric moisture content

$$\theta_{\text{opt}} = w_{\text{opt}} \gamma_{\text{dmax}} / \gamma_{\text{water}}$$

$$\begin{aligned} S_{opt} &= \theta_{opt} / [1 - \gamma_{dmax} / (\gamma_{water} G_s)] \\ \theta_{sat} &= \theta_{opt} / S_{opt} \end{aligned}$$

Where:

w_{opt} = the optimum moisture content as determined by means of the Proctor test,
 γ_{dmax} = maximum dry density determined by means of the Proctor test,
 G_s = specific weight of the solids.

$$\theta_w = C(h) * [\theta_{sat} / [\ln [\exp(1) + (h / a_f)^{b_f}]]^{c_f}]$$

$$C(h) = 1 - [\ln (1 + h / h_r) / \ln (1 + (1.45 * 10^5 / h_r))]$$

Where h = suction in [psi]

The coefficients in the equation are calculated in the following way

a. If $P_{200} * PI > 0$

$$a_f = [0.00364 * (P_{200} * PI)^{3.35} + 4 * (P_{200} * PI) + 11] / 6.895$$

$$b_f / c_f = -2.313 * (P_{200} * PI)^{0.14} + 5$$

$$c_f = 0.0514 * (P_{200} * PI)^{0.465} + 0.5$$

$$h_r / a_f = 32.44 * e^{0.0186(P_{200}*PI)}$$

b. If $P_{200} * PI = 0$

$$a_f = 0.8627 * (D_{60})^{-0.751} / 6.895$$

$$b_f = 7.5$$

$$c_f = 0.1772 * \ln D_{60} + 0.7734$$

$$h_r / a_f = 1 / (D_{60} + 9.7 * e^{-4})$$

$$[a_f, h_r] = [\text{psi}]$$

P_{200} = percentage passing the no.200 sieve [not in % but in decimal!]

PI = plasticity index

D_{60} = effective grain size corresponding to 60% passing by weight

Reference [31] mentions that P_{200} and D_{60} can be determined from a grain-size distribution test according to AASHTO T27. In table 15 the sieve sizes used in AASHTO T27 as well as the sizes in [mm] are shown. In [31] it is not specified whether the D_{60} is specified in [mm] or [inches] but it is assumed that it is in [mm] because this unit is used in figure 76 which is taken from [31].

When direct measurements of w_{opt} , γ_{dmax} , and G_s are not made they can be estimated following relationships.

$$G_s = 0.041 * (P_{200} * PI)^{0.29} + 2.65$$

$$S_{opt} = 6.752 * (P_{200} * PI)^{0.147} + 78$$

If $P_{200} * PI > 0$ then $w_{opt} = 1.3 * (P_{200} * PI)^{0.73} + 11$

If $P_{200} * PI = 0$ then $w_{T99} = 8.6425 * (D_{60})^{-0.1038}$

If the layer is not a base course then $w_{opt} = w_{T99}$

If the layer is a base course then $w_{opt} = w_{T99} - \Delta w_o$

$\Delta w_o = 0.0156 * w_{T99}^2 - 0.1465 * w_{T99}$

$\gamma_{d \text{ max comp}} = G_s * \gamma_{\text{water}} / (1 + w_{opt} * G_s / S_{opt})$

If the layer is a compacted material $\gamma_{d \text{ max}} = \gamma_{d \text{ max comp}}$

If the layer is a natural in-situ material $\gamma_d = 0.9 * \gamma_{d \text{ max comp}}$

One comment should be made with respect to the units to express suction. In the past it was common practice to express suction pF in terms of the log of the water head "h" expressed in [cm].

So: $pF = \log h$ and with 100 cm water head pF would be: $pF = \log 100 = 2$.

Later on suction was expressed in [kPa] or [psi]. This is how suction is expressed in the equations given above. Some relations to translate the one unit into the other are given below.

Suction [kPa] = $0.098 * e^{2.30267 pF}$

kPa = $0.098 * [\text{cm waterhead}]$

Sieve Size in (mm)	
3½	(90)
3	(75)
2½	(63)
2	(50)
1½	(37.5)
1	(25.0)
¾	(19.0)
⅝	(16.0)
½	(12.5)
⅜	(9.5)
¼	(6.3)
No. 4	(4.75)

Table 15: Sieve sizes used in AASHTO T27.

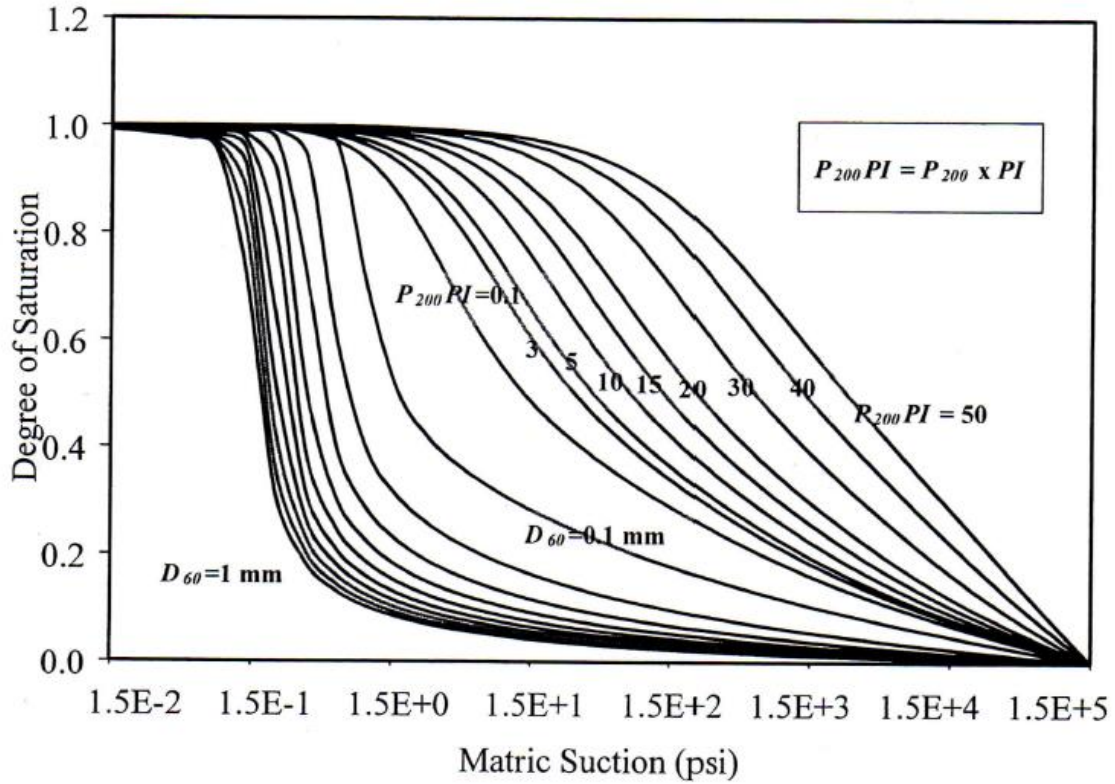


Figure 76: Degree of saturation in relation to matric suction D_{60} , P_{200} and PI .

Côté and Konrad presented an elegant procedure to estimate the hydraulic characteristics of unsaturated base-courses [32]. They used a schematized representation of the suction curve as shown in figure 77. The three most important parameters in this figure are θ_s (saturated volumetric water content which is equal to the porosity of the soil n), ψ_a (air entry value) and the slope of the curve λ (pore size distribution index). These parameters can be estimated using the following equations.

$$\log \psi_a = 3.92 - 5.19 n_f$$

Where: ψ_a = air entry value [kPa],
 n_f = porosity of the fine fraction = n / n_c ,
 n_c = porosity of the coarse fraction = $n + (1 - n) F$,
 n = porosity of the entire skeleton including coarse and fine fraction = $1 - \rho_d / \rho_s$,
 ρ_d = dry density [kg/m^3],
 ρ_s = density of the particles [kg/m^3],
 F = fines content (particles smaller than $50 \mu\text{m}$) [%].

$$\lambda = 0.385 - 0.021 n_f^{0.65} S_{sf}$$

Where: S_{sf} = specific area of the fines fraction (to be determined in the laboratory) [m^2/g].

As a crude estimation, the specific surface area can be calculated from the grain size following

$$\log S_{sf} = -1.4657 \log d - 5.7402 \text{ with } [S_{sf}] = [\text{m}^2/\text{g}] \text{ and } [d] = [\text{m}]$$

Also the saturated hydraulic conductivity, $k_{s,r}$, can be estimated using:

$$\log (k_s * S_{sf}) = 9.94 n_f - 12.64 \quad [k_s] = [m / s]$$

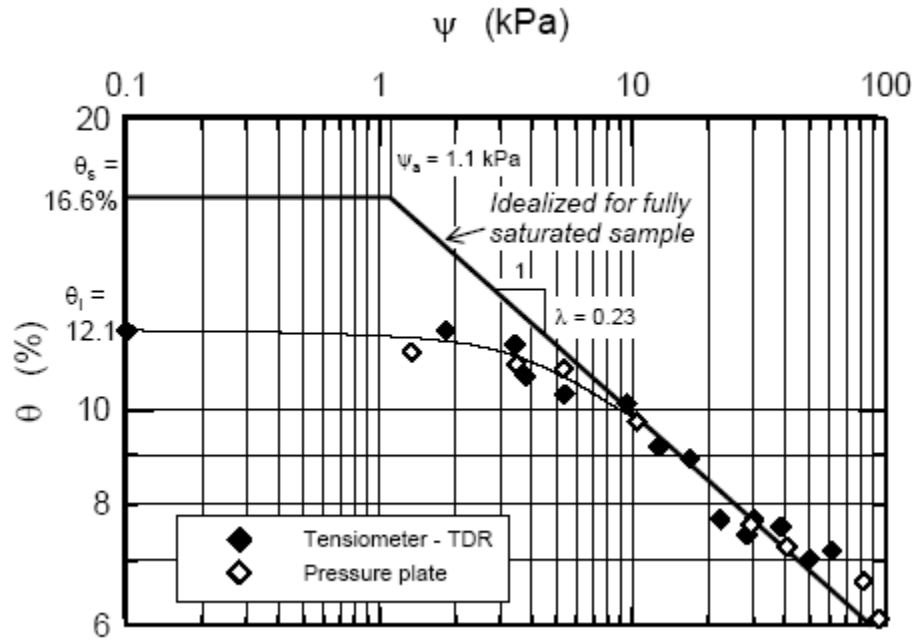


Figure 77: Idealized suction curve according to Côté and Konrad.

Although techniques are available to estimate the equilibrium moisture content using soil suction information, the equilibrium moisture content is also quite often estimated from regression equations developed from field observations. Examples of such equations [135] are given hereafter.

Unbound subgrade:

$$EMC / OMC = 0.0084 LL^{0.7} P_{0.425}^{0.3} + 0.34 \ln (100 + Im) + 0.11 P_{75} / OMC - 0.0036 P_{0.425} - 0.89$$

Non plastic subgrade:

$$EMC / OMC = 0.19 P_{75} / OMC + 0.0040 Im - 0.0036 P_{0.425} + 0.53$$

Where: EMC = equilibrium moisture content [%],
 OMC = optimum moisture content determined by means of the modified Proctor test,
 LL = liquid limit [%],
 $P_{0.425}$ = percentage passing the 0.425 mm sieve,
 P_{75} = percentage passing the 75 μ m sieve,
 Im = Thornthwaite moisture index.

$$Im = 100 * P / PET - 1$$

Where: P = annual precipitation [mm],
 PET = potential annual evaporation [mm].

PET is calculated following:

$$PET = \sum_{i=1}^{12} MPET$$

Where D_i = daylength correction factor for month I,
 N_i = number of days in month i.

$$\begin{aligned} \text{MPET} &= 16 * [10 * T_i / \text{TE}]^a \text{ [mm/month]} \\ a &= 6.75 * 10^{-7} * \text{TE}^3 - 7.71 * 10^{-5} * \text{TE}^2 + 1.792 * 10^{-2} * \text{TE} + 0.49239 \\ \text{TE} &= {}_1\Sigma^{12} (T_i / 5)^{1.514} \end{aligned}$$

Where: T_i = mean air temperature in month i [$^{\circ}\text{C}$]

Typical values for Thornthwaite moisture index are given in table 16.

Thornthwaite Index			Climate classification
	Im	>100	peri-humid
20<	Im	<100	humid
0<	Im	<20	moist sub-humid
-20<	Im	<0	dry sub-humid
-40<	Im	<-20	semi-arid
	Im	<-40	arid

Table 16: Typical Thorthwaite Index values.

It is suggested to use the unsoaked CBR values for subgrade design if $\text{EMC} / \text{OMC} < 1.7$.

8. Asphalt mixtures

8.1 Introduction




Asphalt concrete is a mixture of aggregates (very often crushed aggregates), sand, fines or filler and bitumen. We will not discuss in these notes the types of asphalt mixtures, and the production, laying and compaction of asphalt mixtures. The reader interested in those topics is referred to e.g. [134]. In this chapter we will focus on the mechanical characteristics of asphalt concrete which need to be known in order to be able to design the thickness of a flexible pavement. These characteristics are the stiffness of the mixture as well as its resistance to fatigue and permanent deformation. In this chapter we will discuss extensively how information on these characteristics can be obtained, which tests need to be done and which techniques are available to estimate these parameters from simple indicators like volumetric composition of the mixture and the characteristics of the bituminous binder.

The binder properties have a huge effect on the mixture properties so ample attention will be paid to the assessment of the binder properties. These properties are dependent on the type of bitumen, on temperature and loading time, and on climatic conditions in general which affect the level of aging (hardening) of the bituminous binder.

Although volumetric composition and binder characteristics do have a huge effect on the mixture properties, one should never forget that also the interaction between the aggregates and the bituminous binder is very important especially when it comes to the resistance of the mixture to water (as fluid and vapor). Therefore attention will also be paid to the factors that control the adhesion between the bituminous binder and the aggregates.

Before we discuss how to obtain information on mixture stiffness and resistance to fatigue and permanent deformation etc a short presentation will be given about similarities between soils and asphalt mixtures. Let us recall the three basic soil structures which are shown in figure 78.

Three physical states of soil aggregate mixtures

A	B	C
		
High stability when confined	High stability when confined	High stability when confined AND dry
No cohesion	High cohesion when dry	High cohesion when dry, low when wet
High angle of internal friction	High angle of internal friction	No angle of internal friction when wet
Not affected by moisture conditions	Moderately affected by moisture conditions	Greatly affected by moisture conditions
Very difficult to compact	Moderately difficult to compact	Not difficult to compact at right moisture level

TU Delft

Figure 78: Three basic soil structures.

Not only soils but also asphalt mixtures can be categorized in these three groups. Structure A is typical for a stone skeleton mixture like porous asphalt concrete while structure C is typical for a mastic type of asphalt concrete.

In case of soils, the binder (being the fine material) plays an important role and the characteristics of the fines are dependent on the type of fines and the moisture content. The type of fines are characterized by means of the liquid limit (LL) and the plastic limit (PL) which are in fact parameters indicating the viscosity of the soil/water mixture. The moisture content determines whether the fines are behaving more like a solid or more like a fluid.

In asphalt concrete the "fine fraction" (the binder) is formed by the mastic which is the mixture of bitumen with the fine aggregate fraction ($< 72 \mu\text{m}$). The characteristics of the mastic are highly influenced by the viscosity characteristics of the bitumen. Temperature and loading time determine whether the bitumen and so the mastic behaves more like a fluid or more like a solid. The analogy between soils and asphalt concrete is therefore as follows:

Soils	Asphalt concrete
Fines	Mastic
Plasticity characteristics	Viscosity characteristics
Moisture	Temperature and loading time
Confinement is important	Confinement is important

All this means that if one has a good understanding of the behavior of soil structures one also has a basic understanding of the behavior of asphalt mixtures.

8.2 Mixture stiffness

8.2.1 Mixture stiffness determined by means of testing

Repeated load tests are needed to obtain the stiffness characteristics of asphalt mixtures in relation to the loading time and temperature. Tests which are suitable to determine the mixture

stiffness are the 2 point, 3 point and 4 point bending test, the tension test, the tension – compression test and the indirect tension test; figure 79 is showing some of these tests.

Figure 79. doesn't show the triaxial test but that certainly doesn't mean that this test is considered to be of less importance. It is true that the triaxial test is a bit more complex than the tests shown in figure 79 but it is an essential test when mixture characteristics need to be determined at higher temperatures and longer loading times and in cases when the mixture is subjected to a 3D compressive stress field. Such conditions occur in the top layer of the pavement under slow moving traffic and high temperatures. Since at those conditions the bituminous binder has a limited stiffness, most of the "strength" of the mixture has to be "delivered" by the aggregate skeleton which, as we know from our classes on soils and aggregates, is very much dependent on the amount of confinement. It will be clear from this description that the triaxial test is a very important one in characterizing the permanent deformation resistance of asphalt mixtures. The triaxial test will therefore be discussed extensively in the section on permanent deformation.

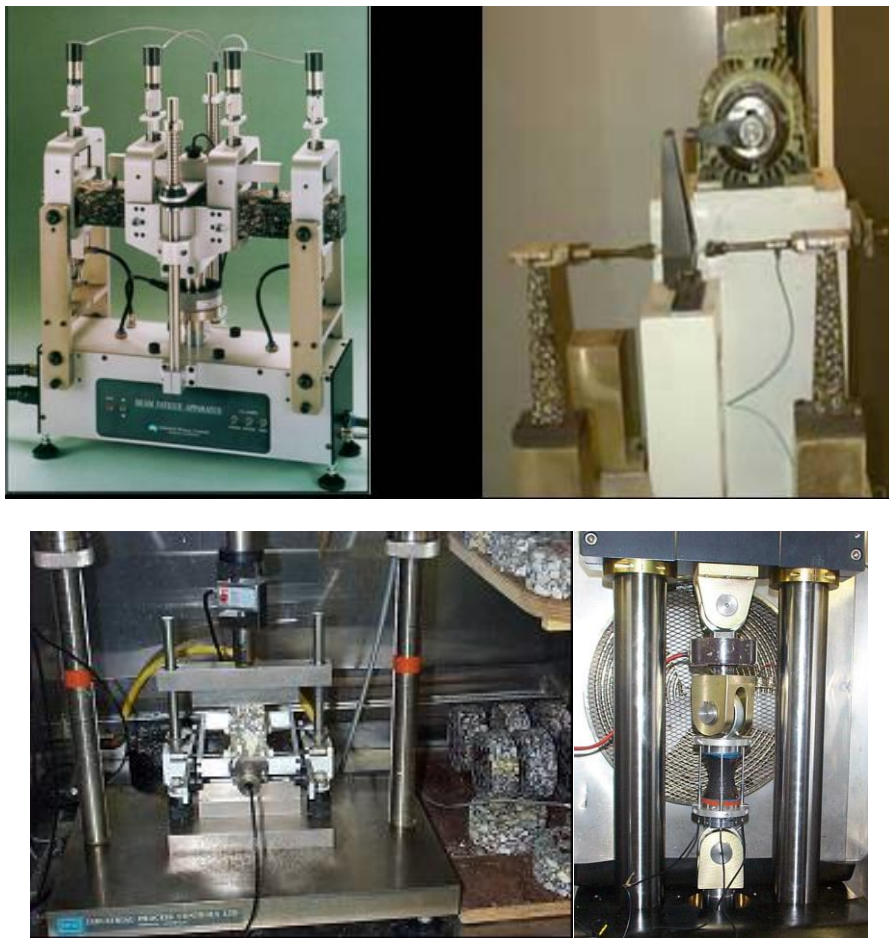


Figure 79: Examples of tests to determine mixture stiffness. Upper left: 4 point bending test. Upper right: 2 point bending test. Lower left: indirect tension test. Lower right: direct tension test.

Figure 80 is showing the response of beam or tension – compression test specimen when subjected to a sinusoidal load signal. One clearly observes a time lag θ (phase angle) between the load a displacement signal. This is caused by the visco-elastic behavior of the asphalt mixture.

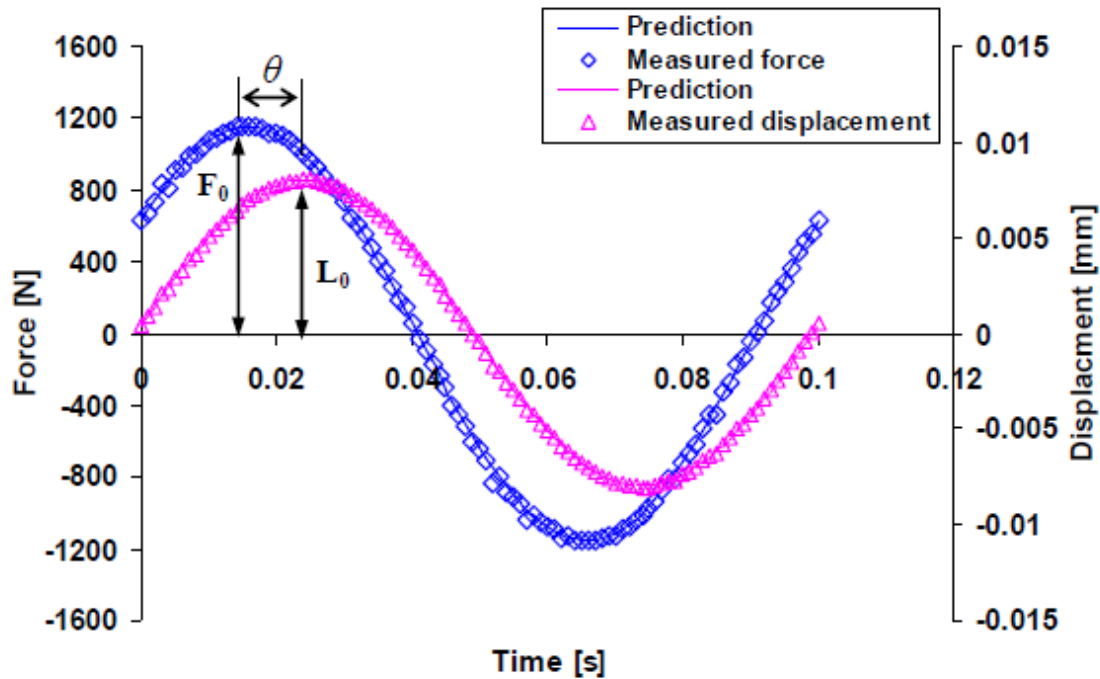


Figure 80. Displacement response observed in a tension – compression test when the specimen is subjected to a sinusoidal load signal.

The question now is why asphalt mixture is showing a visco-elastic behavior. This is because the bituminous binder is a visco-elastic material. It behaves like a fluid, as a viscous material, at high temperatures (this property is very important because it allows us to mix the aggregates with the bitumen) and as a solid, as an elastic material, at low temperatures. In between the material behaves visco-elastically. This will be discussed in more detail when discussing the time – temperature dependency of the bitumen stiffness.

Figure 81 is an example of the dependency of mixture stiffness on loading time and temperature as determined by means of the 4 point bending test. Figure 81 tells us that the stiffness of the mixture decreases with increasing loading time and with increasing temperature. The loading time/temperature dependency of the asphalt stiffness is of course caused by the bitumen which is a fluid at high temperatures and a solid at low temperatures.

The figure also shows that a master curve for the mixture stiffness at 15 °C has been developed. This master curve shows the relation between mixture stiffness at a particular temperature and the loading time over a very large loading time range. It is constructed by moving the stiffness vs loading time relations obtained at different temperature horizontally such that a continuous stiffness vs loading time curve at 15 °C is obtained. Several computational techniques are available for construction of master curves such as the Arrhenius equation and the Williams – Landel – Ferry (WLF) equation. This will be described in more detail when discussing the loading time/temperature dependency of the bitumen stiffness.

Also the phase angle shows a dependency on loading time and temperature. At low temperatures when the bitumen is a solid and behaves elastically, the phase angle will be zero. At those conditions the maximum value for the stiffness of the asphalt mixture will be obtained. Figure 82 shows, as an example, the master curves for the mixture stiffness and phase angle at 20 °C as determined for a particular mixture.

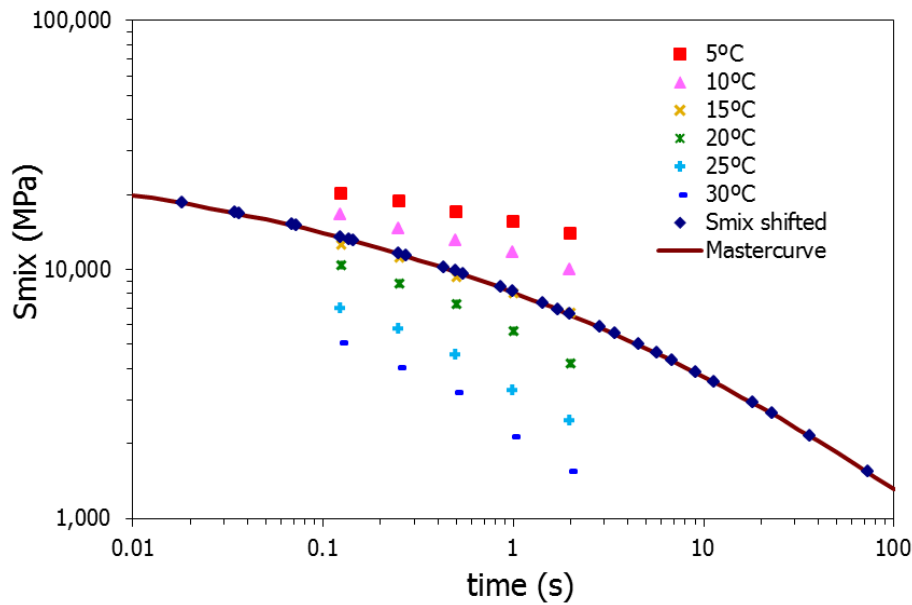


Figure 81. Example of the relation between mixture stiffness, temperature and loading time.

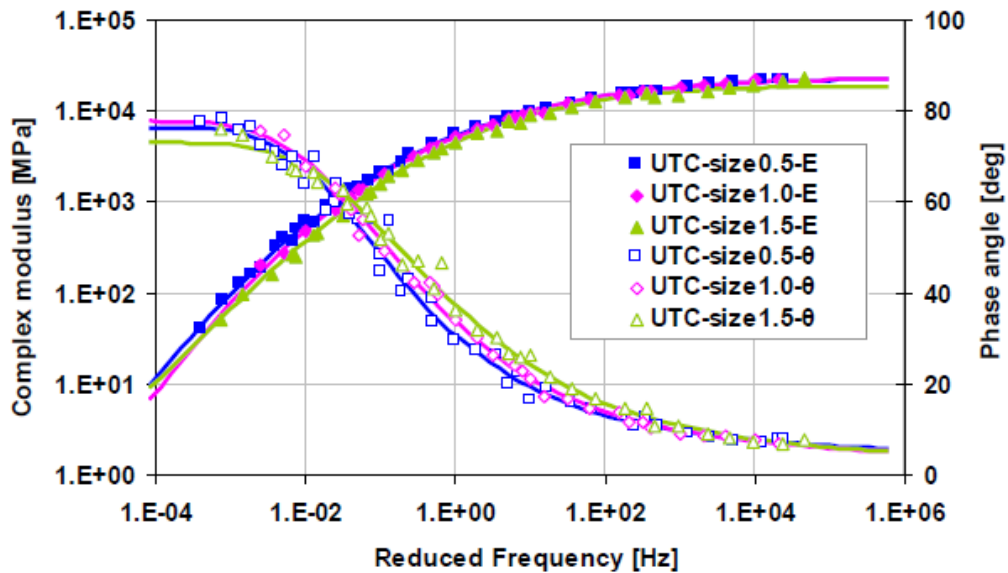


Figure 82. Master curves for mixture stiffness and phase angle at 20 °C as determined by means of the uniaxial tension – compression (UTC) test for a particular mixture using different specimen sizes indicated with "size 0.5" etc.

Figure 82 [41] shows that there was no specimen size effect (meaning the results were not affected by the dimensions of the specimen) when determining the mixture stiffness with the UTC test. It was furthermore shown in [41] that there was also no specimen size effect on the mixture stiffness when determined with the 4 point bending test or the indirect tension test.

In our stress and strain analyses we normally assume that the asphalt mixtures behave like isotropic materials; this however can be disputed. Especially in case of coarse grained mixtures and the presence of flaky aggregates (aggregate particles are never perfect spheres) it can very

well be that the asphalt mixture should be treated as an anisotropic material which implies that the stiffness in the vertical direction differs from the stiffness in the horizontal direction. It will be clear that anisotropic behavior can very well be further "enhanced" during compaction. In a pavement, compaction is in the vertical direction forcing somewhat elongated particles to lay flat. All these effects might also cause differences in properties between laboratory and field compacted specimens.

Figure 83 [41] shows the stiffness modulus of a particular mixture in relation to test type, temperature, loading time and specimen size. The mixture was a dense asphalt concrete mixture which is used for wearing courses. The maximum grain size was 8 mm and it contained 6.5% bitumen by mass of a 45 pen bitumen. It was compacted with a shear box compactor (figure 84) to a design void content of 4%. In this way blocks with dimensions of 450 * 160 * 150 mm were produced from which specimens were cut.

From figure 83 one can conclude that the differences in mixture stiffness determined with the 4 point bending tests and UTC test are small and, as mentioned before, also the effect of specimen size is negligible. At lower temperatures (e.g. 10 °C) the differences between the modulus values obtained with the indirect tension test and those determined with the other test methods are also very small. At higher temperatures the stiffness values as determined with the indirect tension test is clearly lower than those determined with the other two test methods. This might be due to the differences in stress conditions between the indirect tension test and the other two test methods.

Strain (or stress) dependency of the mixture stiffness was shown by Medani [121] in his research on the performance of wearing courses for steel bridge decks. Figure 85 shows the stiffness master curve of a mastic asphalt concrete in relation to the applied strain level. The maximum grain size used in this mixture was 8 mm, it contained 8.8% SBS modified bitumen and the void content was 1.5%.

Figure 85 shows that at 20 °C the strain dependency of the mixture stiffness appears to be higher at lower frequencies. This also implies that the strain dependency increases with increasing temperature since a higher temperature has the same effect on the stiffness of bituminous mixtures as a lower loading frequency (longer loading time).

At 0.5 Hz this dependency could be written as:

$$S_{mix} = 4169 \varepsilon^{-0.386}$$

While for the 10 Hz data the dependency could be written as

$$S_{mix} = 2389 - 0.953 \varepsilon$$

In both equations S_{mix} is the mixture stiffness in [MPa], ε is the applied tensile strain in the 4 point bending test in [$\mu\text{m}/\text{m}$].

These results indicate that it is wise to do modulus testing at several strain levels especially if fairly high strain levels and temperatures are to be expected in the asphalt mixture.

The stress/strain dependency of the asphalt mixture stiffness will be discussed in greater detail when discussing the resistance to permanent deformation.

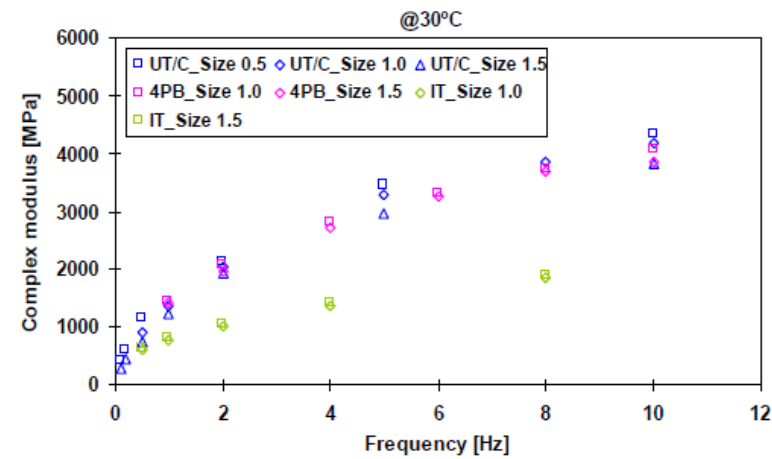
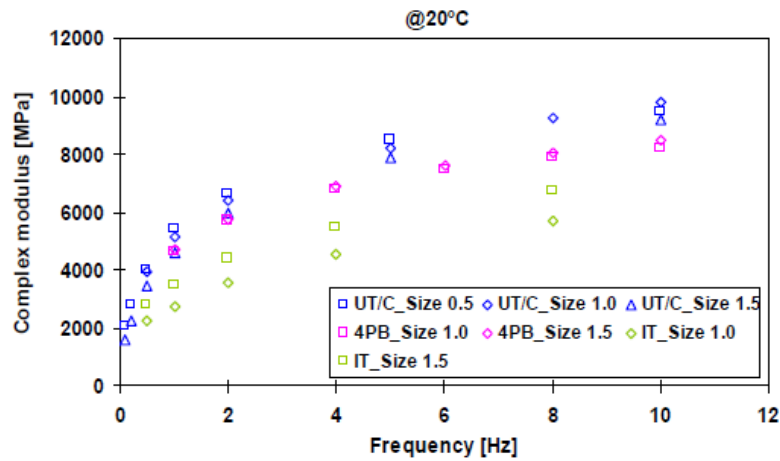
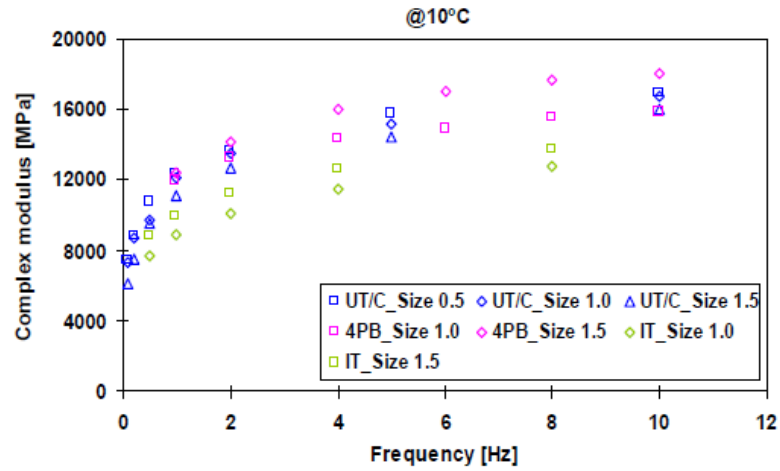


Figure 83. Mixture stiffness in relation to temperature, loading time and test type



Figure 84a. Shear box compactor.

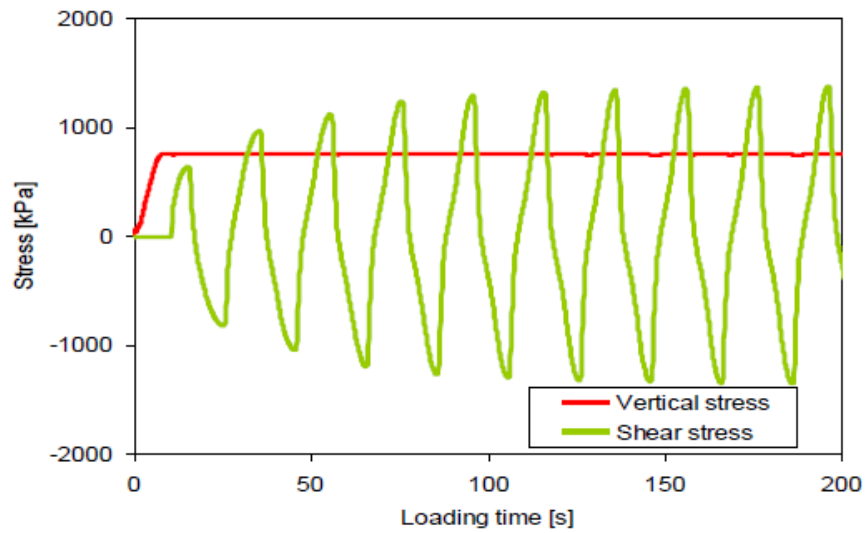


Figure 84b. Stresses applied on the specimen during compaction with the shear box compactor

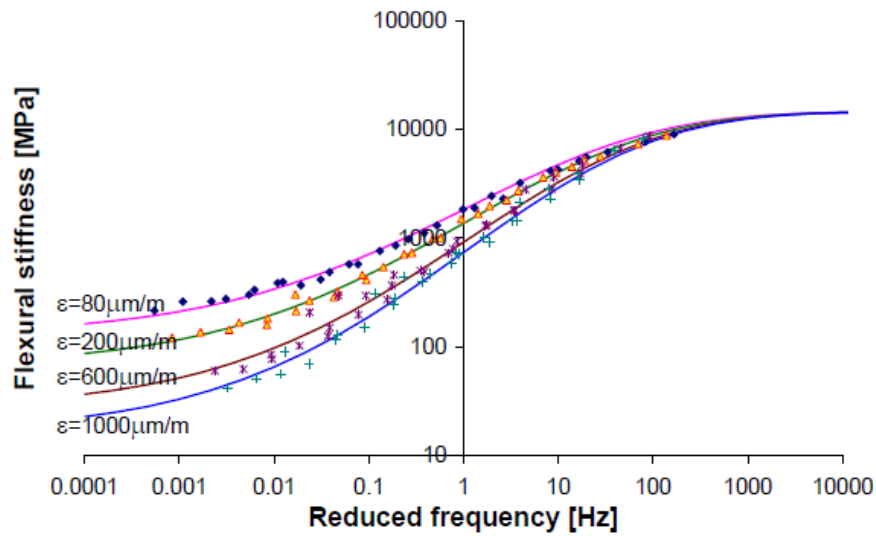


Figure 85. Strain dependency of the mixture stiffness at 20 °C [121].

8.2.2 Mixture stiffness determined with nomographs and equations

If testing of the mixture is too cumbersome, one can estimate the mixture stiffness by using one of the available nomographs to predict the mixture stiffness from the bitumen stiffness and the volumetric composition. Examples of such nomographs are those developed by Shell (figure 86 [33]) and the one developed by the Belgian Road Research Centre (figure 87 [34]). The bitumen stiffness can be obtained from direct tension tests as was done by Shell and by e.g. dynamic shear rheometer tests (figure 88) that give the stiffness of the bitumen in relation to the loading time and temperature.

When a tension test is performed on a bitumen sample we can calculate its stiffness from

$$E_{t,T} = \sigma / \varepsilon_{t,T}$$

Where: $E_{t,T}$ = modulus as a function of temperature and loading time
 σ = applied stress
 $\varepsilon_{t,T}$ = deformation as a function of temperature and loading time

The time/temperature dependency plays a role because bitumen is a solid at short loading times and low temperatures and is a fluid at high temperatures and long loading times. This behavior also makes the stiffness of the asphalt mixture dependent on temperature and loading time (see e.g. fig 81).

Because of the loading time/temperature dependency of E , Shell decided not to use the symbol "E" but to replace it by S_{bit} to characterize the bitumen stiffness and S_{mix} to characterize the mixture stiffness.

The bitumen stiffness can also be determined using a dynamic shear rheometer test (figure 88) but keep in mind that such a test will provide a complex shear modulus G^* which is not the same as S_{bit} used in the Shell nomograph. The relation between S_{bit} and G^* can be written as:

$$G^* = S_{bit} / 2 (1 + \mu) \text{ where } \mu \text{ is Poisson's ratio}$$

The equations from which the Shell nomograph (figure 86) has been derived are as follows.

$$\log S_{mix} = \{(\beta_4 + \beta_3) / 2\} * (\log S_{bit} - 8) + \{(\beta_4 - \beta_3) / 2\} * |\log S_{bit} - 8| + \beta_2$$

$$[S_{mix}, S_{bit}] = [\text{Pa}]$$

$$\beta_1 = 10.82 - [1.342 * (100 - V_g)] / (V_g + V_b)$$

$$\beta_2 = 8 + 0.00568 * V_g + 0.0002135 * V_g^2$$

$$\beta_3 = 0.6 * \log [(1.37 * V_b^2 - 1) / (1.33 * V_b - 1)]$$

$$\beta_4 = 0.7582 * (\beta_1 - \beta_2)$$

V_g = volume percentage of aggregates (stone + sand + fines) [%]

V_b = volume percentage of bitumen [%] (this is the effective binder content)

Figure 87 shows that according to the Belgian Road Research Centre, the modulus of the mixture can be determined from G^* of the bitumen, the ratio V_g / V_b and E_∞ . E_∞ is the maximum modulus an asphalt mixture can obtain and can be determined from:

$$E_{\infty}(V_b, V_a) = 14360 * (V_g / V_b)^{0.55} * e^{(-0.0584 * V_a)} \quad [E_{\infty}] = [\text{MPa}]$$

V_b = volume percentage bitumen [%]

V_g = volume percentage of aggregates [%]

V_a = void content

Finally also the so called Hirsch model [35] is presented; it is shown in figure 89. Also this model shows that the stiffness of the bitumen and the volumetric composition of the mixture control the stiffness of the asphalt mixture. At the bottom of figure 89 it is mentioned that the gradation doesn't play a role in the prediction of the modulus of the asphalt concrete. This comment was made because in the prediction model that is proposed to be used in AASHTO's MEPD [31] also the gradation is taken into account. This model will not be discussed here since it doesn't result in better predictions.

One aspect should be especially mentioned which is the value of the bitumen stiffness which is used in the nomographs and equations. This author could not find in the literature whether this value was determined on the bitumen before mixing or whether the bitumen stiffness was determined on bitumen samples retrieved from the completed mixture. This is important to know because during mixing with the hot aggregates (at around 180 °C) significant hardening of the bitumen can occur making the mixture stiffer. These hardening effects will be discussed in the section on "bitumen stiffness".

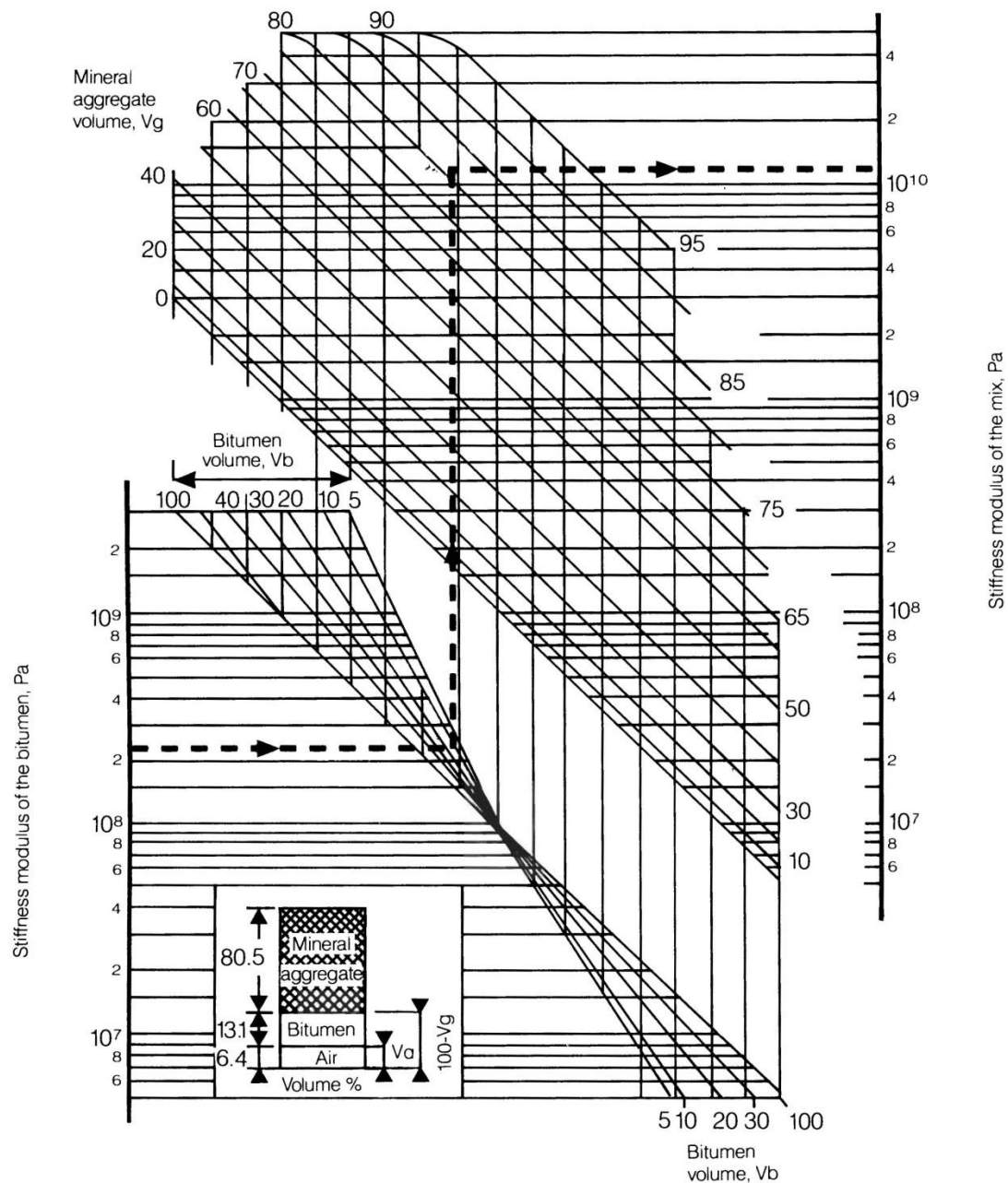
It is therefore strongly recommended that the effect of hardening during mixing on the stiffness of the bitumen is taken into account when using the nomographs and equations to predict the mixture stiffness using the bitumen stiffness as input.

In conclusion we can state that the stiffness of the asphalt mixture is highly dependent on:

- bitumen stiffness,
- loading time and temperature,
- volumetric composition,

and at higher temperatures and longer loading times (lower load frequencies)

- stress cq strain level.



Example

Stiffness modulus of the recovered bitumen, 2.2×10^8 Pa

V_b : Volume of bitumen, 13.1%

V_g : Volume of mineral aggregate, 80.5%

Stiffness modulus of the mix

1.1×10^{10} Pa

Figure 86: Shell nomograph to predict the stiffness of asphalt mixtures.

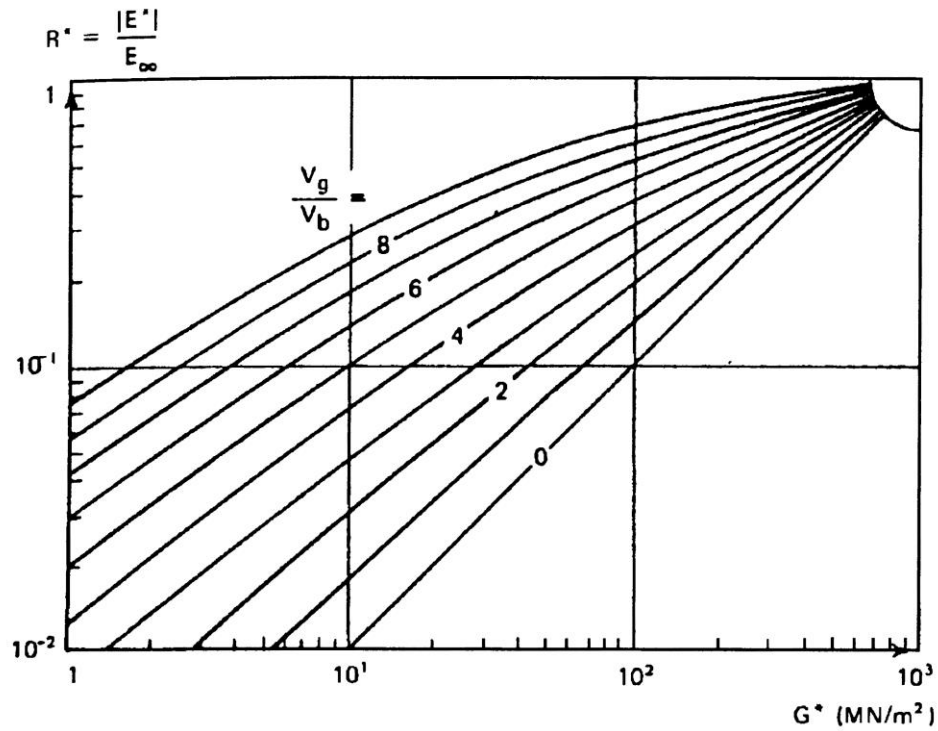


Figure 87: Nomograph of the Belgian Road Research Centre to predict asphalt mixture stiffness.

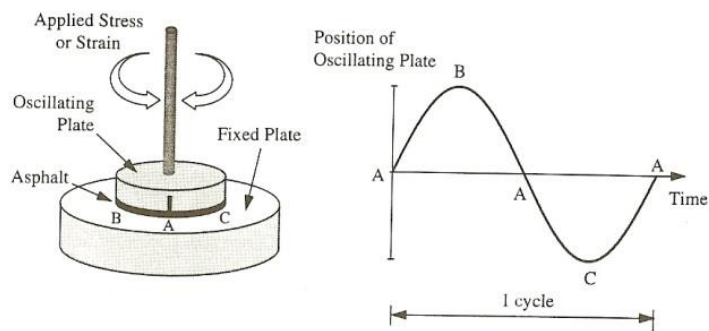


Figure 88: Principle of the dynamic shear rheometer test.

Hirsch model

$$E^* = P_c [4200000 * (1 - VMA/100) + 3G^* * (VFA * VMA/100)] + (1 - P_c) [(1 - VMA/100)/4200000 + VMA/(3VFA * G^*)]^{-1}$$

$$P_c = [(20 + VFA * 3G^*/VMA)^{0.58}] / [650 + (VFA * 3G_b/VMA)^{0.58}]$$

E^* = dynamic modulus [psi]
 G^* = dynamic shear modulus of the binder [psi]
VMA = voids in mineral aggregate skeleton [%]
VFA = voids in aggregate skeleton filled with mastic [%]
 $VFA = 100 (VMA - V_a)/VMA$
 V_a = voids content [%]

Note that gradation is not taken into account

October 11, 2017

47



Figure 89: Hirsch model to predict the modulus of asphalt concrete.

8.3 Bitumen stiffness

We have shown that the stiffness of the asphalt concrete mixture strongly depends on the stiffness of the bitumen and in this section we will extensively discuss the factors that control the stiffness of the bituminous binder. But before we go into detail about the bitumen stiffness and the factors controlling it, first some general information on bitumen will be given as well as ways how to characterize its behavior.

8.3.1 Composition of bitumen

Bitumen is a product resulting from the refinery process of crude oil. Details about this refinery process can be found in [33] and will not be repeated here. As is shown in figure 90, different amounts of bitumen are produced from different types of crude oil.

Bitumen is highly complex in its chemical structure. Although Carbon and Hydrogen are by far the most important elements, C – H chains of different length and molecular weight can be recognized. Figure 91 gives an overview of the chemical composition of some crude oils.

It is common practice to separate the bitumen into several fractions. A common way of separating bitumen is shown in figure 92. In the first step the bitumen is separated in "asphaltenes" and "maltenes", the later one being the solubles. The maltene fraction is then separated into aromatics, resins and saturates.

Bitumen is made of crude oil. Not each crude produces same and same amount of bitumen.

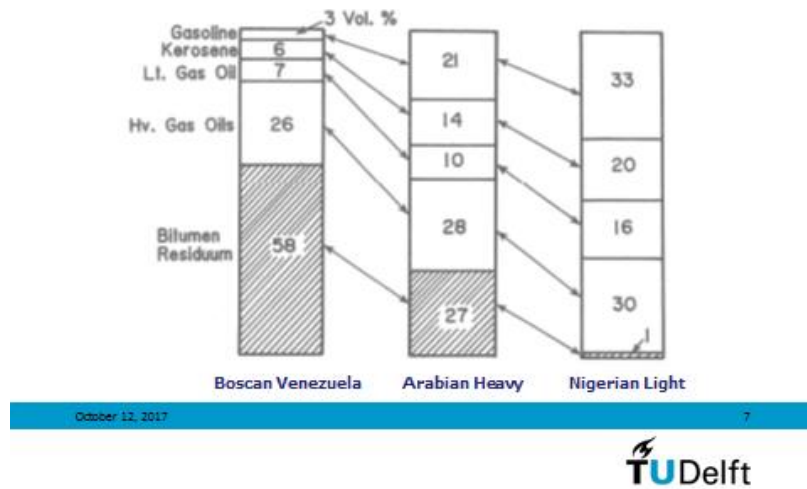


Figure 90: Different amounts of bitumen are produced from different types of crude oil.

Chemical composition of different types of bitumen

Elements	Mexican Blend B-2959	Arkansas-Louisiana B-3036	Boscan B-3051	California B-3602
Carbon %	83.77	85.78	82.90	86.77
Hydrogen %	9.91	10.19	10.45	10.93
Nitrogen %	0.28	0.26	0.78	1.10
Sulfur %	5.25	3.41	5.43	0.99
Oxygen %	0.77	0.36	0.29	0.20
Vanadium ppm	180	7	1380	4
Nickel ppm	22	0.4	109	6

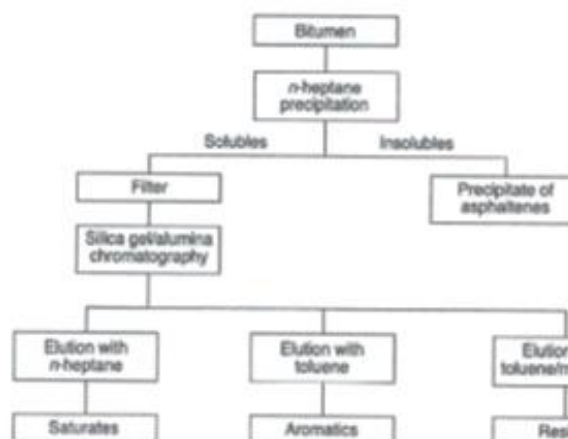
Vanadium content is "fingerprint" of origin of bitumen



Figure 91: Chemical composition of some bitumens.

It should however be noticed that the n-heptane separation technique is just one way of separating the fractions of the bitumen. How the selected separation technique affects the grouping of the various constituents of the bitumen is shown in figure 93. All this implies that if one is given "the composition" of a certain bitumen, one always should ask "how was the composition determined, which procedure was used".

Separation of bitumen into fractions



This is just one way of classifying, other methods give different results

October 12, 2017

10



Figure 92: Separation of bitumen into fractions.

Different methods give different compositions (Q8 70/100)

Column separation		Iatroscan		Clay gel hydrocarbon (Besamusca 2005)	
	% (m/m)		% (m/m)		% (m/m)
Saturates	8.5	Saturates	3.3	Saturates	10.2
Naphthene aromatics	50.7	Aromatics	55.6	Aromatics	46.5
Polar aromatics	30.3	Polars (I)	23.2	Polar components	36.7
Asphaltenes	10.5	Polars (II)	17.9	Asphaltenes	6.6

October 12, 2017

11



Figure 93: Different separation techniques result into different compositions.

Pictures of the different constituents of bitumen are shown in figure 94. As one will observe, the constituents are black, dark brown and colorless.



Figure 94: The various constituents in bitumen.

8.3.2 Characterizing bitumen by means of Pen, $T_{R\&B}$ and PI

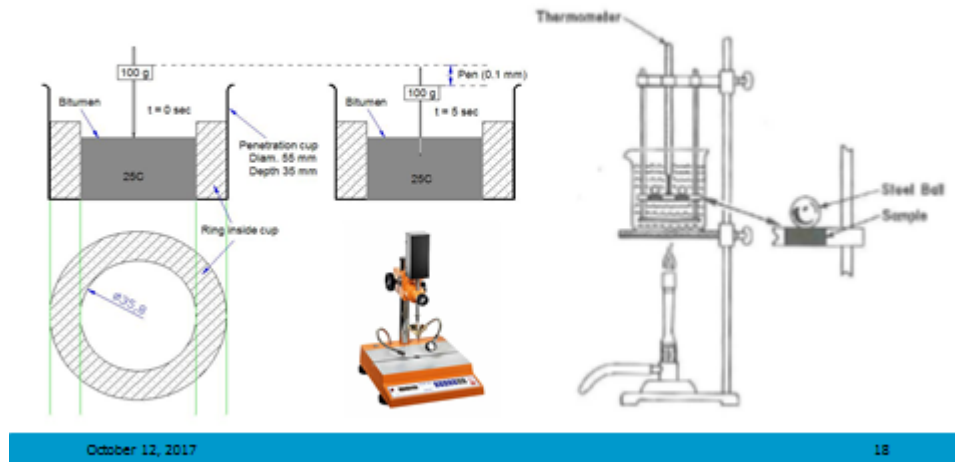
Since bitumens do have such a complex chemical structure, and because its chemical composition is strongly related to its viscosity properties, defining a bitumen by means of its chemical composition is not done; instead bitumens are characterized by means of their viscosity characteristics. At very low temperatures and/or short loading times bitumens behave like a solid and have elastic properties. At high temperatures and/or long loading times bitumens behave like a fluid and are viscous. In between these two extreme conditions bitumen behaves like a visco-elastic material. Two very simple tests are used to characterize the viscosity characteristics of bitumen. They are the "penetration test" and the "ring and ball test". Both tests are schematically shown in figure 95.

In the penetration test a needle, with a specified mass and specified dimensions, is allowed to penetrate the bitumen during a specified time period. The penetration is reported in tenth of a mm (pen 80 = 8 mm penetration). So the "knowns" in this test are the mass and loading conditions, the loading time and the temperature. The "unknown" is the penetration which is to be measured.

In the ring and ball test, a ball of specified dimensions and mass is placed on a layer of bitumen with specified dimensions. The ball will sink through the bitumen layer and the temperature is measured at which a specified distance is travelled by the ball. This temperature is reported as $T_{R\&B}$ or softening point. So the "knowns" in this test are the mass and the loading conditions, the

loading time and the displacement. The “unknown” in this test is the temperature at which the specified displacement is travelled within the specified time.

We characterize viscosity by means of penetration and ring and ball test



October 12, 2017

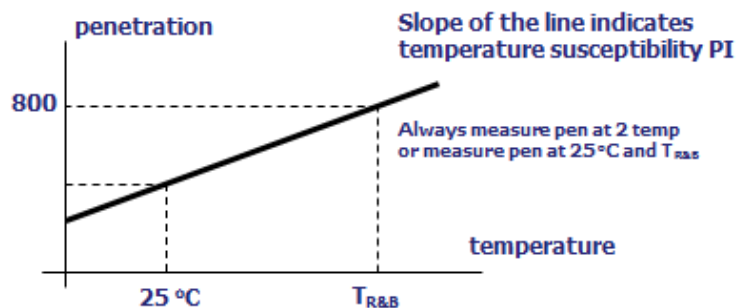
18



Figure 95: Penetration (left) and Ring and Ball test (right).

By combining the results of the penetration and ring and ball test, information is obtained about the temperature susceptibility of the bitumen. This is shown in figure 96.

Penetration (pen) and penetration index (PI)



October 12, 2017

19



Figure 96: Penetration and penetration index.

For most of the bitumens the penetration equals 800 at $T = T_{R\&B}$.

The temperature sensitivity of bitumen is characterized by means of the penetration index PI. The PI is calculated in the following way:

$$PI = 20 * (1 - 25 * A) / (1 + 50 * A)$$

$$A = \{\log \text{pen at } T_1 - \log \text{pen at } T_2\} / (T_1 - T_2)$$

Assuming that the penetration equals 800 at $T_{R\&B}$, which by the way is not true for all bitumens, PI can then be written as:

$$PI = \{1952 - 500 * \log \text{pen}_{25\text{ C}} - 20 * T_{R\&B}\} / (50 * \log \text{pen}_{25\text{ C}} - T_{R\&B} - 120)$$

$\text{pen}_{25\text{ C}}$ = penetration at 25 °C

$T_{R\&B}$ = softening point [°C]

Based on vast experience Shell defined that bitumens to be used for road construction should have $-1 < PI < 1$.

A bitumen with a high positive PI value (e.g. $PI = +3$) is less sensitive to changes in temperatures, needs however a high mixing temperature and is brittle and sensitive to cracking at low temperatures. The resistance to permanent deformation is high.

A bitumen with a high negative PI value (e.g. $PI = -3$) is sensitive to changes in temperature, needs lower mixing temperatures, is still somewhat flexible at low temperatures but its resistance to permanent deformation is low.

8.3.3 Bitumen stiffness nomograph

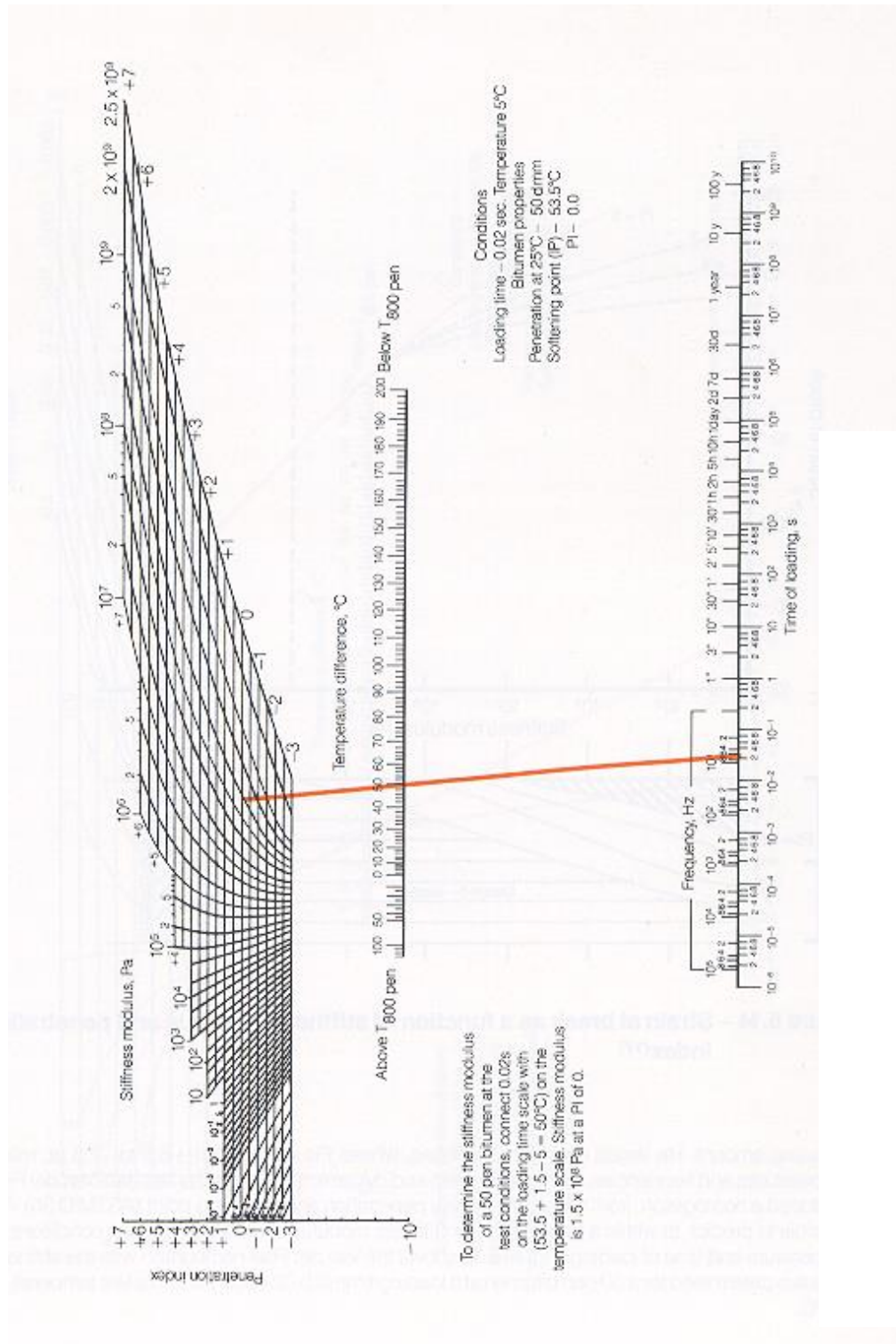
Based on these three parameters (pen, $T_{R\&B}$, PI) van der Poel of the Shell laboratories has developed his famous nomograph (figure 97 [33]) which allows the stiffness of the bitumen to be determined as a function of temperature and loading time. As one will notice, input parameters for the nomograph are the loading time or loading frequency, the temperature difference between the actual temperature and $T_{800\text{ pen}}$ (which for most bitumen is equal to the ring and ball temperature or softening point $T_{R\&B}$), and the PI which is dependent on the penetration and the softening point.

Shell also developed a simple model (the Burgers model) to describe the behavior of bitumen in relation to temperature and loading time. A spring is used to model the elastic behavior, a dashpot is used to model the viscous behavior and a set consisting of a dashpot parallel to a spring is used to model the delayed elastic behavior. This model is shown in figure 98. Figure 99 shows the contribution of the elastic, delayed elastic and viscous deformation in the total deformation as a function of the stiffness of the bitumen and the PI. Figure 98 e.g. shows that at $S_{bit} = 10^6$ Pa and $PI = 0$, 75% of the total deformation is delayed elastic deformation and will recover after some time and 25% of the total deformation is viscous deformation which will not recover and is permanent. In case PI would be +2, then all deformation would recover after some time.

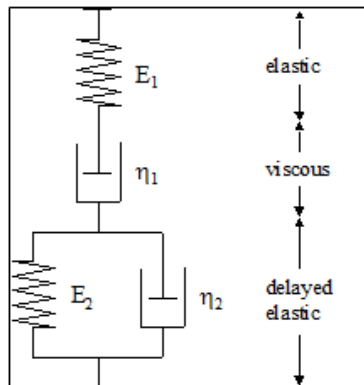
Later on Shell developed the computer program BANDS (the computerized version of the van der Poel nomograph) which allows the stiffness of the bitumen as well as the stiffness of the mixture to be determined in a very quick and easy way. The program uses as input the PI of the bitumen, the temperature and loading time as well as the volumetric composition of the mixture. An example of the output generated by the BANDS program is shown in appendix B.

When using the nomograph and the program BANDS one should be aware of the fact that the frequency f is not equal to $1/t$ where t is the loading time in [s]. The reason for this is that the

frequency used in the nomograph is the angular frequency and there is a difference of 2π between the angular frequency used in the nomograph and the frequency calculated with $f = 1/t$.



Burgers' model



October 12, 2017

28

Visco-elastic behavior

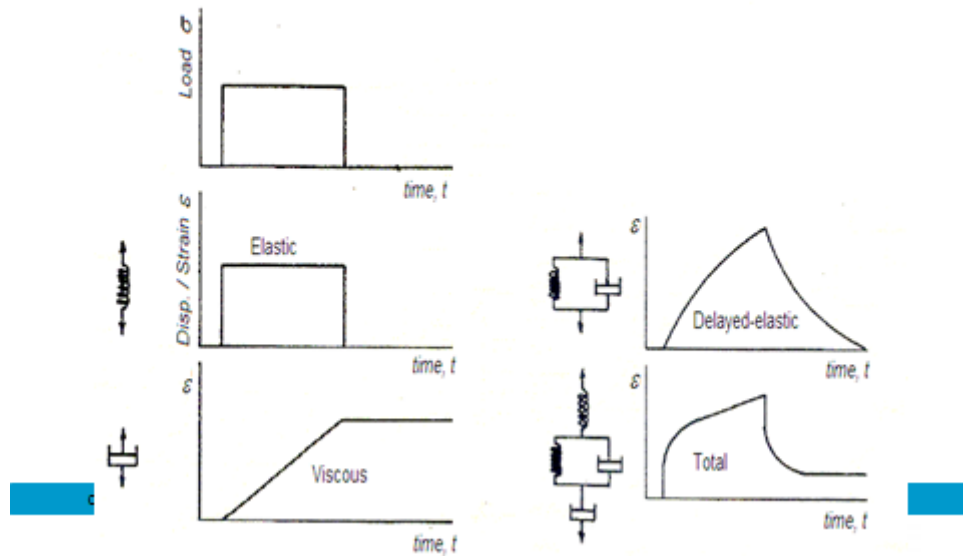
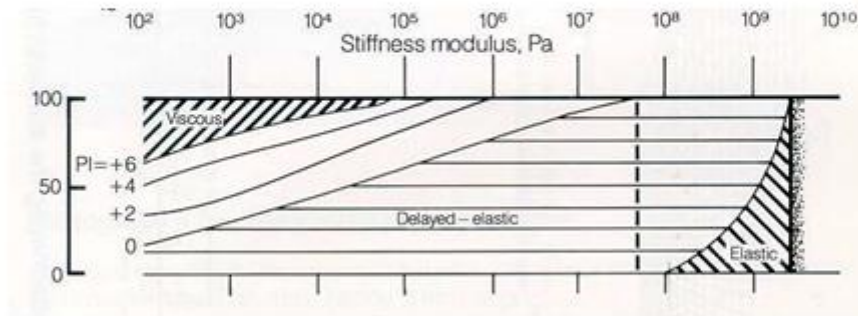


Figure 98: Burgers' model and the contribution of the various components to the total deformation.

Viscous, delayed elastic and elastic response in relation to bitumen stiffness and PI



October 12, 2017

31

TU Delft

Figure 99: Response of a bitumen in relation to its stiffness and PI.

It is important to know that the nomographs and equations do not give a precise and accurate answer. One always has to deal with a “model error” which implies that the value predicted with nomographs or equations can easily be a factor of 1.5 lower or higher than the real, measured, one. This will be discussed in greater detail in the chapter on probabilistics.

8.3.4 Measuring bitumen stiffness by means of the Dynamic Shear Rheometer DSR

It has already been mentioned that the bitumen stiffness can also be measured by means of the DSR (see figure 88). The principle of the DSR test is shown in figure 100.

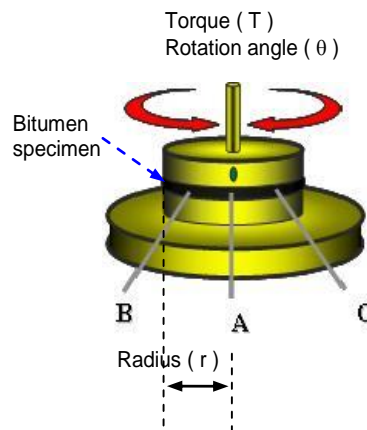


Figure 100: Principle of the DSR test.

The testing mode can either be torque or displacement controlled and the load or displacement can be applied in a static or dynamic way. Figure 101 shows the outcomes of a repeated load DSR test. As one will observe there is a phase lag between the load and displacement signal.

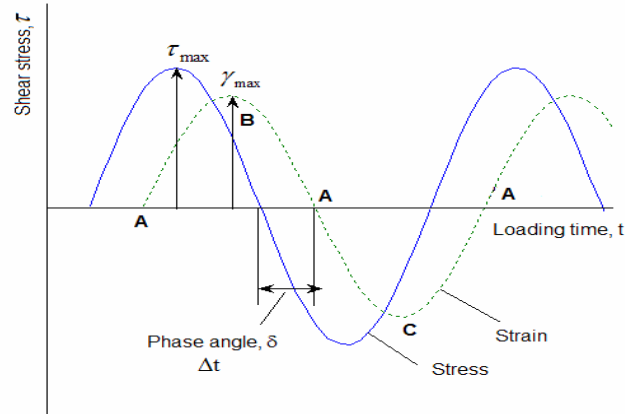


Figure 101: Outcomes of a repeated load DSR test.

Figure 102 show the shear stresses and strains which develop during the test.

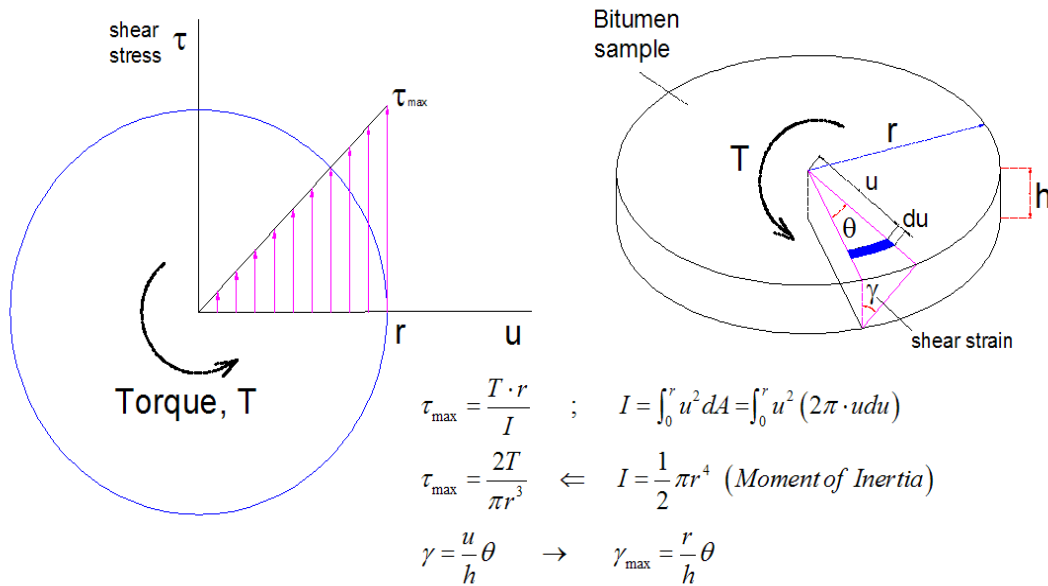


Figure 102: Shear stresses and strains in the DSR test.

The complex shear modulus G^* is calculated in the following way from the test results.

$$G^* = \tau_{\max} / \gamma_{\max}$$

The complex modulus E^* (which was called Sbit by Shell) is calculated following

$$S_{bit} = E^* = G^* (1 + 2 \mu) \quad \text{where } \mu = \text{Poisson's ratio.}$$

Mainly due to the capacity of the DSR devices and the changing “fluidity” of the bitumen at different temperatures (hard and stiff at low temperatures and fluid like at high temperatures), DSR tests are usually performed using the plate geometries shown in table 17 and figure 103.

Temperature range [°C]	G* range [MPa]	Plate diameter [mm]	Sample thickness [mm]
0 < T < 40	0.1 – 30	8	2
40 < T < 80	0.001 – 0.1	25	1
T > 80	< 0.001	40	< 1

Table 17: Plate diameter and specimen thickness as used in DSR tests.

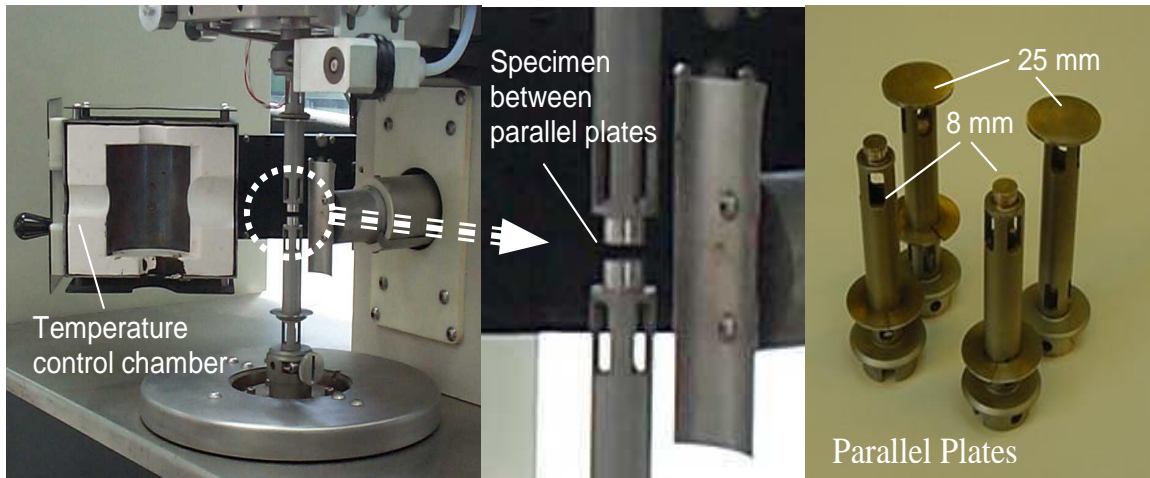


Figure 103: DSR setup and plate sizes.

Figure 104 gives an example of DSR test results obtained at different temperatures and loading frequencies. The results are obtained on specimens which were subjected to long term aging procedures. Aging procedures are described in detail in appendix D.

Figure 104 shows that the results obtained at various temperatures are used to construct a master curve which shows the G* at a particular temperature, in this case 20 °C, over a very wide range of frequencies. This master curve is obtained by shifting horizontally the curves obtained at other temperatures to the 20 °C curve in such a way that they form one continuous curve. The figure shows also the shift factors that apply. The shift factor implies that the G* at 20 °C and a reduced frequency of 5.105×10^{-4} was obtained from the measured G* at 50 °C and 1 Hz.

The principle of the shift factor is as follows. Boltzman has shown that the temperature dependency of the viscosity (η) of purely viscous materials can be written as:

$$\eta' = \eta_0 * e^{b/T}$$

Furthermore we can write $\tau = \eta' * (d\gamma / dt)$ resulting in $\gamma(t) = \tau * t / \eta'$ and $G_t = \eta' / t$. By substituting η' and taking the logarithm we obtain

$$\log (G_{t,T}) = \log \eta_0 + (b / T) * {}^{10}\log e - \log t$$

If for example we obtain G_i at temperature X and loading time t_1 and the same stiffness is obtained at temperature Y and t_2 , we obtain:

$$(b / 2.3) * [1 / T_y - 1 / T_x] = \log t_2 - \log t_1$$

This equation is very much alike the Arrhenius equation which is very often used for shifting procedures. The Arrhenius equation is:

$\log \alpha_T = C * (1 / T - 1 / T_s)$ with T is temperature from which the data are shifted and T_s is the reference temperature. Furthermore:

$C = \Delta H / (2.303 * R)$ where ΔH is the activation energy and R is the universal gas constant.

Comparison shows that:

$$\log t_2 - \log t_1 = \log \alpha_T \quad \text{and} \quad b = \Delta H / R$$

Also other shift procedures exist like the WLF equation which was used for shifting the data in figure 104. No further explanation will be given here about those procedures. The interested reader is referred to available literature on these methods.

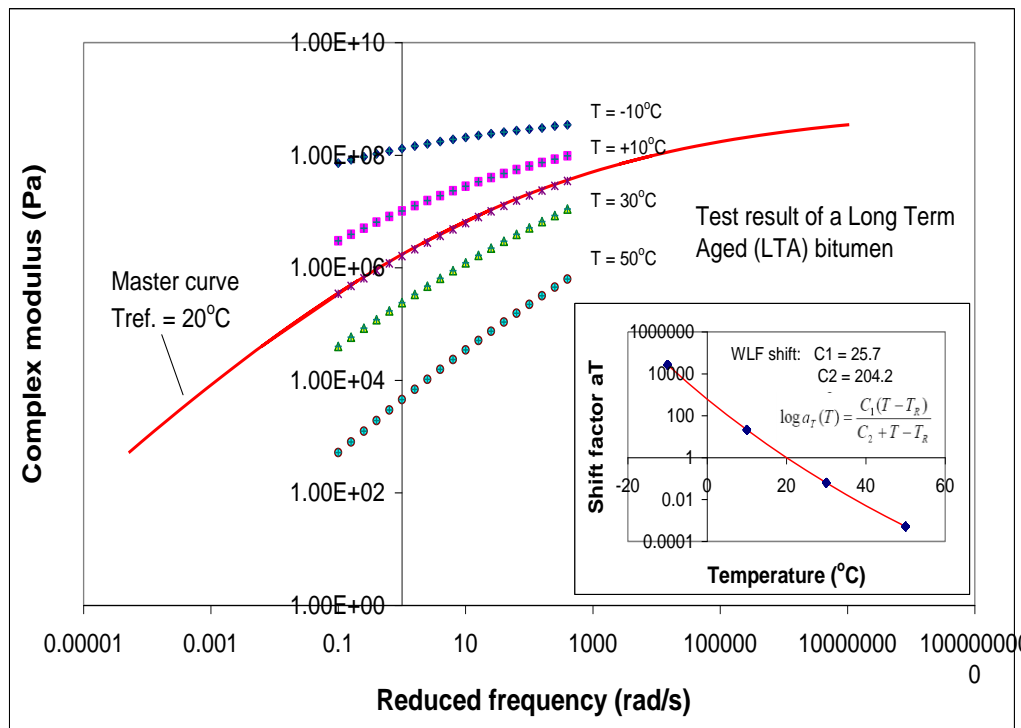


Figure 104: DSR results and master curve

The complex modulus G^* can be split into a part that represents the elastic behavior and a part that represents the viscous behavior. This is shown in figure 105. The elastic component, the storage modulus G' , is calculated via: $G' = G^* \cos \delta$ and the viscous component, the loss modulus G'' , is calculated via: $G'' = G^* \sin \delta$

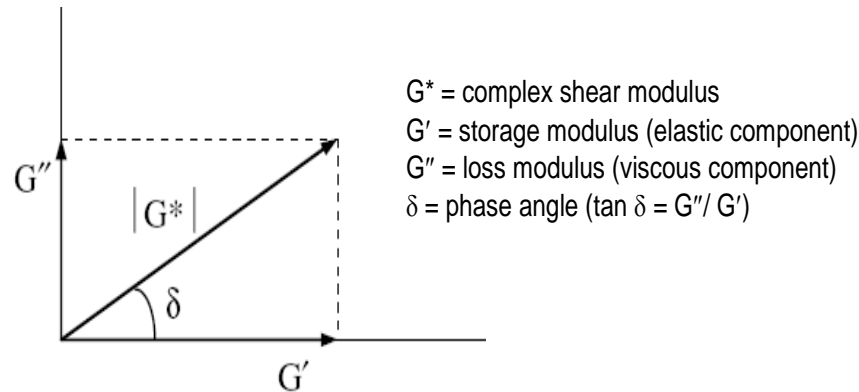


Figure 105: Complex, storage and loss modulus

In the USA minimum values are set for the storage modulus ($G^* \cos \delta = G' / \sin \delta$) in order to ensure a good resistance to permanent deformation. Also maximum values are set for the loss modulus ($G^* \sin \delta$) to ensure a good resistance to fatigue.

Also the so called Black diagram (G^* vs δ) and Cole – Cole diagram (G' vs G'') are used to represent the characteristics of the bitumen (see figures 106 and 107). Later on it will be shown how the Black diagram is used to characterize the sensitivity of the binder to cracking due to hardening.

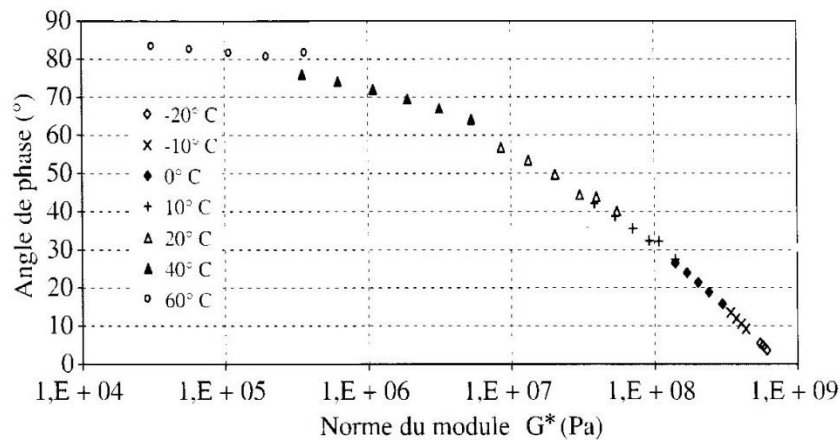


Figure 106: Black diagram.

Until now we have been discussing viscosity parameters like G^* , pen , $T_{R\&B}$, and PI and the question is whether there is some relation between those parameters. The only relationship known by the author is the one between pen and G^* which is:

$$\log G^* = 2.923 - 1.9 \log \text{pen}$$

Where $[G^*] = [\text{MPa, at } 0.4 \text{ Hz and } 25^\circ\text{C}]$; $[\text{pen}] = [\text{dmm at } 25^\circ\text{C}]$.

Because of the inaccuracies involved, estimating the penetration via G^* is much more accurate than actual pen measurements especially when the pen is low.

8.3.5 Bitumen stiffness and chemical composition

Shell [33] has developed a relation between the penetration index (PI) of the bitumen and its composition. This relationship is shown in figure 108. The figure nicely shows that the higher the

asphaltene content, the higher the PI. Depending on the concentration of asphaltenes in the bitumen, Shell [33] has defined two typical structural compositions for bitumen being the so called "Gel" and "Sol" structure. These structures are schematically shown in figure 109. The existence of such colloidal structures has been criticized by other researchers who claim that bitumen is a more homogeneous system in which sharp distinctions between groups cannot be made.

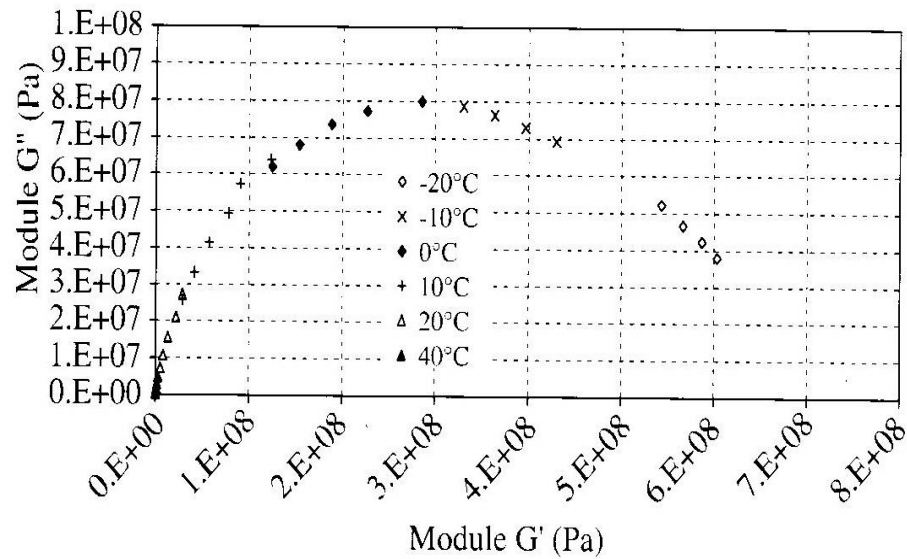


Figure 107: Cole – Cole diagram.

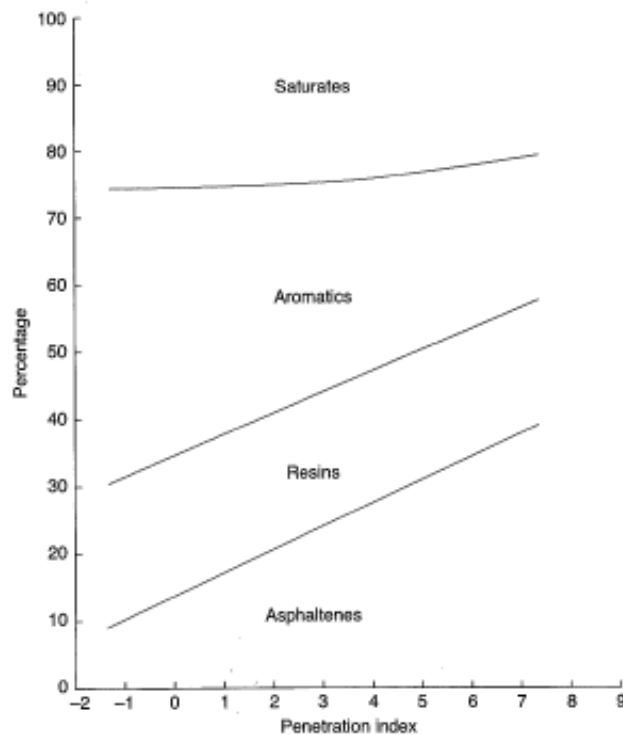


Figure 108: Relation between the broad chemical composition of bitumen and the PI

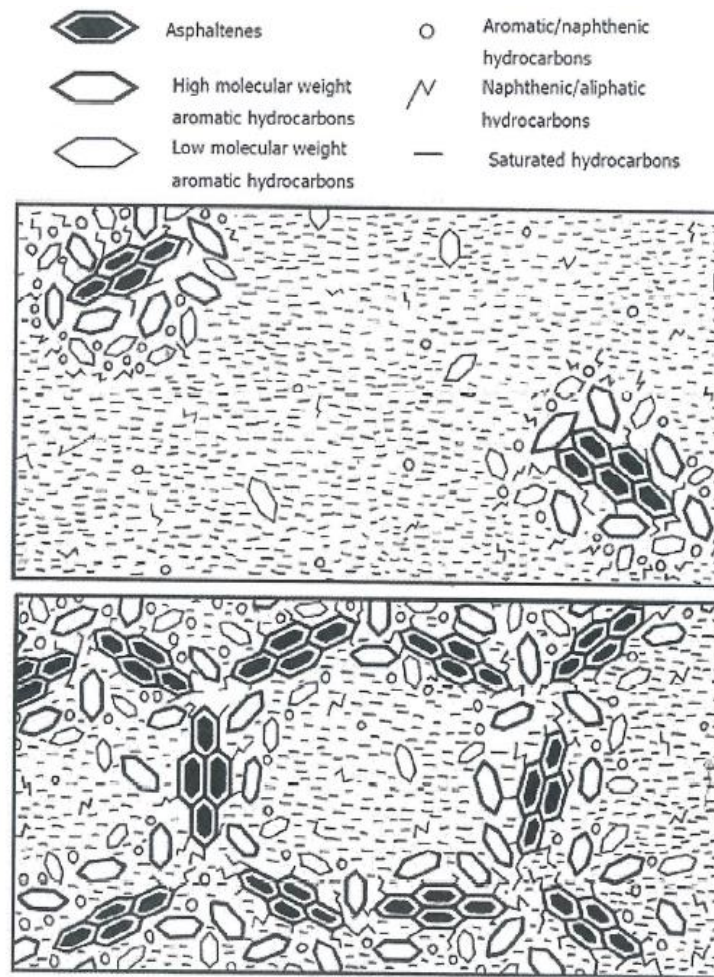


Figure 109: Colloidal bitumen structures as proposed by Shell;
top: Sol structure (PI = -2.3)
bottom: Gel structure (PI = +5)

Figure 110 shows the relation between S_{bit} and loading time and temperature for the bitumen structures shown in figure 109. By linking all this information it becomes clear that chemical and viscosity characteristics of the bitumen are indeed strongly related. Note that the slope of the S_{bit} curves of the Sol bitumen are much steeper than those of the Gel bitumen. The importance of the slope of the stiffness vs loading time curves will be discussed in detail later on.

8.3.6 Bitumen stiffness and aging

The original penetration of the bitumen will decrease and the softening point ($T_{R\&B}$) will increase due to ageing which results in hardening/stiffening of the bitumen. Significant hardening already occurs during production and laying because of loss of volatiles and oxidation at high temperatures; this is the so called short term aging. Later on, when the asphalt mixture is exposed to the influences of climate, further hardening occurs due to oxidation of the binder. Loss of volatiles might also be the result of exudation which is the penetration of the light bitumen fraction in the pores of the aggregates. Exudation will only occur when the bitumen is less stable and when the aggregates are porous.

Depending of the type of mixture, the production, storage, transportation and laying conditions and depending on the climate, about 60% of the hardening of dense mixtures (with around 4% void content) takes place during production and laying.

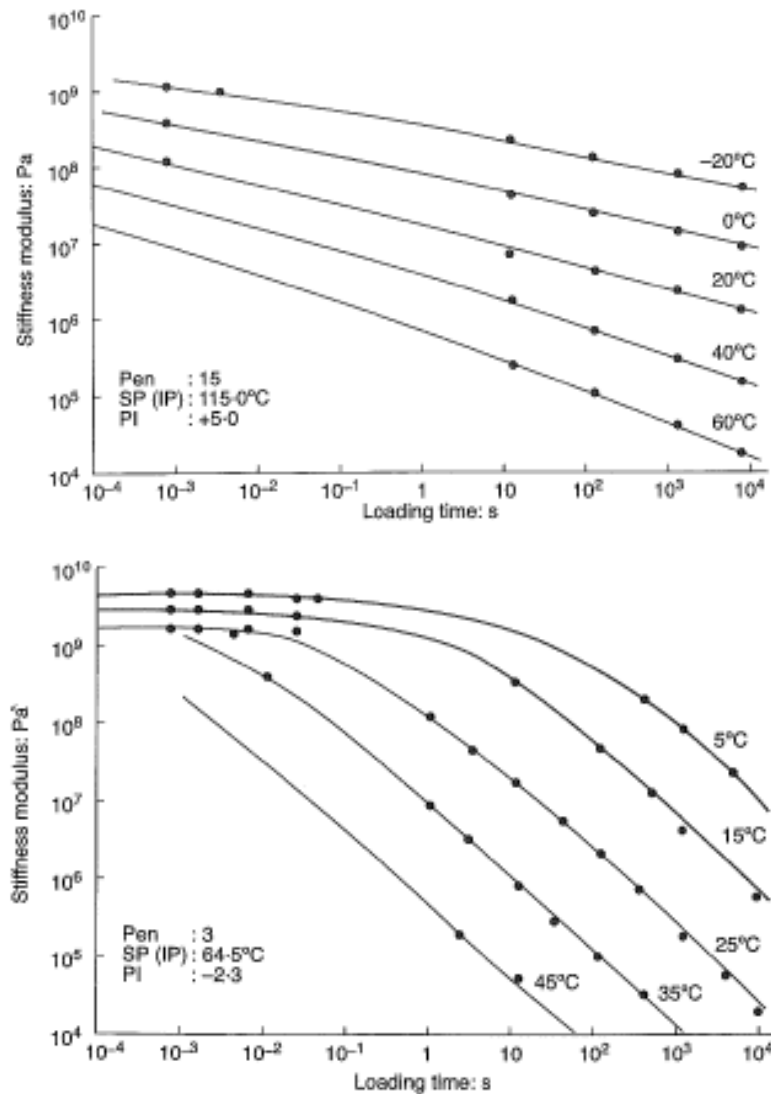


Figure 110: Stiffness of the Gel (top) and Sol (bottom) bitumen shown in figure 103.

Figure 111 [37] shows how the G^* of bitumen samples retrieved from the top 25 mm of porous asphalt concrete (void content around 20%, this makes the mixture very sensitive for aging) wearing courses has increased in time due to aging. All sections were constructed with virgin bitumen of the same penetration and $T_{R\&B}$ class. The amount of aging can be quantified by comparing for instance the G^* at 1 Hz of the bitumen of section 11 (EL, 12 years) with the G^* at 1 Hz of the virgin bitumen; one will notice an increase of G^* with a factor of around 42 ($G^*_{\text{section 11}} = 10 \text{ MPa}$, $G^*_{\text{virgin}} = 0.237 \text{ MPa}$). The G^* of the bitumen retrieved from section 12 (SL, 12 years) shows an increase of around 13 times when compared to the virgin bitumen (3.16 MPa vs 0.237 MPa). Furthermore it is interesting to note that the G^* of the bitumen of the newly laid section 4 is already 7.5 times higher than that of the virgin bitumen (1.77 MPa vs 0.237 MPa). For section 11 most of the aging happened after construction while for section 12 almost 56% of the aging occurred during production and laying and around 45% during the 12 years the section was in

service. The figure also shows that the RTFOT short time aging (STA) procedure (label 2), which is believed to simulate aging during production and laying, is too mild. The G^* curve for label 2 is much lower than that of section 4. The same is true for the RCAT long term aging (LTA) procedure (label 3). The G^* curve for label 3 is lower than the curves obtained from the field samples. Details of the RTFOT and RCAT aging tests as well as of other aging tests can be found in references [37] and [137].

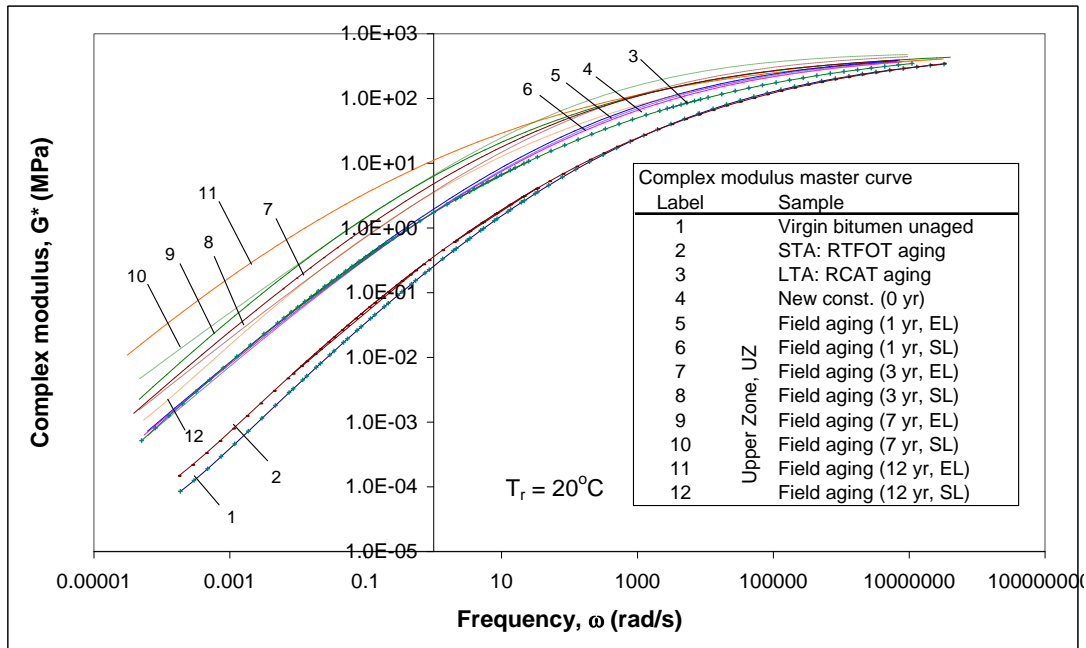


Figure 111: G^* master curves at $T = 20\text{ }^{\circ}\text{C}$ for virgin bitumen, laboratory aged bitumen (RTFOT and RCAT) and bitumen recovered from the top half of cores taken from porous asphalt concrete wearing courses of different age (EL = emergency lane, SL = slow lane of highway).

Figure 112 and 113 show how the penetration and softening point of bitumen samples taken from the upper 25 mm of porous asphalt concrete wearing courses did change in time because of aging

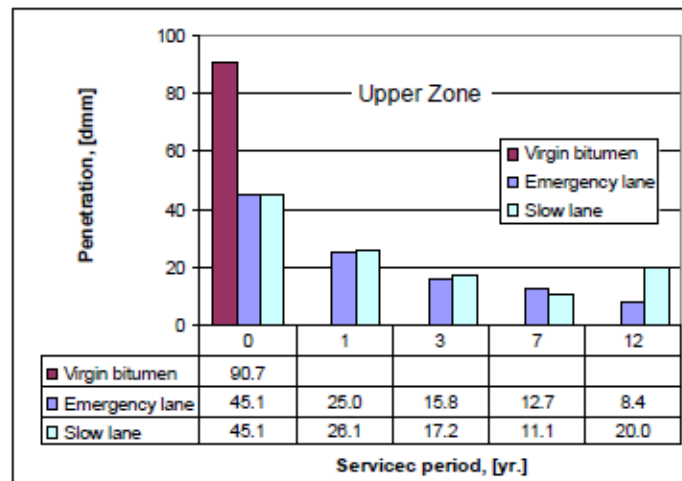


Figure 112: Decrease in penetration due to aging.

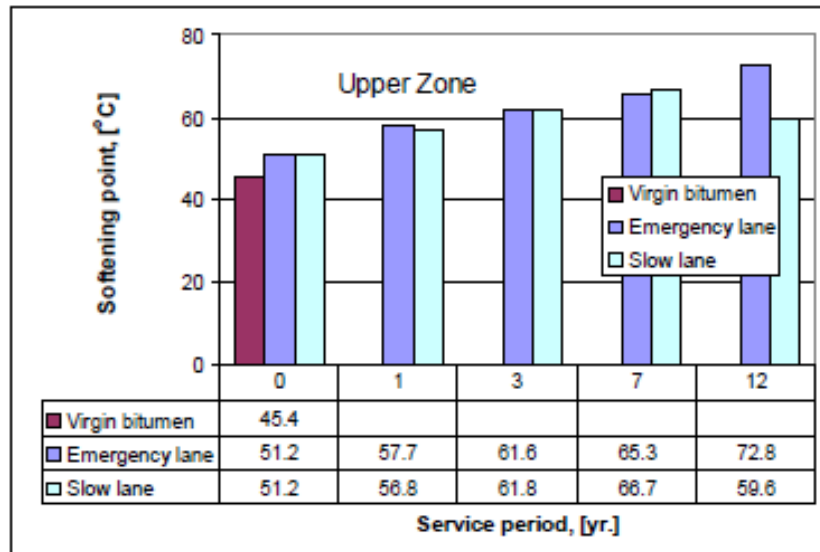


Figure 113: Increase in softening point $T_{R\&B}$ due to aging.

The field aging data shown in figures 112 and 113 apply to porous asphalt concrete which has a void content of around 20%.

An example of field aging of a base course mixture with approximately 6% voids can be found in [23]. These data are shown in table 18.

	penetration (0.1 mm)		softening point Ring & Ball (°C)		penetration index	
	1991	1996	1991	1996	1991	1996
top layer	45		52.0		-1.0	
0-1 cm		31.5 (1.0) n=2 ^a		53.9 (0.1) n=2		-1.3
1-2 cm		34.4 (10.3) n=3		53.1 (3.1) n=3		-1.3
2-4 cm		40.3 (7.8) n=4		51.7 (1.6) n=4		-1.3
4-7 cm		40.2 (3.5) n=3		51.5 (1.0) n=3		-1.3
bottom layer	47		51.0		-1.1	

^a average, (standard deviation), number of samples

Table 18: Aging observed in test section

The data shown in table 18 were obtained from a test section consisting of a 70 mm top and 80 mm bottom layer both made of a gravel asphalt concrete base course mixture with a void content of about 6% and a bitumen content of 4% by mass (per 100% aggregates). The table clearly shows that a significant decrease in penetration occurred during the 5 years the section was exposed to climatic influences. Also an aging gradient over the height of the asphalt layer is visible. These results clearly show that even in a rather dense mixture, aging will occur in time over a fairly large depth. It is clear that these influences should be taken into account when predicting pavement performance.

The question now is whether we are able to model this aging behavior. In [31] the following equations are given to estimate the amount of hardening/aging during production and laying.

$$\log \log \eta_{t=0} = 0.054405 + 0.004082 * \text{code} + (0.972035 + 0.010886 * \text{code}) * \log \log \eta_{\text{original}}$$

Where:

$\eta_{t=0}$ = mix/lay-down viscosity [cP]

η_{original} = original viscosity [cP]

code = hardening ratio (HR)

HR = $\log \log$ viscosity after RTFO (rolling thin film oven test) / $\log \log$ original viscosity

HR \leq 1.030 then code value = -1

1.03 < HR \leq 1.075 then code value = 0

1.075 < HR \leq 1.100 then code value = 1

HR > 1.100 then code value = 2

The relation between viscosity and penetration as given in [31] is:

$$\log \eta = 10.5012 - 2.2601 \log (\text{pen}) + 0.00389 \log (\text{pen})^2$$

Where:

η = viscosity [P]

pen = penetration [mm/10]

In [31] also equations are given to estimate the long term viscosity aging occurring at the top of the pavement as well as an equation to estimate the aging occurring at a certain depth of the pavement surface. These equations are not given here because long term aging is so much dependent on the climatic conditions and type of surface layer mixture which might be completely different from the conditions for which those equations were developed. This is clearly visible when the data shown in figure 112 are compared with those given in table 18. Figure 112 e.g. shows that in the porous asphalt concrete with a void content of around 20% a drop in penetration of around 25 points was obtained after 3 years (figure 112), while table 18 shows that in the much denser base course mixture (around 6% voids) a drop in penetration of around 14 points was obtained after 5 years. For the sake of completeness it is mentioned that both data were obtained on sections in the Netherlands where the climatic differences over the country are (very) limited.

In any case, the estimation of the bitumen and mixture stiffness for design purposes should take the effects mix/lay-down hardening into account, which can be estimated using the provided equations, as well as hardening that takes place in time. For the later an "educated estimation" should be made.

8.4 Mixture stiffness at high temperatures, long loading times and high confining pressures

Bending tests, uni-axial tension-compression and indirect tension tests were used to determine the mixture stiffness as discussed in paragraph 8.2. In the top layer, or wearing course, however high vertical compressive stresses are acting together with high horizontal compressive stresses. During the summer high temperatures (as high as 60 °C) will occur in the top layer and in such conditions the behavior of the asphalt mixture strongly depends on the characteristics of the stone skeleton especially in case of stone skeleton mixtures like stone mastic asphalt (SMA) and porous asphalt concrete (PAC). Furthermore one knows that under those conditions, asphalt mixtures are prone to permanent deformation.

Research done by Antes e.a. [36] has shown that the stiffness modulus of asphalt mixtures becomes stress dependent at elevated temperatures. This dependency can be modeled as follows:

$$M_r = k_1 \{(\sigma_3 + k_3) / \sigma_{30}\}^{k_2}$$

Where: σ_3 = confining pressure [kPa],
 σ_{30} = reference pressure = 1 kPa,
 k_1, k_2, k_3 = constants,
 M_r = resilient modulus = 0 if $\sigma_3 \leq -k_3$.

Some results are shown in table 19.

Mixture type	Test temperature [$^{\circ}$ C]	Loading frequency [Hz]	k_1	k_2	k_3
STAC	40	25	0.0008	1.879	3143.40
		8	0.0008	1.894	2408.23
		0.5	0.0002	2.054	1600.58
	50	25	0.0002	1.929	2795.66
		8	0.0003	1.945	1880.27
		0.5	0.0001	2.104	1592.74
PAC	40	25	0.0006	1.925	2065.65
		8	0.0008	1.890	1681.70
		0.5	0.0003	2.029	1362.47
	50	25	0.0005	1.971	1347.48
		8	0.0006	1.928	1206.74
		0.5	0.0003	2.050	1052.94
DAC	40	25	0.0005	1.835	4518.63
		8	0.0004	1.926	2579.78
		0.5	0.0001	2.141	1845.23
	50	25	0.0003	1.835	4518.63
		8	0.0002	2.020	1828.18
		0.5	0.0001	2.141	1845.23

Table 19: Constants of the stress dependent resilient modulus for three asphalt mixtures.

Table 20 gives some details on the composition of the mixtures.

Property	STAC Stone Asphalt Concrete, base course mixture	PAC Porous Asphalt Concrete, wearing course mixture	DAC Dense Asphalt Concrete, wearing course mixture
Bitumen content [% m / m] "on" 100% aggregate	4.6	4.6	5.9
Pen of recovered bitumen	33	64	31
Void content [%]	5.5	18.1	4.2
Degree of compaction [%]	98.7	104.5	99.4

Table 20: Composition of the mixtures of table 19.

Some results are also shown in tables 21 and 22.

T [°C]	f [Hz]	$\sigma_3 = 0$ kPa	$\sigma_3 = 300$ kPa	$\sigma_3 = 590$ kPa
30	0.1	1034	1374	1882
30	8	4012	4681	5465
30	25	6128	6731	7608
40	0.5	935	1254	1789
40	8	1981	2437	3084
40	25	3027	3582	4198
50	0.5	652	845	1386
50	8	907	1153	1669
50	25	1230	1651	2337

Table 21: Stress dependent stiffness modulus for STAC as determined by means of repeated load triaxial tests.

T [°C]	f [Hz]	$\sigma_3 = 0$ kPa	$\sigma_3 = 300$ kPa	$\sigma_3 = 590$ kPa
30	0.3	635	1069	1502
30	8	1999	2312	2783
30	25	3027	3366	4041
40	0.5	816	1188	1567
40	8	1435	1624	2014
40	25	1931	3131	2641
50	0.5	721	886	1191
50	8	815	986	1318
50	25	908	1106	1431

Table 22: Stress dependent stiffness modulus for PAC as determined by means of repeated load triaxial tests.

The values shown in tables 21 and 22 clearly show that the modulus determined in compression ($\sigma_3 = 0$) is significantly lower than the modulus determined when a certain confinement was applied. The effect of confinement can therefore not be ignored when estimating the asphalt mixture stiffness at high temperatures in the presence of high confining stresses.

It is recalled that at the bottom of the asphalt layer a combination of horizontal tensile stresses (due to bending of the layer as a result of the applied wheel load) and much smaller vertical compressive stresses (due to load spreading) occurs. Because of the significant difference in stress conditions at the top (3D compression) and bottom (mainly 2D tension) of the asphalt layer, different values for the mixture stiffness for the bottom and top part might need to be used for design purposes.

In addition to this Molenaar [39] and Pramesti [38] have shown that the modulus in tension is lower than the modulus in compression at higher temperatures and longer loading times. An example of this is shown in figure 114 which is taken from [38].

From the material presented so far it will have become clear that assigning a single modulus value for e.g. a 150 mm thick asphalt layer made of the same type of asphalt mixture is a rather crude simplification of reality because we have seen that the modulus depends on:

- temperature, which will not be a constant over the entire thickness,
- loading time, which will not be a constant over the entire thickness,
- degree of aging, which will not be a constant over the entire thickness,
- stress conditions, which will not be a constant over the entire thickness.

We will see later on however that in most of the design analyses a single modulus value is assigned for the entire asphalt thickness. The consequences of such a simplification will be discussed later on.

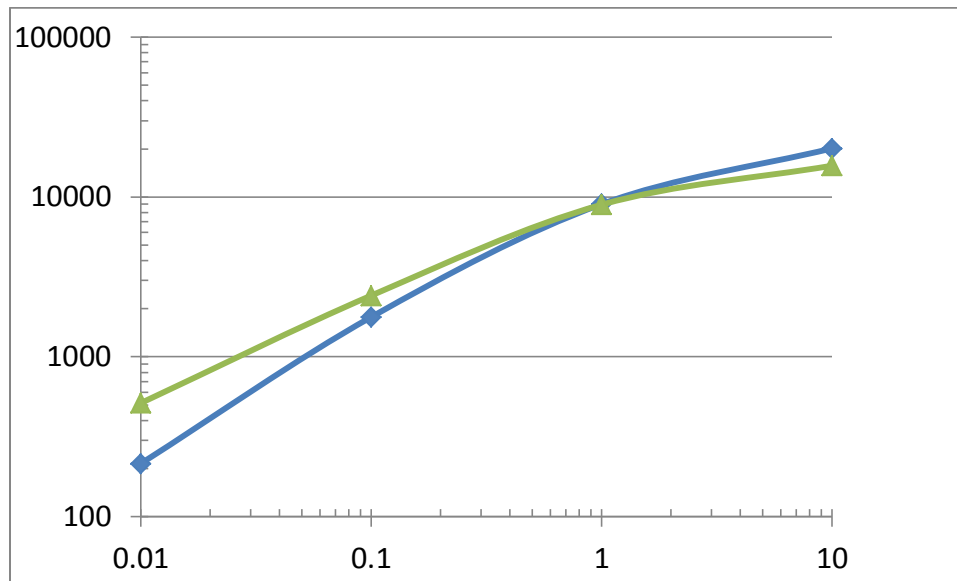


Figure 114: Modulus (vertical axis in MPa) in tension (blue line) and modulus in compression (green line) in relation to the strain rate (horizontal axis in %/s)) as determined at 20 °C for a base course mixture.

8.5 Poisson's ratio of asphalt mixtures

Next to the modulus of the asphalt layer, its Poisson's ratio should be known. Compared to the vast amount of information that is available on how to determine/estimate the stiffness of asphalt mixtures, only little information is available on how to estimate a value for Poisson's ratio. It doesn't however very much explanation to understand that Poisson's ratio takes a lower value when the temperature is low and the loading time is short making the asphalt mixture behaving like a solid, than when the temperature is high and the loading time is long making the material more viscous. Figure 115 developed by Sayegh [40] was/is very often used at the Delft University for making an estimate for the Poisson ratio value.

In the AASHTO MEPD system [31] an equation is proposed for estimating Poisson's ratio which is:

$$\mu = 0.15 + 0.35 / \{1 + e^{(-1.63 + 3.84 \cdot 10^{-6} \cdot S_{mix})}\}$$

Please note that in this equation $[S_{mix}] = [psi]!$ 100 psi = 0.7 MPa

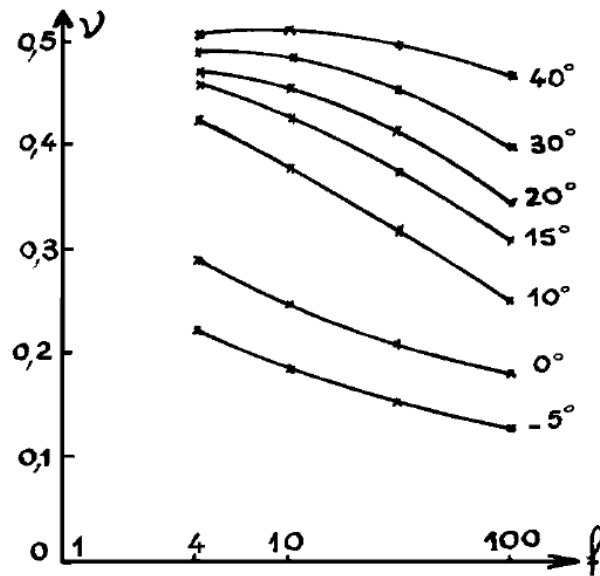


Figure 115: Chart for estimating Poisson's ratio values as developed by Sayegh.

8.6 Fatigue resistance

Fatigue is the process of the initiation of micro cracks and the gradual development of these cracks to macro cracks until failure occurs as a result of repeated loads. Fatigue damage shows itself as cracking although not all cracks visible at the pavement surface are due to repeated loads. Traffic loads are the best known type of repeated loads but also repeated low temperature cycles cause fatigue cracking. Fatigue cracks due to traffic loads are believed to be initiated at the bottom of the asphalt layer although many cracks visible at the pavement surface in the wheel paths are initiated at the pavement surface.

Fatigue tests are commonly done using equipment shown in figure 79 but they can also be done using the so called BOEF test, beam on elastic foundation test, which is shown in figure 116. With so many test methods available, the question that has to be asked is "which test is the best one and which test simulates reality in the best way". This is an important question since we will see that test type, testing mode and specimen size are factors which influence the test results. The next question which then immediately arises is "are we measuring material properties by means of these tests or are we measuring specimen properties implying that the result is affected by the type of test, geometry of the specimen etc?".

All these items will be discussed to some depth in in this chapter and based on this discussion the reader should be able to make a proper decision on how to characterize asphalt fatigue for design purposes.

Since in the Netherlands traffic induced fatigue is a much more important defect type than temperature induced fatigue, we will focus on traffic induced fatigue.

Beam on elastic foundation (BOEF) test

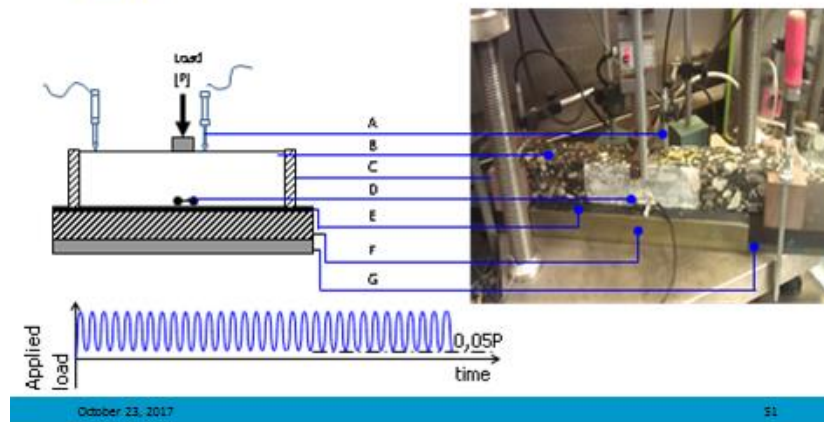


Figure 116: Beam on elastic foundation (BOEF) test.

8.6.1 Strain signals in pavements

It is generally accepted that repeated tensile strains are the cause for fatigue cracking. The question then is how these tensile strain signals look like. It is common practice to measure in test pavements longitudinal (in the direction of traffic) and transversal (perpendicular to the direction of traffic) tensile strains. Such measurement results are reported in e.g. [23] and some examples are shown in figures 117, 118 and 119. These tensile strains were measured at the bottom of the asphalt layer of simple "asphalt on a sand subgrade" test pavements. These test pavements were trafficked by means of the Delft University Accelerated Pavement Testing (APT) device LINTRACK which is shown in figure 120.

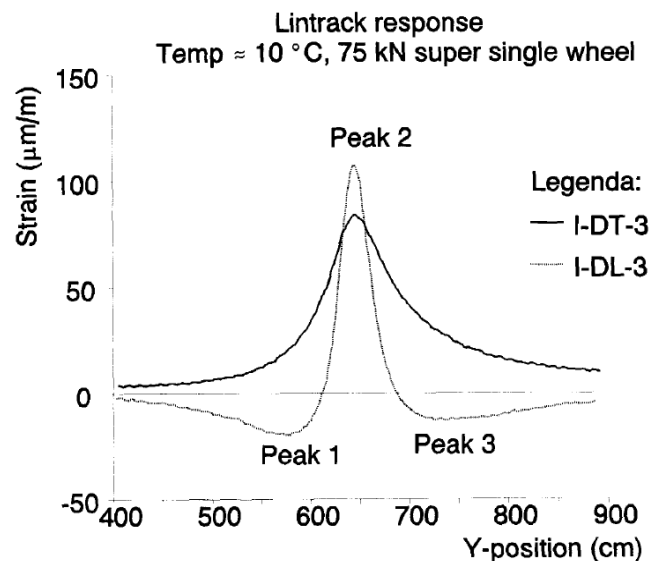


Figure 117: Longitudinal (I-DL-3) and transversal (I-DT-3) strain signals as measured in a test pavement.

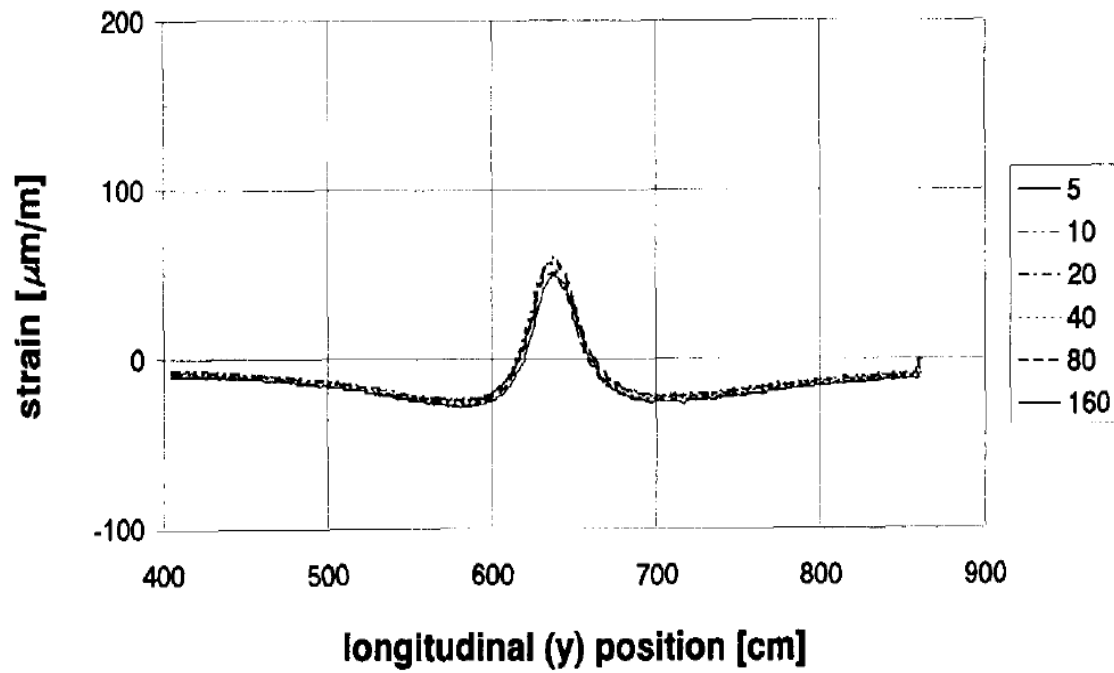


Figure 118: Build-up of longitudinal strain as function of the number of load repetitions; the numbers in the legend indicate the number of load repetitions.

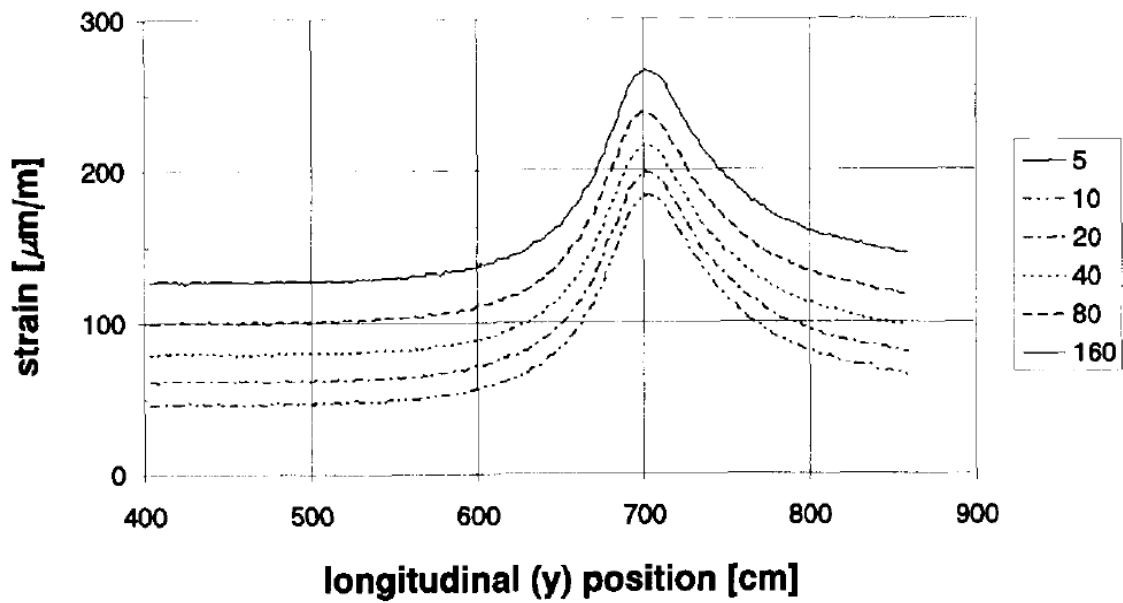


Figure 119: Build-up of transversal strain as function of the number of load repetitions; the numbers in the legend indicate the number of load repetitions.



Figure 120: Delft University LINTRACK APT device.

Figure 117 shows that the longitudinal strain signal is completely different from the transversal signal. Furthermore it shows that the peak values are not the same. If we would have calculated the strains by means of BISAR assuming a circular wheel load and a uniform contact pressure then both peak values would be the same. Measurements however showed that the print of the super single tire used in the LINTRACK experiments was rectangular instead of circular and that the vertical contact pressure distribution was far from uniform (see also chapter 6).

Figure 118 shows that there is no build-up of longitudinal strain with increasing number of load repetitions while figure 119 shows there is a significant build-up of transversal strain. Figure 119 shows that from the 5th to 160th load repetition, the peak value is not increasing but there is a significant build-up of permanent strain. The permanent strain builds up from 65 $\mu\text{m}/\text{m}$ after the 5th cycle to 145 $\mu\text{m}/\text{m}$ after the 160th cycle. This build-up of transversal strain cannot be ignored because it can lead to some kind of creep failure.

8.6.2 Tensile strains and cracking caused by permanent deformation

Cracking which is visible at the pavement surface might be caused by permanent deformation. This is often overlooked when designing pavements but as will be shown, permanent strains due to permanent deformation will be developing at the bottom and surface of the asphalt layer which can become so high that they will result in cracking. Figure 121 shows e.g. the permanent deformation development in one of the test pavements tested by Groenendijk [23]. This test pavement consisted of a 150 mm thick asphalt layer on top of a sand subgrade. Measurements showed that the permanent deformation visible at the pavement surface was caused by deformation of the sand subgrade and not by the asphalt layer. As one will notice, the radius of the deformation pit is gradually decreasing with increasing number of load repetitions. The tensile strain (ε) that develops at the bottom of the asphalt layer because of the deformation development can be calculated via:

$$\varepsilon = h / 2R$$

With h = asphalt thickness
 R = radius of curvature of the deformation pit

Figure 122 shows the permanent deformation which developed in a 80 mm thick asphalt pavement resting on the same sand subgrade. Also in this case the deformations were completely due to deformation of the sand subgrade. As one will observe two ridges develop on

either side of the deformation pit. In this case not only tensile strains develop at the bottom of the asphalt layer but also at the top of the asphalt layer, on the top of both ridges. Figure 123 [38] shows the how the permanent deformation is related to the radius of curvature of the deformation pit.

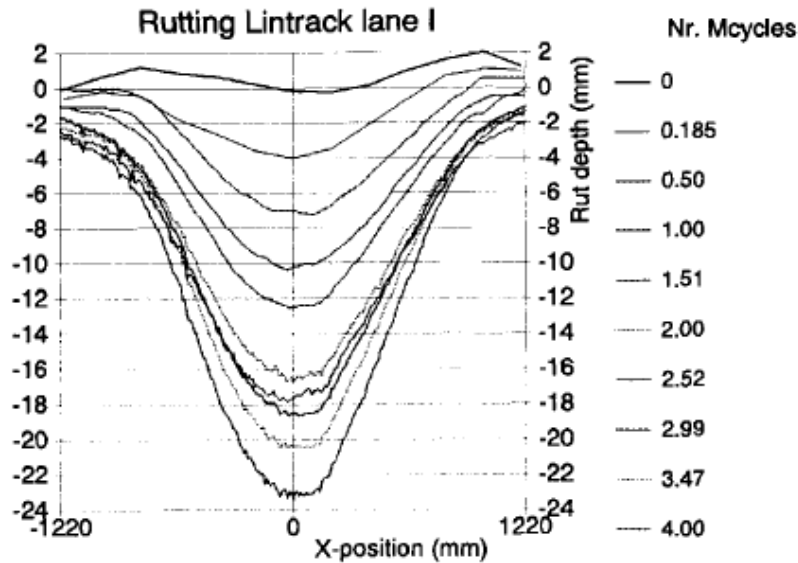


Figure 121: Permanent deformation developing in a test pavement consisting of 150 mm asphalt on top of a sand subgrade.

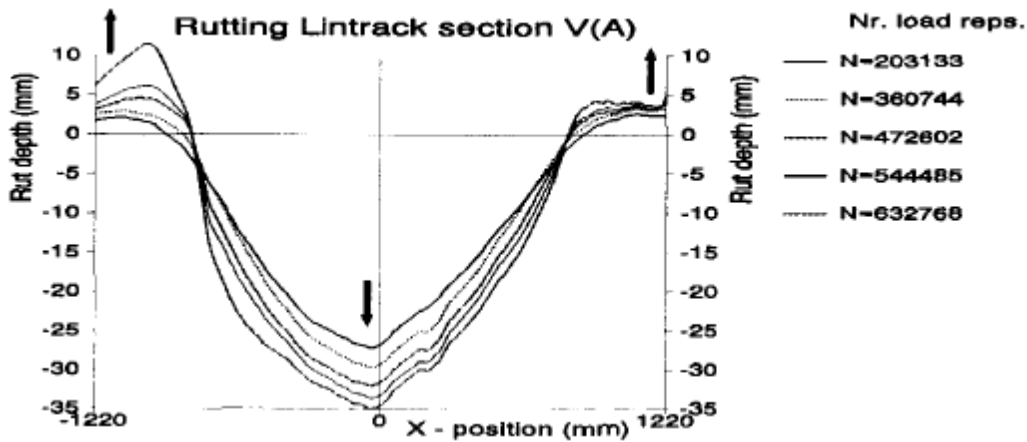


Figure 122: Permanent deformation developing in a test pavement consisting of 80 mm asphalt on top of a sand subgrade. NOTE THE DEVELOPMENT OF RIDGES next to the deformation pit.

Figure 124 [38] shows how permanent deformation and permanent strain are related.

The results obtained on the test pavements showed that in general the rate of cracking started to increase when the permanent deformation was around 15 mm resulting in a permanent strain of around 0.25%. This seems to indicate that at higher permanent deformation levels, cracking due

to permanent deformation becomes a serious issue and that a permanent strain of around 0.25% can be taken as the failure strain under creep conditions for the mixture used in the test pavements.

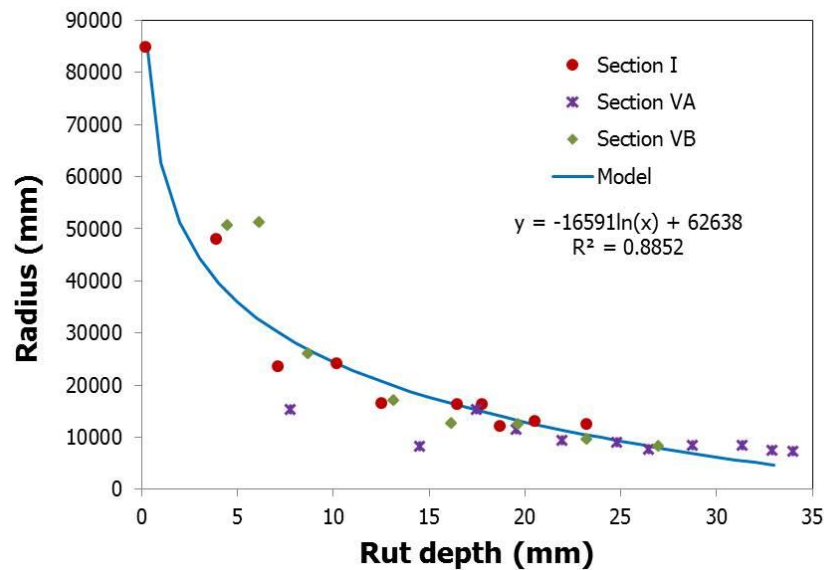


Figure 123: Permanent deformation (rut depth) in relation the the radius of curvature of the permanent deformation pit.

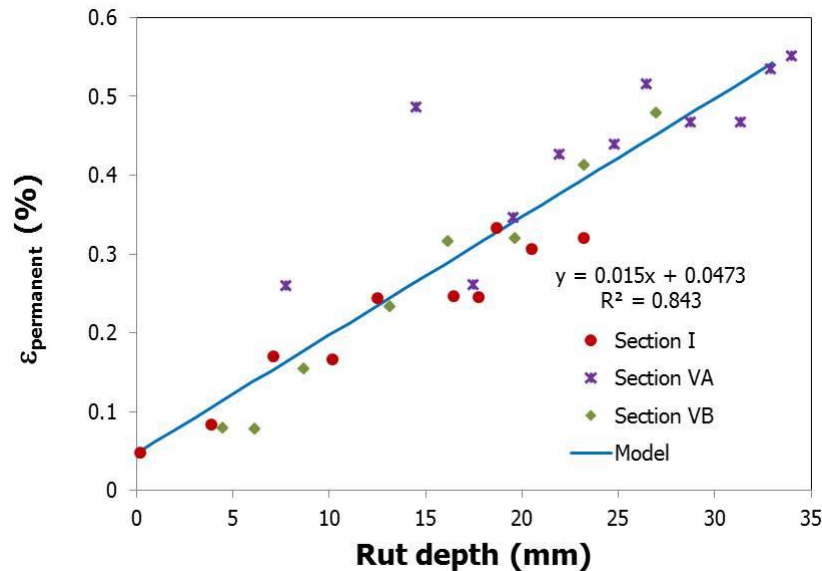


Figure 124: Relation between permanent deformation (rut depth) and permanent strain.

It should be stressed that the relation between cracking and permanent deformation presented here is only valid when the the permanent deformation is caused by deformations in the layers below the asphalt layer causing the asphalt layer to bend. Figure 125 shows an example of permanent deformation which is clearly caused by deformation of the layers below the asphalt layer. Please note the longitudinal cracks at the edge of the rutdepth bowl (on the left side where

the beam touches the pavement) which most probably are due to the permanent strain which developed at the top of the asphalt layer as a result of rutting.



Figure 125: Permanent deformation caused by deformations in the layer(s) below the asphalt layer. Note the cracks!

8.6.3 Stress and strain signals in fatigue tests.

Two point and four point bending tests as well as uni-axial tension/compression tests can be performed in the load or displacement controlled mode. Sinusoidal as well as haversine, or half sine, load and displacement signals can be applied. In the indirect tension fatigue tests only load controlled half sine or haversine signals can be applied. Be aware of the fact that "constant load fatigue tests" are often called "constant stress tests" while "constant displacement tests" are often called "constant strain tests" but keep it mind that it is not the stress or strain that is kept constant during the test but the load or displacement.

Let us discuss a load and displacement controlled 3 point bending test (figure 126) in which one uses sinusoidal load or displacement signals. Figure 127 gives a schematic overview of what is happening in such tests.

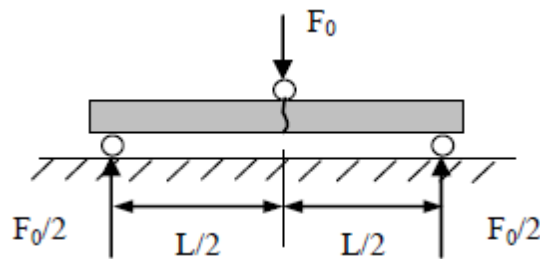


Figure 126: 3 Point bending test.

In the 3 point bending test, the maximum bending moment and maximum bending stress occur at midspan. Also the maximum deflection/displacement occurs at midspan. When the load signal is sinusoidal the maximum stress and strain will alternately occur at the bottom and top of the beam at midspan.

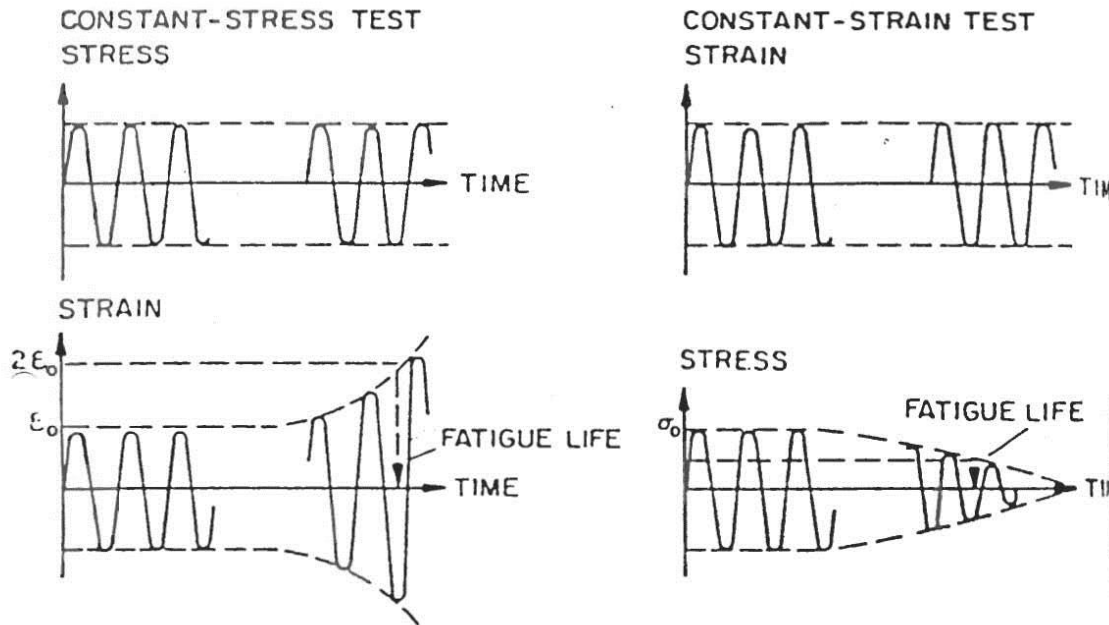


Figure 127: Constant load/stress and constant displacement/strain bending fatigue tests with sinusoidal load or displacement signal.

In the constant load test, the amplitude of the sinusoidal load signal is kept constant. After a certain number of load repetitions, damage will develop in the specimen which results in a decrease of the effective stiffness. Because the load is kept constant, the displacement will rapidly increase until collapse of the beam occurs (remember: displacement at midspan = $F \cdot L^3 / [4 \cdot E \cdot b \cdot h^3]$; b and h are resp. width and height of beam).

In the constant displacement test, the amplitude of the displacement signal is kept constant. After a certain number of load repetitions, damage will develop. This results in a decrease of the effective stiffness of the specimen which in turn results in a decrease of the load because less load is needed to get the same displacement. Collapse of the specimen does not occur in this test and "failure" is therefore defined as the number of load repetitions at which the stiffness of the beam (calculated from the load, displacement and geometry of the beam) has reduced to 50% of its initial stiffness.

If two beams of exactly the same composition and dimensions are tested under exactly the same initial conditions (same initial stress and same initial strain), but one is tested in the constant load mode and the other in the constant displacement mode, then the number of load repetitions to initiation will be exactly the same. The difference is in the damage propagation phase which will be much shorter in the constant load test than in the constant displacement test. Therefore the number of load repetitions to failure in the constant load test will be less than in the constant displacement test.

When the fatigue test is performed at different load/displacement levels, one will notice that the lower the load/displacement the higher the number of load repetitions will be. It is common practice to relate the number of load repetitions to the initial stress or strain in the specimen by means of the equation given below:

$$N = a \varepsilon^{-b} \quad \text{or} \quad N = c \sigma^{-d}$$

Since $\sigma = E \varepsilon$ we can write the stress based equation as $N = c E^{-d} \varepsilon^{-d}$.

It is also common practice to present the fatigue relationship in a plot which shows $\log N$ vs $\log \epsilon$ which is a straight line. If we however plot the fatigue results on a linear – linear scale we obtain a plot like shown in figure 128.

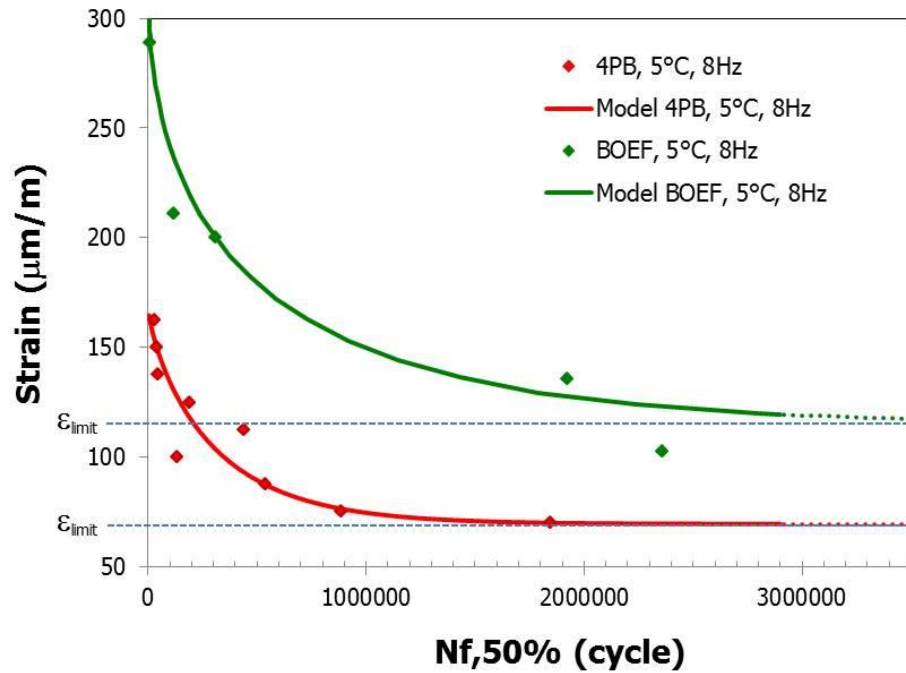


Figure 128: Graph of fatigue test results when using a linear – linear representation instead of $\log - \log$ [38] .

Figure 128 shows some interesting aspects. First of all Beam on Elastic Foundation (BOEF) test resulted in a much longer fatigue life than the four bending (4PB) fatigue test. Why there is a difference between the BOEF and 4PB test will be discussed later on.

Secondly, there seems to be a strain threshold value below which no fatigue occurs. This limit is called the endurance limit. This limit is around 70 $\mu\text{m/m}$ in the 4PB test and around 115 $\mu\text{m/m}$ in the BOEF test.

Figure 129 shows an example of the sinusoidal signals as used in 2, 3, and 4 point bending tests as well as in uni-axial tension/compression (UTC) tests. Note the phase difference between load and displacement.

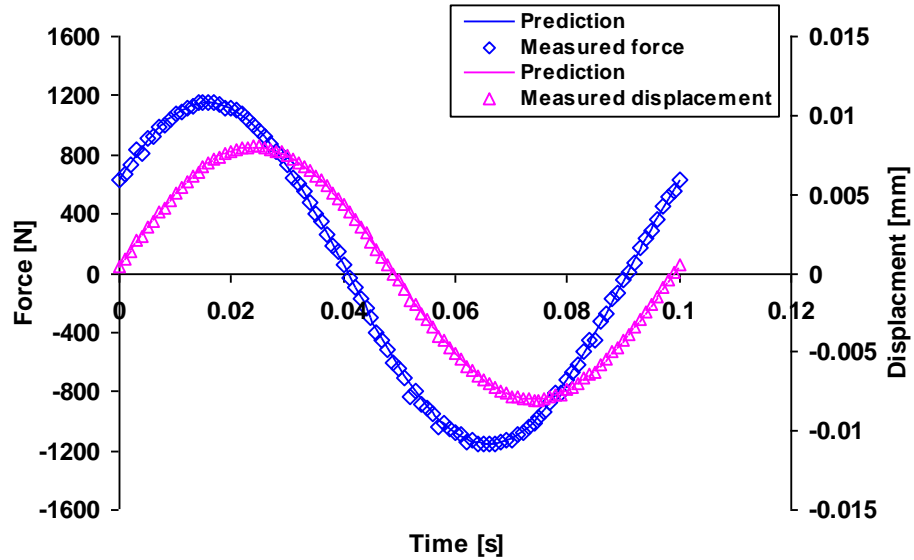


Figure 129: Sinusoidal signals as used in bending tests and UTC tests [41].

Figure 130 shows an example of the haversine load and resulting horizontal displacement signal as obtained in a load controlled indirect tension test. Figure 131 shows where the horizontal LVDT's (displacement transducers) are placed.

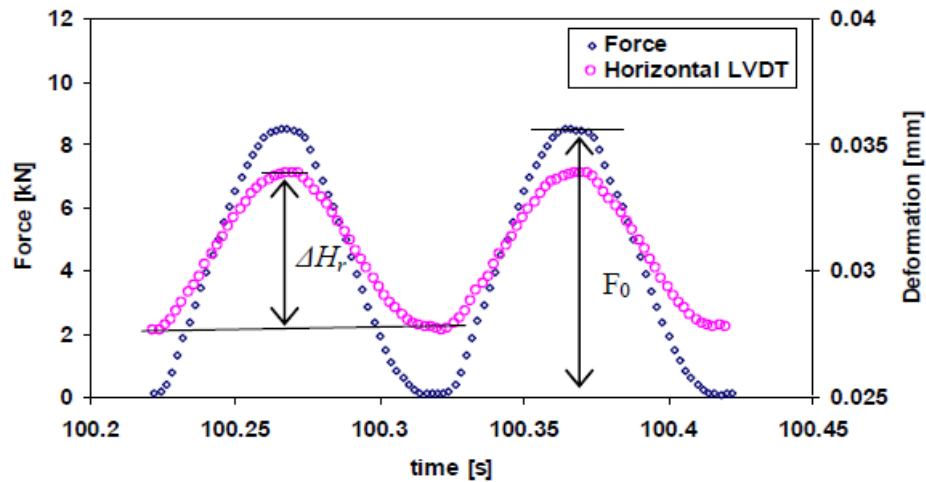


Figure 130: Haversine load signal and resulting horizontal displacement signal as applied in an indirect tension test [39].

In the indirect tension test, the stresses in the specimen can be calculated from the load, the geometry of the specimen and the width of the loading strips. The modulus of the specimen is calculated from the load, geometry of the specimen and the measured vertical and horizontal displacement. If the vertical displacement is not measured then a value for Poisson ratio has to be estimated for the calculations.

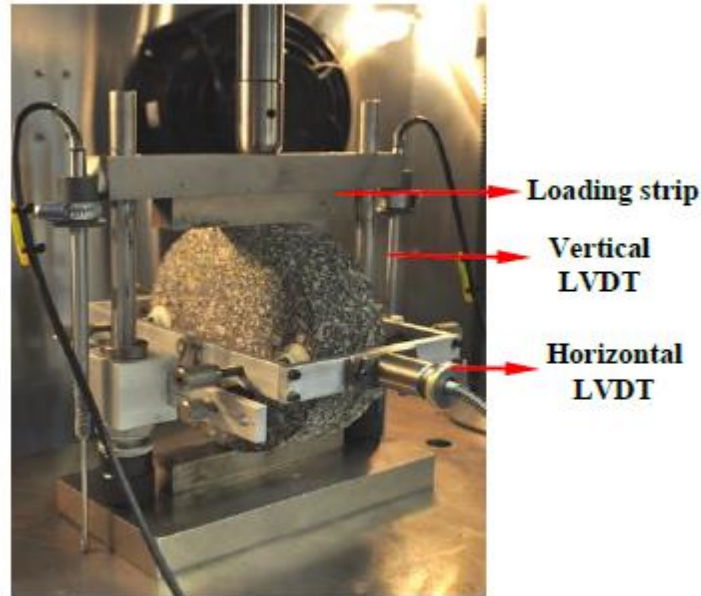


Figure 131: Indirect tension test.

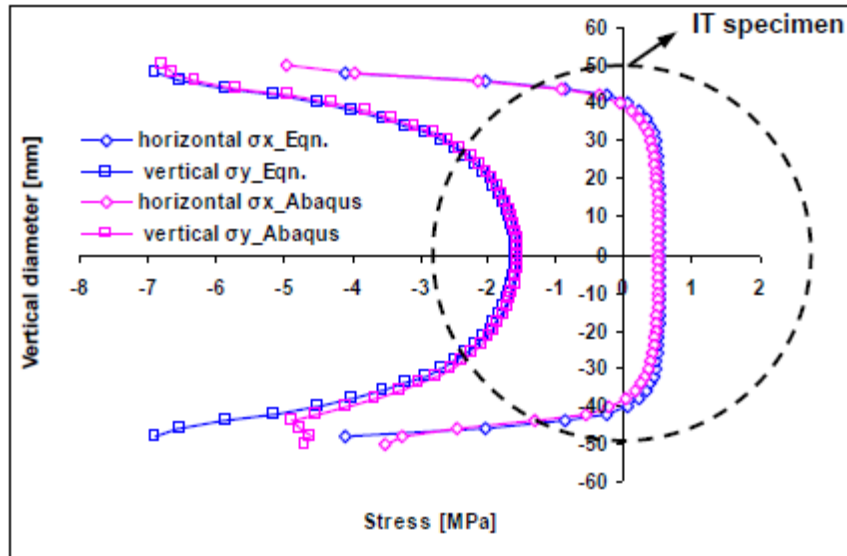
Figure 132 shows the horizontal and vertical stress and strain distribution along the vertical diameter of the specimen. The figure shows that at the center of the specimen the vertical compressive stress has a value which is 3 times the horizontal tensile stress. This horizontal tensile stress (σ_t) at the center of the specimen is calculated using:

$\sigma_t = 2 F / \pi t D$ where F is the applied load, t is the thickness of the specimen and D the diameter.

The vertical compressive stress (σ_c) at the center of the specimen is $\sigma_c = - 3 \sigma_t$

One will notice that the horizontal tensile stress and strain are rather constant over the mid 80 mm of the specimen. However the maximum tensile strain occurs 14 mm below the upper loading strip and 14 mm above the lower loading strip. At these locations damage will initiate and NOT in the center of the specimen which is often believed to be the case.

Since the indirect tension test always need to be performed with a haversine or half sine load cq displacement signal (when using a sinusoidal signal the load strips would loose contact with the specimen), also permanent deformation is developing during the test. Examples of such deformations are shown in figure 133 [41]. As one can observe from figure 133b and 133c, both the elastic deformation D_r and cumulative permanent deformation D_p start to increase rapidly after the same number of load repetitions.



(a)

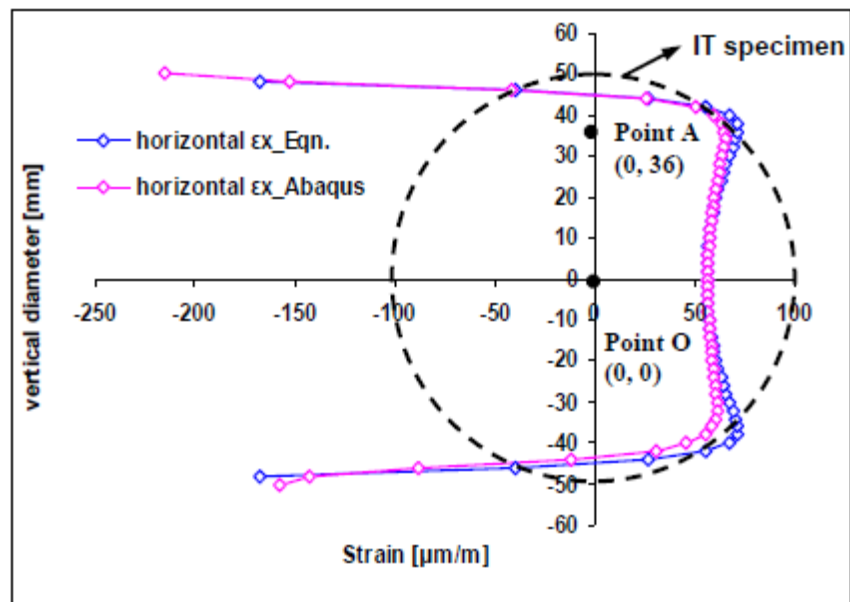


Figure 132: Horizontal and vertical stresses and strains along the vertical diameter of a 100 mm diameter indirect tension specimen as calculated analytically and with the finite element program ABAQUS [41].

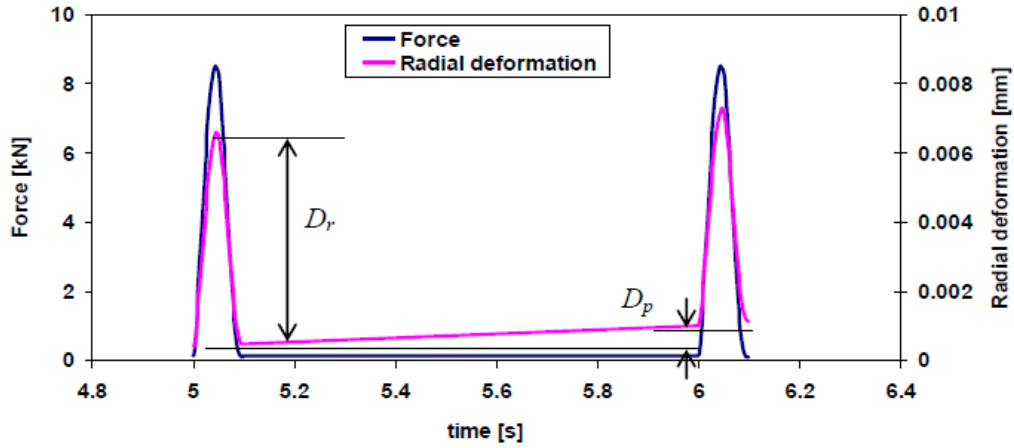


Figure 133a: Load and horizontal radial deformation during an indirect tension test. D_r is elastic deformation, D_p is permanent deformation.

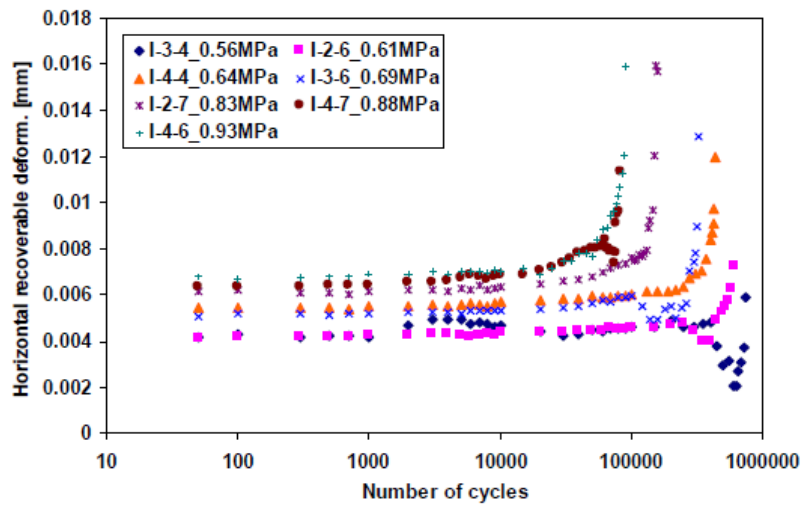


Figure 133b: Development of the horizontal recoverable/elastic deformation D_r during some indirect tension fatigue tests.

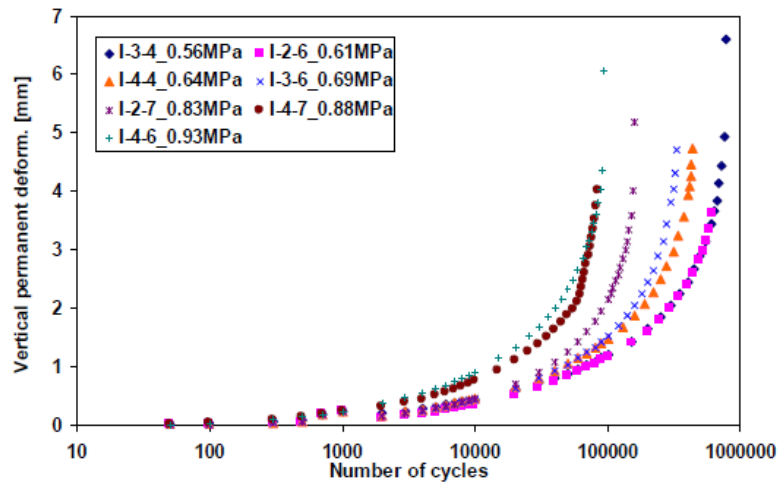


Figure 133c: Development of the cumulative vertical permanent deformation D_p during some indirect tension fatigue tests.

It should be noted that permanent deformations will also develop in the 2 point, 3 point and 4 point bending fatigue test as well as the UTC test when haversine or half sine load or displacement signals are used in these tests.

One aspect should be discussed when performing displacement controlled fatigue tests using a haversine or half sine signal. Initially the force signal as a result of the induced displacement will also be a haversine or half sine but will rapidly change into a full sine. This is because residual stresses will develop as a result of the visco-elastic behavior of the asphalt mixture; an example of the development of such residual stresses is shown in figure 134.

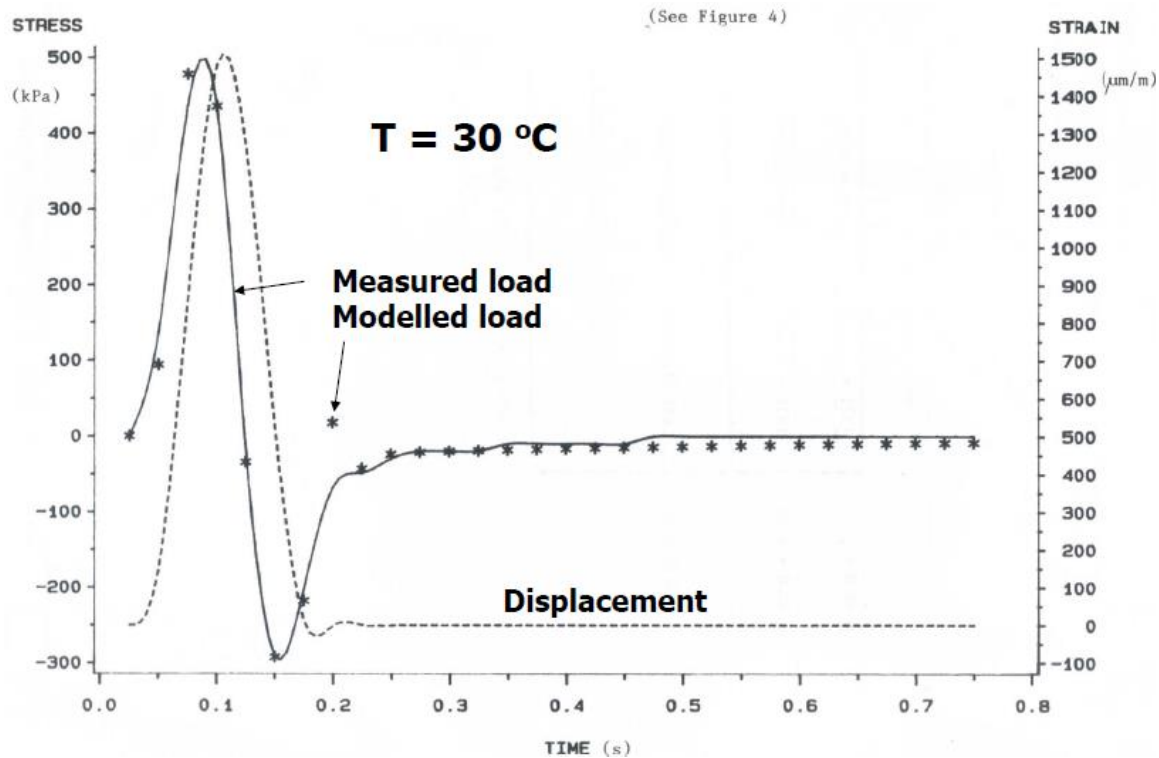


Figure 134: Development of residual stresses in a direct tension test with a displacement controlled haversine signal.

If however sufficient long rest periods are applied between the successive displacement pulses, then the residual stresses have time to relax and the resulting load signal is more or less a haversine or half sine as well.

Since the development of residual stresses is related to the visco-elastic behavior, such stresses will mainly develop at conditions where the viscous nature of the mixture is important which is at the higher temperature and longer loading time conditions. At low temperatures and short loading times, the build-up of residual stresses is of (far) less importance since at such conditions asphalt mixtures behave more elastically.

8.6.4 Discussion on differences between laboratory and field conditions and their consequences for pavement design

Comparison of the strain signals as observed in practice with the strain signals which are applied in laboratory tests immediately tells us that the longitudinal signals observed in practice are not matched by any of the fatigue tests. The transversal strain signals as measured in practice are only matched to a fair degree by laboratory tests if they are performed in the load controlled mode with a half sine or haversine signal. Unfortunately the rate of damage propagation as

observed in the load controlled laboratory fatigue tests is “explosive” because the samples are not fully supported as they asphalt layer is in practice by the supporting layers.

In practice, the asphalt layer will bend because of the applied traffic load. Stress conditions like those occurring in the UTC and indirect tension test do not occur in practice.

Bending fatigue tests seem therefore most appropriate to simulate what is happening in practice however in reality one is dealing with a 3D stress condition in the pavement while in all bending tests one has a 1D stress condition. Furthermore there is a difference between the thickness of a real asphalt pavement and the beam and, perhaps most importantly, an asphalt layer in a pavement is fully supported while the laboratory test beams are not; this difference does have a great impact on the damage propagation rate in beams tested in the lab and in the asphalt layer of a real pavement.

All in all this means that some major steps have to be made to match field conditions by means of lab conditions.

8.6.5 Discussion on the differences between the various fatigue tests and potential size effects

Figure 135 gives an overview of the stress conditions which occur in the tests discussed so far.

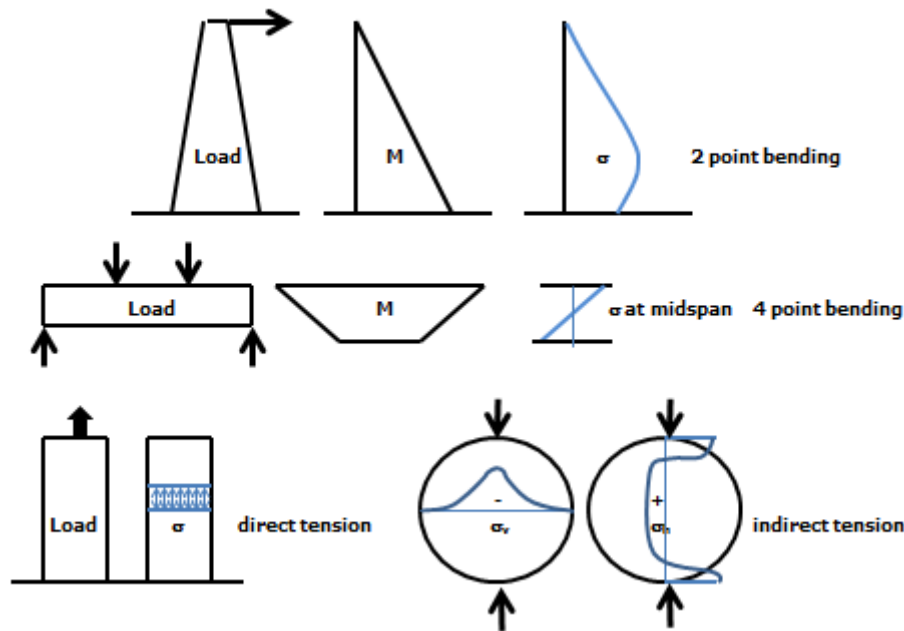


Figure 135: Stress conditions in some of the fatigue tests used.

It seems logical to assume that there is an effect of the thickness of the specimen on the fatigue results in the bending tests since in a higher beam the crack should propagate over a longer distance than in a lower beam. Furthermore it seems logical to assume that a direct tension test specimen will fail earlier than a 4 point bending specimen when the stress in the direct tension test specimen is equal to the stress at the bottom of the 4 point bending specimen. It is also not unreasonable to assume that the indirect tension specimen will give the shortest fatigue life because of the bi-axial stress conditions.

The effect of the specimen size on 2 point bending fatigue test results has been shown by Bodin [42] while Li [41] showed the effect of specimen size on 4 point bending tests. Li [41] also

showed that significant differences exist between the results of UTC, 4 point bending and indirect tension fatigue tests. Li [41] reported the following results (table 23).

Size	0.5	1	1.5
4 point bending	1.95	1	0.71
UTC	0.41	0.37	0.35

Table 23: Relative fatigue lives at a tensile strain of 100 $\mu\text{m}/\text{m}$ of UTC and 4 point bending test samples of different sizes compared to the fatigue life of 4 point bending samples of size one; all specimens tested at 20 °C and 10 Hz in the displacement controlled mode.

The meaning of "size 0.5, size 1 and size 1.5" is given in table 24. As one will observe, the "sizes" are related to the diameter of the specimen or the height of the specimen. Only for the 4 point bending specimens they also relate to the critical cross sectional area.

For UTC specimens the difference between load controlled and displacement controlled tests is shown in figure 136. The figure also shows the effect of temperature and specimen size.

Test type	Specimen size	Dimension [mm]	Cross area in critical location [mm^2]
UT/C	Size 0.5	$\phi \times h = 25 \times 62.5$	491
	Size 1.0	$\phi \times h = 50 \times 125$	1964
	Size 1.5	$\phi \times h = 75 \times 187.5$	4418
4PB	Size 0.5	$l \times w \times h = 400 \times 50 \times 25$	1250
	Size 1.0	$l \times w \times h = 400 \times 50 \times 50$	2500
	Size 1.5	$l \times w \times h = 400 \times 50 \times 75$	3750
IT	Size 1.0	$\phi \times h = 100 \times 30$	2100
	Size 1.5	$\phi \times h = 150 \times 45$	4725

Note: size 0.5 = small size; size 1.0 = medium size; size 1.5 = large size
 $\phi \times h$ = diameter \times height, $l \times w \times h$ = length \times width \times height

Table 24: Different specimen sizes as used by Li [39].

At 5 °C and a strain level of 100 $\mu\text{m}/\text{m}$ there is a difference of a factor of 3.2 in fatigue life between the displacement and load controlled fatigue test.

Figure 137 shows the results of the load controlled fatigue tests performed in 4 point bending, UTC and indirect tension. The tensile stress is either the tensile stress at the bottom of the beam (4PB) the stress over the entire cross sectional area (UTC) or the tensile stress at the center of the specimen (indirect tension).

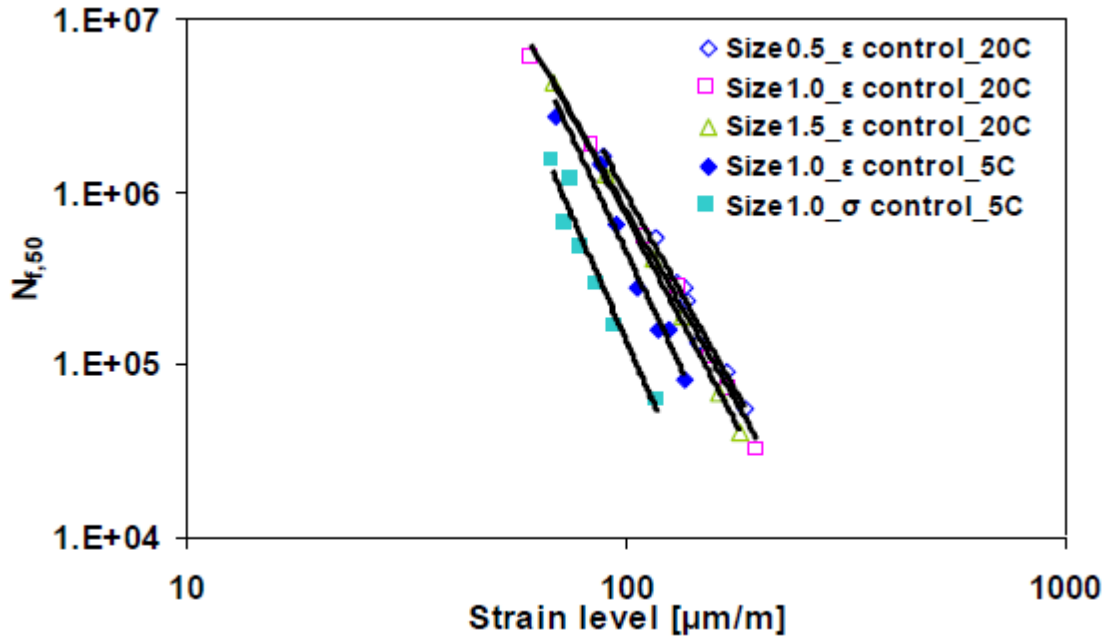


Figure 136: Fatigue results obtained at 5 °C with the UTC test in the displacement (ϵ) controlled and load (σ) controlled mode. Also the effect of temperature on the fatigue results is shown (compare: size 1.0_ε control 20C with size 1.0_ε control 5C).

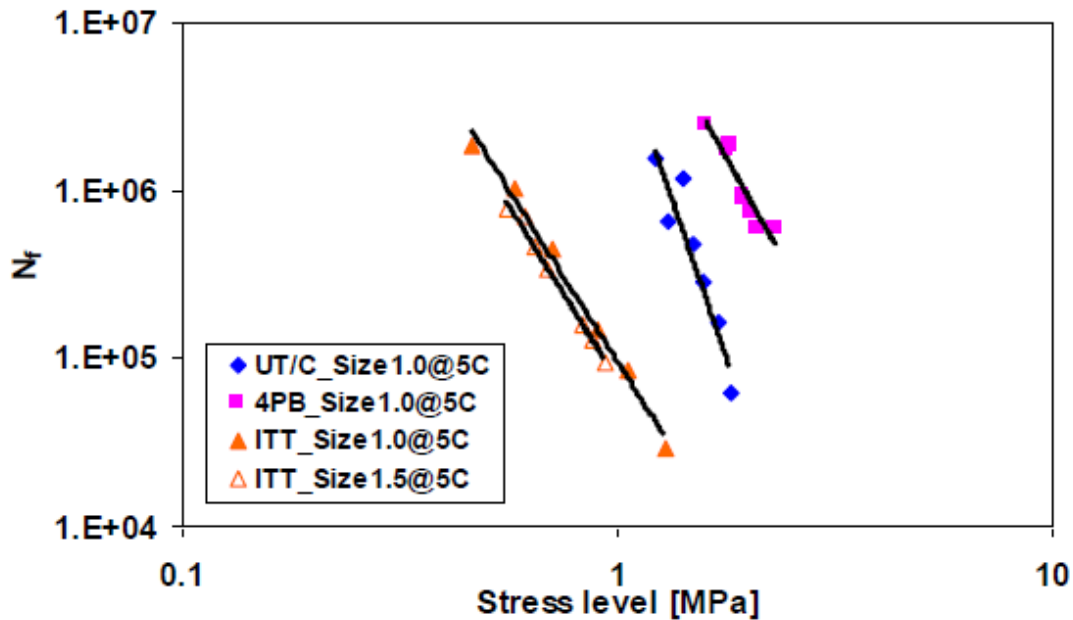


Figure 137: Difference in fatigue life as determined in the load controlled mode by means of 4 point bending tests, UTC tests and indirect tension tests.

Summarizing what has been discussed so far, we come to the following conclusions:

- Beam bending fatigue tests suffer from a size dependency being that the higher the specimen the lower the fatigue life will be.
- There is also some size dependency in the UTC and indirect tension fatigue tests results but that is much smaller than in the 4 point bending test.

- There is a significant difference between the results of load and displacement controlled fatigue tests.
- Different tests result in significantly different results.

The question now is whether the differences can be explained and if not which test should be used for pavement design purposes.

Let us discuss first the size effect that is affecting the bending beam test results. Groenendijk [23] has shown that by using fracture mechanics principles the fatigue relation can be written as:

$$N = \frac{h^{(1-\frac{n}{2})} c_f/h}{A[S_{mix}]^n \int_{c_0/h}^{c_f/h} \frac{d(c/h)}{\left[1.99\left(\frac{c}{h}\right)^{0.5} - 2.47\left(\frac{c}{h}\right)^{1.5} + 12.97\left(\frac{c}{h}\right)^{2.5} - 23.17\left(\frac{c}{h}\right)^{3.5} + 24.8\left(\frac{c}{h}\right)^{4.5}\right]^n}} \cdot \epsilon^{-n}$$

Where:

N = number of cycles to fatigue

S_{mix} = mixture stiffness

h = specimen thickness/height

A = constant from Paris' crack growth law $dc/dN = A K^n$

A = f(S_{mix}, tensile strength, fracture energy, slope of the relation log S_{mix} vs log t)

t = loading time

K = stress intensity factor at the tip of the crack

n = exponent of Paris' crack growth law = f(slope log S_{mix} vs log t relation)

c₀ = initial crack length

c_f = final crack length = specimen height

ε = applied tensile strain

Since n takes a positive value (depending on type of mixture, temperature and loading time $3 < n < 7$), the exponent value $(1 - n/2)$ takes a negative value implying that a thicker beam will show a shorter life time than a thinner beam.

It should be noted that the long c/h polynomial function is describing the change in stress intensity factor in a 4 point bending test in relation to and increasing crack length. This function will take a different form for UTC and indirect tension tests.

All in all this means that bending tests are indeed affected by the specimen thickness/height.

The differences between the UTC and the 4 point bending tests can be explained in the following way. As shown in figure 135, there is a uniform stress distribution over the cross sectional area in a UTC test. In a 4 point bending test however that same tensile stress would only occur at the bottom of the beam (a triangular stress distribution is present across the height of the beam). Li [41] has shown that there would be perfect agreement between the UTC test and the 4 point bending test if one would not consider the failure of the entire beam but only failure of the outer fiber of the beam; this is shown in figure 138.

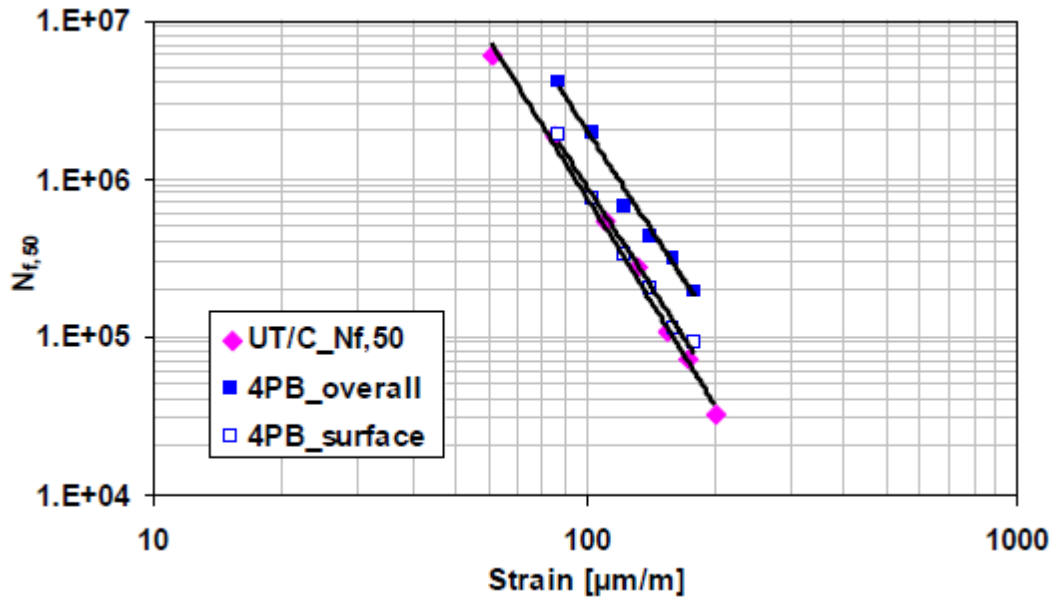


Figure 138: Comparison of the fatigue life of the outer fiber of a 4 point bending fatigue beam with that of the UTC test and the overall fatigue life of the 4 point bending beam.

Comparing the results of the load controlled indirect tension fatigue results with those obtained by any of the other load controlled tests is rather complicated because of the rather complex stress conditions in the indirect tensile test. Furthermore only a comparison of results obtained by means of haversine or half sine load controlled signals would be a fair one because in such cases permanent deformation of the specimen occurs which certainly affects the fatigue life.

We have seen in figure 132 that the tensile strain in an indirect tension specimen is rather constant over most of the vertical diameter (line of loading) of the indirect tension specimen. Because in a UCT specimen the tensile strain is constant over the cross sectional area, it might be fair to make a strain based comparison between the UCT and the indirect tension test. Such a comparison is given in figure 139.

Figure 139 shows that there is not too much difference between the "UTC size 1.0_σ_5°C" fatigue line and the "IT size 1.0_σ_5 °C" fatigue line. At a tensile strain of 100 μm/m they produce almost the same result. The comparison is made a bit complicated by the fact that the slope of the fatigue relations of the UTC and indirect tension test is not the same. Why these slopes are not the same is hard to explain because they should be the same. Furthermore one should be aware of the fact that permanent deformation did develop in the indirect tension fatigue test and not in the UCT test. The noticed "agreement" might therefore be lucky shot.

From the material presented above it becomes clear that we can explain to some extent why we obtain different fatigue test results from different tests but it is not yet clear which test is to be preferred for pavement design purposes.

8.6.6 Fatigue based on dissipated energy

During each load cycle, energy is induced in the test sample. When the material is elastic, this energy will be completely released when unloading. No energy is stored in the material itself. Asphalt mixtures however are visco-elastic materials and because of this visco-elastic behavior energy will be dissipated and will be transformed into heat and some will be used for damage development. Example of the energy dissipation that takes place during a load/stress and displacement/strain controlled fatigue test is given in figure 140.

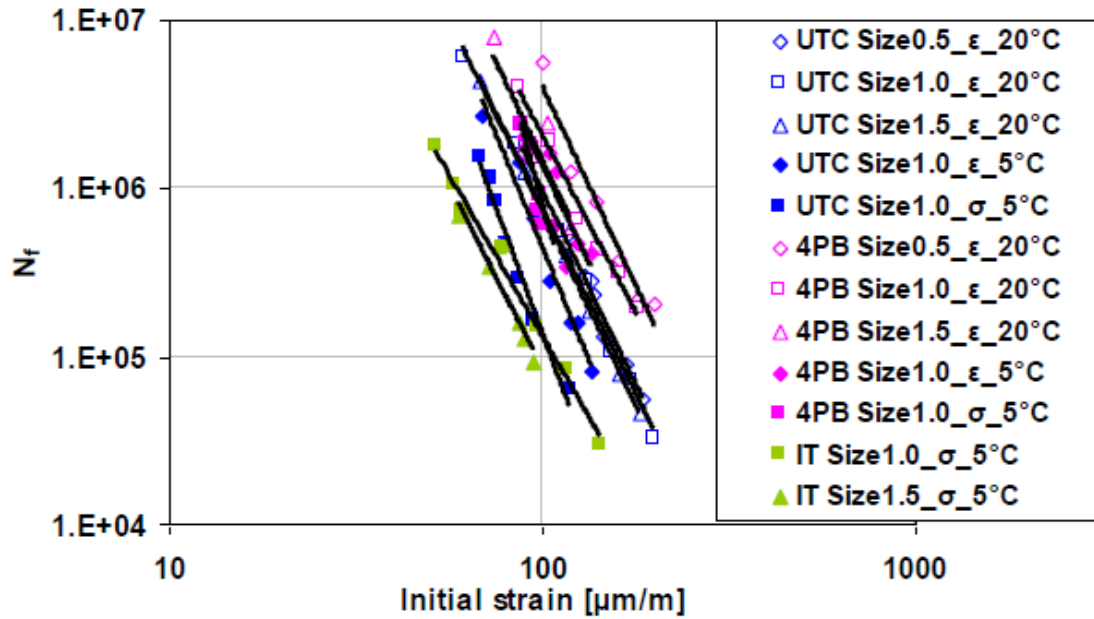


Figure 139: Comparison between different fatigue lives obtained with different fatigue tests.

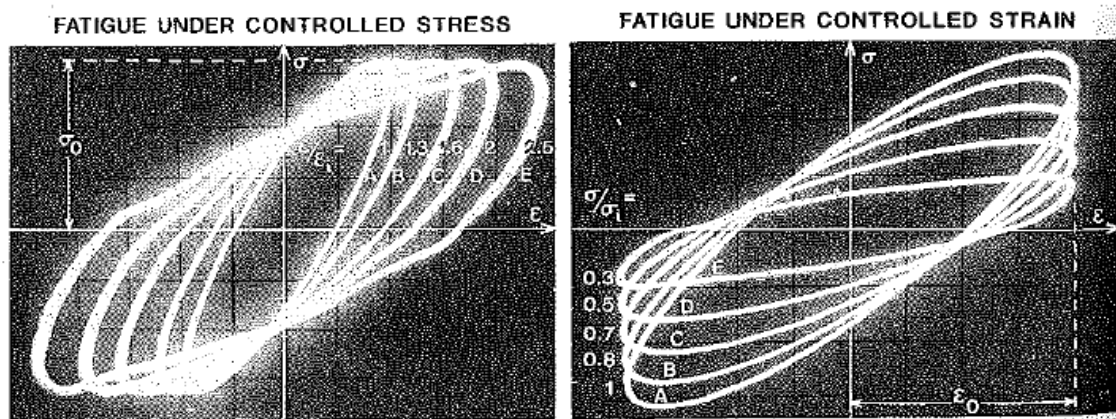


Figure 140: Energy dissipation in a load/stress and displacement/strain controlled fatigue test.

The amount of dissipated energy is equal to the area enclosed by the stress – strain hysteresis loop. In a load controlled test the dissipated energy per load cycle will increase during the test (hysteresis loop will increase) while in a displacement/strain controlled test the dissipated energy per cycle will decrease during the test. The change in amount of dissipated energy is because of damage development.

In a fatigue test where a sinusoidal load/displacement signal is used, the total amount of energy that is dissipated during a test can be calculated using:

$$W_{fat} = \pi * \sum_{i=1}^n \sigma_i * \epsilon_i * \sin \phi_i$$

Where:

W_{fat} = total amount of dissipated energy at which fatigue failure occurs

σ, ϵ, ϕ = respectively the stress amplitude, strain amplitude and phase angle between σ and ϵ at load cycle i

Van Dijk [43] has shown that for each mixture a unique relationship exists between the number of load repetitions to fatigue N_{fat} and W_{fat} which he claimed was independent on the type of test. This relationship is shown in figure 141 and can be written as $W_{fat} = A * N_{fat}^z$.

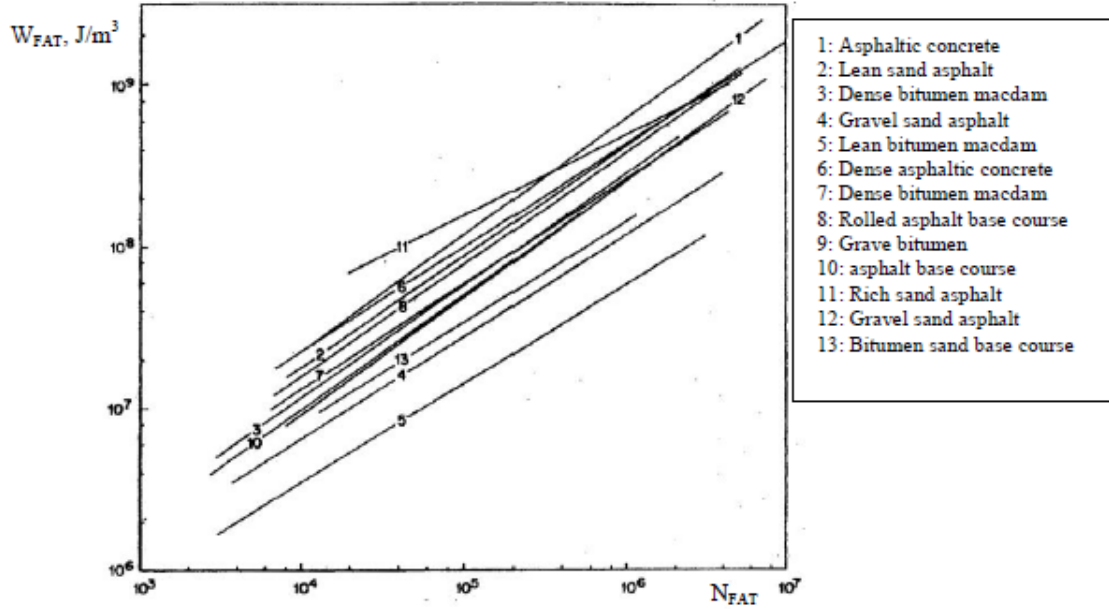


Figure 141: Relationship between N_{fat} and W_{fat} according to van Dijk [41].

If we assume that the relation between N_{fat} and W_{fat} is independent of the type of mixture, we can develop a dissipated energy based fatigue relation in the following way.

$W_{fat} = \sum_{i=1}^{n=N_{fat}} W_i = N_{fat} * W_1 / \psi$ where ψ is a factor taking care for the change in dissipated energy per cycle during the test and W_1 is the energy dissipated in the first load cycle. Following this we can write

$$W_{fat} = N_{fat} * \pi * \sigma_1 * \epsilon_1 * \sin \phi_1 / \psi = A * N_{fat}^z$$

Since $\sigma = \epsilon * S_{mix}$, we arrive after rewriting to

$$N_{fat} = (\pi * S_{mix_1} * \sin \phi_1 / \psi * A)^{1/(z-1)} \epsilon_1^{2/(z-1)}$$

It is recalled that fatigue relations are usually written as $N_{fat} = k_1 \epsilon^{-n}$ so:

$$-n = 2/(z-1) \text{ and } k_1 = (\pi * S_{mix_1} * \sin \phi_1 / \psi * A)^{1/(z-1)}$$

As has been mentioned before, a certain part of the dissipated energy is transformed into heat and therefore doesn't contribute to the development of damage. It can be hypothesized that when the amount of dissipated energy per cycle starts to change, the physical condition of the test specimen starts to change which. This occurs when damage starts to propagate after a damage initiation phase. In order to be able to separate the initiation phase from the propagation phase the so called dissipated energy ratio (DER) has been introduced which is defined as:

$$DER = \sum_{i=1}^{n=k} W_i / W_k = \Lambda / W_k$$

Where:

DER = dissipated energy ratio

Δ = total amount of energy dissipated during cycle 1 to k

W_k = dissipated energy in cycle k

Figure 142 shows how the dissipated energy is changing in a load and displacement controlled UTC fatigue test. The figure also shows how a new fatigue life parameter N_R can be defined as being the number of load repetitions at which damage initiation is completed and damage propagation starts.

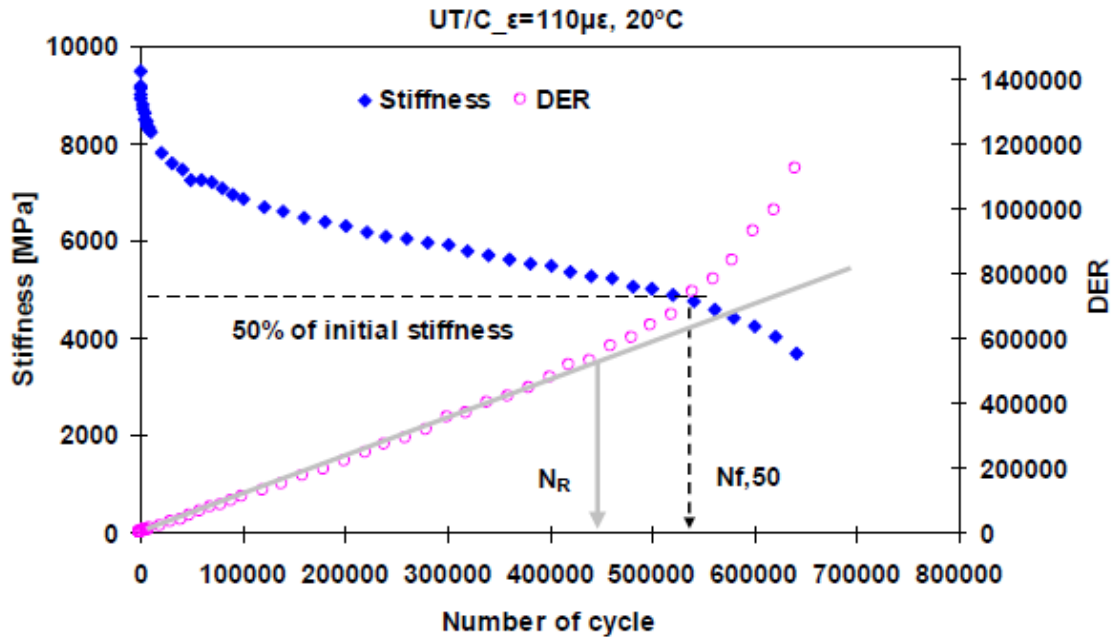


Figure 142a: Development of DER in a displacement controlled UTC fatigue test.

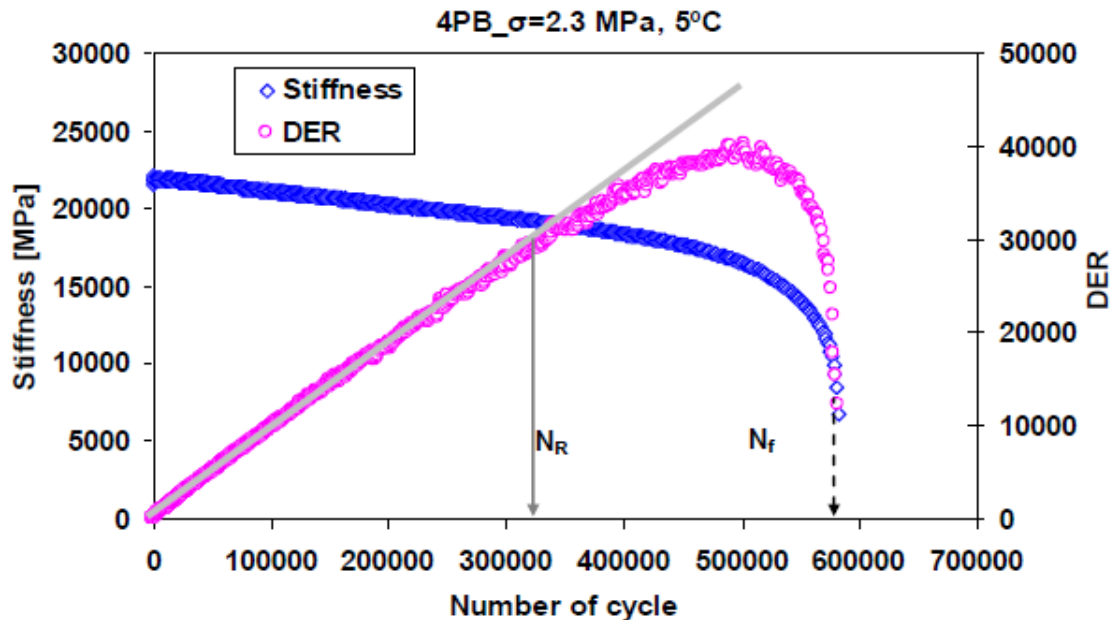


Figure 142b: Development of DER in a load controlled UTC fatigue test.

One will notice that N_R in case of the displacement controlled test is approximately 82% of the fatigue life $N_{f,50}$ at which the stiffness of the specimen has reduced to 50% of its initial value. At N_R the stiffness is still around 56% of its initial value.

In the load controlled test $N_R \approx 0.56 N_f$. At that number of load repetitions the stiffness is still around 86% of the initial value.

As has been mentioned before, damage initiation in a load controlled test should start after the same number of load repetitions as in a displacement controlled test when the initial conditions (stress, strain and modulus are the same). This implies that the same amount of energy should have been dissipated after N_R load repetitions have been applied irrespective of the type of test. Data produced by Li [41] (figure 143) however show that this independency is not completely true. The size dependency of the 4 point bending test results is e.g. still visible. All in all however all W_{fat} vs N_R relations are in rather good agreement with each other.

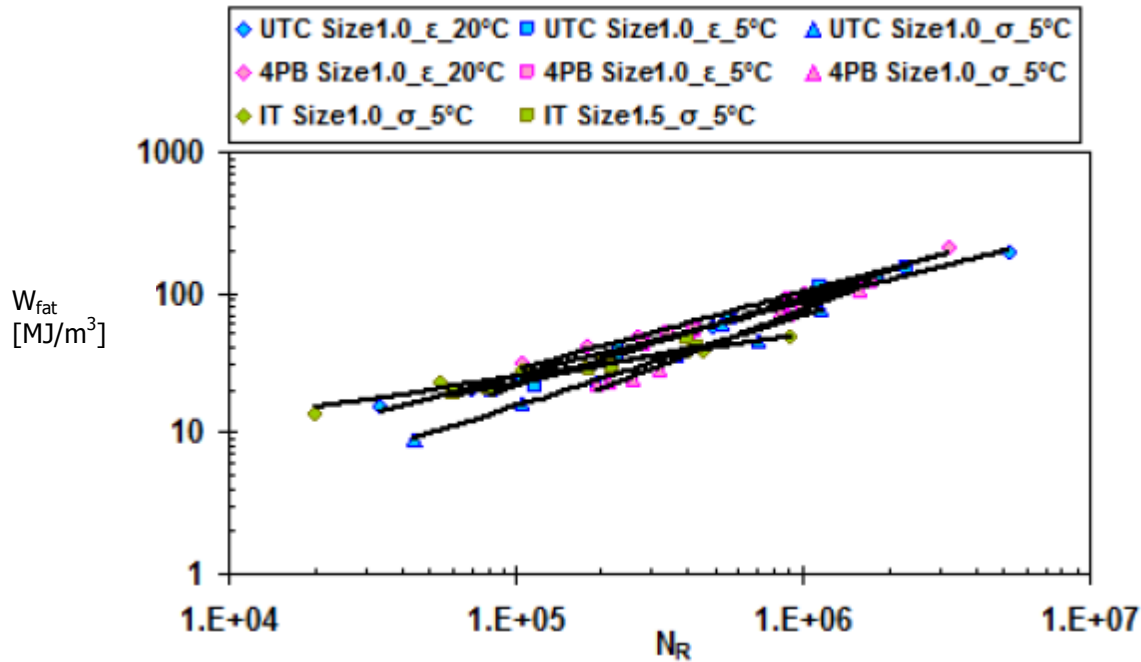


Figure 143: W_{fat} vs N_R relationships as determined on one type of mixture using different types of fatigue tests performed at different temperatures using different loading modes.

In conclusion this means that the number of load repetitions to initiation of fatigue damage (N_R) seems to be fairly independent of the type of test and test conditions. This implies that N_R seems to be a unique fatigue parameter and in any case a much better fatigue parameter than $N_{f,50}$ (fatigue = number of load repetitions to a 50% reduction in stiffness) used in the displacement controlled tests and the N_f (fatigue = number of load repetitions to failure/collapse) used in load controlled tests.

All this also implies that pavement design analyses based on initiation of fatigue damage preferably should be based on the total amount of dissipated energy, which is a scalar and accounts for the 3 D stress/strain conditions) and not on tensile strain, which is a vector and only takes account for the stress/strain conditions in one direction. This in turn implies that a visco-elastic analysis systems should be used instead of system which are based on linear elastic theory because a visco-elastic system can give the dissipated energy as a result of a passing wheel load.

In [44] an elegant procedure is presented which allows the number of load repetitions to fatigue to be calculated from the energy of distortion which is held responsible for fatigue damage. As we have seen, $U_{\text{distortion}}$ is calculated by means of the multi-layer linear elastic system BISAR. We can derive an $U_{\text{distortion}}$ based fatigue relation in the following way. We know that:

$$U_{\text{volume}} = \{3(1 - 2\mu) / 2E\} \sigma_{\text{hyd}}^2 = \{(1 - 2\mu) / 6E\} \{\sigma_1^2 + \sigma_2^2 + \sigma_3^2 + 2\sigma_2 \sigma_3 + 2\sigma_1 \sigma_2 + 2\sigma_1 \sigma_3\}$$

Since $U_{\text{distortion}} = U_{\text{total}} - U_{\text{volume}}$ we find

$$U_{\text{distortion}} = \{(1 + \mu) / 3E\} [(\sigma_1 - \sigma_2)^2 + (\sigma_2 - \sigma_3)^2 + (\sigma_3 - \sigma_1)^2] / 2]$$

In a uni-axial test $U_{\text{distortion}} = (1 + \mu) * \varepsilon * \sigma / 3$ so $\sigma * \varepsilon = 3 * U_{\text{distortion}} / (1 + \mu)$. Since we have seen that:

$$N_{\text{fat}} * \pi * \sigma_1 * \varepsilon_1 * \sin \phi_1 / \psi = A * N_{\text{fat}}^z \text{ we arrive to}$$

$$N_{\text{fat}} = (\pi * 3 * U_{\text{distortion}} * \sin \phi / [(1 + \mu) * A * \psi])^{1/(z-1)}$$

One might wonder why U_{volume} should also not be taken into account. Of course it can be taken into account as well but from the equations for U_{volume} and $U_{\text{distortion}}$ one can easily derive that in a uni-axial test, U_{volume} is only a fraction of $U_{\text{distortion}}$ and at $\mu = 0.5$ $U_{\text{volume}} = 0$.

8.6.7 Some practical aspects with respect to 2 point and 4 point bending tests as well as UCT and indirect tension tests

Doing a test is something that is easily said but doing it in the correct way and taking into account all the boundary conditions is another thing. In this paragraph some practical aspects will be discussed with respect to the fatigue tests that have been mentioned in the previous paragraphs. It will be shown that it is not that easy to comply to the conditions which are assumed when interpreting the test results.

2 Point bending test:

The (big) advantage of the 2 point bending test is that the shape of the specimen is such that the maximum stress doesn't occur at the location where the load is introduced and doesn't occur at the support of the system (see figure 135); this means that fatigue damage can "freely" develop. The disadvantage is that cutting the specimen is considered to be (somewhat) cumbersome. Furthermore restrictions need to be set to the thickness of the specimen in order to comply to the plain stress conditions which are assumed in the analysis.

4 Point bending test:

The problem with the 4 point (and also with the 3 point) bending test is that although the support system consists of rollers, some clamping forces need to be applied to fix the specimen. Furthermore, some clamping forces need to be applied in order to introduce the load. Figure 144 shows the support and load introduction arrangement in a particular 4 point bending test. One will observe the clamping system and how clamping forces are introduced.

It will be obvious that the clamping forces should be as low as possible and in this particular setup this was done by keeping the torque force by which the screws were tightened as low as possible. The influence of the clamping forces is shown in figure 145.

If the clamping forces are too high (this also depends on the type of mixture) than failure will occur at the location where the load is introduced instead of somewhere in the middle of the beam (see figure 146).

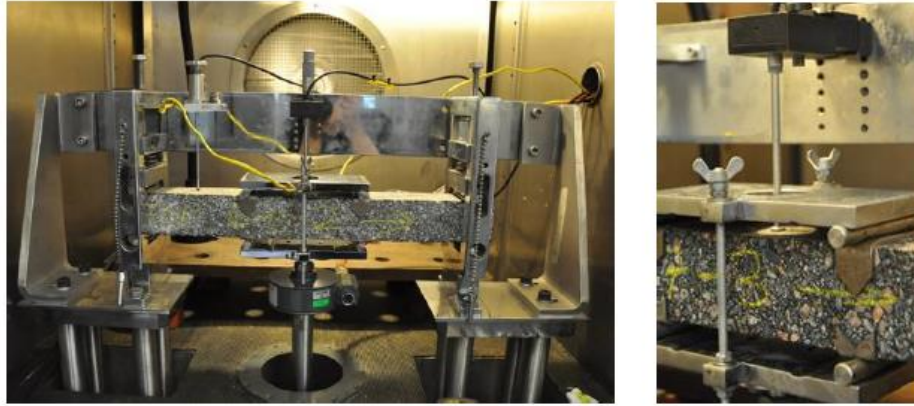


Figure 144: Support and load introduction arrangement in a 4 point bending test.

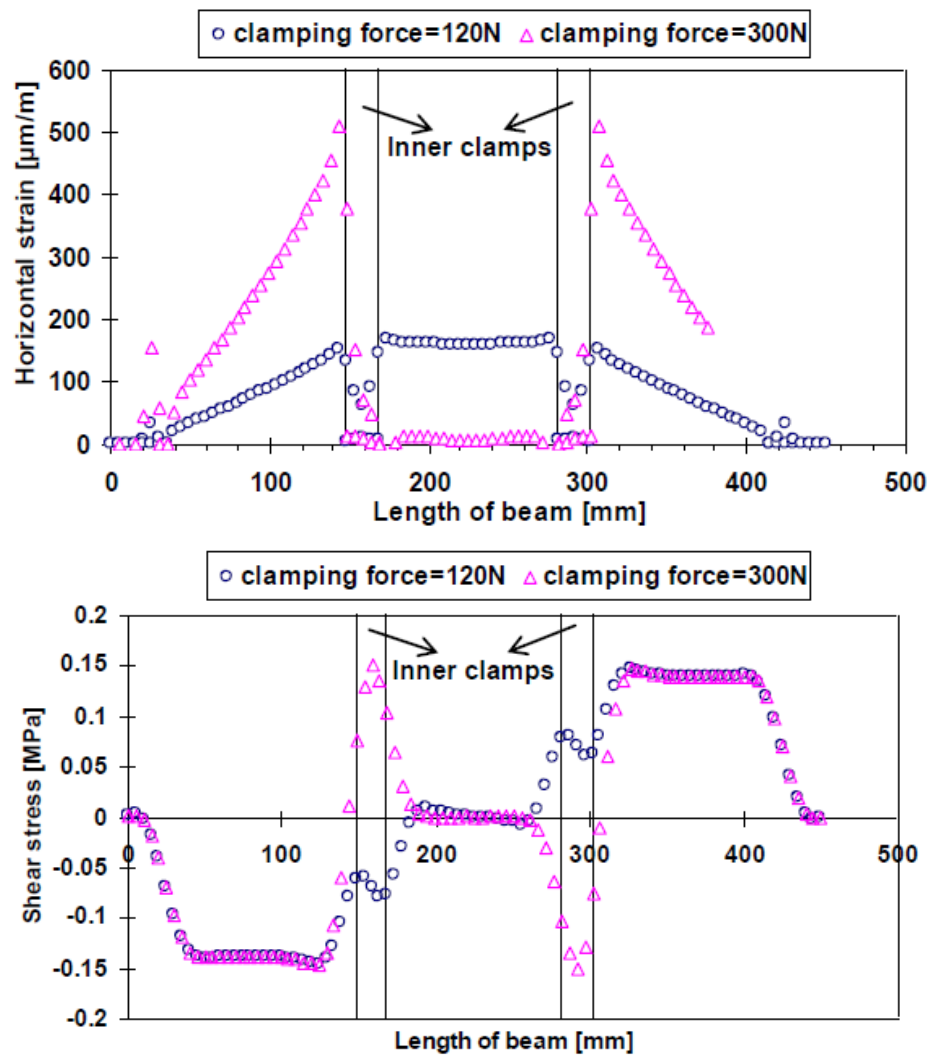


Figure 145: Tensile strain at the outer fiber of a 4 point bending beam (top) and shear stress in the middle of the beam (bottom) in relation to the applied clamping force.

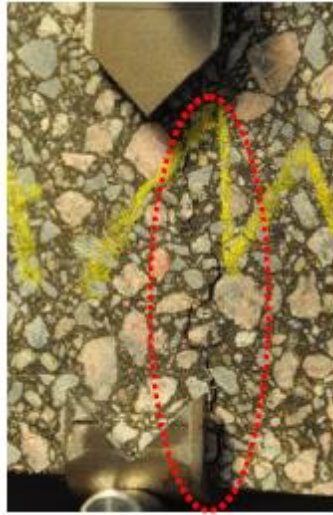


Figure 146: Failure near one of the inner clamps due to a too high clamping force.

UCT test

The stress distribution in a UCT test is considered to be very simple but this is not the case at the top and bottom of the specimen where it is glued to the loading platens. Because of the applied tension force, the specimen should be allowed to contract freely in the lateral direction. This is not possible at the top and bottom of the specimen since there lateral movement is equal to zero because of the glue. This results in horizontal stresses at the bottom and top of the specimen and it is therefore likely that the specimen will fail closely to the bottom or top of the specimen and not somewhere in the middle what is expected. This problem can be overcome by applying extra adhesive so that a ring of confining glue is around the top and bottom end of the specimen (see figure 147).

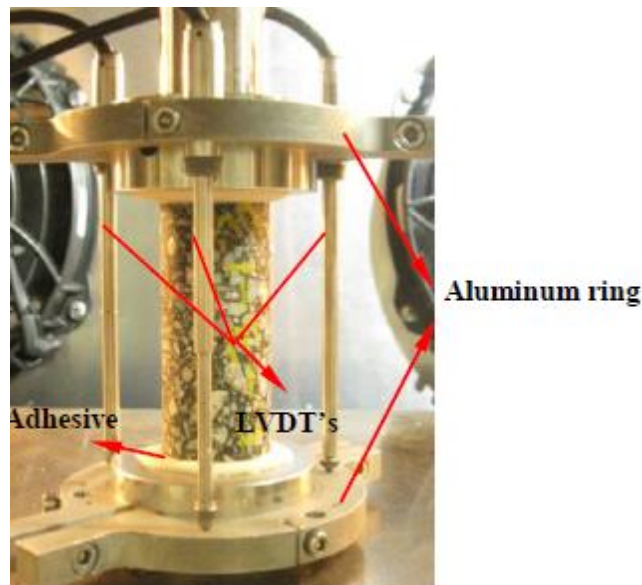


Figure 147: Ring of adhesive around top and bottom of specimen for providing confinement.

Another issue with the UCT test is that a perfect alignment of the specimen is absolutely needed.

Indirect tension test

The equations that are used to calculate the stresses inside an indirect tension test specimen are valid if a plain stress condition occurs in the specimen. Plain stress conditions do occur if the ratio diameter : thickness is equal or larger than 3. The specimen shown in figure 148 is actually too thick to fulfill the plain stress condition.

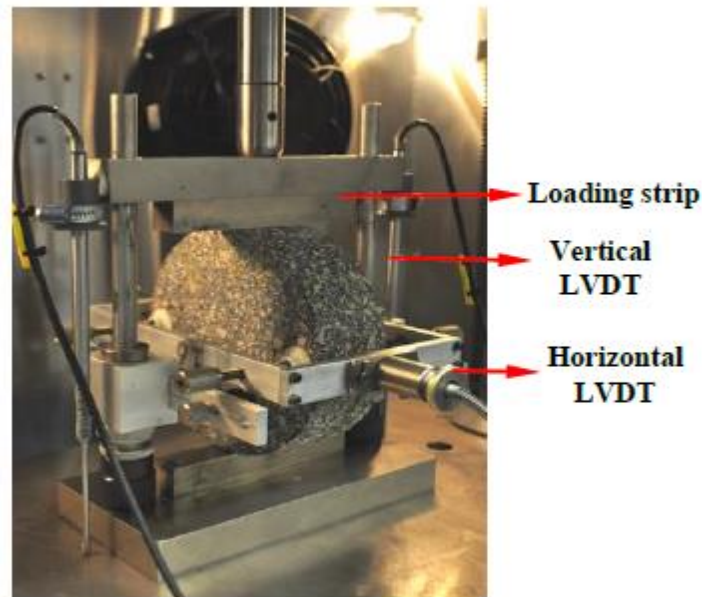


Figure 148: Indirect tension test specimen which is too thick to comply with the assumed plain stress conditions.

The plain stress criterion results in rather thin specimens and when the test is performed at temperatures of 10 °C and higher the chance that the upper and lower loading strip are penetrating the specimen is very likely (see figure 149). It is obvious that such failure has little to do with tensile failure. It is therefore strongly recommended to do indirect tension tests on specimens that fulfill the plain stress criterion (diameter : thickness ratio ≥ 3) at temperatures of 5 °C and lower. Of course the penetration of the upper and lower loading strip can be overcome by using thicker specimens but then the plain stress equations are not valid anymore.



Figure 149: Indirect tension test specimen where loading strips have penetrated the specimen. Failure is a combination of shear, compression and tension.

Figure 148 shows that a special rig is used to which the horizontal LVDT's are attached. This rig is clamped to the specimen. Also in this case the clamping forces should be as low as possible since they provide confinement and will influence the measured displacements.

8.6.8 Tests on slabs and beam on elastic foundation (BOEF) tests

We have seen that by using the energy approach we might be able to make reasonable predictions of the initiation of fatigue life in terms N_R but pavements can still sustain large numbers of load repetitions after initiation of fatigue damage. Depending on the structure and the materials used the crack propagation phase might be very significant. None of the presented fatigue tests however allows a realistic prediction of crack propagation to be made.

The solution to all this uncertainty is of course to perform fatigue tests on fully supported slabs by means of rolling wheel loads. The MMLS3 (figure 150) is excellently suited to perform such tests.

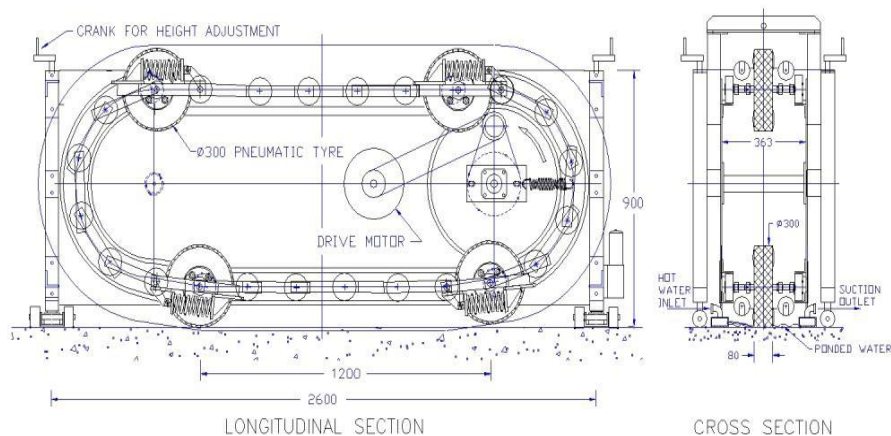


Figure 150: MMLS3.

The “power” of using such a system has however been shown by Shell [45] which used such a system to determine which type of fatigue test (controlled load or controlled displacement test) gives a relationship which is the most appropriate one for pavement design purposes. The test setup as used by Shell is shown in figure 151.



During the test, the increase in tensile strain as well as the developments of cracks were carefully monitored; see figure 152. Figure 152 clearly shows that the crack propagation period during which the initially formed hairline cracks had developed to some kind of network and later on to real cracks is quite long; this is made visible in figure 153.

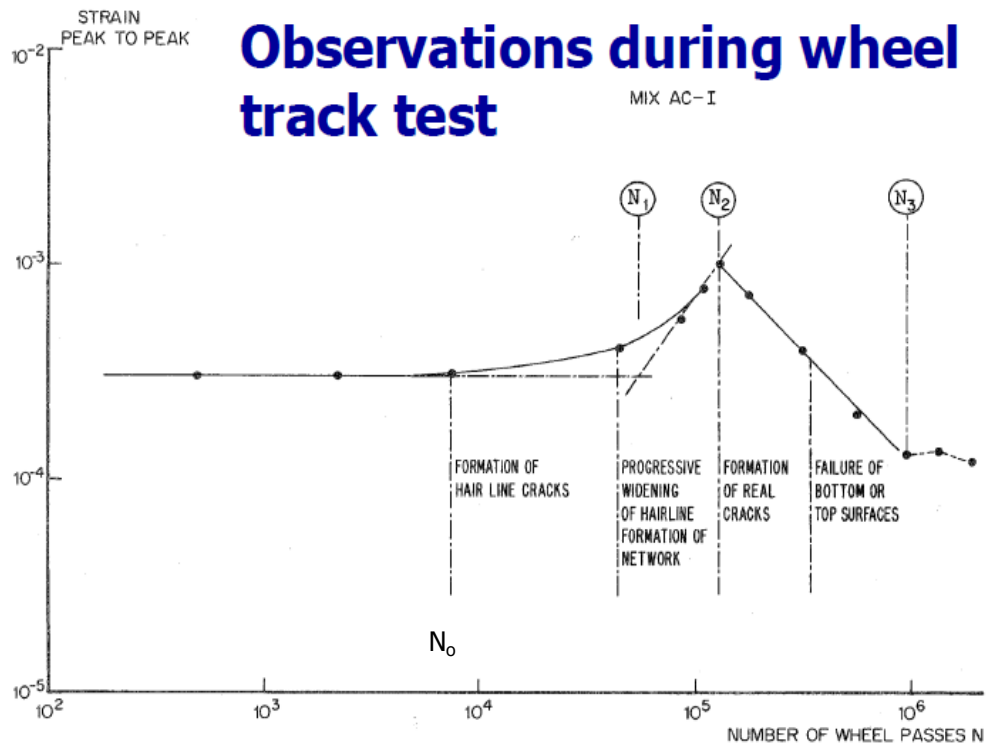


Figure 152: Tensile strain and visible cracking as observed in Shell's slab testing.

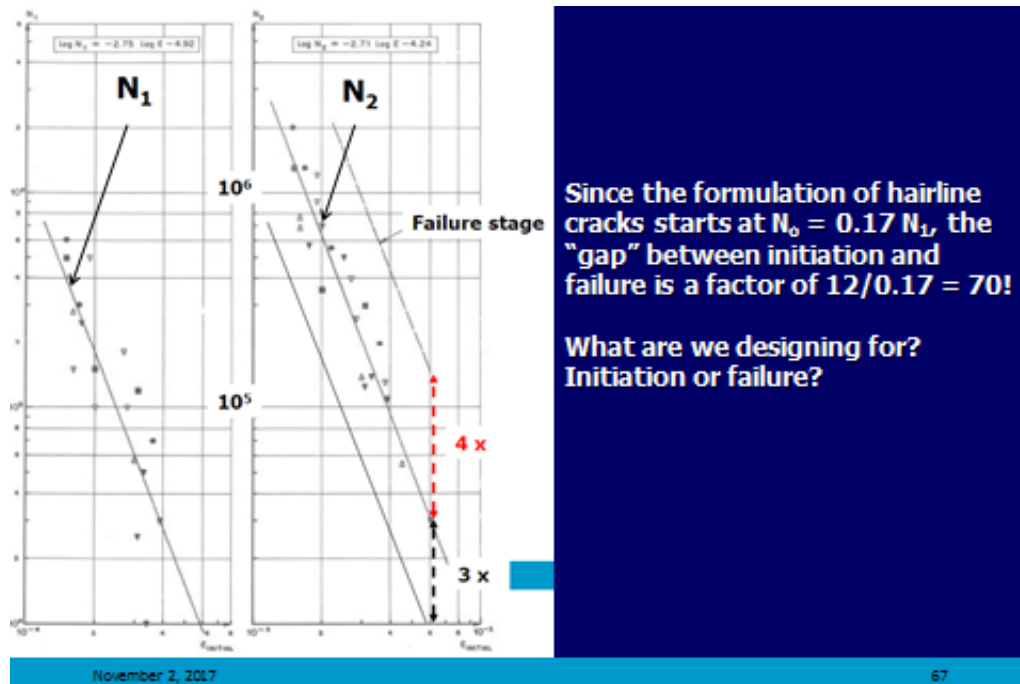


Figure 153: Number of load repetitions to various crack stages vs tensile strain at the bottom of the asphalt slab.

Shell then correlated the results obtained on the slabs to the results of 3 point bending fatigue tests which were performed on specimens having dimensions of 230*30*20 mm (much smaller than the size of 4 point bending specimens which are used nowadays!). The beam fatigue tests were done in the constant load, the constant displacement and the constant energy dissipating mode. The results of these comparisons are shown in figure 154.

Based on these comparisons Shell concluded that the displacement controlled beam fatigue tests correlated best with the ϵ vs N_2 relationship developed from the slab tests and therefore it was concluded that the constant displacement beam fatigue test results could best be used for design purposes.

Given the fact that real asphalt pavements, especially in the USA, Europe, China, Japan etc are much thicker than the 40 mm thick slab used by Shell, and because of the fact that in Shell's 3 point bending test (very) small specimens were used, the validity of Shell's conclusion on recommending displacement controlled fatigue tests is questionable for today's conditions.

Although fatigue tests on slabs by means of the MMLS3 or similar equipment is extremely important from a research point of view in making an effort to match laboratory conditions with practice, such tests are not feasible from a practical point of view (1. too much material is needed, from one slab one can take many beams, 2. test will take too long since fatigue tests are usually done at a frequency of at least 10Hz which means that 36000 repetitions are applied in one hour compared to the 7200 in the MMLS3 test).

A reasonable alternative to the slab test might therefore be the slab on elastic foundation (BOEF) test which is shown in figure 155 [38]. In this test a beam similar to the ones used in 4 point bending tests is placed on a layer of rubber. In between the rubber and the beam a layer of Teflon is placed which limits to a very large extent the friction between the beam and the rubber layer. In this way one ensures tensile stresses and strains to be generated at the bottom of the beam and that the beam behaves independently from the rest of the structure (test setup). The fully supported beam is then subjected to a constant load or displacement signal which could have a haversine or a half sine shape. The test can be done with and without rest periods between the load pulses. The tensile strain at the bottom of the beam is calculated from the horizontal displacement which is measured just above the bottom of the beam. Wooden clamps are attached to either side of the beam to make sure that the beam is not "moving away" during the repeatedly applied load cycles. This can happen because the interface between the beam and the rubber subgrade is extremely slippery because of the applied Teflon layer.

Figure 156 shows how the cyclic and accumulated strain develop during the test.

The accumulated strain shown in figure 156 [38] is a combination of permanent strain and resilient strain which had no chance to recover completely. Remember that the response of a visco-elastic material to a load consists of an elastic part, a delayed elastic part and a viscous part. The cyclic displacement in figure 156 represents the elastic response while the accumulated displacement represents the delayed elastic part which could not recover because of continuous loading and the viscous part. Figure 157 [38] further explains this.

This immediately implies that the strain accumulation would have been less if rest periods would have been applied between the successive load pulses. In that case the delayed elastic deformation would have time to recover completely (if the rest period is long enough).

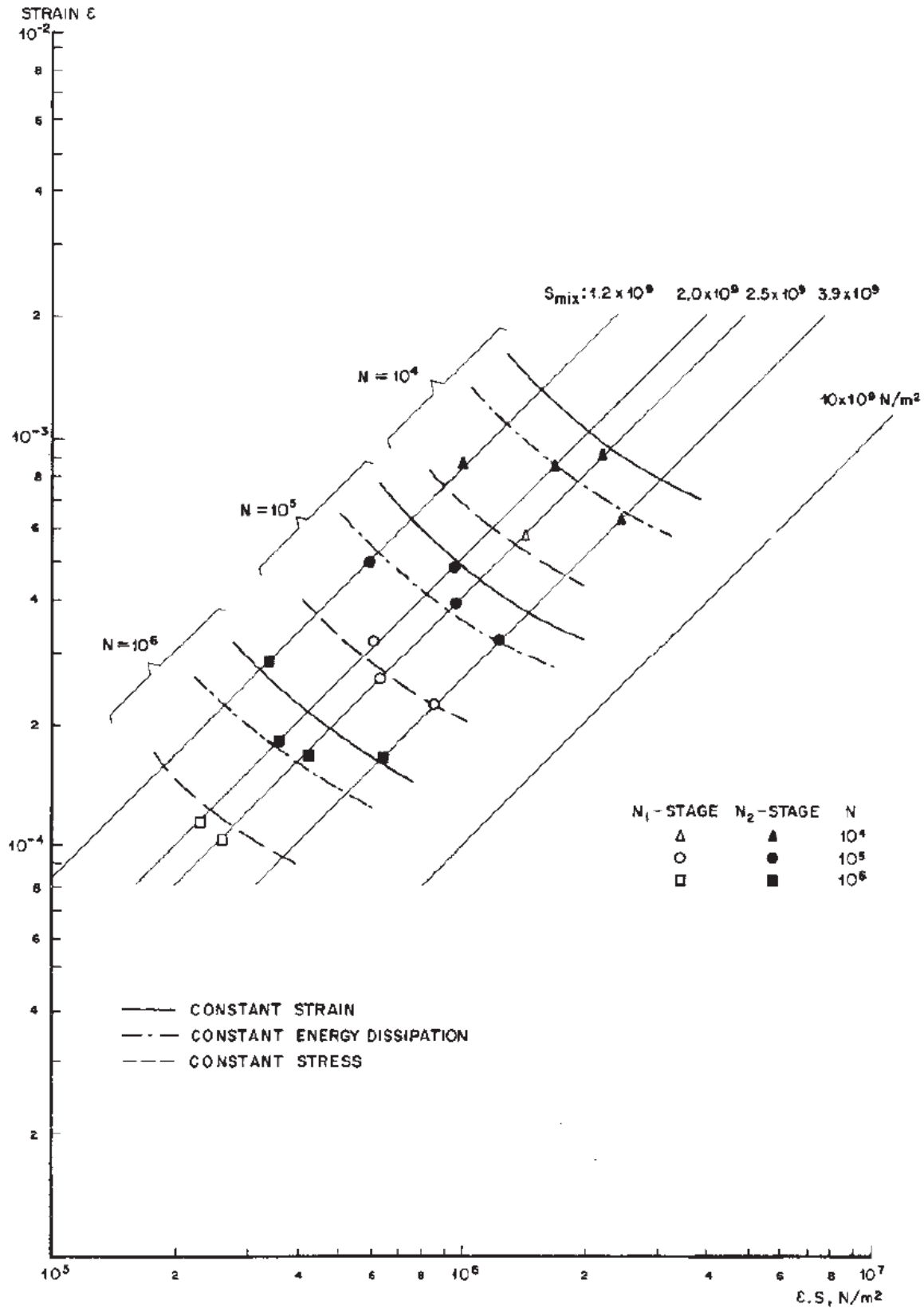
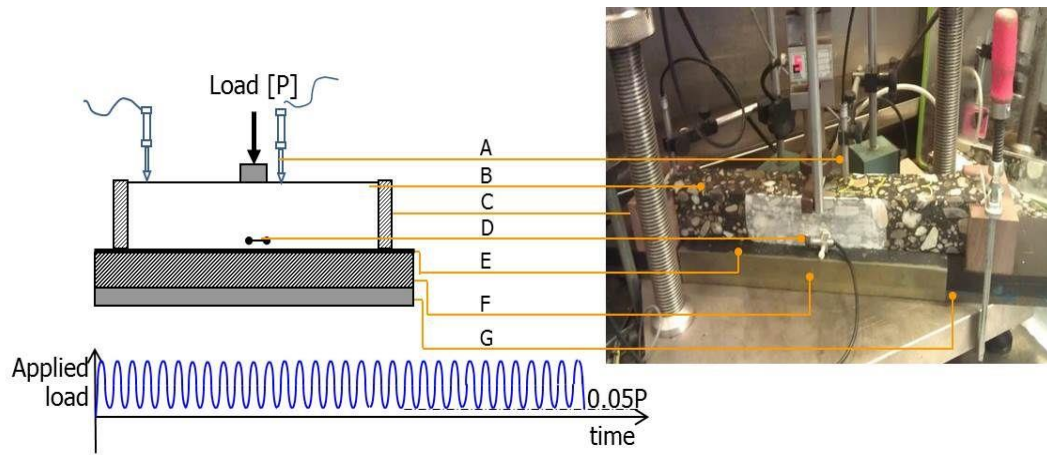


Figure 154: Comparison of Shell's slab and beam fatigue test results.



(a)



(b)

Figure 155: (a) The setup of the BOEF test and the haversine loading applied to the beam, where $0.05P$ is the preload. Where A: LVDT for vertical displacement; B: Beam $50 \times 50 \times 400$ mm; C: Wooden C-Shape Support; D: LVDT for horizontal displacement; E: Latex sheet; F: Rubber foundation; G: Steel plate. (b) Artist impression of BOEF test setup.

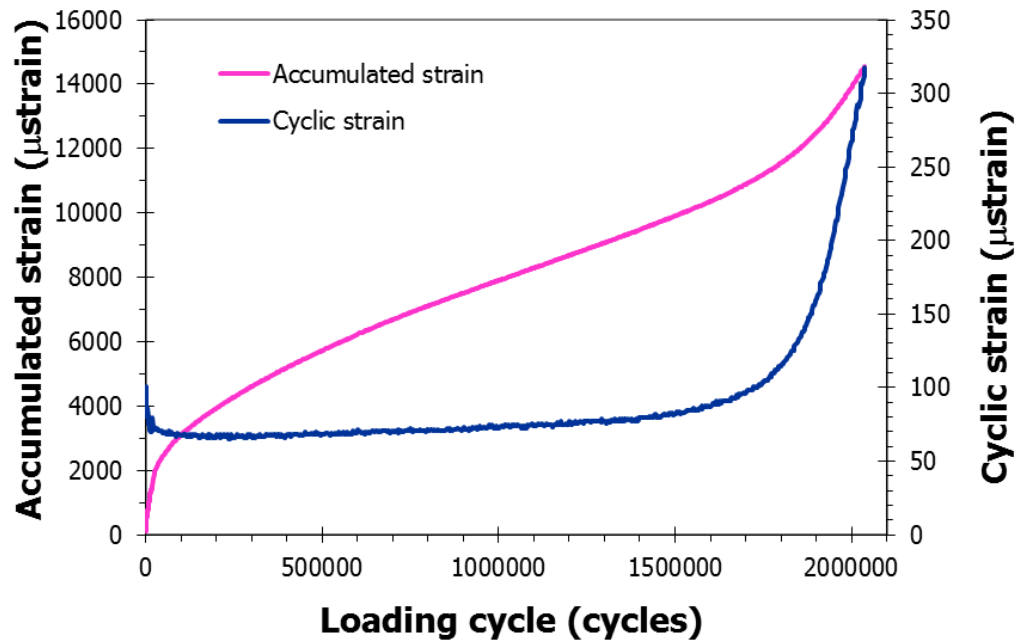


Figure 156: Typical development of the cyclic and accumulated strain during the BOEF fatigue test ($P=1.75$ kN) measured at 8 mm from the bottom of the beam using horizontal LVDT on position D.

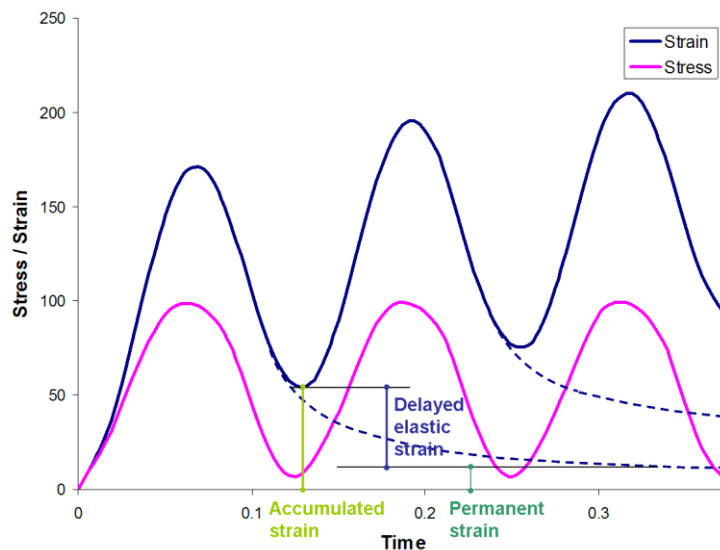


Figure 157: Sketch of the development of permanent, delayed and accumulated strain due to the haversine cyclic loading used in the BOEF test as a function of time.

The question now is how the results of the BOEF test compare with the results obtained with the commonly used 4 point bending test. Such a comparison is shown in figure 158 [38] which shows that there is a significant difference between both tests. The BOEF tests were performed in the

controlled load mode with a continuous haversine signal while the 4 point bending tests were performed in the controlled displacement mode using a continuous sinusoidal signal.

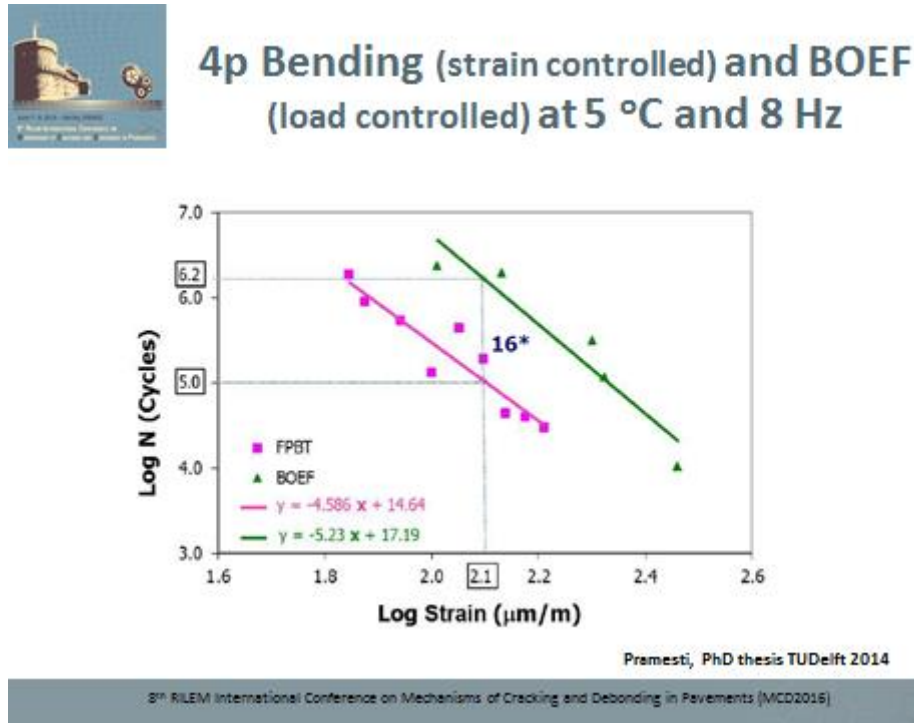


Figure 158: Differences between the results about with the BOEF and 4 point bending tests.

It is recalled that the results shown in figure 158 were already shown in figure 128 be it in a different way. It should be noted that in both tests "end of life" was defined as the number of load repetitions at which the modulus had reduced to 50% of its initial value. The main differences between the two tests are the fact that the BOEF test is performed on a fully supported beam while the 4 point bending test is not. The fact that the beam is fully supported has an effect on the redistribution of stresses after damage initiation and has a large effect on the crack propagation phase. Another reason might be that the amount of energy dissipation per load cycle in both tests is not the same. In the 4 point bending test the outer fiber of the beam is subjected to alternating tension and compression conditions implying that both conditions are contributing to the development of dissipated energy. In the BOEF test however there are only tension conditions implying that energy is only dissipated in the tension cycle. Unfortunately no stress – strain loops were measured during the BOEF tests to prove this point. On the other hand however creep occurs in the load controlled BOEF test which also contributes to damage development while such a creep doesn't occur in the displacement controlled 4 point bending test.

As has been shown, accumulated horizontal strain did develop during the BOEF test. This was explained as being accumulation of not fully recovered delayed elastic strain and creep. From figure 159 [38] however one can deduce that this so called "creep" might also be due to an increase of the width of the crack that develops during the test. From the development of the cyclic strain one can determine that at B, the beam stiffness had decreased to 50% of its initial value which corresponds with a crack that has grown over approximately 30% of the beam height. After that point, the cyclic as well as accumulated strain and the crack length increase rapidly.

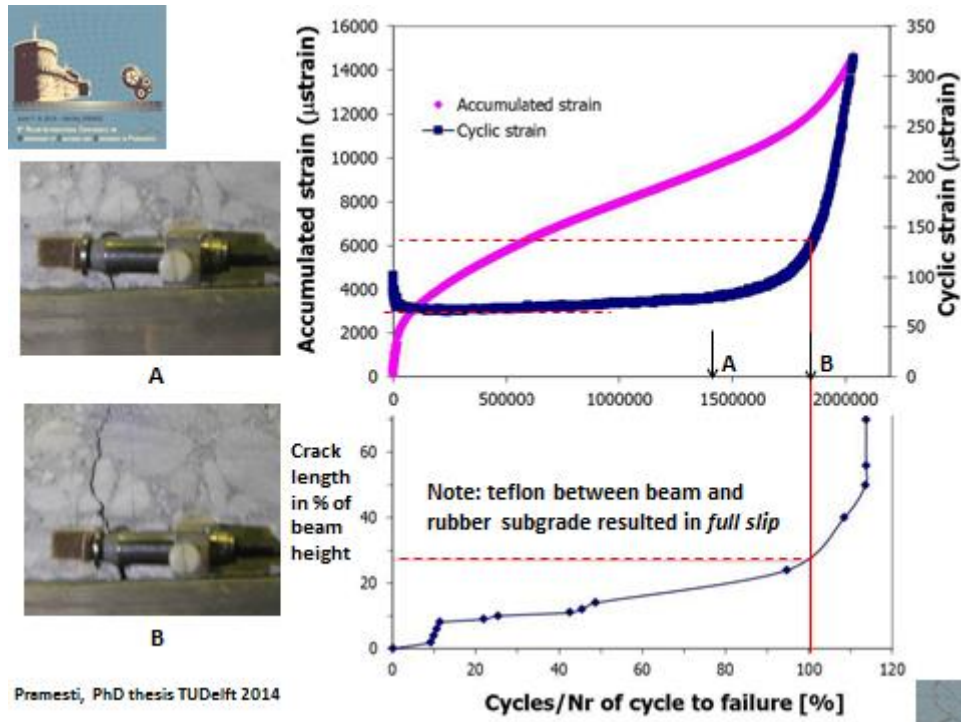


Figure 159: Cyclic and accumulated strain in relation to number of load repetitions and crack development.

In figure 158 a clear difference between the 4 point bending displacement controlled test and BOEF load controlled test has been shown. We do observe a difference in slope value "n" and a significant difference in intercept value "k" of the relationship $N = k \varepsilon^{-n}$. Let us first discuss why the slope values should be different.

The reason for this difference is because the 4 point bending tests were performed in the controlled displacement mode and the BOEF tests were done in the controlled load mode. Molenaar [39] has shown why these two testing modes result in different values for "n" and how these "n" values can be estimated. He showed that:

$$n = \{(2/m)\} / (-0.93 + 0.65 V_a) \text{ for displacement controlled tests and}$$

$$n = \{2 * (1 + 1/m)\} / (-0.93 + 0.65 V_a) \text{ for load controlled tests}$$

where m = the slope of the relation between log t (t = loading time) and log S_{mix} and V_a is void content in [%]. The "m" parameter is a material parameter and is independent of the type of test and is therefore the same for the BOEF and 4 point bending tests. The average void content of the BOEF specimens was 4.68% while for the 4 point bending specimens the average void content was 4.47%. The difference in testing mode together with the difference in void content explains why the slope of the 4 point relationship is 4.586 while it is 5.23 for the BOEF test at m = 0.221.

The difference in "k₁" value (remember $N = k_1 * \varepsilon^{-n}$) between the two tests is due to the differences in support conditions and loading conditions. The outer fibers of the beam in the mid third part of the 4 point bending test are only subjected to a tensile stress. At the bottom of the BOEF specimen however there is a longitudinal horizontal stress, a transversal tensile stress which is about 5% of the longitudinal stress, and a vertical stress which also is about 5% of the

longitudinal stress (*please note that the 5% values are valid for the test/specimen geometry and test conditions used in the particular BOEF test, 5 °C and 8 Hz, $S_{mix} \approx 20000$ MPa; the 5% values change when the mentioned conditions change*). This implies that at the bottom of the BOEF beam there is a 3D state of stress while at the bottom of the 4 point bending beam there is a 1D stress situation (there is also a very small tensile stress in the lateral direction at the bottom of the 4 point bending beam but this is so small that it can be neglected). The stresses at the bottom of the BOEF beam are dependent on the magnitude of the load, the beam geometry and the stiffness ratio $S_{mix} / E_{rubber\ subgrade}$. The stresses at the bottom of the 4 point bending beam are however only dependent on the load and the test specimen geometry. All this implies that the shift factor between the BOEF and 4 point bending fatigue results not only depends on the support conditions and the mode of loading but also on the stiffness of the mixture. It is therefore NOT a unique parameter which is independent of the test conditions!

8.6.9 Which test should we preferably use?

In the previous sections we have extensively discussed test methods, testing modes, effects of specimen size etc and we have compared the stress and strain signals as used in the various tests with those that actually occur in a pavement. From what has been presented we can conclude the following:

- The fatigue life as determined by means of laboratory tests is highly affected by the type of test, mode of testing and in a number of cases by the specimen size. This makes the fatigue characteristics as determined by means of the different tests are a specimen property rather than a material property.
- Each of the mentioned tests however can be used for comparing fatigue resistance of different mixtures and assessing the influence of modifiers etc.
- Only tests performed with wheel load simulators and to large extent BOEF tests are good to fair simulations of reality.
- Given the differences between the test conditions and the conditions occurring in practice (e.g. stress/strain signals and support conditions) the fatigue life as predicted by using laboratory determined fatigue relations need to be multiplied with a certain factor in order to match predicted fatigue life with observed fatigue life.
- The less representative the test is, the larger the value of this multiplication factor (also called calibration factor) will be.
- A huge amount of information on fatigue of asphalt mixtures is based on 2, 3 and 4 point bending; to a lesser extent this is the case with the indirect tension and UCT tests. Although none of these tests is perfect, their advantage is the large amount of experience and information obtained with these tests.
- The indirect tension test is very attractive since it can be performed on samples which can be cut from cores taken from the pavement. The test should however be performed at fairly low temperatures in order to avoid excessive damage of the sample near the loading strips.
- The 2 point bending test on trapezoidal specimens is to be preferred over the 4 point bending test since damage development is not influenced by clamping forces etc. Cutting 2 point bending specimens is unfortunately more complex than cutting 4 point bending specimens.
- The UCT test has the advantage of being a uniaxial test in which "simple" stress conditions occur. The disadvantage however is that UCT samples might be hard to obtain from field cores. Furthermore the test is not as simple as it seems because high requirements have to be set to the stiffness and rigidity of the test set up, the alignment of the specimen and the gluing of the end caps.
- Based on all this, the author tends to conclude that the BOEF test is to be preferred for practical fatigue testing of asphalt mixtures. This is because of the realistic loading and support conditions, the absence of any clamping forces and the fairly simplicity of the test. Unfortunately little practical experience has been built up with this test yet.

8.6.10 Equations and nomographs to predict fatigue relationships

As is the case for the mixture stiffness, various equations and nomographs have been produced in time to estimate the fatigue performance of asphalt mixtures. It goes too far to present here each and every equation and nomograph. Only a few will be presented, the selection of which is based on whether the equation/nomograph is often used, whether the test method on which it is based is still used and whether the equation makes sense. This later aspects needs to be explained.

We have seen that asphalt mixtures are visco-elastic materials which behave like an elastic solid at low temperatures and short loading times and more viscous at high temperatures and long loading times. This of course also affects the fatigue and fracture behavior of asphalt concrete. Let us discuss in an as simple as possible way how these effects can be described. In order to be able to do so we will be using principles of fracture mechanics.

Fracture mechanics principles

Figure 160 shows that three modes of cracking can be discriminated.

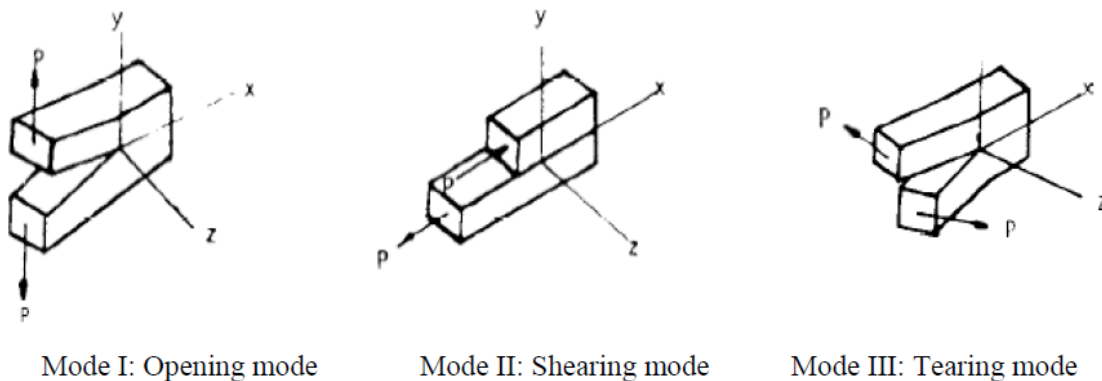


Figure 160: Three modes of cracking; the opening mode occurs in cases of tension and bending.

The rate at which a crack will propagate is of course dependent on the stresses at the tip of the crack and the resistance of the material to cracking. This is schematically shown in figure 161.

Assume we have a specimen that is subjected to a tensile stress σ . In the middle of the specimen we have a small crack with length "c" on either side of the specimen. Because of this crack we have stress concentrations at the tip of the crack and the stress distribution in the cross sectional areas at the location of the crack is certainly not uniform as it is at all other cross sectional locations in the specimen. As is shown in figure 161, this stress concentration is characterized by means of the parameter K called the stress intensity factor. K is dependent on the tensile stress σ and the crack length "c". It will be clear that the crack will grow faster when K gets higher which happens when "c" gets larger. The crack growth rate can be described by means of the so called Paris' law which is:

$$dc/dN = A K^n$$

where dc/dN is the increase in crack length "dc" per load cycle "dN" and "A" and "n" are material parameters. Theoretical justification for the use of Paris' law for visco-elastic materials was given by Schapery [46, 47, 48]. He showed that the "constant" A could be written as follows:

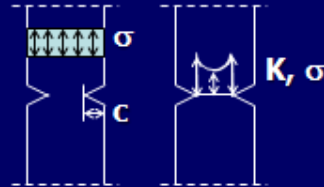
Crack growth

The stresses at the tip of the crack are characterized by the stress intensity factor K

$$K = f(\sigma, \sqrt{c})$$

σ = tensile stress

c = crack length



Crack growth per load cycle $dc/dN = A K^n$

A, n = material parameters

23.11.2017



Figure 161: Stress intensity factor and crack growth

$$A = \frac{\pi}{6 \sigma_m^2 I_1^2} \left(\frac{(1-\nu^2) D_2}{2 \Gamma} \right)^{\frac{1}{m}} \left| \int_0^{\Delta t} w(t)^2 \left(1 + \frac{1}{m} \right) dt \right|$$

Where:

$I_1 = \pi K_1 / 2 \alpha \sigma_m$

α = size of failure zone in front of the crack tip [mm]

σ_m = tensile strength [MPa]

K_1 = stress intensity factor for mode I loading [$N/mm^{1.5}$]

$D(t) = D_0 + D_2 t^m$

D_0 = creep compliance at $t = 0$ s [MPa^{-1}] (creep compliance = $1/E$ or $1/S_{mix}$)

Γ = fracture energy [Nmm/mm^2]

t = time [s]

m = slope of the double logarithmic creep compliance curve

ν = Poisson's ratio

$d\Delta t$ = period of one loading cycle [s]

$w(t)$ = pulse shape of the stress intensity factor related to time

He assumed a non-linear relation between stress and strain following

$$\sigma / \sigma_0 = b_0 \varepsilon^{b_1}$$

Where σ = applied stress and σ_0 = stress at failure.

He then showed that

$$n = 2 (1 + 1/m)$$

when the tensile strength and fracture energy are assumed to be constant along the path of the crack growth. It was hypothesized that this occurs in constant load (stress) fatigue tests.

When the length of the failure zone ahead of the crack tip and the fracture energy are assumed to be constant then

$$n = 2 / m$$

It was hypothesized that this occurs in constant displacement fatigue tests.

Also a third case was defined in which the failure zone and the crack opening distance are assumed to be constant. In that case

$$n = 2 / \{m * (1 + b_1)\}$$

Molenaar [39] showed that the n calculated in this way should be corrected for the effects of voids in the mixture if the void content is larger than 3%. This resulted in

$$n = \{(2/m)\} / (-0.93 + 0.65 V_a) \text{ for displacement controlled tests and}$$

$$n = \{2 * (1 + 1/m)\} / (-0.93 + 0.65 V_a) \text{ for load controlled tests.}$$

Groenendijk [23] showed that beam bending fatigue relations could be written as:

$$N = \frac{h^{\left(1 - \frac{n}{2}\right)} \int_{c_0/h}^{c_f/h} \frac{d(c/h)}{\left[1.99\left(\frac{c}{h}\right)^{0.5} - 2.47\left(\frac{c}{h}\right)^{1.5} + 12.97\left(\frac{c}{h}\right)^{2.5} - 23.17\left(\frac{c}{h}\right)^{3.5} + 24.8\left(\frac{c}{h}\right)^{4.5}\right]^n}}{A[S_{mix}]^n} \cdot \epsilon^{-n}$$

which can be simply written as $N = k_1 \epsilon^{-n}$. *Please note that the slope of the fatigue relationship is the same as the slope of Paris' crack growth relation and that this value is related to the slope of the log S_{mix} vs log t relation!*

The material presented above implies that equations and nomographs developed to predict fatigue relationships should comply to the following requirements:

- the slope of the fatigue relationship cannot take a constant value; it should be dependent on loading time and temperature;
- the intercept value of the fatigue relationship should at least show dependency on the stiffness modulus and the tensile strength and fracture energy of the asphalt mixture. Or at least a dependency on parameters which control stiffness, tensile strength and fracture energy.

Equations and nomographs to predict fatigue relationships

In [31] the following equation is presented, which is a modified version of the one developed by the Asphalt Institute [49], to predict fatigue life of asphalt mixtures.

$$N = 0.00432 * C * \epsilon^{-3.9492} * E^{-1.281}$$

$$C = 10^M$$

$$M = 4.84 * \{ (V_b / (V_a + V_b)) - 0.69 \}$$

V_a = void content [%], V_b = volumetric bitumen content [%]. The units for $[E]$ and $[\varepsilon]$ are not given in [31].

This equation is developed from constant load fatigue tests. As will be shown later on multipliers are added to the equation to predict the amount of fatigue cracking visible on the pavement surface.

The disadvantage of this relationship is that the slope of the relationship is a fixed value and we have seen that this cannot be the case.

Francken and Clauwaert [50] developed the following equation from controlled load fatigue tests on 30 mixtures using the 2 point bending test on trapezoidal specimens:

$$\sigma / E^* = \varepsilon = K N^{-a}$$

With:

$$K = G * \{ V_b / (V_b + V_a) \} * \exp (-5 * V_g / 100)$$

$$a = 0.194 B + 0.3 * V_g / 100 - 0.109$$

V_b = volumetric bitumen content [%]

V_a = void content [%]

V_g = volumetric aggregate content [%]

B = $d \log (\text{pen}) / d \log t$

pen = penetration

t = loading time [s]

If $B \leq 0.43$ then $G = 75.3 * 10^{-4}$

If $B > 0.43$ then $G = 0.874 B^2 - 0.86 B + 0.216$

The mixtures tested varied in volumetric bitumen content (6.3 – 17.5%), void content (2.9 – 22%), bitumen penetration (47 – 99) and B value (0.321 – 0.438) so a wide range of mixtures was tested. A comparison between the measured fatigue strain and calculated fatigue strain showed that almost all values were within the +20% to – 20% range.

Medani and Molenaar [51] developed the following equations based on over 100 displacement controlled 4 point bending fatigue test results (beams were all 50 mm thick) reported in literature:

$$N = k_1 \varepsilon^{-n}$$

$$\log k_1 = 6.589 - 3.762 n + 3209 / E^* + 2.332 \log V_b + 0.149 V_b / V_a + 0.928 \text{PI} - 0.0721 T_{R\&B}$$

Where: E^* = complex modulus [MPa],

V_b = volume percentage of bitumen [%],

PI = penetration index.

$T_{R\&B}$ = softening point [$^{\circ}\text{C}$].

For “ n ” they developed the following equation for which over 30 different results were available:

$$n = 2 / \{ m (0.541 + 0.346 / m - 0.0352 V_a) \}$$

Where: m = slope of the $\log t$ vs $\log E^*$ relationship,
 V_a = void content [%].

Figure 162 shows the comparison between the predicted and observed $\log k_1$ values while figure 163 shows the comparison between the predicted and observed “n” values.

In figure 162 we see that all predicted $\log k_1$ values are within a range of -10% to 10% of the experimental values which looks good but keep in mind that we are talking about logarithmic values! Figure 163 shows that in 33 out of the 38 cases “nest” correlated very well with the experimental “nexp” values! This is important since “n” is a material property not affected by the type of test and it seems to be possible to estimate this property with a rather high degree of accuracy!

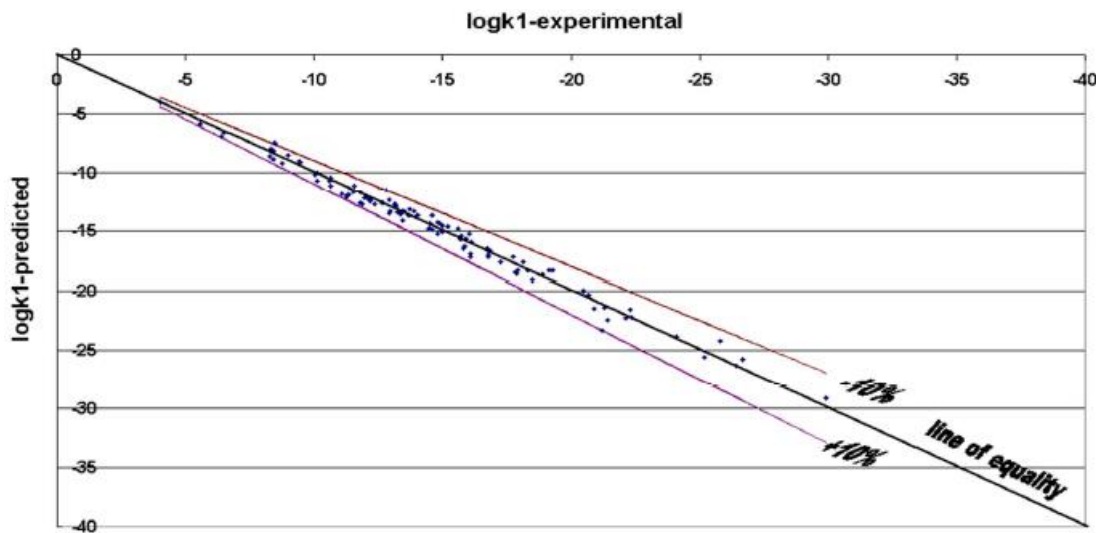


Figure 162: Comparison between experimentally determined $\log k_1$ values and $\log k_1$ values calculated with the Medani/Molenaar equation.

Shell has also produced equations as well as a nomograph to predict the fatigue characteristics of asphalt mixtures under controlled and controlled displacement conditions. The input for those equations and nomographs are the volume percentage of bitumen, the PI of the bitumen and the mixture stiffness. The disadvantage of these equations is that the slope of the relationships is fixed at a value of 5 while the slope, as we have seen, cannot take a constant value; it depends a.o. on loading time and temperature. Furthermore the relationships are based on 3 point bending tests on rather small specimens which are not used anymore. Therefore it was decided not to present the Shell equations and nomograph in these notes.

From the presented discussion it has become clear that both the Francken/Clauwaert and Medani/Molenaar equations fulfill the requirements which were set earlier being:

- The slope of the fatigue relationship cannot take a constant value; it should be dependent on loading time and temperature.
- The intercept value of the fatigue relationship should at least show dependency on the stiffness modulus and the tensile strength and fracture energy of the asphalt mixture. Or at least a dependency on parameters which control stiffness, tensile strength and fracture energy.

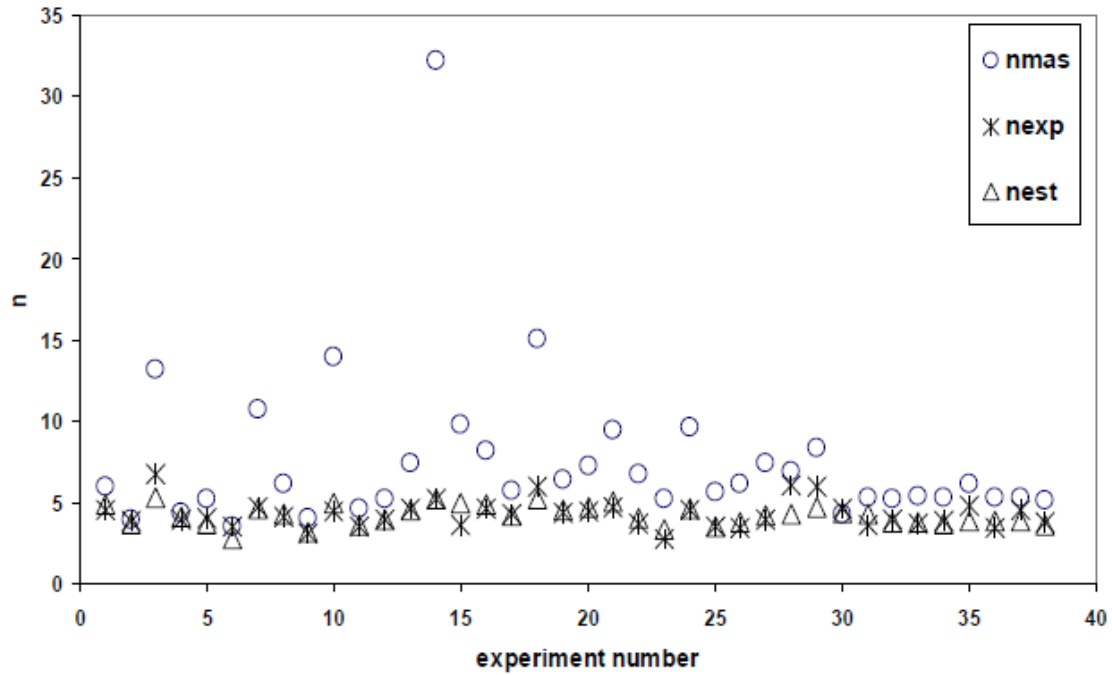


Figure 163: Comparison between experimentally determined “n” values and “n” values calculated with the Medani/Molenaar equation (“nest”). The given “nmas” values are calculated with $n_{mas} = 2/m$ so no correction for V_a and “m” was applied on these values.

The Francken/Clauwaert equation is therefore recommended if fatigue characteristics under controlled load conditions are to be estimated while the Medani/Molenaar equation is recommended for controlled displacement conditions.

Let us now return to fatigue relationships based on dissipated energy. We recall that dissipated energy based fatigue relations can be written as:

$$N_{fat} = (\pi * S_{mix1} * \sin \phi_1 / \psi * A)^{1/(z-1)} \varepsilon_1^{2/(z-1)}$$

We have seen that N_{fat} includes the number of load repetitions to crack initiation plus the number of load repetitions to crack propagation. The number of load repetitions to crack propagation is unfortunately affected by the type of test. This makes that N_{fat} is not a unique number. The number of load repetitions to crack initiation N_R (based on the dissipated energy ratio) should be independent on the type of test and the results shown in figure 143 has shown that this seems indeed to be the case (although some scatter and some geometry influences are still visible). So we might rewrite the dissipated energy based fatigue relation such that we predict the number of load repetitions to crack initiation. In that case we obtain:

$$N_R = (\pi * S_{mix1} * \sin \phi_1 / \psi * A)^{1/(z-1)} \varepsilon_1^{2/(z-1)}$$

Let us now investigate whether we can also estimate the parameters of this fatigue equation from mixture composition data.

Since the dissipated energy per cycle is not changing until N_R , we can take $\psi = 1$. We have also seen that the slope of the fatigue relation “n” and the slope of the dissipated energy based fatigue relation “z” are correlated via:

$$-n = 2 / (z - 1)$$

Earlier in this section it was explained how the value of "n" can be estimated from the slope of the log t vs log S_{mix} relationship and the void content of the mixture. This implies that the value of "z" can be estimated as well. Furthermore we have seen that S_{mix} can be estimated from the volumetric mixture composition and bitumen characteristics. By means of the equation given in section 8.5 we can estimate Poisson's ratio. Finally the phase angle can be estimated using figure 164, which is shown below, and which is taken from [28].

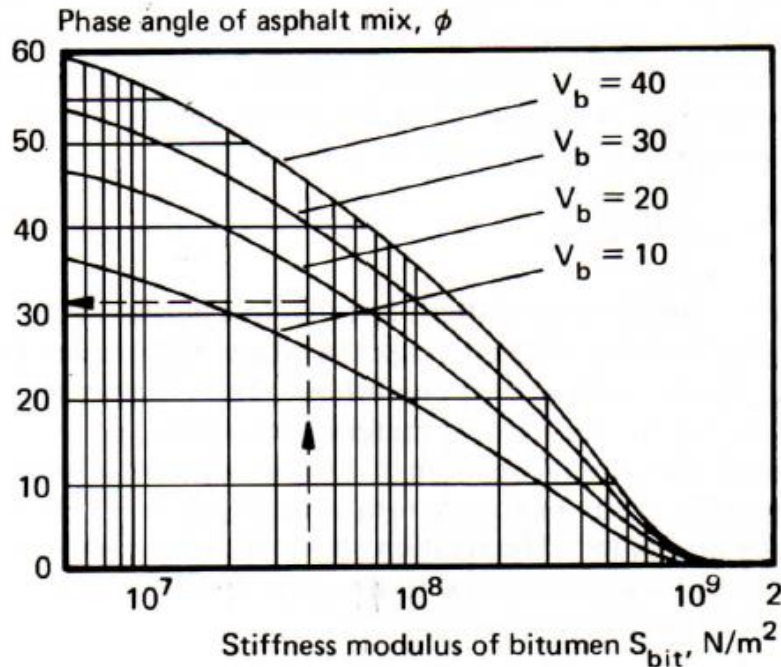


Figure 164: Chart to estimate the phase angle of asphalt mixtures.

The only unknown parameter which needs to be estimated is the "A" parameter. Unfortunately this author was not able to find enough N_R based fatigue test results which would allow him to make a relationship between "A" and mixture composition parameters. It should certainly be possible to develop such an relationship.

8.7 Healing

Healing is the potential of a material to repair itself. An excellent example of a material that has the capacity to heal is water. If you dive from the diving tower into a swimming pool (hopefully filled with water) you will severely damage the water. Depending on how you dive into the water there is an enormous amount of splash and spray. As soon as you are in the water, the "gap" you have made in the water surface closes immediately and it looks as if nothing has happened. The water returns to an undamaged state. It is clear that this healing is because of the excellent capacity of water to flow.

The other prerequisite for healing is that it can only occur when the crack is closed, when the crack faces are in close contact with each other.

Bitumen also has an excellent capacity to flow when it is hot and/or when the loading time is long. Because bitumen can heal, also asphalt mixtures can heal but only when the conditions are such that the bitumen/asphalt mixture will flow. This implies that temperatures should be high and the time to recover is long. It will be clear that also the type of bitumen will have an influence on the capacity to heal. A bitumen with a low penetration (e.g. pen = 15) will hardly flow, especially not at lower temperatures, while a soft bitumen (e.g. pen = 180/200) will easily flow even at lower temperatures.

So for bitumen we can define the following parameters influencing its healing capacity:

- Viscosity characteristics of the bitumen.
- Temperature.
- Healing time.

Since bitumen is the only component in an asphalt mixture that is capable to heal, these three factors also influence the healing capacity of asphalt mixtures. Next to that however the amount of bitumen plays an important role. So in conclusion we can state that a mixture with a low bitumen content, made of a hard bitumen which is allowed to heal for a short time at a low temperature will hardly show any healing or might even show no healing at all.

It will be clear that even a material with a high healing capacity will show no healing at all if a crack stays open, if the two crack faces are not touching each other. Healing can only occur at crack closure. Most cracks we see at the pavement surface have a certain width and because of this, it is very unlikely (actually impossible) that these macro cracks will heal. Micro cracks which are not visible with the naked eye might very well close when the material is unloaded so healing of micro cracks can/will occur.

The other factor that plays a role is the amount of micro cracking. It will be obvious that a mixture with a large amount of micro damage will take a longer time to heal than a mixture with a small amount of micro damage.

Figure 165, which was derived by Molenaar using data given in [50] shows the effect of the mixture composition on healing. The results were obtained using a rest period to loading pulse time ratio of 20.

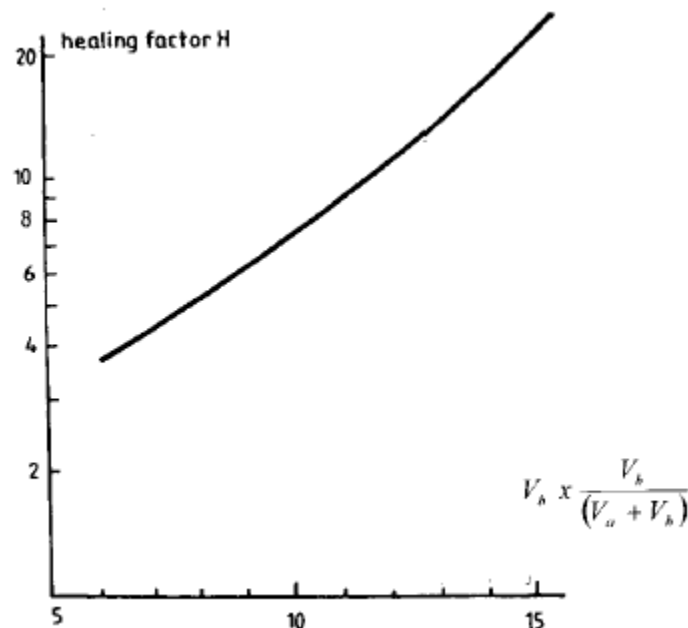


Figure 165: Effect of the amount of bitumen expressed as $V_b * V_b / (V_a + V_b)$ on healing. V_b and V_a are volume % of bitumen and void content respectively.

The data used to derive figure 165 were obtained on mixtures which had a volumetric bitumen content ranging between 10.7 – 17.5 %, void contents between 2.9 and 7.6 % and the

penetration of the bitumen was between 47 and 58. These numbers imply that we are dealing with fairly bitumen rich mixtures. The fatigue tests were load controlled tests performed on trapezoidal specimens (2 point bending).

Figure 166 [52], which is based on fatigue data by Shell shows the influence of the viscosity characteristics on healing. These test results are most probably obtained on 4 point beam bending displacement controlled tests.

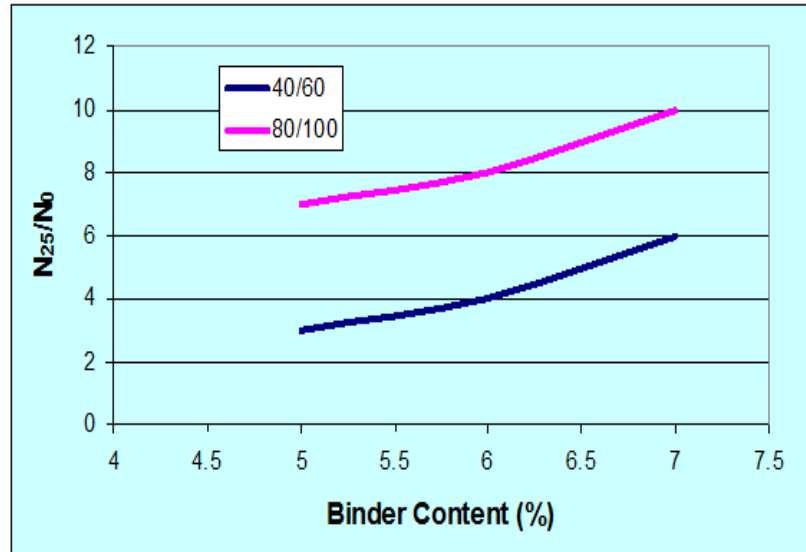


Figure 166: Influence of bitumen content and type of bitumen on healing of asphalt mixtures. N₂₅ is the number of load repetitions to fatigue with a t_{rest} / t_{load} ratio = 25. N₀ is the number of load repetitions without rest periods. Binder content is in mass %.

Figure 167 [38] shows the amount of healing which was measured on a base course mixture after the originally tested beams were stored for 18 months at 15 °C. The originally tested beams were tested to $E_n / E_1 = 0.5$. The retested beams were the same as the originally tested beams.

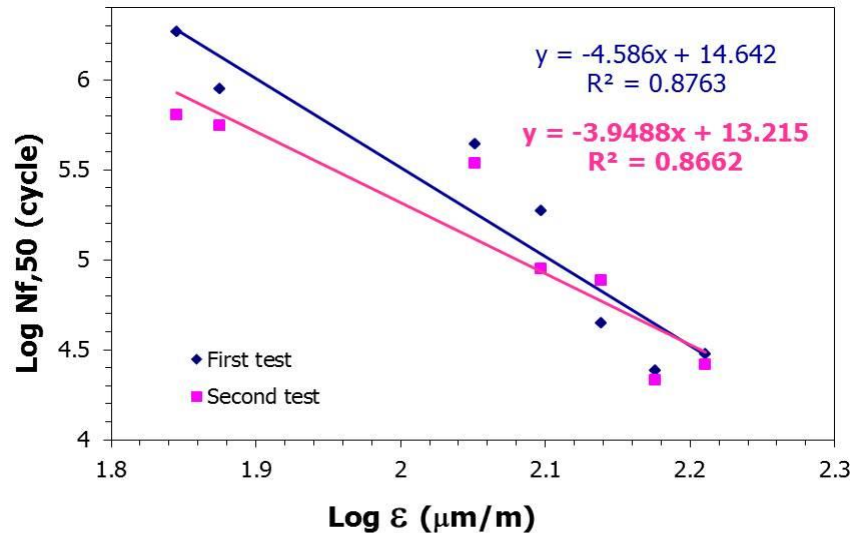


Figure 167: Original fatigue relation ($y = -4.586x + 14.642$) and after retesting ($y = -3.9488x + 13.215$) both determined at 5 °C and 8 Hz.

None of the originally tested beams showed any signs of damage. The beams were tested in the controlled displacement mode.

The results shown in figure 166 were obtained on a mixture with a void content between 4.08 and 4.82% and a bitumen content by volume between 8.85 and 8.92%. The penetration of the bitumen was 19. The results show that after this long rest period, healing in terms of fatigue strength did occur at the high strain levels but not at the low strain levels. Furthermore it should be noted that the initial stiffness of the retested beams was roughly speaking the same as the stiffness of the originally tested beams.

Figures 168 and 169 [41] show similar results but in this case the original beams were tested to a damage level of $E_n / E_1 = 0.3$ so at the end of the tests the beams had a higher damage level than the ones shown in figure 166. The original tests as well as the retesting were performed at 20 °C and 10 Hz. The mixture was a fine graded wearing course mixture with a maximum grain size of 8 mm. The void content was 3.42% on average and the bitumen content (45 pen bitumen) was 6.5 % by mass. In this case the storage period was 6 months at 15 °C.

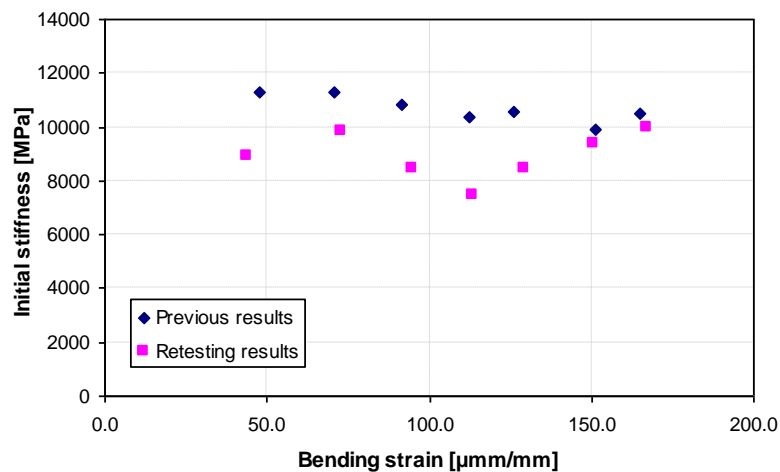


Figure 168: Initial stiffness of original and retested 4 point bending specimens. Retested at $E_n / E_1 = 0.3$. 8 month storage at 15 °C.

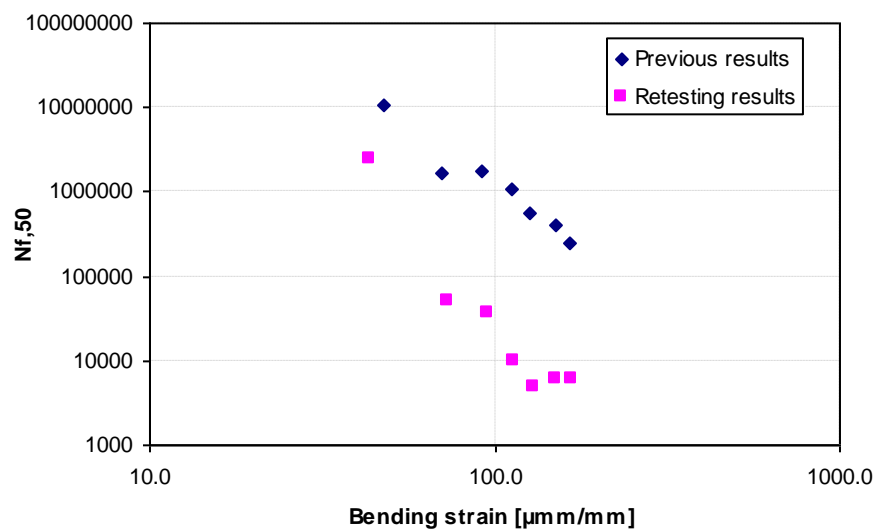


Figure 169: Fatigue life of original and retested 4 point bending specimens. Retested at $E_n / E_1 = 0.3$. 8 month storage at 15 °C.

When the results of figures 168 and 169 are compared with those in figure 167 one will notice that although the mixture of figures 168 and 169 had a higher bitumen content, a lower void content, and were made of a softer bitumen, the healing is less than the healing of the mixture shown in figure 167. This might have to do with the fact that the mixture of figure 167 had a longer time to heal but more probably this difference is caused by the higher damage level in the mixture of figures 168 and 169.

Healing tests on mixtures by means of fatigue tests with rest periods are quite cumbersome. Therefore it is more practical to do healing tests on bitumen and bituminous mastics and mortars since these are the composites in the mixture responsible for healing. Excellent work on this has been done by Qiu [53]. He tested mastics made of Q8 70/100 pen bitumen (pen = 95; $T_{R\&B} = 45^\circ\text{C}$) mixed with a limestone filler in a bitumen : filler mass ratio of 1 : 1; he called these mastics Pbmas. He also made similar mastics in which he replaced the Q8 70/100 bitumen by a SBS modified bitumen produced by Shell (pen = 65; $T_{R\&B} = 70^\circ\text{C}$) and called these mastics SBSmas. He tested diabolo shaped specimens (figure 170) till fracture, put them in the mold again and stored them for some time and a specific temperature and then retested them (figure 171). The results are shown in figure 172.

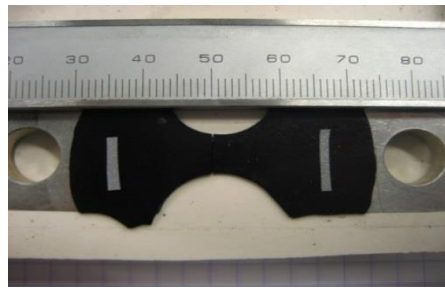


Figure 170: Diabolo shaped mastic specimens as used by Qiu.

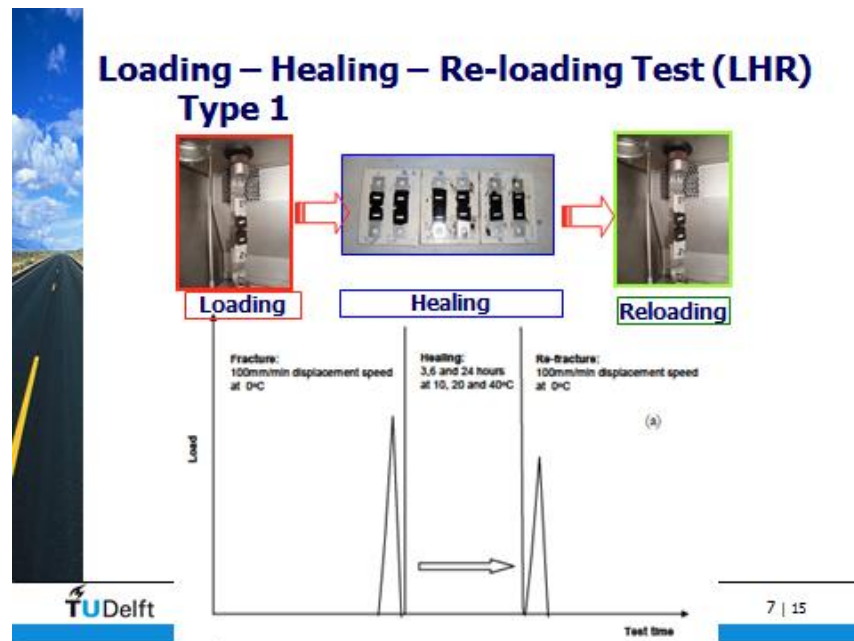


Figure 171: Test procedure as used by Qiu. Tension tests at 100 mm/min and 0°C

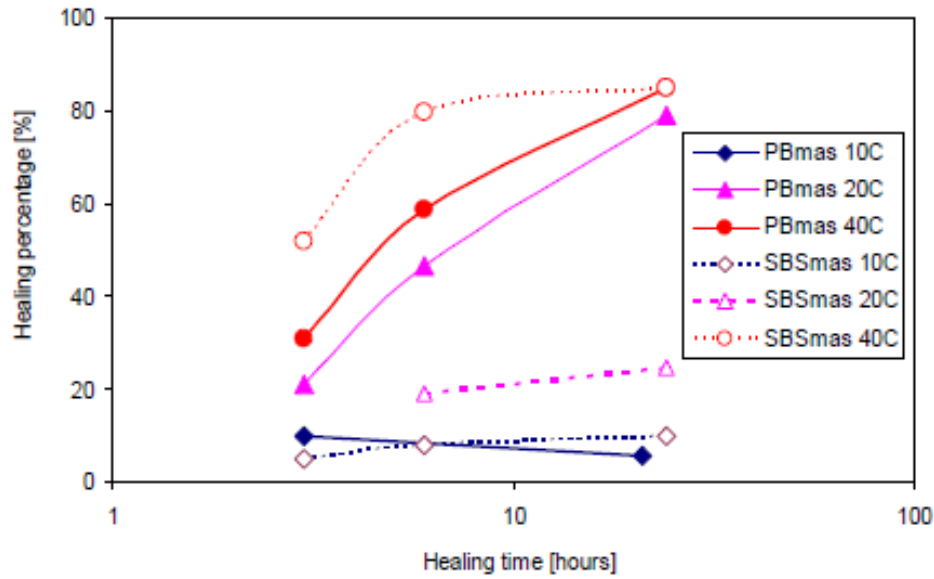


Figure 172: Test results obtained by Qiu in his fracture – healing – re-fracture tests. Healing percentage is fracture load after healing / initial fracture load.

Figure 172 shows that cracked mastic specimens heal. It also shows that temperature has a very large effect on the healing process. The figure furthermore implies that a healing times of less than an hour or even a few minutes (these healing times occur in practice) healing of fractured specimens will not be significant not even at elevated temperatures (this in spite of the fact that the crack was forced to close).

Qiu also studied the healing of mastic specimens which were not fractured but did show a certain amount of damage. For this he performed tests shown in figure 173.

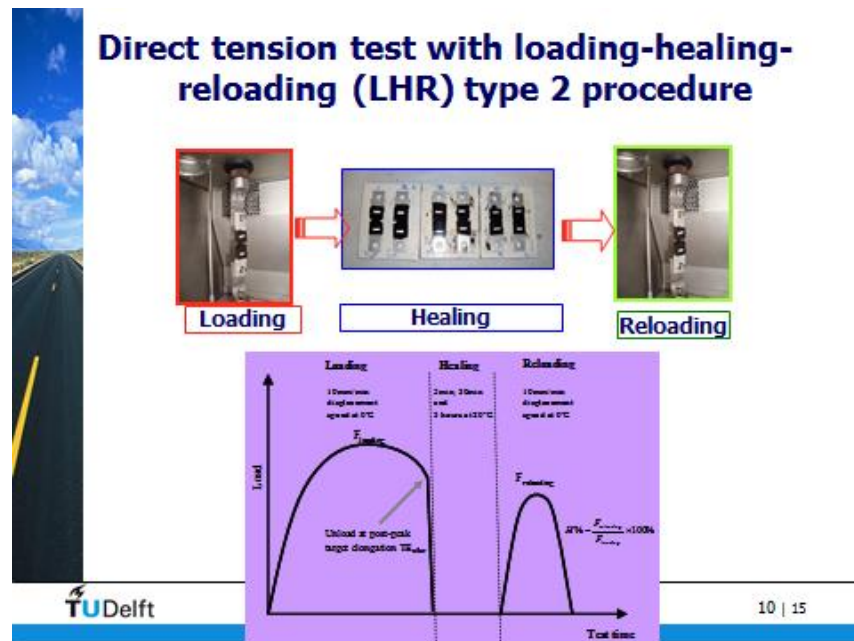


Figure 173: Qiu's healing type 2 tests. Note that in this case displ. rate is 10 mm/minute at 0 °C.

Qiu related the total amount of deformation applied to the specimen to a so called single crack width (SCW) (see figures 174 and 175).

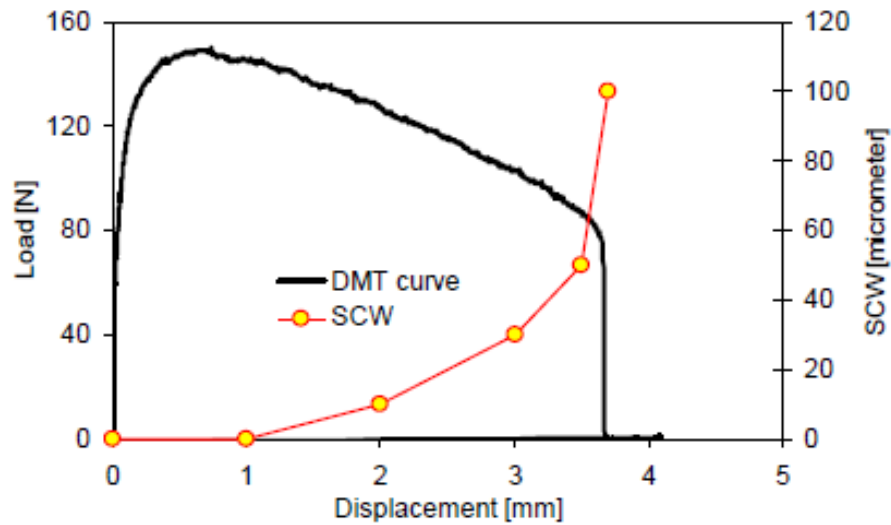


Figure 174: Load – displacement curve of a direct tension test on mastics and relation between the applied displacement to the so called single crack width.

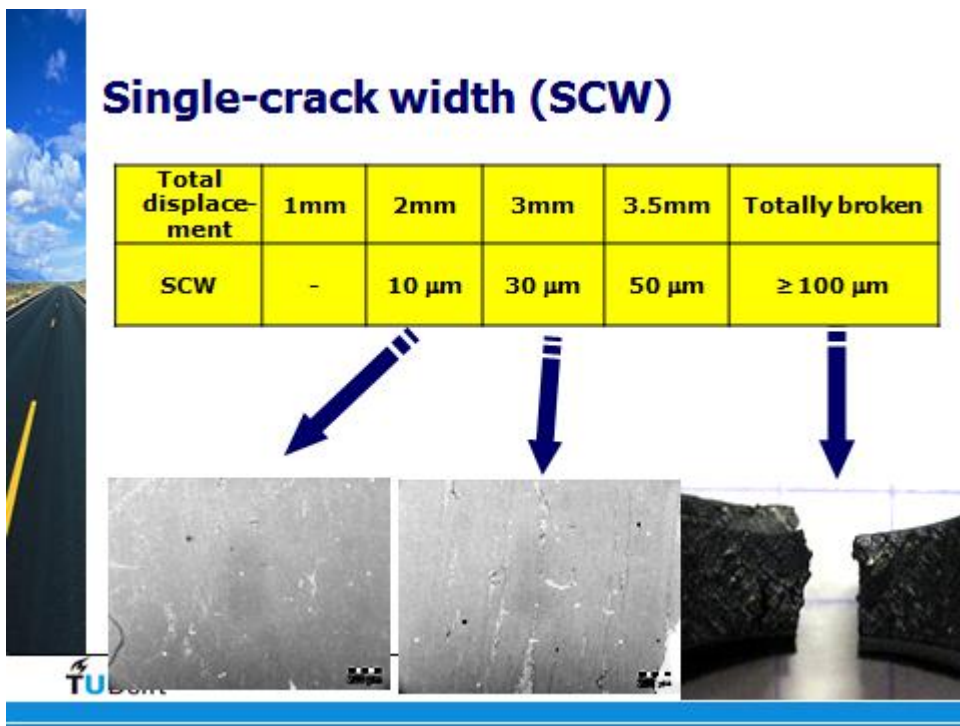


Figure 175: Appearance of some single crack width.

Figure 175 clearly shows that a SCW of 30 μm is nothing more than some “scratches” in the material.

The results Qiu obtained in this way are shown in figure 176.

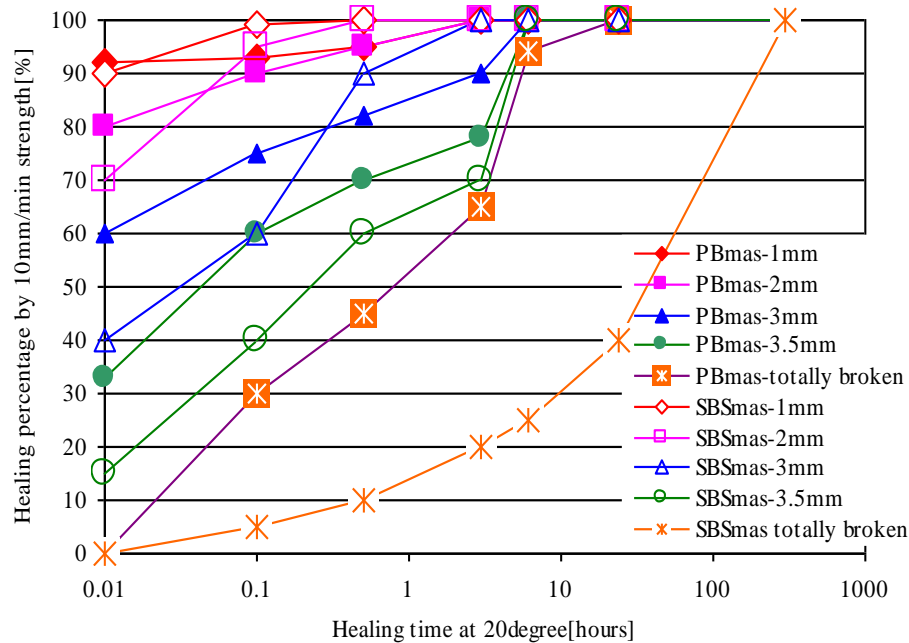


Figure 176: Healing of Pbmas and SBSmas in Qiu's phase 2 testing program. Pbmas-2mm means that the total displacement was 2 mm implying a SCW of 10 μm

Figure 176 shows the healing master curves at 20 °C. This temperature was selected because it is most relevant for the Netherlands. The figure shows very important information in that it appears that a large amount of healing will occur within 6 minutes (0.1 hour) if the micro cracks have a width of less than 10 μm ! This amount of damage does occur well beyond the peak in the load vs displacement curve (SCW = 10 μm implies a total displacement of 2 mm which is beyond the displacement at peak load shown in figure 173).

Although figure 176 shows that micro cracking in mastics heal fairly well, one should realize that in an asphalt mixture the mastic only composes about 15% of the total volume of the asphalt mixture. The other 85% are voids, sand and coarse aggregates. We should also keep in mind that figure 175 only presents healing of cracks in the mastic and these cracks are called cohesive cracks. In reality there are however we also have adhesive cracks which form around the coarse aggregates and the question is to what extent these adhesive cracks will heal. Figure 177 gives a schematic overview of cohesive and adhesive cracking while figure 178 clearly shows the difference between the two types of cracking.

To the knowledge of the author only little work has been done on healing of adhesive cracking. The question is whether such healing will occur. Adhesive healing in the ceramic waste aggregate mixture shown in figure 178 will certainly not occur. Since the limestone aggregate shown in figure 178 on the right hand side shows some mortar "beard" some healing might occur in that interface

All this implies that we also have to pay attention to the adhesive zone and have to pay attention to the factors that control adhesive cracking.

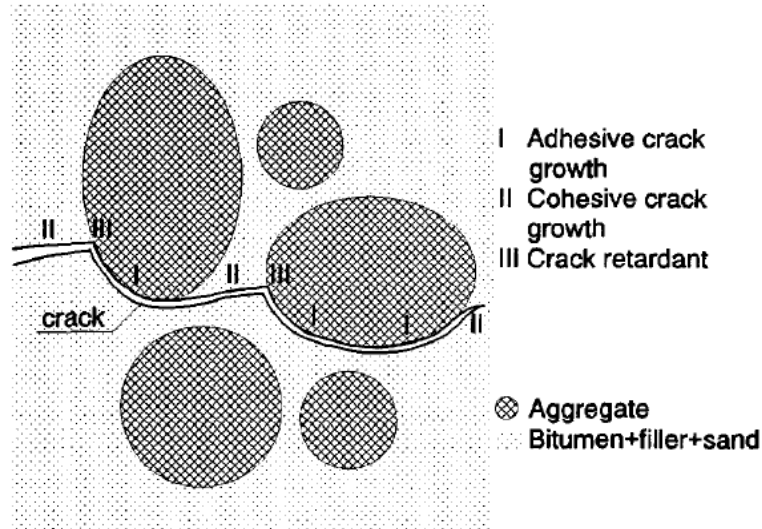


Figure 177: Crack growth process, adhesive and cohesive cracking.



Figure 178: Adhesive cracking in a mixture made with crushed ceramic waste aggregate (left) and cohesive/adhesive cracking in a mixture with limestone aggregate.

8.8 Adhesive cracking

Whether cracking will be mainly adhesive or cohesive depends of the affinity of the mastic with the aggregates. This affinity is highly affected by the acidity level, whether the aggregates are mainly positively or negatively charged and by the texture of the aggregate surface. Figure 179 e.g. shows the texture of the ceramic and limestone aggregates and one will not be surprised that bituminous mastic will adhere much better to the rough limestone surface than to the very smooth ceramic surface. This finding implies that the specific surface area of the aggregates play an important role in the adhesion between the bituminous mastic and the aggregates.

Adhesion between a solid (aggregate particle) and a liquid (bituminous mastic) depends on how much the solid and liquid "like each other". A nice example of this is shown in figure 180. The liquid drop on the left has a high affinity with the aggregate surface since the liquid is spreading over the aggregate surface. The liquid drop on the right doesn't have affinity with the aggregate surface since the drop stays the drop.

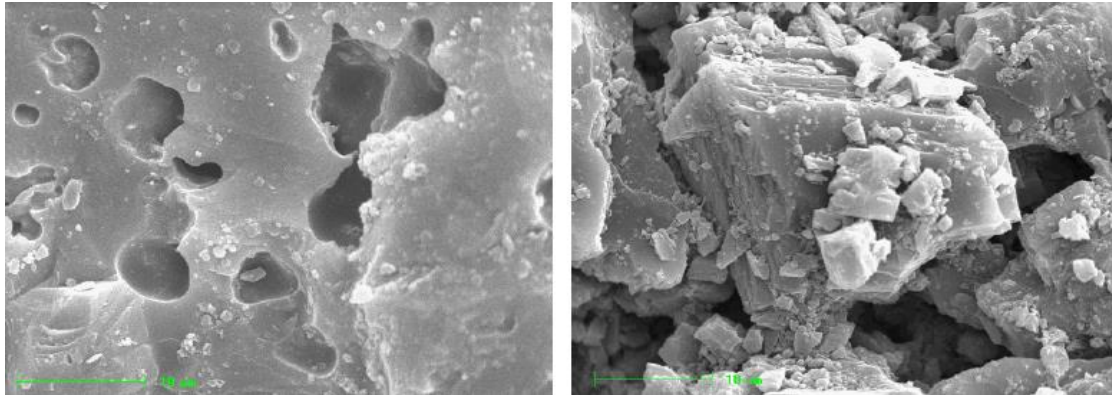


Figure 179: Texture of the ceramic (left) and limestone (right) aggregate (magnification 2500 *).



Figure 180: High affinity between liquid and aggregate (left) and no affinity (right) [54].

The wetting of a surface by a liquid can be described by means of the model shown in figure 181.

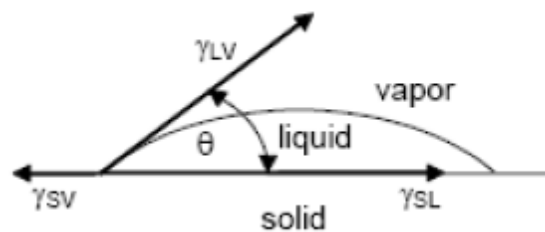


Figure 181: Forces involved in the wetting of a surface.

We can write:

$$\gamma_{sv} = \gamma_{sl} + \gamma_{lv} \cos \theta_{sl}$$

Where: γ_{sv} = interfacial energy between solid and vapor,
 γ_{sl} = interfacial energy between solid and liquid,
 γ_{lv} = interfacial energy between liquid and vapor,
 θ_{sl} = contact angle between solid and liquid.

After some manipulation and neglecting the influence of the spreading pressure we obtain:

$$\gamma_l * (1 + \cos \theta_{sl}) = \gamma_s + \gamma_l + \gamma_{sl}$$

Where: γ_l = surface energy of liquid,
 θ_{sl} = contact angle between solid and liquid,
 γ_s = surface energy of solid,
 γ_{sl} = interfacial energy between solid and liquid.

Hefer and Little [55] showed that the total energy that is needed to split two materials from each other can be written as:

$$W^a = -\Delta G_{12}^a = \gamma_1 + \gamma_2 + \gamma_{12}$$

Where: W^a = work of adhesion
 ΔG_{12}^a = change of Gibbs free energy per unit area
 γ_1 = surface energy of material 1
 γ_2 = surface energy of material 2
 γ_{12} = interfacial energy between materials 1 and 2

By combining the equations given above we arrive to:

$$W^a = -\Delta G_{12}^a \approx \gamma_l * (1 + \cos \theta_{sl})$$

There are several methods to determine the surface free energy of bitumen and aggregates. It goes too far to describe them in detail here; a detailed discussion on this topic can be found in [54]. Well known methods are the Sessile drop method, the Wilhelmy plate method and the Universal Sorption Device (see e.g. [56]). For the discussion on adhesion between bitumen and aggregates it is sufficient to know that surface energies play an important role in whether bitumen and aggregates adhere well or poor to each other. Table 25 shows the Gibbs free energy of adhesion as determined for different bitumen (B1 – B6) and aggregate (A2 – K2) combinations.

ΔG	A2	B2	C2	D2	E2	F2	G2	H2	I2	K2
B1	125.84	116.56	107.42	106.56	113.24	128.61	160.06	107.84	120.16	129.08
B2	154.59	150.49	145.83	127.14	149.35	165.23	189.68	140.45	154.73	173.90
B3	141.66	131.69	122.79	116.23	128.91	145.98	184.04	122.55	136.24	149.11
B4	173.28	171.90	169.97	139.41	172.24	188.70	211.34	161.20	176.79	202.84
B5	138.70	129.46	121.30	113.27	127.01	143.51	180.01	120.61	133.94	147.31
B6	106.98	95.48	83.95	94.33	90.79	105.36	137.16	87.40	98.35	100.63

Table 25: Gibbs free energy (G_f) of adhesion as determined for different bitumen – aggregate combinations [56].

As is shown in table 25, some bitumen – aggregate combinations adhere (much) better (indicated by a high ΔG value) than other combinations. In particular using bitumen B4 results in a good adhesion with all aggregate types while bitumen B6 gives the poorest adhesion. Also using aggregate types G2 and K2 results in a good adhesion. Unfortunately the names of the bitumens and aggregates cannot be given since this is propriety information belonging to the contractor who invested in this investigation.

It will be clear that the adhesive characteristics are also influencing the fatigue resistance. We have seen that beam fatigue relationships can be written as:

$$N = \frac{h^{\left(1-\frac{n}{2}\right)} c_0^{\frac{n}{h}}}{A[S_{mix}]^n} \int_{c_0/h}^{\frac{c}{h}} \frac{d(c/h)}{\left[1.99\left(\frac{c}{h}\right)^{0.5} - 2.47\left(\frac{c}{h}\right)^{1.5} + 12.97\left(\frac{c}{h}\right)^{2.5} - 23.17\left(\frac{c}{h}\right)^{3.5} + 24.8\left(\frac{c}{h}\right)^{4.5}\right]^n} \cdot \epsilon^{-n}$$

Lytton has shown that the parameter A depends a.o. parameters on the Gibbs free energy. This dependency is shown in figure 182.

$$A = \frac{k}{\sigma_t^2 \cdot I_i} \left(\left[\frac{D_1^{(1-m_t)} \cdot E_t}{\Delta G_f} \right]^{\frac{1}{m_t \cdot n_{BD} + 1}} \right) \int_0^{\Delta t} w^n(t) dt$$

A, n	= Paris' law fracture coefficients
m_t	= exponent obtained from the tension RM master-curve (slope of the log relaxation modulus versus log time graph)
D_1	= time-dependent creep compliance at 1.0 s (MPa^{-1})
E_t	= elastic modulus from tension RM master-curve (MPa)
k	= material coefficient (~ 0.33)
ΔG_f	= surface energy due to fracture or dewetting (mJ/m^2)
	So high ΔG_f is good!
σ_t	= maximum HMAC mixture tensile strength at break (kPa)
I_i	= dimensionless stress integral factor in crack failure zone, ranging between 1 and 2
n_{BD}	= dimensionless brittle-ductile factor, ranging between 0 and 1
Δt	= repeated loading time (s) (~ 0.01 s)
$\int_0^{\Delta t} w^n(t) dt$	= load pulse shape factor, ranging between 0 and 1
t	= time (s)

Remember: $dc/dN = A K^n$ and $N = f(1/A) * f(h) * f(c/h) * \epsilon^{-n}$ **TU Delft**

Figure 182: Effect of Gibbs free energy on the fracture parameter "A".

Together with table 25, figure 182 clearly shows that it makes quite some difference in fatigue resistance whether bitumen – aggregate combination B6 – C2 is selected or combination B4 – G2. It also shows that one has to be careful with changing the type of aggregate or bitumen during a project because such changes can have a significant effect on mixture performance.

Although the author only referred a little to the work done at Texas A&M University, he likes to mention that excellent ground breaking work in this field has been done by Texas &M researchers such as Little, Lytton, Bashir and the MSc and PhD students working under their supervision. Work reported in [56] e.g. was done at Texas A&M under the supervision of the researchers mentioned above.

The question now is which type of cracking is dominant is it adhesive, cohesive or do we see mixed mode cracking? In [57] a relationship between bitumen film thickness and cohesive and adhesive strength is presented (figure 183). This figure implies that at a bitumen film thickness of 0.008 inch (0.2 mm) and less adhesive failure is going to be dominant.

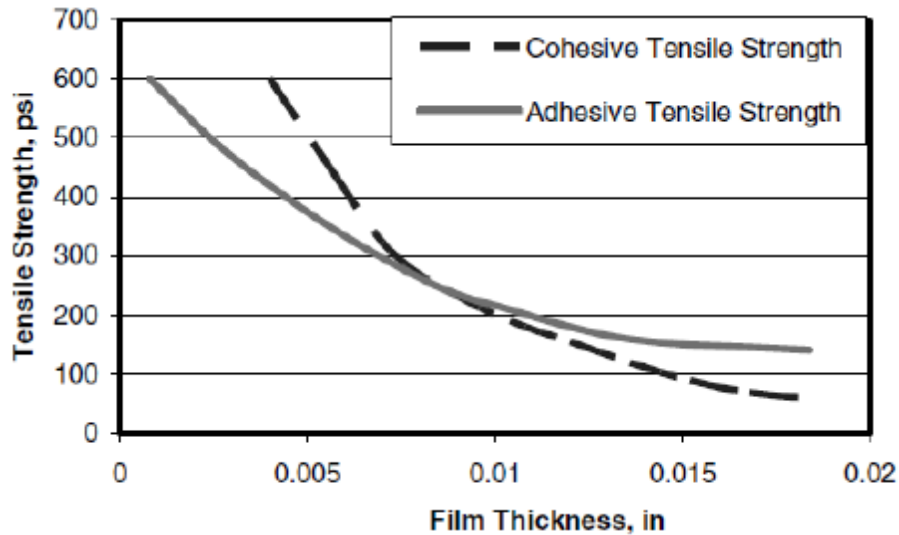


Figure 183: Cohesive and adhesive strength in relation to bitumen film thickness.

Mo [58] in his research showed that the type of cracking is also dependent on the temperature and type of aggregate (figure 184).

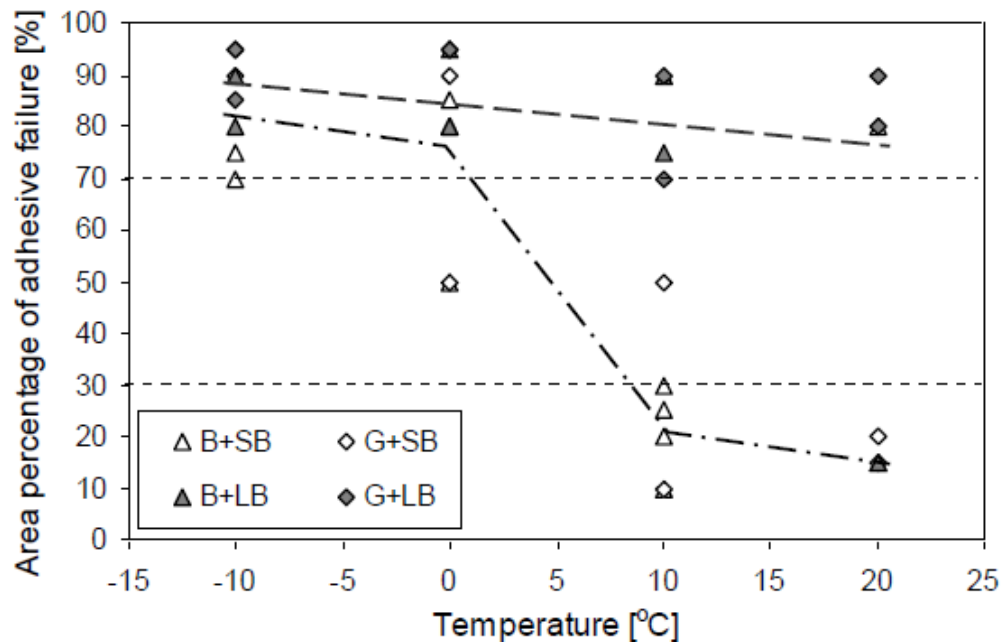


Figure 184: Type of cracking in relation to temperature and aggregate type (B = Bestone, G = Greywacke; SB = short time aging of the binder, LB = long time aging of the binder).

Mo obtained these results by testing stone – bitumen – stone columns in which a 15 μm thick bitumen film was placed between two stone columns (see figure 185) which had a diameter of 6.5 mm. The aggregates used were a sandstone (Bestone) and Greywacke. The bitumen used was a SBS modified bitumen provided by Shell (Cariphalt XS).

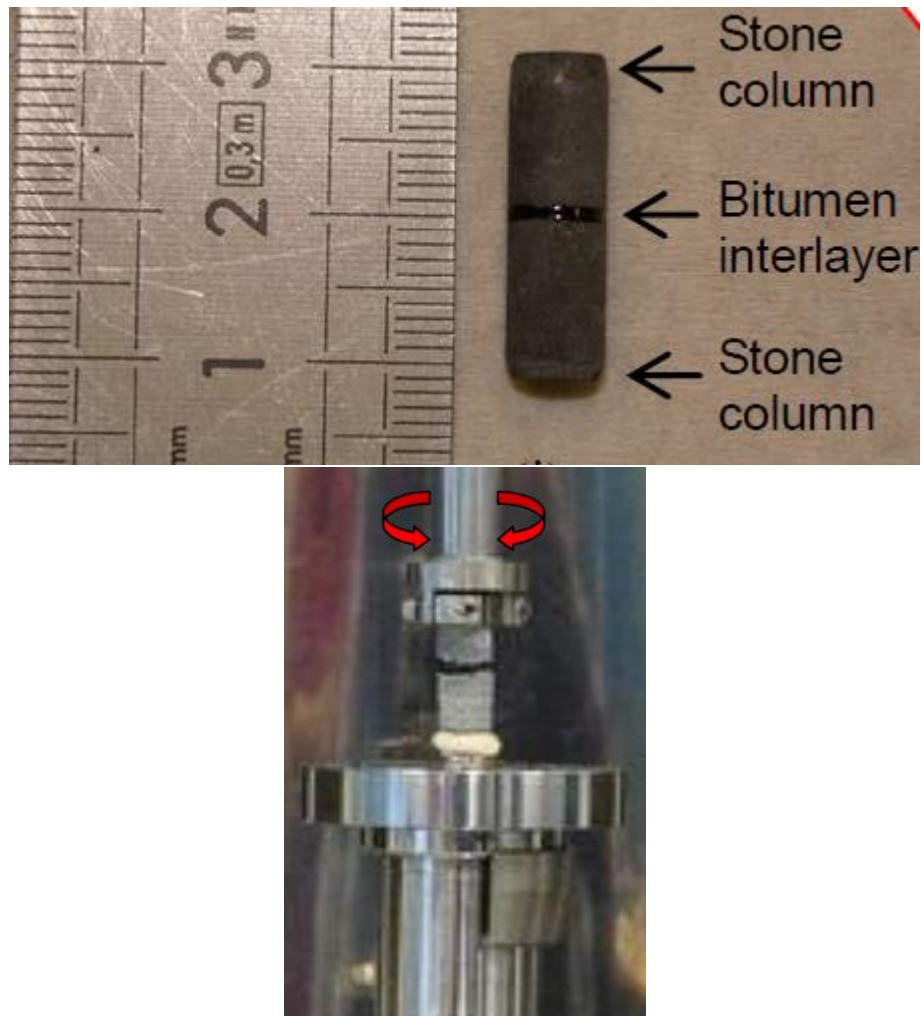


Figure 185: Stone – bitumen – stone columns as used by Mo and placement of such specimens in the DSR.

From figure 184 it can be concluded that in case of the sandstone (Bestone) adhesive cracking was clearly dominant over the entire temperature range. In case of the Greywacke more than 50% of the failure surface showed adhesive cracking at temperatures of 5 °C and lower. All in all this means that the dominance of adhesive cracking over cohesive cracking depends on the type of aggregate, type of bitumen and temperature (which also implies loading time).

The results given in table 25 can be interpreted in this way that adhesive cracking is more likely to occur than cohesive cracking for those bitumen – aggregate combinations which have a low ΔG .

The low ΔG combinations also point to another problem which is the water resistivity of those mixtures. If water has the chance to penetrate to the bitumen – aggregate interface through cracks then it will try to “push away” the bitumen. This is because water is a very strong dipole and has therefore by definition a greater affinity to aggregates than bitumen. However, the higher the ΔG of the specific bitumen – aggregate combination is the more difficult it is for water to replace the bitumen.

All in all this means that the fatigue resistance of asphalt mixtures which is normally determined in dry conditions might be disappointingly low when the mixture is facing wet conditions in reality. This is of course dependent on the void content of the mixture. The lower the void content, the less the mixture will be vulnerable for moisture influences. Mixtures with a void content < 4 à 5% are believed to be hardly affected by moisture since the voids will not be connected at these low void contents. If however (micro) cracks start to develop also these dense mixtures will become vulnerable for moisture.

8.9 Aging related cracking

As we have previously discussed aging resulting in hardening of the bitumen occurs during production and laying and during the service life of the pavement. Aging is caused by loss of volatiles (mainly during production and laying), oxidation (during the service life) and exudation (during the service life). Exudation is the process of the lighter fractions being absorbed by the aggregates; the aggregates should of course be porous otherwise absorption cannot take place. This is caused by the fact that the bitumen itself is not stable. Shell [33] has developed an exudation test which acts as follows.

Defined quantities of bitumen are placed in drilled recesses of a marble plate of specific Italian origin. The plates are heated to $60\text{ }^{\circ}\text{C}$ for four days under a nitrogen blanket (to prevent oxidation). During this period oily rings develop which are measured with a microscope under ultraviolet light. For a pen 60 material a ring width of less than 2 mm is an indicator for good performance.

Oxidation of bitumen causes an increase in polarity through formation of carbonyls and sulfoxides primarily in the asphaltene fraction and an increase in polarizability through conversion of aromatic resins to asphaltenes. As polarity and dispersion forces increase, asphaltene particles bind more tightly resulting in layering. This effect increases with increased oxidation. The layering of the asphaltene particles imparts rigidity which in turn leads to cracking as visco-elastic properties are lost. The increase in overall polarity of the bitumen increases its viscosity. One could say that due to aging the bitumen changes from a more sol type bitumen to a more gel type bitumen.

Aging can result in cracking even when no traffic loads are applied. Figure 186 shows an example of such cracking.



Figure 186: Example of cracking due to aging/hardening of the binder.

Rowe e.a. [59] showed that the development of such cracking can be related to the change of the Black diagram in time (figure 187).

Black diagram and non load associated cracking

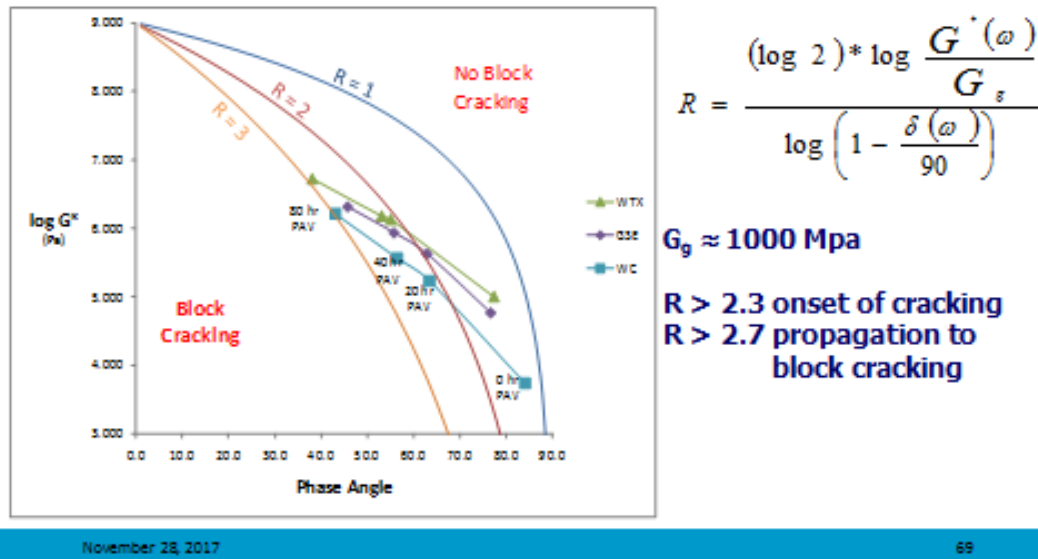


Figure 187: Black diagram and non-load associated cracking.

Figure 187 also shows how the Black diagram of three bitumens was changing in relation to the nr of hours (0, 20, 40, 80 hrs) aging in the PAV (pressure aging vessel). The figure shows that bitumen WC shows the fastest change and is therefore the bitumen which is the most sensitive of the three to show aging related cracking.

From the material presented here it becomes obvious that if one has to work with a bitumen of unknown/unspecified quality, doing aging tests in combination with viscosity/DSR tests and exudation droplet tests is a good way to find out whether one is dealing with a bitumen of good or marginal quality.

8.10 Permanent deformation in asphalt mixtures

Figure 188 is a typical example of severe rutting in the asphalt layers of a flexible pavement. The permanent deformation shown in this picture is not only due to viscous densification of the asphalt layer but also due to shear deformation; notice the ridges next to the wheel paths. From what have been discussed in the previous sections it will be clear that permanent deformation is controlled by:

- the wheel load and, more importantly, the contact pressure distribution,
- temperature and loading time,
- the viscosity characteristics of the bitumen,
- the type and amount of filler which, together with the bitumen, makes the mastic,
- the stone skeleton (gradation and angularity of the aggregates).



Figure 188: Permanent deformation in the asphalt layer.

Let us first discuss the stresses that occur in the asphalt wearing course and binder course due to a wheel load and which are responsible for the permanent deformation.

Wang [60] analyzed the stresses at mid depth of the wearing course of the pavement shown in figure 189.

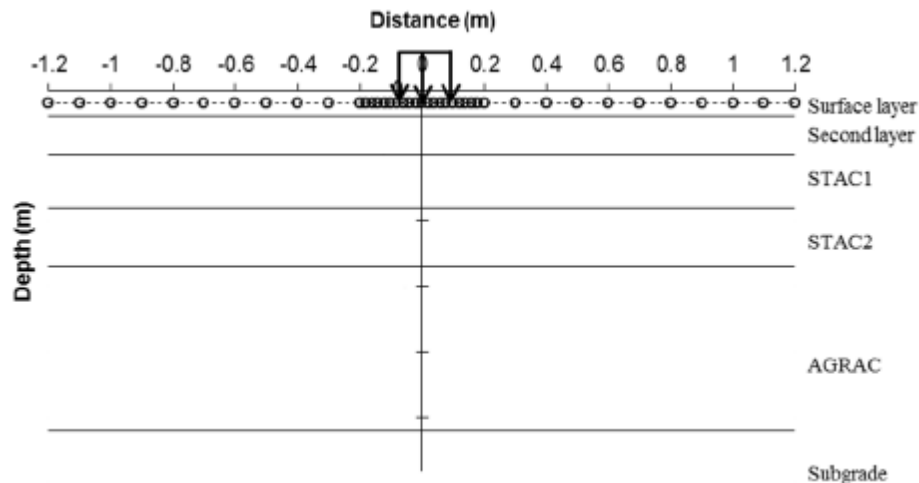


Figure 189: Pavement structure analyzed by Wang.

The wearing course was a 50 mm thick porous asphalt concrete (PAC) or dense asphalt concrete layer (DAC). The second, third and fourth layer consisted of stone asphalt concrete (STAC) which is a base course type of mixture with a thickness of 60, 80 and 90 mm respectively containing RAP. The 250 mm thick AGRAC layer was a layer of 85 % crushed old asphalt and 15 % river sand mixed with 3.5 % by mass cement. The subgrade was a sand subgrade. The load applied was a 45 kN load with a contact pressure of 0.94 MPa.

In the analysis the following temperature distribution was assumed (table 26).

Depth [mm]	T [°C]
25	40
80	39.5
150	38
235	36.5

Table 26: Temperature distribution as used by Wang in his analyses.

The stiffness characteristics of the asphalt layers were assumed to be stress dependent; the stress dependent relationships were taken from [36]. An example of the stress dependency of the stiffness modulus of the dense asphalt concrete (DAC) wearing course at 40 °C is given in figure 190.

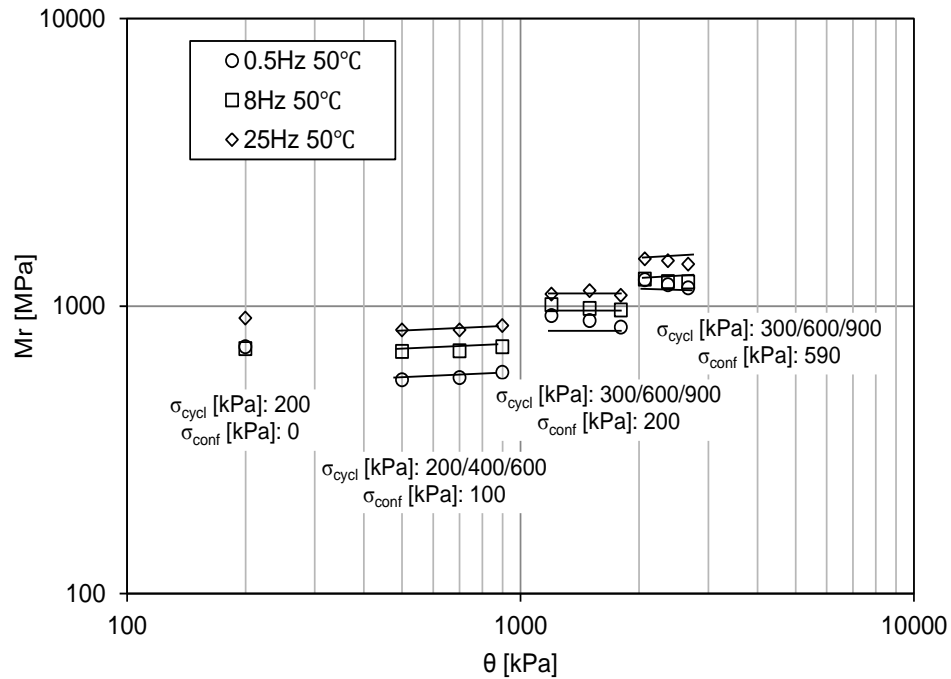


Figure 190: Stress dependency of the modulus of the dense asphalt concrete wearing course at 40 °C.

Figure 191 shows the maximum and minimum principal stresses that were calculated at mid depth of the DAC layer. As is the case with granular materials, the stress ratio being maximum principal stress at the occurring confinement stress : stress at failure at that same confinement pressure (σ_1 / σ_{1f}) is an important indicator for whether permanent deformation will occur or not. Information on the failure strength of the asphalt mixtures at different temperatures and confining pressures was taken from Muraya [61] who tested the same mixtures. Using this information Wang calculated the stress ratios $R = \sigma_1 / \sigma_{1f}$ at different locations and obtained in this way figure 192. It is interesting to note that the two sharp peaks of $R = 0.25$ occurred at the edge of the wheel load. At these locations the maximum permanent deformation will occur and this is exactly what is shown in figure 188.

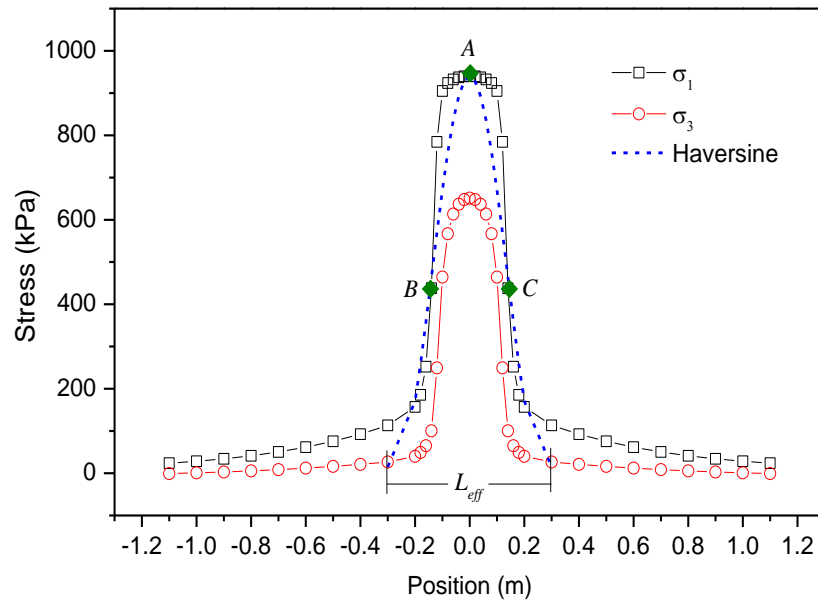


Figure 191: Maximum and minimum principal stress at mid depth of the DAC layer at 40 °C.

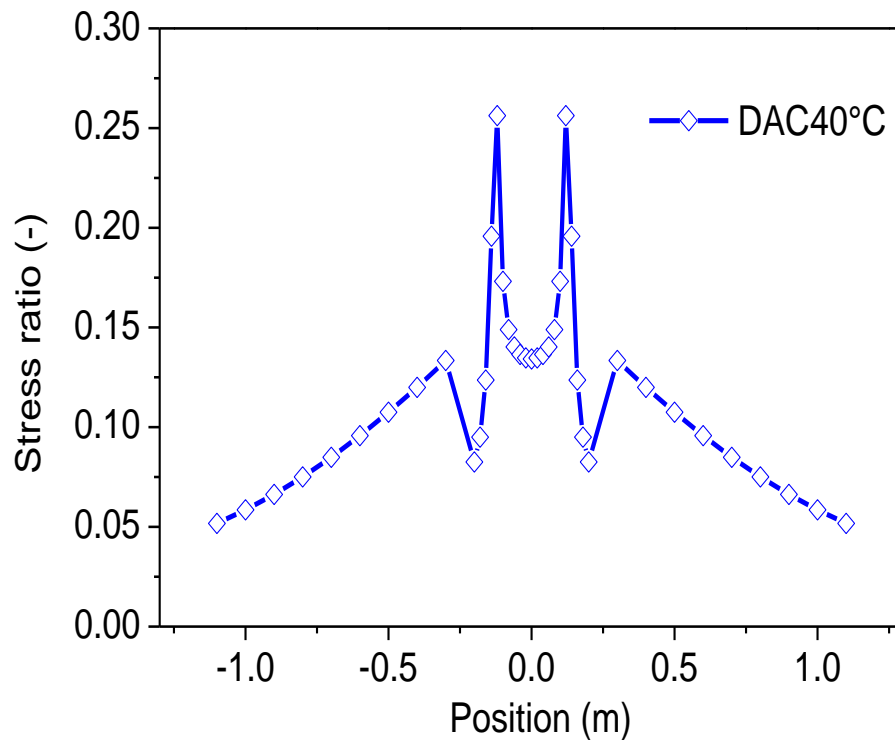


Figure 192: Stress ratio $R = \sigma_1 / \sigma_{1f}$ at mid depth of the DAC wearing course at 40 °C.

From the behavior of granular materials we know that if $R < 0.3$ permanent deformation is not likely to occur. Unfortunately no guidelines with respect to allowable R values in asphalt concrete are available. Furthermore asphalt concrete contains bitumen as a binder and this binder shows viscous flow at high temperature and therefore contributes to the development of permanent deformation. It is nevertheless interesting to know to what the contribution of the stone skeleton

is in giving the mixture its resistance to permanent deformation. Information on this is given in figure 193 for DAC and in figure 194 for PAC.

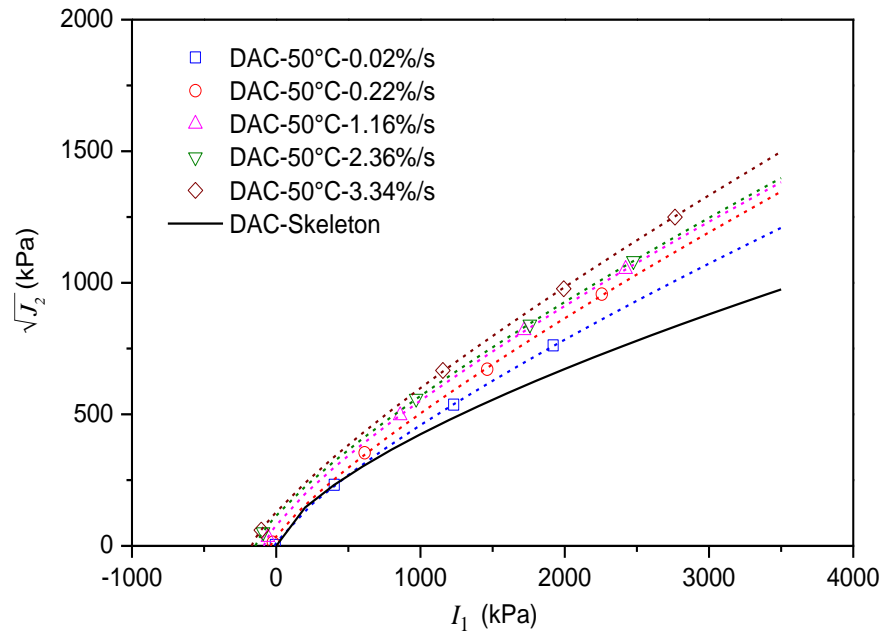


Figure 193: Failure envelope for the DAC stone skeleton and mixture at 50 °C and several deformation rates.

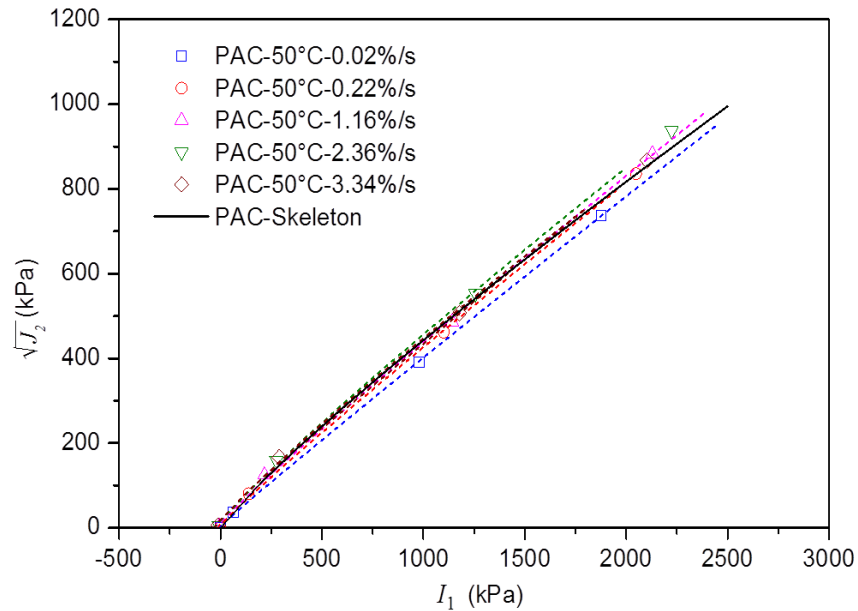


Figure 194: Failure envelope for the PAC stone skeleton and mixture at 50 °C and several deformation rates.

Figures 193 and 194 show the failure envelopes for the DAC and PAC stone skeletons and the DAC and PAC mixtures. By comparing figures 193 and 194 we learn that the stone skeleton is the main contributor to the (triaxial) strength of both mixtures. In case of PAC the strength completely depends on the stone skeleton; the bitumen doesn't contribute to the shear

conditions at the prevailing loading and temperature conditions. In case of DAC however we notice that the presence of bitumen improved the shear resistance. Furthermore we notice that when the strain rate increases (resulting in a higher stiffness) the contribution of the bituminous mastic to the shear strength of DAC also increases. The PAC results also show why PAC should not be used as a bottom layer in an asphalt structure. The strength of PAC is dependent on confinement and at the bottom of an asphalt package there is no confinement but there are horizontal tensile stresses. Such stress conditions can hardly be taken by PAC.

Or the sake of completeness it is recalled that the stress invariants I_1 and J_2 are calculated as follows:

$$I_1 = \sigma_1 + \sigma_2 + \sigma_3$$

$$J_2 = [(\sigma_1 - \sigma_2)^2 + (\sigma_2 - \sigma_3)^2 + (\sigma_3 - \sigma_1)^2] / 6$$

For pavement design purposes, there is a need to predict the development of permanent deformation in relation to the number of wheel loads and their weight, the mixture composition and the climatic conditions (mainly temperature). In general permanent deformation can be described in the way shown in figure 195.

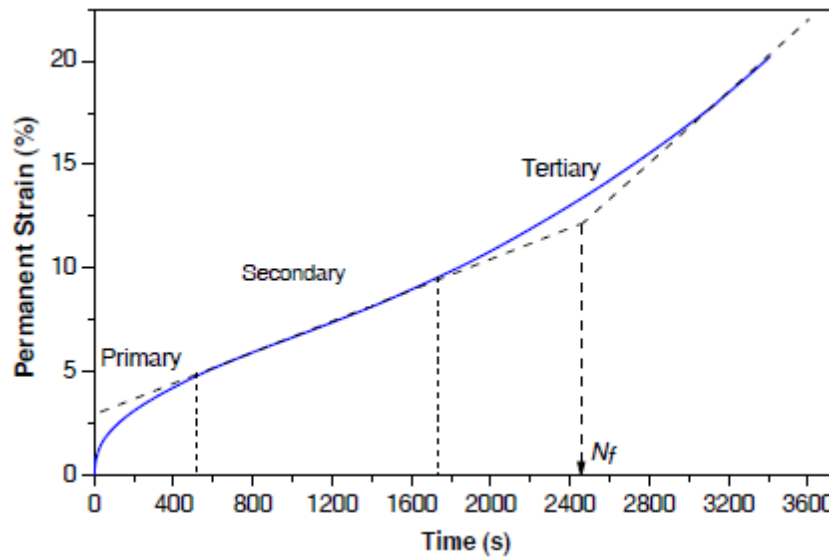


Figure 195: Development of permanent vertical strain in a repeated load triaxial test. Number of load repetitions = time / load frequency.

The permanent deformation is a result of densification (volume decrease), viscous flow and shear deformation (dilation resulting in volume increase). The primary and secondary phases are considered to be the result of densification, whereas shear dilation occurs in the tertiary phase. The point at which tertiary flow starts to occur is often defined as the flow number. Many researchers (e.g. Kenis [63]) have shown that the steady secondary stage starts after a limited number of load repetitions (e.g. after 200 repetitions) and that the development of the permanent strain (ϵ_p) can be written as:

$$\epsilon_p = a N^b$$

Where N is number of load cycles and a and b are material parameters.

The increase of the permanent deformation per load cycle can then be written as:
 $d\varepsilon / dN = a b N^{(b-1)}$

Many researchers (a.o. Wang [60], Kenis [63]) have shown that the ratio of permanent strain ε_{pn} to resilient (elastic) strain ε_{en} per cycle takes a constant value after let say 200 load repetitions. We can then write:

$$\varepsilon_{pn} / \varepsilon_{en} = (a * b / \varepsilon_{en}) N^{(b-1)}$$

If we call $\mu = (a * b / \varepsilon_{en})$ and $\alpha = 1 - b$ we obtain:

$$\varepsilon_{pn} / \varepsilon_{en} = \mu N^{-\alpha}$$

This is the basis for permanent deformation calculations within the visco-elastic pavement analysis system VESYS [63].

In AASHTO's MEPD [31] a similar approach is followed and the final lab equation that was proposed for the field validation/calibration process is as follows

$$\varepsilon_p / \varepsilon_e = 10^{-3.5552} * T^{1.734} * N^{0.09937}$$

where T is the temperature in [°F].

It is recalled that this is the selected laboratory equation; it needs to be multiplied with a number of calibration factors in order to be able to predict in situ permanent deformation. These calibration factors will be presented when we discuss pavement design systems.

Also the prediction model as developed by the Belgian Road Research center follows similar lines. Francken e.a. [50] have shown that the permanent deformation of asphalt mixtures as determined by means of repeated load triaxial tests can be described by:

$$\varepsilon_p = ((\sigma_0 - \sigma_h) / (0.65 * E * F)) * (t / 1000)^{0.25}$$

Where: ε_p = cumulative permanent strain,
 σ_0 = $\sigma_v / 2$ [MPa],
 σ_v = vertical stress [MPa],
 σ_h = horizontal stress [MPa],
 E = complex modulus at the given temperature and loading time conditions [MPa],
 F = $5.5 * 10^{-2} (1 - 1.02 V_b / (V_b + V_a))$,
 V_b = volume percentage of bitumen [%],
 V_a = void content [%],
 t = total loading time [s] = $N f$,
 N = number of load repetitions,
 f = load frequency [Hz].

This equation appears to be a much better one than the one used in MEPD. In the MEPD equation the effect of the material properties is only reflected in ε_e which is calculated using a linear elastic multi layer systems where the stiffness of the asphalt layer is needed as one of the material parameters. The asphalt modulus is also one of the parameters controlling the permanent deformation in the Belgian equation but this equation also takes into account the volumetric composition. The ratio $V_b / (V_b + V_a)$ gives the amount of pores in the skeleton that are filled with bitumen. It will be clear that if this ratio is too high, if the mixture is over-filled, permanent

deformation will easily occur. If the degree of filling ratio increases, E as well as F will decrease and ε_p will increase.

Francken's equation shows that a high stiffness is effective in the reduction of permanent deformation. This was already implied in figure 100 which shows how the viscous deformation of bitumen is controlled by the stiffness of the bitumen and the PI. That figure implies that using a bitumen with a high PI (e.g. $PI = 3$) is effective in reducing permanent deformation but increasing the PI also implies that the mixture gets brittle and will crack easily; this is not really what we like! So the question how can we stiffen the bitumen without using a higher PI bitumen.

Let us therefore have a look in what material is actually the "glue" in an asphalt mixture. As mentioned earlier, it is not the bitumen that binds the aggregates together but it is the mastic (binder + filler). Therefore the viscosity characteristics of the mastic are of importance when it comes to resistance to permanent deformation and not so much those of the bitumen. The viscosity characteristics of the mastic are heavily influenced by the type and amount of filler; this is shown in figure 196.

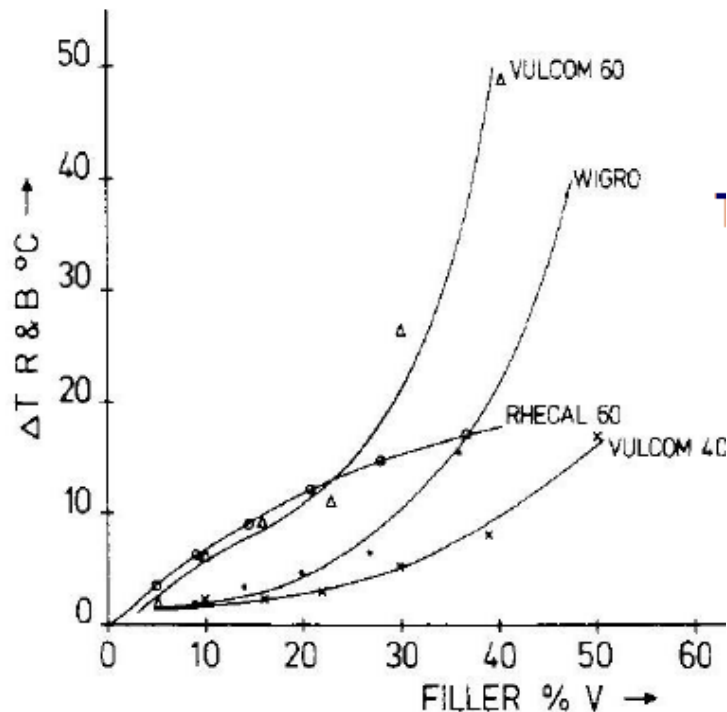


Figure 196: Increase in $T_{R\&B}$ as function of amount and type of filler [64].

It should be noted that the fillers shown in figure 196 are specially produced fillers. This is common practice in the Netherlands while in other countries crusher dust is used as filler (also called fines). When crusher dust is used it is highly recommendable to determine the effect it has on the $T_{R\&B}$ since depending on the type and amount of fines the mastic can become either very stiff or not stiff enough.

Information on the bitumen used to produce figure 196 is given in table 27 while tables 28 and 29 give information on the fillers.

Softening point ring and ball	47 °C
Penetration at 25 °C	87
Penetration index	- 0.6
Density	1030 kg/m ³
Acidity	0.28 mg KOH/g

Table 27: Properties of the bitumen used to produce figure 194 [64].

	Wigro	Vulcom 40	Rhecal 60	Vulcom 60	
Density	2748	2379	2650	2295	kg/m ³
Bitumen-carrying capacity	44	43	58	57	-
Voids per cent according to Rigden	37	40	44	48	%V
Retained on sieve to 63 µm	12.2	16.0	14.8	15.7	%
Passing sieve 63 µm	87.8	84.0	85.2	84.3	%
Susceptibility to stripping	1.4	0.0	traces	0.0	%
Loss of mass on heating to 150 °C	0.2	0.1	0.3	0.2	%
Swell	1	1	0	3	%

Table 28: Properties of the fillers used to produce figure 194 [64].

Weak filler		Medium filler		Mineral composition
Filler with bitumen-carrying capacity ("van der Baan's ratio") 40-50		Filler with bitumen-carrying capacity ("van der Baan's ratio") 54-60		
Wigro	Vulcom 40	Rhecal 60	Vulcom 60	
100%	5 - 15% 60 - 70% 10 - 20% 10 - 15% 2 - 5%	55 - 65% 35 - 45%	10 - 20% 60 - 80% 5 - 15% 10 - 15% 2 - 5%	Limestone Coal fly ash Lignite fly ash Mineral silicates Calcium hydroxide

Table 29: Properties of the fillers used to produce figure 194 [64].

An increase in $T_{R\&B}$ will give the mixture certainly a higher resistance to permanent deformation.

Figure 196 also points to another important aspect of the effect of the filler and that is its effect on the mixture stiffness; a higher $T_{R\&B}$ will definitely result in a higher mixture stiffness. As one will recall the mixture stiffness nomograph of Shell, next to S_{bit} and V_b only requires V_g , the volume % of aggregates (aggregates + sand + filler) as input. This means that the stiffening effect of the type of filler is ignored in the mixture stiffness nomograph of Shell.

9. Granular materials

9.1 Introduction

In many countries around the world, granular base and subbase layers comprise a very important part of the pavement structure. An example of a pavement structure the bearing capacity of which highly depends on the structural capacity of unbound layers is given in figure 1, South African pavement structure I. In order to be able to properly design such pavements knowledge on the behavior of unbound granular layers and the factors which influence that behavior is essential.

As has been shown in the Lecture Notes on Soils and Unbound Granular Materials [62], the stiffness and strength characteristics of unbound granular are strongly influenced by the stress conditions to which these material are subjected as well as by other important factors like degree of compaction, moisture content as well as characteristics of the material itself like gradation etc. All that has been discussed in [62] will not be repeated here. In this chapter we will focus on how important parameters like stiffness, cohesion, angle of internal friction etc can be estimated. Firstly we will discuss estimation methods that have been developed as part of AASHTO's MEPD system. Then we will discuss the equations that have been developed to predict the mechanical characteristics of Dutch sands and Dutch base course materials made of mixtures of crushed concrete and crushed masonry.

9.2 Estimation of the resilient characteristics of unbound base materials and sands

In reference [65] several regression equations are presented which give the resilient modulus as a function of the stress conditions and material parameters like gradation, plasticity etc. These equations will be given hereafter.

The first equation is for **crushed stone** materials.

$$M_r = [0.7632 + 0.0084 * P_{3/8} + 0.0088 * LL - 0.0371 * W_{opt} - 0.001 * \gamma_{opt}] * p_a * [\theta / p_a]^A * [(\tau_{oct} / p_a) + 1]^B$$

$$A = 2.2159 - 0.0016 * P_{3/8} + 0.0008 * LL - 0.038 * W_{opt} - 0.0006 * \gamma_{opt} + 2.4 \text{ E-}7 * (\gamma_{opt}^2 / P_{40})$$

$$B = -1.1720 - 0.0082 * LL - 0.0014 * W_{opt} + 0.0005 * \gamma_{opt}$$

For **crushed gravel** the proposed equation is:

$$M_r = [-0.8282 - 0.0065 * P_{3/8} + 0.0114 * LL + 0.0004 * PI - 0.0187 * W_{opt} + 0.0036 * W_s + 0.0013 \gamma_s - 2.6 \text{ E-}6 * (\gamma_{opt}^2 / P_{40}) * p_a * [\theta / p_a]^C * [(\tau_{oct} / p_a) + 1]^D$$

$$C = 4.9555 - 0.0057 * LL - 0.0075 * PI - 0.0470 * W_s - 0.0022 * \gamma_{opt} + 2.8 \text{ E-}6 * \gamma_{opt}^2 / P_{40}$$

$$D = -3.514 + 0.0016 * \gamma_s$$

For **uncrushed gravel** the equation is:

$$M_r = [-1.8961 + 0.0014 * \gamma_s - 0.1184 * W_s / W_{opt}] * p_a * [\theta / p_a]^E * [(\tau_{oct} / p_a) + 1]^F$$

$$E = 0.4960 - 0.0074 * P_{200} - 0.0007 * \gamma_s + 1.6972 * \gamma_s / \gamma_{opt} + 0.1199 * W_s / W_{opt}$$

$$F = -0.5979 + 0.0349 * W_{opt} + 0.0004 * \gamma_{opt} - 0.5166 * W_s / W_{opt}$$

For **sand** the equation is:

$$M_r = [-0.2786 + 0.0097 * P_{3/8} + 0.0219 * LL - 0.0737 * PI + 1.8 \text{ E-}7 * \gamma_{opt}^2 / P_{40}] * p_a * [\theta / p_a]^G * [(\tau_{oct} / p_a) + 1]^H$$

$$G = 1.1148 - 0.0053 * P_{3/8} - 0.0095 * LL + 0.0325 * PI + 7.2 \text{ E-}7 * \gamma_{opt}^2 / P_{40}$$

$$H = -0.4508 + 0.0029 P_{3/8} - 0.0185 * LL + 0.0798 * PI$$

Where:

M_r = resilient modulus [MPa]

θ = $\sigma_1 + \sigma_2 + \sigma_3$ [kPa]

τ_{oct} = $\{\text{sqrt}[(\sigma_1 - \sigma_2)^2 + (\sigma_2 - \sigma_3)^2 + (\sigma_1 - \sigma_3)^2]\} / 3$ [kPa]

$\sigma_1, \sigma_2, \sigma_3$ = principal stresses [kPa]

P_a = atmospheric pressure [kPa] (normally air pressure is around 1000 mbar)

The other parameters are defined in table 30.

Variable	Description	Unit
$P_{3/8}$	Percentage passing 3/8" sieve	%
P_{40}	Percentage passing No. 40 sieve	%
LL	Liquid limit	%
W_{opt}	Optimum moisture content	%
γ_{opt}	Optimum dry density	kg/m ³
W_s	Actual moisture content	%
γ_s	Actual dry density	kg/m ³
PI	Plasticity Index	%
P_{200}	Percentage passing No. 200 sieve	%

Table 30: Variables used in the regression equations.

The question with regression equations is always whether they are physically correct, for which materials they have been developed and how good there predictive capability is. These issues will be discussed hereafter.

It is a well-known fact that the resilient modulus depends on the stress conditions and that the so called $M_r - \theta$ model is doing a fairly good job when the stresses stay well below the failure stress. We recall that this model is written as

$$M_r = k_1 \theta^{k_2}$$

It is also known however that model is incorrect from a fundamental point of view because it implies that a high θ , so a high modulus can be achieved having a high vertical stress and no confinement. In such a case however the material would fail. This implies that the influence of the confinement should be taken into account in a more explicit way. This is done by taking into account the τ_{oct} . All this means that the model is correct from a mechanical point of view by taking into account both θ and τ_{oct} .

Determining whether the influence of the physical parameters is correct is much more complicated since there are so many variables involved. Furthermore some of these variables are related to each other. An example of this are the W_{opt} and γ_{opt} ; if for instance the compaction effort is increased one will notice that a higher γ_{opt} is achieved at a lower W_{opt} . Therefore it is always better to also take the influence of compaction into account and report density not as an absolute value but as a relative number being "density of the sample : specific weight of the material".

An overview has been made of the parameters that control the "constant" of the M_r equations and how they affect that "constant". This "constant" value should preferably as high as possible. This overview is shown in table 31.

Parameter	Crushed stone	Crushed gravel	Uncrushed gravel	Sand
$P_{3/8}$	+	-		+
LL	+	+		+
W_{opt}	-	-		
γ_{opt}	-			
PI		+		-
W_s		+		
γ_s		+	+	
γ_{opt}^2 / P_{40}		-		+
W_s / W_{opt}			-	

Table 31: Parameters taken into account in the "constant" of the M_r relationships and their effect. The table shows how an increase in the value of the parameter affects the "constant". If + the value of the "constant" will increase if - , its value will decrease.

From table 31 we can conclude that there is no parameter that affects the "constant" of all four materials. Especially the difference between the parameters that affect the "constant" of the crushed and uncrushed gravel is striking and this author could not find an explanation why this should be the case. Also the fact that an increase in W_s should result in an increase in the value of the "constant" in case of crushed gravel is not clear; it is in fact counter intuitive. The fact that a higher γ_s results in a higher value of the "constant" for crushed gravel makes sense.

One could also wonder whether each and every parameter really contributes to the value of the "constant". These can easily be checked by considering the value of " α " the constant by which each parameter is multiplied (α * parameter). Since all parameters except the density parameters are expressed as a % value one can determine the contribution of each α * parameter value. In case of the crushed stone equation, one can conclude that $P_{3/8}$ and LL are not really contributing to the value of the "constant" since the multiplier α has a very low value in those cases. In case of the crushed gravel $P_{3/8}$, LL, PI, and W_s don't contribute to much while in case of sand it is again the $P_{3/8}$ parameter.

The question arises whether the equations couldn't have been simplified without losing the predictive capability.

The equations have been determined for different types of materials; tables 32, 33, 34 and 35 give an overview of the range in the values of the parameters of the materials that were tested. This overview helps to determine whether the equations can be useful for other conditions.

LTPP BASE MATL. CODE: 303 – Crushed Stone
No. of Resilient Modulus Tests: 57

Parameters	Min	Max	Median	Mean
$P_{3/8"}$	39.0	90.0	64.0	63.5
$P_{No. 4}$	21.0	77.0	49.0	46.9
$P_{No. 40}$	8.0	47.0	25.0	25.6
$P_{No. 200}$	3.0	32.4	12.2	13.4
LL	0.0	27.0	0.0	6.1
PI	0.0	8.0	0.0	1.3
$w_{opt}\%$	4.0	11.0	6.0	6.4
$\gamma_{d, opt} (kg/m^3)$	1874.3	2354.9	2242.8	2218.6
$w_s\%$	3.1	12.9	6.3	6.6
$\gamma_s (kg/m^3)$	1723.6	2236.2	2095.2	2082.3
$\gamma_s/\gamma_{d, opt}$	0.80	1.00	0.94	0.94
w_s/w_{opt}	0.52	1.42	1.00	1.03
$(\gamma_{d, opt})^2/P_{No. 40}$	74747.9	665211.9	198342.0	220732.2

Table 32: Range of the values of the parameters used in the M_r equation for crushed stone.

LTPP BASE MATL. CODE: 304 – Crushed Gravel
No. of Resilient Modulus Tests: 27

Parameters	Min	Max	Median	Mean
$P_{3/8"}$	49.0	98.0	69.0	69.5
$P_{No. 4}$	30.0	91.0	53.0	53.7
$P_{No. 40}$	8.0	69.0	28.0	28.2
$P_{No. 200}$	3.5	59.9	12.3	16.3
LL	0.0	33.0	0.0	9.7
PI	0.0	16.0	0.0	2.1
$w_{opt}\%$	5.0	11.0	6.0	7.2
$\gamma_{d, opt} (kg/m^3)$	1986.5	2419.0	2194.7	2195.3
$w_s\%$	4.3	11.3	5.9	6.9
$\gamma_s (kg/m^3)$	1875.8	2285.8	2061.6	2072.8
$\gamma_s/\gamma_{d, opt}$	0.92	0.96	0.94	0.94
w_s/w_{opt}	0.69	1.30	0.95	0.96
$(\gamma_{d, opt})^2/P_{No. 40}$	57189.9	584658.9	172031.6	210196.2

Table 33: Range of the values of the parameters used in the M_r equation for crushed gravel.

LTPP BASE MATL. CODE: 302 – Uncrushed Gravel
 No. of Resilient Modulus Tests: 31

Parameters	Min	Max	Median	Mean
$P_{3/8"}$	60.0	90.0	76.0	76.6
$P_{No. 4}$	32.0	81.0	59.0	61.2
$P_{No. 40}$	9.0	45.0	25.0	25.6
$P_{No. 200}$	3.5	18.1	6.9	8.5
LL	0.0	23.0	0.0	3.0
PI	0.0	8.0	0.0	0.7
$w_{opt}\%$	5.0	10.0	6.0	6.7
$\gamma_{d, opt} (kg/m^3)$	2018.5	2371.0	2194.7	2190.1
$w_s\%$	3.7	13.8	6.0	6.4
$\gamma_s (kg/m^3)$	1882.1	2215.5	2057.0	2049.9
$\gamma_s/\gamma_{d, opt}$	0.89	1.00	0.94	0.94
w_s/w_{opt}	0.62	1.38	0.98	0.95
$(\gamma_{d, opt})^2/P_{No. 40}$	93439.9	535209.3	193843.1	215727.5

Table 34: Range of the values of the parameters used in the M_r equation for uncrushed gravel.

LTPP BASE MATL. CODE: 306 – Sand
 No. of Resilient Modulus Tests: 35

Parameters	Min	Max	Median	Mean
$P_{3/8"}$	80.0	100.0	98.0	94.6
$P_{No. 4}$	69.0	100.0	95.0	91.1
$P_{No. 40}$	28.0	97.0	59.0	60.9
$P_{No. 200}$	1.7	32.3	9.4	10.5
LL	0.0	26.0	0.0	2.0
PI	0.0	4.0	0.0	0.1
$w_{opt}\%$	5.0	16.0	10.0	9.5
$\gamma_{d, opt} (kg/m^3)$	1666.1	2226.8	1906.4	1943.0
$w_s\%$	5.0	14.7	9.1	8.9
$\gamma_s (kg/m^3)$	1574.6	2108.9	1797.3	1831.5
$\gamma_s/\gamma_{d, opt}$	0.90	0.97	0.95	0.94
w_s/w_{opt}	0.55	1.21	0.96	0.95
$(\gamma_{d, opt})^2/P_{No. 40}$	30172.0	151323.7	64972.0	78238.9

Table 35: Range of the values of the parameters used in the M_r equation for sand.

Figures 197, 198, 199 and 200 show how well the predicted modulus values did match the measured ones

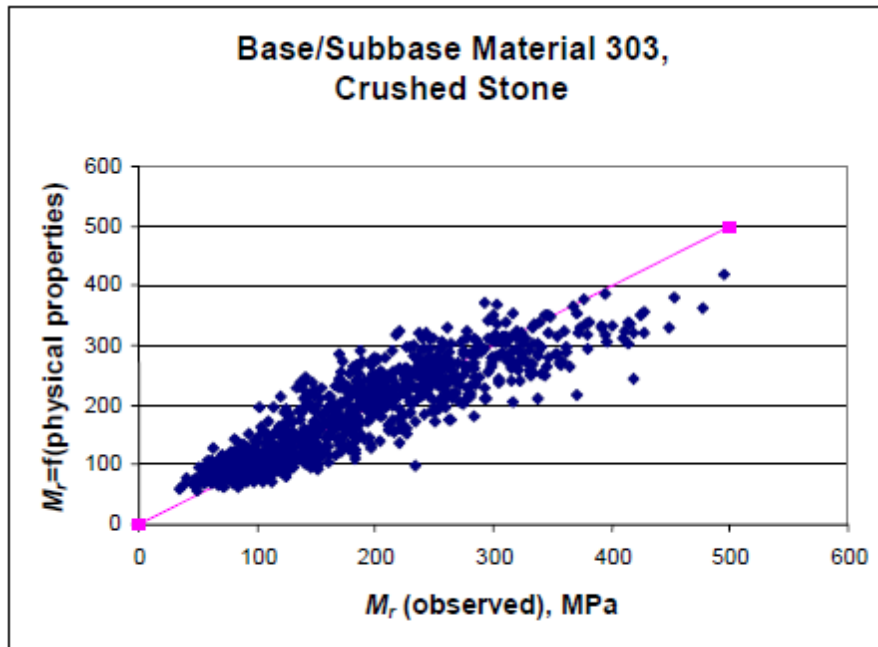


Figure 197: Match between measured and predicted M_r values for crushed stone.

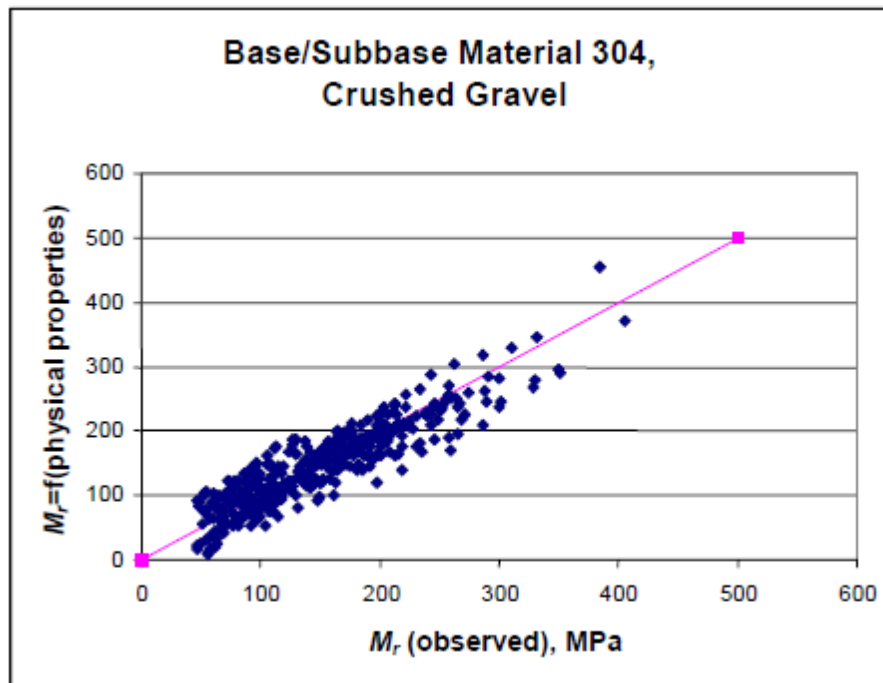


Figure 198: Match between measured and predicted M_r values for crushed gravel.

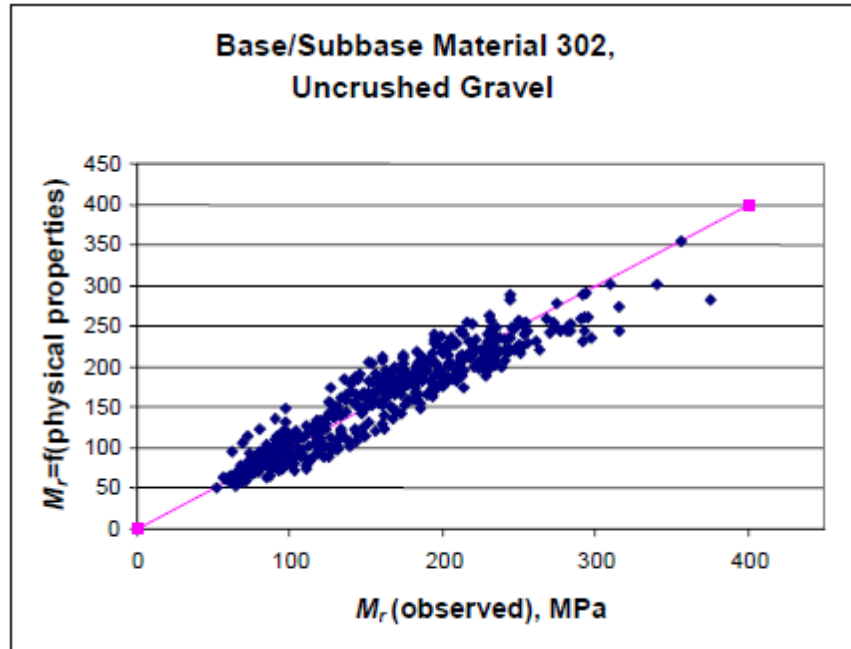


Figure 199: Match between measured and predicted M_r values for uncrushed gravel.

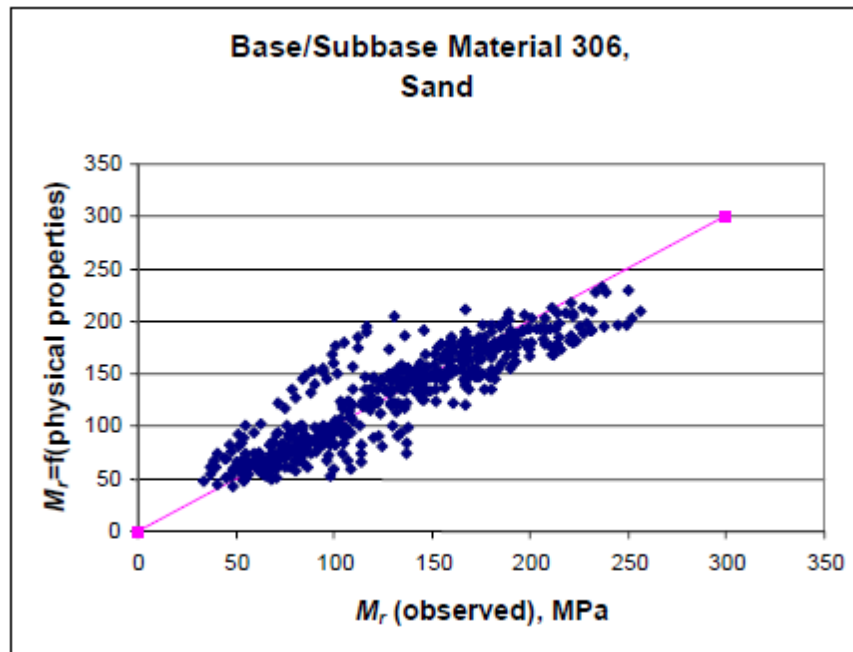


Figure 200: Match between measured and predicted M_r values for sand.

It can be concluded that the equations for the crushed and uncrushed gravel do a pretty good job in predicting the resilient modulus. Also the equation for crushed stone gives reasonable good predictions. For the sands it looks as if there an additional dataset (located above the line of equality) the modulus values of which are not too well predicted.

Although the $M_r - \theta$ is incorrect from a fundamental point of view it is still doing a fairly good job when the stresses stay well below the failure stress. For this reason it is used in many pavement design systems like e.g. KENLAYER. The question now is whether the constants of this model can be estimated with a fair degree of accuracy. For the sake of completeness we recall that this model is written as

$$M_r = k_1 \theta^{k_2}$$

Van Rutten [87] has done an analysis to determine whether relationships that allowed to predict values for k_1 and k_2 could be developed as well as relationships that could be used to estimate the cohesion and angle of internal friction. The materials involved in his analysis were:

- Crushed gravel,
- Limestone,
- Lava,
- Porphyry,
- Sand,
- Crushed masonry,
- Crushed concrete,
- Several mixtures of crushed concrete and crushed masonry.
- Silicon-manganese slag

The following relationships were developed:

$$\ln C = 3.909 + 9.602 * \ln (\text{DOC}) + 8.558 * 10^{-2} * Z_{\text{fines}}$$

Where:

C = cohesion [kPa]
 DOC = degree of compaction defined as $\rho_{\text{dry}} / \text{MPD}$
 ρ_{dry} = dry density [kg/m^3]
 MPD = maximum proctor density [kg/m^3]
 Z_{fines} = % passing the 75 μm sieve

No correlation for the angle of internal friction was developed since it appeared that in all cases this angle was approximately 40° .

$$k_1 = -357.9 + 51.8 * \ln (\text{vol density grains}) - 0.431 * D_{85} + 3.627 * 10^{-2} * C_u \text{ [MPa]}$$

Where:

$C_u = D_{60} / D_{10}$
 $\text{Vol density grains}$ = density of the grains including the pores in the particles [kg/m^3]
 D_x = sieve size through which x % is passing

$$\ln k_2 = -4.432 - 1.542 * 10^{-2} * k_1 - 7.619 * 10^{-4} * D_{(\text{PSDC-FC})} + 3.402 * 10^{-4} * C_u$$

$D_{(\text{PSDC-FC})}$ is obtained by adding up the absolute values at each of the sieve sizes of the differences in percentage passing of the particle size distribution curve (PSDC) and the Fuller curve (FC). So if the percentage passing at 2mm is 20% for the PSDC and 15% for the Fuller curve then the difference is 5%. This difference is determined for each sieve size and then the sum is taken of the absolute values of these differences.

9.3 Estimation of the resilient characteristics of Dutch sands and unbound base materials made of recycled concrete and masonry

Sands in the Netherlands are normally fine grained materials which a maximum grain size of 2 mm; they are non-plastic and provide beautiful yellow colored beaches. Extensive research on these typical Dutch sands is done by Huurman [66] and van Niekerk [67] and they showed that the dependency of the resilient modulus of **sands** to the state of stress should be described by means of the equation given below.

$$M_r = k_1 (\sigma_3 / \sigma_0)^{k_2} \cdot (1 - k_3 (\sigma_1 / \sigma_{1,f})^{k_4})$$

Where: σ_3 = confining stress [kPa],
 σ_0 = reference stress = 1 kPa,
 σ_1 = applied total vertical stress [kPa],
 $\sigma_{1,f}$ = total vertical stress at failure at the given confining stress [kPa],
 k_1 = model parameter [MPa],
 k_2 to k_4 = model parameters [-].

In their research they also developed equations to predict the values for the different constants in the M_r equation.

The parameter k_1 is determined using the following relationship.

$$k_1 = k_{11} \cdot \left(\frac{d_{50}}{1mm} \right)^{k_{12}} \cdot \left(\frac{VVS}{100\%} \right) \cdot qc^{k_{13}}$$

Where: k_{11} = model parameter = 24.616 [MPa],
 k_{12} = model parameter = -0.645 [-],
 k_{13} = model parameter = 4.01 [-],
 qc = compaction parameter which can be estimated by means of figure 201,
 VVS = angularity of the material as determined by means of the outflow test according to the Dutch standards (information on this tests is given in appendix D),
 d_{50} = sieve diameter through which 50% of the mass passes [mm].

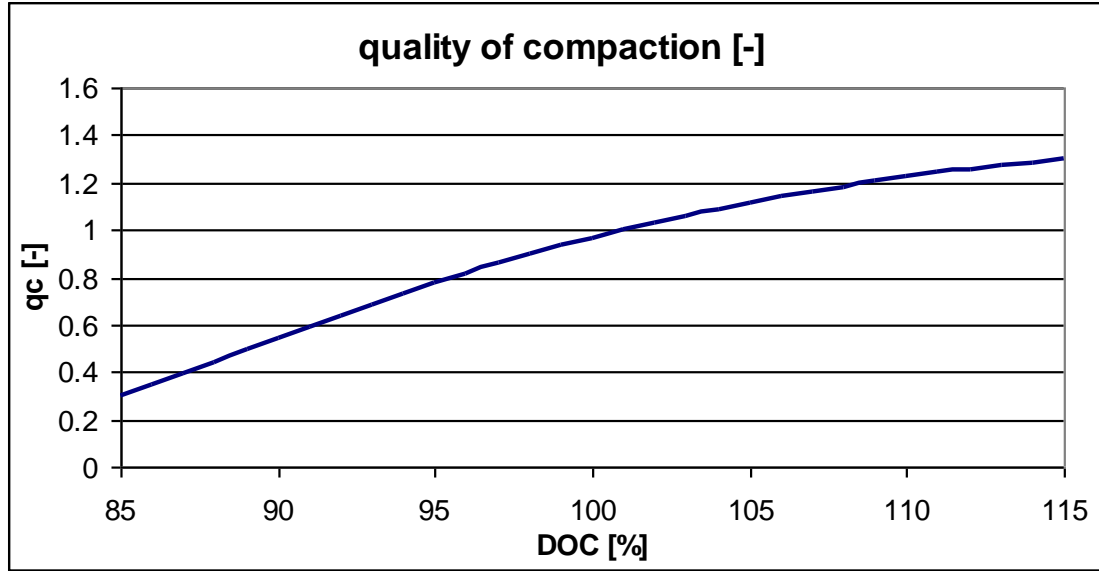


Figure 201: Chart to estimate qc

k2 is determined using the following relationship.

$$k2 = \frac{\ln\left(\frac{Mr_{1000}}{k1}\right)}{\ln(1000)} \quad \text{with} \quad Mr_{1000} = k21 + k22 \cdot \left(\frac{VVS}{100\%}\right)^{k23} Cu$$

Where: Mr_{1000} = Mr at 1000 kPa confining pressure combined with small vertical load [MPa],
 $k21$ = model parameter = 1023.25 [MPa],
 $k22$ = model parameter = 30.22 [MPa],
 $k23$ = model parameter = -8.264 [-],
 Cu = $d60 / d10$,
 $d60$ = sieve diameter through which 60% of the mass passes [mm],
 $d10$ = sieve diameter through which 10% of the mass passes [mm].

k3 is determined using:

$$k3 = k31 \cdot \left(\frac{1}{Cu}\right)^{k32}$$

Where: $k31$ = model parameter = 2.56 [-],
 $k32$ = model parameter = 0.5511 [-].

k4 is determined using the following relationship.

$$k4 = k41 \cdot \left(\frac{d50}{1mm \cdot Cu}\right)$$

Where: $k41$ = model parameter = 46.87 [-]

In the Netherlands unbound granular base and subbase courses are not made of natural materials but of mixtures of recycled crushed old concrete and crushed old masonry. Excellent work done by van Niekerk [67] has shown that unbound layers with high mechanical properties

can be made in such a way. Since environmental policies enforce recycling of old building materials as much as possible and because of the high quality that can be achieved approximately 90 – 95% of the old concrete and masonry is recycled and used in base and subbase layers. Huurman [66, 68] and van Niekerk developed also equations to predict the resilient modulus as a function of the stress conditions, the composition and the degree of compaction.

Although the stress dependency of the resilient modulus of these **coarse grained unbound base and sub-base materials** can be described by means of the same model as used for sands, the well-known $M_r - \theta$ model is used for these materials. We recall:

$$M_r = k_1 \theta^{k_2}$$

The equations for k_1 and k_2 for **unbound base materials** are given below. The degree of compaction and gradation have a large influence on the k_1 value while k_2 strongly depends on k_1 .

$$k_1 = \frac{k_{11}}{qg} \cdot qc^{k_{12}} \cdot qp^{k_{13}}$$

$$k_2 = \frac{\ln\left(\frac{Mr_{5000}}{k_1}\right)}{\ln(5000)}$$

$$Mr_{5000} = k_{21} \cdot qc^{k_{22}}$$

Where: k_{11} = 34.1855 [MPa],
 k_{12} = 1.8183 [-],
 k_{13} = 1.6502 [-],
 k_{21} = 1016.275 [MPa],
 k_{22} = 1.5568 [-],
 qc = compaction parameter as described before,
 qp = composition parameter = $(0.4 \cdot \text{mass percentage masonry} + \text{mass \% concrete}) / 100$.

Figure 202 shows how the predicted modulus values match with the measured ones.

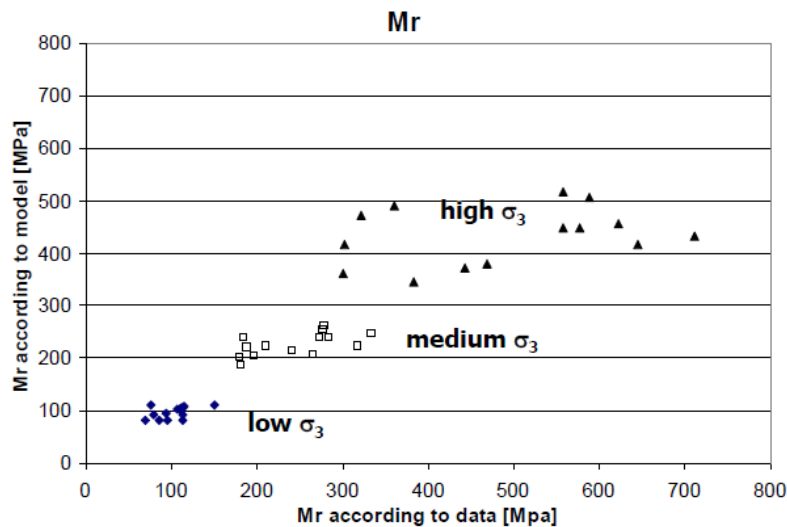


Figure 200: Measured and predicted resilient modulus values.

When the parameters that characterize the stress dependent nature of granular materials have been quantified, the modulus of the granular (and the variation therein over the height and width of the layer) can be determined by means of an iterative procedure; this will be discussed in detail later on in the lecture notes.

Stress dependency implies that the stiffness modulus of unbound granular materials varies over the height and width of the granular layer. It is clear that this cannot be analyzed by means of programs like BISAR since such programs assume the layer stiffness to be constant in the horizontal direction. A much better approach of course is using a finite element program which allows stress dependency to be modeled in the vertical and horizontal direction.

In spite of all this linear elastic multi-layer systems are still very popular to be used for pavement analyses purposes because they are so easy to use. In such a case the only solution for taking into account the stress dependent nature of pavement layers is to divide the unbound base and subbase into a number of sublayers and determine the stress dependent stiffness modulus by means of an iterative procedure. This means however that the modulus of the granular layers only varies over the depth and not over the width of the layer. When dividing the granular layers into sublayers one has to take into account the fact that the minimum sublayer thickness is about 2.5 – 3 times the maximum grainsize of the granular material. This implies that with a maximum grainsize of 35 mm, the minimum sublayer thickness is around 80 – 100 mm.

Such a procedure, dividing granular layers into sublayers is adopted in the program KENLAYER [70] which is linear elastic multilayer program allowing the modulus of granular layers and soils to be stress dependent. The question however is to what extent an approach as used in KENLAYER is still capable of giving realistic results. An investigation on this was done by Opiyo [71] using the finite element code NOLIP developed by Huurman [66].

He analyzed two pavement structures, one with a 30 mm thick asphalt top layer and one with a 100 mm thick asphalt top layer. In both cases the stiffness modulus of the asphalt was 3000 MPa. The unbound laterite base course had a thickness of 200 mm while the unbound laterite subbase had a thickness of 250 mm. The stress dependency of the stiffness modulus of both laterites was determined in the laboratory by means of repeated load triaxial tests. In order to be able to take the stress dependent nature of the base and subbase into account, Opiyo divided the base into two sublayers with a thickness of 100 mm each. The subbase was divided into two layers as well; the thickness of the top subbase layer was 100 mm and the thickness of the bottom subbase layer was 150 mm. The stiffness of the subgrade was assumed to be 80 MPa. Some results of this work are shown in figures 203, 204 and 205.

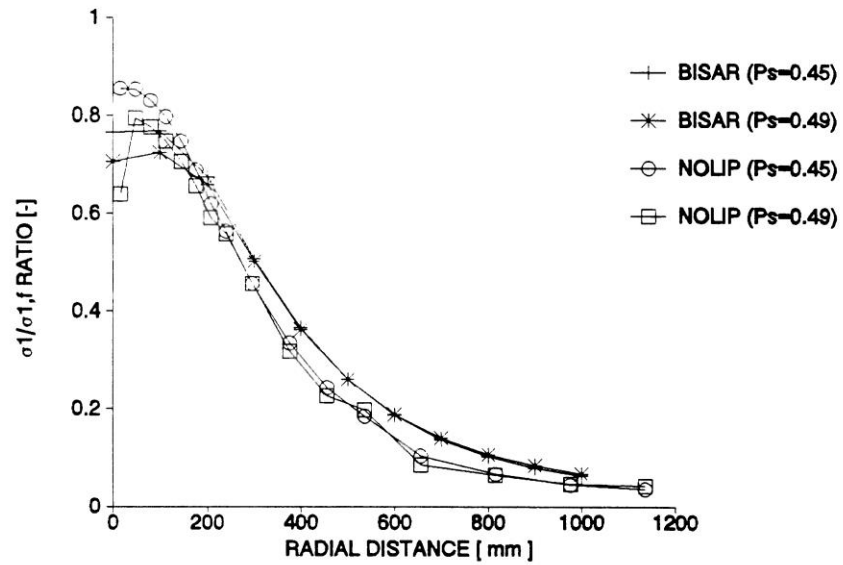


Figure 203: Variation of the failure ratio in the top of the base course for the 100 mm asphalt pavement at a depth of 137.5 mm from the pavement surface.
Note: Ps = Poisson's ratio.

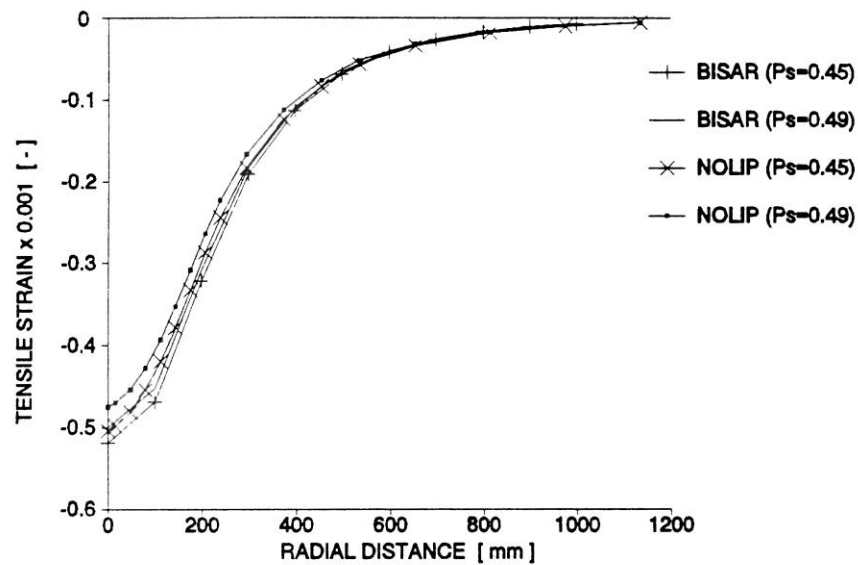


Figure 204: Tensile strains at the bottom of the 100 mm thick asphalt layer.

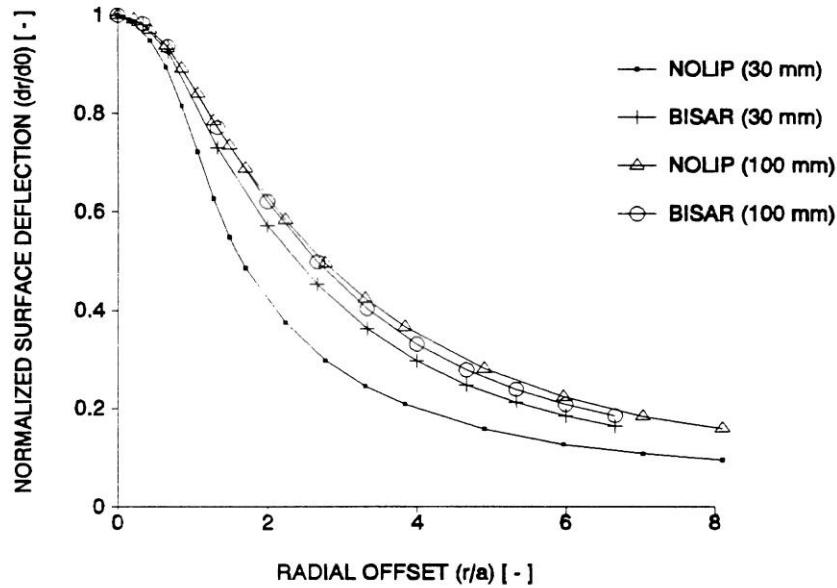


Figure 205: Normalized surface deflections for both pavements.

From these figures one can conclude that the influence of using BISAR, in combination with subdividing the base and subbase into sublayers and assigning the modulus of these layers in a stress dependent way, on the calculated stresses, deflections and tensile strains is only marginal when the results are compared with the results obtained with the finite element program NOLIP in which the modulus of the granular layers was varying in both the vertical and horizontal direction. However this was only true for the 100 mm asphalt pavement. Significant differences and even unrealistic results were obtained when using BISAR for the 30 mm asphalt pavement. The conclusion therefore is that the stress dependent behavior of granular materials can be successfully simulated using a linear elastic multilayer program like BISAR and subdividing the base and subbase layer, provided that the top asphalt layer is not too thin. It is estimated that realistic results will already be obtained when the asphalt thickness is 70 mm.

When taking into account the stress dependent nature of unbound granular materials one should not forget to take into account the stresses due to the dead weight of the material. The vertical dead weight stresses can simply be calculated following:

$$\sigma_{v,dw} = \gamma * z$$

Where: $\sigma_{v,dw}$ = vertical stress due to the dead weight of the material,
 γ = volume weight of the material,
 z = depth below the surface.

In principle, the horizontal dead weight stresses are not equal to the vertical stresses as is the case in fluids. We can write:

$$\sigma_{h,dw} = K * \sigma_{v,dw}$$

Where: $\sigma_{h,dw}$ = horizontal stress due to the dead weight of the material,
 K = constant depending on a large number of factors.

The constant K depends a.o. on the degree of compaction, the tendency of the aggregate skeleton to dilate when loaded, the angle of internal friction. The effect of compaction can be compared with the development of passive earth pressure behind/in front of retaining walls. We know from soil mechanics principles that for cohesion-less soils the active soil pressure constant K_a can be calculated using:

$$K_a = (1 - \sin \phi) / (1 + \sin \phi)$$

While the passive soil pressure constant K_p can be calculated with:

$$K_p = (1 + \sin \phi) / (1 - \sin \phi) \text{ where } \phi \text{ is the angle of internal friction.}$$

K can easily take a value of 2, but because very little information can be found on compaction affects the value of K , a value of 1 is recommended for design purposes.

Figure 206 shows an example of how the horizontal earth pressure ($\sigma_h = K \sigma_v$) can develop behind a retaining wall as a result of compaction.

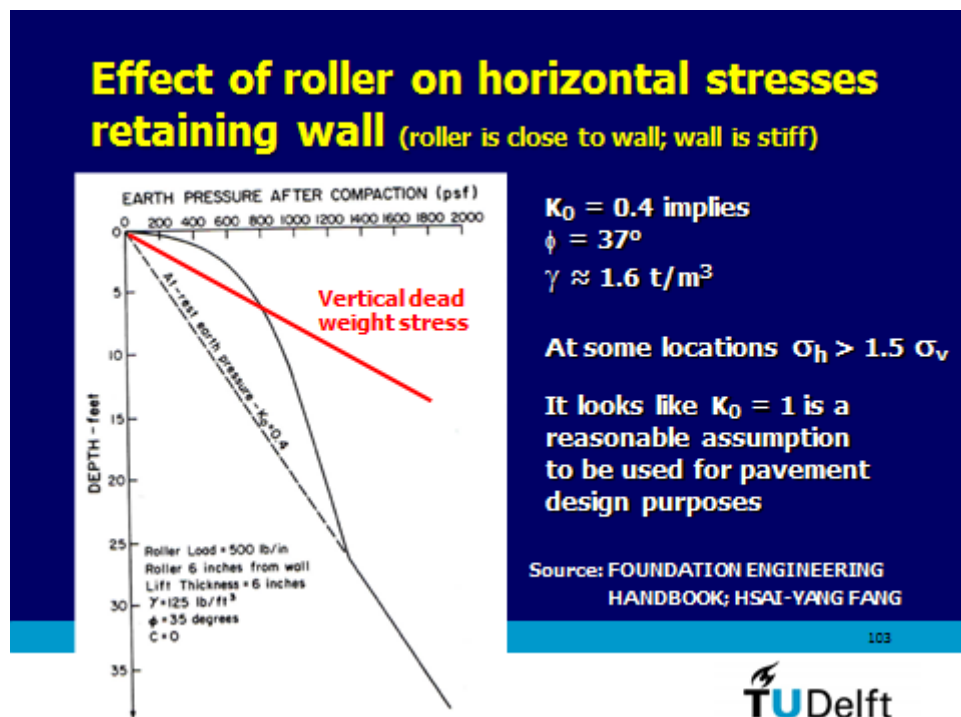


Figure 206: Development of horizontal stresses behind an earth retaining wall as a result of compaction.

9.4 Estimating the stiffness by means of graphs and tables

The procedure which was described in the previous paragraph on how to estimate the stress dependent parameters and to determine the stiffness modulus of the granular layers by means of an iterative procedure is quite often considered to be a cumbersome one. Therefore procedures have been developed to make fair estimates of the stiffness values and tables have been set up to give the designer some guidance about the stiffness values to select. An example of such a table is table 36 [69].

When using the values mentioned in table 36 one should be aware of the specifications which are applicable for these materials; these are given in table 37. Special attention is called for the high compaction levels that are required and achieved in South Africa; they might be very difficult to achieve when different materials are used under different climatic conditions.

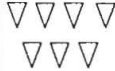
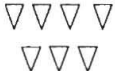

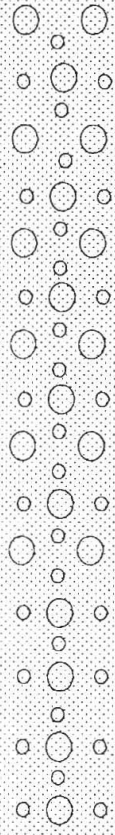
Material code	Material description	Over cemented layer in slab state	Over granular layer or equivalent	Wet condition (good support)	Wet condition (poor support)
G1	High quality crushed stone	250 – 1000 (450)	150 – 600 (300)	50 – 250	40 – 200
G2	Crushed stone	200 – 800 (400)	100 – 400 (250)	50 – 200	40 – 200
G3	Crushed stone	200 – 800 (350)	100 – 350 (230)	50 -150	40 – 200
G4	Natural gravel (base quality)	100 – 600 (300)	75 – 350 (225)	50 – 150	30 – 200
G5	Natural gravel	50 – 400 (250)	40 – 300 (200)	30 – 200	20 – 150
G6	Natural gravel (sub-base quality)	50 – 200 (150)	30 – 200 (120)	20 – 150	20 – 150

Table 36: Stiffness values for granular bases and sub-bases as recommended in South Africa.

It should be noted that the grading modulus GM which is mentioned in table 37 is calculated as:

$$GM = \{300 - [P_{2mm} + P_{0.425mm} + P_{0.075mm}]\} / 100$$

Cynical readers might state that table 36 is not very helpful for selecting modulus values for design purposes since the range that is given for the different materials at different conditions is rather wide. In spite of its cynicism the comment is right; one needs to be an experienced engineer to pick an appropriate value for design purposes. In any case table 36 shows that there is no such thing as THE stiffness modulus of e.g. a G3 material.

SYMBOL	CODE	MATERIAL	ABBREVIATED SPECIFICATIONS
	G1	Graded crushed stone	Dense - graded unweathered crushed stone; Maximum size 37,5 mm; 86 - 88 % apparent relative density; Soil fines PI < 4
	G2	Graded crushed stone	Dense - graded crushed stone; Maximum size 37,5 mm; 100 - 102 % Mod. AASHTO or 85 % bulk relative density; Soil fines PI < 6
	G3	Graded crushed stone	Dense - graded stone and soil binder; Maximum size 37,5 mm; 98 - 100 % Mod. AASHTO ; Soil fines PI < 6
	G4	Crushed or natural gravel	Minimum CBR = 80 % @ 98 % Mod. AASHTO; Maximum size 37,5 mm; 98 - 100 % Mod. AASHTO; PI < 6; Maximum Swell 0,2 % @ 100 % Mod. AASHTO. For calcrete PI ≤ 8
	G5	Natural gravel	Minimum CBR = 45 % @ 95 % Mod. AASHTO; Maximum size 63 mm or 2/3 of layer thickness; Density as per prescribed layer usage; PI < 10; Maximum swell 0,5 % @ 100 % Mod. AASHTO. *
	G6	Natural gravel	Minimum CBR = 25 % @ 95 % Mod. AASHTO; Maximum size 63 mm or 2/3 of layer thickness; Density as per prescribed layer usage; PI < 12; Maximum swell 1,0 % @ 100 % Mod. AASHTO. *
	G7	Gravel / Soil	Minimum CBR = 15 % @ 93 % Mod. AASHTO; Maximum size 2/3 of layer thickness; Density as per prescribed layer usage; PI < 12 or 3GM** + 10; Maximum swell 1,5 % @ 100 % Mod. AASHTO. ***
	G8	Gravel / Soil	Minimum CBR = 10 % @ 93 % Mod. AASHTO; Maximum size 2/3 of layer thickness; Density as per prescribed layer usage; PI < 12 or 3GM** + 10; Maximum swell 1,5 % @ 100 % Mod. AASHTO. ***
	G9	Gravel / Soil	Minimum CBR = 7 % @ 93 % Mod. AASHTO; Maximum size 2/3 of layer thickness; Density as per prescribed layer usage; PI < 12 or 3GM** + 10; Maximum swell 1,5 % @ 100 % Mod. AASHTO. ***
	G10	Gravel / Soil	Minimum CBR = 3 % @ 93 % Mod. AASHTO; Maximum size 2/3 of layer thickness; Density as per prescribed layer usage;

* For calcrete PI ≤ 15 on condition that the Linear Shrinkage (LS) does not exceed 6 %.

** GM = Grading Modulus (TRH14, 1985) =
$$\frac{300 - [p_{2,00mm} + p_{0,425mm} + p_{0,075mm}]}{100}$$
 where $p_{2,00}$ etc., denote the percentage passing through the sieve size .

*** For calcrete PI ≤ 17 on condition that the Linear Shrinkage (LS) does not exceed 7 %.

Table 37: Specifications for granular materials in South Africa.

A graphical procedure is available for the estimation of the stiffness modulus of the base and sub-base material by Barker e.a. [72] which is presented in figure 207.

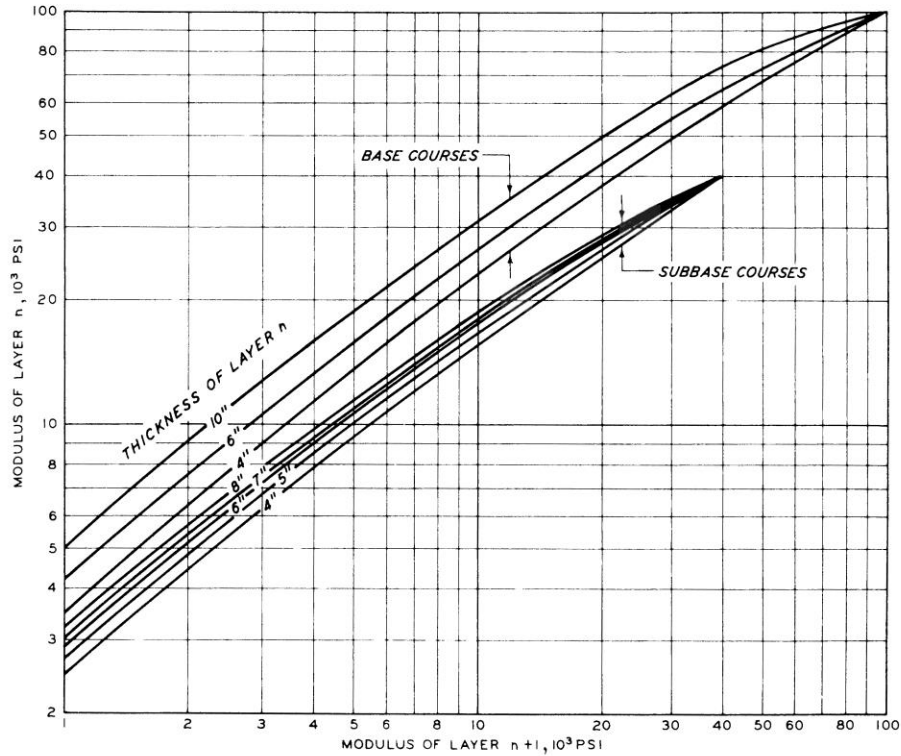


Figure 207: Relationship between modulus of layer n and modulus of layer n + 1 for various thicknesses of unbound base and subbase layers.

Please note that in figure 207, the maximum value for the stiffness modulus of the subbase layer is set at 40,000 psi (280 MPa), while the maximum stiffness for the base layer is set at 100,000 psi (700 MPa). The use of the chart will be illustrated by means of an example. Let us assume that the stiffness modulus of the subgrade equals 4,000 psi. If we place an 8 inch subbase on top of the subgrade, the stiffness of that subbase will be 10,000 psi (enter the horizontal axis at 4,000 psi and determine the subbase stiffness at the point where the vertical line through the 4,000 value crosses the 8 inch subbase line). To know the stiffness of a 6 inch base placed on top of the subbase, we have to enter 10,000 on the horizontal axis and determine where the vertical line through the 10,000 value crosses the 6 inch base line. In this way we determine that the base stiffness equals 27,000 psi.

Barker e.a. [72] also presented the equations which are the background for figure 207. For the sake of completeness they are given here as well because they show that some assumptions had to be made to derive figure 207.

$$E_n = E_{n+1} (R + S \log t - T \log t \log E_{n+1} + W \log E_{n+1})$$

Where: E_n = stiffness modulus of the upper layer [psi],
 E_{n+1} = stiffness modulus of the lower layer [psi],
 $R = a - X \log b + \{(a - 1) / Y\} \log c$,
 $S = X + T \log c$,
 $T = X / Y$,
 $X = (a - 1) / \log (b / e)$,
 $Y = \log (d / e)$
 $W = T \log b - (a - 1) / Y$

- t = thickness of the upper layer [inch],
- a = ratio E_n / E_{n+1} for a layer with thickness b over a material having modulus of c, this means one have to set a certain thickness b (e.g. 4" or 6" for which a certain modulus ration (e.g. 1.5 or 2) is obtained,
- d = maximum limiting modulus value for the particular material,
- e = layer thickness [inch] for which the modulus ratio equals 1.

Summarizing it means that assumptions have to be made for the parameters a, b, d and e. Furthermore the stiffness modulus of the lower layer (c) should be known.

In case of figure 207, Barker e.a. assumed the following values:

For the subbase course: a = 2, b = 6", d = 40,000 psi, e = 1".

For the base course: a = 3, b = 6", d = 100,000 psi, e = 1".

One could argue whether or not the selected a values are a bit on the high side (this author would have used a = 1.5) and whether the selected e values are a bit on the low side (this author would have selected e = 2" since it is impossible that a thin layer produces any appreciable stiffness).

A very simple relationship to estimate the stiffness modulus of the base course has been developed by Shell [29]. This relationship is written as:

$$E_b = k * E_{sg}$$

Where: E_b = stiffness modulus of the base course [MPa],
 E_{sg} = stiffness modulus of the subgrade [MPa] ,
 $k = 0.2 * h_b^{0.45}$, $2 \leq k \leq 4$,
 h = thickness of the base course [mm].

The question now is to what extend realistic stiffness modulus values are predicted using e.g. the Shell equation. In order to determine this, a comparison was made between the base layer stiffness as estimated by means of the Shell equation and the stiffness as estimated by means of an analysis in which the stress dependency of the base material was taken into account. Figure 208 [73] shows the variation of the stiffness modulus of a base course of different thicknesses when placed on subgrades with different stiffness values. KENLAYER was used for the analysis.

One can easily derive from figure 208 that for this particular case, the Shell equation produces a stiffness value for the base course which seems to be on the safe side. For a 200 mm thick base course k equals 2.17 giving the base course a stiffness of 217 MPa if the subgrade stiffness is 100 MPa. According figure 208, the mean stiffness would be approximately 275 MPa. For a 400 mm thick base course k equals 2.96 giving the base course a stiffness of 148 MPa if the subgrade stiffness is 50 MPa. According to figure 208 the mean base stiffness would be approximately 225 MPa. It is recalled once more that the observations made here are only valid for the material under consideration. If weaker materials are used which are compacted to a lesser degree of compaction, the Shell rule might very well over-predict the value of the stiffness modulus of the base course.

9.5 Resilient modulus of granular layers determined with the repeated load CBR test

The results reported in section 9.3 were determined by means of a large scale triaxial cell (diameter 300 mm, height 600 mm) which is available at the Delft University of Technology [67, 68]. Such a large cell is needed to fulfill all the requirements with respect to the size of the

aggregate particles and diameter of the cell and the diameter to height requirements. This large triaxial cell is shown in figure 209; it is clear that because of its complexity and size this type of equipment is not feasible to be used in e.g. consultancy projects. The complexity is not only because of the testing device but also because of the large size compaction equipment that is needed (figure 210). All this makes that only a few of these large scale cells are available in the world.

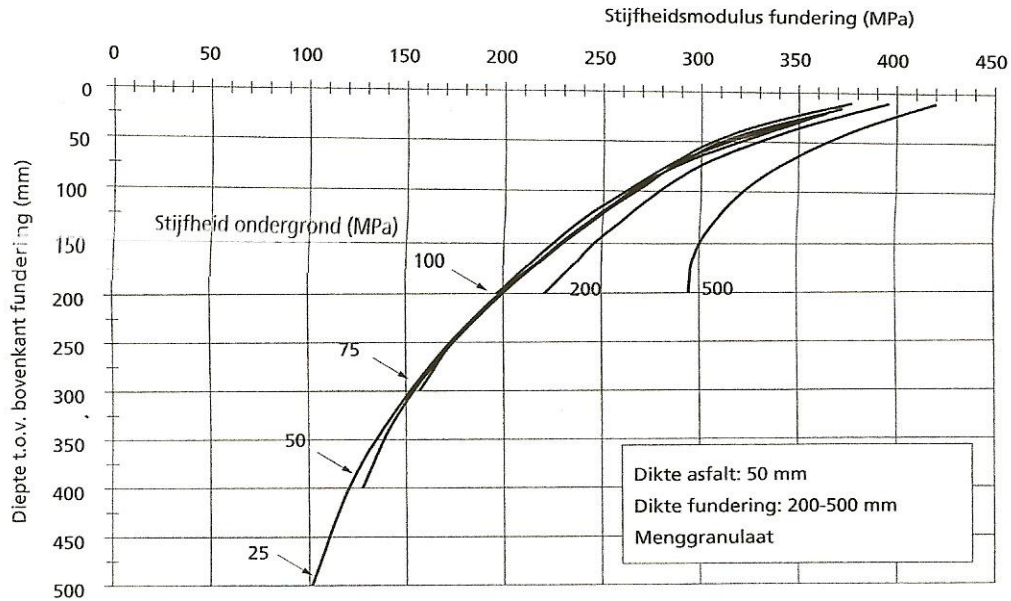


Figure 208: Variation of the stiffness modulus over the thickness of a granular base course.
Note: Vertical axis gives depth below pavement surface [mm]; horizontal axis gives stiffness modulus of the base [MPa]; Stijfheid ondergrond = subgrade stiffness; fundering = base; menggranulaat = mixture of crushed concrete and crushed masonry.

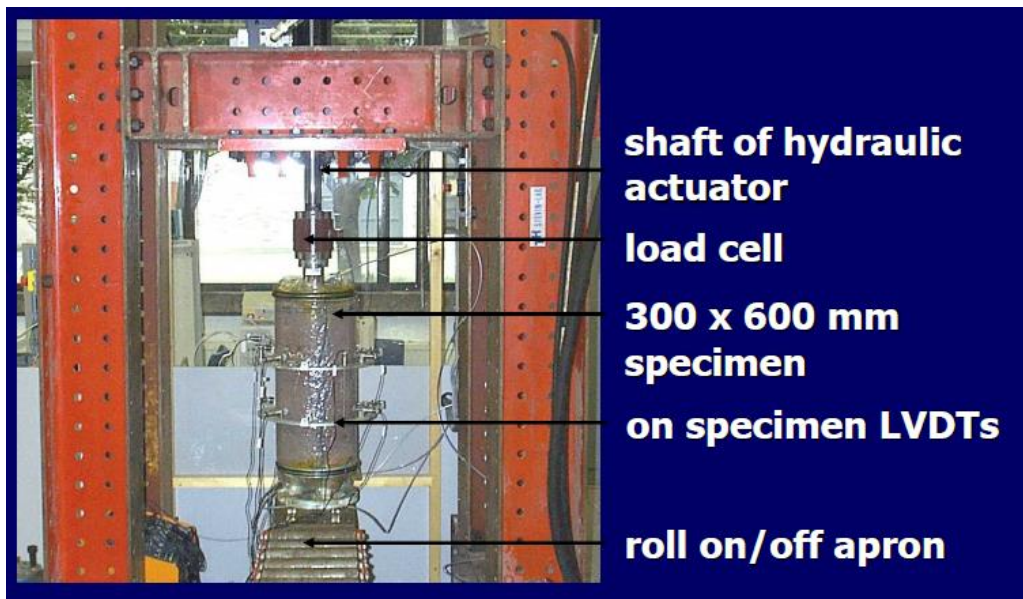


Figure 209: Large scale triaxial cell as in use at the Delft University of Technology.

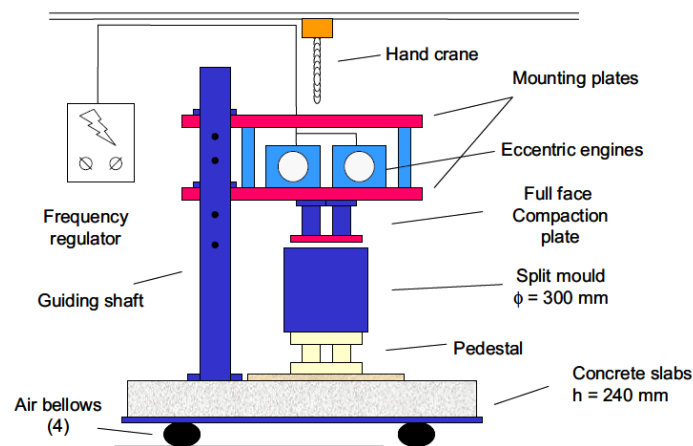


Figure 210: Delft University compaction device for preparing the ϕ 300 mm, h = 600 mm triaxial specimens.

Because large triaxial cell is not feasible for day to day practice, extensive research has been done at the Delft University to replace this test by a more practical test which allows full gradations to be tested. This has resulted in the development of the repeated load CBR test. This device is shown in figure 211 [74].



Figure 211: Repeated load CBR test setup for coarse grained granular materials (left) and test mold (right).

As one can see in figure 211, both the size of the mold as well the size of the plunger are much bigger than those of the normal CBR test. The diameter of the standard mold is 152.4 mm while for the large mold it is 250 mm. The diameter of the plunger in the standard CBR test is 49.64 mm while it is 81.5 mm for the plunger use in the repeated load CBR test. It is recalled that the large mold is needed to test full gradations of base course material which have a maximum grain size up to 45 mm.

Figure 212 [74] shows the differences in size of the aggregate particles and the stress conditions in the large triaxial cell, the large CBR mold and the standard CBR mold.

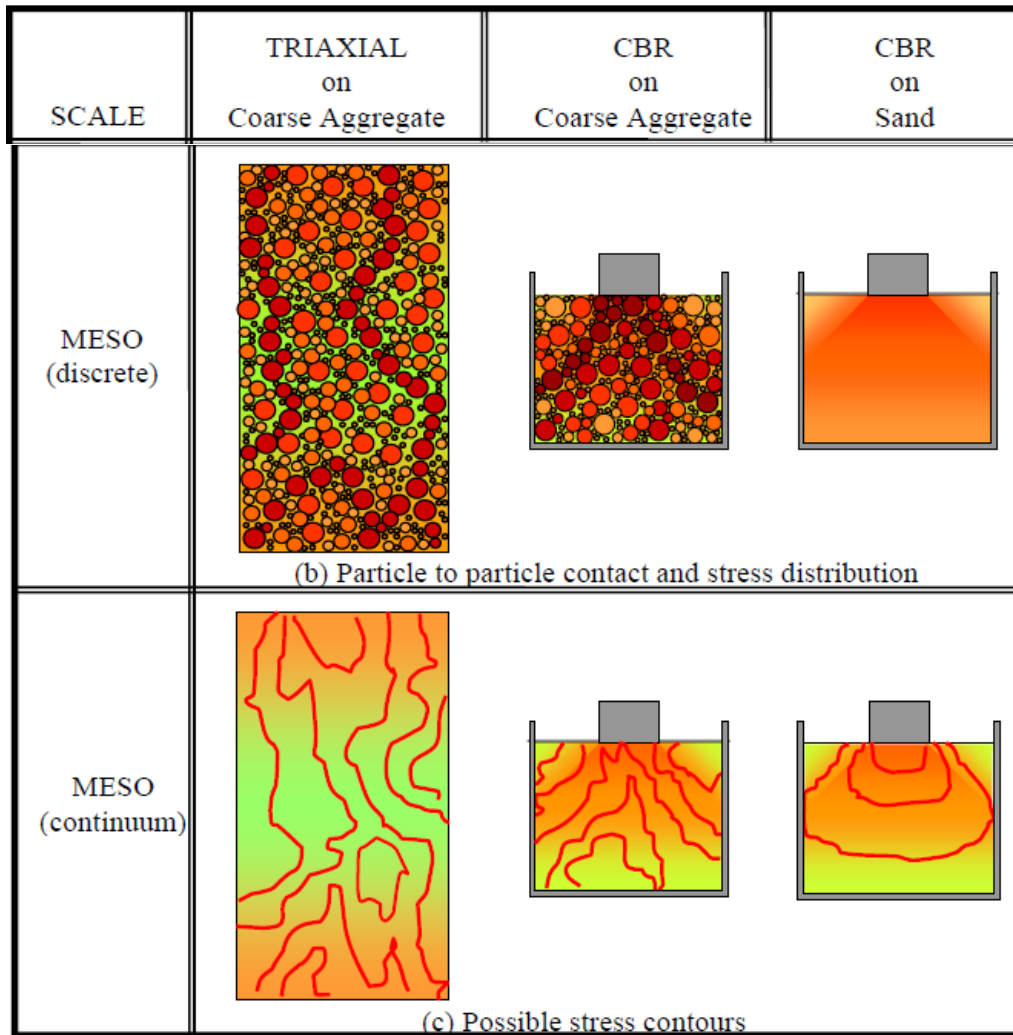


Figure 212: Particle to particle contact and stress conditions in the large triaxial, large CBR and standard CBR test.

Figure 213 shows the loading sequence of the repeated load CBR test.

As one will have observed in figure 211, quite a large, stiff testing frame and a loading piston with sufficient capacity is needed for doing the test; the normal CBR setup cannot be used. So although the repeated load CBR test with the large mold is much simpler than the large scale triaxial test, it is certainly not as simple as the standard CBR test in which the small mold is used. During the test steel rings with a total weight of 16 kg are placed on top of the granular material representing the weight of 80 mm of asphalt concrete. As is the case with the normal CBR test the load is applied directly on the granular material through a circular opening in the steel discs.

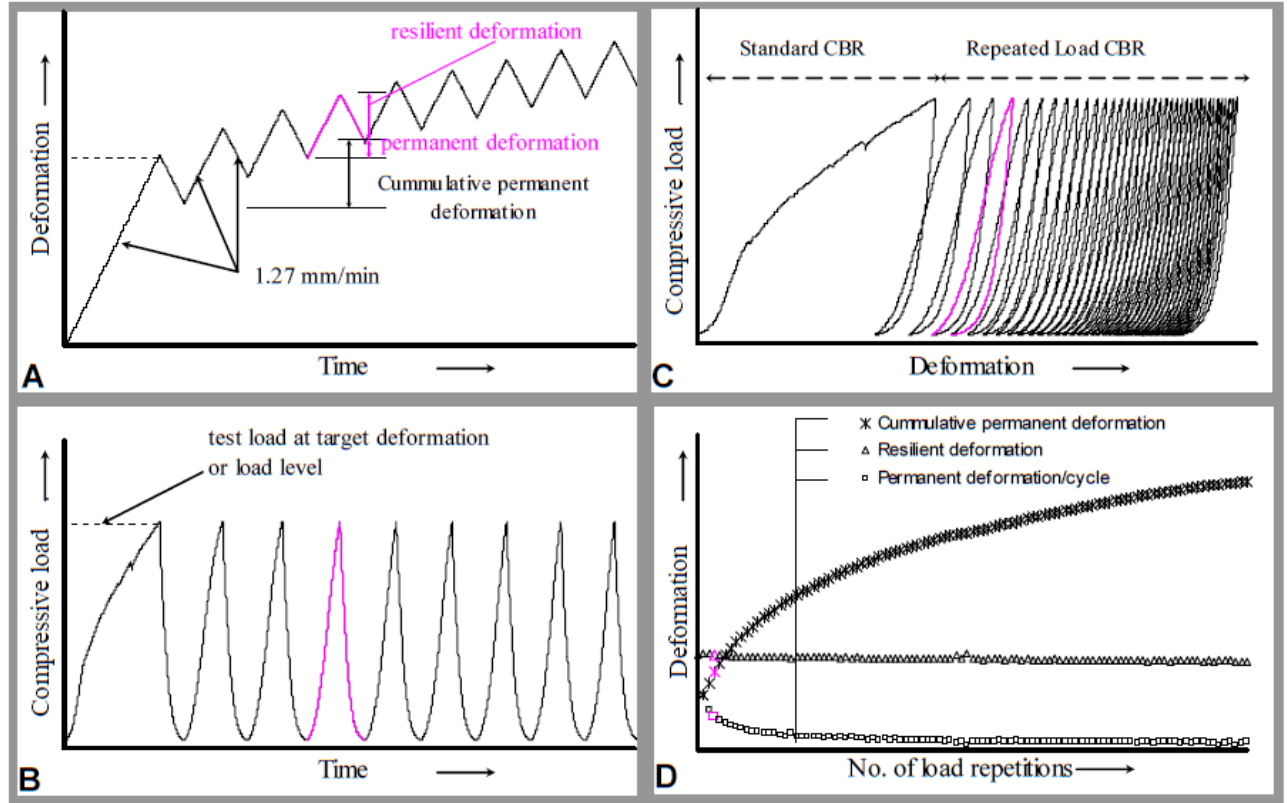


Figure 213: Test sequence in a repeated load CBR test.

Based on finite element analyses by using ABAQUS, Alemgena [74] was able to develop a relationship between the equivalent resilient modulus of the sample (E_{equ}) and the stress and displacement under the plunger. This relationship is:

$$E_{\text{equ}} = 1.513 * (1 - \mu^{1.104}) * \Delta\sigma_p * r / \Delta u^{1.012}$$

Where:

E_{equ} = equivalent modulus of the sample [MPa]

μ = Poisson's ratio (to be estimated / assumed)

$\Delta\sigma_p$ = difference in maximum and minimum plunger stress in a loading cycle [MPa]

r = radius of the plunger [mm]

Δu = difference between max. and min. elastic displacement in a loading cycle [mm]

Figure 214 shows, as an example, the relation that was obtained for a particular granular material between E_{equ} and the plunger stress. As one will observe this relation looks very much alike the $M_r - \theta$ relationships that are obtained with triaxial tests.

As one will observe from figure 214, moisture content and degree of compaction don't seem to have a large effect on the relationship between plunger stress and E_{equ} . Degree of compaction and moisture content do however have a significant influence on the resistance to permanent deformation. This is shown in figure 215.

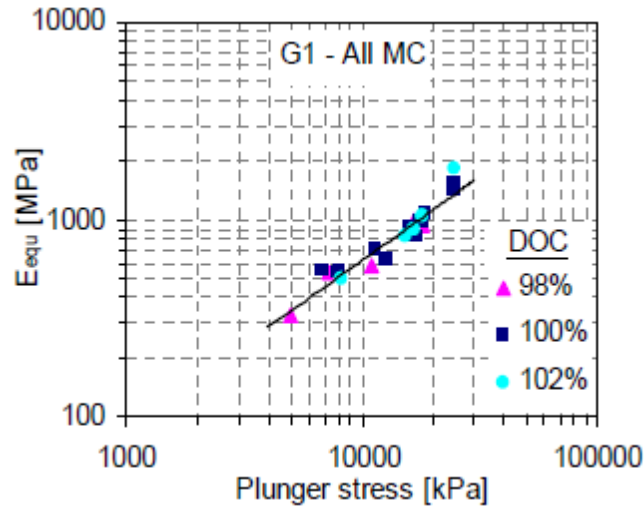


Figure 214: Relation between plunger stress and E_{equ} for a G1 (South African) base course material.

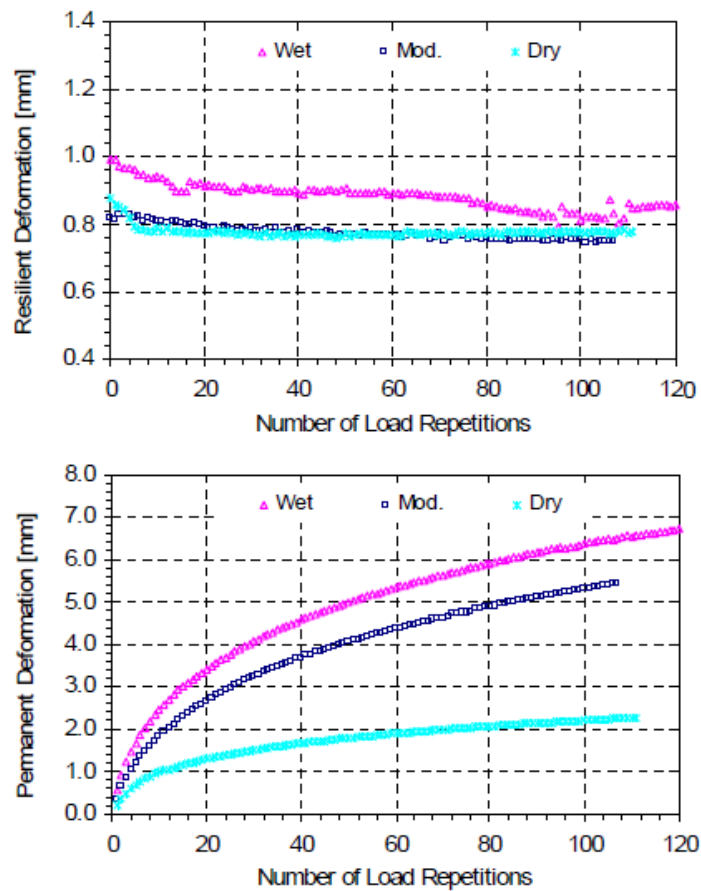


Figure 215: Effect of moisture content on the resilient and permanent deformation behavior of a G1 material at 100% degree of compaction and a plunger stress of 16 MPa. Wet = 6% moisture, mod = 4% moisture, dry = 2% moisture.

Figure 216 shows the difference between test results obtained with the large size triaxial test and the large size CBR test. The reason for these differences is the large difference in stress conditions in both test and because of the high confinement stress in the CBR test. Given the nature of the repeated load CBR test, E_{equ} should be taken as a specimen property.

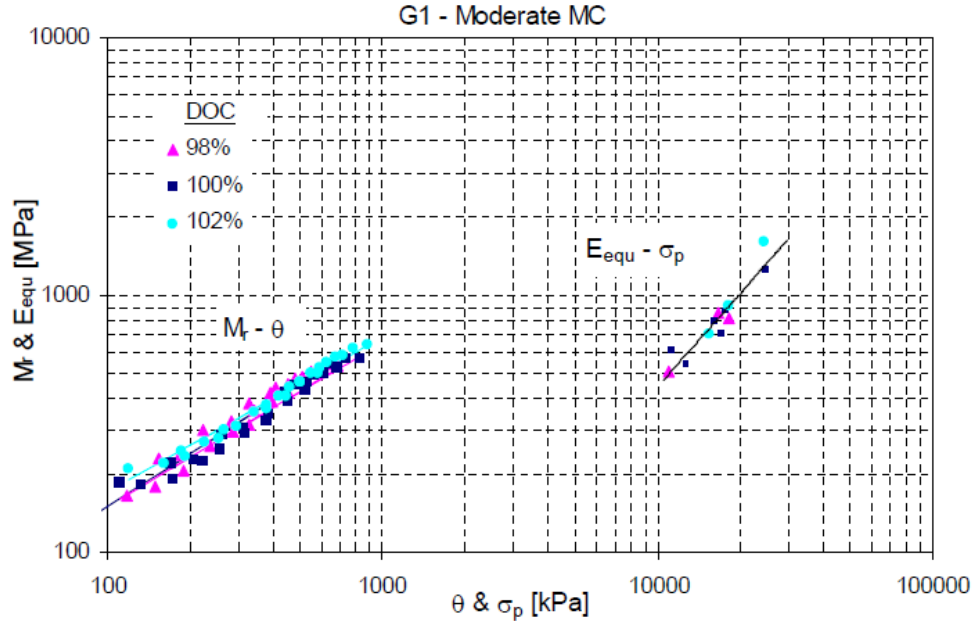


Figure 216: Difference in results obtained with the triaxial and CBR test.

Figure 217 shows that the stress and strain conditions in the CBR test are very inhomogeneous and nothing like those in the middle third part of the triaxial sample (over which the displacements are measured); in that part of the triaxial sample both the vertical and horizontal stress take a constant value. This inhomogeneity in stress conditions in the CBR test explains why the test results obtained with this test are specimen and not material properties.

Alemgena [74] also developed a procedure which allows to determine at which plunger stress E_{equ} values will be obtained which are the same as those which would be obtained with the repeated load large triaxial test. The procedure is as follows: as a first step we divide the granular layers in the pavement into sublayers and assign a modulus to each of the sublayers. Then we calculate the stresses in each sublayer and calculate the value for θ . The next step is to perform repeated load CBR tests to determine the relationship between the plunger stress and the E_{eq} . Since we have calculated θ , we can determine a corrected plunger stress using the equation given below.

$$\log(\sigma_{cp}) = a_1 + a_2 S + a_3 e + a_4 \log \theta$$

Where:

- σ_{cp} = corrected plunger stress [MPa],
- S = degree of saturation [%],
- e = void ratio [%/100],
- θ = $\sigma_1 + \sigma_2 + \sigma_3$ [kPa].

The plunger stress vs E_{eq} relationship provides us with new moduli value for each of the granular sublayers. Then the stresses in the granular sublayers are calculated again and new value for θ are determined. This in turn provides a new values for σ_{cp} , and new values for E_{eq} . The iteration

is completed when the “new” modulus differs less than 2 - 5% from the previous one. Of course values for “S” and “e” should be determined as well.

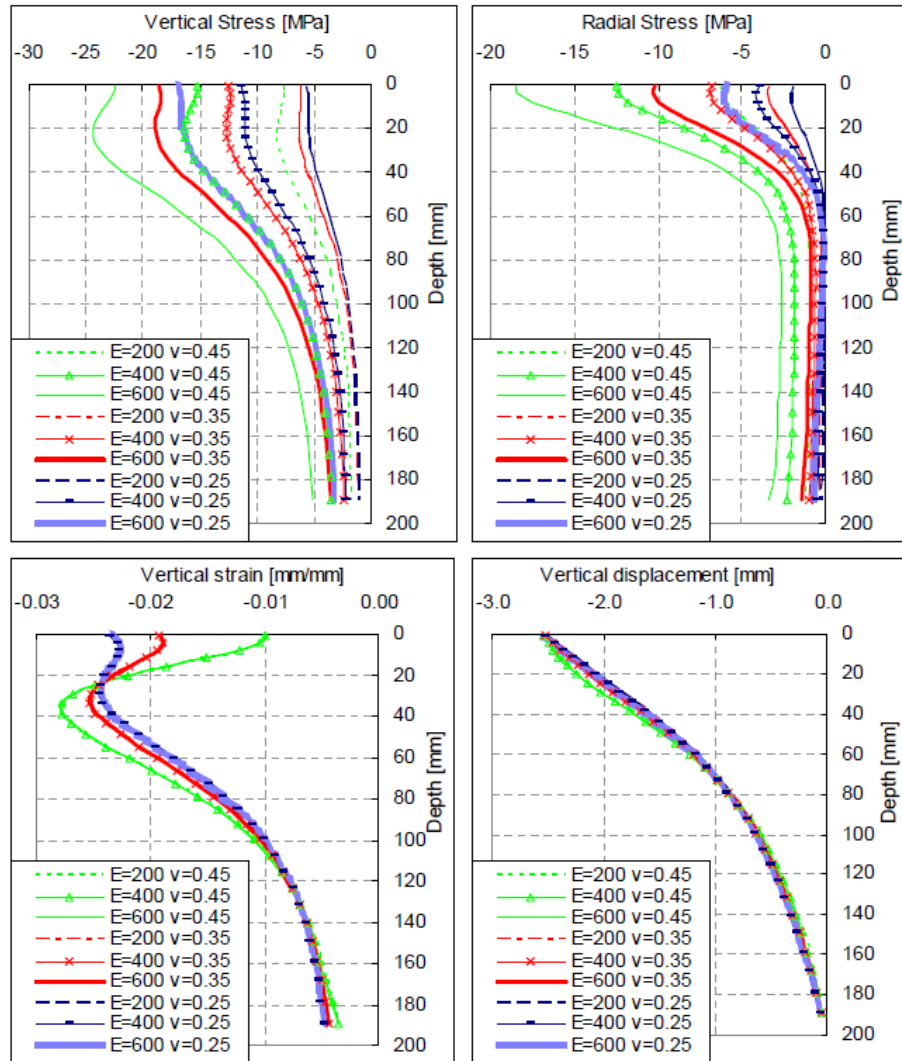


Figure 217: Stresses, strains and displacements in a CBR test as function of the modulus and Poisson ratio of the tested material.

Table 38 gives the values for the various constants, while figure 218 shows the predictive capability of the equation.

Material	a ₁	a ₂	a ₃	a ₄	R ²
G1	-1.069	0.072	1.030	0.641	0.96
FC	1.504	1.860	2.150	0.375	0.71
WB	-0.241	0.025	-1.101	0.469	0.63
all	0.164	-0.668	-1.317	0.479	0.68

Table 38: Values for the various constants. G1 = a South African base course material, FC = ferricrete from South Africa, WB = weathered basalt from Ethiopia.

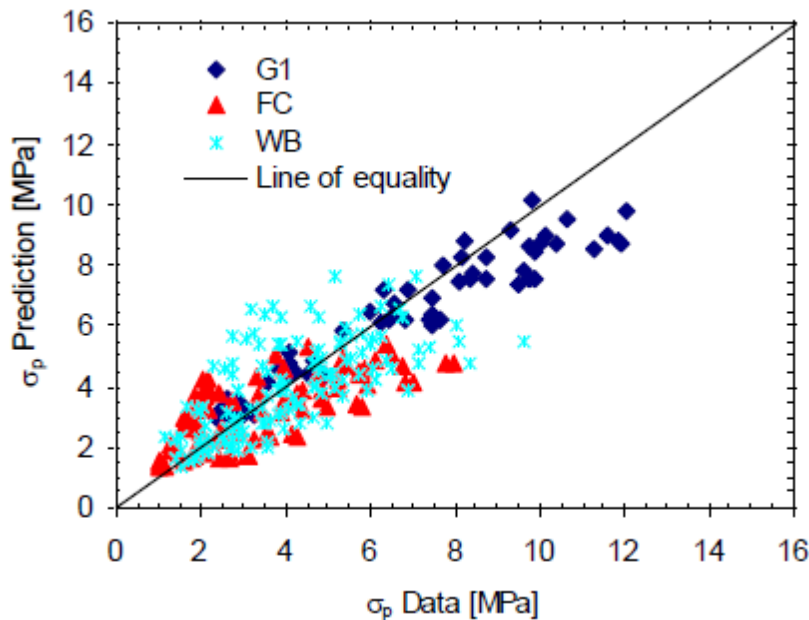


Figure 218: Fit between actual and predicted plunger stresses.

Although the repeated load large scale CBR test is not a perfect test, it fills the (huge) gap that exists between the fundamentally correct large scale triaxial test and estimating/"guessing" resilient parameters by means of empirical relations. It allows to determine in a fairly simple way the effect of gradation, moisture content and compaction on the resilient and permanent deformation characteristics of granular materials.

9.6 Estimation of the failure characteristics of unbound materials

In order to prevent that excessive deformations occur in a granular base or subbase, the stresses in these layers should be well below the stresses at which shear failure occurs. We recall that the vertical stress at which shear failure occurs in a granular material depends on the amount of confinement as well as the cohesion and angle of internal friction of the material considered. We can write:

$$\sigma_{1,f} = [(1 + \sin \varphi) \cdot \sigma_3 + 2c \cdot \cos \varphi] / (1 - \sin \varphi)$$

Where: $\sigma_{1,f}$ = vertical stress at which failure occurs [kPa],

σ_3 = confining pressure [kPa],
 φ = angle of internal friction,
 c = cohesion [kPa].

Values for the cohesion and angle of internal friction of granular materials need to be determined by means of the triaxial test. For coarse grained granular materials we need the large scale triaxial setup and as we have discussed earlier this is not a practical test for day to day purposes. Fortunately procedures have been developed to estimate the failure characteristics of sands and unbound base course materials.

An example of such a procedure is the one developed by van Niekerk for sands that are commonly used in the Netherlands as well as base course materials made of mixtures from crushed concrete and crushed masonry [67]. These equations will be presented hereafter.

Based on the triaxial test results obtained on the **sands**, the following equation could be developed to predict the cohesion (c) and the angle of internal friction (φ) of the sands.

$$c = c1 \cdot qc^{c2} \cdot \left(\frac{d50}{1mm} \right)^{c3} \cdot Cu^{c4} \cdot \left(\frac{VVS}{100\%} \right)^{c5} \quad \phi = \phi1 \cdot qc^{\phi2} \cdot \left(\frac{VVS}{100\%} \right)^{\phi3}$$

Where:

c1: model parameter = 0.1375 [kPa]	$\phi1$: model parameter = 45.71 [degr.]
c2: model parameter = 2.553 [-]	$\phi2$: model parameter = 0.833 [-]
c3: model parameter = -1.698 [-]	$\phi3$: model parameter = 0.091 [-]
c4: model parameter = 2.959 [-]	d50 sieve diameter through which 50% of the mass passes [mm]
c5: model parameter = 0.384 [-]	VVS angularity of the material as determined by means of an outflow test according to the Dutch standards [%]
	Cu d60 / d10 [-]

The strength characteristic of **unbound granular base materials** in relation to their gradation, compaction quality index and ratio amount of crushed masonry to amount of crushed concrete has been determined in a similar way.

$$c = c6 \cdot qg \cdot qp \cdot qc^{c7} \quad \phi = \phi4 + \phi5 \cdot qc \cdot qg$$

Where:

c6 model parameter = 134.506 [kPa]	qc: see figure 201
c7 model parameter = 2.2495 [-]	qp: (0.4 * mass % masonry + mass % concrete) / 100 [-]
$\phi4$ model parameter = 30.27 [degr.]	qg: grading quality [-],
$\phi5$ model parameter = 18.86 [degr.]	(UL=1 / FL=1 / CO=0,9 / AL=0,89 / LL= 0,75 / UN=0,63, see also figure 219)

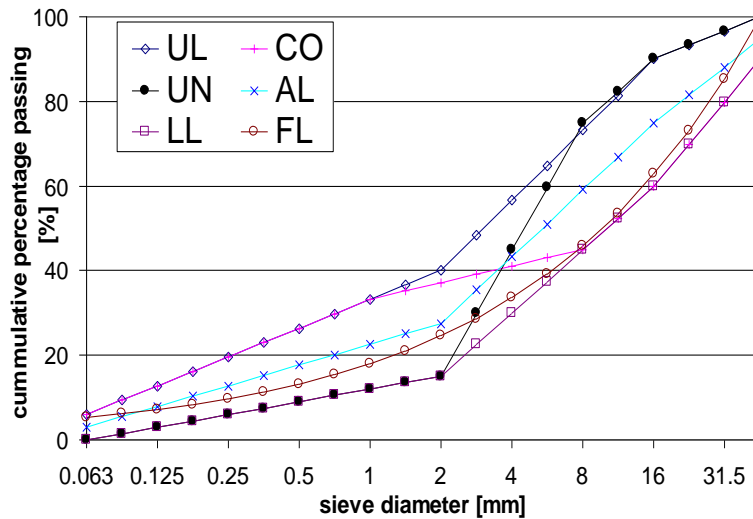


Figure 219: Gradations of the base course materials for which the equations have been developed.

The South-African pavement design procedure [69] also contains a method to evaluate the resistance of granular material to the applied stress levels and, in other words, to determine whether excessive permanent deformation occurs due to the applied stresses. In order to do so, a safety factor has been derived which is calculated using the following equation.

$$F = \{ \sigma_3 [K (\tan^2 (45 + \phi/2) - 1) + 2 K c (\tan (45 + \phi/2))] / (\sigma_1 - \sigma_3) \}$$

This equation can be rewritten as:

$$F = (\sigma_3 \phi_{\text{term}} + c_{\text{term}}) / (\sigma_1 - \sigma_3)$$

Where: F = safety factor,
c = cohesion [kPa],
K = constant = 0.65 for saturated soils, 0.8 for moderate moisture conditions and 0.95 for normal conditions,
 ϕ = angle of internal friction,
 σ_1, σ_3 = major and minor principle stress in the layer [kPa].

It should be noted that the F factor is in fact the inverse of the σ_1/σ_{1f} ratio which was used earlier in the description of the chance on failure and excessive permanent deformation. The only difference is that in the F equation, the factor K is introduced which takes care for the effect of the moisture conditions in the layer.

Values for the c_{term} and ϕ_{term} are given in table 39.

	Dry conditions	Dry conditions	Moderate conditions	Moderate conditions	Wet conditions	Wet conditions
Material code	ϕ_{term}	C_{term}	ϕ_{term}	C_{term}	ϕ_{term}	C_{term}
G1	8.61	392	7.03	282	5.44	171
G2	7.06	303	5.76	221	4.46	139
G3	6.22	261	5.08	188	3.93	115
G4	5.50	223	4.40	160	3.47	109
G5	3.60	143	3.30	115	3.17	83
G6	2.88	103	2.32	84	1.76	64

Table 39: Values for the ϕ_{term} and C_{term} .

9.7 Allowable stress and strain conditions in granular materials, permanent deformation models

If the stress conditions in the granular base or sub-base are becoming too high, permanent deformation or even shear failure will occur. Figure 220 is a nice example of excessive deformation in a pavement due to excessive deformation in the unbound layers.



Figure 220: Excessive pavement deformation due to deformation of the unbound base and/or sub-base layer.

The deformation shown in figure 220 is clearly due to deformation in the base or sub-base because the permanent deformation bowl is rather wide. In case of asphalt rutting a much narrower deformation bowl would have appeared.

There are two options to analyze the resistance to permanent deformation in the unbound layers. The first one is making predictions of the development of the permanent deformation as a function of the number of load repetitions, the stress conditions and the material characteristics. The second one is based on keeping the stress conditions in the unbound layers below a certain level such that excessive deformation will not occur. It is obvious that the latter procedure is a more simple and straightforward one.

Work by van Niekerk [67] has shown that if the stress ratio σ_1 / σ_{1f} stays below 0.4, no excessive deformation (< 5%) will occur (see figure 221). This ratio is valid for gradations UL and AL and compaction levels of 97 – 103%. For the coarser LL gradation the stress ratio could go up to 0.45 if the degree of compaction is 100% and even to 0.62 at a degree of compaction of 103%; the ratio is for gradations containing more fines (see figure 219 for gradation codes).

According to the South-Africans however, F values of smaller than one can still be allowed for a significant number of load repetitions. From the results presented above it is clear that these South-African findings should be treated with great care. Ratios not higher than 0.5 for σ_1/σ_{1f} or lower than 2 for F are strongly recommended to avoid excessive deformation in unbound granular layers to take place.

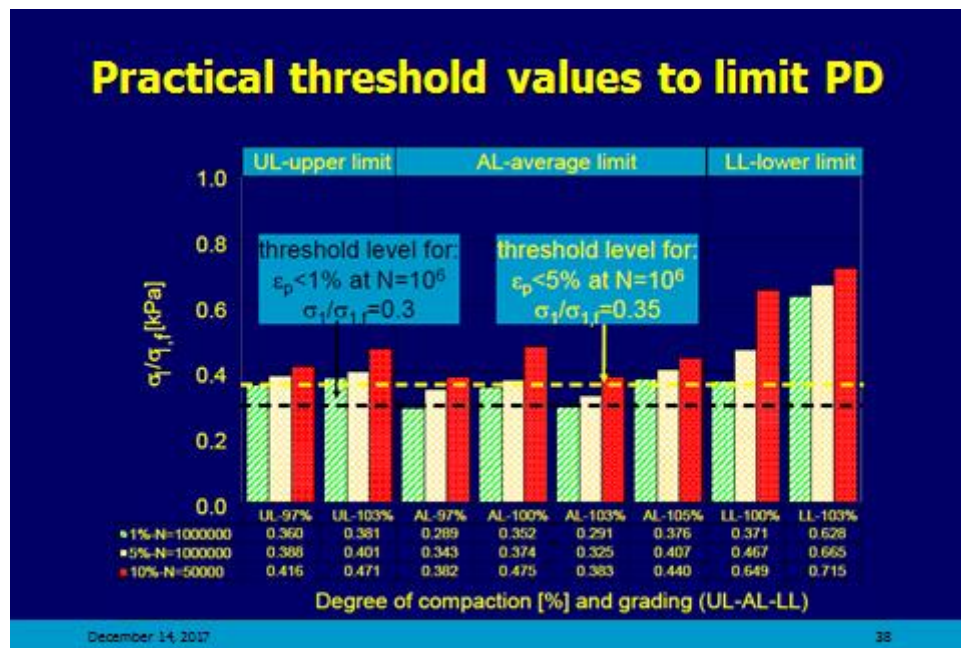


Figure 221: Effect of stress ratio σ_1 / σ_{1f} , gradation and degree of compaction on permanent deformation development in base course materials.

Similar work has been done at the Belgian Road Research Center by Descornet [75]. Based on extensive triaxial testing he defined a relationship between the compacted density of the granular layer and a so called R value which is defined as:

$$R = 1 + (\sigma_v - \sigma_h) / \sigma_h$$

If the R ratio in the granular layer is below the R value that belongs to a certain compacted density, then no significant permanent deformation will occur. The relation between the compacted density and the R value is given in figure 222.

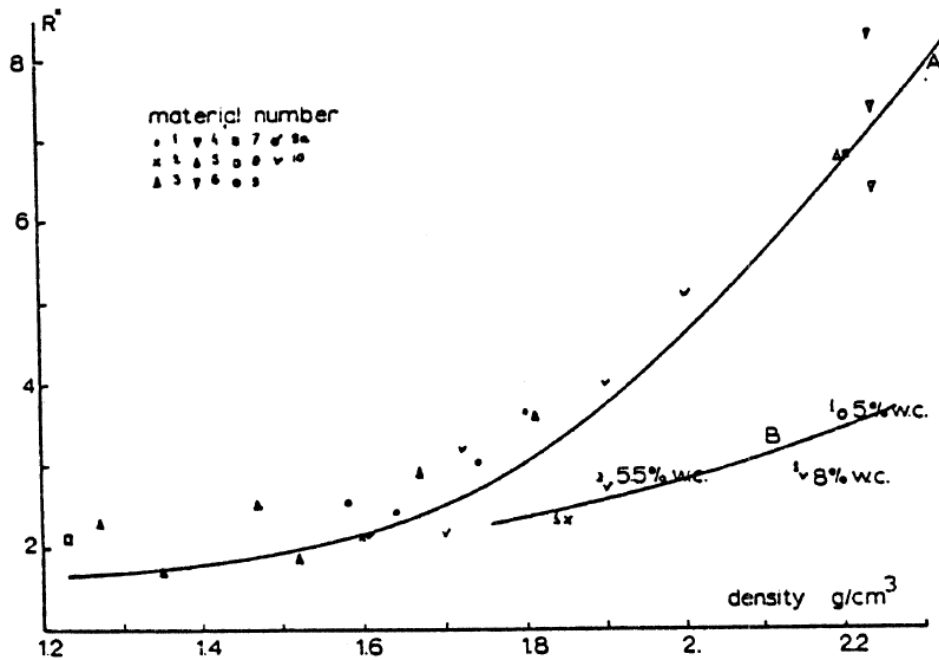


Figure 222: Relation between compacted density and R. B line to be used when material is wet.

Van Niekerk's work has also been used to develop allowable vertical compressive strain in the unbound base or subbase criteria [76]. The resilient strain level (ϵ) in the granular layer is calculated as:

$$\epsilon = (\Delta_{\text{top}} - \Delta_{\text{bottom}}) / h$$

Where:

- Δ_{top} = vertical displacement at the top of the layer [mm],
- Δ_{bottom} = vertical displacement at the bottom of the layer [mm],
- h = thickness of the layer [mm]

The resilient strain was then correlated to a permanent strain of 4% of the total thickness of the granular layer; the relationships developed in this way are shown in figure 223. If we take a 300 mm thick granular layer made of material CO-65-J-100 as an example, then figure 223 shows that at a resilient strain of 631 $\mu\text{m/m}$ ($\log \epsilon = 2.8$), 4% permanent deformation of the layer would occur after 10^6 load repetitions. So if the elastic deformation of the layer ($h * \epsilon$) would be $631 * 10^{-6} * 0.3 = 1.893 * 10^{-4}$ m, then the permanent deformation of that layer after 10^6 load repetitions would be $0.04 * 300 = 12$ mm.

If figure 223 would be plotted on a linear scale then we would obtain relationships which would look similar to the ones shown for asphalt fatigue (fig. 128). Also in this case a threshold value does appear which takes a value of 450 $\mu\text{m/m}$ for all materials shown in figure 223. This implies that the maximum amount of permanent deformation in a 300 mm thick granular layer would be 12 mm if the elastic deformation of that layer ($\Delta_{\text{top}} - \Delta_{\text{bottom}}$) would be limited to $450 * 10^{-6} * 0.3 = 1.35 * 10^{-4}$ m.

Work by Huurman and Van Niekerk on **sands** showed that for these materials much higher σ_1/σ_{1f} ratios can be allowed before permanent deformation occurs. A typical ratio value is 0.9.

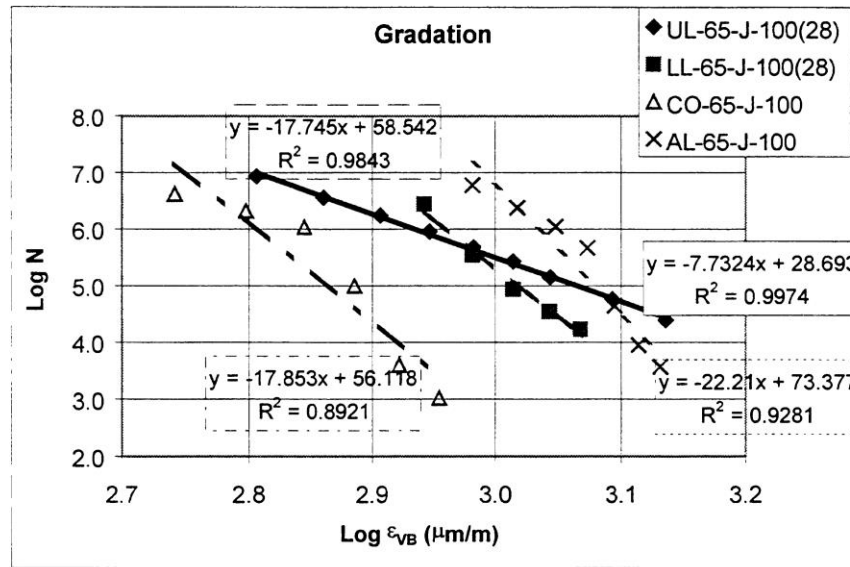


Figure 223: Allowable vertical strain levels in unbound base materials.

A number of researchers have developed permanent deformation models for granular materials. An example is given hereafter which was developed for the AASHTO MEPD system [31].

$$\delta = 1.673 * (\epsilon_0 / \epsilon_r) * e^{-A} * \epsilon_v * h$$

Where:

$$A = (\rho / N)^\beta$$

δ = permanent deformation after N load repetitions [in]

ϵ_v = average resilient strain in the granular layer [in/in]

h = thickness of the granular layer [in]

$\log \beta$ = $-0.6119 - 0.01736 * W_c$

$\log (\epsilon_0 / \epsilon_r)$ = $\{(e^B * a_1 E^{b_1}) + (e^C * a_9 E^{b_9})\} / 2$

B = ρ^β

C = $(\rho / 10^9)^\beta$

C_0 = $\ln\{(a_1 * E^{b_1}) / (a_9 * E^{b_9})\}$

ρ = $10^9 * [C_0 / (1 - D)]^{1/\beta}$

D = $(10^9)^\beta$

W_c = $51.712 * [(E/2555)^{1/0.64}]^F$

F = $-0.3586 * GWT^{0.1192}$

E = modulus of granular layer [psi]

GWT = depth to groundwater table [ft]

$a_1 = 0.15$; $a_9 = 20$; $b_1 = b_9 = 0$

The equations given here are copied from [31]. This is especially mentioned since a few times we see E^{b_1} or E^{b_9} which makes the equations look impressive. However b_1 and b_9 are equal to zero so E^{b_1} and E^{b_9} become equal to 1 and the equations could have been simplified because of that. C_0 e.g. could have been written as $\ln(0.15/20) = -4.893$

Also the Belgian Road Research Center has developed a permanent deformation equation for granular layers which is much simpler and is written as:

$$U_p = U_{el} * 2 * N^b$$

Where:

$$b = 2 - 3$$

U_{el} = the elastic deformation in the granular layer = $U_t - U_b$,

U_t = elastic deformation as calculated with e.g. BISAR at the top of the granular layer [m],

U_b = elastic deformation at the bottom of the granular layer [m],

U_p = permanent deformation in the granular layer [m]

10. Base courses showing self cementation

In the Netherlands, but also in many other countries, many secondary materials are used for base courses. A number of these materials show self-cementing action and in this part of the lecture notes some attention is paid to the mechanical characteristics of these materials as they were determined as part of a large research program [77] to determine whether or not these recycled materials could be used successfully in pavements. The following materials were investigated (table 40).

Number	Base course material	Code
1	Crushed masonry	MG
2	Mixture of crushed masonry and crushed concrete (50% - 50%)	FF
3	Lava	LA
4	Pelletized blast furnace slag	SS
5	Sand cement	ZC
6	Blast furnace slag	HO
7	Crushed concrete	BG
8	Phosphorous slag	FO
9	MG + 15% electro furnace slag	ME

Table 40: Investigated base course materials.

Test pavements were constructed with these materials. These pavements were placed on a sand subgrade; the base thickness applied was 250 mm. On top of the base materials which didn't show self-cementation (being MG, FF, LA and SS), a 180 mm thick asphalt layer was placed. A 120 mm thick asphalt layer was placed on layers which were expected to show self-cementation (ZC, HO, BG, FO and ME).

Falling weight deflectometer tests were performed at different moments in time to evaluate the increase of the stiffness modulus as a function of time of the base course materials. Figures 224, 225, 226 and 227 are summarizing the findings.

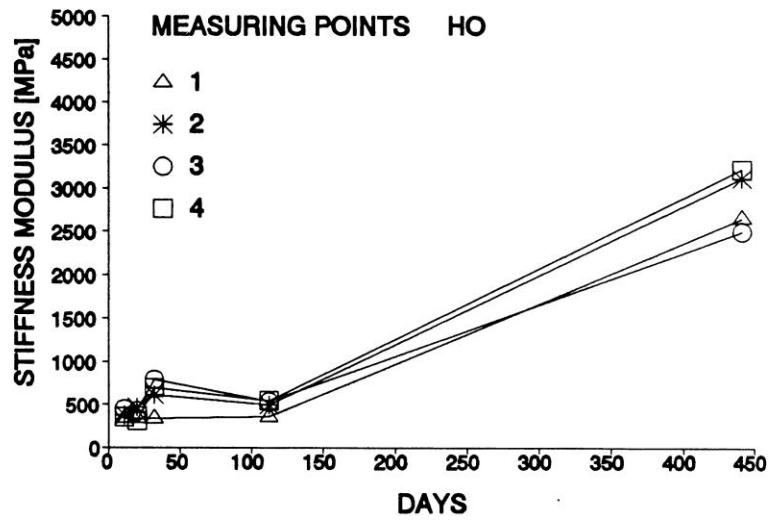


Figure 224: Increase of the stiffness modulus in time of the base course made of blast furnace slag.

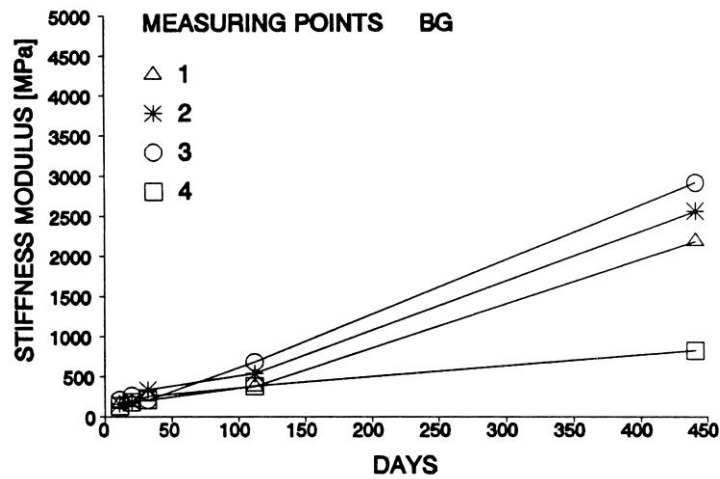


Figure 225: Increase of the stiffness modulus in time of the base course made of crushed concrete.

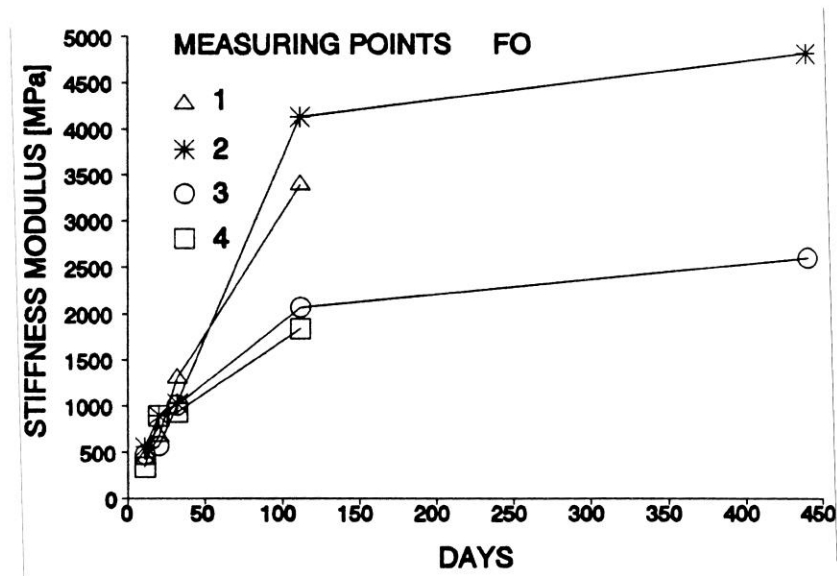


Figure 226: Increase of the stiffness modulus in time of the base course made of phosphorous slag.

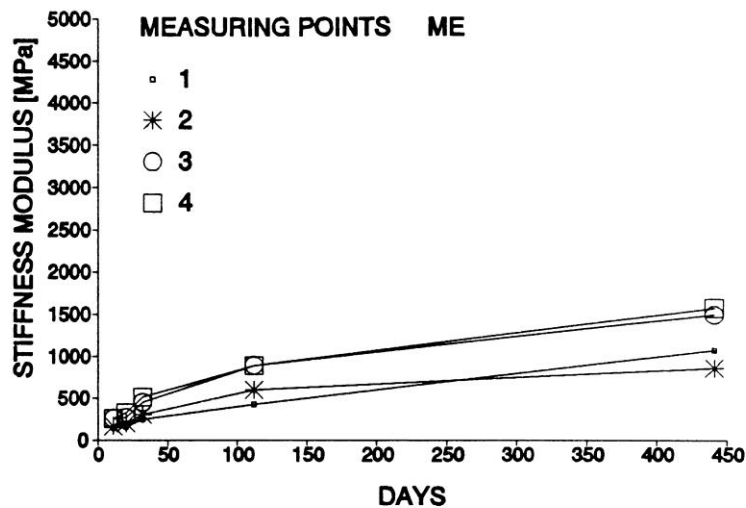


Figure 227: Increase of the stiffness modulus in time of the base course made of crushed masonry mixed with electro furnace slag.

Three aspects are calling the attention.

- there is a strong increase of the stiffness modulus in time,
- there is a relatively large amount of scatter in the data,
- the sections were not subjected to traffic loads which implies that any damage caused by traffic loads was not taken into account; early traffic might have a significant negative effect on the stiffness development.

Similar trends have been reported by van Niekerk [67]. He analyzed the development in time of crushed concrete – crushed masonry mixtures (63% crushed concrete) without and with addition of 10% blast furnace slag. Figures 228 and 229 show the M_r relationships that were obtained.

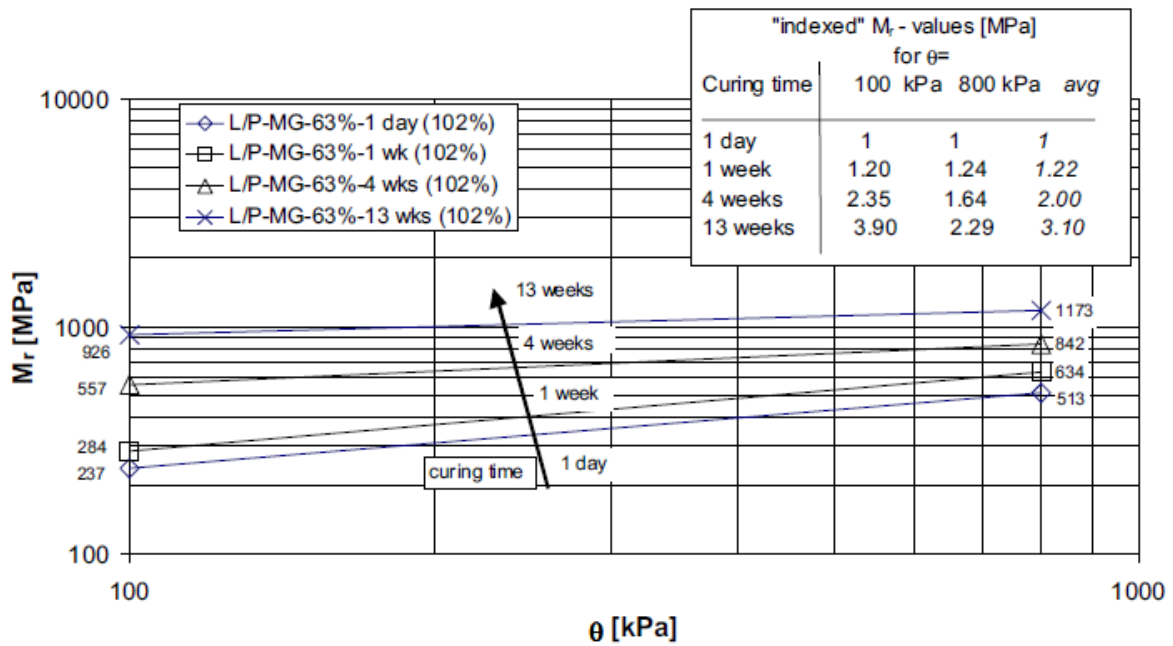


Figure 228: Development in time of the stiffness of a crushed concrete – crushed masonry mixture.

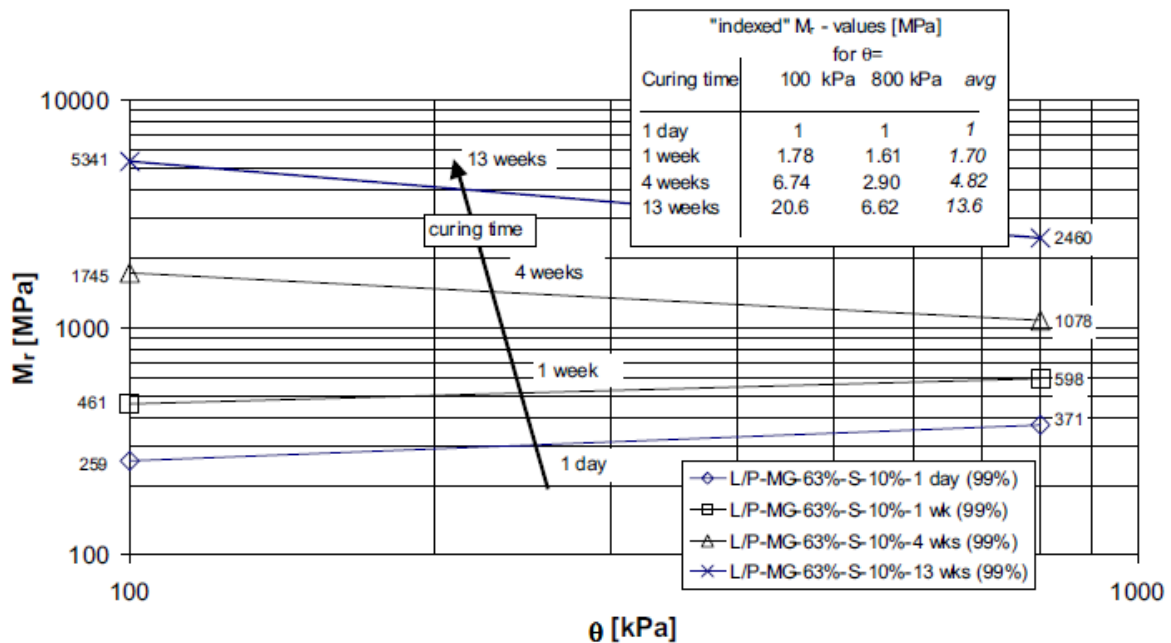


Figure 229: Development in time of the stiffness of a crushed concrete – crushed masonry mixture to which 10% of blast furnace slag is added.

These figures clearly show an increase of the stiffness in time and also show that the stiffer the materials becomes, the less dependent the stiffness is from the stress conditions. One also

observes that a sharp increase in stiffness occurred in cases where blast furnace slag was added. However, when the stiffness was taking high values, it was negatively affected by the stress conditions. At high θ values a decrease in stiffness was observed indicating that the bonds that were formed were partly broken because of the high stresses.

Figure 230 shows the permanent deformation behavior of the masonry – concrete base material when mixed with 10% slag. The figure shows that the permanent deformation is very small but also that the permanent deformation suddenly increases rapidly if the stress ratio reaches values of 0.47 and higher. At a stress ratio of 0.4 no significant deformation develops. It is recommended to use this value for design purposes.

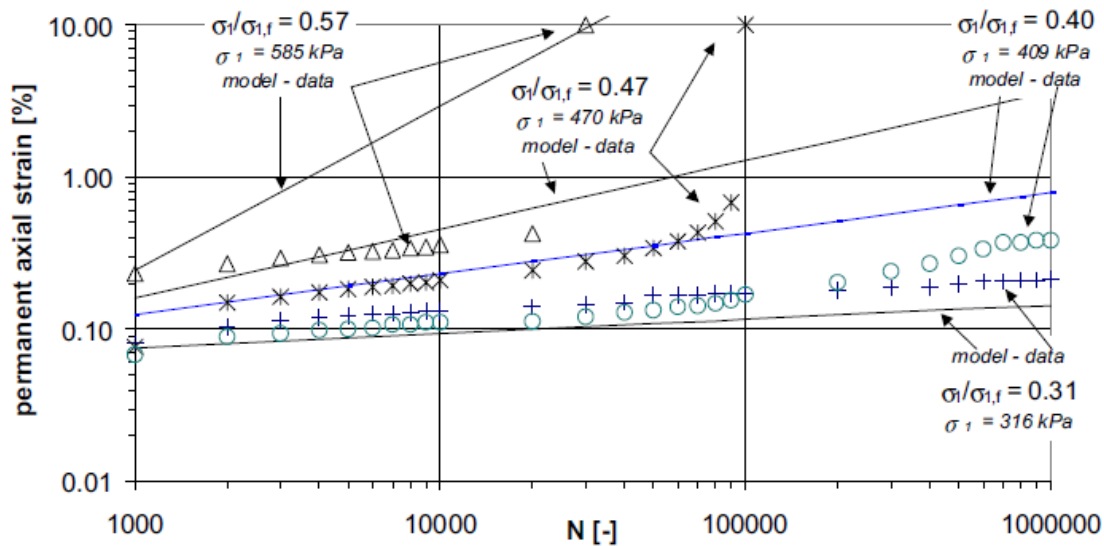


Figure 230: Permanent strain as a function of the σ_1 / σ_{1f} ratio for a crushed concrete – crushed masonry base (63% concrete) to which 10% of blast furnace slag is added, after 4 weeks curing.

The rapid increase in strength in time as a result of self-cementation is also shown in figure 231. After 13 weeks the failure stress has reached a value of about 1.7 MPa and seems to be independent of the confining stress level.

From the results presented in figure 231, it is clear that these types of material can provide significant stiffness and strength to the pavement structure.

One should however be aware of the fact that the all the results presented so far (including those of the test sections shown in figures 224 to 227) are obtained on undisturbed material. The material was allowed to develop self-cementation and during the curing time no loads were applied. In reality however (heavy) construction traffic will use the prepared base course as a roadway which means that significant stresses and strains will be induced which might result in premature damage. The effect of this has also been studied by van Niekerk [67] and some of his findings will be presented hereafter.

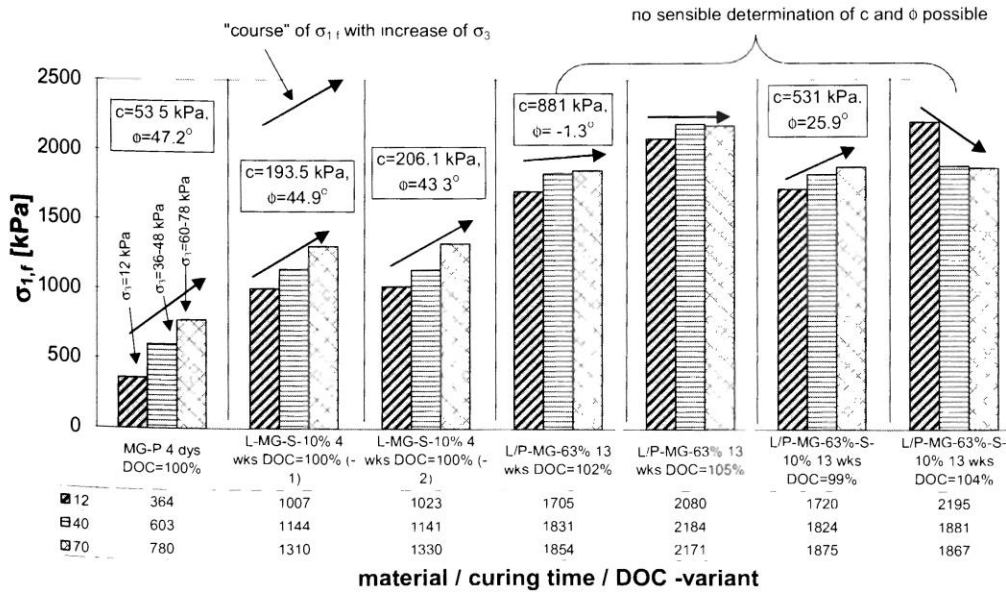


Figure 231: Stress at failure (σ_{1f}) at different confinement levels (σ_3) for crushed concrete – crushed masonry mixtures (63%) crushed concrete, indicated with MG-63%) and a similar mixture with 10% blast furnace slag (indicated with MG-63%-S-10%), at different moments in time.

In his study to determine the effect of early loading of a self cementing material, a 300 mm base layer consisting of a mixture of crushed concrete – crushed masonry mixed with 10% blast furnace slag was placed on a sand subgrade. The base was compacted to a degree of compaction of approximately 105%. A double surface treatment was applied to protect the base from climatic influences. After construction of the base, the loading schedule as shown in figure 232 was applied.

Type of load	# of points	Code	Week													
			0	1	2	3	4	5	6	7	8	9	10	11	12	13
Construction traffic 70 kN	2	CT-70	construction													
Traffic load 70 kN	2	T-70														
Traffic load 50 kN	2	T-50														
Traffic load 30 kN	2	T-30														
Traffic load 10 kN	2	T-10														
Delayed traffic 50 kN	2	DT-50														
Reference point	2	R														
Total	14															

Figure 232: Loading schedule.

The traffic loads were not real traffic loads but repeated falling weight deflectometer tests. A total of 100 load repetitions per day was applied per loading position. The stiffness modulus of the self-cementing base course was back calculated using the measured deflection bowls as input. Some results are shown in figure 233.

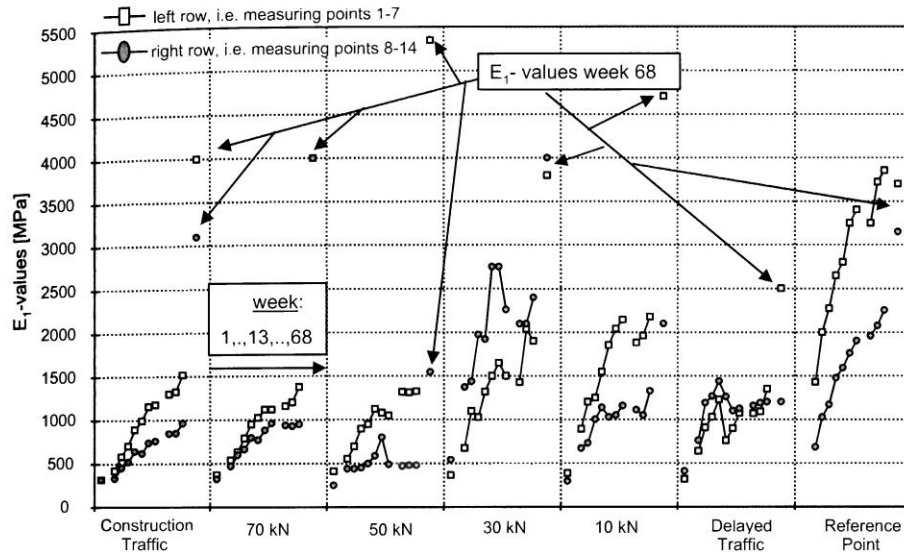


Figure 233: Development in time of the stiffness of a self-cementing base course as a function of the applied load.

Figure 233 clearly shows that the stiffness development of the base course is strongly influenced by the loading schedule. Also a significant amount of healing was observed during the period in which the section was not subjected to repeated loading by means of the falling weight equipment (period between week 13 and week 68). Furthermore quite some scatter in the results can be observed.

The figure also shows that "heavy construction traffic", simulated with FWD loads, has a significant influence on the stiffness development. Due to the high stresses and strains, self-cementation is disturbed and only develops slowly (compare the data of the loaded sections with those of the reference).

Since the falling weight loads were directly applied on the base course, an analysis was made to determine which falling weight load would simulate more or less the tensile strain at the bottom of the base when it had been covered with a 150 mm thick asphalt layer. It appeared that the 10 kN load simulated that the strain level fairly well. From figure 233 we can conclude that due to the 10 kN load, the stiffness modulus reduces to about 50% of its undisturbed value.

In conclusion this means that the negative effect of traffic in general and construction traffic in particular should be taken into account when designing pavements with self-cementing base courses. For design purposes, it is recommended to adopt a stiffness value that is 50% of the value determined in the laboratory on undisturbed samples.

11. Stabilized base courses

11.1 Introduction

In many countries, locally available materials are mixed with cement to obtain better characteristics with respect to stiffness, strength, moisture resistance etc. For the background and principles of modifying or stabilizing materials with cement or lime, the reader is referred to the vast amount of literature available on this topic like e.g. [78, 79] and these will not be repeated. Here only the most important issues with respect to pavement designs in which stabilized base courses are used will be discussed.

Before we go into that discussion, the reader should be aware of the fact that there is a distinct difference between a cement treated soil on one hand and a cement treated granular material or

a cement treated sand on the other. In general one could state that the less fines are present in the soil mixture, the more the cement is suited to be used as a stabilizing agent. This implies that in most cases it is not feasible to treat a fine grained soil with cement. In such cases modification with lime is much more feasible than mixing it with cement.

One should also be aware of the fact that the characteristics of lime and cement treated materials strongly depend on aspects like:

- pulverization of the existing soil,
- homogeneity of spreading,
- homogeneity of mixing,
- homogeneity in moisture content,
- amount of lime or cement,
- compaction.

When mixing is done in place, a significant amount of variation in the characteristics of the treated material might occur due to variations in the above mentioned factors. One should therefore not be surprised when the characteristics determined on cores taken from the field are less than the characteristics of the same material when mixed in the laboratory. It should be mentioned however that nowadays spreading and mixing equipment are developed to such an extent that, when the equipment is well operated, the differences between the lab and field characteristics are limited.

Figure 234 shows which type of stabilizer is most suited for which type of soil.

Designation	Fine clays	Coarse clays	Fine silts	Coarse silts	Fine sands	Coarse sand	Aggregate
Particle size (mm)	<0.0006	0.0006-0.002	0.002-0.01	0.01-0.06	0.06-0.4	0.4-2.0	>2.0
Volume stability	Very Poor	Fair	Fair	Good	Very Good		
Stabilizing agent	Lime	Range of maximum efficiency			Effective, but quality control is difficult		
	Cement	Range of maximum efficiency			Effective, but quality control is difficult		
	Bitumen	Range of maximum efficiency			Effective, but quality control is difficult		

Figure 234: Type of preferred stabilizer in relation to type of soil.

From figure 234 one can conclude that cement is the preferred stabilizing agent in case of course grained subbase and base course layers.

11.2 Cement stabilized base and subbase courses

11.2.1 Cement treated sands

In many parts in the world, sand is readily available while good quality crushed stone is not. Unfortunately the stiffness and strength characteristics of sands are not exceptionally good meaning that treating the material with cement is a viable option to improve those characteristics. In this part of the notes attention will be paid to relationships that are helpful to estimate the mechanical characteristics of cement treated sands. Most of the available information is related to sand cement as was used in the Netherlands. For that reason the presented equations hold particularly for that type of material.

In order to be able to estimate the **compressive and indirect tensile strength of Dutch sand cement**, a laboratory investigation [80] was carried out to determine the strength characteristics of this material. The sand was a fine grained sand typical for the sands used in the western part of the Netherlands for road construction. Some characteristics are given hereafter.

d10 = 125 μm ,
d50 = 200 μm ,
d60 = 230 μm ,
dx = sieve size through which x% passes.

The cement contents used were: 6%, 8%, 10% and 12% by weight. The moisture contents used were also 6%, 8%, 10% and 12%. The unconfined compressive strength after 28 days could be predicted using:

$$\text{UCS} = 40.5 - 23 X_1 - 13.6 X_2 + 20.7 X_3 - 108.5 W^2 + 123.2 D W^2 - 35 W^2 D$$

The indirect tensile strength could be predicted using:

$$\sigma_t = 32.17 - 3.81 X_1 - 1.91 X_2 + 2.02 X_3 + 0.097 W - 15.98 D$$

In these equations: UCS = unconfined compressive strength [kgf / cm²]
X_i = dummy variable,
W = moisture content [% m/m],
D = dry density [gr / cm³],
1 kgf / cm² = 100 kPa.

The dummy variables are defined as follows:

Cement content [% m/m]	X ₁	X ₂	X ₃
6	1	0	0
8	0	1	0
10	0	0	0
12	0	0	1

No equations were developed to estimate the **stiffness modulus** of the cement treated sand. Therefore the author tested two equations that were available in literature for the prediction of the stiffness modulus from the compressive strength of the material. The used equations are:

$$E_f = 1435 \sigma_c^{0.885} \quad (a) \quad \text{and} \quad E_f = 1284 \sigma_c \quad (b)$$

When used together with the Dutch specifications, the following results were obtained.

Strength requirement	Stiffness modulus [MPa] using	
	Equation (a)	Equation (b)
Lab. specimens after 28 days mean compressive strength 5 MPa	5963	6420
Field specimens after 28 days minimum compressive strength 1.5 MPa	2054	1926

The estimates obtained by means of both equations are considered to be very reasonable and therefore it is believed that both equations can be used for design purposes.

The fatigue relation as determined for a particular sand cement in the Netherlands is:

$$\log N = 10 - 0.08 \varepsilon$$

Where: ε = tensile strain at the bottom of the sand cement layer [$\mu\text{m} / \text{m}$].

An extensive analysis was made of the performance of a number of road sections in the SHRP-NL database that have a cement treated sand base [81]. It was possible to derive from this analysis a field fatigue relation which, together with the laboratory determined fatigue relation, is shown in figure 235. From this picture one can conclude that a design made using the laboratory determined fatigue relation is on the save side because that fatigue line more or less corresponds with the field line indicating a 85% probability of survival. Furthermore it is quite clear that there is a significant amount of variation around the mean fatigue line.

The field fatigue relation can be written as:

$$\text{Log } N = 8.5 - 0.034 \varepsilon$$

Where: N = allowable number of equivalent 100 kN axles (probability of survival is 50%),
 ε = tensile strain at the bottom of the cement treated base [$\mu\text{m} / \text{m}$].

11.2.2 Cement stabilized granular layers

A large amount of information is available on the characteristics of cement stabilized granular layers. Of course the strength, stiffness and fatigue characteristics can be determined by means of testing. In this way the effect of the following parameters can be determined:

- type of material,
- gradation,
- moisture content,
- degree of compaction,
- cement type,
- amount of cement,
- curing conditions and curing time.

Testing is however time consuming and is therefore not considered feasible for most projects and one therefore heavily relies on estimating procedures. Xuan [86] in his PhD study made a detailed literature study on this topic and the procedures presented hereafter are taken from his PhD thesis. No reference will be made here of the original sources.

With respect to estimating the **dynamic modulus** of stabilized granular layers, Xuan referred to Kolas & Williams who did put forward the following equation:

$$E_d = 40 * (\text{UCS}^{0.5}) * (D / 1000 * m)^{1.5}$$

Where:

E_d = dynamic modulus [MPa]
 UCS = compressive strength [MPa]
 D = dry density [kg/m^3]
 m = moisture content [%]

In South Africa [69] the following relationships have been proposed

$$E_f = 1284 \sigma_c \text{ for cemented fresh crushed aggregates}$$

$$E_f = 1784 \sigma_c \text{ for cemented natural weathered gravel}$$

Where: E_f = modulus in flexure [MPa] and σ_c = compressive strength [MPa]

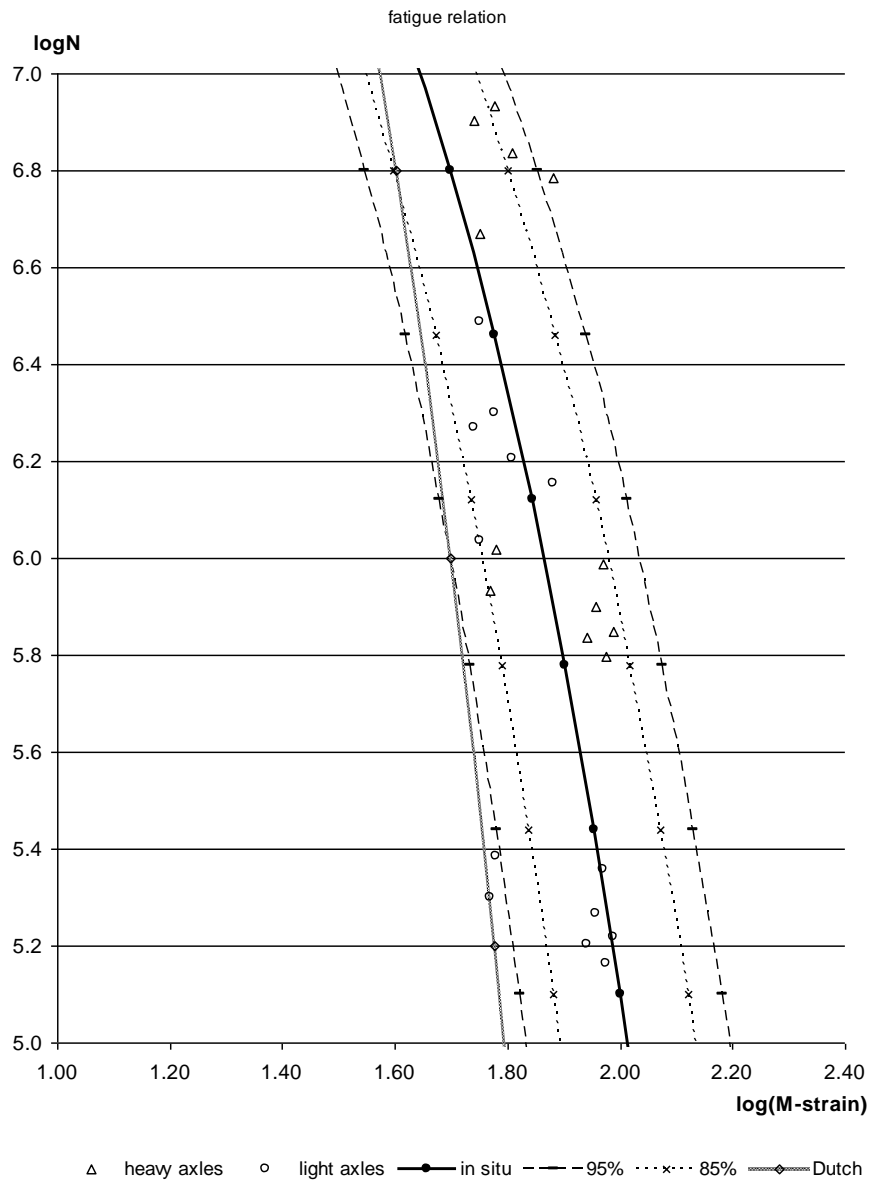


Figure 235: Field fatigue relation for sand cement base courses.

Typical **fatigue** relations that are reported are given below.

For an A-1-a soil treated with 5.5% cement (moisture content 7.5% and a density of 2200 kg/m³) the following relation was given:

$$\log N = 9.110 - 0.0578 \varepsilon \quad [\varepsilon] = [\mu\text{m} / \text{m}]$$

In South Africa the following relationship is used.

$$\log N = 9 (1 - \varepsilon / \varepsilon_t)$$

In both equations:

ε = applied strain level,

ε_t = strain at break

For fresh crushed rock material the strain at break varies between 100 and 250 $\mu\text{m}/\text{m}$. The mean value was reported to be 160 $\mu\text{m}/\text{m}$. For natural weathered material, the strain at break seems to be dependent on the stiffness modulus following the trend shown below.

E [MPa]	Strain at break [$\mu\text{m}/\text{m}$]
2500	188
5000	141
7500	118
10000	112
15000	106

One should however be aware of the large amount of scatter around the trend line. At a stiffness of 3000 MPa, strain at break values ranging between 120 and 280 $\mu\text{m}/\text{m}$ have been reported while at a stiffness of 6000 MPa the range is still between 100 and 200 $\mu\text{m}/\text{m}$. At high stiffness values, the variation in strain at break values is less.

In Australia a fatigue relation was developed for cement treated base courses using the results of accelerated load testing experiments and laboratory testing. The fatigue relation is given below.

$$N = \{(A E^{-B} + C) / \varepsilon_t\}^D$$

Where: E = stiffness modulus [MPa],
 ε_t = tensile strain at the bottom of the cement treated base [$\mu\text{m}/\text{m}$],
A = 112664
B = 0.804
C = 190.7
D = 12

In his literature survey Xuan [86] also reported fatigue relationships for cement stabilized granular materials, these are shown in figure 236. The gradations of the tested mixtures are shown in figure 237.

Figure 236 uses SN as independent variable, this means that the flexural strength should be known. This parameter can be estimated from the compressive strength using:

$$\sigma_f = -0.0042 + 0.1427 \sigma_c$$

Where: σ_c = compressive strength [MPa],
 σ_f = flexural strength [MPa],

Xuan, in his thesis, reported results of work done by Kolias and Williams who produced the following relationship:

$$\sigma_f = 0.25 * \sigma_c^{0.75}$$

This equation is based on the data shown in figure 238.

It is interesting to note that it is not always clear how the compressive strength is determined. Kolias and Williams used cube testing for determining the compressive strength while the relationships developed in South Africa are based on testing of cylinders. These tests do not give the same compressive strength! In general one could say that the compressive strength

determined on cylinders with a diameter of 150 mm and a height of 300 mm is around 80% of the strength determined on cubes with dimensions 150 * 150 * 150 mm.

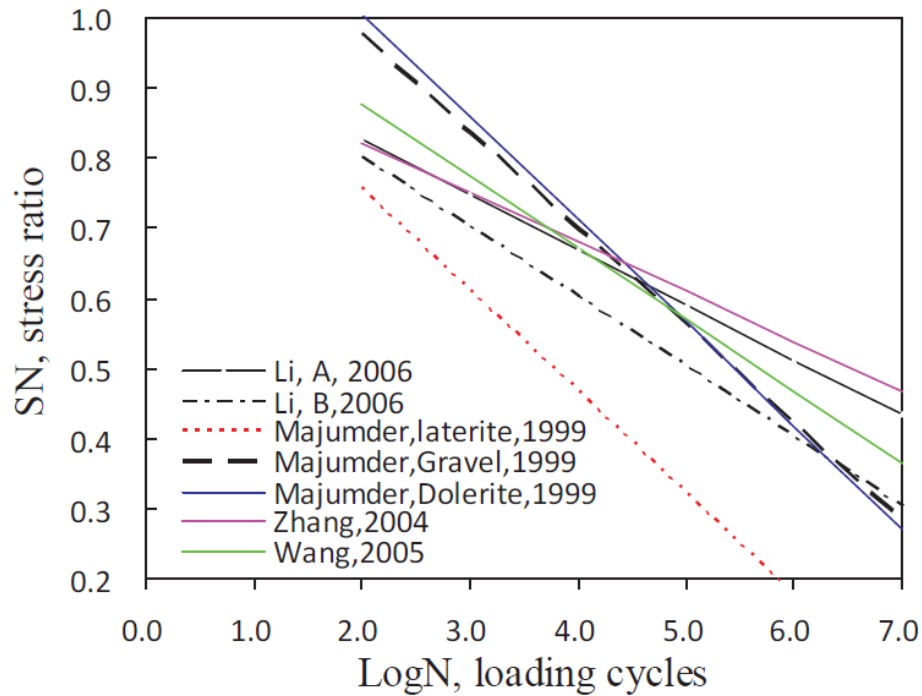


Figure 236: Fatigue relationships as reported by Xuan in his literature survey. SN = stress ratio = applied tensile stress / tensile strength.

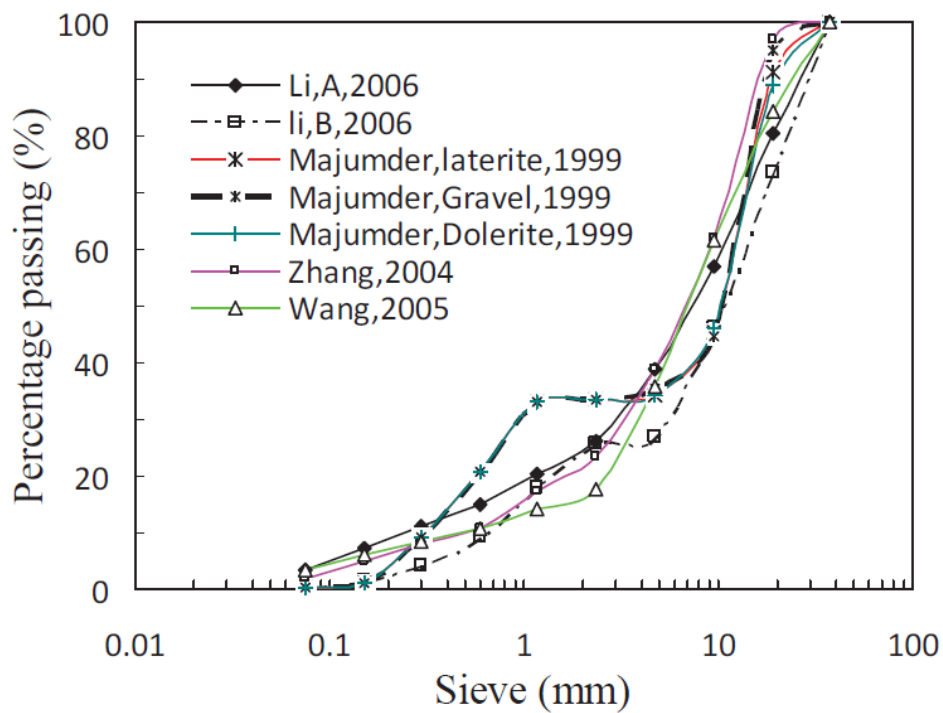


Figure 237: Gradations of the mixtures shown in figure 236.

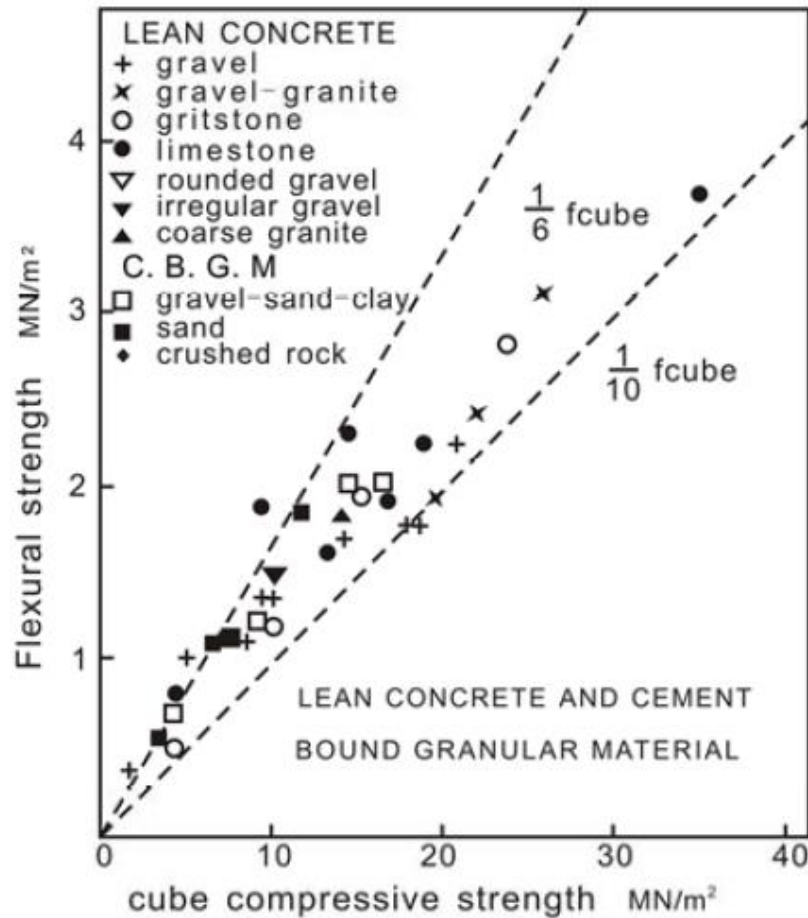


Figure 238: Relation between compressive and flexural strength as reported by Kolas and Williams.

11.2.3 Cement treated RAP and recycled crushed concrete – masonry mixtures

In the Netherlands large amounts of secondary materials have to be recycled. Re-use of these materials in road constructions is very feasible and quite often those materials are cement treated to give them the required mechanical characteristics and to prevent leaching of contaminating material. In this section we will present the main findings of the research done by Xuan [86] on cement treated mixtures of crushed recycled concrete and crushed recycled masonry. First of all we will present results obtained on cement treated recycled crushed asphalt.

RAP (recycled asphalt pavement) is sometimes treated with cement to obtain a good quality base course material. The reason to treat RAP with cement and not to re-use it in hot mix asphalt can be because the bitumen has hardened to such an extent that proper hot recycling has become rather difficult. Furthermore treating RAP with cement becomes a feasible option when the RAP is not sorted so one is dealing with a pile of RAP consisting of different types of mixtures.

The cement treated asphalt aggregate is called AGRAC in the Netherlands. A typical value for the **compressive strength** of cement treated crushed asphalt aggregate is 3.1 MPa. This value is obtained for an asphalt aggregate treated with 3.3% cement [m/m] having. The cement treated mixture has a density of approximately 1970 kg/ m³. By means of falling weight deflection measurements **stiffness values** of around 4500 MPa were obtained for a mixture that was subjected to construction traffic. On areas that were not subjected to construction traffic stiffness values of 6000 MPa were obtained. These values show once more the damaging effect construction traffic can have.

Stiffness values of 11000 MPa were obtained on beams that were tested in the laboratory using a four point bending test set up. This value was obtained at a temperature of 0 °C and a load frequency of 30 Hz. At 20 °C and 30 Hz a stiffness of 8000 MPa was obtained. Also **fatigue tests** were performed at the same temperatures and using the same loading frequency. The results are presented below.

For 0 °C and 30 Hz: $\log N = -38.69 - 11.42 \log \varepsilon$
For 20 °C and 30 Hz: $\log N = -24.95 - 7.72 \log \varepsilon$

In both cases $[\varepsilon] = [m/m]$.

The values for the slope of the fatigue relation (11.42 and 7.72) show that this material is a very brittle one at low temperatures. Furthermore the results show that the RAP still adds some visco-elastic behavior to the material since the slope of the fatigue relation is clearly affected by temperature.

As mentioned above Xuan [82] extensively researched the characteristics of recycled crushed concrete/masonry mixtures that were treated with cement.

It is clear that not all old concrete and masonry can be re-used or recycled. The material must e.g be free of asbestos and should not be contaminated by ink, oil or other residues. On top of that additional requirements are set in the Netherlands which are listed in table 41 [67].

Constituent		Description	Limit
			% [mass/mass]
Main	A	Crushed gravel concrete and crushed-stone concrete, with a particle density of at least 2100 kg/m ³	Min A+B: 50 ¹ with min A: 45
	B	Other crushed stone and stony material, with a particle density of at least 2100 kg/m ³	
	C	Crushed masonry, other crushed stone and stony material, with a particle density of at least 1600 kg/m ³	Max C: 50 ¹
Secondary		Other crushed stone and stony material	Max D+E: 10 with max E: 5
	D	Light weight concrete, glass, ceramics, slags,	
	E	Crushed asphalt	
Impurity	F	Gypsum and non-stony material ((non)-ferro metal, plastics, rubbers, polystyrene etc.)	Max F: 1
	G	Decomposable organic material (wood, rope, paper, plants remains, etc.)	Max G: 0.1

¹: at A+B > 80% a granulate classifies as a concrete granulate, while at C > 50% the granulate classifies as a masonry granulate

Table 41: Requirements to be set on stony materials to be recycled.

Based on his research results, Xuan was able to derive a number of predictive equations which are listed hereafter (e.g. table 42). The parameters used in these equations have the following meaning:

UCS = unconfined compressive strength [MPa],
ITS = indirect tensile strength [MPa],
E_r = resilient modulus at loading pulse duration of 200 ms with 800 ms rest period [MPa],
C = cement content by mass of aggregates [%],
W = water content by mass of aggregates [%],

D = dry density [kg/m³],
M = amount of crushed masonry in the mixture [% by mass],
t = curing time at 20°C in a fog room. [days].

Model and Parameters	$A \cdot \left(\frac{C}{W}\right)^{n1} \cdot D^{n2} \cdot e^{k1 \cdot M} \cdot e^{S \left[1 - \left(\frac{28}{t}\right)^{k2}\right]}$						
	A	n1	n2	K1	S	K2	R ²
UCS (MPa)	0.0747	1	8	0.0088	2.31	0.1	0.92
E_{static} (MPa)	161.3	0.71	7.4	0.0053	2.52	0.1	0.82
$E_{dynamic}$ (MPa)	124.9	0.35	7.5	0.0069	1.33	0.1	0.83
Relations	$E_{static} = 366.8 \cdot D^{3.8} \cdot UCS^{0.56}$						0.83
	$E_{dynamic} = 1.18 \cdot E_{static}$						0.66
	$E_{dynamic} = 0.84 \cdot E_{static} + 3565$						0.81
	$E_{dynamic} = 28.94 \cdot E_{static}^{0.65}$						0.83
Poisson's ratio	Between 0.09 and 0.15						

Table 42: Equations developed by Xuan to predictive compressive characteristics of cement treated recycled crushed concrete/masonry mixtures.

$$ITS = 0.0293 * (C / W)^{1.3} * (D / 1000)^7 * e^{0.008M} * e^Z$$

$$Z = 1.6 * [1 - (28 / t)^{0.2}]$$

$$E_r = 1577.8 * (C / W)^{0.65} * (D / 1000)^{4.1} * e^{0.0037M} * e^Y$$

$$Y = 0.28 * [1 - (28 / t)^{0.65}]$$

$$E_r = 6365.3 * D^{1.15} * ITS^{0.45}$$

Xuan also developed a model to predict shrinkage due to hardening and drying. This model is shown in figure 239. The parameters in this model have the following meaning. Please note that in this model "t" has a different meaning than in the strength and stiffness models.

S = deformation due to shrinkage [m/m],
S_{min} = minimum deformation due to shrinkage after 7 days [m/m],
S_{max} = maximum deformation due to shrinkage after 365 days [m/m],
t = curing time in days at 50% relative humidity.

Shrinkage model

$$S(t) = S_{\min} + (S_{\max} - S_{\min}) \cdot \left[1 + \left(\frac{t}{t_r}\right)^k\right]^{-m/k} \quad t > 7 \text{ days}$$

$$S_{\min} = 8 \times 10^{-6} M^3 + 0.01 M^2 - 0.312 M - 56.21$$

$$S_{\max} = 32.05 W + 32.29 C + 6.89 DC - 4.30 M - 541.00$$

$$t_r = 37.92$$

$$k = -1.0 \times 10^{-5} M^3 + 6.0 \times 10^{-4} M^2 - 0.014 M - 1.61$$

$$m = 6 \times 10^{-6} M^3 - 8 \times 10^{-4} M^2 + 0.028 M - 2.28$$

M = recycled masonry content, %;
DC = degree of compaction, %;
C = cement content, %;
W = moisture content, %;

December 13, 2017

91

TU Delft

Figure 239: Shrinkage model as developed by Xuan.

Also a model to predict the coefficient of thermal expansion was presented which is:

$$CTE = \frac{2.65}{1 + e^{(0.13 \cdot M - 6.04)}} + 0.51 \cdot \ln(C) + 0.37 \cdot \ln\left(\frac{DC}{100}\right) + 6.87$$

In this model DC is the degree of compaction in [%]. CTE is given in [$10^{-6} / ^\circ\text{C}$]. Information on shrinkage behavior and the coefficient of thermal expansion is important since cement stabilized material show hardening and drying shrinkage and will change in volume due to temperature changes. Both types of movement can result in significant cracking if special measures are not taken. It is because of this behavior that the cement content should not be too high! Cement contents should preferably stay below 5%!

The question is whether these equations are really able to predict reality. In order to check this the compressive strength of a similar type of material as produced and laid in a project in Spain were predicted and compared with the test data obtained on cores taken from the pavement. The result is shown in table 43.

Curing days (d)	Cement content (%)	Water content (%)	Masonry content (%)	Dry density (kg/m ³)	Measured UCS (MPa)	Estimated UCS (MPa)	Deviation (%)
7	3	11.53	15	1990	3.43	3.87	12.80
		12.45	22	1960	3.52	3.37	-4.13

Table 43: Comparison between predicted and measured UCS values.

In conclusion one can state that the predicted values were in good agreement with the measured values.

An analysis has been made to determine to what extend cement treated crushed concrete/masonry mixtures could be used as base or base course material. The requirements that are set in different countries with respect cement treated subbase and base courses are shown in table 44. The results of this analysis are shown in table 45; it is clear that these materials can indeed very well be used in pavement structures especially as a subbase; the cement contents needed for the base course are considered to be too high.

Country	Curing	Unconfined compressive strength (MPa)			
		C1	C2	C3	C4
South Africa	7 days at 100% compaction	6~12	3~6	1.5~3	0.75~1.5
	7 days at 97% compaction	4	2	1	0.5
United Kingdom	7 days cube compressive strength	CBM1 2.5~4.5	CBM2 4.5~7.5	CBM3 6.5~10.0	CBM4 10.0~15.0
China	7 days compressive strength	Top base of highway >4	Bottom base of highway >3	Subbase of highway >2	

Table 44: Requirements set on cement treated subbase and base courses.

Composition Masonry : Concrete	C/W for base course	Cement content for base course [%]	C/W for subbase	Cement content for subbase [%]
100 : 0	0.73	8.6	0.36	4.2
65 : 35	0.73	8	0.35	3.8
35 : 65	0.64	6.7	0.32	3.3
0 : 100	0.59	5.6	0.29	2.8

Table 45: Cement contents needed for several crushed concrete/masonry mixtures to fulfill the Chinese requirements.

The last item to be discussed is stress relaxation. Relaxation is a very important property in case temperature stresses are combined with traffic stresses. The first ones will relax as a function of

time making the combination of temperature and temperature stresses less damaging. The relaxation behavior of these materials can be described with:

$$R(t) = 2.22 t^{-0.25}$$

Where:

$R(t)$ = stress at time t / initially induced stress (for temperature stresses $\sigma = E * \alpha * \Delta T$,
 E = elastic modulus [MPa],
 α = coefficient of thermal expansion,
 ΔT = temperature drop [$^{\circ}\text{C}$],
 t = number of days.

12. Subgrade soils

12.1 Introduction

Subgrades usually consist of fine grained cohesive or non-cohesive soils. All these materials exhibit a stress dependent behavior implying that both the stiffness and the shear strength increase with increasing confinement. The dependence of the stiffness modulus on the stress conditions is shown in figure 240. The figure shows that non-cohesive soils react quite differently to various states of stress than cohesive soils. This stress dependency should ideally be taken into account when designing a pavement.

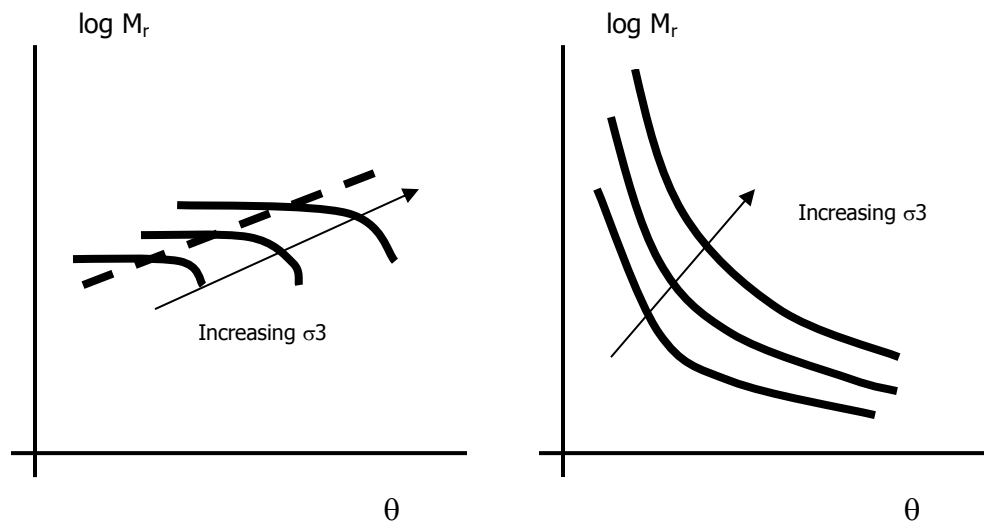


Figure 240: Stress dependent stiffness (resilient) modulus of non-cohesive (left) and cohesive (right) soils.

12.2 Models to predict the resilient modulus of soils

Because repeated load triaxial testing is still considered to be an “advanced” test it is not used very often for the characterization of pavement subgrades. Therefore one relies quite often on procedures that allow to predict the stiffness of subgrade soils. In [65] a set of those equations

have been presented. It is recalled that similar equations were presented when discussing the estimation of the stiffness of granular base and subbase layers.

Course grained gravel soils

$$M_r = [1.3429 - 0.0051 * P_{3/8} + 0.0124 * \%Clay + 0.0053 * LL - 0.0231 * W_s] * p_a * [\theta / p_a]^A * [(\tau_{oct} / p_a) + 1]^B$$

Where:

$$A = 0.3311 + 0.001 * P_{3/8} - 0.0019 * \%Clay - 0.0050 * LL + 0.0093 * W_s$$

$$B = 1.5167 - 0.0302 * P_{3/8} + 0.0435 * \%Clay + 0.0626 * LL + 0.0377 * PI - 0.2353 * W_s$$

Coarse grained sand soils

$$M_r = [3.2868 - 0.0412 * P_{3/8} + 0.0267 * P_4 + 0.0137 * \%Clay + 0.0083 * LL - 0.0379 * W_{opt} - 0.0004 * \gamma_s] * p_a * [\theta / p_a]^C * [(\tau_{oct} / p_a)]^D$$

$$C = 0.5670 + 0.0045 * P_{3/8} - 2.98 * 10^{-5} * P_4 - 0.0043 * \%Silt - 0.0102 * \%Clay - 0.0041 * LL + 0.0041 * W_{opt} - 3.41 * 10^{-5} * \gamma_s - 0.4582 * (\gamma_s / \gamma_{opt}) + 0.1779 * (W_s / W_{opt})$$

$$D = -3.5677 + 0.1142 * P_{3/8} - 0.0839 * P_4 - 0.1249 * P_{200} + 0.1030 * \%Silt + 0.1191 * \%Clay - 0.0069 * LL - 0.0103 * W_{opt} - 0.0017 * \gamma_s + 4.3177 * (\gamma_s / \gamma_{opt}) - 1.1095 * (W_s / W_{opt})$$

Fine grained silt soils

$$M_r = [1.0480 + 0.0177 * \%Clay + 0.0279 * PI - 0.370 * W_s] * p_a * [\theta / p_a]^E * [(\tau_{oct} / p_a)]^F$$

$$E = 0.5097 - 0.0286 * PI$$

$$F = -0.2218 + 0.0047 * \%Silt + 0.0849 * PI - 0.1399 * W_s$$

Fine grained clay soils

$$M_r = [1.3577 + 0.0106 * \%Clay - 0.0437 * W_s] * p_a * [\theta / p_a]^G * [(\tau_{oct} / p_a) + 1]^H$$

$$G = 0.5193 - 0.0073 * P_4 + 0.0095 * P_{40} - 0.0027 * P_{200} - 0.0030 * LL - 0.0049 * W_{opt}$$

$$H = 1.4258 - 0.0288 * P_4 + 0.0303 * P_{40} - 0.0521 * P_{200} + 0.0251 * \%Silt + 0.0535 * LL - 0.0672 * W_{opt} - 0.0026 * \gamma_{opt} + 0.0025 * \gamma_s - 0.6055 * (W_s / W_{opt})$$

The variables used are the same as those mentioned in table 30 which is presented again hereafter.

Variable	Description	Unit
$P_{3/8}$	Percentage passing 3/8" sieve	%
P_{40}	Percentage passing No. 40 sieve	%
P_4	Percentage passing No. 4 sieve	%
LL	Liquid limit	%
W_{opt}	Optimum moisture content	%
γ_{opt}	Optimum dry density	kg/m ³
W_s	Actual moisture content	%
γ_s	Actual dry density	kg/m ³
PI	Plasticity Index	%
P_{200}	Percentage passing No. 200 sieve	%

In table 46, 47 and 48 the range in characteristics of the subgrade soils for which the equations were developed are given. This allows to determine whether the equations can be used for a particular soil if one wants to estimate the resilient behavior by means of the equations given here.

Parameters	Min	Max	Median	Mean
$P_{3/8}$	45.0	100.0	75.0	75.3
$P_{No. 4}$	34.0	99.0	61.0	62.1
$P_{No. 40}$	13.0	90.0	36.0	37.3
$P_{No. 200}$	1.9	37.0	15.9	17.4
LL	0.0	44.0	0.0	10.4
PI	0.0	18.0	0.0	2.7
W_{opt} %	4.0	19.0	8.0	8.5
$\gamma_{d, opt}$ (kg/m ³)	1682.1	2451.1	2114.6	2099.8
w_s %	3.5	20.5	7.9	8.5
γ_s (kg/m ³)	1557.0	2332.0	2005.5	1985.3
$\gamma_s/\gamma_{d, opt}$	0.85	1.06	0.95	0.95
w_s/w_{opt}	0.36	1.46	0.99	1.01
$(\gamma_{d, opt})^2/P_{No. 40}$	37058.9	412457.8	117658.0	141567.2

Table 46: Coarse grained soils aggregate mixture

Parameters	Min	Max	Median	Mean
$P_{3/8}$	58.0	100.0	94.5	92.3
$P_{No. 4}$	36.0	100.0	89.5	87.4
$P_{No. 40}$	20.0	98.0	66.0	67.2
$P_{No. 200}$	4.1	96.1	18.0	23.9
LL	0.0	30.0	0.0	5.4
PI	0.0	12.0	0.0	1.6
W_{opt} %	5.0	13.0	9.0	9.0
$\gamma_{d, opt}$ (kg/m ³)	1746.2	2467.1	1986.5	2001.8
w_s %	4.7	14.2	8.3	8.5
γ_s (kg/m ³)	1608.3	2391.6	1871.0	1889.8
$\gamma_s/\gamma_{d, opt}$	0.86	1.01	0.94	0.94
w_s/w_{opt}	0.45	1.29	0.96	0.95
$(\gamma_{d, opt})^2/P_{No. 40}$	33188.6	304324.2	58296.3	69574.2

Table 47: Fine grained soils

Parameters	Min	Max	Median	Mean
$P_{3/8}$	53.0	100.0	96.0	92.3
$P_{No. 4}$	30.0	100.0	92.0	87.4
$P_{No. 40}$	18.0	99.0	71.0	69.3
$P_{No. 200}$	1.0	99.0	35.0	40.2
% Silt	0.0	92.7	23.2	26.6
% Clay	0.0	75.5	10.3	13.5
LL	0.0	73.0	22.0	19.7
PI	0.0	46.0	5.0	7.9
$w_{opt}\%$	6.0	95.0	12.0	13.2
$\gamma_{d, opt} (kg/m^3)$	352.4	2226.8	1890.4	1865.5
$w_s\%$	3.0	33.2	11.6	12.7
$\gamma_s (kg/m^3)$	1215.8	2160.0	1804.5	1790.3
$\gamma_s/\gamma_{d, opt}$	0.816	4.231	0.957	0.966
w_s/w_{opt}	0.239	1.357	0.973	0.964
$(\gamma_{d, opt})^2/P_{No. 40}$	1380.2	275475.0	49524.3	58883.4

Table 48: All subgrade soils.

In spite of the availability of these “impressive” regression equations, common practice is that one relies on relationships between e.g. CBR and the stiffness modulus of the subgrade. Some of these relationships are given hereafter

12.3 Estimation of the subgrade modulus using empirical equations

Some well- known rules which can be applied to estimate the stiffness modulus of fine grained soils are given below.

Organisation	Equation
Shell	$E = 10 \text{ CBR}$
US Army Corps of Engineers	$E = 37.3 \text{ CBR}^{0.711}$
CSIR South Africa	$E = 20.7 \text{ CBR}^{0.65}$
Transport and Road Research Laboratory UK	$E = 17.25 \text{ CBR}^{0.64}$
Delft University, Ghanaian laterite	$E = 4 \text{ CBR}^{1.12}$

Table 49: Equations to estimate the subgrade modulus $[E] = [\text{MPa}]$, $[\text{CBR}] = [\%]$.
Note: The relationship for the Ghanaian laterite was determined by means of the repeated load CBR test.

It is clear that there is no unique relationship to predict the stiffness modulus of fine grained materials from the CBR. Therefore one should be very cautious in adopting these equations. Furthermore it should be noted that these relationships show a significant amount of scatter. An example of the scatter that can occur is given in figure 241.

In the AASHTO MEPD system [31] also an equation is presented to estimate the CBR. This equation is:

$$\text{CBR} = 75 / (1 + 0.728 * P_{200} * \text{PI})$$

All parameters have been explained above. It is remarkable to see that the moisture content is not taken into account while it has a significant influence (see e.g. the equations to predict M_r for subgrade soils which were given above. The influence of moisture on the resilient modulus is also clearly shown in figure 242. The conclusion therefore is that the effect of moisture on the

stiffness and the strength of the subgrade soil should always be checked. The same holds for the effect of compaction.

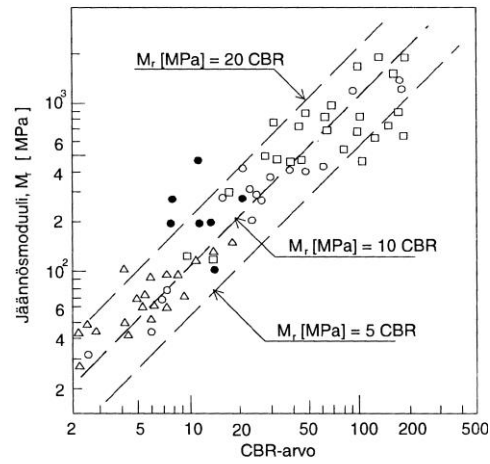


Figure 241: Scatter around the relationship $E = 10 \text{ CBR}$.

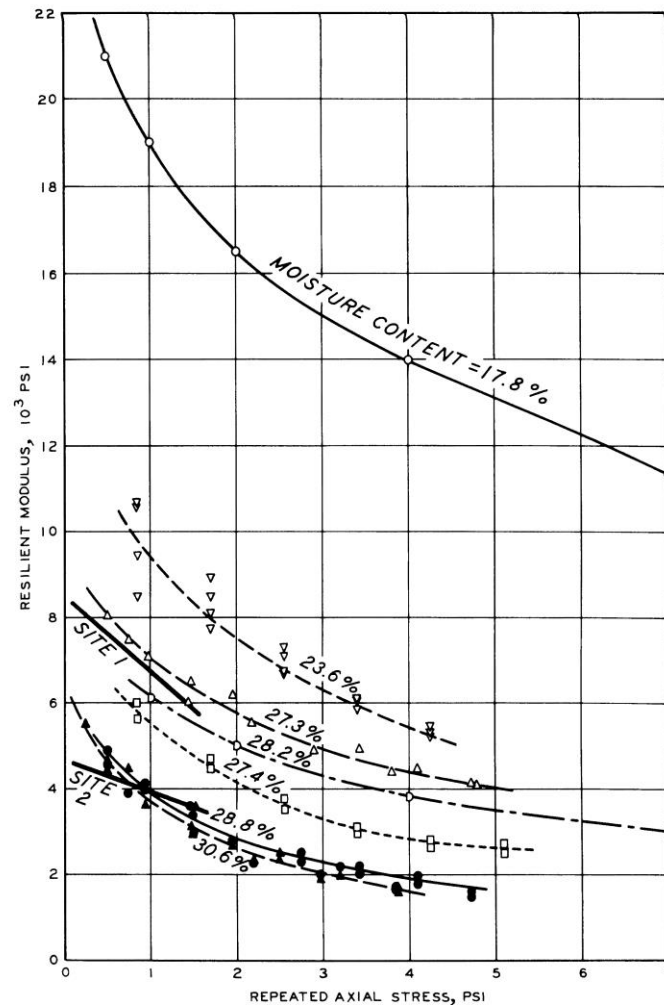


Figure 242: Influence of the moisture content on the resilient modulus of a silty clay subgrade.

The repeated load CBR test can of course also be used to determine the resilient modulus of fine grained materials. The standard size CBR mold and plunger can be used for this purpose. For the type of sand used as subgrade for most road projects in the western part of the Netherlands it has been found that the resilient modulus as determined by means of the repeated load CBR test is the same as the resilient modulus determined from a repeated load triaxial test performed at 20 kPa confinement stress. For other confinement levels one could write:

$$M_r = 0.211 \sigma_3^{0.563} M_{\text{rep CBR}}$$

Where: M_r = resilient modulus
 σ_3 = confining stress [kPa],
 $M_{\text{rep CBR}}$ = resilient modulus obtained from the repeated load CBR test.

Let us now discuss transfer functions for subgrade soils that allow to determine the number of load repetitions before excessive deformation will occur.

12.4 Allowable subgrade strain

A number of organizations have developed relationships between the vertical elastic strain at the top of the subgrade and the number of load repetitions at which a significant amount of permanent deformation in the subgrade occurs. In the Netherlands e.g. results from accelerated pavement tests done at the Delft University on asphalt pavements placed on a sand subgrade allowed to develop a subgrade strain relation for the sand subgrade material. The test results showed that the observed permanent deformation was entirely due to the deformation of the subgrade. The subgrade strain relationship was then developed by correlating the vertical compressive strain at the top of the sand subgrade to the number of load repetitions needed to obtain a rut depth of 18 mm. The following relationship was obtained.

$$\log N = -7.461 - 4.33 \log \varepsilon_v$$

Where: ε_v = vertical compressive strain at the top of the subgrade [m/m],
 N = number of load repetitions to a rut depth of 18 mm.

Similar relationships have been developed in South Africa and are shown below.

$$\log N = A - 10 \log \varepsilon_v$$

Where: N = allowable number of load repetitions to a specific rut depth,
 A = constant depending on the allowable rut depth; see table 50,
 ε_v = vertical compressive strain at the top of the subgrade [$\mu\text{m} / \text{m}$].

Terminal rut depth [mm]	Reliability level [%]	A
10	95	33.30
10	90	33.38
10	80	33.47
10	50	33.70
20	95	36.30
20	90	36.38
20	80	36.47
20	50	36.70

Table 50: A values for the South African subgrade strain relationships.

As mentioned above similar relationships have also been developed by other institutions and they are listed in table 51.

Agency	A	B	Rut depth
Asphalt institute	1.365 E-9	4.447	12.5 mm
Shell 50% reliability	6.15 E -7	4.0	
Shell 85% reliability	1.94 E-7	4.0	
Shell 95% reliability	1.05 E-7	4.0	
TRRL 85% reliability	6.18 E-8	3.95	
Belgian Road Research Centre	3.05 E-9	4.35	10.2 mm

Table 51: Subgrade strain relationships as developed by different agencies. In all equations the subgrade strain (ϵ_v) is in $\mu\text{m/m}$. The equation is $\log N = \log A + B \log \epsilon_v$

Also the relationship developed by the US Corps of Engineers (CoE) should be mentioned which is:

$$N = 10000 * (a / \epsilon_v)^b$$

Where:

$$a = 0.000247 + 0.000245 * \log (M_r)$$

$$b = 0.0658 * (M_r)^{0.559} \quad [M_r] = [\text{psi}]$$

It should be noted that the original Shell relationship (50% relationship) is related to the number of load repetitions at which the pavements in the AASHTO Road Test reach a present serviceability index of 2.5. The CoE relationship was developed on test sections with a fine grained clay subgrade.

Finally the relationship used in the French design manual [138] is mentioned which is:

$$\epsilon_v = 0.012 NE^{-0.222}$$

Where:

NE = number of equivalent 130 kN single axles

As one will notice the different relationships predict a different number of load repetitions at the same strain level. This is of course rather confusing because the question then is which relationship should be used! Fortunately the subgrade strain criterion is seldom the decisive criterion when designing pavements so in most cases selecting the proper relationship is therefore not much of an issue. This will be discussed in great detail later on.

12.5 Prediction of subgrade deformation

Although using the subgrade strain criterion is mostly used to determine whether the subgrade can sustain the applied loads, permanent deformation in the subgrade can also be predicted. This is e.g. done in AASHTO's Mechanical Empirical Pavement Design (MEPD) system. The equation is exactly the same as the one which is used for granular layers which was presented earlier. The only difference however is the "constant" used in the equation which is 1.35 for subgrade materials instead of 1.673 which was used for granular materials.

$$\delta = 1.35 * (\epsilon_0 / \epsilon_r) * e^{-A} * \epsilon_v * h$$

All variables are discussed earlier. The complicating factor here is the value of “h”. This value should in fact be equal to the subgrade thickness over which elastic vertical deformations occur. It is therefore suggested to divide the top 8ft of the subgrade into sublayers and calculate the permanent deformation in each sublayer and take the sum of these. This is a rather tedious procedure and because the predictive capability of the subgrade model is not very good, this model is not advised for use in practice.

A much simpler and more practical model is the one developed by the Belgian Road Research Center for fine grained soils. This model is:

$$U_p = U_{el} * (1.3 + 0.7 * \log N)$$

Where:

U_p, U_{el} = permanent respectively elastic deformation at the top of the subgrade [m],

N = applied number of load repetitions.

13. Lime treated Soils

13.1 Introduction

Stabilization of soils with cement is not feasible for fine grained soils. Cement can be very effectively used on materials like sand and coarser grained materials. The Portland Cement Association e.g. gives the following estimates for cement requirements for different soil groups.

AASHO soil group	Usual range in cement requirements [% m/m]
A-1-a	3 – 5
A-1-b	5 – 8
A-2	5 – 9
A-3	7 – 11
A-4	7 – 12
A-5	8 – 13
A-6	9 – 15
A-7	10 – 16

Table 52: Cement requirements in relation to soil group.

The table shows that for the finest graded coarse grained soil (A3) cement percentages of 7 – 11% might be needed to obtain a material which fulfills the requirements. Such high cement contents inevitably result in (severe) problems such as reflective cracking. This is one of the reasons why the Dutch Ministry of Transport doesn't allow anymore the use of cement stabilized sand layers in pavement structures.

Next to the cement requirement issue, use of cement in (very) fine grained soils is complicated because of construction issues like mixing, required pulverization when dry and workability when wet.

Fine grained soils can therefore much better be treated with lime because use of lime will make the fine material coarser, reduces the plasticity values and reduces the moisture content especially when quick lime (CaO) is used. Little e.a. [81] state that lime stabilization will only be effective if the soil has at least 25% passing the 75 μ m sieve and a PI of at least 10%. Lime stabilization will not be very effective if the soil contains more than 1% organic material and the soluble sulfate content should be less than 0.3% by weight in a 10:1 water to soil solution.

As has been discussed in the lecture notes on Soils and Unbound Granular Materials [62], the “quality” of fine grained soils, and in particular clayey soils, depends on the size of the clay platelets and the thickness of the water layer that is attached to the clay particle. Montmorillonite clay e.g. consist of small clay platelets surrounded by a relatively thick water layer. Kaolinite clays on the other hand characterize themselves by their relatively large, stable clay platelets which are surrounded by a relatively thin layer of water. The stability of clay structures also strongly depends on the type of exchangeable ion. The general order of replace-ability of the common cations associated with soils is:

$$\text{Na}^+ < \text{K}^+, \text{Ca}^{2+} < \text{Mg}^{2+}$$

So K^+ will replace Na^+ , Ca^{2+} will replace K^+ and so on. It has been shown that the thickness of the bound water layer around the clay particle will decrease substantially if e.g. sodium ions are replaced by the calcium ions coming from the lime. It has also been shown that under such conditions development of flocculent structures is promoted. In itself such reactions are mainly influencing soil characteristics as plasticity, shrinkage and workability but are not responsible for the observed rapid increase in strength. The reason for the rapid strength development is believed to be an immediate reaction between the alumina at the edges of the clay particles with the lime which is absorbed at the clay particle faces. This means that plasticity, shrinkage and swelling and other normal clay – water interactions are distinctly inhibited. Thus the clay becomes ameliorated but not really stabilized since the flocs have not been bound together well enough to retain any significant strength after soaking. Any immediate reduction in plasticity results in an immediate increase in shear strength.

13.2 Example of the effects of lime

As an example of how a lime treatment affects the characteristics of a soil, the results of a study performed at the Delft University on how a lime treatment would affect the characteristics of the notorious Ethiopian Black Cotton clay are shown in figures 243 to 247 and tables 53 and 54 [82, 83].

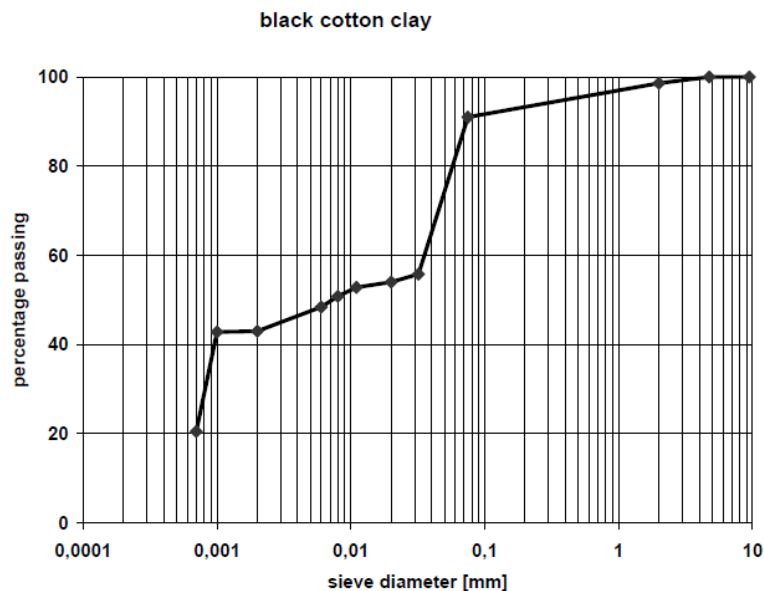


Figure 243: Gradation of the Back Cotton Clay (LL = 99%, PI = 45%)

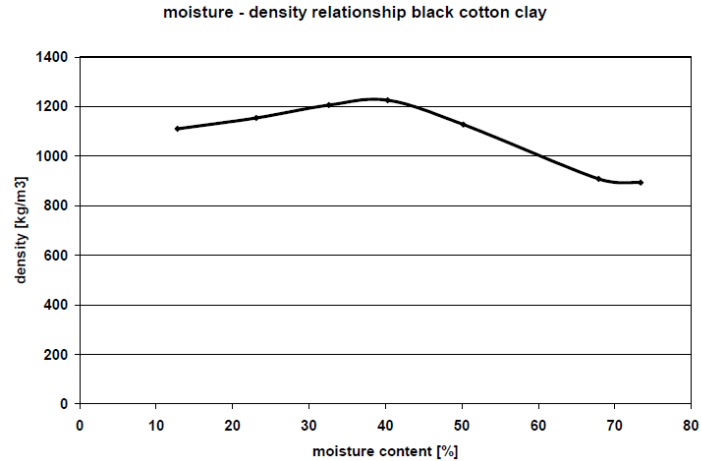


Figure 244: Moisture density relation of the Black Cotton Clay
CBR at moulding water content and after soaking

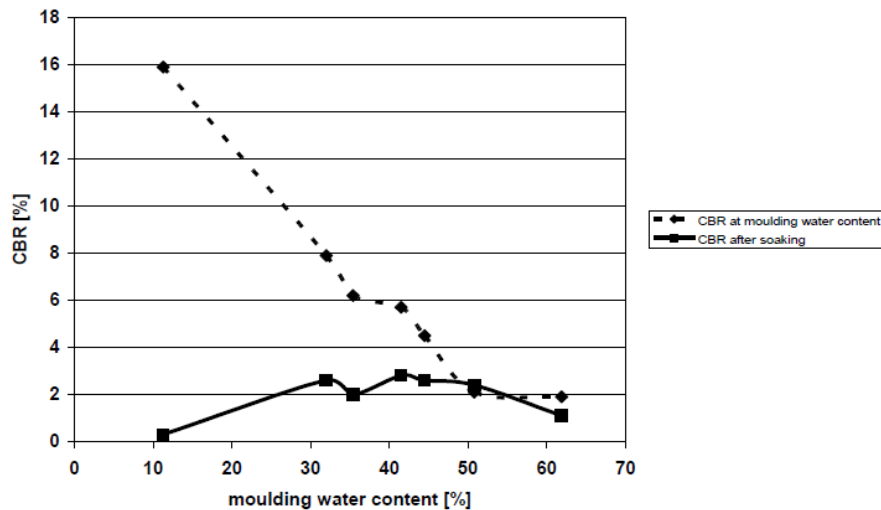


Figure 245: CBR vs moulding water content and after soaking for the Black Cotton Clay (drawn line is after soaking, dashed line is CBR at moulding water content).

Figures 243 to 245 clearly show that this particular clay is a rather poor one especially in the presence of water. After 17 hours being submerged in water the occurring swell appeared to be around 20%.

Figure 246 shows that the plasticity indices significantly improved by treating the clay with lime. At lime percentages higher than 5% no significant further improvement developed so it appeared that 5% lime is the preferred amount of lime to be used.

As shown in figure 247, no further increase in pH level occurred at lime percentages higher than 5%. At 5% lime the pH is slightly higher than 12 indicating the presence of free lime. This also indicates that adding more than 5% lime makes no sense since this higher amount will not react with the soil.

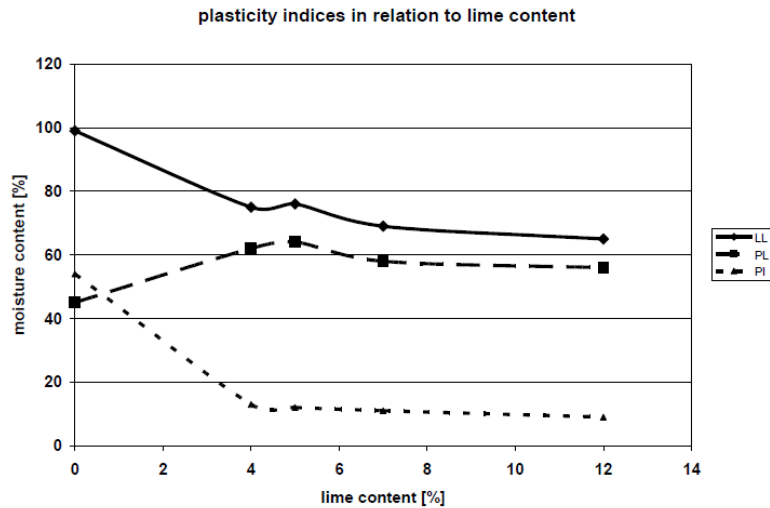


Figure 246: Plasticity indices of the Black Cotton Clay in relation to lime content.

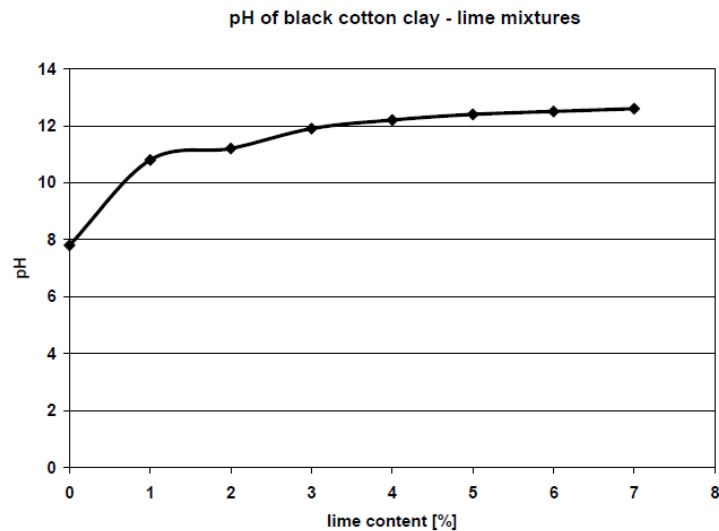


Figure 247: pH of Black Cotton Clay – lime mixtures.

At an initial moisture content of 15%, the swell of the clay mixed with 5% lime reduced to 5.1% after 96 hours being submerged in water.

The effect of the lime treatment on the CBR is shown in table 53. The samples were prepared at an initial moisture content of around 40%.

	0 days curing	7 days curing	28 days curing
0% lime	4.5		
5% lime	12	27	27
7% lime	20	35	39

Table 53: Effect of lime treatment on the CBR value [%].

Also the resilient modulus of the lime treated samples was determined. This was done by means of the repeated load CBR test. The results that were obtained are shown in table 54.

	0 days curing	7 days curing	28 days curing	After 48 hours soaking
0% lime	18			
5% lime		169	139	34
7% lime		226	312	456

Table 54: Effect of lime treatment on resilient modulus Mr [MPa].

Although figures 243 and 244 showed that adding more than 5% lime did not have an effect on the plasticity indices and that at those percentages free lime occurred, tables 53 and 54 show that adding a bit more lime (7% instead of 5%) does significantly increase the CBR and resilient modulus. The Mr values after soaking show that, from a mechanical point of view, adding 7% lime is to be preferred over 5% lime.

It has been mentioned above that adding lime results in flocculation and this may give the soil a totally different appearance. A clay with 10% of loam e.g. was stabilized with lime and after 14 days it looked like a sandy loam while after 20 days it looked like a sand!

As mentioned above, siliceous and aluminous materials in the soil react with lime to produce a gel of calcium silicates and aluminates. This gel cements the soil particles together in a manner that is similar to that of hydrated cement. Minerals in the soil that react with lime to produce a cementing compound are known as pozzolans. This lime-cementing action however is usually a slow process and it takes considerable more time than required for hydration of Portland cement.

It should be noted that carbonation occurs when the hydrated lime reacts with the CO₂ from the air. Although the formed carbonates (CaCO₃) add some strength (not much!!), carbonation "eats" so to say the lime and will therefore deter pozzolanic reactions.

13.3 Mechanical properties of lime stabilizations

As has already been discussed many times in the previous sections, mechanical properties like stiffness modulus and fatigue resistance which are needed to make an analytical based pavement design are very often based on relationships between a parameter that is rather easy to determine by means of simple laboratory tests and parameters like tensile strength, stiffness and resistance to fatigue. Such relationships are also developed for lime treated materials and some of them will be presented here-after.

Although his name doesn't appear in the list of references, Marshall Thompson, emeritus professor at the University of Illinois at Urbana-Champaign, should be given a lot of credit since he did a lot of work in characterizing lime treated materials.

Tensile and flexural strength

Little [84], in referring to Thompson reported the following relationships between the unconfined compression test on one hand and the tensile or flexural strength on the other.

$$\begin{aligned}\sigma_{it} &= 0.13 q_u \\ \sigma_f &= 2 \sigma_{it} \\ \text{So: } \sigma_f &= 0.25 q_u\end{aligned}$$

Where:

$$\begin{aligned}\sigma_{it} &= \text{indirect tensile strength,} \\ \sigma_f &= \text{flexural strength,} \\ q_u &= \text{unconfined compressive strength.}\end{aligned}$$

Modulus in flexure

Little [84] also reported a relationship between the unconfined compressive strength and the modulus of lime treated materials. This relationship is shown in figures 248 and 249.

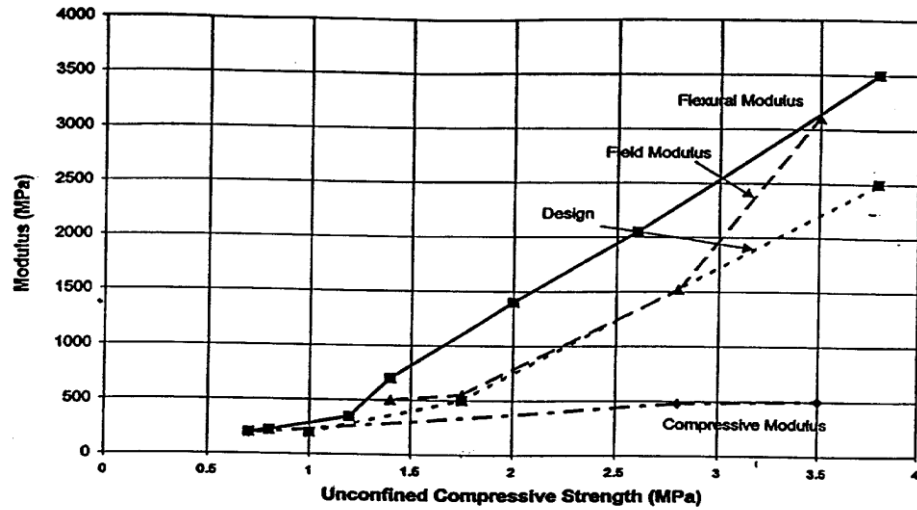


Figure 248: Relation between unconfined compressive strength and flexural modulus for lime treated materials [84].

Figure 248 presents a relationship between unconfined compressive strength and flexural modulus (based on data from Thompson e.a.), unconfined compressive strength and back calculated field moduli (determined from FWD data) and unconfined compressive strength and compressive moduli (based on data from Thompson e.a.). From this figure, it can be seen that the relationship between unconfined compressive strength and flexural modulus and between unconfined compressive strength and field (FWD back calculated) modulus are in reasonable agreement. The compressive modulus approximated from unconfined compressive strength data appears to be a conservative approximation of the modulus of the lime stabilized layer. Based on the findings summarized in Figure 248, a realistic and conservative approximate modulus for the lime stabilized layer that can be used in design approximations is presented by the dashed line in Figure 248. For clarity, this relationship is reported in Figure 249.

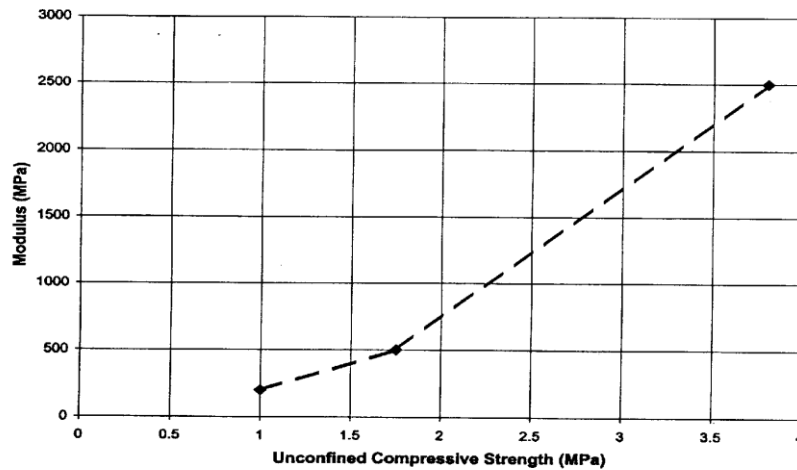


Figure 249: Relationship between unconfined compressive strength and the modulus of lime treated materials.

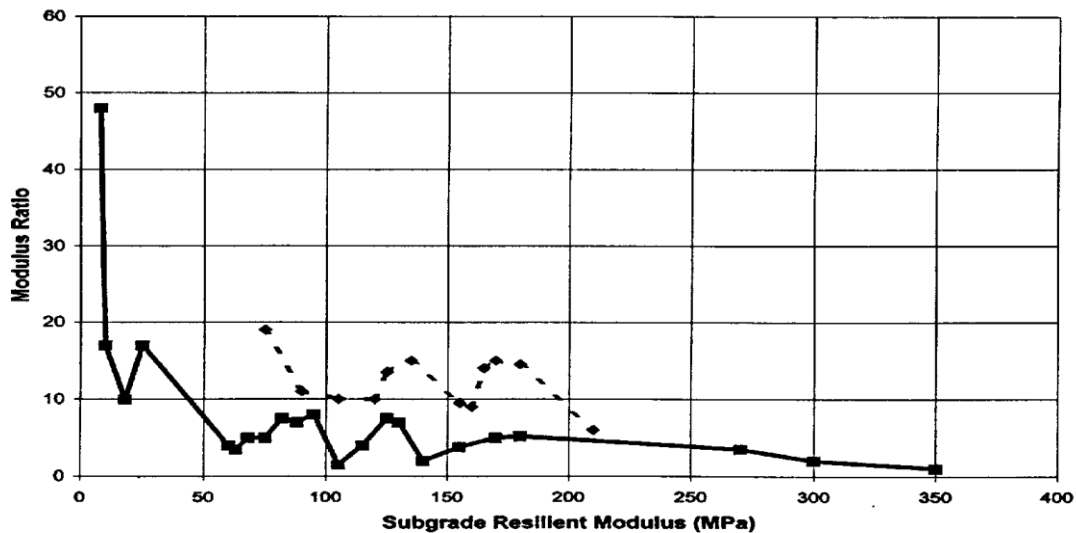


Figure 250: Ratio between the modulus of the lime treated subbase and the modulus of the original subgrade [84].

Figure 250 shows the ratio between the modulus of the lime stabilized subbase and the modulus of the subgrade. This figure was derived from layer moduli which were back-calculated from falling weight deflectometer measurements. These figure indicates that for natural subgrade moduli below about 50 MPa, the modulus ratio is typically 10 or above. For subgrade moduli between 50 MPa and 200 MPa, the modulus ratio is between 5 and 10, and for subgrade moduli exceeding 200 MPa, the modulus ratio is less than about 5.

Little et al also recommended a process by which to assign structural significance to lime-stabilized layers. The first step is to assign a realistic approximate resilient modulus to the layer. This can be done by either laboratory resilient modulus testing or from pre-existing field data. If laboratory testing is selected, then the resilient modulus should be determined in accordance with AASHTO T-294-94 after curing for 5-days at 38 °C. If laboratory testing facilities for such testing is not available, the resilient modulus can be approximated from unconfined compressive strength testing when compressive strength testing is performed in accordance with ASTM D 5102 or Texas Method TEX-121-E following a curing period of 5 days and at a temperature of 38 °C. Then, based on an empirical relationship between laboratory derived unconfined compressive strength and resilient modulus, determine the approximate resilient modulus of the lime-stabilized layer.

Fatigue

It will be no surprise that there is no unique fatigue relationship for lime stabilized materials. Type of soil, amount of lime, degree of compaction etc all have an effect on the fatigue resistance of the material. The fatigue relationships shown in figure 251 [79] can be written as follows:

Sable B	$\log N = 11.878 - 12.245 \sigma / \sigma_f$
Illinoisan till	$\log N = 15.882 - 17.882 \sigma / \sigma_f$
Bryce B	$\log N = 16.114 - 17.143 \sigma / \sigma_f$
Champaign County till	$\log N = 23.25 - 25 \sigma / \sigma_f$

Where: N = number of load repetitions to failure,
 σ = applied flexural stress,
 σ_f = flexural strength.

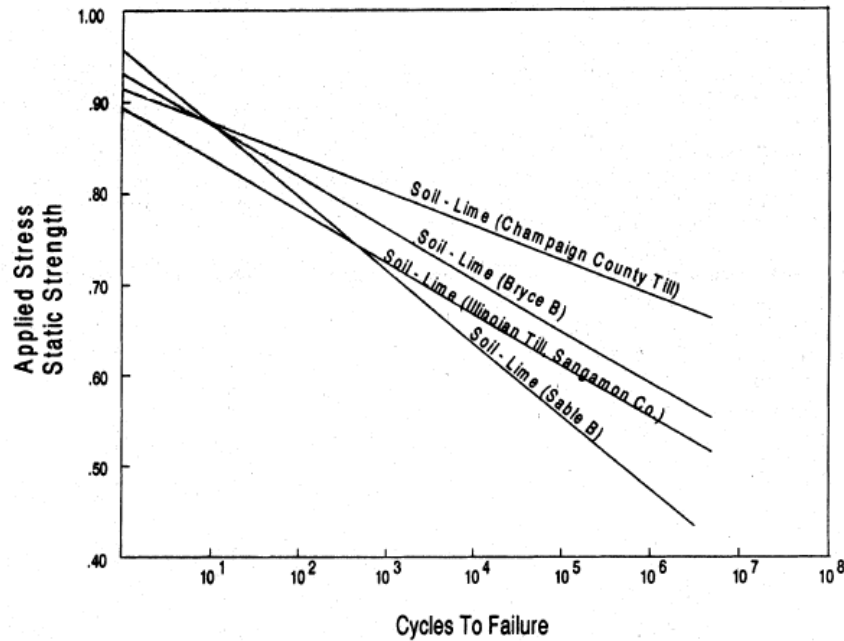


Figure 247: Fatigue relationships for lime stabilized soils as reported in [79].

Based on work done by Thompson e.a., Little [84] reported the following relationship:

$$\log N = 15.914 - 17.241 \sigma / \sigma_f$$

This relationship is shown in figure 252. As shown in figures 251 and 252, the stress ratio, ratio of induced tensile flexural stress to flexural strength, should be less than 0.50 to insure a fatigue resistant layer. Since the flexural strength is approximately 0.25 times the unconfined compressive strength and since the ratio of tensile strength induced within the stabilized layer should be less than 0.50, the critical flexural stress within the stabilized layer should not exceed 12 percent of the compressive strength.

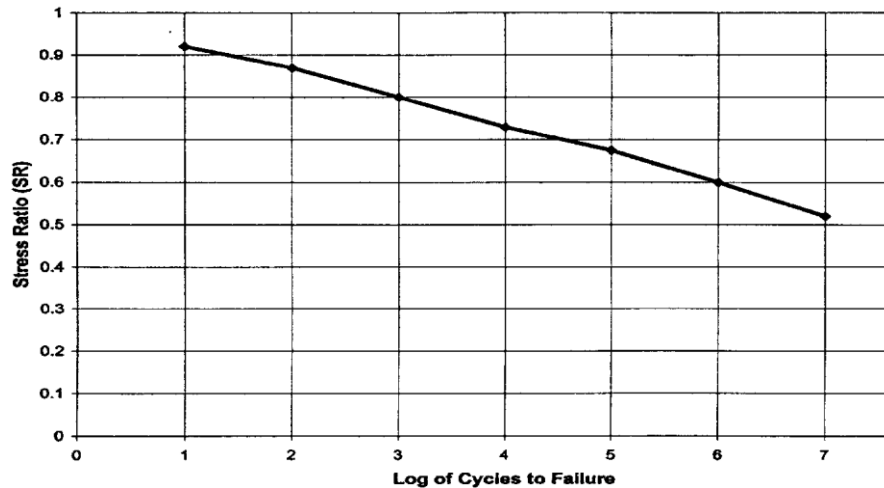


Figure 252: Fatigue relationship as reported by Little [84].

Like cement bound layers, also lime stabilized layers will show a development in strength in time and based on data given in [79], Molenaar developed the following relationship to make a rough estimate the flexural strength as a function of time:

$$\sigma_{ft} / \sigma_{f, t = 24 \text{ hours}} = -1.315 + 0.736 \ln(t)$$

t = time in hours

Durability

The reported strength values were obtained on properly manufactured and cured samples and an important question is what the strength characteristics would be after soaking. In [79] it is reported that the unconfined compressive strength after soaking is 70% to 85% of the strength which was obtained on specimens prepared under optimal conditions. It was also reported that in case lime stabilizations get "wet", the degree of saturation in most cases was limited to 90% to 95%.

14. Factors affecting pavement design and performance

14.1 Introduction

At this stage we have discussed how stresses and strains in pavements due to traffic loads can be calculated and how the input which is needed for pavement design and performance predictions can be obtained/estimated. Before we discuss how the design process is carried out, we need to discuss first of all some factors that affect pavement design and performance. Such factors are:

1. lateral wander,
2. the limited width of the pavement,
3. design considerations when using cemented bases and subbases,
4. design considerations when using bases and subbases of e.g. blast furnace slags.

14.2 Lateral wander

It is a well-known fact that cars and trucks don't drive in a perfectly straight line; in practice some ***lateral wander*** always occurs. Because of this lateral wander, the maximum stresses and strains don't always occur in the same location. This again implies that the allowable number of wheel passages is actually larger than the number of peak tensile strain repetitions that can be taken in a specific location. The amount of lateral wander that occurs depends mainly on the lane width. Furthermore the stiffness of the pavement determines the load spreading and determines whether e.g. the tensile strain is fairly constant at the bottom of the asphalt layer or whether high strains occur locally (see figure 253).

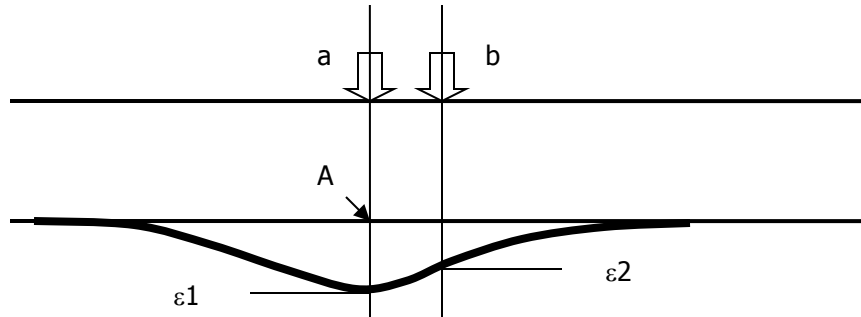
CROW [73] has developed a procedure to estimate the positive effect of lateral wander. This procedure is outlined hereafter.

First of all the radius of relative stiffness is calculated using:

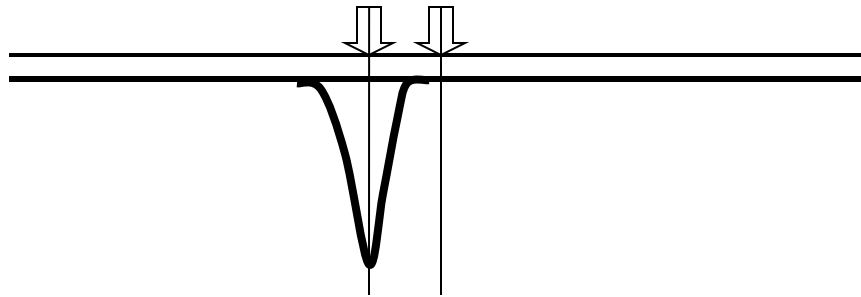
$$L_k = [E_1 h_1^3 (1 - \nu_s^2) / 6E_s (1 - \nu_1^2)]^{0.33}$$

Where: L_k = radius of relative stiffness [mm],
 E_1 = stiffness modulus of the asphalt layer [MPa],
 E_s = combined stiffness modulus of all layers below the asphalt layer [MPa],
 ν_1 = Poisson's ratio of the asphalt layer,
 ν_2 = Poisson's ration of the layers below the asphalt layers.

Figure 254 is then used to determine the lateral wander that will occur. That number together with L_k is then used in figure 255 to determine the correction factor on pavement life due to lateral wander.



The load at position a causes a tensile strain ε_1 in location A, the load in position b still causes a tensile strain ε_2 in point A. The effect of lateral wander is therefore limited.



In this case the load in position b causes no tensile strain in location A. The effect of lateral wander is therefore large.

Figure 253: Principle of the effect of lateral wander.

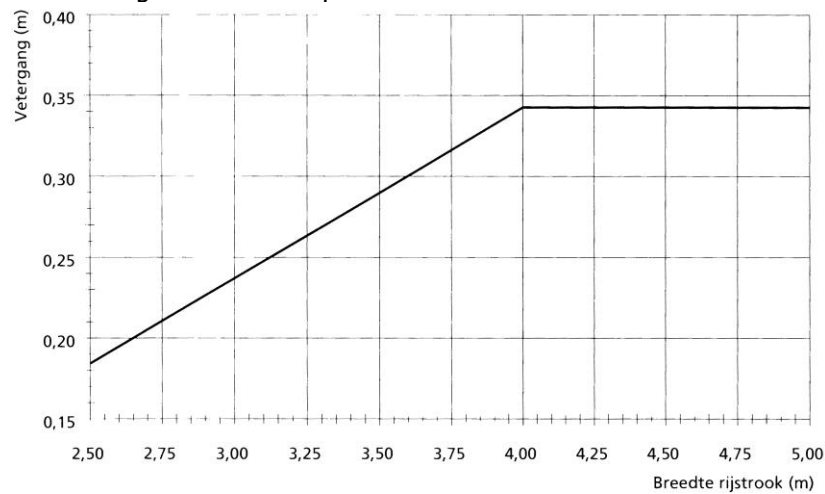


Figure 254: Lateral wander in relation to lane width.

Note: Breedte rijspoor = lane width; vetergang = lateral wander

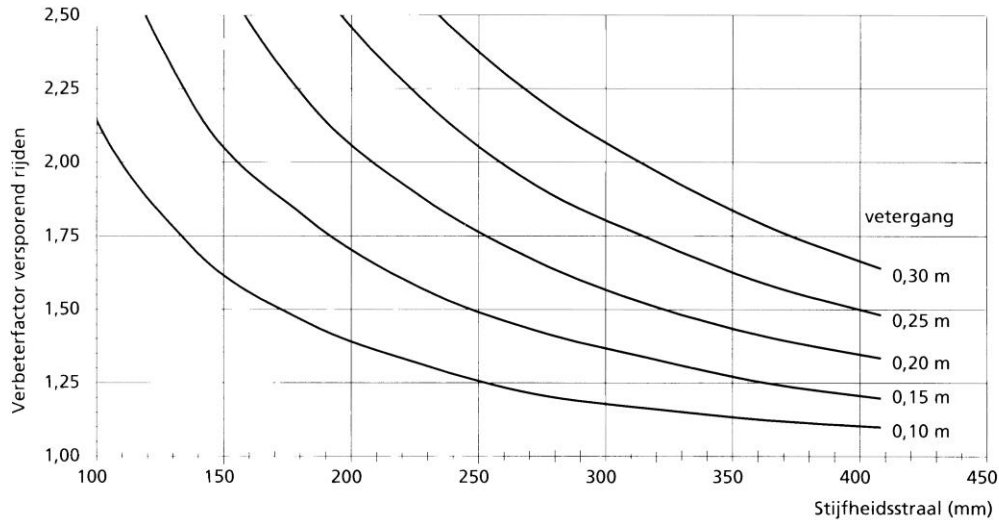


Figure 255: Correction factor on pavement life as a function of the lateral wander and pavement stiffness.

Note: stijfheidsstraal = radius of relative stiffness; vetergang = lateral wander; verbeterfactor versprend rijden = multiplication factor on pavement life due to lateral wander

Pvement life N is then calculated using:

$$N = \text{multiplication factor} * N_{fat}$$

Where:

N_{fat} = pavement life calculated based on the maximum tensile strain in the asphalt layer and a fatigue relationship.

14.3 Effect of limited pavement width

When a multi-layer linear elastic program is used for the calculation of stresses and strains, one implicitly assumes that the pavement has an infinite length and width, or in other words, one neglects the fact that the edge of the pavement can be very close to the wheel load. On narrow roads however, the wheel load can be very close to the edge of the pavement. An example of edge loading as well as the consequences is shown in figure 256.



Figure 256: Edge loading and its consequences.

In [73] also a procedure has been presented for the assessment of the edge effects. This procedure is presented hereafter.

First of all the distance to the edge of the pavement is determined using:

$$b_{\text{edge}} = (b_{\text{traffic lane}} - 2.50) / 2 - b_{\text{lateral wander}}$$

Where: b_{edge} = distance to the pavement edge [m],
 $b_{\text{lateral wander}}$ = as determined by means of figure 254.

Next we determine the radius of relative stiffness L_k using the relationship when discussing lateral wander. L_k is then used as input for figures 257 and 258.

Figure 257 shows the multiplication factor that has to be applied on the tensile strain at the bottom of the asphalt layer. Figure 258 shows the correction factor that has to be applied on the vertical stress at the top of the base layer. One should be cautious in using figures 257 and 258 because of the fact that lack of lateral support (figure 256 shows that in that case there is hardly any lateral support!) can have a very negative influence on the stiffness of the base and subbase. This effect is not taken into account in developing figures 257 and 258.

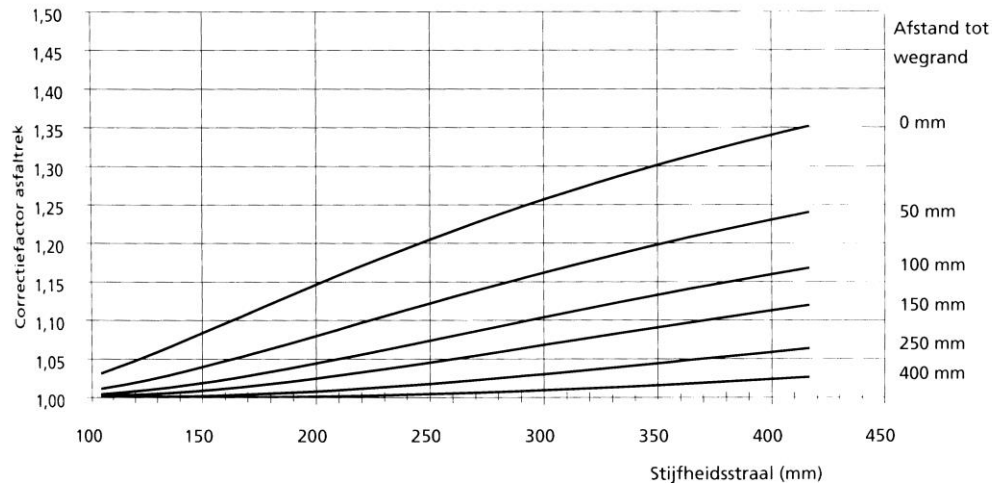


Figure 257: Edge effect on the tensile strain at the bottom of the asphalt layer.

Note: stijfheidsstraal = radius of relative stiffness; afstand tot wegrand = distance to the edge of the pavement; vertical axis gives factor by which calculated tensile strain should be multiplied.

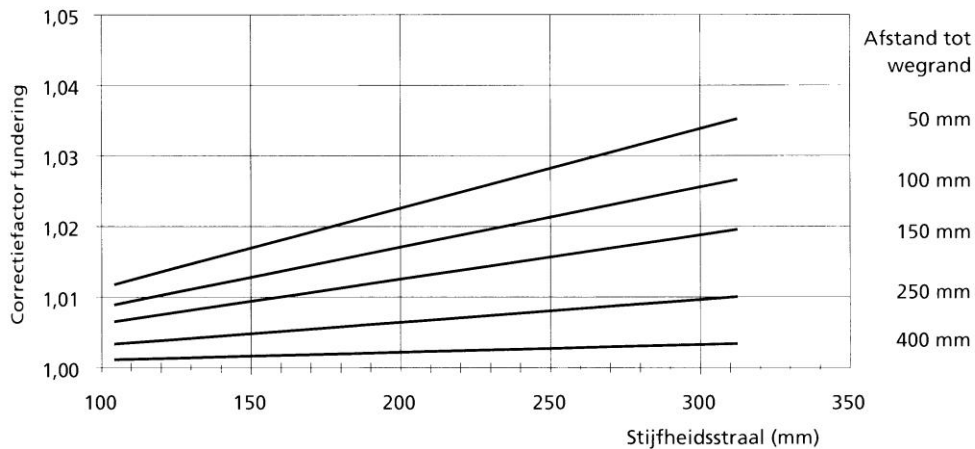


Figure 258: Edge effect on the vertical stress at the top of the base.

14.4 Design considerations when using cemented bases and subbases

In the previous sections ample attention has been paid to the fatigue characteristics of cement treated materials. Fatigue cracking is however a type of cracking that appears after many load repetitions. In reality transverse shrinkage cracks due to hardening and thermal movements might already develop shortly after the pavement has been constructed. Depending on the load transfer across these cracks, significant traffic induced tensile strains might develop parallel to these cracks resulting in longitudinal cracking. This phenomenon is schematically shown in figure 259 and figure 4 shows a real example.

In [85] some practical design guidelines have been developed to analyze the occurrence of these longitudinal cracks. It was shown that in winter time when the transverse cracks are usually open and the load transfer across the crack is limited, the tensile strain along the transverse crack is about 1.46 times the tensile strain that is calculated for an undamaged area. In summer time when the crack is closed, this multiplication factor amounts 1.2.

Furthermore it was shown that the probability of traffic induced cracking in sand cement bases like the ones used in the Netherlands is very low when the strain level is below $60 \mu\text{m/m}$ in the area between two transverse cracks.

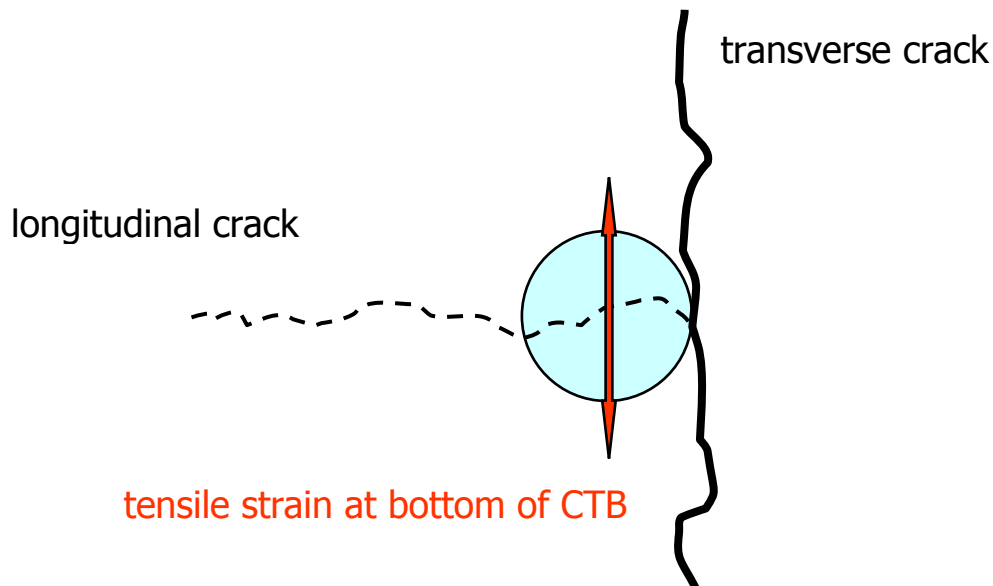


Figure 259: Principle of the development of a longitudinal crack in a cement treated layer near a transverse crack.

14.5 Design considerations when using bases and subbases of blast furnace slags (the text of this section is taken from [88]).

Slag mixtures are widely used in base and subbase layers for roads. These products are byproducts from the steel energy. In the Netherlands e.g. more than 1 million tons of granulated blast furnace slag sand (GBFS) was produced in 2011 which is mainly used for the production of cement. In the same year 0.6 million tons of steel slag was produced as well as 25000 tons of air cooled blast furnace slag (AC-BFS). Almost 100% of these slags were re-used and much of it was used in pavement construction. Figure 260 gives a schematic overview of the production of these slags.

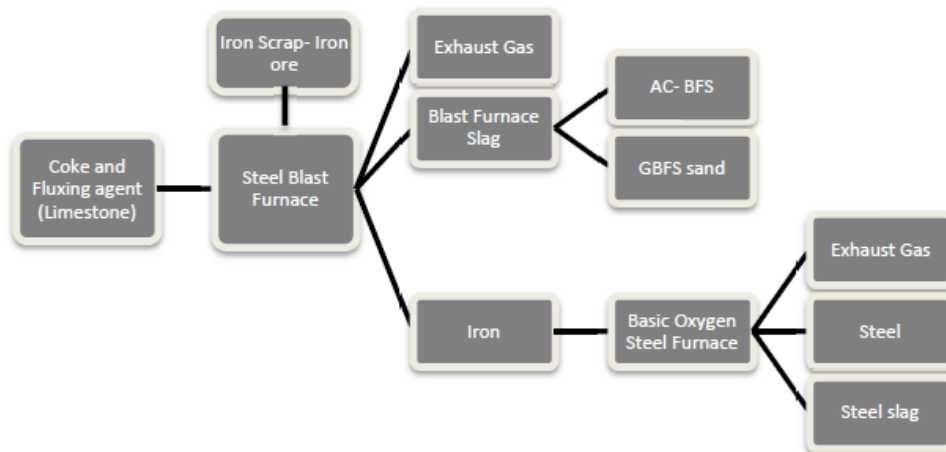


Figure 260: Schematic representation of the production of slags.

AC-BFS is formed when the liquid slag is poured into beds and slowly cooled under ambient conditions and crushed when cooled down. Crushed AC-BFS is angular, roughly cubical and has textures ranging from rough, vesicular (porous) surfaces to glassy (smooth) surfaces. There can be a considerable variation in properties depending on the iron production process. Some information on the composition of AC-BFS and its properties is given in tables 55 and 56.

CaO	SiO ₂	Al ₂ O ₃	MgO	FeO or Fe ₂ O ₃	MnO	S
34-45	27-38	7-12	7-15	0.2-1.6	0.15-0.76	1-1.9

Table 55: Composition of AC-BFS by mass.

Specific gravity [kg/m ³]	Los Angeles abrasion [%]	Sodium sulphate soudness loss ASTM C88	Angle of internal friction [°]	CBR maximum grain size 19 mm [%]	Water absorption [%]
2000-2500	35-45	12	40-45	Up to 250	6-8

Table 56: Some properties of AC-BFS.

The water absorption may seem high but little water is held in pores and most is held in shallow pits on the surface.

GBFS is formed when hot, molten blast furnace slag is rapidly chilled (quenched) by immersion in water. It is a granular product with little crystal formation and is cementitious in nature. Rapid quenching converts the slag into fine aggregate (usually smaller than 4.75 mm). When crushed or milled these fine aggregates have cementitious properties and can be used as replacement for cement. Generally the oxide analyses of AC-BFS and GBFS are similar.

The cementitious action of granulated blast furnace slag is to a large extent dependent on the glass content. Slowly (air) cooled slags are predominately crystalline and therefore not possess significant cementitious properties.

As table 57 shows, GBFS sand is basically a mixture made up of the same oxides as Portland cement but not in the same composition. This implies that the hydration reactions in GBFS sand will be slower than in Portland cement.

	SiO ₂	Al ₂ O ₃	Fe ₂ O ₃	CaO	MgO	SO ₃	Na ₂ O	K ₂ O	Cl
Portland cement	21.7	4.9	3.2	62.4	3.58	1.84	0.35	0.95	0.017
GBFS sand	33.03	10.87	0.25	38.45	10.26	<0.1	0.65	0.78	0.007

Table 57: Composition by mass of GBFS sand.

Steel slag from the basic oxygen furnace and electric arc furnace contains free unhydrated lime (CaO) which can cause volume instability.

It is this volume instability which can cause significant problems in terms of unevenness when these slags are used in pavements; examples of this are shown in figures 261.

To improve the strength of base courses made of BF slag, GBFS sand is often added which gives cementitious properties to the material. This not only means that the strength and stiffness are increased but also that BF slag base courses will shrink and expand due to a drop and rise of temperature. Furthermore volume changes might occur due to aging, moisture effects and freeze thaw cycles. Also an increase in volume might occur due to the formation of hydration products during the hydration process. Since hydration of these materials is a relatively slow process that can go on for a large number of years, these volume changes will develop slowly. Cracking does influence the process since moisture will enter the structure through the cracks and will affect the hydration process.

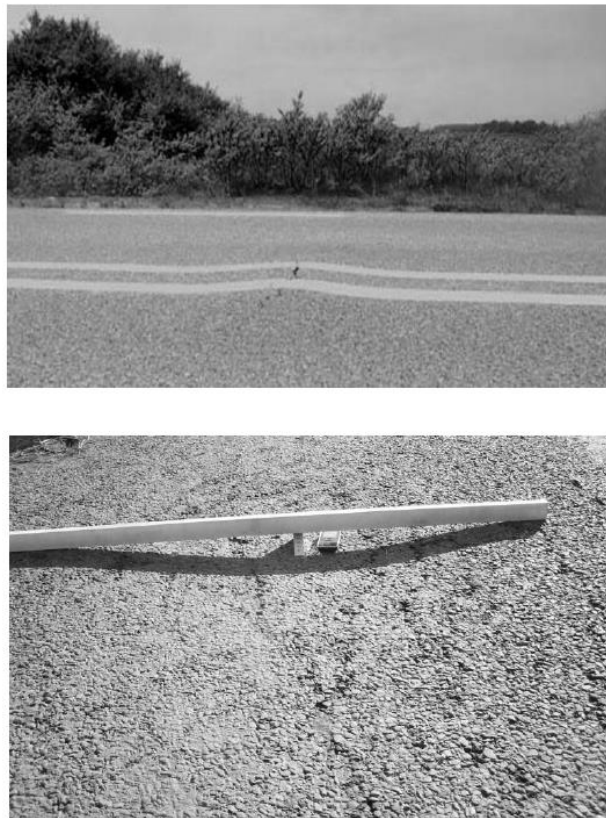


Figure 261: Heave and depression together with transverse cracking as observed on a Dutch highway in which a blast furnace base course was applied.

When the material expands, buckling might occur which results in heaves shown in figure 261. When the compressive stresses become too high, crushing might occur resulting in a loss of the stiffness of the material. Such a loss has been observed at the locations where the heaves, shown in figure 261, occurred.

Figure 262 shows the falling weight deflectometer deflections measured on a Dutch highway with a base course made of blast furnace slags. Heaves were present at the locations where the high peak deflections were measured.

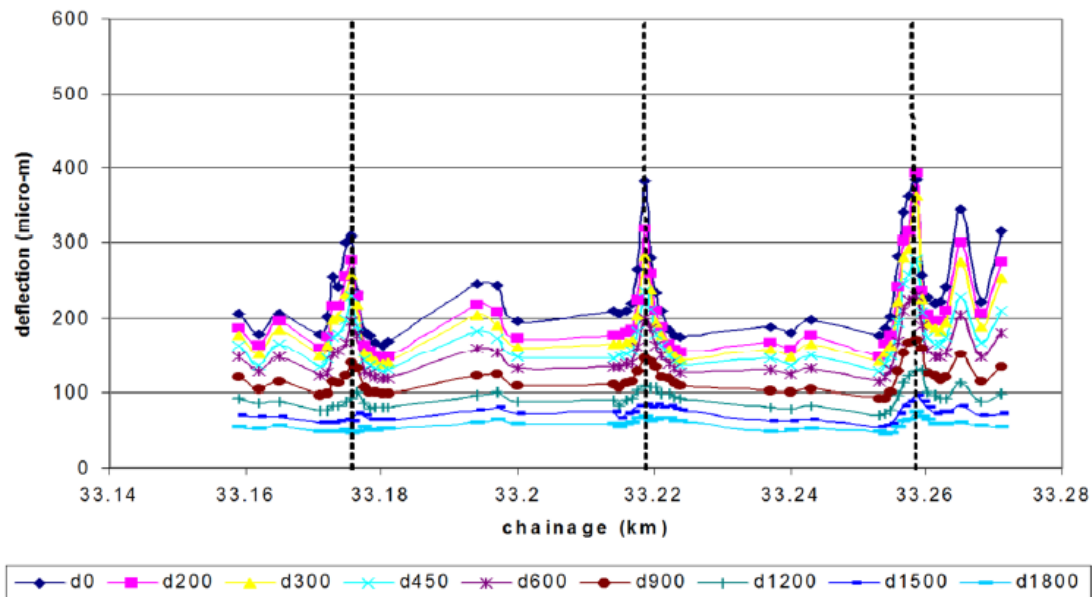


Figure 262: Deflections measured on a highway with a BFS base course on which heaves occurred.

It will be no surprise that the modulus of the BFS base course was very low at the locations of the heaves where the high deflections were measured. This is shown in figure 263.

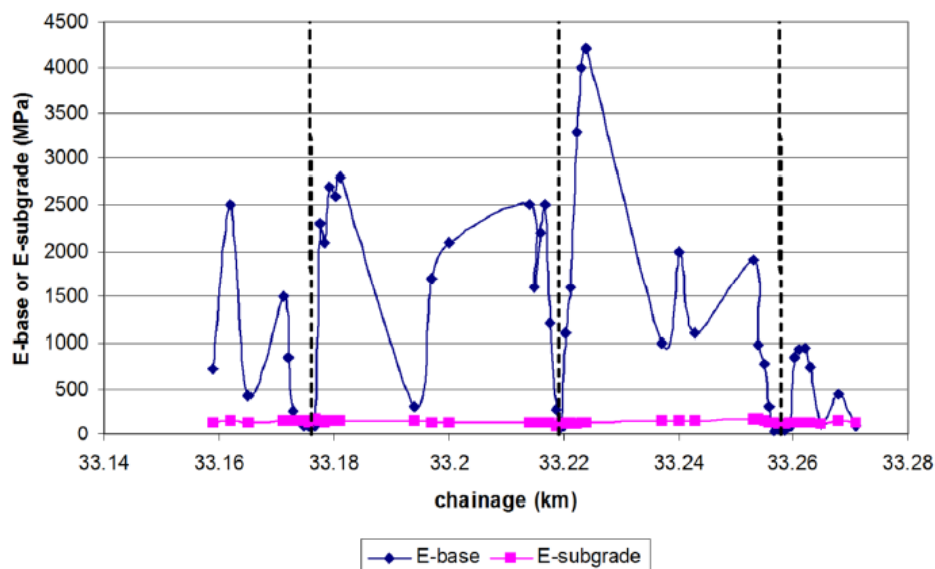


Figure 263: Back calculated modulus values for the BFS base and subgrade.

Akbarnejad [88] did extensive research on the characterization of base courses made of BFS, GBFS, steel slag and mixtures thereof and concluded that the sensitivity to volume change of these materials could be determined with:

$$\Delta V = (0.15 + 0.05 * \ln (S + 0.1)) * A$$

Where:

S = GBFS content (% by mass),

A = (CaO + MgO + Al₂O₃) / SiO₂ (% by mass).

If ΔV is larger than 1.5% then volume stability problems might occur.

Akbarnejad also developed a protocol to determine whether or not volume stability or other problems will occur with these types of materials. This protocol is shown in figure 264.

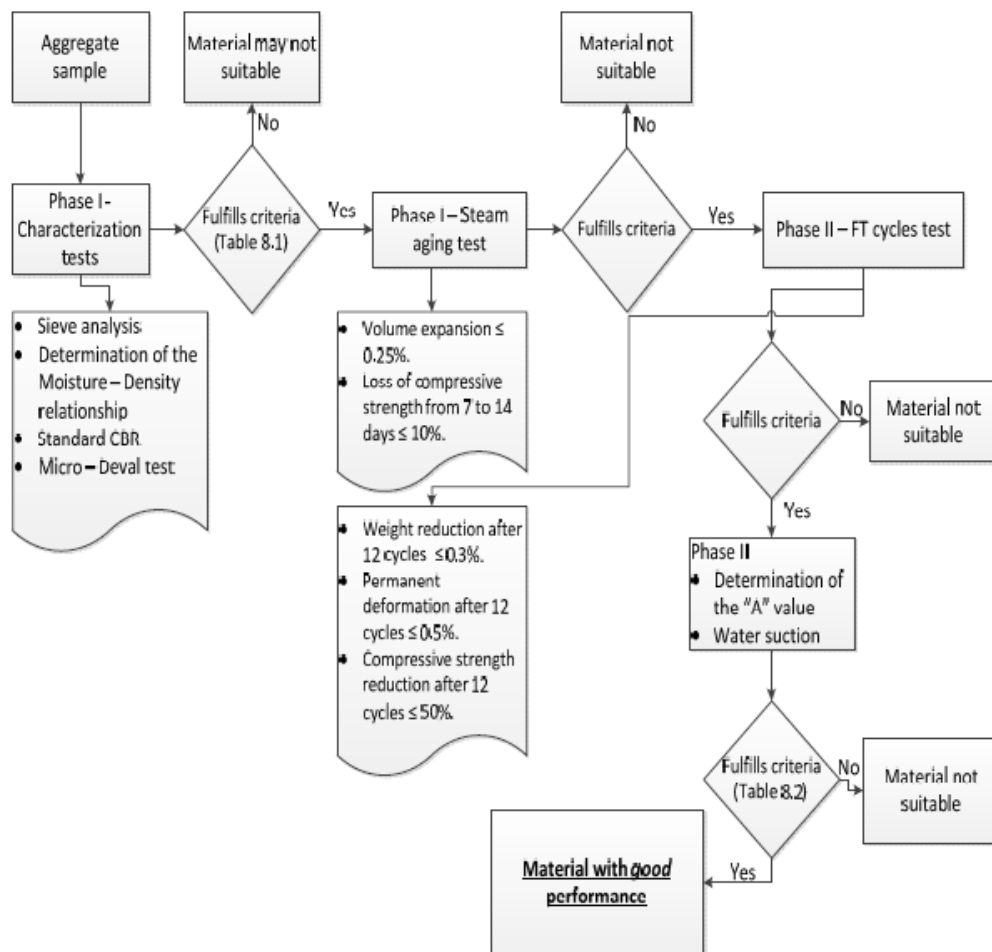


Figure 264: Protocol developed by Akbarnejad [88].

In the protocol reference is made to table 8.1 and 8.2. These tables are shown here as tables 58 and 59.

Aggregate Tests	Recommended Test Methods	Recommended Criteria
Sieve analysis	EN 933-1	
Determination of the Moisture – Density relationship	EN 13286-2	
Standard CBR	EN 13286-47, ASTM D1883 and Section 5.3.4	ΔCBR_{28} should be limited. The recommended value is $\leq 40\%$. Volume expansion $\leq 0.25\%$
Steam aging	See Section 7.7.3	Loss of compressive strength from 7 to 14 days $\leq 10\%$
Micro - Deval test	EN 1097-1	Micro – Deval coefficient $\leq 25\%$

Table 58: Table 8.1 as mentioned in the protocol.
Note: section 7.7.3 refers to section 7.7.3 in reference [88].

Aggregate Tests	Recommended Test Methods	Recommended Criteria
Freezing and Thawing (FT) test	See Section 6.3.5	Weight reduction after 12 cycles $\leq 0.3\%$. Permanent deformation after 12 cycles $\leq 0.5\%$. Compressive strength reduction after 12 cycles $\leq 50\%$.
Percentage of binding materials	XRD, XRF or Microprobe	By limiting GBFS sand content to 5% and steel slag content to 9% an acceptable performance can be expected.
Water suction	See Section 5.3.3	Weight increase (due to the suction) shall be less than 6% after 21 days. If higher than 6%, particular attention to the frost action is necessary.

Table 59: Table 8.2 as mentioned in the protocol.
Note: section 6.3.5 and section 5.3.3 refer to section 6.3.5 and section 5.3.3 in reference [88].

From the discussion given above it will have become clear that a proper investigation into the strength and volume stability characteristics of these slag type of materials is important to avoid unexpected failures to occur and premature maintenance to be needed.

15 Design aspects not related to thickness design

15.1 Introduction

Before we are going to discuss the thickness design process, we will first pay attention to some defect and damage types which are not related to thickness design. Such defects are:

1. shrinkage cracking,
2. reflective cracking,
3. top down cracking,

4. raveling and bleeding,
5. skid resistance,
6. noise production,
7. roughness/unevenness.

Occurrence of these defect types doesn't immediately affect the structural integrity of the pavement but do affect the amount of maintenance that should be applied and, when not maintained properly also will affect the structural life of the pavement. Moisture e.g. might enter the pavement structure through the shrinkage and reflected cracks causing weakening of the subgrade and reducing in this way the subgrade's stiffness and strength as well as the lifetime of the entire pavement. Even if the pavement is designed and built such that it can carry millions of load repetitions from a structural point of view, the above mentioned defect types might still occur and can therefore have a significant influence on the maintenance that is required.

15.2 Shrinkage cracking

An analysis of the development of shrinkage cracks in cement treated base courses made of crushed concrete and masonry is made by Xuan [86]. In his work Xuan made use of a very powerful EXCEL based analysis tool which was developed by Houben [89]. Some of the results obtained by Xuan when using Houben's program will be presented here.

When we assume a certain temperature drop to occur in an infinitely long cement treated base course, then the tensile stress as a result of that temperature drop can be calculated using:

$$\sigma_T = E * \alpha * \Delta T$$

Where:

- σ_T = induced tensile stress
 α = coefficient of thermal expansion
 E = elastic modulus of the cement treated base
 ΔT = temperature drop

Cracking will occur when the tensile stress becomes greater higher than the tensile strength.

At that stage the situation shown in figure 265 occurs and temperature induced stresses will develop again at a given ΔT because friction between the layer and the subgrade hinders free contraction of the slab.

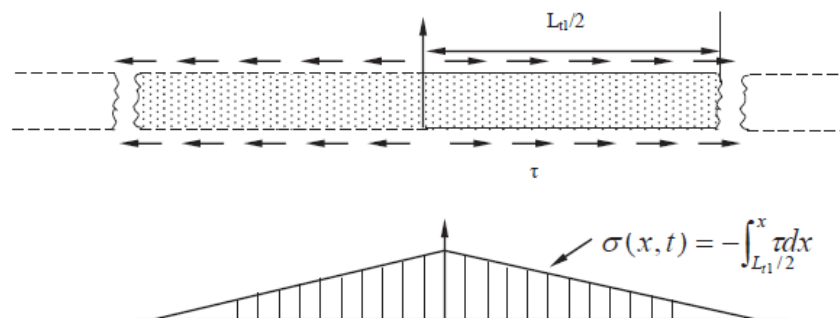


Figure 265: Shrinkage stresses in a cement treated base.

Because of equilibrium, the summation of the friction forces formed from the center of the slab to the free end is equal to the restrained tension force in the slab. So:

$$\sigma(t_1) * b * h = -L_{t1}/2 \int_0^0 \tau dx = \gamma * \rho * g * b * h * L_{t1} / 2$$

Where:

b = width of CTB [m]
h = thickness of CTB [m]
 γ = coefficient of sliding friction
 ρ = unit weight of the material [kg/m³]
g = 9.8 m/s²
L_{t1} = crack spacing at time t₁

When the induced stress equals the tensile strength, the crack spacing can be calculated using:

$$L_{t1} = 2 * \sigma(t_1) / (\gamma * \rho * g)$$

The initial crack (W₁) width can be calculated using:

$$W_1 = \sigma(t_1)^2 / (\gamma * \rho * g * E(t_1))$$

After cracking in the center of the slab, a reduction of the maximum tensile stress occurs which is equal to:

$$\Delta\sigma(t_1) = 0.5 * \sigma(t_1) + 0.5 * \sigma(t_1) * W(t_1) / L_{t1}$$

Accordingly the tensile stress in the slab becomes

$$\sigma'(t) = \sigma(t) - \Delta\sigma(t_1)$$

Where $\sigma'(t)$ = tensile stress after cracking at time t.

The change in crack width ΔW becomes:

$$\Delta W(t) = \sigma'(t)^2 / (\gamma * \rho * g * E(t)) - \sigma'(t_1)^2 / (\gamma * \rho * g * E(t_1))$$

and the crack width before the following crack develops equals

$$W(t) = W(t_1) + \Delta W(t)$$

The following remark should be made with respect to the induced tensile stress due to shrinkage. Shrinkage deformation only slowly changes because the daily and seasonal temperature are changing slowly. This implies that relaxation of the induced tensile stress does occur. Xuan adopted a stress relaxation model of the form:

$$R(t) = a * t^{-b}$$

Where R(t) is the amount of stress relaxation in [%] at time t. Figure 266 shows the shape of the model for different values of a and b which were assumed by Xuan.

Houben's model takes into account the effects of curing, implying that the strength slowly increases in time, and the effects of dry shrinkage are reduced. The total shrinkage is the sum of thermal shrinkage and the dry shrinkage.

Seasonal and daily temperature changes are assumed to be sinusoidal. For the Netherlands, the amplitude of the seasonal temperature change in the cement treated base course was calculated

to be 5 °C around an average temperature of 10 °C. On top of that a daily temperature variation with an amplitude of 3 °C was calculated.

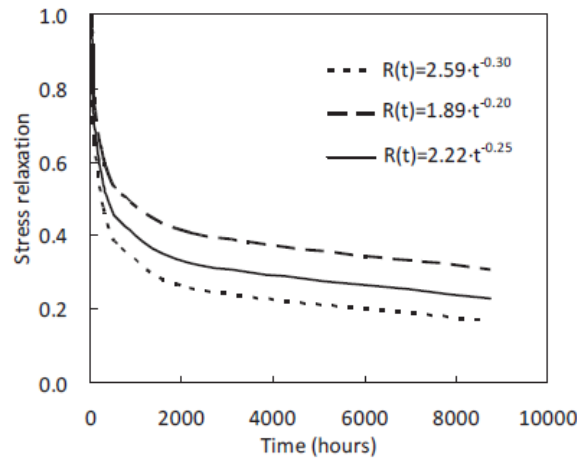


Figure 262: Stress relaxation models as adopted by Xuan.

Figure 263 shows the results of crack development analysis for a cement treated mixed granulate base course constructed on the first of May at 10 am, containing 65% recycled masonry and 35% recycled concrete. The mixture contained 4% cement, was prepared at a moisture content of 11% and was compacted to 101% degree of compaction.

As can be seen from the figure, the final average crack spacing was calculated to be 5m and crack widths as wide as 6mm and as narrow as 1mm were obtained. As we will see hereafter; especially these wide cracks can give rise to problems.

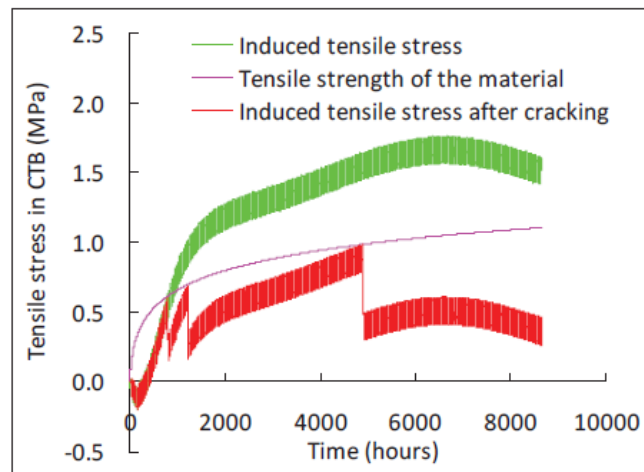
When no special precautions are taken, shrinkage cracking will occur at random and we will see cracks which are widely spaced and cracks which are rather closely spaced to each other. As we have seen from the equations given above, wide cracks are always associated with large crack spacings.

As mentioned before, moisture can easily enter these wide cracks and will soften the subgrade resulting in a loss of bearing capacity. Furthermore the load transfer across a wide crack will be poor and be the reason for additional cracking. Also this has been discussed before. The question therefore is how to avoid large crack spacings and wide cracks, how to regulate/control the shrinkage cracking? A simple but very effective solution is to cut so called shrinkage joints in the cemented base course just like this is done in concrete pavements. By means of sawing, the effective height of the base can be reduced to 60 – 66% of the original thickness. At these weakened joints, the shrinkage stresses will be much higher and shrinkage cracking will therefore happen at these joints. When the joint spacing is limited to about 7m, the joint/crack opening will be limited and because of this the load transfer across the joint/crack will still be good and the tendency of the cracks in the stabilized layer to reflect through the asphalt layer(s) on top will be significantly reduced.

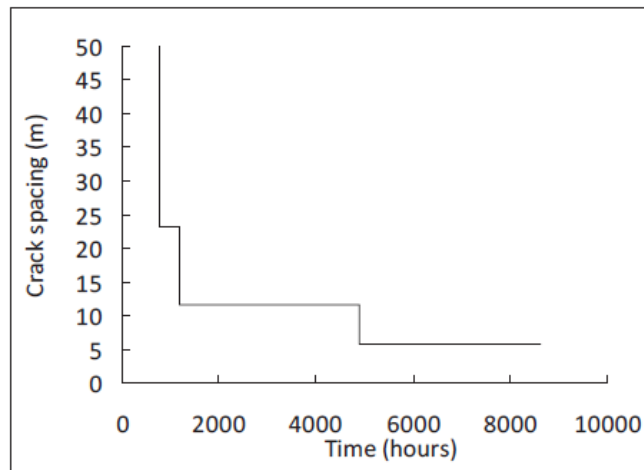
15.3 Reflective cracking

15.3.1 Introduction

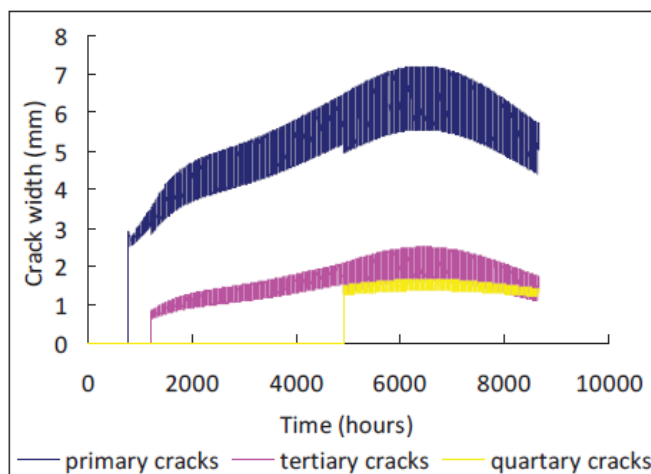
Shrinkage cracks which develop in a cementing base course (this could be a cement treated base or a base made of self-cementing materials) and these cracks will reflect sooner or later through the asphalt layers placed on top of the base. The speed by which this reflection of cracks will occur depends on the "activity" of the cracks which implies the magnitude of the horizontal movement at the crack due to shrinkage and the amount of vertical movement due to passing traffic loads. Both effects are schematically represented in figures 268, 269 and 270.



(a) Built-up of tensile stress



(b) Crack spacing



(c) Crack width

Figure 267: Crack development in a cement treated base course as calculated by Xuan [88] using Houben's computer program [89].

Thermal stresses due to shrinkage

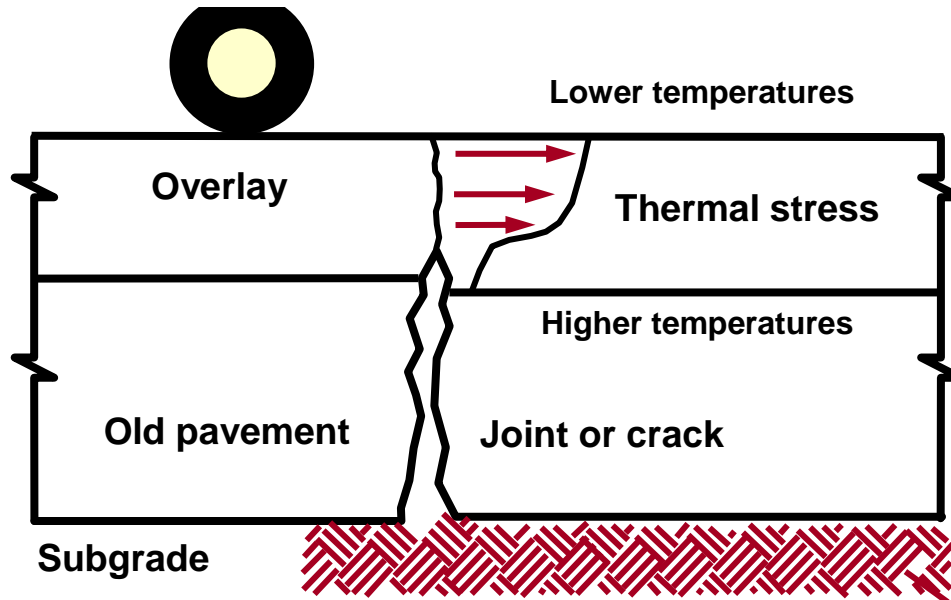


Figure 268: Crack reflection because of (thermal) shrinkage of the base course.

Thermal stress due to curling

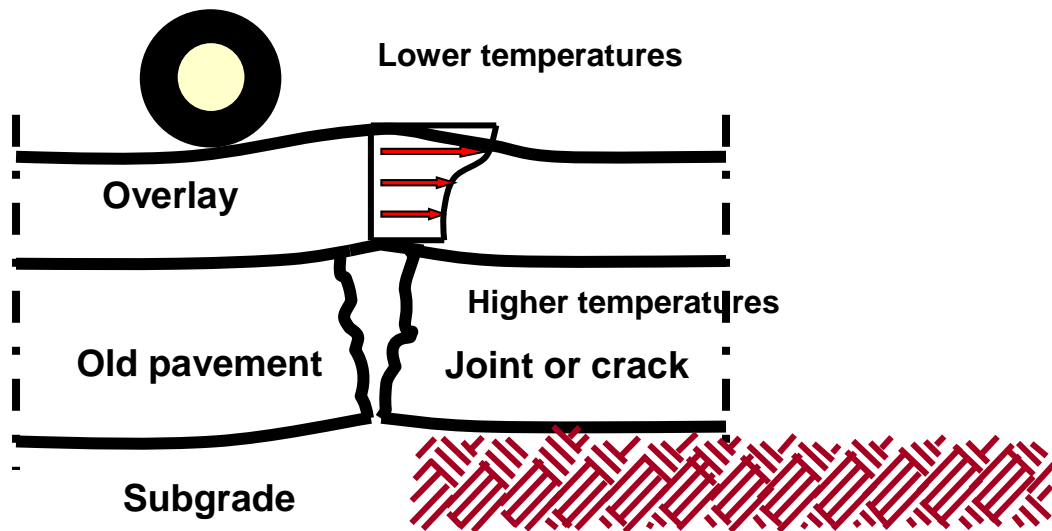


Figure 269: Crack reflection due to temperature induced curling of the cement treated base.

Shearing and Bending in HMA Overlay

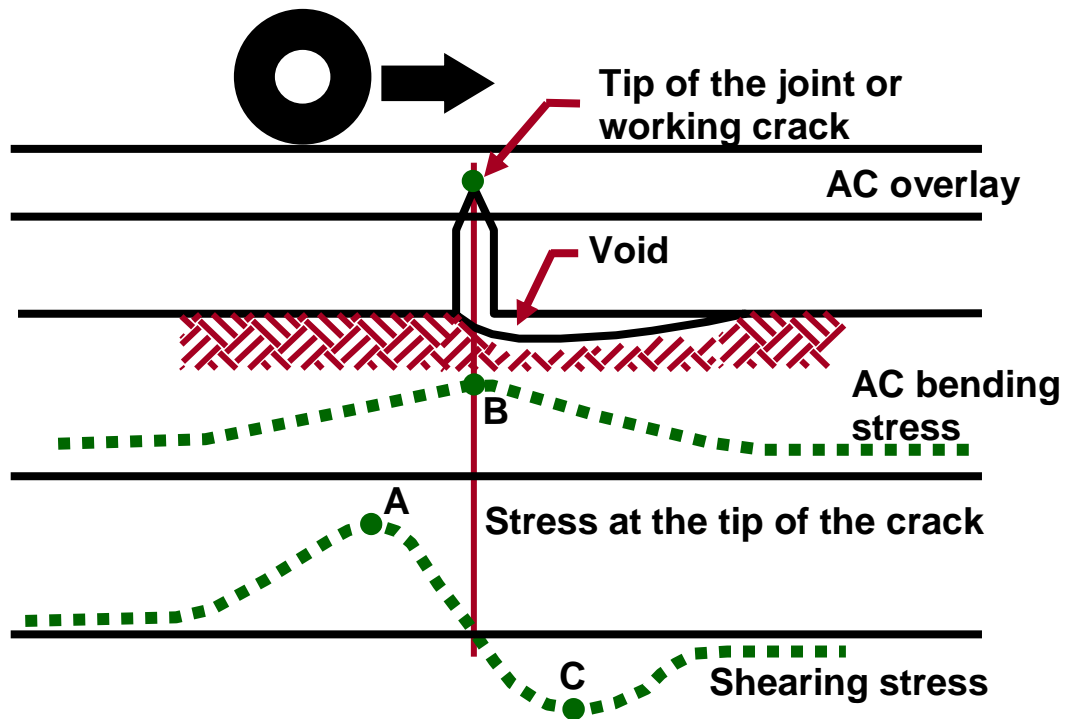


Figure 270: Crack reflection due to traffic loads.

As mentioned before, the effect of the mechanisms shown in figures 268 and 269 can be greatly reduced if the cement treated base is pre-cracked by sawing shrinkage joints in the base every 5 – 7 m just like in concrete pavements. What remains to be analyzed is the effect of traffic loads.

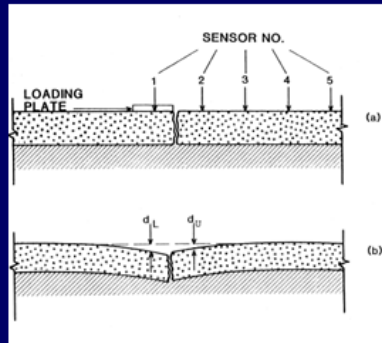
15.3.2 Measuring crack activity

The first thing that needs to be known is the activity of the crack. This activity can be measured by means of a falling weight deflectometer (figure 271) and placing the geophones as shown in figure 272.



Figure 271: Falling weight deflectometer.

Placement of geophones

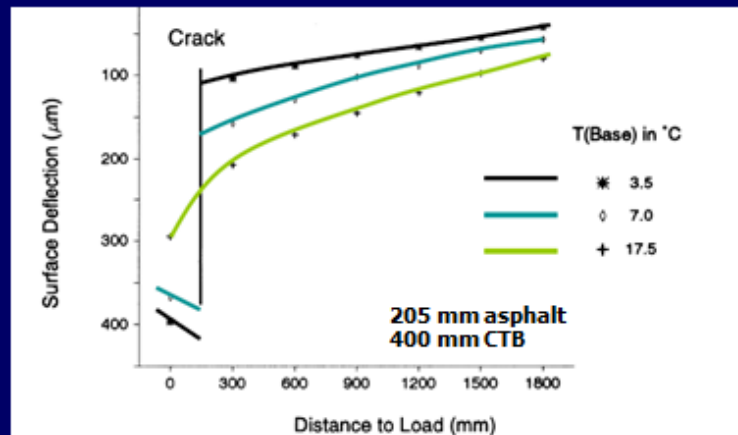


TU Delft

Figure 272: Placement of the geophones for load transfer measurements.

Figure 273 shows the deflections measured on either side of a transversal crack in a pavement consisting of 205 mm of asphalt on top of a 400 mm cement treated base [90]. Notice the very large differences in deflection between the measurements done at 17.5 °C (base temperature) and when taken at 3.5 °C.

Effects of bending and shear due to load in combination with crack width

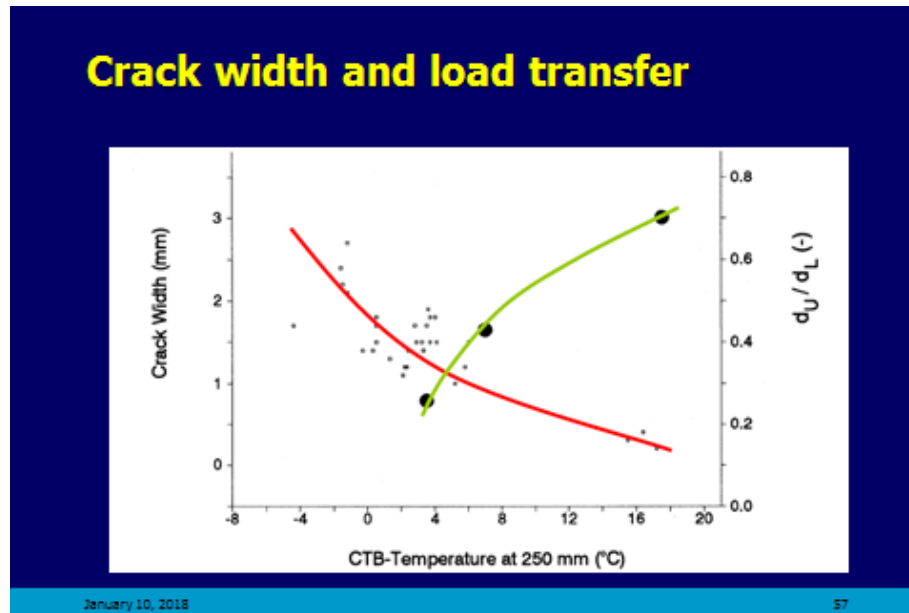


TU Delft

Figure 273: Deflections measured at a reflected crack at different temperatures.

Figure 274 [90] shows for the same transverse crack as discussed in figure 273, the ratio d_U / d_L in relation to the temperature in the base and the crack width. A high d_U / d_L relation indicates a good load transfer across the joint. At 4 °C the crack width appears to be approximately 1.2 mm while the d_U / d_L ratio is only approximately 0.28. This low ratio is due to the fact that the crack face in the cement treated sand base is rather smooth because of the small particle size of the sand. This implies that there will not be aggregate interlock because of the crack opening

combined with the rather smooth crack face. Figure 273 and 274 clearly show that a lot of vertical differential movement occurs at the crack at temperatures below 4 °C. Because of this the crack can be considered to be “active” at those temperatures. On the other hand, the d_u/d_L ratio at higher temperatures is much higher implying that much less differential movement is occurring. Under these conditions the crack can be rated as “not active”.



TU Delft

Figure 274: Load transfer and crack width determined for the pavement shown in figure 268.

Other interesting deflection test results are shown in figure 275 [90]. The figure shows that some very high d_{600}/d_{900} ratios are measured at a number of transverse cracks. These deflections are much higher than those which were measured between transverse cracks. The cracks with the high d_{600}/d_{900} ratios can therefore be considered as active cracks. It should be noted that the deflections shown in figure 275 were taken on the same pavement on which the results shown in figure 273 and 274 were obtained.

It will be no surprise at at locations where the cracks show a high “activity” fairly rapid propagation of the crack in the cement treated base through the asphalt top layer will occur.

15.3.3 Analysis tools for predicting propagation of reflection cracks through overlays

Crack growth analyses cannot be made by means of multi-layer linear elastic programs like BISAR; one has to use a finite element program in order to be able to do a proper job on this. An excellent example of such a program is the TxACOL program developed at the Texas Transportation Institute (TTI) at the Texas A&M University [91]. The program takes into account cracking due to shrinkage as well as cracking due to wheel loads. It calculates the development of reflective cracking using fracture mechanics principles in relation to the number of load repetitions as well as the permanent deformation development. The stress intensity factor K due to bending and shearing as a result of traffic loads as well as the stress intensity factor K due to temperature induced shrinkage cracking are calculated and the growth of the crack is determined using Paris' law:

$$dc/dN = A * K^n$$

Deflection measurements at cracks and between cracks tell about severity of cracks

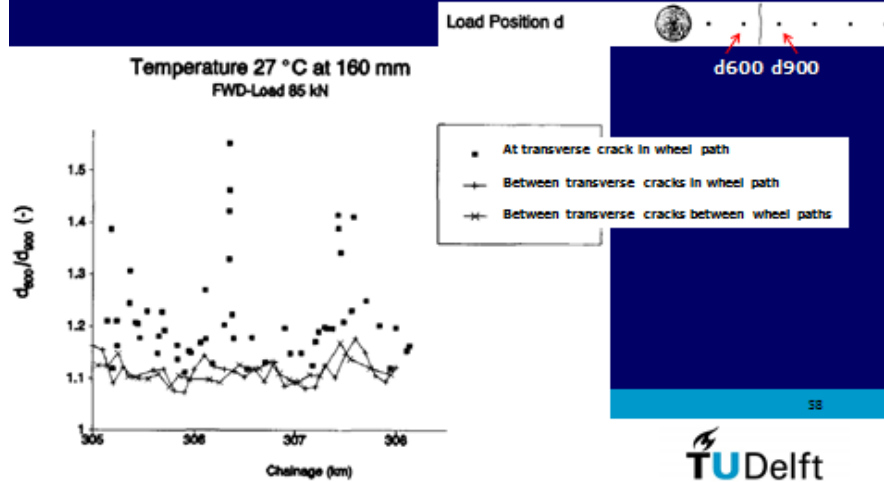


Figure 275: Deflection ratio d_{600} / d_{900} as determined on a pavement with a 400 mm thick cement treated sand base and 205 mm of asphalt concrete.

Input parameters are traffic and climate data, layer thickness and modulus values, fracture properties A and n, coefficients of thermal expansion, resistance to permanent deformation data. Figure 276 shows an examples of the output.

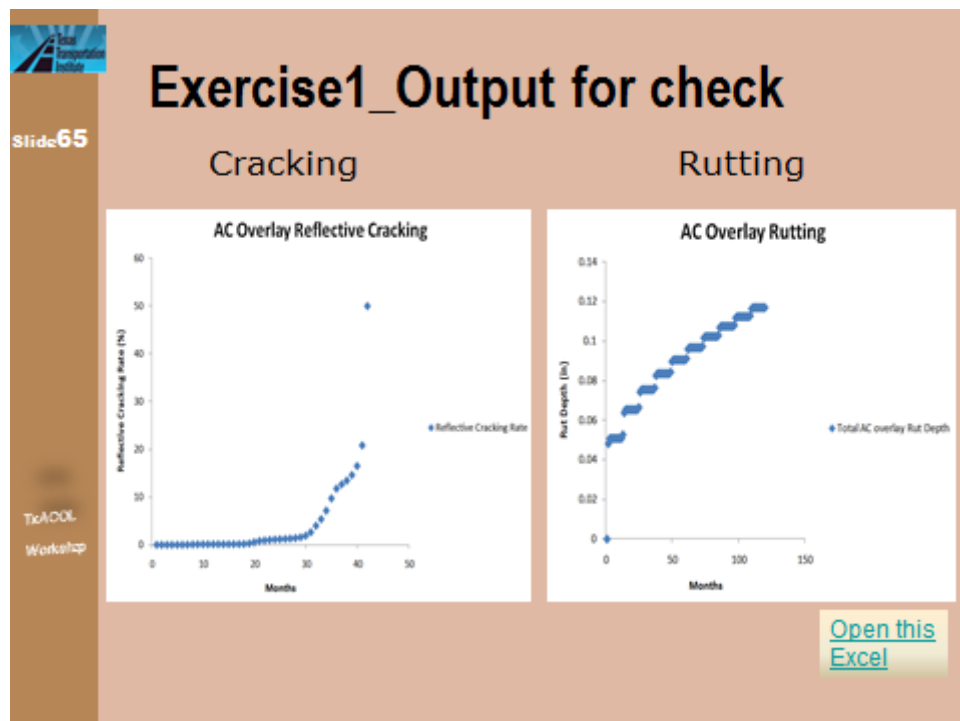


Figure 276: Example of the TxACOL output.

TxACOL itself is not a finite element program. The values for the crack intensity K due to shrinkage and traffic loads are obtained from regression equations which are based on a large number of finite element analyses. The regression equations for K_{bending} and K_{shearing} are based on more than 1,600,000 runs on 4 layer pavement structures (figure 277). The bending mode refers to the situation when the wheel load is precisely on top of the crack. The shearing mode refers to the condition when the wheel load is adjacent to the crack.

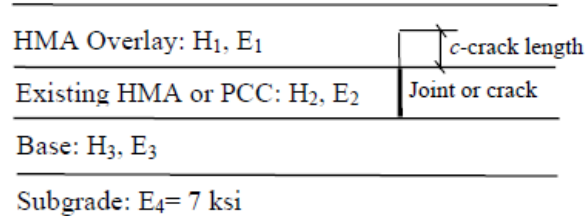


Figure 277: Pavement structures analyzed for the development of the TxACOL regression equations.

The K value due to bending and shearing is calculated following:

$$K_{\text{bending/shearing}} = K_a [K_b * (c/H_1)^3 + K_c * (c/H_1)^3 + K_d * (c/H_1)^3 + K_e]$$

The crack growth ΔC as a function of the increasing number of load repetitions (ΔN_i) is calculated using:

$$\Delta C = k_1 * A * (K_{\text{bending}})^n * \Delta N_i + k_2 * A * (K_{\text{shearing}})^n * \Delta N_i + k_3 * A * (K_{\text{thermal}})^n$$

An overview of the equations to predict K_a to K_e in case of an asphalt overlay on top of a concrete pavement (PCC) [91]. The term LTE stands for load transfer efficiency. Similar equations have been developed to calculate the stress intensity factor due to thermal shrinkage. These equations will not be reproduced here, the interested reader is referred to the literature [91].

Although TxACOL allows the crack growth to be analyzed for many pavement problems, it is clear that application of a general finite element tool like e.g. ABAQUS is needed for analyzing problems not covered by TxACOL and to analyze the effect of e.g. stress absorbing interlayers and reinforcements which are often used to retard or even stop crack reflection. Use of such advanced finite element packages however is still considered not to be feasible for solving every days engineering problems.

Before TxACOL came available simple approximation methods were developed and some of these methods will be presented hereafter. They are interesting because they allow a "quick and dirty" analysis to be made of e.g. the effect of using a polymer modified asphalt mixture relative to using a standard asphalt mixture.

A general applicable simple design system has been developed by Lytton [92]; this method is based on the propagation of cracks in fully supported beams. In the text hereafter the equations given in [92] will be reproduced. This is followed by an explanation of how this method can be used for analyzing crack reflection in pavements.

Let us consider the two loading conditions as shown in figure 278.

- HMA/PCC: $K_{bending}$ under single axle load of 18 kip

$$K_a = (-1.5900 \log H_3 + 7.5670 (\log E_3)^{-0.6674} + 2.9689 (\log H_2)^2 - 20.2856 \log H_2 - 0.6100 (\log E_2)^2 + 4.0389 \log E_2 + 31.0721) \times (1.9882 \log H_1 - 0.1908 (\log E_1)^2 + 1.0080 \log E_1 - 7.6964) \quad (2-6)$$

$$K_b = 7.1018 \times 10^{-6} (12.4974 (\log E_1)^2 - 76.5328 \log E_1 + 0.2502 f_1^2 - 16.9600 f_1 + 110.5739) \times ((\log E_3)^{0.5383} \times (\log E_2)^{7.7583} \times (\log E_1)^{-3.6878} - 22.2688) \times (-5.9056 (f_0 c)^{-0.8594} + 1.0855) \times (-18.4093 f_0 - 1.3660 \times 10^{-6}) \quad (2-7)$$

$$K_c = 0.0035 (-8.9941 (\log E_1)^2 + 102.1921 \log E_1 - 3.4384 f_1^2 + 17.7353 f_1 - 196.7209) \times ((\log E_3)^{-1.6440} \times (\log E_2)^{-9.2183} \times (\log E_1)^{7.8892} - 0.0595) \times (0.1618 (f_0 c)^{1.1273} + 1.0769) \times (27.6264 f_0 + 4.4900) \quad (2-8)$$

$$K_d = 0.0014 (-13.6682 (\log E_1)^2 + 57.5807 \log E_1 + 3.0213 f_1^2 - 90.3137 f_1 - 89.0447) \times ((\log E_3)^{0.0535} \times (\log E_2)^{4.7219} \times (\log E_1)^{-2.0160} + 21.3984) \times (-0.3612 (f_0 c)^{0.0255} + 0.4002) \times (9.0514 f_0 - 0.3287) \quad (2-9)$$

$$K_e = (0.0253 (\log E_1)^2 - 0.2021 \log E_1 + 0.3703) \times ((\log E_3)^{-1.6612} \times (\log E_2)^{-7.5751} \times (\log E_1)^{9.8212} - 2.8501) + 0.1013 \quad (2-10)$$

where f_0 , f_1 , Y , and I are defined below:

$$f_0 = (H_1 + H_2)^2 \times \left(1 - \frac{c + H_2}{(H_1 + H_2)}\right)^2 \times \left(\frac{YE_1}{6I}\right) \quad (2-11)$$

$$f_1 = YE_1 \frac{(H_1 + H_2)^2}{I} \quad (2-12)$$

$$Y = \frac{0.5E_1H_1^2 + E_2H_2H_1 + 0.5E_2H_2^2}{E_1H_1 + E_2H_2} \quad (2-13)$$

$$I = E_1 \left(\frac{H_1^3}{12} + H_1(Y - 0.5H_1)^2 \right) + E_2 \left(\frac{H_2^3}{12} + H_2(Y - H_1 - 0.5H_2)^2 \right) \quad (2-14)$$

- HMA/PCC: $K_{shearing}@LTE=10\%$ under single axle load of 18 kip

$$K_a = (-0.1070 \log H_3 + 10.6812 (\log E_3)^{-0.0835} - 0.5013 (\log H_2)^2 + 2.5971 \log H_2 - 0.2433 (\log E_2)^2 + 1.9193 \log E_2 - 15.7217) \times (-2.9156 \log H_1 + 0.7873 (\log E_1)^2 - 6.3932 \log E_1 + 22.6415) \quad (2-15)$$

$$K_b = 0.1304 (28.8189 (\log E_1)^2 - 136.1341 \log E_1 - 0.3764 f_1^2 + 6.9661 f_1 + 174.7384) \times ((\log E_3)^{-6.0701} \times (\log E_2)^{-2.2051} \times (\log E_1)^{-9.2409} + 1.3280) \times (-5.8771 (f_0 c)^{-0.0043} \times (f_0(c + H_2)))^{0.0073} + 5.8969 \quad (2-16)$$

$$K_c = 0.0942 (-0.2358 (\log E_1)^2 + 1.8967 \log E_1 + 0.0176 f_1^2 - 0.2746 f_1 - 2.5255) \times ((\log E_3)^{1.8761} \times (\log E_2)^{-0.3751} \times (\log E_1)^{3.3863} + 26.2623) \times (1.1298 (f_0 c)^{2.9561} \times (f_0(c + H_2)))^{-3.1189} - 0.0637 \quad (2-17)$$

$$K_d = 0.0020 (1.2828 (\log E_1)^2 + 13.3342 \log E_1 - 0.3373 f_1^2 + 4.8902 f_1 - 35.7626) \times ((\log E_3)^{3.3716} \times (\log E_2)^{0.4688} \times (\log E_1)^{-3.5661} + 3.8379) \times (-0.0850 (f_0 c)^{-0.7944} \times (f_0(c + H_2)))^{1.6155} + 2.2735 \quad (2-18)$$

$$K_e = (18.8600 (\log E_1)^2 - 102.7152 \log E_1 + 135.3821) \times ((\log E_3)^{0.0122} \times (\log E_2)^{-0.0183} \times (\log E_1)^{-0.0447} - 0.9054) + 0.3806 \quad (2-19)$$

Table 60: Example of K factors algorithms as used in TxACOL.

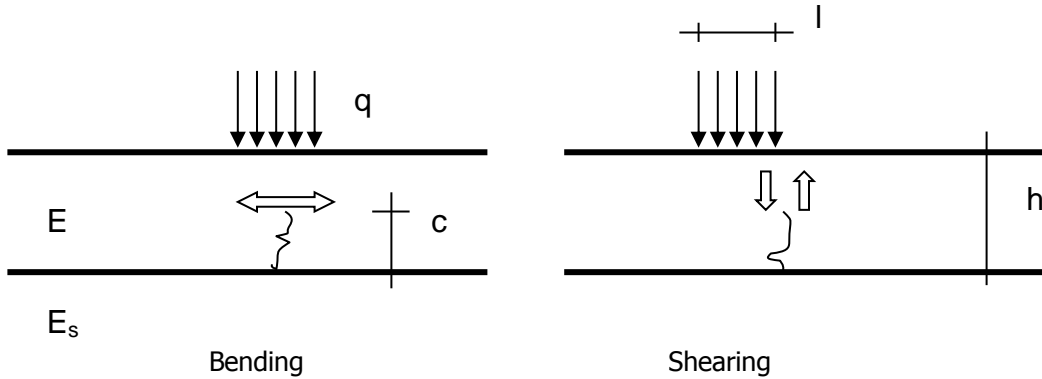


Figure 278: Crack propagation in a fully supported beam as a result of bending and shearing.

The stress intensity factors at the tip of the crack due to bending and shearing can be calculated in the following way.

$$K_{\text{bending}} = k_b \cdot q \cdot e^{-\beta/2} \cdot \sin(\beta \cdot l / 2) / \beta^2 d^{1.5}$$

$$K_{\text{shearing}} = k_s \cdot q \{1 + e^{-\beta l} \cdot [\sin(\beta \cdot l) - \cos(\beta \cdot l)]\} / 4 \beta \sqrt{d}$$

$$\beta = (E_s / E)^{0.33} / 0.55 d$$

Where: k_b = dimensionless stress intensity factor due to bending,
 k_s = dimensionless stress intensity factor due to shearing,
 q = contact pressure [MPa],
 l = width of loading strip [mm],
 c = length of the crack [mm],
 d = thickness of the beam [mm],
 E = modulus of the beam [MPa],
 E_s = modulus of the supporting layer [MPa].

Figure 279 shows how the dimensionless stress intensity factors change in relation to the ratio c / d . As one will observe, the stress intensity factor due to shearing increases with increasing crack length. This is logical because with increasing crack length, the area that has to transfer the load decreases so the stresses in that area increase.

Figure 279 however also shows that the stress intensity factor due to bending increases first with increasing crack length but then decreases to a value of zero. This is because of the fact that at a given moment the crack reaches the neutral axis of the pavement and penetrates the zone where horizontal compressive stresses are acting. Then the cracks stops to grow since the driving tension force has disappeared.

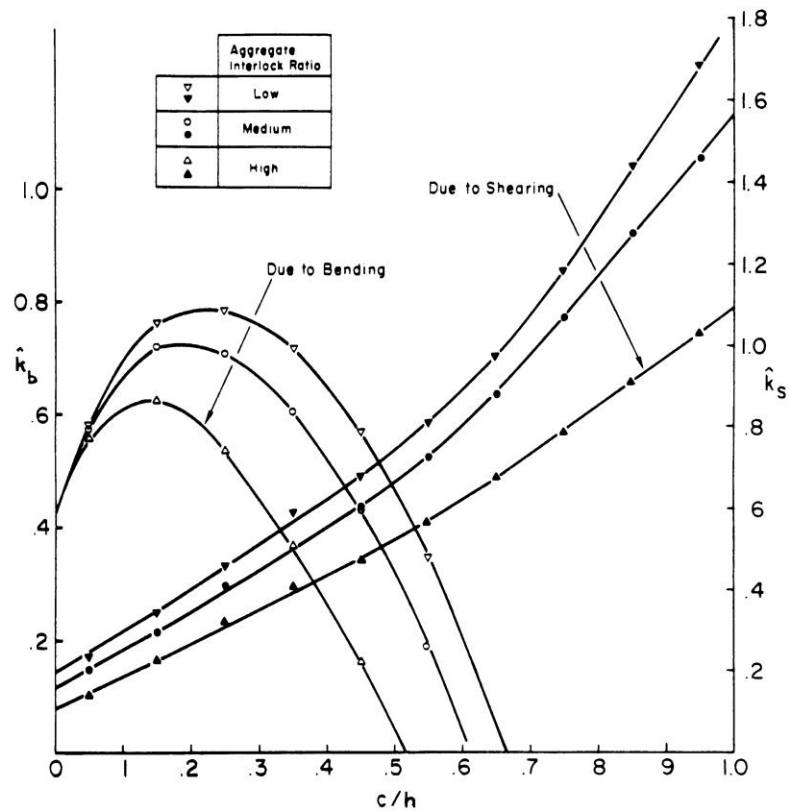
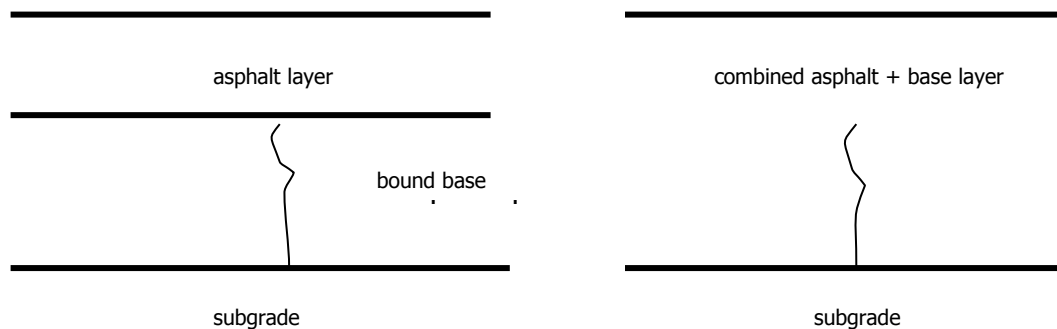


Figure 279: Relationship between c/h and the dimensionless stress intensity factors.

The question now of course is how this beam approach can be used for the design of overlays on cracked pavements. The first step how to schematize a cracked pavement is shown in figure 280.



- c = $h_{\text{bound base}}$
- h = $h_{\text{bound base}} + h_{\text{existing asphalt}}$
- E_s = E_{subgrade}
- E = combined modulus of asphalt layer and bound base

Figure 280: Schematization of structures with a cracked base.

The question now is how to arrive to the combined modulus values of the asphalt layer and the cement treated base. This is done using Nijboer's equation.

$$E = E_b \cdot \{[b^4 + 4 b^3 n + 6 b^2 n + 4 b n + n^2] / [(b + n) \cdot (b + 1)^3]\}$$

Where: E = combined modulus of asphalt layer and cement treated base,
 E_b = modulus of the cement treated base,
 b = thickness of cement treated base / thickness asphalt layer,
 n = modulus of asphalt layer / modulus of cement treated base.

The procedure is illustrated by means of an example.

Example:

Assume a given pavement that consists of a 100 mm thick asphalt layer on a 300 mm thick base which in turn is placed on a subgrade. The modulus of the asphalt layer is 6000 MPa. The base has a stiffness modulus of 3000 MPa and the subgrade a modulus of 100 MPa.

This means that: b = 3 and n = 2

First of all the E value of the combined asphalt – base layer was calculated using the above mentioned equation; this resulted in E = 4059 MPa.

Assume the contact pressure is 0.7 MPa and the width of the loaded strip equals 300 mm.

The value of β was calculated to be $\beta = 1.339 \cdot 10^{-3}$.

Given the fact that the c / h ratio equals 300 / 400 = 0.75, $k_s \approx 1.1$ if we assume medium load transfer.

Given all this information we calculate $K_s = 4.642 \text{ N} / \text{mm}^{1.5}$.

Please note that the product βl in $\sin(\beta l)$ and $\cos(\beta l)$ is in radians!

Since K_s is known, the crack propagation rate can be calculated using:

$$dc / dN = A K_s^n$$

Where: dc/dN = increase in crack length per load cycle,

A, n = material constants,

n = slope of the fatigue relation,

$\log A = -2.890 - 0.308 n - 0.739 n^{0.273} \log S_{mix}$,

S_{mix} = stiffness modulus of the asphalt mixture [MPa].

The number of load repetitions that is needed for the crack to reflect through the asphalt layer is calculated.

$$N = \int_c^d h_{asphalt} / K_s(c) dc$$

Where: $K_s(c)$ = stress intensity factor due to shear as a function of the crack length c.

The question now is to what extent beam theory is representative for real pavement problems. This is of course not the case and some shift factors resulting in similar stress conditions in the beam as in the real pavement are therefore necessary. The easiest way to do this is to compare the stresses at the bottom of the beam with the stresses that would occur at the bottom of the top layer (combined layer asphalt + bound base with modulus E) in the two layer system when calculated with a program like BISAR. Most probably the stresses at the bottom of the beam are higher than the stresses at the bottom of the layer. The correction factor that is needed to fit the stresses at the bottom of the beam to the stresses at the bottom of the layer can also be used as correction factor for the stress intensity factors.

Another simple analysis tool is the one developed by de Bondt [90]. He determined the stress intensity factors due to shearing and bending for a crack entering the overlay placed on a flexible pavement structure. Details of the structures and loading conditions analyzed by him are shown in figure 281.

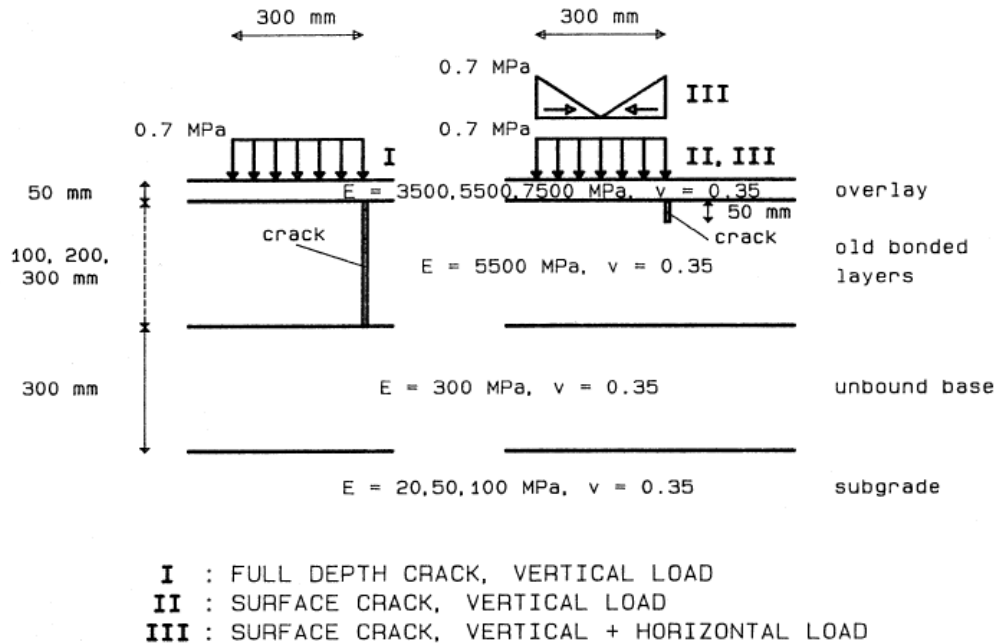


Figure 281: Pavement structures analyzed by de Bondt [90].

When analyzing crack growth due to traffic loads the stress intensity factor due to bending as well as the shearing have to be taken into account. Jacobs e.a. [93] developed a method to combine these two stress intensity factors into an equivalent mode one stress intensity factor $K_{I,eq}$. The magnitude of $K_{I,eq}$ for the structures and loading conditions shown in figure 281 are given in table 61.

$K_{I,eq}(c = 1 \text{ mm}) = p + qh_1^{-1} + rh_1 + sE_0 + tE_0^2 + uh_1E_0^2 + vh_1^3E_0 + wh_1^4E_0^4$									
	E_3 (MPa)	p (*e-2)	q (*e+2)	r (*e-3)	s (*e-5)	t (*e-8)	u (*e-11)	v (*e-12)	w (*e-26)
I	100	852	-1.00			5.00	-38.6	7.86	5.35
	50	446	1.32	13.6	38.9	-2.43	-14.5	-12.1	7.79
	20	612		7.91	66.5	-4.42	-22.6	-7.78	8.72
II	100	66.9	3.67		6.50				
	50	-4.23	3.73	1.87	22.4		-8.70		1.58
	20	35.6	3.78		29.4	-1.46	-5.67		1.47
III	100	-74.6	4.81	2.21					
	50	419	-1.36	-7.66	12.5		-9.59		3.31
	20	194			28.3	-2.29		-10.6	4.08

Table 61: Equation to calculate $K_{I,eq}$ for the structures shown in figure 276 and a 50 mm thick overlay.

Furthermore Jacobs e.a. developed an equation to calculate the so called K_{eff} that takes into account the fact that the stress intensity factor is changing when the crack is growing. How K_{eff} is calculated is shown in table 62.

$K_{eff}/K_{I,00}(c=1\text{ mm}) = p + (qh_1^{-1} + rh_1 + sE_0 + tE_0^2 + uh_1E_0^2 + vh_1^3E_0 + wh_1^4E_0^4)n^{-b}$										
	E_3 (MPa)	b	p (*e-1)	q (*e+1)	r (*e-4)	s (*e-4)	t (*e-9)	u (*e-11)	v (*e-13)	w (*e-27)
I	100	0.3	9.67		-7.97	1.98	-16.8	4.04		-7.90
	50	0.35	10.3	-1.29	-13.1	2.11	-10.3		15.9	-6.19
	20	0.35	10.4		-7.41	1.28	-3.69	1.03	11.2	-7.65
II	100	0.35	10.1	-1.94		2.14	-11.7			
	50	0.35	10.1	-1.82		2.16	-11.7			
	20	0.35	10.2	-1.87		1.96	-9.53		1.62	
III	100	0.35	10.7	-5.28	-35.9	3.55	-22.5	1.96	32.7	-12.3
	50	0.55	11.2	12.2	-70.5	1.93	-13.3	3.94	112	-39.2
	20	0.55	11.1	16.4	-64.9			8.66	123	-73.8

Table 62: Equation to calculate K_{eff} for the structures shown in figure 276 and a 50 mm thick overlay.

It should be noted that these equations were developed using a 2D finite element program and that no load transfer across the crack was assumed to occur.

15.3.4 Construction techniques to overcome reflection crack problems.

In principle there are four ways to limit/reduce reflective cracking being:

1. Application of a stress retarding system such as a SAMI together with a thin overlay.
2. Application of a reinforced overlay.
3. Application of an overlay with improved crack resistance characteristics.
4. Crack and seat or rubblizing the existing pavement.
5. In situ recycling.

Crack and seat techniques or rubblization the existing pavement and in situ recycling are powerful techniques to get rid of all the movements near joints and cracks. They are however not applied on new pavements and will therefore not be discussed here. The other techniques will be discussed hereafter into some detail. Readers who are interested in rubblizing techniques are referred to *Transportation Research Circular Nr. E-C087, January 2006* which is downloadable from www.trb.org/publications/circulars/ec087.pdf

Although methods 1 and 2 are mainly used when applying an overlay on a cracked pavement, they can of course also be applied in new pavements between a cementitious base layer and the asphalt top layer.

Application of a stress retarding system such as a SAMI together with a thin overlay

It has already been mentioned that reflection of shrinkage cracking in cement treated base courses can be controlled by sawing shrinkage joints in the base just like this is done in plain concrete pavements. But even in that case, horizontal movements will occur at the crack due to thermal shrinkage. When the structural capacity of the pavement is still sufficient and the vertical (shear) movements at the crack due to passing wheel loads is limited, the use of stress absorbing membrane interlayers is very effective to retard or even prevent reflection of the joints or cracks

through the asphalt overlay. A stress absorbing interlayer is a layer that allows the overlay to behave independently of the pavement on which it is placed. The interlayer should therefore have a low stiffness but also a high flexibility and should adhere very well to the top of the existing pavement as well as to the bottom of the overlay.

A SAMI (stress absorbing membrane interlayer) can be a polymer modified bitumen sprayed at a rate of 2 - 3 kg/m² on top of which a layer of chips is prayed, or a geotextile which is soaked in a polymer modified binder (pmb) or a bitumen-rubber. In such a case the geotextile act as a container for the sprayed binder. In such applications first a layer of pmb is sprayed after which the geotextile is placed on top of which another layer of pmb is sprayed. An example of a (non-woven) geotextile that can be used for such purposes is shown in figure 282.

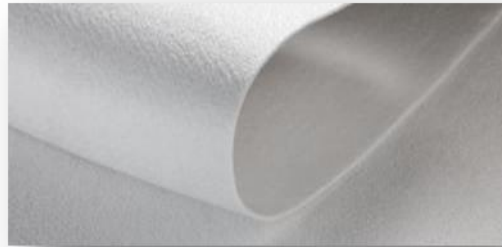


Figure 282: Example of a (non-woven) geotextile that can be used as a SAMI when soaked in polymer modified bitumen.

It should be mentioned that it is unrealistic to assume that such saturated non-woven geotextiles will act as reinforcement. These materials and SAMI's like thick layers of modified bitumen, are all of the "crack arresting family". They don't have any reinforcing effect.

Figure 283 summarizes some important aspects of SAMI's.

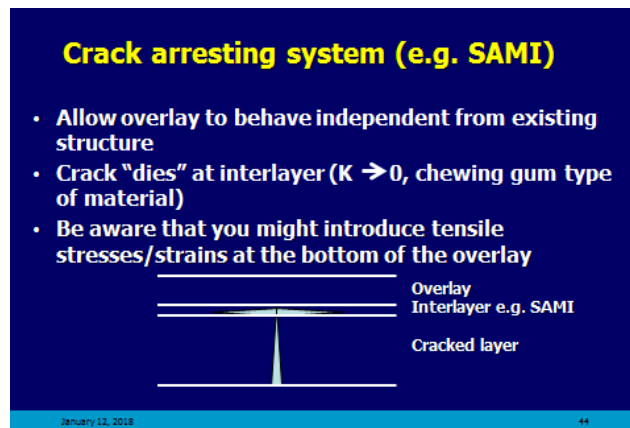


Figure 283: Summary of the most important aspects of SAMI's.

Figure 283 mentions that the crack "dies" in the SAMI because of its "chewing gum" type of behavior; figure 284 shows that this is indeed the case.

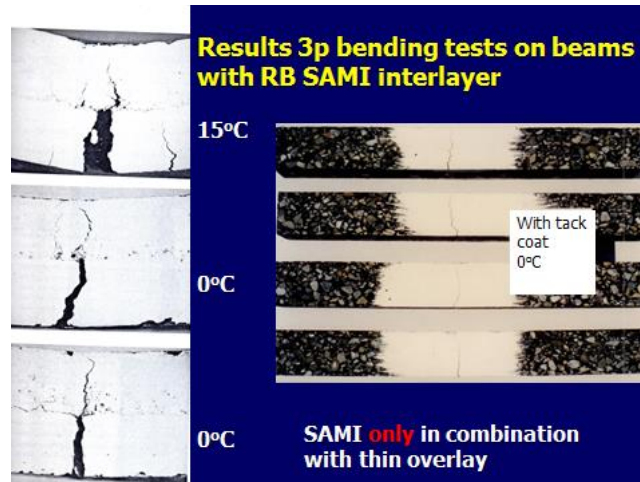


Figure 284: The left hand three pictures show that the crack is arrested at interface between two layers when a SAMI is applied at the interface. The three pictures at the right hand side show that the crack has easily propagated through both layers in case a tack coat was applied.

In figure 283 it is also mentioned that the overlay that is placed on top of a SAMI should be thin. This is because otherwise the overlay will attract too much stresses and will therefore fail early. In order to prove that this is really the case, Molenaar [39] analyzed a number of structures on which an overlay was placed assuming various thickness and stiffness values of the overlay and assuming a smooth interface between the overlay and the existing pavement. Such a smooth interface is in fact provided by a SAMI. The analyzed structures are shown in figure 285.

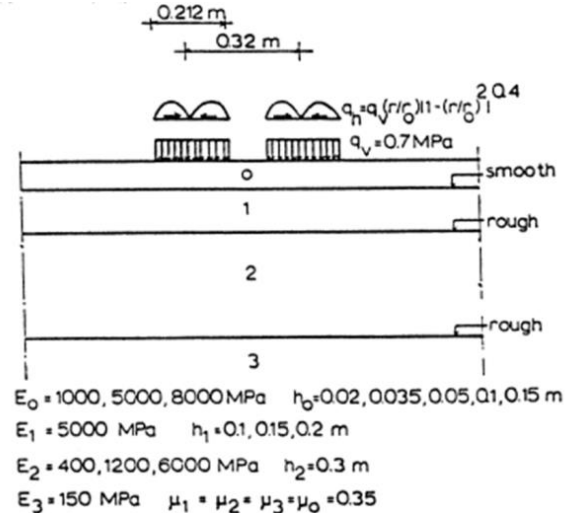


Figure 285: Structures as analyzed by Molenaar [39].

Figure 286 shows how the surface curvature index (SCI) of the deflection bowl due to a 50 kN load, decreased after placement of the overlay. The SCI is defined here as the difference between the maximum deflection (between the two wheel loads) and the deflection at a distance of 500 mm. As one will notice, the overlays will hardly add bending stiffness to the entire structure if a SAMI is applied between the overlay and the existing structure.

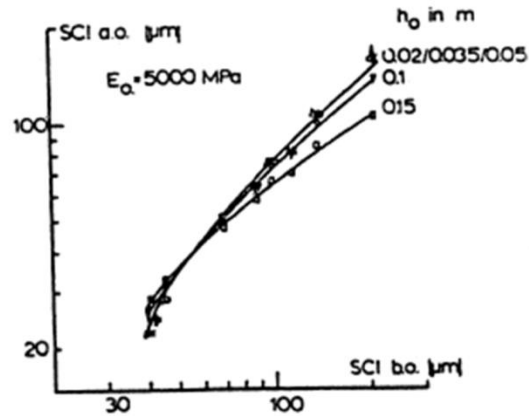


Figure 286: Increase in bending stiffness (decrease of SCI) after placement of an overlay which is "smoothly" connected to the existing pavement.

Figure 287 shows the tensile strain at the bottom of the overlay in relation to its thickness (h_o) and stiffness (E_o) and the SCI of the entire structure after placement of the overlay ($SCI_{a.o.}$) in case a SAMI is placed between the overlay and the existing structure. The figure clearly shows that placement of a thin overlay is the most effective solution because the lowest tensile strain will develop in that case.

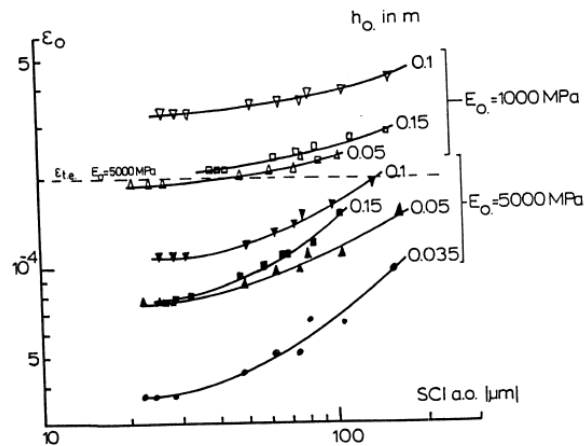


Figure 287: Tensile strain at the bottom of the overlay in case of using a SAMI between overlay and existing structure.

When discussing figure 286, it was already mentioned that a thin overlay which is "smoothly" bonded to the old pavement doesn't contribute too much to the bending stiffness of the entire pavement. Such an overlay will therefore also be not very helpful in reducing the tensile strains at the bottom of the asphalt layer of the existing pavement. This is clearly shown in figure 288; this figure shows that only in case of a thick overlay a reduction in the tensile strain in the existing asphalt layer will occur.

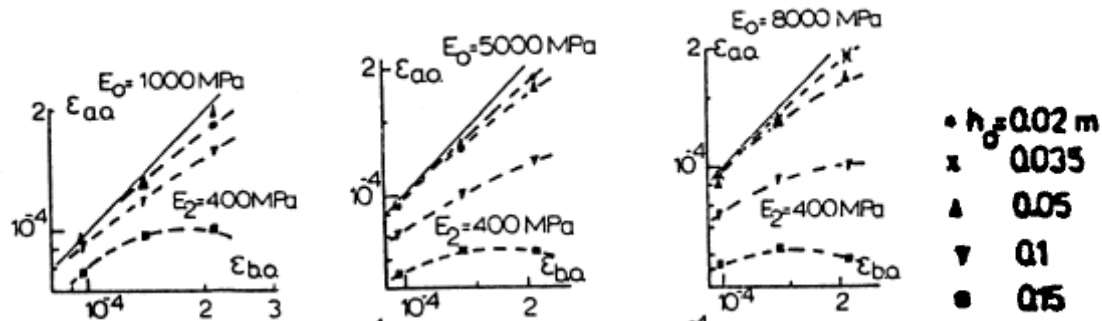


Figure 288: Relation between the tensile strain at the bottom of the existing asphalt layer after overlaying ($\epsilon_{a.o.}$), the thickness (h_o) and stiffness (E_o) of the overlay and the tensile strain in the existing asphalt layer before overlaying ($\epsilon_{b.o.}$) in case a SAMI is applied.

Once again, all these results show that a crack arresting (SAMI) system together with a thin overlay should preferably be used when the pavement still has sufficient bearing capacity and does show only a limited amount of vertical/shear displacements at the cracks due to wheel loads. Such a pavement could look like the one shown in figure 289 which shows no signs of permanent deformation or lack of bearing capacity (the visible cracking is most probably block cracking that reflected from a cement treated base) or could be a pavement which only suffers from top-down cracking.



Figure 289: Example of a pavement which could well be treated with a SAMI system.

Application of a reinforced asphalt concrete overlay

When a cracked pavement lacks structural capacity, the overlay to be placed needs to reduce the stresses and strains in the existing pavement. It is very important in such a case that the overlay is tightly bonded to the existing pavement. The disadvantage of this however is that the crack in the existing pavement that wants to grow through the overlay will not be "arrested" at the interface between the existing pavement and the overlay (which would be the case when a SAMI) would be applied, see above) but will propagate rather easily through the overlay when no special measures are taken. Reinforcement of the overlay is then an option to reduce the crack propagation rate. The requirements that should be set to a reinforcement in asphalt are in fact the same as those which are set for reinforcement of cement concrete. Some of the most important requirements are listed below.

1. The reinforcement should have a high $E \cdot A$ value (modulus * cross sectional area).
2. An excellent bond between the reinforcement and the mixture in which it is placed is absolutely required.
3. The mesh size of the reinforcement should be such that the asphalt mixture can go easily through the meshes; otherwise the reinforcement will act as a separating layer. This

- implies that the maximum grainsize of the aggregates in the mixture (D_{\max}) should be $D_{\max} = \frac{3}{4}$ of mesh opening and minimum mesh opening is 50 mm.
4. The reinforcement should preferably be able to provide some confinement because in that case it will also be helpful in reducing/limiting permanent deformation. The capacity of reinforcements reducing permanent deformation becomes very obvious when reinforcements are used in unbound layers (see figure 290).



Figure 290: Use of reinforcement in unbound layers to provide confinement and reduce the amount of permanent deformation.

Figure 290 shows a steel reinforcement on the left side and a cell structure on the right hand side. In principle the cell structure provides a much better confinement provided the unbound material can easily enter the cells and can be compacted properly after placement. Research by Kwon at the University of Illinois at Urbana Champaign showed that application of a reinforcement is equivalent to adding an additional confining stress of around 60 kPa.

Reinforcements for asphalt layers are available in grids and nets (figure 291).



Figure 291: Reinforcing grid (left) and net (right).

A grid is characterized by its stiff joints which connect the longitudinal bars with the transverse ones. Transfer of the load is realized through anchoring through the mesh and adhesion. Furthermore the transverse bars are activated.

Nets on the other hand have soft joints and the load is transferred through adhesion between the longitudinal strands and the asphalt mixture.

Which is the best solution cannot be said a priori, testing has to provide the answer.

Also composite systems, figure 292 gives an example, are available which try to combine the function of a SAMI with that of a reinforcement.



Figure 292: Composite system combining the function of a SAMI with that of a reinforcement.

The author is however a bit puzzled on the effectivity of the product since he has a feeling that the reinforcement is not really reinforcing the asphalt but is reinforcing the SAMI because it looks to him that the reinforcement is more or less buried in the SAMI. To him it seems that the main purpose of the non-woven shown in figure 292 is mainly to simplify the placement of the reinforcing net. Figure 293 e.g. shows what might go wrong when placing a reinforcing net. The wrinkles in the net shown in that figure should of course not occur. When a composite system is used such placement errors are far less likely to occur.

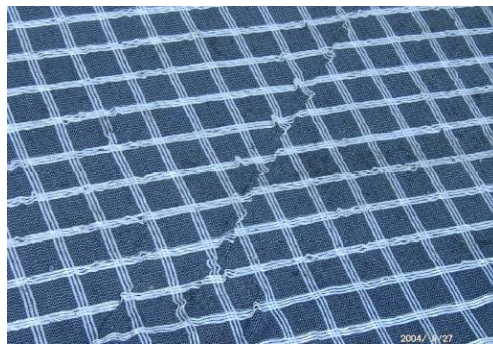


Figure 293: Faulty placement of a reinforcing net.

The question which reinforcing systems is the best, is difficult to answer. The reinforcing system starts to act when the crack is entering the layer in which the reinforcement is placed and one of its main purposes is to keep the crack closed allowing effective load transfer to develop. The other purpose is of course acting as a tension bar just like reinforcement is acting in a reinforced concrete beam; this is shown in a very simplified way in figure 294.

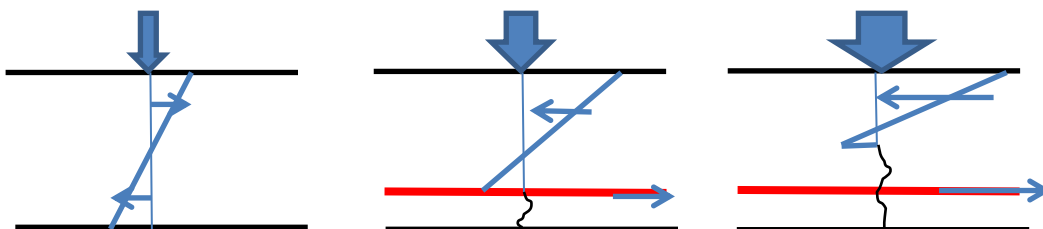


Figure 294: Simplified stress conditions in a reinforced concrete beam when subjected to a bending moment.

When a plain concrete beam is subjected to bending, the stress conditions in the concrete will be like shown in the left sketch of figure 294. When the load is increasing and the tensile stress at

the bottom of the beam is equal to the tensile strength of the concrete, cracking will start and will propagate rather quickly. There should be equilibrium between the bending moment applied on the beam (the magnitude of the bending moment depends on the magnitude of the load and the supporting conditions) and the moment that is offered by the resultant compressive stress in the concrete and the resultant tensile stress in the concrete. Since the tensile strength of concrete is much lower than its compressive strength, the bending moment that can be taken by the beam is actually determined by the tensile strength of the concrete. When a reinforcement is applied, the reinforcement will take the tensile stresses as soon as the crack has passed the reinforcement. This is shown in the middle and right hand sketch of figure 294. Now equilibrium is provided by the resultant compressive stress in the concrete and the tension in the reinforcement. In this case one can say that the maximum bending moment that can be sustained by the beam is controlled by the compressive strength of the concrete. As mentioned above, the compressive strength of concrete is much higher than its tensile strength so the bending moment at which failure occurs is much higher for a reinforced beam than for an unreinforced beam. Of course the description given above is a very rude one of the real conditions but it is good enough to explain why a reinforcement adds structural capacity to a bending beam. In principle the same applies for reinforced asphalt layers.

From this simple description we can also easily understand why the bond between the reinforcement and the surrounding material is so important. If the bond strength is low, the reinforcement will become loose in the surrounding material very easily and will lose its function. For the same reason, also the stiffness of the bond between the reinforcement and the surrounding material should be high.

De Bondt [90] has done excellent work in characterizing the bond strength and stiffness of different reinforcing materials as well on the load transfer that takes place across reinforced cracks. The interested reader is referred to his thesis for further details. In his thesis he presented some examples of the effectivity of various reinforcing systems, which were characterized by their $E \cdot A$ product, in relation to the bond stiffness in extending pavement life. One of these examples is shown in figure 295.

The upper right hand picture in figure 295 shows a farm to market road in the western part of the Netherlands. In this area the subgrade is very weak ($CBR \approx 2\%$) and the groundwater level is high. As one will notice the verge on the canal side is narrow implying that very little lateral support is provided to the pavement. The problem on this particular road was severe longitudinal cracking especially in the traffic lane closest to the canal. A finite element analysis was made to investigate the effectiveness of various reinforcing systems; the finite element mesh is shown in the upper right hand side of figure 295. The bottom part of the figure shows the improvement in overlay life for various reinforcing systems. As was to be expected the systems with the highest $E \cdot A$ product will give the best improvement BUT a high bond stiffness, indicated with $C_{eq,rf}$ on the horizontal axis is needed to get full benefit of a system with a high $E \cdot A$ value.

In his research de Bondt tested several products; they are listed in table 63. It should be noted that some of the products listed in the table might not be available anymore, might be available under a different name or might have been modified in time. The $E \cdot A$ values of some of these products are shown in figure table 64 as well as the bond stiffness values realized with these products.

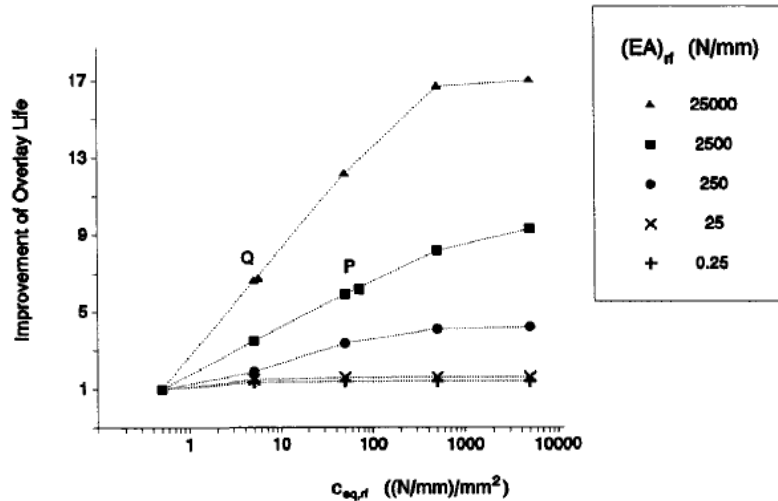
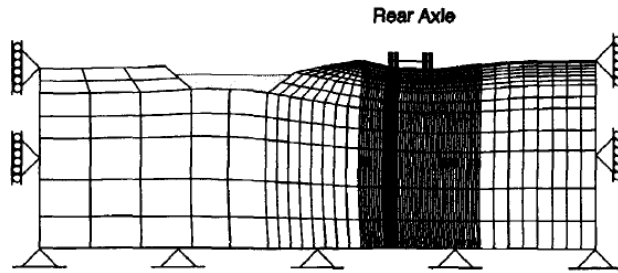


Figure 295: Effect of reinforcement on lifetime overlay.

- 1: GlasGrid 4031 + 0.4 kg/m² Tack Coat Emulsion + 0.5 kg/m² Chippings 2/6 mm
- 2: GlasGrid 8501 + 0.4 kg/m² Tack Coat Emulsion + 0.5 kg/m² Chippings 2/6 mm
- 3: Tensar AR-1 + 1.5 kg/m² Tack Coat Emulsion + 10 kg/m² Chippings 8/11 mm
- 4: GlasGrid 8501 + > 2.5! kg/m² SAM-C + 7 kg/m² Chippings 8/11 mm
- 5: Tack Coat Emulsion 0.4 kg/m² + Rotatex WG2303G1
- 6: Tack Coat Emulsion 0.4 kg/m² + Hatelit 30/13
- 7: Mesh Track + 0.4 kg/m² Tack Coat Emulsion
- 8: only 0.4 kg/m² Tack Coat Emulsion (see section 6.4.1)
- 9: Esha Stick Pes

Table 63: Products tested by de Bondt [90].

Product number	E * A [N/mm per mm ¹ width)	Bond stiffness [N/mm/mm ²]
1	4000 – 8000	20
3	350	400
6	330	900
7	24750	20

Table 64: E * A values for some reinforcing systems.

Table 64 shows that de Bondt did not find combinations of a high E*A value AND a high bond stiffness. For the example in figure 295, the steel reinforcement (product 7) is giving the best improvement (10*) in spite its relatively low bond stiffness. Product 6 (Hatelit) would give an improvement of about 5* this in spite of its low E*A product which is compensated by the bond

stiffness . The final choice depends of course on how severe the problem is as well on the effect : cast ratio for the various products.

At the Belgian Road Research Center research on the effectivity of reinforcing systems in case of horizontal (shrinkage induced) movements at cracks and joints was performed. The test setup used is shown in figure 296 while figure 297 shows some results.

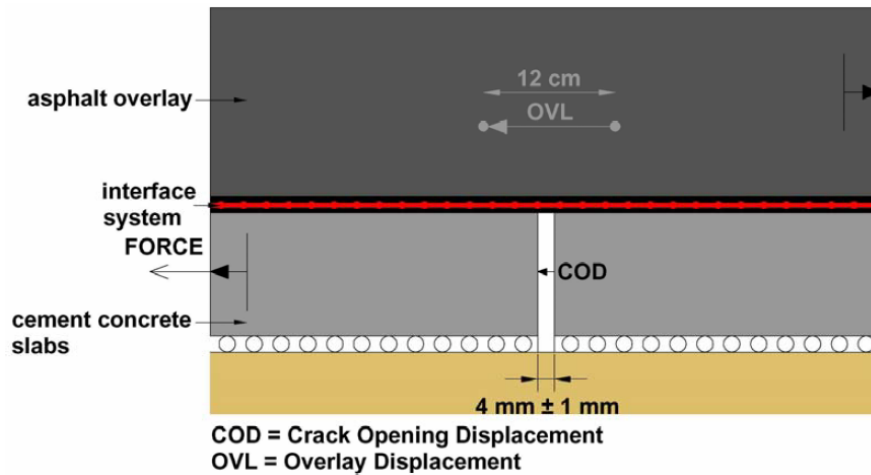


Figure 296: Test setup used by the Belgian Road Research Center to test the effectivity of reinforcing systems.

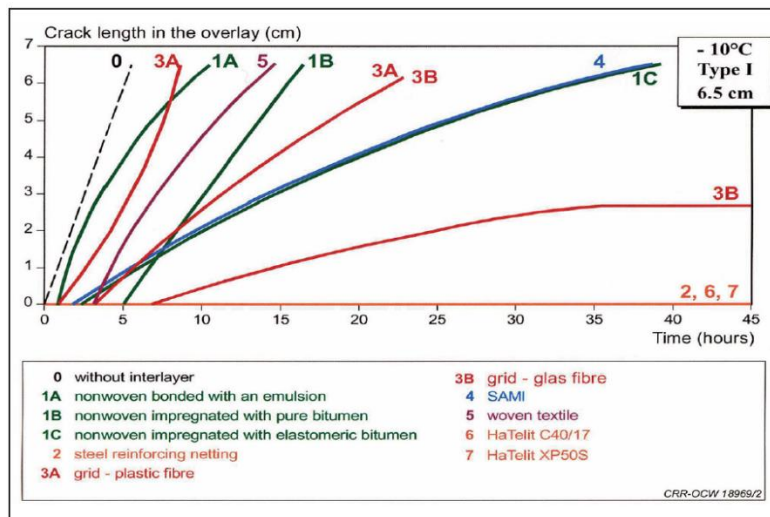


Figure 297: Results obtained by the Belgian Road Research Center.

Figure 297 shows again the excellent performance of the Mesh Track steel reinforcement as was the case in the example shown in figure 295. Also the Hatelit products performed very well in this case.

The improvement factors shown might look ridiculously high but are realistic which is shown in figure 298 where pictures are shown of a pavement very near to where the author is living. In this case a steel reinforcement was applied.

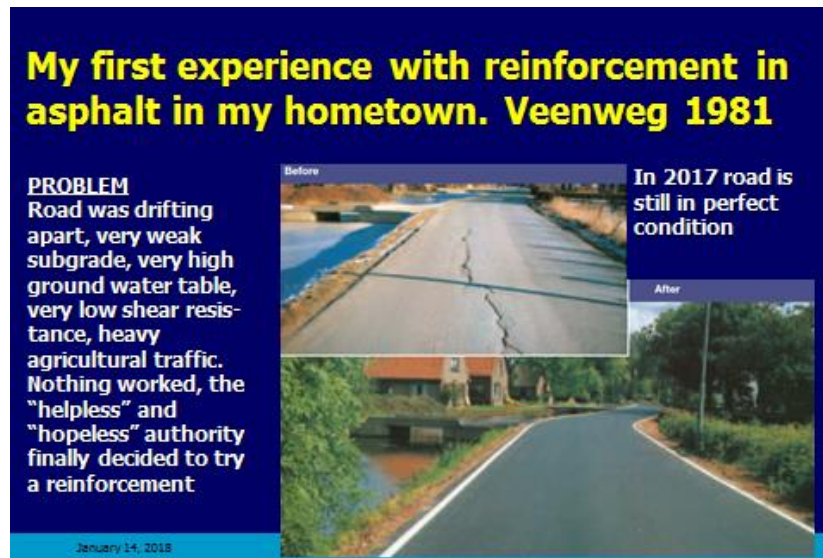


Figure 298: The author's experience with reinforcements in asphalt pavements.

During the 36 years the pavement was in service after being overlaid with a steel (Mesh Track) reinforced overlay, only a few seal coats and finally a thin surfacing were applied for skid resistance and cosmetic purposes.

Application of an overlay with improved crack resistance characteristics

Of course much of the crack reflection problem can already be solved by using an overlay with a wearing course with enhanced characteristics. Improved crack resistance can be obtained by e.g. modifying the bitumen with a polymer, rubber etc.

We have seen that crack growth in an asphalt mixture can be described by means of Paris' law which is:

$$dc/dN = A * K^n$$

where: dc/dN = crack growth per loading cycle, K = stress intensity factor at the tip of the crack and "A" and "n" are material parameters.

It is recalled that:

$$A = \frac{\pi}{6 \sigma_m^2 I_1^2} \left(\frac{(1-\nu^2) D_2}{2 \Gamma} \right)^{\frac{1}{m}} \left| \int_0^{\Delta t} w(t)^2 \left(1 + \frac{1}{m} \right) dt \right|$$

Where:

$$I_1 = \pi K_1 / 2 \alpha \sigma_m$$

α = size of failure zone in front of the crack tip [mm]

σ_m = tensile strength [MPa]

K_1 = stress intensity factor for mode I loading [N/mm^{1.5}]

$$D(t) = D_0 + D_2 t^m$$

D_0 = creep compliance at $t = 0$ s [MPa^{-1}] (creep compliance = $1/E$ or $1/S_{\text{mix}}$)
 Γ = fracture energy [Nmm/mm^2]
 t = time [s]
 m = slope of the double logarithmic creep compliance curve
 ν = Poisson's ratio
 $d\Delta t$ = period of one loading cycle [s]
 $w(t)$ = pulse shape of the stress intensity factor related to time

Furthermore:

$$n = 2 (1 + 1/m)$$

when the tensile strength and fracture energy needed to produce a unit crack surface are assumed to be constant along the path of the crack growth. It was hypothesized that this occurs in constant stress fatigue tests.

When the length of the failure zone ahead of the crack tip and the fracture energy are assumed to be constant then

$$n = 2 / m$$

It was hypothesized that this occurs in constant displacement fatigue tests.

It was mentioned by Molenaar [39] showed that the n calculated in this way should be corrected for the effects of voids in the mixture if the void content is larger than 3%.

All this has been discussed in the chapter on asphalt mixtures.

As one will notice, the parameter A is a function of the components as given in the formula below:

$$A = f \left\{ \frac{1}{f_t^2}, \left(\frac{1}{\Gamma} \right)^{\frac{1}{m}}, \left(\frac{1}{E^2} \right)^{\frac{1}{m}}, (1 - \mu^2)^{\frac{1}{m}} \right\} \text{ (please note } E = 1 / D \text{)}$$

So if one wants to make a relative comparison of the crack resistance of a specific modified mixture with that of a reference mixture one just has to determine $A_{\text{reference}} / A_{\text{modified}}$. This implies that the testing needed to get this comparison can be limited to modulus testing to obtain " E " and " m " and to tension tests to obtain " f_t " and " Γ ". These tests however should cover the loading time and temperature regime to which the mixtures will be subjected.

Since " m " is almost always smaller than 0.5, one can easily see that " E " is the most influential parameter. This is easily shown assuming $m = 0.5$, since then the influence factors become f_t^2 , Γ^2 and E^4 . Unfortunately a high E and high Γ is a combination which is not yet seen by this author. This is nicely shown in figure 299 which shows how the three properties are changing with reduced frequency.

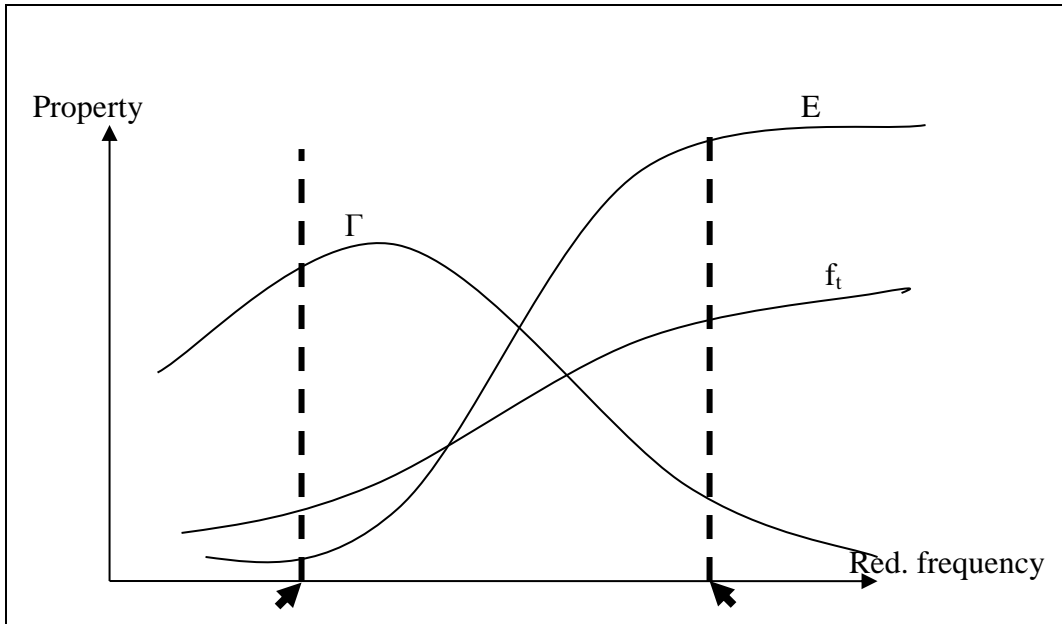


Figure 299: Change of Γ , f_t and E with changing reduced frequency.

Molenaar in his work for Amsterdam's Schiphol Airport in the early 1990's showed that the indirect tensile test is a very useful and practical tool to compare in a relative way the crack resistance of modified mixtures. In the research program one of the mixtures was modified with poly-ethylene while the other ones were modified with three different types of SBS. The indirect tension tests were performed at 5 °C and at a speed of 0.85 mm/s. Some results are shown in figure 300 and in table 65. From the results it became clear that mixture C, a SBS modified mixture, was to be preferred on the basis of having the best combination of tensile strength, tangent modulus and fracture energy.

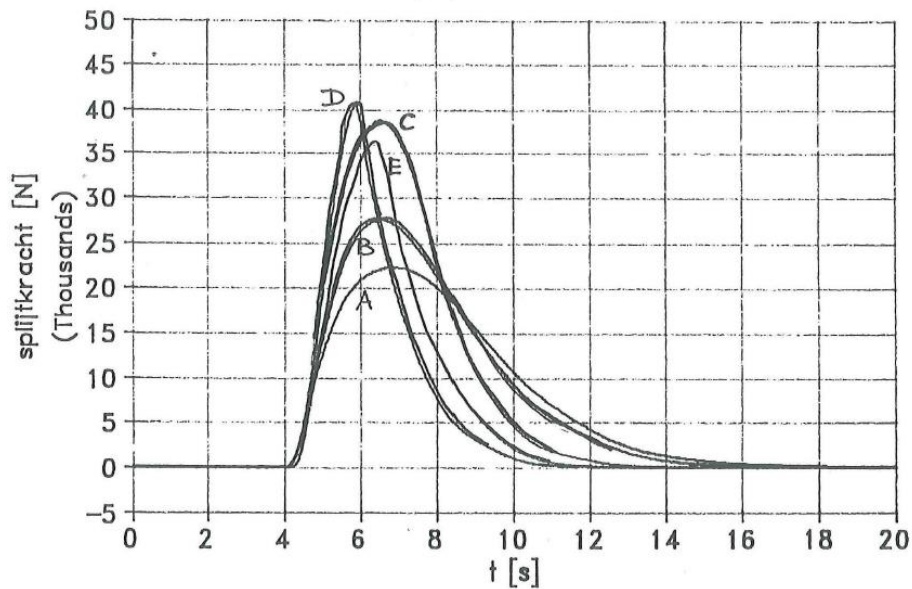


Figure 300: Indirect tensile test results obtained on four polymer modified mixtures.
Note all specimens had exactly the same size.

Mixture Type	Indirect tensile strength [MPa]	Fracture energy [Nmm/mm ²]
A	2.44	16.63
B	2.98	17.54
C	4.21	18.71
D	4.45	12.26
E	3.97	13.81

Table 65: Indirect tension test results obtained at 5 °C and 0.85 mm/s on five polymer modified mixtures initially selected for use on Amsterdam's Schiphol Airport.

In the previous sections we have discussed several techniques to reduce reflection cracking but what about applications? A very interesting combination of techniques has been used extensively at Schiphol airport where extensive reflection crack problems occurred in the late 1980's. The pavement consisted of 600 mm lean concrete on top of a 100 mm sand layer which was laying on a weak subgrade with CBR = 2%. On top of the lean concrete base, asphalt concrete layers were placed with a total thickness of 270 mm. Because of the lean concrete base, reflection cracking occurred resulting in crack spacings of up to 45m and rather wide cracks of up to 25 mm. Such cracking can be dangerous to aircraft operations since loose material can collect in the wide crack openings which might lead to foreign object damage (FOD) to aircraft engines etc. Since a large runway and taxiway renovation project was started, the authorities decided that the new pavements should not suffer from reflection cracking. Therefore a design was made consisting of 600 mm lean concrete which was cut at distances of 7.5 m to force shrinkage cracking to occur on those locations. Then a SAMI was sprayed after which polymer modified asphalt layers were placed in a total thickness of 200 mm. Modifier C, mentioned above, was used in the mixtures. Details cannot be given since it is a propriety product. However some viscosity data can be given which are listed in table 66.

In time this combination of techniques has proven to be very successful in preventing/retarding reflection cracking.

Penetration	55
Softening point	95 °C
PI	6.4
density	1014 kg / m ³

Table 66: Some properties of the SBS modified bitumen used at Schiphol airport.

15.4 Top down cracking and lack of bond between layers

15.4.1 Introduction

Another defect that has nothing to do with the structural thickness design of pavements is top down cracking. As the words already say, these cracks do initiate at the surface of the pavement and grow downwards to a depth of approximately 50 mm. A lot has already been said about this defect type and there is not yet a final definite conclusion on why these cracks occur. It is clear however that hardening of the pavement surface due to aging and traffic loads have a significant influence on the development of these cracks. Top down cracking in the wheel paths is of course strongly related to traffic. Furthermore it is believed that loss of bond between the surface layer and the underlying structure does have a significant influence. Figure 301 is a beautiful example of debonding related cracking.



Figure 301: Cracking in wheel path limited to the wearing course probably due to loss of adhesion between wearing course and underlying structure.

The crack shown in figure 301 might have been developed due to loss of bond causing high tensile strains to develop at the bottom of the wearing course or might have been initiated at the top and has progressed downwards. Ingress of water through the crack that has initiated at the top will certainly have accelerated the debonding.

The presence of these surface cracks makes us wonder where the cracks are coming from we see in the wheel paths at the pavement surface? Are they classical fatigue cracks that initiated at the bottom of the bound layers and have propagated upwards or do these cracks have other reasons?

A long time ago, Dauzats and Linder [94] presented results of investigations on the appearance of cracks and figure 302 is one of the results they presented.

with separation between wearing course and roadbase	NEW PAVEMENT OVERLAYS %	without separation between wearing course and roadbase	NEW PAVEMENT OVERLAYS %			
	25	3,4		2	0,8	LONGITUDINAL CRACK
	8	-		5	3,5	
	5	45,8		18,5	34,8	TRANSVERSE CRACK
	3,5	4,1		8	1,8	
	10	2,4			3,4	
	10	-		5	-	

Figure 302: Appearance of cracks as reported by Dauzats and Linder.

The figure clearly shows that by far, cracking must have originated in the top layer since only a small amount of the cracks visible at the pavement surface are bottom up.

What is a bit “alarming” in figures 301 and 302 is the fact that separation of the top layer from the lower layers seems to occur regularly. This seems to indicate that the interface between the top layer and the lower layer is the weakest part. In our design analyses however we seldomly take into account the potential lack of strength of the interlayer can have in damage development. Xiao [116] in his research showed the significant difference in shear strength of interfaces compared to the shear strength of asphalt mixtures. Some of his test results are shown in figure 303.

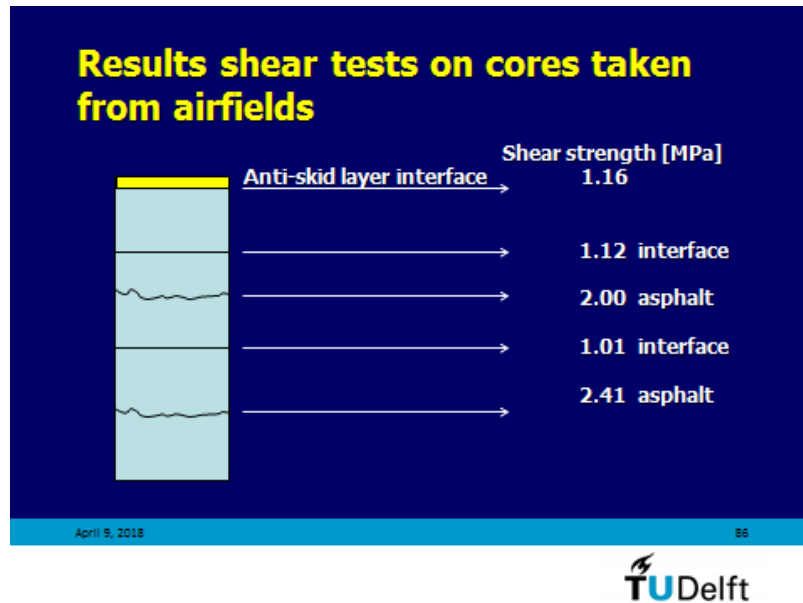


Figure 303: Shear strength of the interface between layers compared to shear strength of the asphalt mixture.

Figure 303 shows that the shear strength of the interfaces is approximately 50% of the shear strength of the asphalt mixtures. Next to this Molenaar (unpublished research) showed that the shear fatigue resistance of the interface is much lower than the shear fatigue resistance of asphalt mixtures. This is shown in figure 304.

The data shown in figure 303 and 304 were obtained by means of the Leutner shear device which is shown in the upper right hand corner of figure 304.

It is not unlikely that debonding occurs between the top layer and the lower layer because of the fact that rather high shear stresses do occur at a depth of about 40 – 50 mm below the pavement surface (= thickness wearing course) and the rather poor fatigue performance of the interface. It will be clear that the “strength” of the interface is affected by a number of reasons such as:

- is a tack coat used or are the layers placed “hot on hot”; “hot on hot” placement will most probably give the best adhesion between the layers;
- cleanliness of the pavement surface when spraying the tack coat;
- was the pavement surface dry and not too cold when spraying the tack coat;
- amount and type of tack coat.

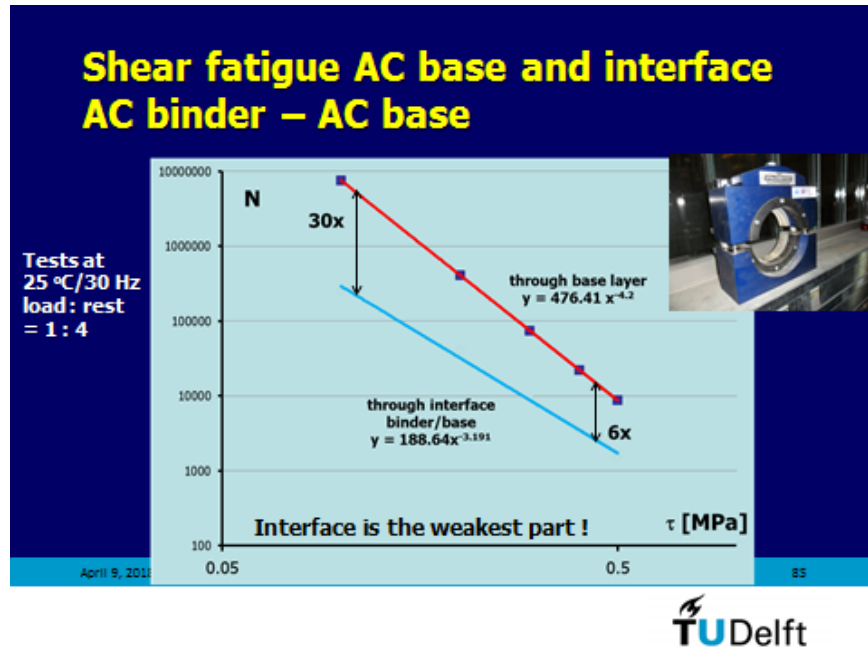


Figure 304: Shear fatigue resistance of the interface compared to the shear resistance of an asphalt mixture.

All in all it is clear that a good bond between layer is essential to prevent problems like early cracking of the top layer. It is therefore surprising that the effects of lack of bond between layers is hardly taken into account in thickness design procedures where usually full friction is assumed between the layers.

The importance of top-down cracking was also shown by van Dommelen and Schmorak [95]. In their paper presented at a SHRP conference in Prague in 1995, they reported about investigations on cracking in pavements in the Netherlands. Some of their results are shown in figure 305.

Figure 305 shows two remarkable things. The first one is that we are not very good in predicting what we see and secondly most of the observed cracking (63%!!) is surface cracking! Schmorak furthermore reported that in thicker pavements all wheel path cracking is in fact surface cracking (see table 67)!

Asphalt thickness > (m)	Test sections with full crack propagation (%)
0.04	26.9
0.08	25.5
0.12	20.0
0.16	3.2
0.20	4.2
0.24	0.0

Table 67: Appearance of surface cracking on the SHRP-NL sections in the Netherlands.

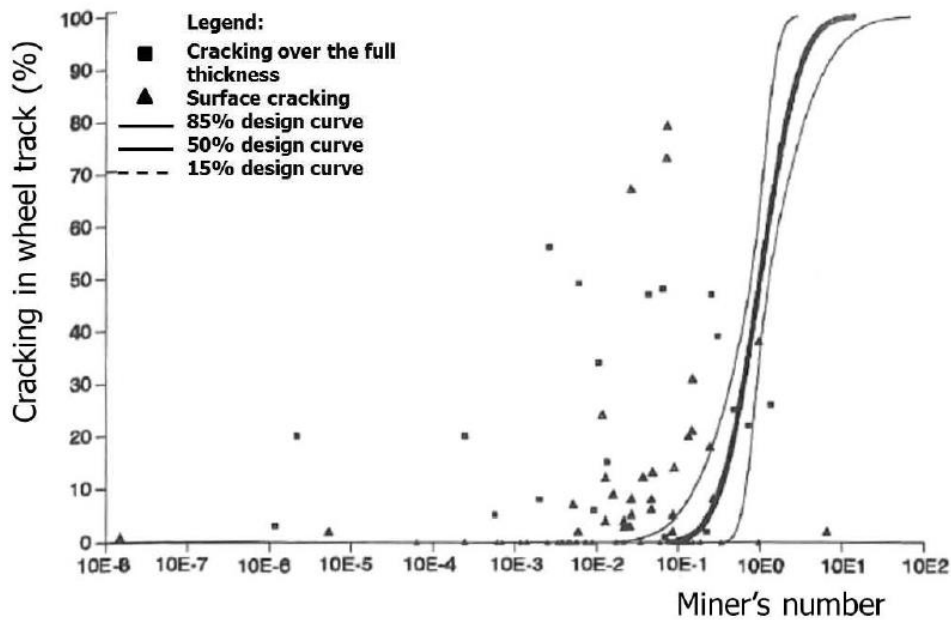


Figure 305: Observed and predicted wheel path cracking in SHRP-NL test sections in the Netherlands.

The conclusion we have to draw so far is that we do not take into account surface cracking in our thickness design system and therefore do overlook a damage type that can cause extensive maintenance. In the section hereafter we will discuss in some detail the stresses and strains that might occur at the pavement surface due to wheel loads.

15.4.2 Stresses at the pavement surface due to the complex pressure distributions in the tire – pavement contact area

Already in 1983, Molenaar [39] showed that rather high tensile strains could develop at the pavement surface due to lateral shear forces underneath the tire. The loading model he used is represented in figure 285 (25 kN per wheel, contact pressure 700 kPa). For this particular loading condition he showed that a direct relationship between the tensile strain at the pavement surface due to inward shear forces underneath the tire on one hand and the stiffness of the wearing course on the other. This relation is:

$$\log \varepsilon_{te} = 4.822 * 10^{-2} - 1.049 \log E_1$$

Where: ε_{te} = tensile strain at the edge of a dual wheel load [m/m],
 E_1 = modulus of the wearing course [MPa]

The equation shows that at $E_1 = 1000$ MPa the tensile strain equals $7.966 * 10^{-3}$, while at $E_1 = 8000$ MPa the tensile strain equals $8.995 * 10^{-5}$.

Jacobs [96], in his research modelled the stresses under a wheel in a much more accurate way. Inspired by data taken from literature [97] he developed the contact pressure distribution as shown in figure 306 which are acting under a 50 kN wheel load with a tire pressure of 650 kPa. As one will notice, the lateral shear force is at some locations rather high. This might be caused by the fact that the tire pressure is a bit on the low side for the vertical load so some peak lateral stresses at the edge of the tire could be expected. Jacobs simulated the distributions shown in figure 306 by means of BISAR, so he modelled the load as a large number of circular loads. He

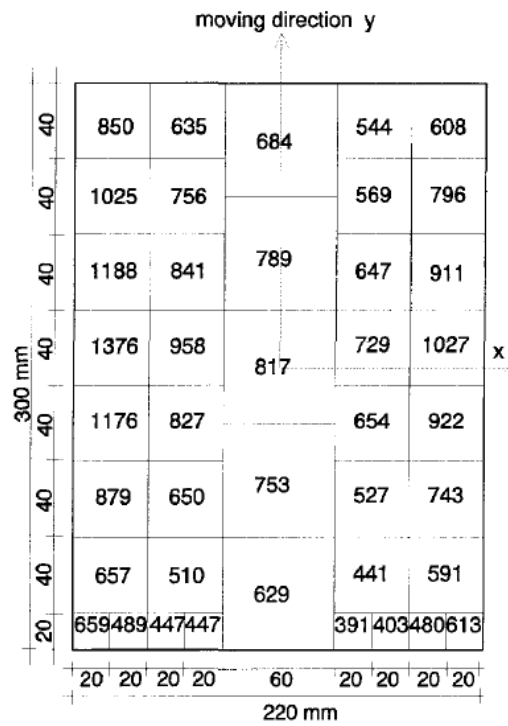
then placed the load on a pavement consisting of 200 mm of asphalt having a modulus of 1500, 5500 and 10000 MPa, on a 300 mm thick base layer with a modulus of 300 MPa on a subgrade with a modulus of 100 MPa. Figure 307 shows some of the lateral stress distributions that were calculated.

As one can see in figure 307, the lateral σ_{xx} stress at the tire edge varies from approximately -0.8 MPa ($y = 160$ mm) to approximately 2.9 MPa ($y = 10$ mm) and then returning to approximately -0.3 MPa ($z = -160$ mm).

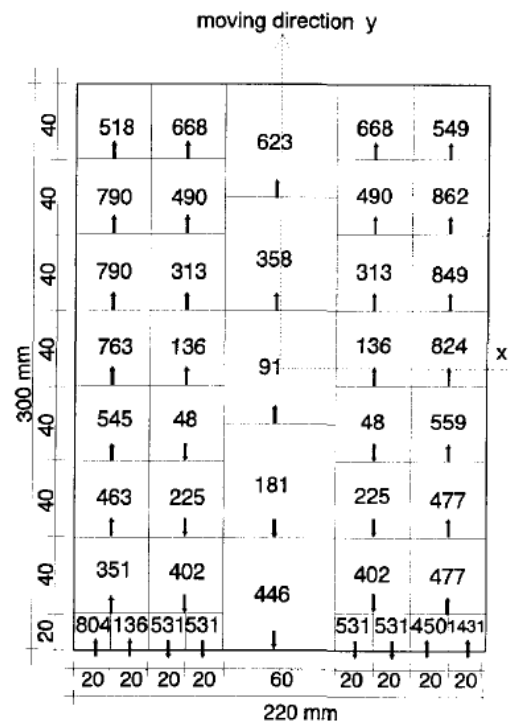
Table 68 shows the tensile stresses at the bottom of the asphalt layer when the wheel contact area is assumed to be a circle and the contact pressure is assumed to be equal to the tire pressure (1D stress) and when the contact pressure distribution shown in figure 299 is taken into account (3D stress). Also the tensile stresses at the pavement surface at the edge of the tire are shown.

S_m [MPa]	$\sigma_{xx,max}$ ($z = 200$ mm) 1D stress	$\sigma_{xx,max}$ ($z = 200$ mm) 3D stress	$\sigma_{xx,max}$ ($z = 0$ mm) 3D stress
1500	0.43	0.52	3.15
5500	0.94	1.09	2.79
10000	1.17	1.34	2.62

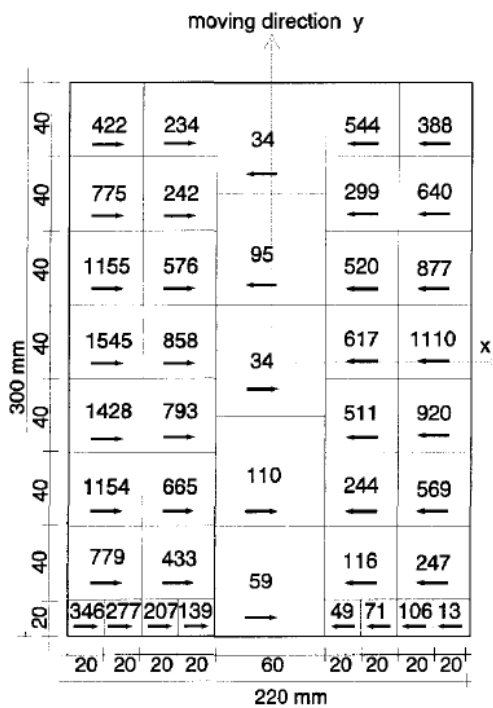
Table 68: Stress values at different locations in the pavement assuming different contact pressure distributions.



(a) The vertical stress distribution



(b) The longitudinal shear stress



(c) The transverse shear stress

Figure 306: Contact pressure distributions as used by Jacobs.

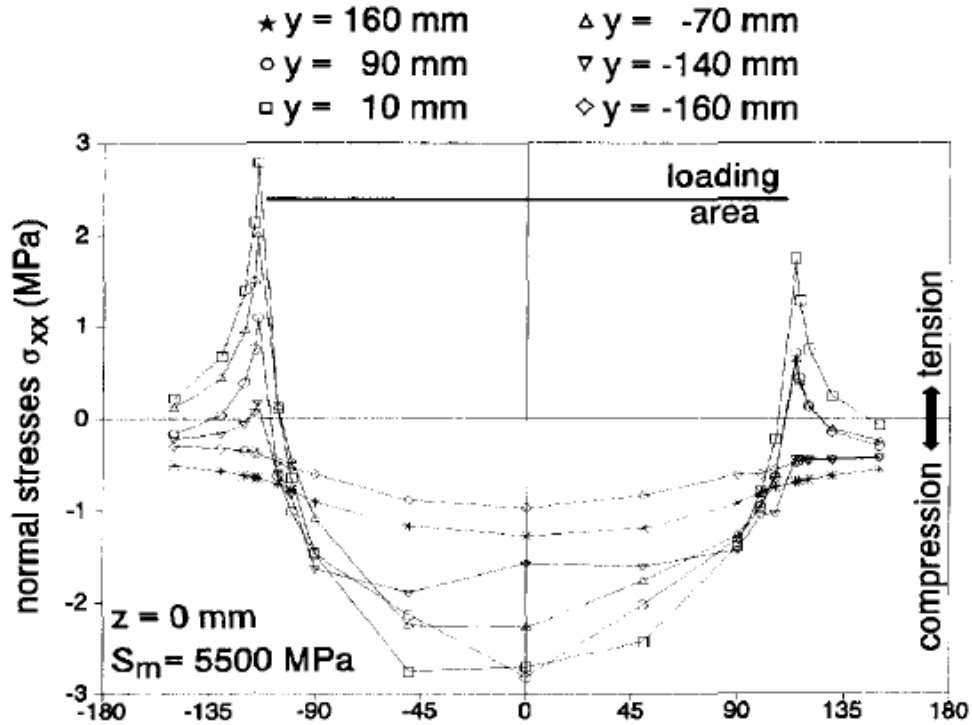


Figure 307: Stresses in the lateral direction under the tire at $E_1 = 5500$ MPa as calculated by Jacobs.

Note: "y" is the longitudinal direction; $y = 160$ mm is the front edge of the tire, $y = -160$ mm is the rear edge of the tire. Center of the wheel is at $x = y = z = 0$ mm

Table 69 gives the same information but now in terms of tensile strains.

E_1 [MPa]	1500	5500	10000
ϵ_{\max} (1D) [m/m] max strain occurs at bottom of asphalt layer	$2.31 \cdot 10^{-4}$	$1.17 \cdot 10^{-4}$	$7.84 \cdot 10^{-5}$
ϵ_{\max} (3D) [m/m] max strain occurs at pavement surface next to the tire edge	$1.95 \cdot 10^{-3}$	$4.90 \cdot 10^{-4}$	$2.59 \cdot 10^{-4}$

Table 69: Tensile strains at the bottom and surface of the asphalt layer.

Table 69 shows that the critical location in terms of maximum tensile strain changes from the bottom of the asphalt layer under the load center in case we take only the 1D contact pressure distribution into account, to the pavement surface next to the tire edge in case we take the full 3D contact pressure distribution into account. The critical location is clearly dependent on the magnitude of the horizontal shear forces acting on the pavement surface. We have seen in the chapter on Wheel Loads and Tire Pressures that the contact pressure distribution (including the shear forces) depends on the wheel load and tire pressure; also the type of tire is of importance.

From table 69 the following relationship can be developed between the stiffness of the asphalt layer and the tensile strain at the surface:

$$\log \epsilon_{\text{surface}} = 0.669 - 1.064 \log E_1$$

Of course this relationship is different from the one developed by Molenaar which was given earlier because the wheel loads were different. It is however interesting to note that the value of the slope of both relationships is almost the same.

Table 69 clearly indicates that in Jacobs' analyses, the tensile strains at the pavement surface are higher than those at the bottom of the pavement indicating that cracking will start first at the pavement surface.

Groenendijk [23] was the third person at the Delft University who spent a considerable amount of time in trying to explain surface cracking. He analyzed the effect of contact pressure distributions, ageing of the top layer, and the presence of transversal compaction cracks on the development of surface cracking. Figure 308 shows the contact pressure distribution used in most of these analyses and figure 309 shows the finite element mesh used.

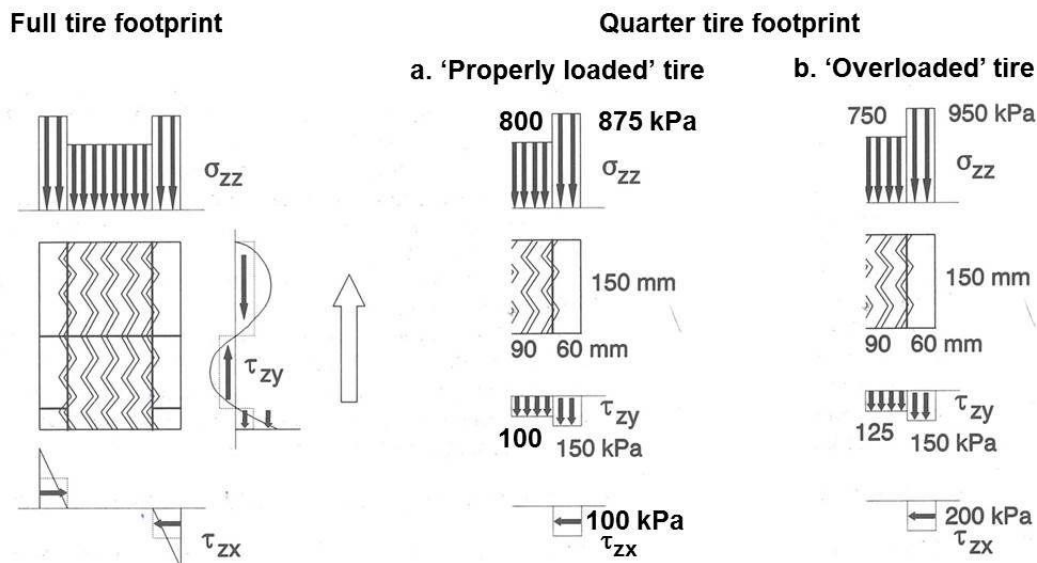


Figure 308: 3D wheel schematization as made by Groenendijk.

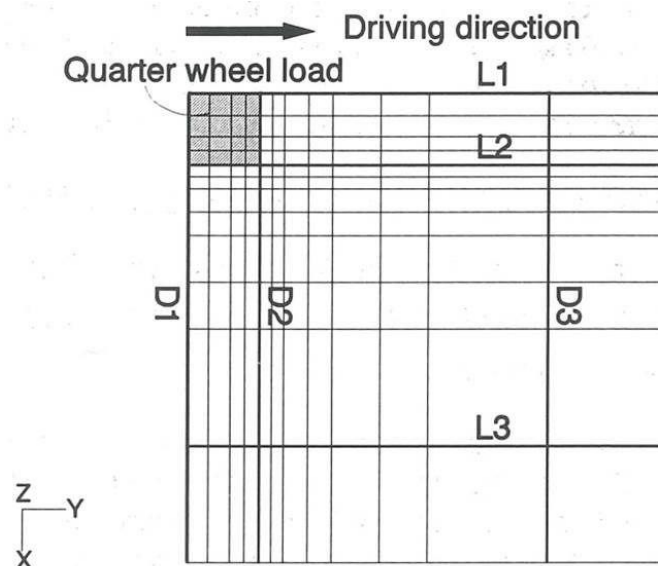


Figure 309: Finite element mesh used by Groenendijk.

After an extensive analyses, Groenendijk concluded that given the rather low inward shear stresses as well as the rather uniform vertical stress distribution under the tire as used in his analyses, top down cracking could not well be explained from the contact pressure distributions. He stated however that surface cracking will be triggered when tires are under-inflated with respect to the wheel load such that very high peak stresses occur at the tire edge (this is what was already shown by Jacobs, see figure 307). He furthermore showed that ageing of the top layer will increase the possibility of surface cracks. He stated that the effect of ageing on the occurrence of surface cracks is larger than the effect of the contact stress distribution. He also concluded that surface cracks which are already there because of shrinkage and, more importantly, those as a result of compaction, will certainly propagate because of the contact stresses. In the situation where the crack tip was at the wheel load edge, both the longitudinal and transversal crack will propagate faster horizontally than vertically. The horizontal cracks, however, would not propagate beyond the wheel path, so the end result could be a type of alligator cracking.

Finally, he concluded *“that it is unlikely that contact stress distributions alone should be held responsible for the surface cracking often found in pavements, but they undoubtedly play an important role together with climatic influences like bitumen ageing and low-temperature cracking. Therefore, it is recommended that close approximations of the actual contact stress distributions should be taken into account in pavement design and analysis”*

Similar work has been done by Pramesti [38], being the fourth person at the Delft University attacking this problem. She modelled the contact stress distribution under a super single tire R160A, 425/65 R 22.5 by means of the computer program Tyrestress[®]. The wheel load was 75 kN and the tire pressure was 950 kPa. She used these data as input in ABAQUS and analyzed the stresses in a two layer pavement system consisting of 150 mm of asphalt concrete ($E = 18850$ MPa at 5 °C and 8Hz also $E = 2000$ MPa at 40 °C and 8 Hz) on a sand subgrade ($E = 160$ MPa). Figure 310 shows how she modelled the tire print while table 70 shows the contact pressures taken into account. Please note that she did not take into account the variation of the contact stresses in the longitudinal direction.

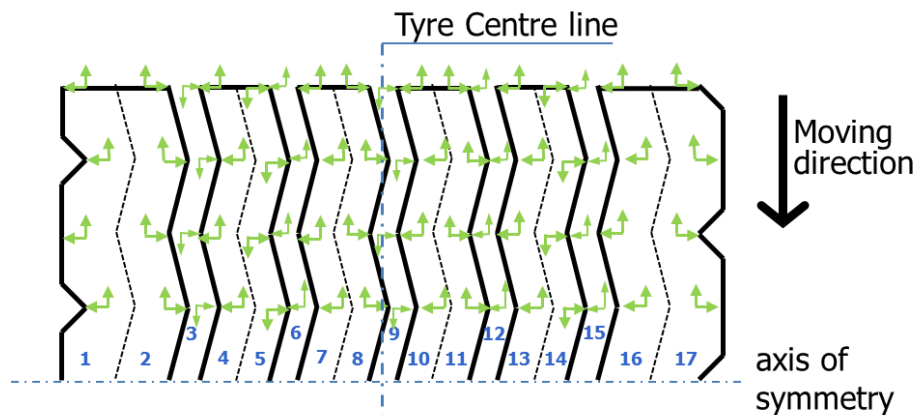


Figure 310: Tire pressure modelling as done by Pramesti.

When comparing table 70 with figure 306, one will notice that the lateral shear forces taken into account by Jacobs are higher than those used by Pramesti. Furthermore Pramesti calculated the stresses and strains just under the tire edge while Jacobs calculated them just outside the tire edge. As a result of all this Pramesti did not predict tensile stresses as was done by Jacobs but she did calculate significant tensile strains near the tire edge.

Surface	Vertical	Transversal	Longitudinal
	Y	X	Z
	(MPa)		
1	-1.738	-0.184	-0.060
2	-1.284	0.197	-0.002
3	-0.307	0.082	0.032
4	-1.199	-0.131	-0.030
5	-1.222	0.176	0.057
6	-0.663	-0.130	-0.033
7	-1.528	-0.017	-0.070
8	-1.528	-0.017	-0.070
9	-0.645	0.106	0.070
10	-1.300	-0.228	-0.098
11	-1.617	0.144	-0.004
12	-0.054	-0.014	0.000
13	-1.406	-0.133	-0.066
14	-0.980	0.145	0.053
15	-0.899	-0.233	-0.097
16	-1.309	-0.154	-0.066
17	-1.412	0.226	-0.090

Table 70: Tire pressure modelling as done by Pramesti.

Note: Figure 310 shows that surfaces 3, 6, 9, 12 and 15 are in fact the grooves of the tire and therefore the stresses at those surfaces should be zero. As table 70 shows, the stresses at these surfaces are not zero. The reason for this discrepancy is that Pramesti used the stress distribution as predicted by Tyrestress which did not predict zero stresses at the surfaces indicated.

Figure 311 shows the maximum and minimum strains immediately under the tire at the pavement surface at 5 °C and 40 °C, while figure 312 shows the maximum and minimum strains at the bottom of the asphalt layer at 5 °C and 40 °C.

Pramesti's results show that although the tensile strains at the pavement surface are lower than those at the bottom, they are of significant magnitude. Although not shown by means of a figure, the tensile strains at the pavement surface are the same as those at a depth of 135 mm from the surface. These values make it plausible that although cracking in this case will start at the bottom of the asphalt layer, the first cracks visible at the pavement surface will most probably be due to the tensile strains at the pavement surface because cracks coming from the bottom need a considerable amount of time before being propagated to the top.

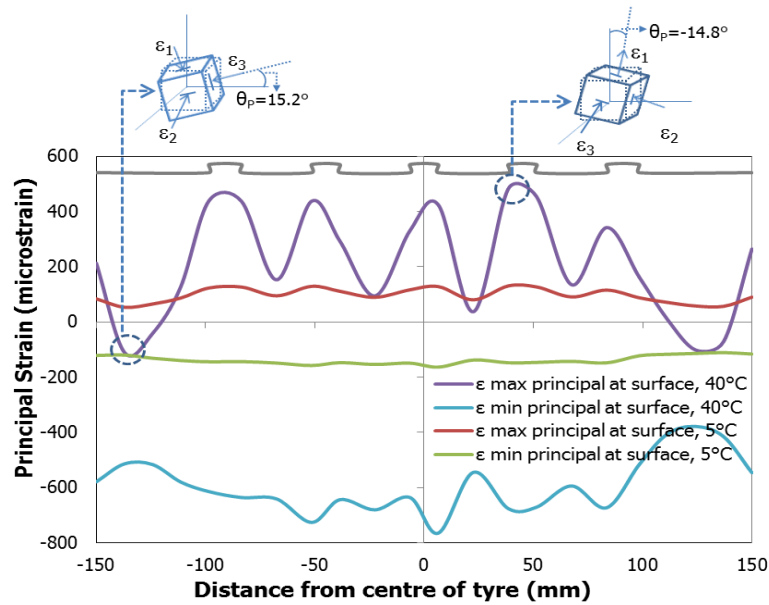


Figure 311: Maximum and minimum strains calculated by Pramesti at the pavement surface immediately under the tire at 5 °C and 40 °C.

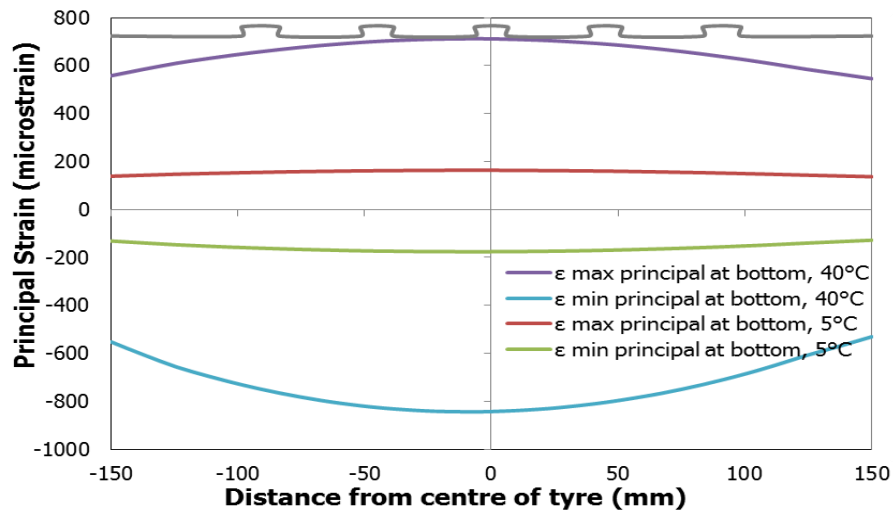


Figure 312: Maximum and minimum strains calculated by Pramesti at the bottom of the pavement at 5 °C and 40 °C.

15.4.3 Field studies on surface cracking

At the time Molenaar [39] was doing his analyses, the Dutch Study Center for Road Construction SCW, later called CROW, had also started research into the reasons behind the occurrence of surface cracking. Surface cracking and raveling had become a problem in the early 1980's on the dense asphalt concrete wearing courses used on highways in the Netherlands. The possible reason for this raveling and surface cracking was believed to be a change in the specifications which took place after the very hot summer of 1976. In those days the prescribed bitumen content for dense wearing courses was between 6 and 7% by mass and the void content had to be between 2 and 5%. Because of the hot weather rutting appeared on many highways and as a counter measure the road authorities had decided to decrease the bitumen content by mass to

5.6 – 6.4%; it was believed that this reduction might have been too large resulting in lean mixtures which are prone to raveling and cracking.

In order to determine the reasons for this extended surface cracking, the SCW B12 study committee did extensive analyses on a e. number of pavements involving falling weight deflectometer measurements, coring, mixture composition tests, analyses on the recovered binders, fatigue tests as well as tests on the buildup and relaxation of temperature stresses. Next to that extensive multilayer analyses were carried out. The results of this extensive research program are reported in [44]. The wearing courses of the test sections in the study, all showed a significant amount of longitudinal surface cracking which was overwhelmingly concentrated in the wheel track area; only very limited transverse cracking was observed. Falling weight deflectometer measurements were taken in and between the wheel paths. These results showed that at 66% of all measurement locations the deflections in the wheel paths were higher than between the wheel paths indicating that structural deterioration had taken place. Although this was the case, only surface cracking was observed on all sections. The penetration of the binders recovered from the wearing courses was ranging from 21 to 36 indicating that significant hardening had occurred since the penetration of the virgin binder was 80/100 in all cases. All wearing courses had a void content of 5.1% or less except for one section where it was 7.2%; this section was showing the highest amount of cracking.

Although the researchers assumed a certain horizontal inward shear distribution under the tire at the pavement surface, the tensile strain at the pavement surface as a result of this could not completely explain the occurrence of surface cracks. However, when the work strain was used in the fatigue relation, it was possible to explain surface cracking. Workstrain ϵ_w was defined as follows:

$$\epsilon_w = \sqrt{\frac{2\Delta W_b}{S_{mix}}}$$

Where:

- ϵ_w = workstrain
- ΔW_b = energy of distortion which can be calculated with any linear elastic multilayer program
- S_{mix} = stiffness of the wearing course

The fatigue life was calculated using

$$N = \left\{ \frac{(3S_{mix} \pi \sin \phi)}{(2(1+\nu) A \Psi)} \right\}^{\frac{1}{(z-1)}} \epsilon_w^{\frac{2}{(z-1)}} \quad (2.1)$$

Where:

- N = number of load repetitions to failure
- ϕ = phase angle between stress and strain as determined by means of stiffness tests
- ν = Poisson's ratio
- A, z = material parameters coming from the relation $W_f = A N^z$
- W_f = total amount of dissipated energy in a fatigue test till failure
- Ψ = $W_f/(N \cdot W_1)$; Ψ depends on whether the fatigue test is load or

displacement controlled
 W_1 = amount of energy dissipated in the first cycle of a fatigue test

The authors came to the following conclusions.

- Although the bitumen in the test sections had hardened to a substantial degree, most of the surveyed cracking had to be attributed to wheel-load induced factors. Nevertheless, thermal stresses seemed to have an effect as well.
- Cracking seemed to be initiated by traffic loads while propagation was probably due to temperature variations.
- Early ageing of the bitumen of the surface course should be prevented implying that attention should be paid to sufficiently thick bitumen films implying a sufficiently high bitumen content and a shift to coarser aggregate compositions. Furthermore, attention needs to be paid to the void content and degree of compaction.
- The work strain parameter seemed to be a powerful parameter since it allows damage due to fatigue to be predicted at locations where this would not be possible using the classical approach which is prediction of cracks based on the maximum tensile strain.

Another field study on cracking performed in the Netherlands should be mentioned as well. In the Netherlands the so called SHRP-NL program has been executed which was considered to be a program parallel to the famous Strategic Highway Research Program which has been executed in the USA. In the SHRP-NL program a number of pavement sections were monitored for a period of approximately 10 years. Data on the visual condition of the pavement as well as deflection data and mixture composition data were collected together with climatic and traffic data. Using Artificial Intelligence techniques, Miradi [98] developed models to predict raveling in porous asphalt concrete wearing courses and cracking and permanent deformation in pavements with a standard dense asphalt wearing course. Using various techniques she also determined the five most important variables that control the amount of cracking 11 years after construction. The results of these analyses are shown in table 71.

Method	Setting	Variable 1	Variable 2	Variable 3	Variable 4	Variable 5
Regression trees	Leave-one-out cross validation	Cold days	Traffic	Voids content	Bitumen content	
Genetic polynomial	Polynomial degree = 3	Cold days	Traffic	Bitumen content	Voids content	Rain
Artificial neural network (WWF)	Leave-one-out cross validation	Traffic	Cold days	Voids content	Bitumen content	Rain
Rough sets	2-class output	Voids content	Bitumen content	Traffic		
Correlation-based subset selection (bidirectional search)	Greedy stepwise search Leave-one-out cross validation	Cold days	Voids content	Bitumen content		
Correlation-based subset selection (genetic search)	Genetic Search Leave-one-out cross validation	Cold days	Bitumen content	Voids content		
Wrappers of ANN (genetic search)	Genetic Search Leave-one-out cross validation	Voids content				
Relief ranking filter	K=20 Nearest neighbor (equal influence) Leave-one-out cross validation	Cold days	Traffic	Bitumen content	Voids content	

Table 71: Five most influential variables on cracking as determined by means of different AI techniques.

Note: "cold days" = number of days with a minimum temperature < 0 °C

It is remarkable to notice that 5 out of the 8 techniques selected the number of “cold days”, a climatic parameter, as the most influential parameter! The voids content was selected two times as the most important parameter and traffic only one time. These results are more or less in line with the findings of the B12 committee which were mentioned above.

15.4.4 Other types of surface cracking

As has been discussed in the chapter on bitumen and asphalt mixtures, surface cracks might also be related to excessive hardening of the binder (see explanation of figure 185) and because of permanent deformation of the unbound base, subbase and subgrade (see figure 125). Sufficient information about the origin of these cracks has been given in the text associated with those figures and this will not be repeated here.

15.4.5 Conclusions on top down (surface) cracking

The cracks we observe at the pavement surface are very often not the classical fatigue cracks which we predict by calculating the tensile strain at the bottom of the asphalt layer and using a fatigue relationship. Such cracks would have grown from bottom to top. As we have seen in this chapter however, most of the cracks we see at the pavement surface, especially in thick pavements, have originated at the pavement surface. From the discussions given in this chapter it is clear that it is difficult to pinpoint a single parameter being responsible for these surface cracks. Although no clear cut conclusions can be made, the contact pressure distribution certainly has a major influence on the development of this type of cracking. The contact pressure distribution depends, as we have seen before, on the wheel load, tire pressure and type of tire. On top of this climatic effects do also have a significant influence since they may have caused hardening of the wearing course mixture which changes the fatigue characteristics and reduces the relaxation capabilities of the mixture (which has an effect on the magnitude of thermal stresses). Although surface cracks are and will remain difficult to predict, they can be limited to a large extent by using well designed and constructed asphalt mixtures for the wearing courses. They should have a fairly low void content, a high degree of compaction (avoid compaction cracks), a sufficient amount of a not too hard binder and a granular skeleton such that rather thick bitumen films will develop. So the solution has to be sought in the wearing course material and not in its thickness; a well-designed mixture laid down by a good quality contractor will solve much of the problem.

15.5 Raveling and bleeding

15.5.1 Introduction

Raveling and bleeding (also called flushing) are surface defects that have nothing to do with the thickness of the pavement but everything with the quality of the top layer in combination with climatic effects and effects of traffic.

Raveling is the loss of aggregates from the pavement surface and might ultimately result in potholes. It needs hardly to be emphasized that potholes affect the riding quality of the pavement very badly and also negatively affect traffic safety. Some examples are shown in figures 313, 314 and 315. Figure 313 shows raveling as observed on the TanZam highway in Africa and figure 314 shows raveling as observed in the Netherlands on a highway with a porous asphalt concrete top layer. In both cases we notice that pothole formation has started. Figure 315 shows raveling as occurred on a freshly laid seal coat; clearly something went (very) wrong during construction.

Bleeding or flushing is the formation of a bituminous skin on the pavement surface giving it a shiny appearance. Examples of bleeding surfaces are shown in figure 316 and figure 317. Because of bleeding, the wheel path will lose its texture and as a result the skid resistance will be

low in wet weather causing dangerous driving conditions. When there is a combination of bleeding and rutting, traffic conditions can really become unsafe in wet weather conditions.

Both raveling and bleeding are well known phenomena in pavements with a seal coat (see figure 315) but both defects also occur on asphalt concrete wearing courses. Here we will only discuss raveling and bleeding occurring in asphalt concrete layers.



Figure 313: Raveling as observed on the TanZam highway.



Figure 314: Raveling as observed on a porous asphalt concrete wearing course in the Netherlands.



Figure 315: Raveling of a seal coat.

Note the pile of aggregates on the right hand side of the road which should be on the pavement surface. Some surveyors would call this "bleeding" but the black appearance of the road is because of loss of aggregates and therefore the defect should be rated as "raveling"



Figure 316: Bleeding observed on a road in the USA.

15.5.2 Bleeding

We do not need to spend a lot of words on the reasons why bleeding occurs. It is simply due to improper construction implying improper mixture design and improper compaction. Hot weather adds to the problem because the bituminous binder will expand when the temperature increases. The Asphalt Institute mentions the following reasons for bleeding:

1. too much bituminous binder is the mixture,
2. too heavy a prime or bond/tack coat,
3. too less voids in the mixture,
4. post compaction due to traffic leading to over-compaction resulting in pushing the binder to the surface.



Figure 317: A “bleeding” wearing course.

That traffic will cause post compaction is rather unthinkable in a country like the Netherlands where a lot of attention is paid to proper compaction. In a number of countries however, post compaction due to traffic occurs, and is even accepted, and in combination with factors 1 to 3 and hot weather this can certainly lead to bleeding of the pavement surface.

15.5.3 Raveling

Raveling is a complex phenomenon since it not only involves the strength of the bituminous mastic/mortar but also the strength of the bond between the aggregate particles and the bituminous binder. The strength of the bond between the bituminous mastic/mortar and the aggregates is affected by the type of aggregates and bitumen used as well as the presence of moisture. Furthermore bitumen content, traffic and climatic loads play an important role.

Using the SHRP-NL data base which contained performance data of 250 road sections, each consisting of 3 * 100 m long sub-sections, that were collected from 1990 till 2000, Miradi [98] determined by means of several AI techniques the five most important factors controlling the raveling of porous asphalt concrete (PAC) wearing courses as used on the Dutch highways (17% of the sections in the SHRP-NL data base had a PAC wearing course). This type of mixture is extensively used on the Dutch highways for noise reducing purposes. More than 90% of the Dutch highways have such a wearing course and raveling is the main reason for doing maintenance. Some of Miradi’s results are shown in tables 72 and 73.

Method	Setting	Variable 1	Variable 2	Variable 3	Variable 4	Variable 5
Regression trees	Leave-one-out cross validation	Bitumen content	Traffic	Cold days	Voids content	%Coarse
Genetic polynomial	Polynomial degree = 3	Bitumen content	Traffic	Cold days	%Coarse	Voids content
Artificial neural network (WWF)	Leave-one-out cross validation	Bitumen content	Traffic	Voids content	Cold days	%Coarse
Rough sets	2-class output	Bitumen content				
Correlation-based subset selection (bidirectional search)	Greedy stepwise search Leave-one-out cross validation	Bitumen content	Traffic	Cold days		
Correlation-based subset selection (genetic search)	Genetic Search Leave-one-out cross validation	Bitumen content	Traffic	Voids content	Cold days	%Coarse
Wrappers of ANN (genetic search)	Genetic Search Leave-one-out cross validation	Bitumen content				
Relief ranking filter	K=20 Nearest neighbor (equal influence) Leave-one-out cross validation	Bitumen content	Traffic	Cold days		

Table 72: Most important parameters affecting the amount of raveling on PAC wearing courses 5 years after construction.

Note: "cold days" is the number of days with a minimum temperature < 0 °C
"Warm days" is the number of days with a maximum temperature > 25 °C

Method	Setting	Variable 1	Variable 2	Variable 3	Variable 4	Variable 5
Regression trees	Leave-one-out cross validation	Bitumen content	Voids content	Cold days	%Coarse	Density
Genetic polynomial	Polynomial degree = 3	Voids content	Bitumen content	Cold days	%Coarse	Density
Artificial neural network (WWF)	Leave-one-out cross validation	Voids content	Cold days	Bitumen content	%Coarse	Traffic
Rough Sets	3-class output	Bitumen content	Voids content			
Correlation-based subset selection (bidirectional search)	Greedy stepwise search Leave-one-out cross validation	Voids content	Bitumen content	Cold days	D50	Density
Correlation-based subset selection (genetic search)	Genetic Search Leave-one-out cross validation	Voids content	Bitumen content	Density	Cold days	D50
Wrappers of ANN (genetic search)	Genetic Search Leave-one-out cross validation	Voids content				
Relief ranking filter	K=20 Nearest neighbor Leave-one-out cross validation	Cold days	Voids content	Bitumen content	Warm days	Density

Table 73: Most important parameters affecting the amount of raveling on PAC wearing courses 8 years after construction.

When comparing table 72 with 73 one will notice that the most important parameter explaining raveling 5 years after construction is the "bitumen content" (8 times out of 8) while the 2nd important parameter is "traffic" (8 times out of 8). For the amount of raveling 8 years after

construction the picture has changed drastically. The bitumen content (2 times out of 8), the void content (5 times out of 8) and the number of cold days (1 time out of 8) have become the most influential parameters. The influence of traffic seems to have disappeared from the picture; it is only mentioned one time as a number 5 important parameter. Furthermore it is remarkable that precipitation did not show up at all as an influential parameter. It is remarkable since raveling can very well be caused by stripping which is a process highly driven by water.

Considering the order of importance of the variables, it should be noted that not all methods make it possible to determine the exact importance ranking. Two of the methods which gave a rather clear ranking were the genetic polynomial regression technique and the artificial neural network technique. The rankings according to the later technique are given in figure 318 and figure 319.

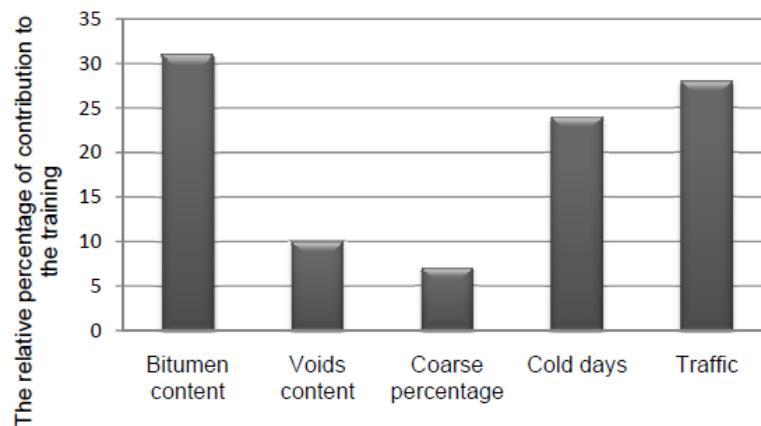


Figure 318: Five most important influence factors on raveling in PAC 5 years after construction based on neural network input selection.

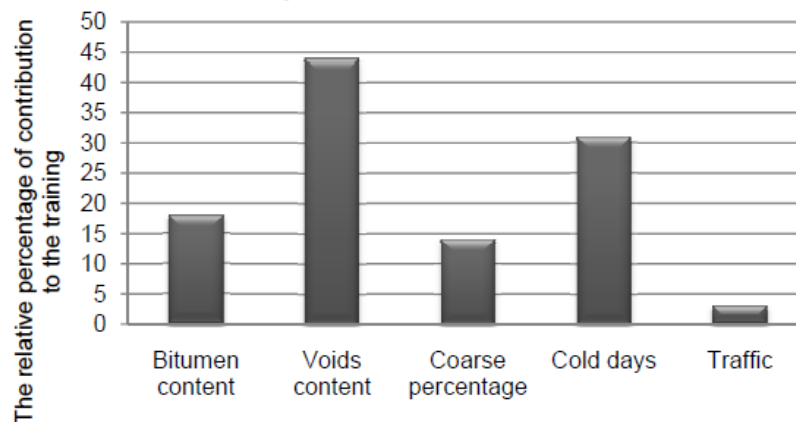


Figure 319: Five most important influence factors on raveling in PAC 8 years after construction based on neural network input selection.

Figures 318 and 319 show that based on the neural network input selection method the number of "cold days" plays a pretty important role in explaining the amount of raveling 5 and 8 years after construction.

As we have seen in chapter 8.8 on "Adhesive Cracking", different types of aggregate have different bond strengths with different types of bitumen. One might therefore wonder why

aggregate and bitumen type were not part in Miradi's analysis. The reasons are quite simple; Dutch crushed siliceous river gravel was used as aggregate in most of the wearing courses that were included in the study. There were some other aggregate types but the number of sections having such a different type of aggregate was so small that it was decided not to take them into account since it is pretty difficult, not to say impossible, to recognize trends from only one or two data points. The reason why the type of bitumen was not taken into account was also because only a few suppliers provided bitumen for the sections and it was not precisely clear where those bitumens were used. All bitumens however complied with the Dutch specifications which implied the use of a pen 70/100 bitumen without the use of any modifier. Other specifications in those days were related to the void content ($> 20\%$) and the bitumen content (4.5% by weight of total aggregates $\approx 8\%$ by volume).

In a parameter study, Miradi determined the effect of some individual parameters on the amount of raveling (expressed in terms of Meq) 5 years after construction. The results are shown in figure 320.

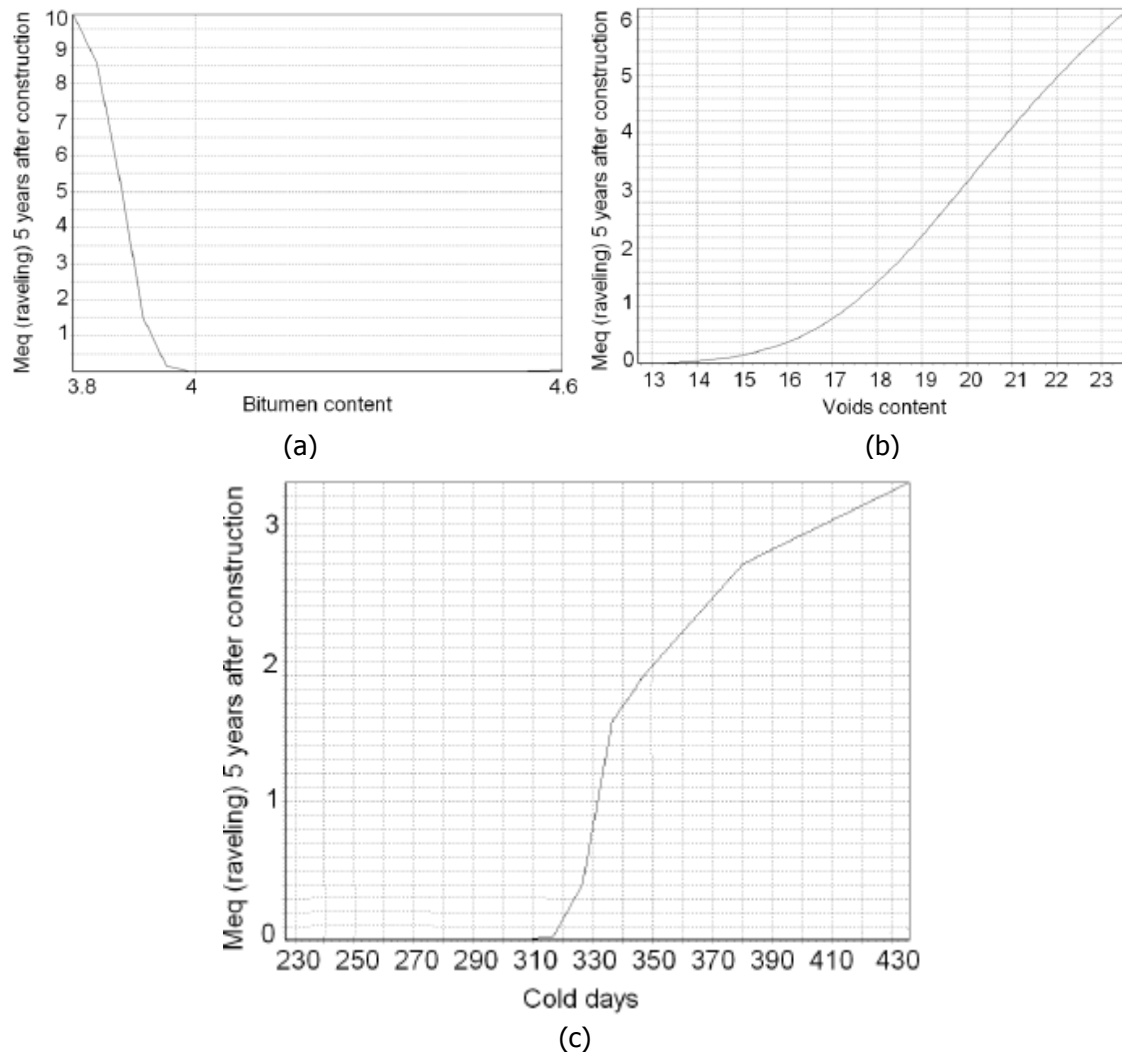


Figure 320: Effect of some parameters on the amount of raveling (Meq) 5 years after construction.

Note: in figure 313c, "cold days" = the cumulative number of "cold days" during a five year period.

For the sake of completeness it should be mentioned that Meq stands for the amount of equivalent moderate raveling. Meq is calculated following:

$Meq = 0.25 * (\text{amount of light raveling} + (\text{amount of moderate raveling}) + 5 * (\text{amount of severe raveling}))$.

The "amount" is in percentage of the area considered. The definitions for "light", "moderate" and "severe" are given in table 74.

Severity of raveling	Percentage of stone loss per m ²
Light	6 – 10
Moderate	11 – 20
Severe	Larger than 20

Table 74: Severity of raveling definitions as used in the SHRP-NL project.

Figure 320a clearly shows that raveling developed rather quick when the bitumen content was below 4% by mass. At the time Miradi was doing her research (2004 – 2008), the Dutch specification required a bitumen content in the PAC of 4.5% by mass on top of 100% aggregates and a minimum void content of 20% because of noise reduction requirements. Unfortunately the amount of bitumen requirement was not always met (see e.g. table 75) and many PAC wearing courses suffered from gravitational drainage of the binder from the top part of the layer to the lower part (in those days PAC was placed in a single layer of 50 mm). Binder drainage is clearly visible in table 75 by comparing the bitumen content data of the upper with those of the lower zone. Bitumen drainage is making the top part of the layer prone to raveling since the bitumen content was below 4% in almost all cases.

Since then a number of things have changed; the bitumen content was raised to 5.5% and crushed siliceous river gravel was not used any longer because of skid resistance issues and was replaced by aggregate types like Bestone, Porphyry, Greywacke etc.

1. Bitumen content %				CT-scan			Laboratory (recovered) bitumen data
Section		Service Year	Sample code	Upper Zone (UZ)	Lower Zone (LZ)	Overall*	
G	EL	0	05041.IPG	3.9	4.4	4.1	4.4
A	EL	1	05033.IPG	3.9	4.5	4.1	4.3
	SL			3.9	4.3	4.1	4.4
B	EL	3	05034.IPG	3.9	4.0	3.9	4.3
	SL			4.2	4.9	4.4	4.3
C	EL	7	05036.IPG	3.5	3.5	3.5	3.9
	SL			3.5	3.7	3.6	3.9
E	EL	12	05039.IPG	3.6	4.1	3.7	4.1
	SL			3.4	4.3	3.6	3.6
Average				3.8	4.2	3.9	4.2

Table 75: Bitumen content in the upper and lower part of PAC cores as determined by means of CT scanning and bitumen content of entire core determined by means of traditional extraction method.

Note: EL = core is taken from emergency lane; SL = core is taken from slow lane.

During the winter 2009/2010, severe raveling occurred on many PAC sections in the Netherlands. The picture shown in figure 314 was taken on one of the sites which showed winter related raveling. Mohan [101] made an analysis of the causes of this winter related raveling which

occurred on such a large scale. He based his work on the Lifetime Optimization Tool (LOT) which was developed by Huurman e.a. [99, 100] and for which a lot of work has been done by Mo [58] under the LOT project leadership of Huurman. Before we will discuss the findings of Mohan, first a short description of LOT will be given.

LOT is a meso-mechanical 2D finite element model (3D version is available) in which the real structure of PAC is transformed into an equivalent structure of spheres (see figure 321).

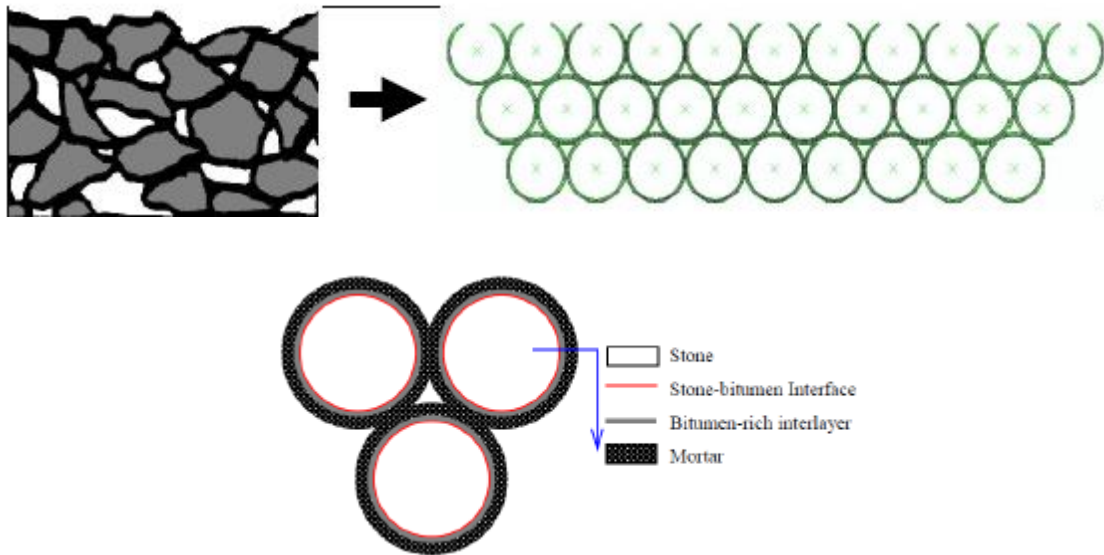


Figure 321: LOT meso-mechanical analysis model.

Figure 321 also shows how the interface between aggregate and mortar was modelled. The spheres were defined as un-deformable rigid bodies. The stiffness, strength and fatigue characteristics of the mortar were determined using stone column – mortar – stone column tests which were described in the chapter on asphalt materials. The test set up which was already shown in figure 183 is shown again here-under as figure 322.

The characteristics of the mortar were determined using the test setup shown in figure 323.

One might comment that representing the aggregates as spheres is a very crude simplification of reality. Although this is a valid comment, one should realize that using a real skeleton instead of spheres (such a version is available) only complicates the picture because the shape of the aggregate particles will highly affect the stress conditions and can therefore make influences of void and bitumen content as well as binder type less visible and therefore making studies on the effects of these parameters more complicated.

In spite of the simplifications made, the LOT model was (and of course still is) very capable of predicting failure in terms of adhesive or cohesive failure. The results obtained agreed very well with those obtained from full scale testing, more precisely: the predicted order of failure of 4 sections which differed from each other in aggregate type and void content, agreed with the observed order of damage development.

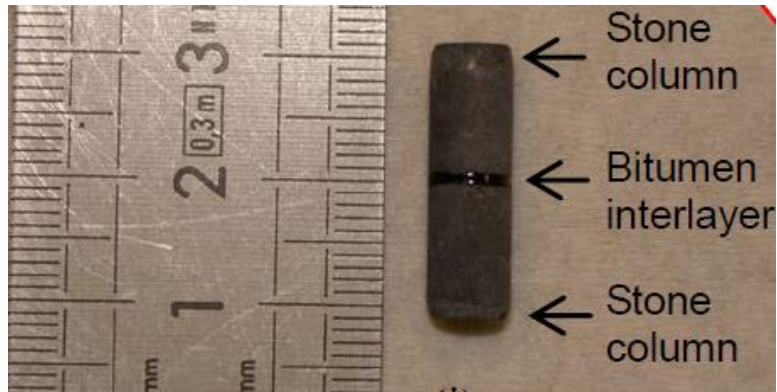


Figure 322: Stone – bitumen – stone column adhesion testing by means of the DSR.

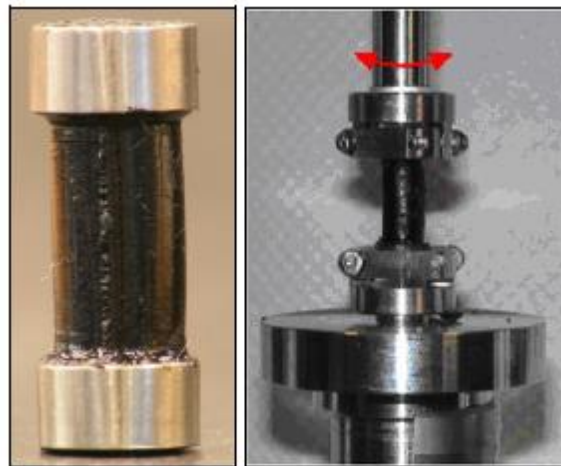


Figure 316: Mortar columns tested by means of the DSR for obtaining stiffness and fatigue characteristics.

With respect to the applicability of LOT it should be mentioned that the tool has been successfully used by Milne [102] and Gerber [103] in their studies on the lifetime of seals.

Mohan in his research modelled PAC according to the LOT protocol. He took into account the effects of wheel loads as well as temperature stresses that develop during winter periods. Special attention was paid to the effect of relaxation of the bituminous mortar. He was able to show that

the winter damage that was observed on a number of sections was clearly due to low bitumen contents of the PAC in those sections and the fact that the bituminous mortar had almost completely lost its relaxation capacity. So according to his findings raveling in PAC due to winter conditions was caused by a too low bitumen content and a low relaxation capacity; the low relaxation capacity is reflected in high stiffness values at low frequencies (figure 324).

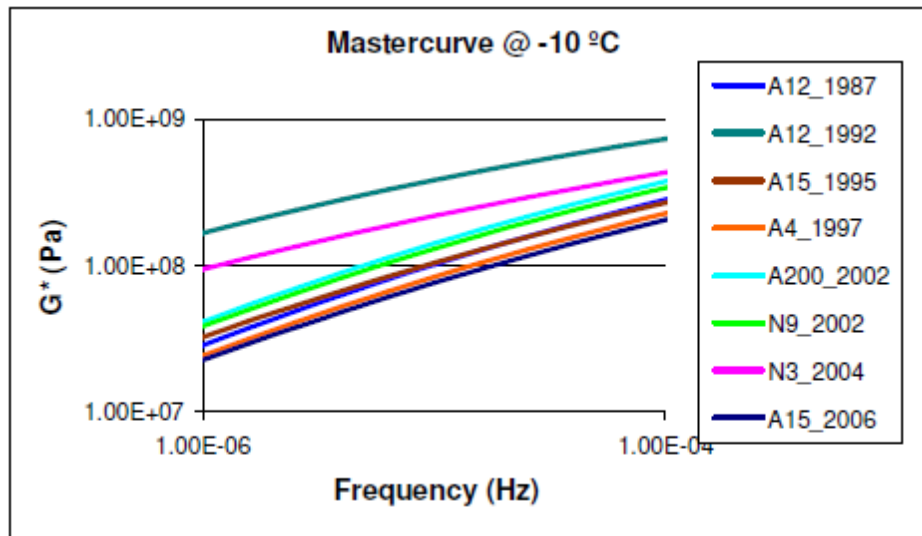


Figure 324: G^* master curves of the bitumen retrieved from the test sections investigated by Mohan.

The A12-1992, N3-2004 and N9-2002 sections were the ones showing much winter related raveling. These sections had void and bitumen contents which as shown in table 76.

Section	A12-1992	N3-2004	N9-2002
Void content [%]	19.1	20.8	21.8
Bitumen content by mass [%]	3.6	3.29	3.03

Table 76: Void and bitumen content of the sections showing severe winter related raveling.

Mohan's results are fully in line with those found by Miradi and in the LOT project, indicating that the bitumen content is a key parameter in controlling the amount of raveling. On top of that he showed that the relaxation capacity of the binder is another key factor.

Although moisture damage is not specifically mentioned in LOT, it can be taken into account via the transfer functions that describe the fatigue resistance of the stone – mortar – stone interface and the fatigue resistance of the mortar with and without water conditioning. The moisture conditioning used by Mo [58] to determine the effect of moisture was to submerge the samples under vacuum in water of 5 °C. He found that the fatigue resistance of the mortar reduced with around 25% (so the resistance of the moisture treated specimens was around 75% of the specimens which did not receive a water treatment). The interface fatigue resistance was roughly halved. This shows that the influence of moisture can be significant; it should be mentioned however that the moisture conditioning treatment as used by Mo was a severe one. All this shows that we should have a more detailed look into the effects of moisture on the condition and mechanical characteristics of asphalt mixtures.

Raveling is also to be caused by moisture effects but keep in mind: this implies moisture not only as fluid but also as vapor. Moisture has a significant effect on the bond between the aggregate –

bituminous mortar but will of course only be of a problem when it can get in the mixture and when it has enough time to cause loss of bond between the aggregate and the mortar. The reason for this loss of bond is the following. Most of the aggregates have a negative electrical charge and when water can reach the interface between the aggregate particle and the bituminous mortar, the extremely strong water dipole will immediately try to “push away” the bitumen from the stone particle. The other possibility of water to reach the aggregate – bitumen interface is through diffusion of the moisture through the bituminous coating. As mentioned before, the prerequisite for both processes is the possibility for the moisture to get into the mixture and to stay there long enough allowing diffusion to take place. Figure 325 [104] shows what is believed the most critical void content range with respect to moisture damage.

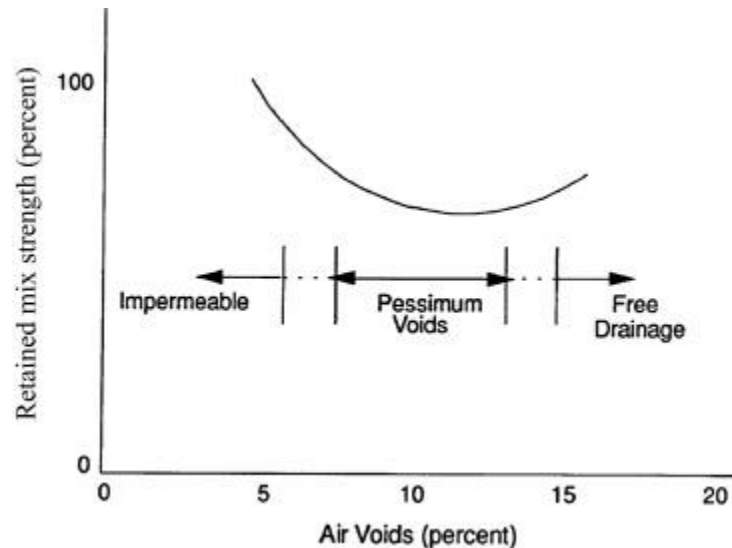


Figure 325: Pessimium air void contents resulting in the highest moisture damage [104].

As mentioned before, moisture will only produce damage when it has a chance to enter the asphalt mixture. This implies that the voids need to be inter connected. Li [105] investigated the relation between the void content and the degree of connectivity of the voids. This relationship is shown in figure 326.

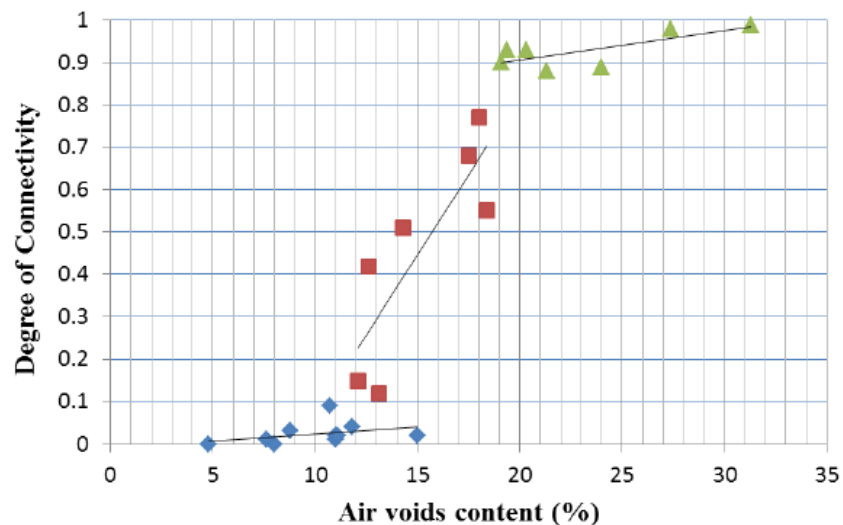


Figure 326: Void content and degree of connectivity of the voids.

Similar information is given figure 327 for a PAC in and in figure 328 for a Stone Mastic Asphalt (SMA). Both mixtures were produced with aggregates having a maximum grain size of 11 mm. The void content in the PAC was 23.7% while the bitumen content was 5.3% by mass. The SMA had a void content of 4.4% and a bitumen content of 6.4% by mass. It is interesting to notice that although the SMA is a rather dense mixture, there is still some connectivity between the voids implying that moisture can also penetrate in a so called dense mixture.

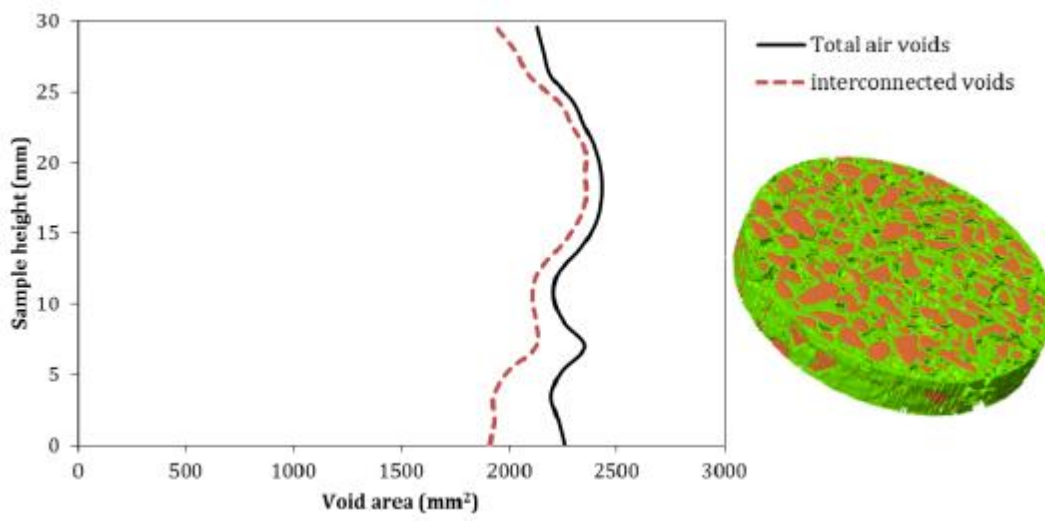


Figure 327: Void content and connectivity over the height of a PAC sample [107].

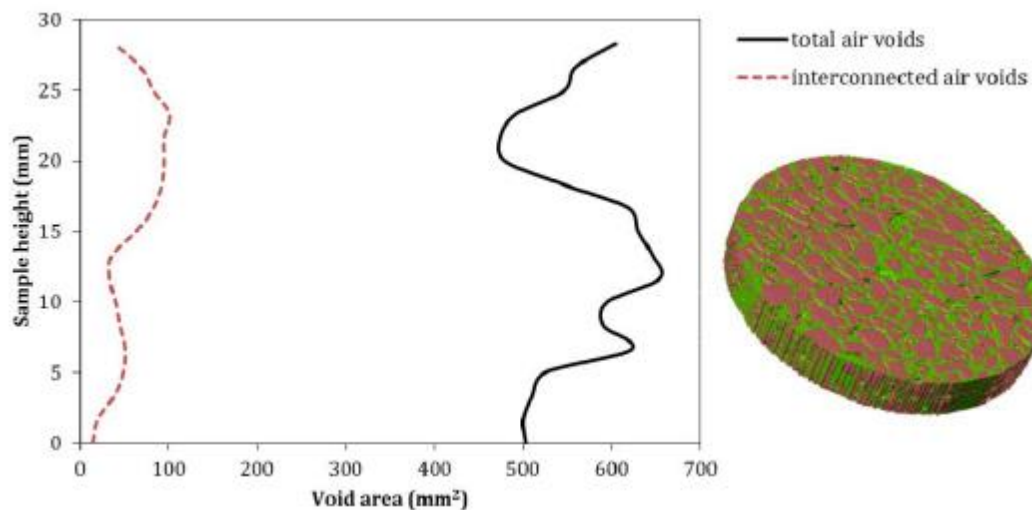


Figure 328: Void content and connectivity over the height of a SMA sample [107].

When moisture is IN the voids, it can diffuse through the bitumen layer surrounding the aggregates.

Wikipedia tells us that "diffusion is the net movement of molecules or atoms from a region of high concentration with high chemical potential to a region of low concentration with low chemical potential".

Fick's second law predicts how diffusion causes the concentration to change with time. For a one dimensional process it is written as:

$$\partial \varphi / \partial t = D * \partial^2 \varphi / \partial^2 x$$

Where:

φ = concentration e.g. [mol/m³]
 t = time [s]
 D = diffusion coefficient [m²/s]
 x = length [m]

Varveri [107] prepared cylindrical mortar samples (total weight 65 gr) made of 25% m/m binder, 25% m/m filler (material < 63 μ m) and 50% m/m sand (125 μ m < d < 1mm). The filler was either a limestone filler called Wigras 60 and a hydrated lime Wigro 60K filler which contained 25% hydrated lime. Three types of bitumen were used being a 70 – 100 pen reference bitumen with a softening point of 43 – 51 °C, a Cariphalte XS SBS modified bitumen with pen 45 – 80 and a softening point > 65 °C, and a Sealoflex 5-50 SBS modified bitumen with pen 60 – 90 and a softening point > 65 °C. The samples were fully submerged in water (20 °C) for a particular time and the uptake of water was measured. The results of these measurements are shown in figure 329. Although the absolute values of water uptake might not seem that high, there is a significant effect of bitumen type and filler type on the water uptake. Pen 70/100-Wigras 60 has a 3 times higher uptake than the Sealoflex 5-50-Wigro60K. It will be clear that the mortar with the lowest moisture uptake is to be preferred.

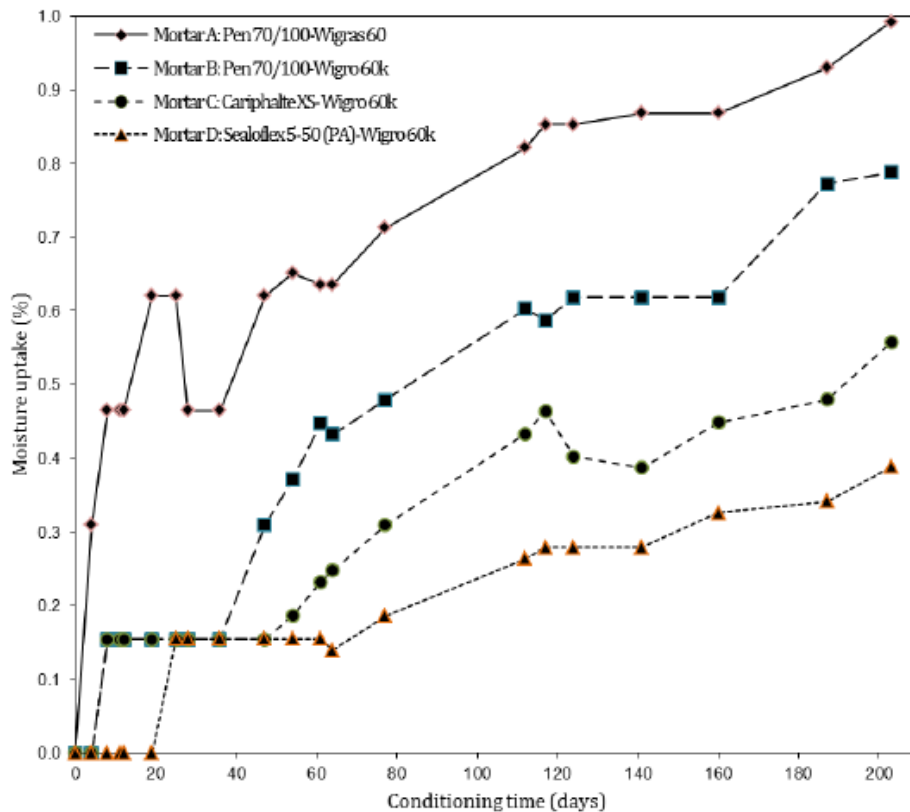


Figure 329: Uptake of moisture of the different mortars. Top: Pen 70/100-Wigras60; Second: Pen 70/100-Wigro60K; Third:Cariphalte XS-Wigro60K; Bottom: Sealoflex 5-50-Wigro60K.

Based on the information given above, we can conclude that in order to increase the **raveling resistance of dense type of asphalt mixtures** one should aim for the following:

- relatively thick mortar/bitumen films around the aggregate particles (to be obtained by means of the mixture design c_q aggregate size selection and bitumen content),
- relatively low void content resulting in a low connectivity of the voids (to be obtained by mixture design and compaction),
- mortar composition with a low moisture uptake capacity,
- good relaxation properties of the bituminous mortar/binder,
- aggregate – binder combination that results in the highest bond strength.

One will notice that these requirements are exactly the same as those mentioned for getting a mixture which is resistant to top-down cracking.

With respect to moisture related raveling damage on dense wearing courses in the Netherlands one should note that the amount of water that can enter the dense layer is only very limited. First of all this is because the amount of rainfall in the Netherlands is not spectacularly high (see figure 330). Secondly, not all the water that comes on the pavement surface will penetrate the pavement because of drainage (run-off because of the cross slope of the pavement surface) and drying of the surface. Thirdly, the maximum void content of dense wearing courses is restricted to 5%. All in all this means that moisture related raveling of dense wearing courses is not really a big issue in the Netherlands. It might however be a big issue in other countries where the conditions are different.

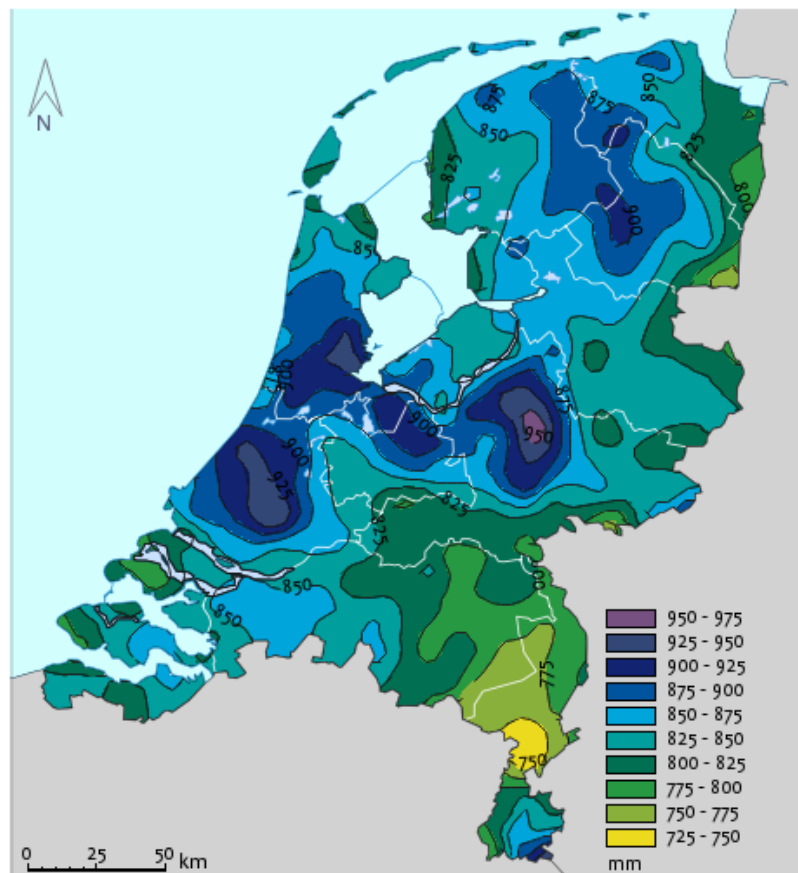


Figure 330: Long-term average rainfall in the Netherlands period 1981 – 2010 [107].

For porous asphalt concrete (PAC) with its high void contents ($> 20\%$) the situation is somewhat different because for these types of mixtures some additional damaging effects need to be considered as well. Kringos [106] defined in her work the following processes (figure 331) that result into the disintegration of PAC.

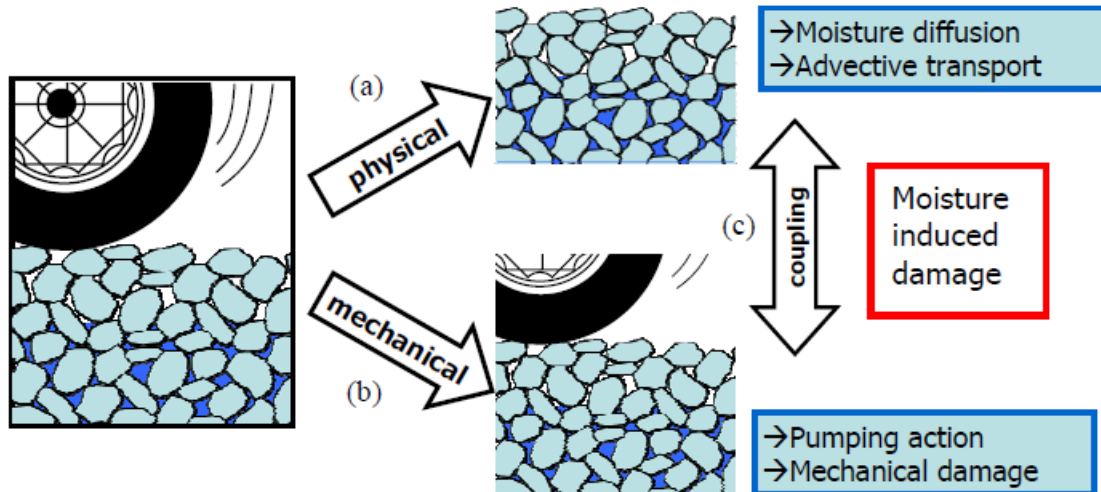


Figure 331: Moisture related damage mechanisms in PAC as defined by Kringos [106].

The physical processes mentioned by Kringos are diffusion of moisture and a “washing away” process of the mastic, which she called advective transport, due to a fast water flow field. The mechanical damage processes includes pumping and refers to the high water pressure fields inside the mixture caused by traffic. The mechanical damage she mentions in figure 324 is in fact the damage which can be explained by design systems like LOT being adhesive and cohesive fatigue due to wheel and temperature loads.

Kringos [106] and Varveri [107] have both been working on the development of models which can describe the above mentioned processes. The reader who is interested in the mathematical background of the how these processes have been modelled are referred to reference [106] and [107].

The question however is whether we can also do tests which mimic the processes described here. Such a test is available and is known as the MiSt test; the equipment is shown in figure 332.

As is shown in figure 332c, a specimen is placed in a container which is then filled with water. After that the whole system is put under pressure. The repeated pressure which is applied is simulating the repeated excessive pore pressure which occur when a wheel load is travelling a saturated PAC layer. Figure 333 shows some results obtained by Varveri [107].

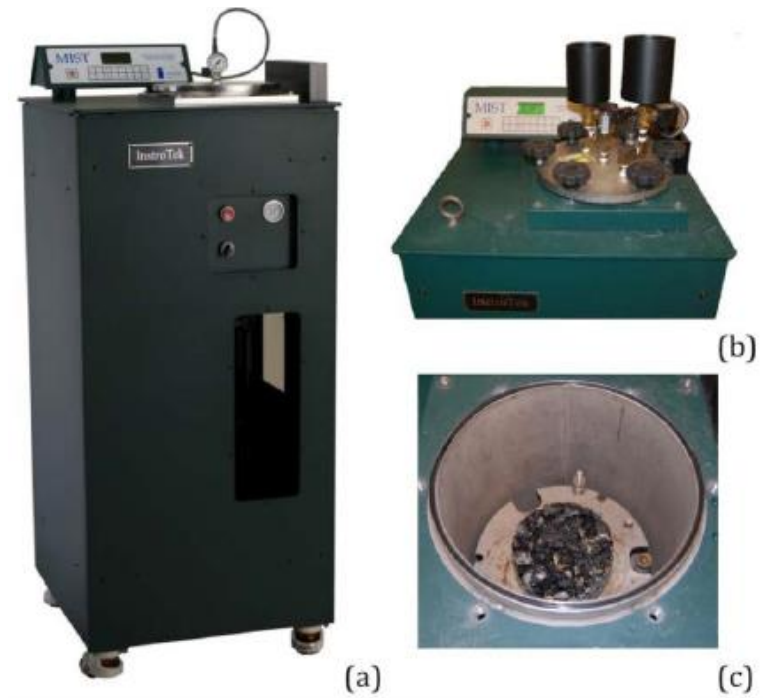


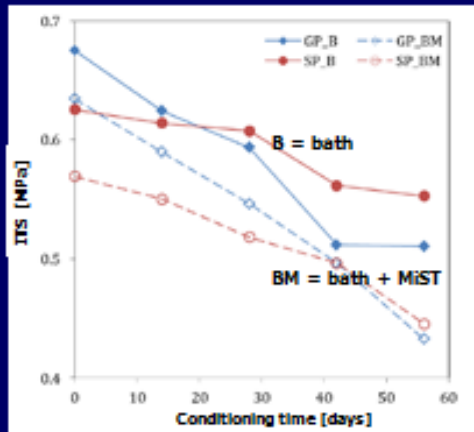
Figure 332: MiST device.

Figure 333 shows some interesting things being:

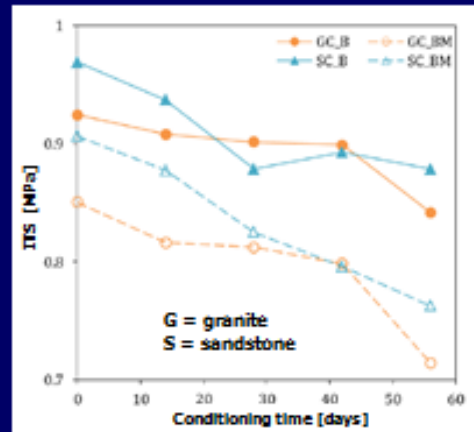
- the water bath treatment has a negative effect on the tensile strength,
- the MiST treatment increases the negative effect of water,
- the bath treatment + MiST lines are more or less parallel to the bath treatment lines,
- the mixtures with the Cariphalt SBS modified bitumen show a significant higher tensile strength than the mixtures with the 70/100 pen bitumen,
- the slope of the strength vs conditioning time is about equal for each mixture and seems not to be affected by the MiST treatment,
- the mixtures with the sandstone aggregates performed somewhat better than those with the granite aggregates.

The question of course is whether the MiST device is simulating reality. This question is a very valid one because in reality a PAC layer will never be completely saturated with water of 60 °C. Further remember that PAC has a high permeability and the chances that it stays saturated for a considerable amount of time are not that high. There might be saturation in some pores because of the presence of fine material in those pores because of clogging and this fine material might retain moisture. Finally it should be mentioned that it was shown by means of coring that raveling of PAC is mainly to almost exclusively observed at the top part of the PAC layer (which dries easily).

porous asphalt concrete 4.5% bitumen by mass, 20% void content
specimen $\phi = 101.6 \text{ mm}$, $h = 50 \text{ mm}$
X days at 60°C + 4000 MiST cycles (water 60°C and 0.48 MPa pressure)
bath treatment affects physio-chemical nature of binders and mortars
MiST treatment simulates mechanical effects



70/100 pen bitumen



Cariphalt SBS bitumen

January 22, 2018

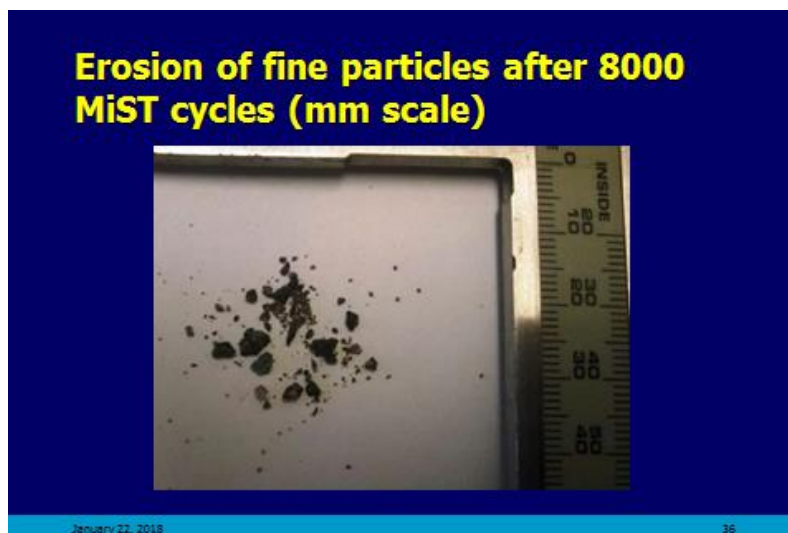
35

Source: PhD thesis Varveri, 2017



Figure 333: Loss in indirect tensile strength of PAC specimens subjected to submerging in water and a MiST treatment. The effects of the bath treatment is given by the draw lines, the effect of the bath + MiST treatment is given by the dashed lines.

Figure 334 shows that erosion of fine particles did take place after a large number of MiST cycles.



January 22, 2018

36



Figure 334: Erosion of fine particles from the PAC mixture as a result of a MiST treatment.

Kringos concluded in her work that pumping is mainly harmful for the cohesive connection between the aggregates. She also showed that erosion of the mortar could certainly take place depending on the moisture sensitivity of the mortar and the bond strength between aggregate and mortar (please note that it was mentioned earlier that Mo did show that moisture has a serious effect on the fatigue strength of the mortar and the fatigue strength of the adhesive zone).

The question now is: "does erosion of the mortar occur in practice?. Do we have data to proof this?" Evidence that this is indeed the case was given by Mohan [101]. In his work he found that the pores were partly filled with dirt assumingly being the result of clogging of the pores (see figure 335).

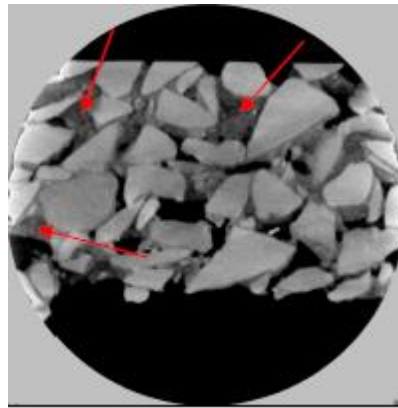


Figure 335: Clogged pores in PAC.

The question however is whether all this dirt is dirt or whether some particles are in fact fines as a result of the erosion process described above. If this would be the case then also traces of bitumen should be in the dirt. Mohan analyzed the composition of the dirt particles < 1mm (which was 90% of the total amount and found the results shown in table 77.

Material	Mass [gr]	Mass %
Filler material < 63 μm	4.2	11.4
Material > 63 μm	30.6	82.9
Bitumen	2.1	5.7
Total	36.9	100

Table 77: Composition of the dirt found in pores of PAC

The question then is how much dirt is present in the pores? This is a difficult question because suction produced by traffic has a self-cleaning effect on the pores of the PAC in the trafficked lane and the pores of the PAC on emergency lanes are cleaned using cleaning machines. Because of these cleaning processes it is difficult to get an idea of the magnitude of the erosion of the mastic. Mohan in his research investigated cores coming from 6 different pavements and he found the dirt content ranging between 1.6% and 8.1%. by mass of the cores.

All in all this means that erosion of the mortar due to fast moving moisture in the pores does occur; unfortunately the amount of erosion that occurs in practice is very difficult to determine.

15.6 Skid resistance

It will be obvious that sufficient skid resistance is necessary to provide the road user a safe driving surface. This becomes clear when we observe the relation between skid resistance and accident rate which is shown in figure 336.

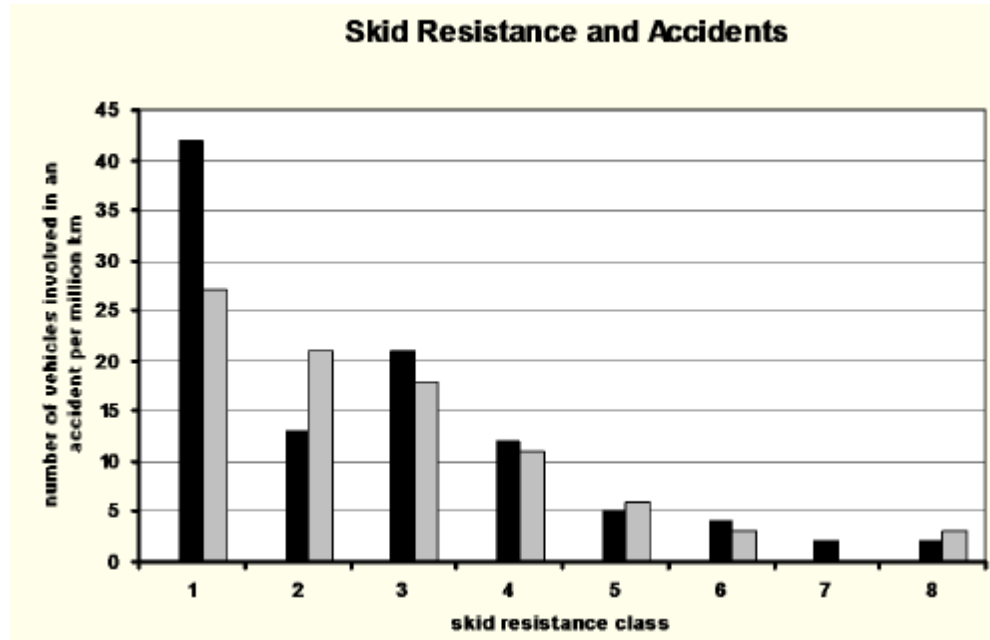


Figure 336: Relation between number of accidents and skid resistance.

Note: black bars indicate person cars and grey bars indicate trucks

From experience we know that the skid resistance of road surfaces is much lower when they are wet then when they are dry and we also know from experience that not all wet surfaces do have the same skid resistance. From experience we know that a pavement surface like the one shown in figure 337 is not only rather uncomfortable to drive on but also very slippery when wet. Nevertheless this type of cobblestone pavement, and preferably it should be in an even in a worse condition, is the big "attraction" in the famous cycle race Paris – Roubaix (see figure 338). Also the pavement of the little square shown in figure 339 will be slippery when wet and one wonders why architects don't understand that also pedestrians need a pavement surface with sufficient skid resistance. We might ask ourselves "why are these pavements slippery when wet?". The answer is quite simple, the surface lacks a "grinding paper" type of structure or, in other words, it lacks micro texture. There is another thing these pavement surfaces are lacking which is macro texture. The definition of micro and macro texture is given in figure 340. As figure 3340 shows, micro texture is provided by the surface roughness of the individual aggregate particles while macro texture is controlled by the size of the aggregate particles. The function of the micro and macro texture is shown in table 78. Pictures of micro and macro texture are shown in figure 341.



Figure 337: Wet cobblestone pavement.



Figure 338: The main "attraction" in the famous Paris – Roubaix cycle race are the stretches with cobblestones.



Figure 339: The pavement of this little square will be slippery when wet.

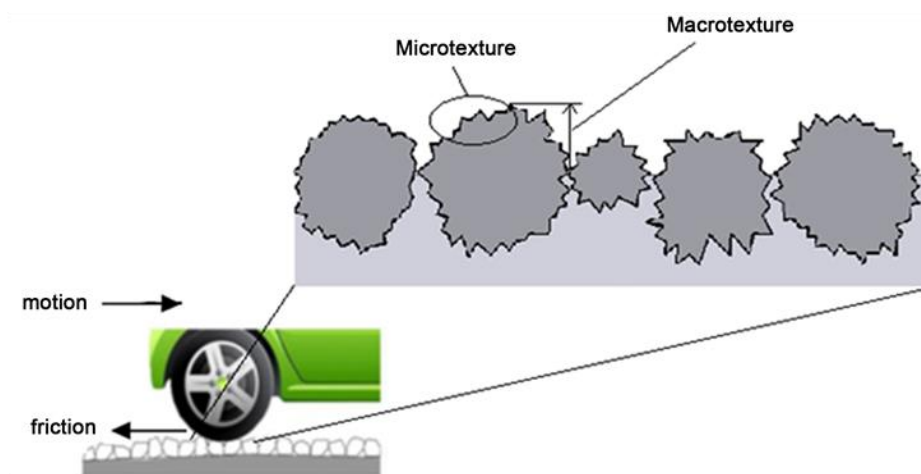


Figure 340: Micro and macro texture.

Component	Main-Function	Main Benefit
Macro texture	Rapid drainage Deformation of tire	Avoid hydroplaning Hysteresis
Micro texture	Penetrates the thin layer of water to provide tire/pavement contact	Adhesion

Table 78: Function and benefits of micro and macro texture.

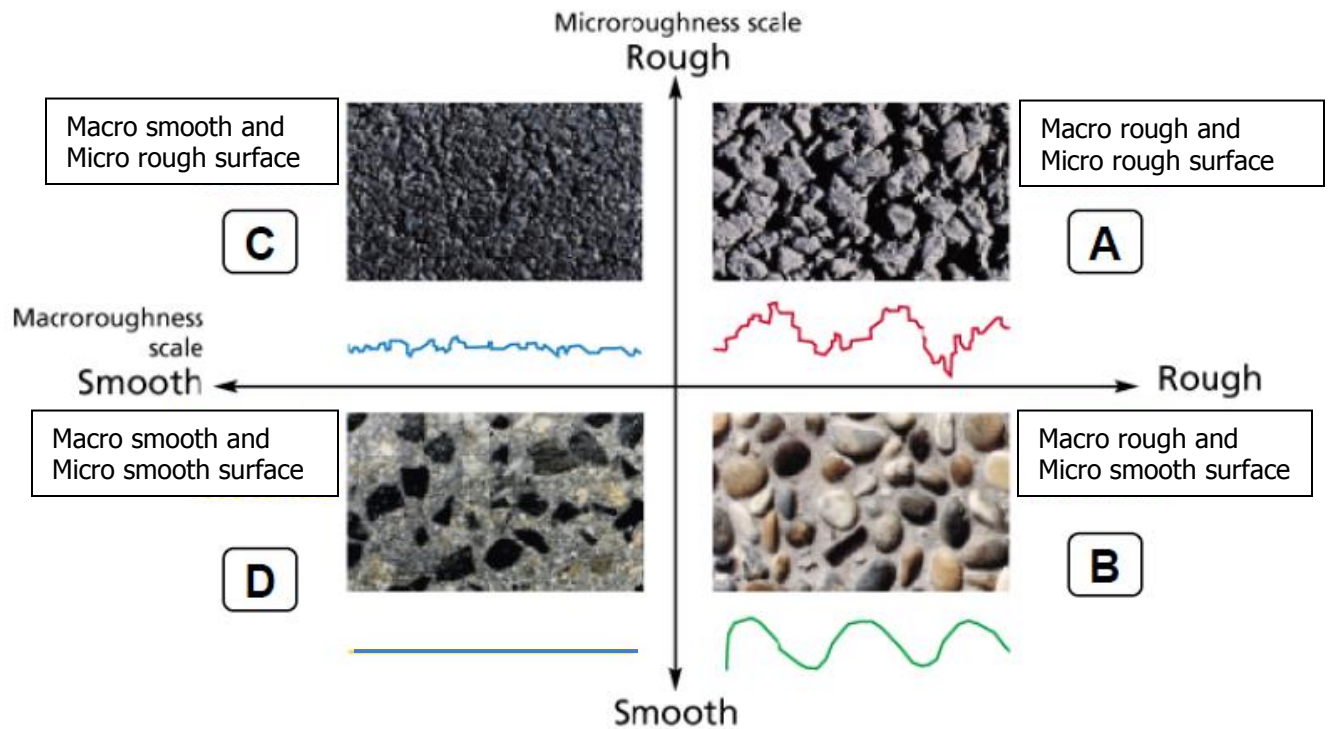


Figure 341: Pictures of micro and macro texture [108].

Figure 342 shows the friction coefficient in wet weather conditions for the four pavement surfaces shown in figure 341.

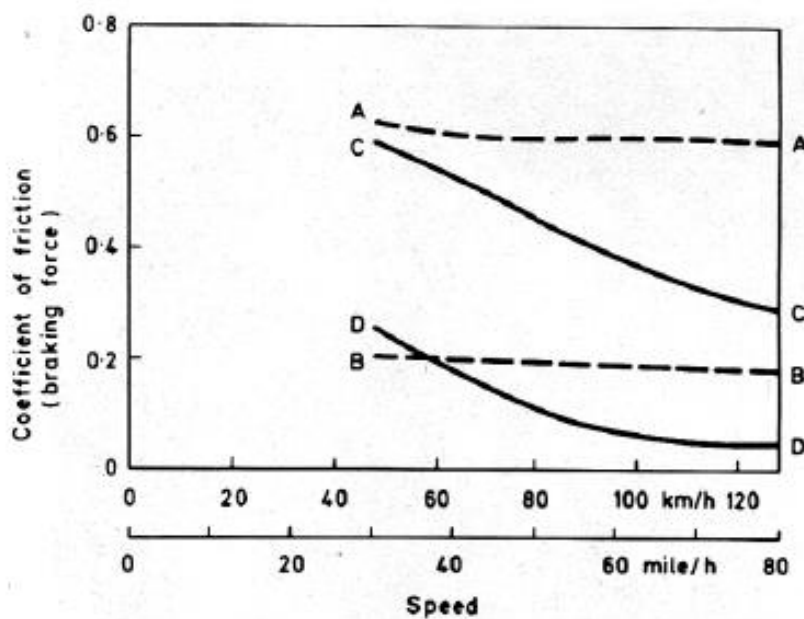


Figure 342: Wet weather coefficient of friction measured with a smooth tire on the four surfaces shown in figure 341 [108].

Figure 342 shows that that macro texture, micro texture, and speed have a great influence on the measured friction coefficient which is defined as $\mu = F_x / F_z$ (horizontal force on the tire divided by the vertical tire force). Of course the tire (type, depth of the grooves) etc and the thickness of the water film on the road also play an important role but this will be discussed later on. In the early 1970's, Dijks of the Delft University of Technology developed a relationship between the friction coefficient on one hand and the macro and micro texture as well as the vehicle speed on the other. This relationship is:

$$\mu = 0.52 + 0.58 \text{ SRT} / 100 - 0.001 * \text{SRT} * V / (100 * \text{TD})$$

Where:

- μ = friction coefficient,
- SRT = friction value measured with the SRT (a measure for the micro texture),
- V = speed [km/h]
- TD = texture depth (a measure for the macro texture) [mm]

The relationship was developed for a tire (specifications unknown) with an inflation pressure of 180 kPa and a tire load of 3.3 kN, and a water film thickness of 0.6 mm.

The equation shows that the friction coefficient decreases when the SRT decreases, the product $\text{SRT} * V$ increases and TD decreases. Later on we will come back to these influence factors in greater detail.

Let us first discuss how the friction coefficient, SRT value and texture depth can be measured.

A large number of devices are available for skid resistance measurements on roads. An excellent overview of these devices can be found in [109]. One device which has gained large popularity is the SCRIM which is pictured in figure 343.



Figure 343: SCRIM device for measuring skid resistance.

The measurement wheel has a slip angle of 20° with the driving direction and a 0.5 mm thick water film is sprayed in front of the tire. The tire pressure is 350 kPa, the tire load is 1960 N and measurements are usually done at 50 km/h. The tire is an "Avon SCRIM smooth profile tire 76/508".

Figure 344 shows the Dutch skid resistance trailer. The measuring wheel operates at 86% slip and in front of the tire a 0.5 mm water film is sprayed. The measurements are done at 50 – 70 km/h. The measurement tire is a "PIARC smooth profile tire" which has an inflation pressure of 200 kPa and operates at a tire load of 1962 N. From the description of these two devices it will be clear that the friction number that is obtained depends on the device that is used. Since there is such of variety in equipment, it is a hell of a job to translate the numbers obtained by one machine into numbers that would be obtained when other devices would have been used.



Figure 344: Dutch skid resistance trailer.

Figure 345 shows the SRT device which produces the SRT number which was mentioned in Dijk's equation (see previous page). This device basically consists of a pendulum with a foot under which a rubber pad is attached. Next to that there is an indicator and a scale. The pendulum and the indicator are lifted to the position shown in figure 345 left. Then both are released and swing over the pavement surface while the rubber pad of the foot is touching the pavement. The higher the skid resistance the less high the pendulum will swing. The indicator is measuring this height (see figure 345 right). The equipment is also used to measure the PSV (polish stone value) of aggregates; these measurements will be discussed later on.



Figure 345: SRT device.

The texture depth TD which is mentioned in Dijk's equation is measured with the so called sand patch method. In this method, a certain amount of sand is spread on the pavement surface such that a circle is obtained. Then the diameter of the sand patch is measured and the texture depth is calculated using:

$$TD = 4 * W / (\gamma * \pi * D^2)$$

Where:

TD = texture depth [mm],
W = weight of the amount of sand used [kg],
D = diameter of the sand patch [mm],
 γ = specific weight of the sand [kg/mm³].

The test itself is shown in figure 346.



Figure 339: Sand patch test to determine texture depth.

As with all these empirical tests, the tools are carefully specified. The sand spreading tool has a diameter of 63.5 mm (2.5 inch) which has at its bottom a 16 mm hard rubber disc of the same size. With the kit comes a measuring cylinder of 24.6 ml. The sand is a silica Ottawa sand (Illinois) which complies to the specifications shown in table 79.

Sieve size [μm]	% retained
420 (No. 40 sieve)	0
300 (No. 50 sieve)	0 – 4
150 (No. 100 sieve)	96 - 100

Table 79: Sand for the sand patch test.

Nowadays texture measurements can be done at high speed user laser technology. This will be discussed in the section on traffic noise.

Because of erosion and wear due to the abrasive action of traffic in combination with moisture, oil spillage and dirt, the aggregate surface might get polished and because of that the skid resistance may decrease. The resistance to polishing is determined by means of the polishing stone machine which is shown in figure 347. The machine itself is shown on the left hand side of figure 347 while an important detail is shown on the right hand side of the figure. Fourteen aggregate samples (88.9 mm long and 44.45 mm wide) are glued in special molds which are

attached to a wheel (see figure 347 right). The aggregate particles should pass the 9.5 mm (3/8") sieve but be retained on the 6.3 mm (1/4") sieve. The particles are loaded by a solid rubber wheel (hardness of the rubber is 69 ± 3 IRHD) with a load of 715 – 735 kN at 315 – 325 rpm. The test is performed in 2 stages; in the first stage 20 – 34 gr/min of corn emery is spread on the samples while rotating and water is applied at 20 – 34 ml/min. After being carefully dried the specimens are subjected to the second stage. In this stage emery flour is used at a rate of 2 – 4 gr/min and water is sprayed at a rate of 5 – 8 ml/min. After the test has been completed the SRT value is determined using the equipment shown in figure 345.

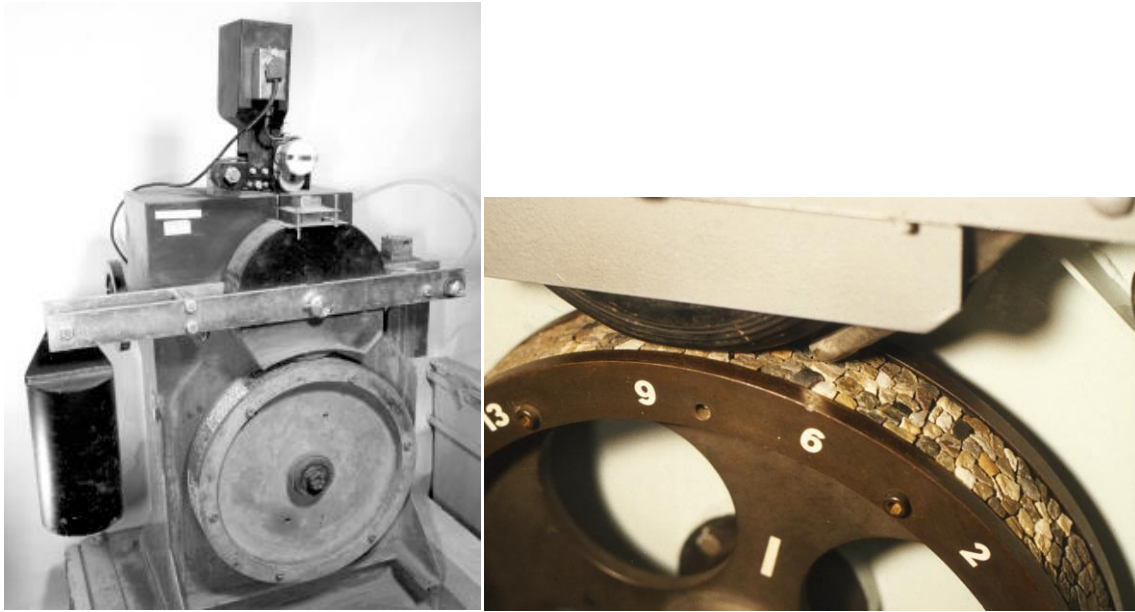


Figure 347: Polishing stone machine.

Also the SRT value of aggregate particles which have not been subjected to polishing is measured. Then the Polished Stone Value PSV is calculated using:

$$PSV = S + X - C$$

Where:

- S = SRT value of the aggregate specimens subjected to polishing,
- C = SRT value of specimens of the same material which were not subjected to polishing,
- X = PSV value of a reference material.

The somewhat complicating factor in all this is the fact that 3 different reference materials are defined being:

- Swd: UK PSV control stone PSV = 52.5
- SbG: 2011 UK PSV control stone PSV = 49.0
- HhG: German PSV control stone PSV = 54.5

Aggregates are natural materials and the beauty of Mother Nature is that the "same thing" cannot be pinpointed with one single number. Table 80 e.g. gives the PSV numbers and Los Angeles abrasion values for a number of aggregates as reported in [110]. The table shows that, in spite of the range in values, Greywacke seems to have the highest PSV values. The table also shows that there is no relation between the Los Angeles abrasion value and the PSV of the aggregates.

Stone type	PSV	LA
	L Av H (nr of tests)	L Av H (nr of tests)
Greywacke	59 61 66 (4)	10 18 20 (6)
Sandstone	45 56 63 (29)	10 11 24 (25)
Diorite	50 53 56 (2)	14 18 22 (4)
Limestone	35 50 58 (4)	19 31 49 (9)
Gabro	45 51 57 (42)	10 19 36 (47)
Hornfels	45 49 54 (9)	9 10 12 (6)
Basalt	44 48 55 (22)	8 10 20 (16)
Porphyry	43 46 58 (11)	10 11 12 (6)
Gneiss	45 52 61 (68)	10 22 60 (97)
Granite	46 51 57 (27)	13 29 49 (49)
Quartzite	46 50 55 (6)	13 20 30 (9)

Table 80: PSV and LA values as reported in [110].

Note: L = lowest value measured, H = highest number measured, Av = average value determined from the indicated number of tested specimens.

Until now we have discussed the influence of the aggregates on skid resistance but one might rightfully argue that when asphalt layers are just laid, all the aggregate particles will be covered with a bitumen film making the pavement look black. This bitumen film at the pavement surface will gradually wear off because of the action of traffic. This process is schematically shown in figure 348.

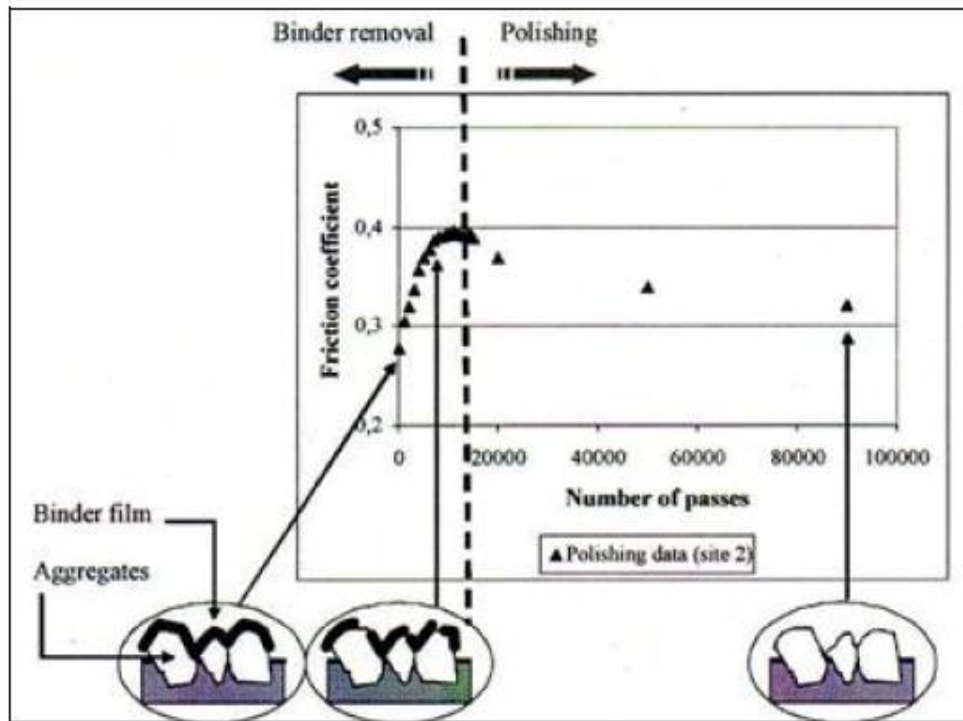


Figure 348: Increase of friction coefficient in the early phase of pavement life due to wear of the bitumen film from the top of the wearing course [108].

The presence of this bitumen film implies that the initial skid resistance of wearing courses can be too low. This is overcome by gritting the surface with fine aggregate particles. Figure 349 shows such a gritted pavement surface.



Figure 349: Gritted pavement surface for early skid resistance [111].

In [111] also some guidelines have been given with respect to the size and amount of gritting material. These guidelines are given in table 81.

Size gritting material [mm]	Maximum aggregate size wearing course ≤ 8 mm	Maximum aggregate size wearing course > 8 mm
1/3	ca 1 kg/m ²	ca 1 kg/m ²
2/5	unsuitable	ca 2 kg/m ²

Table 81: Guidelines for gritting material to provide initial skid resistance[111] .

In time the grits and the bitumen film will be eroded and the aggregate particles at the top of the pavement will be exposed to traffic.

All in all the development (decay) of skid resistance in time shows a pattern like indicated in figure 350.

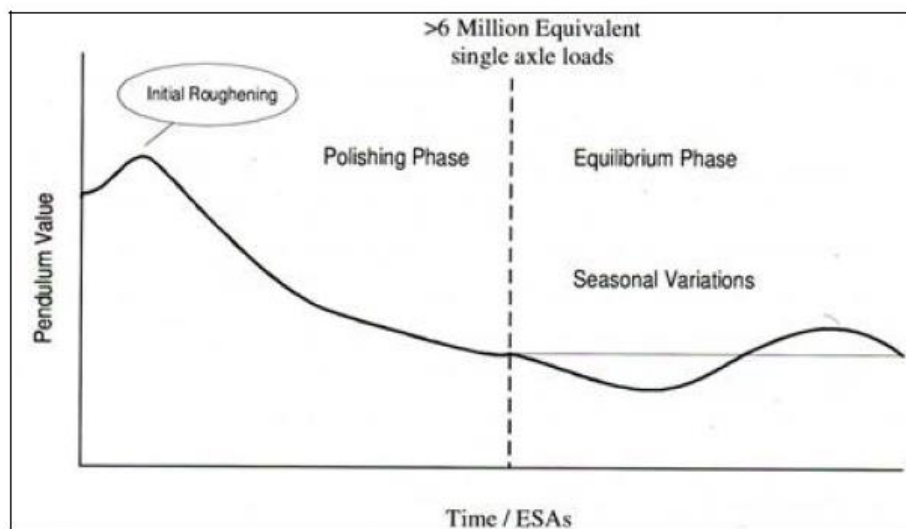


Figure 350: Schematic representation of the decay of skid resistance in time [108].

We have discussed the initial roughening and polishing phase but what about the equilibrium phase? It has been shown that at a given moment, the polishing effect due to traffic becomes in equilibrium with the roughening effect due to climatic influences. Especially after winter periods, the pavement surface will show a rougher texture and a higher skid resistance. In the UK extensive research has been done to establish this equilibrium level. In [112] the following equation has been developed.

$$\text{MSSC} = 0.98 * 10^{-2} \text{PSV} - 0.664 * 10^{-4} \text{CVD} + 0.033$$

Where:

MSSC = mean summer SCRIM coefficient,

CVD = number of commercial vehicles per day.

CVD = $0.97 - 0.385 * 10^{-4} F$

F = 24 hr average annual daily traffic flow

Later on TRL showed in [113] that reality is a bit more complex and showed that the relation should be written as:

$$\text{MSSC} = [A * \text{PSV}] - [B * \ln(\text{CVD})] + K.$$

The constants A, B and K are related to the investigatory level which in its turn is related to the type of road and safety requirements for that type of road. In [113] it is stated that "the investigatory level is the MSSC below which investigation of the site and assessment of any need for remedial work is initiated" (is this the typical English way of saying in a complex way that these levels are the minimum acceptance levels?). The investigatory levels are shown in table 82.

Site category	0.30	0.35	0.40	0.45	0.50	0.55	0.60
A: Motorway		X					
B: Dual carriageway non event		X	X				
C: Single carriage way non event			X	X			
Q: Approaches to and across minor and major junctions; approaches to roundabouts				X	X	X	
K: Approaches to pedestrian crossings and Other high risk situations					X	X	
R: Roundabout				X	X		
G1: gradient 5-10% longer than 50 m				X	X		
G2: gradient >10% longer than 50 m					X	X	
S1: bend radius < 500 m dual carriageway				X	X		
S2: bend radius < 500 m single carriageway					X	X	

Table 82: Investigatory level at 50 km/h [114].

Table 83 shows the relation between the investigatory levels and the constants A, B, and K

Investigatory level	A * 10 ⁻³	B * 10 ⁻²	K
0.35	6.18	2.25	0.252
0.40	3.90	1.95	0.377
0.45	2.94	1.70	0.407
0.50	5.81	1.46	0.193
0.55	4.73	0.98	0.231

Table 83: Constants A, B and K in relation to the investigatory level [113].

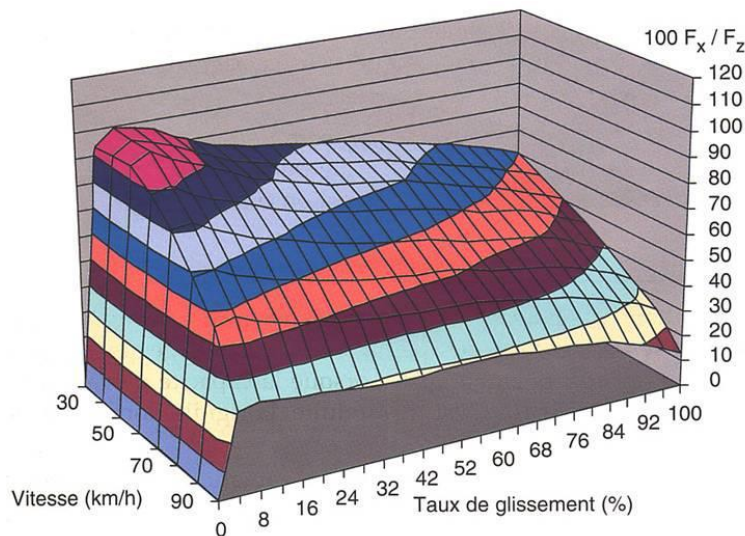
It is needless to say that these relationships are only valid for UK conditions, weather, traffic and types of aggregates used being the most important ones. Nevertheless the relationships provide a tool to estimate the equilibrium skid resistance in cases one is dealing with conditions which are more or less similar to the UK conditions.

As we have seen so far, skid resistance is highly affected by the properties of the pavement surface and the speed of the vehicle. It will be obvious that also the water film thickness and the tire itself play are also important factors. From experience we know that driving on a very wet road with tires that don't have any profile is a very dangerous thing to do. We also know that in formula 1 (F1) racing, the type of tire that is mounted on the race car depends on the weather type and road surface conditions. Typical F1 tires are shown in figure 351.



Figure 351: F1 tires for different road surface conditions.

We also know from experience that it is better to brake with a certain slip percentage than braking with blocked wheels. The car industry has anticipated on this by the introduction of ABS systems. Figure 352 shows an example of how all this affects the friction coefficient.



Friction 352: Friction coefficient in relation to speed (vitesse) and slip percentage (taux de glissement) for a tire with a profile depth of 2mm, 1 mm water film thickness and $TD = 0.5$ mm.

Figure 353 shows how profile depth, water film thickness and speed affect the skid resistance.

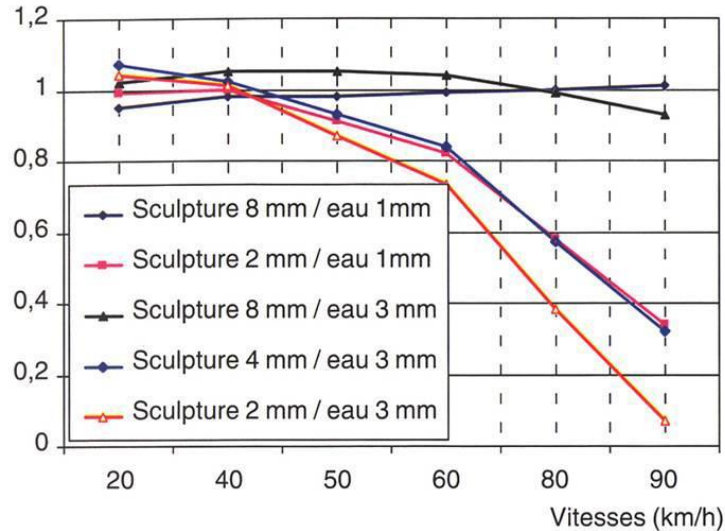


Figure 353: Influence of speed (vitesse), profile depth (sculpture) and water film thickness (eau) on the skid resistance at TD = 0.58 mm.

Figures 352 and 353 clearly indicate that even when a road authority does the utmost to provide skid resistant roads, the road user still carries a high responsibility for her/his own safety. Too fast driving on a wet road with a car having tires with a (very) limited profile depth is putting your safety at risk.

Until now we have discussed a large number of parameters influencing skid resistance but we haven't discussed the fundamentals of skid resistance. So let us spend some words now on some fundamental issues.

Skid resistance requires transfer of frictional forces and is provided through a complex interplay between adhesion and hysteresis forces. Here "hysteresis" is defined as the energy loss due to the deformation of the tire and "adhesion" is defined as the short term bond between atoms of the tire and the road surface. These principles are shown in figure 354. From this description it is clear that the tire indeed plays a very important role in skid resistance and, as mentioned before, this is very well understood by the Formula 1 and other high speed car races.

Next to that we have the effect of water. As we have seen, a water film on the road surface will reduce the skid resistance. Therefore we need to provide drainage which can be achieved by means of the macro texture and by making the wearing course porous; also the grooves in the tire provide drainage.

Figure 355 schematically shows what happens when a tire is rolling over a wet surface. It will be obvious that the actual contact zone decreases when the thickness of the water film increases, when the speed increases (water has no time to be pushed out of the contact area) and if the drainage by the pavement (macro texture) and tire (depth of the grooves) decrease. If conditions are such that a water film develops underneath the entire tire, then we have a situation called hydroplaning in which it is impossible to control the car. Figure 356 is an excellent example of uncontrolled conditions in wet weather.

At the end of this section on skid resistance the question is what kind of wearing course mixture will provide the highest skid resistance. We have seen that macro texture is important and that macro texture is controlled by the aggregate size. Wearing courses which are usually 50 mm thick (or even less) do not give much room to "play" with the maximum grain size in the mixture; usually the gradation is between a 0/8 and a 0/16 mm. In [111] it is recommended to use crushed sand instead of natural, rounded, sand and to "go" for a void content which is in the

middle to upper range of the allowable void content levels. Also a harder binder is advised and the bitumen content of the VFB (voids filled with bitumen) should not be too high. It doesn't need to be emphasized that in the design of wearing course mixtures also durability, crack resistance etc should be taken into account which might lead to e.g. lower void contents and higher bitumen contents. All in all this means that the wearing course mixture should be optimized in such a way that all requirements with respect to skid resistance, durability, crack and permanent deformation resistance etc are fulfilled as good as possible. Such an optimization dilemma is schematically shown in figure 357.

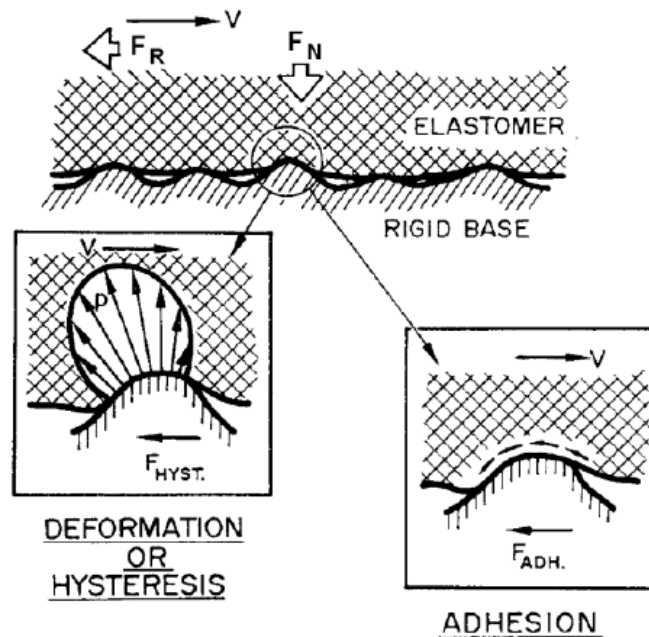


Figure 354: Principles of skid resistance [108].

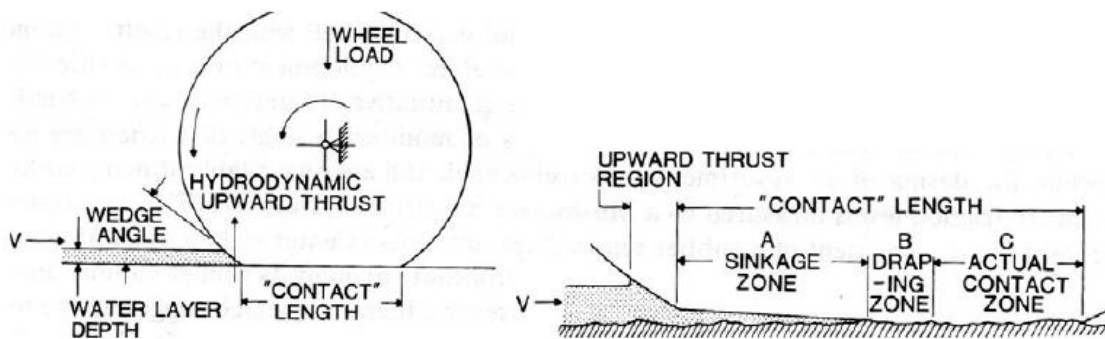


Figure 355: Effect of water, speed and tire profile on actual contact zone [108].



Figure 356: Wet weather skidding in F1 racing involving Alonso (foreground), Verstappen and Raikonen (red car on the right hand side).

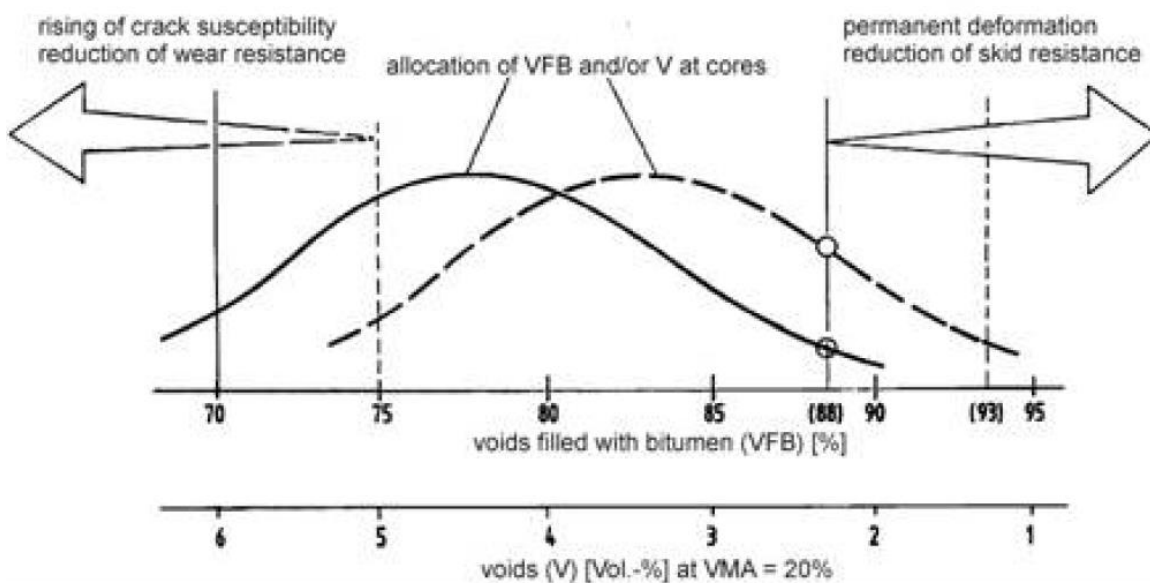


Figure 357: Impact of the void content V and the voids filled with bitumen VFB on the performance of SMA [108].

15.7 Noise and noise reducing pavement surfaces

Traffic produces noise; at speeds below 50 km/h engine noise and noise due to e.g. loose cargo and the exhaust system is dominant but at speeds higher than 50 km/h tire noise becomes the dominating factor. The noise that is generated in the tire – road contact area is because the tire profile blocks "hit" the road and the aggregates at the pavement surface "hit" the tire. There exists a vast amount of literature on the topic of tire – pavement noise and this author did not even try to summarize all this. The interested reader is therefore referred to an excellent book on this topic by Sandberg e.a. [115] and to the very interesting PhD thesis by Li [105] which contains, among a lot of other things, an excellent literature survey on the topic. In spite of having such a vast amount of literature available on the topic, the author decided to repeat some basic principles as an introduction to the topic.

Sound consists of sound waves with a wide variety of wave lengths and pressure levels (see figure 358).

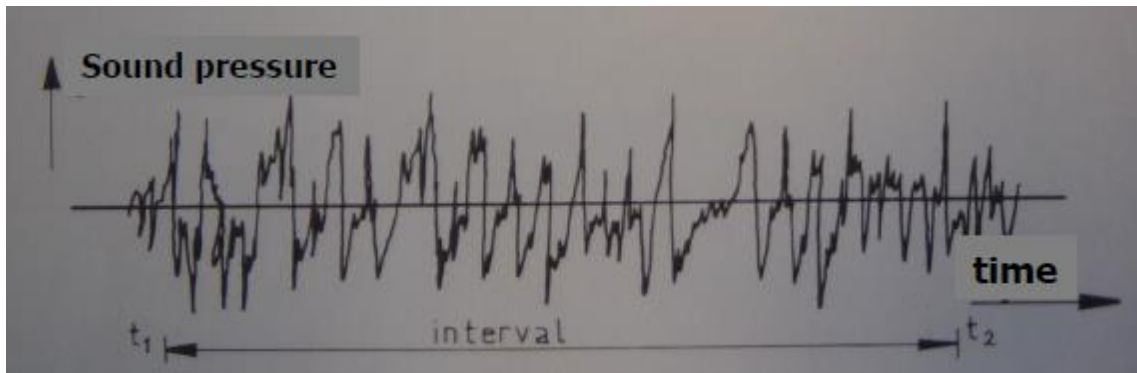


Figure 358: Sound.

The frequency of the sound wave determines the height of the tone. This implies that both pressure and frequency are important factors. We cannot hear the very high and very low tones (frequencies) but we can feel them as pain in the ears (very high tones) or vibrations in the belly (very low ones). The frequencies which we can hear we don't hear them as equally loud; some frequencies we hear better than others. This is shown in figure 359 which gives the lines of equal loudness.

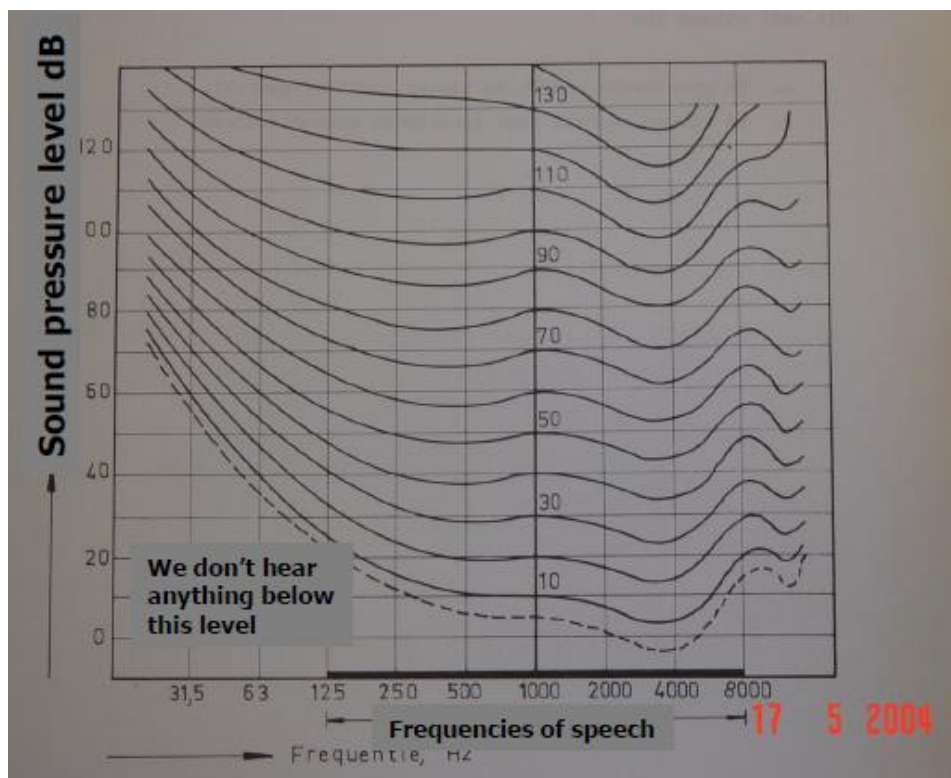


Figure 359: Lines of equal loudness.

Because there is a difference in terms of energy of 25×10^{12} between what we can just hear and what causes pain, we are using log scales to indicate the noise level. We calculate the ratio of the

log of the energy of the occurring changes in air pressure to the log of the energy at what we can just hear (see equation below). This ratio is expressed in decibels (dB).

$$L_{eq} = 10 \log \left\{ (1/T) \int (p_{eff}^2 / p_o^2) dt \right\}$$

As mentioned above, our ear is not equally sensitive to each frequency and therefore we apply a weighing factor; this results in the noise level in dB(A). Several weighing factors have been developed but the most commonly used one is the A filter resulting in dB(A). Some filter characteristics are shown in figure 360.

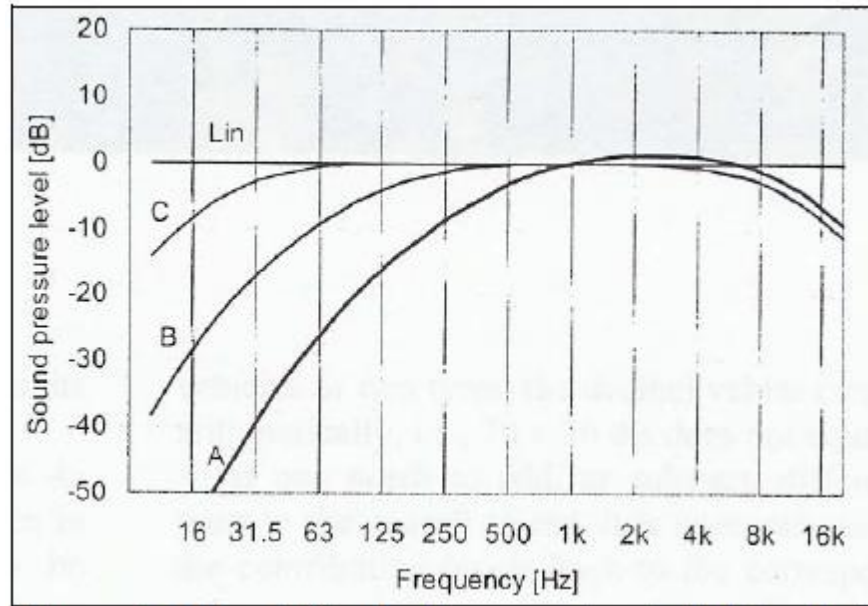
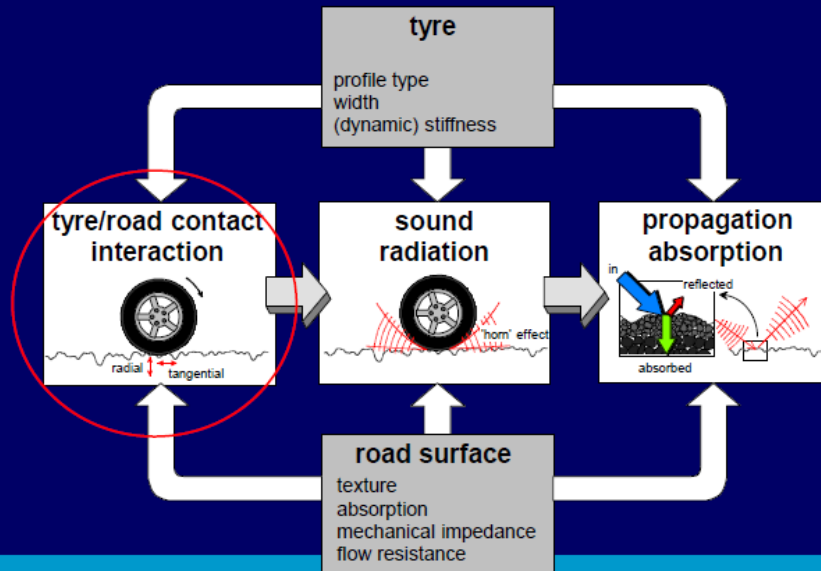


Figure 360: Some filter characteristics used on measured sound levels.

As a further introduction to the topic, a series of pictures (figure 362 a – i) is given hereafter which give an excellent summary on the production of noise and how to control and limit it. These pictures are copies from power point slides that were produced by dr. ir. Wim van Keulen, a Dutch renown expert in traffic noise. Dr. van Keulen also provided a lot of assistance and inspiration to Li's work [105].

Tyre/road noise generation

Both tire and pavement surface have influence



15

Figure 361a

Mechanical mechanisms



- radial vibrations
- sidewall vibrations

Hammer effect

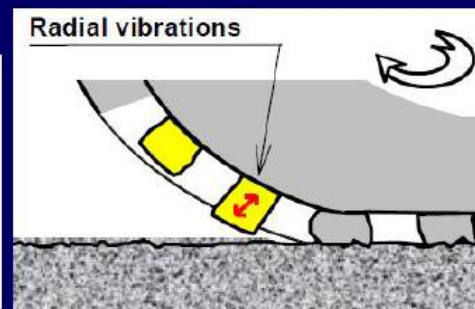


Figure 361b

Adhesion Mechanisms



- stick slip
- sidewall vibrations

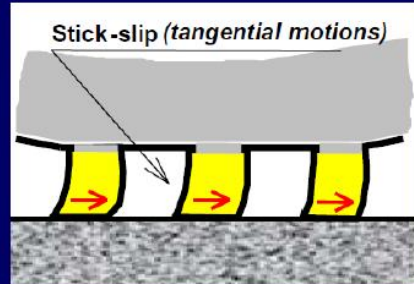


Figure 361c

Adhesion Mechanisms



- stick-snap
- sidewall vibrations

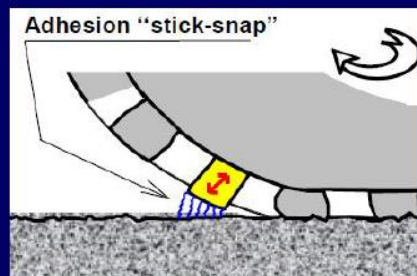


Figure 353d

Aerodynamic Mechanisms



Figure 353e

Tyre/road noise generation

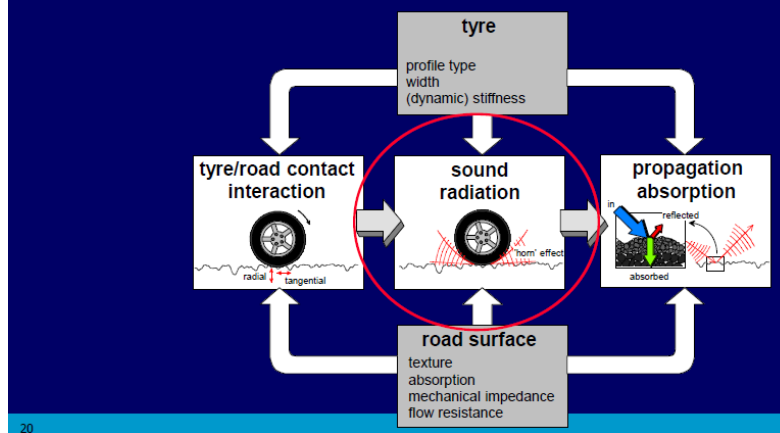


Figure 353f

Sound Radiation

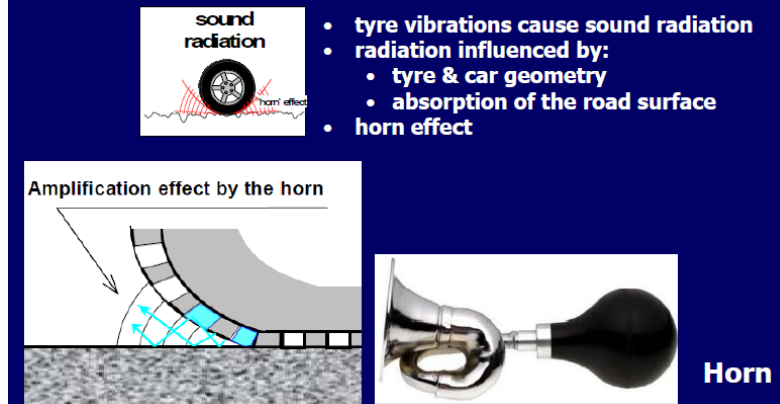
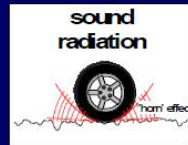


Figure 353g

Sound Radiation



- tyre vibrations cause sound radiation
- radiation influenced by:
 - tyre & car geometry
 - absorption of the road surface
- resonances

Pop Bottle

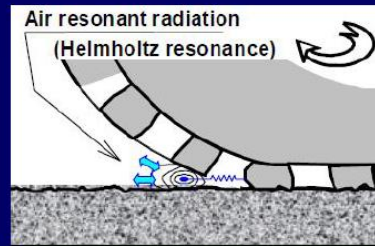
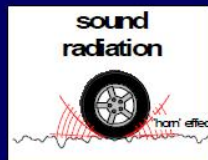


Figure 353h

Sound radiation



- tyre vibrations cause sound radiation
- radiation influenced by:
 - tyre & car geometry
 - absorption of the road surface
- resonances

Organ Pipes



Pipe resonances in channels formed in the tire footprint:

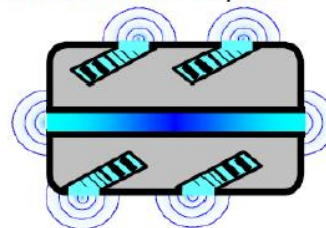


Figure 353i

All these different sources do produce sound at different frequencies. An overview of the sources and frequencies produced is given in table 84.

Vibration	Impact	Tread	300-500 Hz
„	Impact	Texture	800-1250 Hz
„	Impact	Running Deflection	
„	Adhesion	Stick slip	
„	Adhesion	Stick snap	>1000-2000 Hz
Aerodynamics	Air turbulence		300 Hz
„	Air pumping		> 100 Hz
„	Pipe resonance		900-2000 Hz
„	Helmholtz reson.		1000-2500 Hz
Amplific./Reduct.	Horn effect		
„	Acoustical imp.		
Tyre	Belt resonance		600-1300 Hz
„	Torus cavity res.		230-280 Hz

Table 84: Sound sources and frequencies produced.

As pavement engineers we are of course mainly interested in which road surface characteristics are important for noise production and reduction. These characteristics are listed hereunder:

- texture,
- acoustic impedance,
- friction,
- mechanical impedance.

Texture causes the tire to vibrate; the aggregate surface in the wave length range of 1 – 20 mm has an influence on the individual profile blocks of the tire and wave lengths between 20 – 500 mm cause the tire to vibrate. In general we can state that texture wavelengths greater than 10 mm tend to increase noise excited by tire vibrations while wavelengths less than 10 mm tend to reduce noise from air pumping. Furthermore it should be mentioned that a negative texture is more favorable than a positive texture which produces more noise. The meaning of positive and negative texture is explained by means of figure 362. Furthermore we know from experience that the rougher the surface, the more noise is produced. So both texture depth and texture wavelength are important parameters.

In the section on skid resistance we have shown that texture depth is measured by means of the sand patch method. This test doesn't provide enough information to be of use for noise related purposes. Information on texture depth and texture wavelength can easily be obtained by means of laser measurements. Figure 363 shows the device as used by Li [105]. When a detailed picture of the pavement surface (figure 364) is obtained, various texture parameters can be calculated such as the MPD (see figure 365).

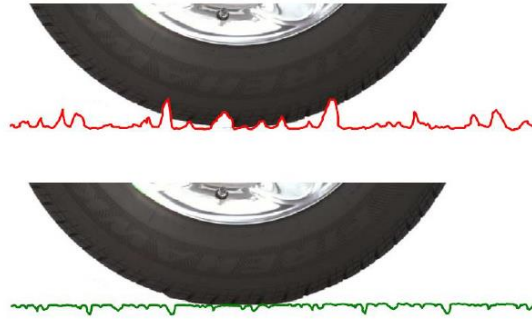


Figure 362: Positive texture (top, red profile) and negative texture (bottom, green profile).

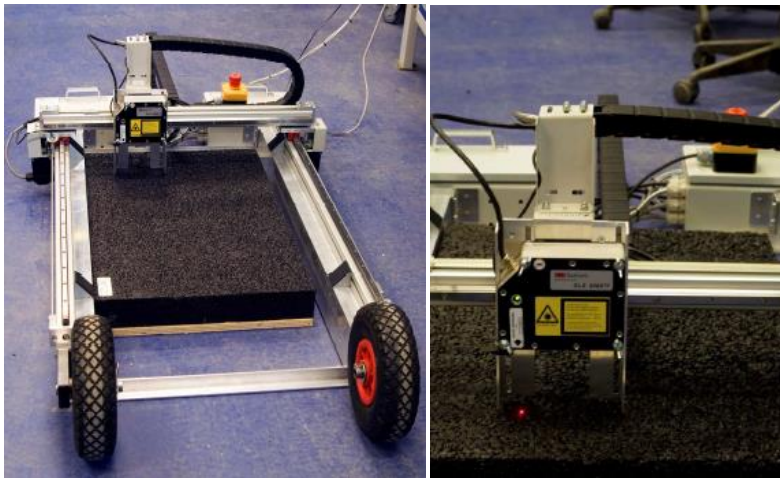


Figure 363: Laser profilometer and laser sensor as used by Li [105].

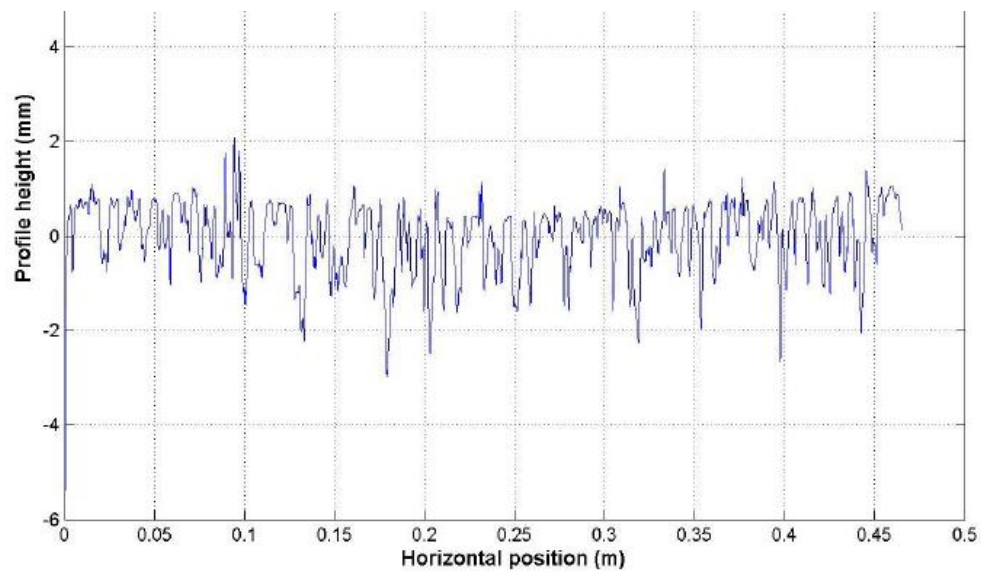


Figure 364: Example of a profile measurement showing negative texture.

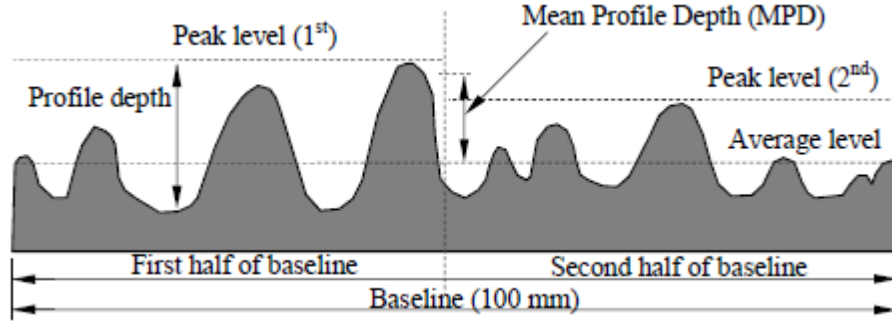


Figure 365: Texture profile.

The mean profile depth MPD is calculated via:

$$\text{MPD} = [\text{Peak level (1st)} + \text{Peak level (2nd)}] / 2 - \text{Average level}$$

The MPD and the TD measured with the sand patch method basically provide the same information and Xiao [116] showed that these two parameters could be related following:

$$\text{TD}_{\text{sand patch method}} = 0.647 + 2.146 * \text{MPD}$$

$$[\text{TD}] = [\text{MPD}] = [\text{mm}]$$

Based on signal processing theories, also spectral analyses can be performed for characterizing the profile. The amplitudes within a certain frequency band can be transformed into a unique indicator defined as texture profile level TL. TL is calculated following:

$$\text{TL} = 20 * \log (\alpha_{t,I} / \alpha_{t,\text{ref}})$$

Where:

TL = texture profile level at octave band with wavelength λ_I (ref 10^{-6} m) [dB],

λ_I = center wavelength of the octave band [mm],

$\alpha_{t,I}$ = root mean square value of the vertical displacement of the surface profile [m],

$\alpha_{t,\text{ref}}$ = reference value [$= 10^{-6}$ m].

The root mean square value (RMS) value is calculated following:

$$\text{RMS} = \sqrt{\int_0^{1m} y^2(x) dx}$$

y = profile height - MPD

An example of such an analysis is given in figure 366.

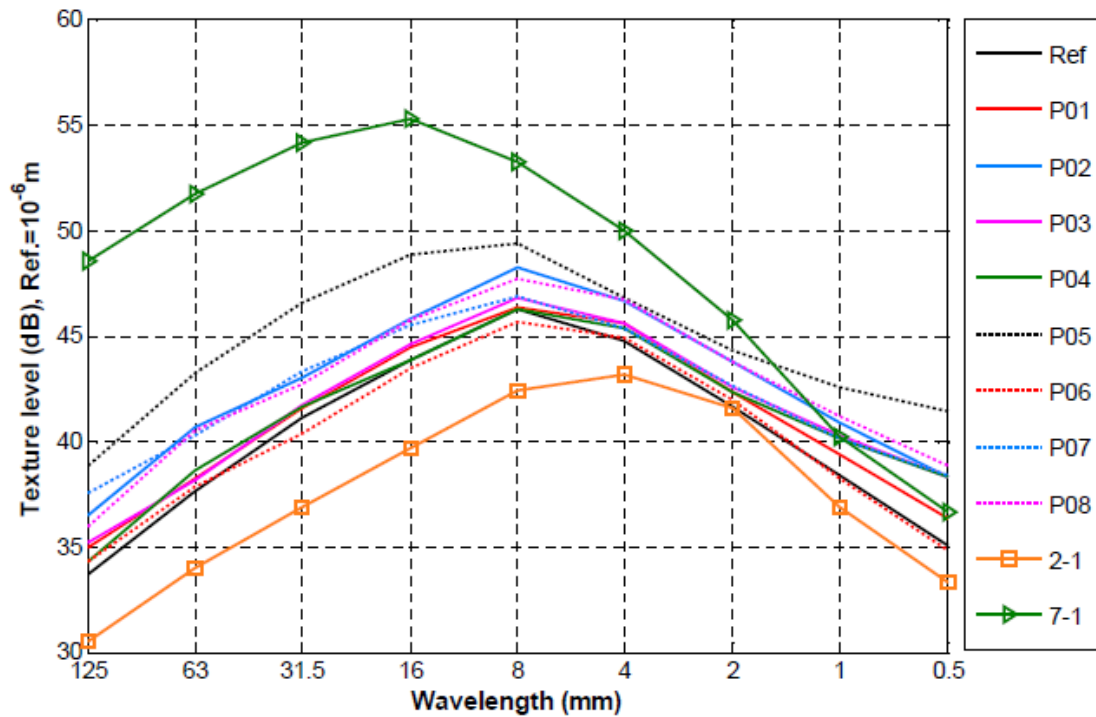


Figure 366: TL values for a porous asphalt concrete (7.1) and nine thin noise reducing layers.

The peak value in the curves appeared at a wavelength which more or less coincided with the maximum grain size of the aggregates in the mixtures. For the porous asphalt concrete (7.1) this was 16 mm, for mixture 2.1 it was 4 mm, for mixture P05 it was 8 mm and for all the other mixtures 6 mm.

Acoustic impedance implies the following. The voids in an open road surface, the shape of the voids, the resistance the airflow experiences in the voids and the thickness of the layer determine the degree of absorption (acoustical impedance) and the position of the absorption peak in the frequency domain. This only holds if we are dealing with interconnected pores and we have seen earlier that such interconnected pores starts to develop in earnest at void contents larger than 12%! Porous surface layers however are sensitive to clogging, a phenomenon which also has been discussed earlier, and because of that the effective thickness of the layer reduces which causes a change in the absorption capacity of the layer.

Li [105] used a new type of device for measuring the acoustic impedance/noise absorption of in situ pavement surfaces, test slabs and cores. The device is developed by the Dutch company Microflown Technologies [117] and is based on measuring the sound pressure (P) and particle velocity (U) at the surface. The device is shown in figure 367.

During the test the loudspeaker emits a continuous sound signal. The sound pressure (P) and the acoustical particle velocity (U) at the same point are measured simultaneously. From these results the acoustical impedance of the free field as well as the acoustical impedance close to the test specimen are measured. From these two measurement results the sound absorption is calculated.

Figure 368 shows two examples of absorption characteristics of two different types of pavement surfaces.

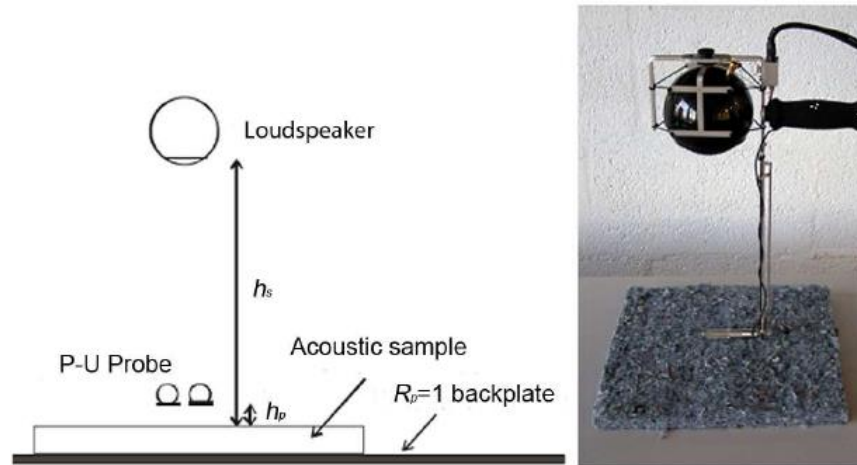


Figure 367: Sound absorption measuring device as developed by Microflow Technologies.

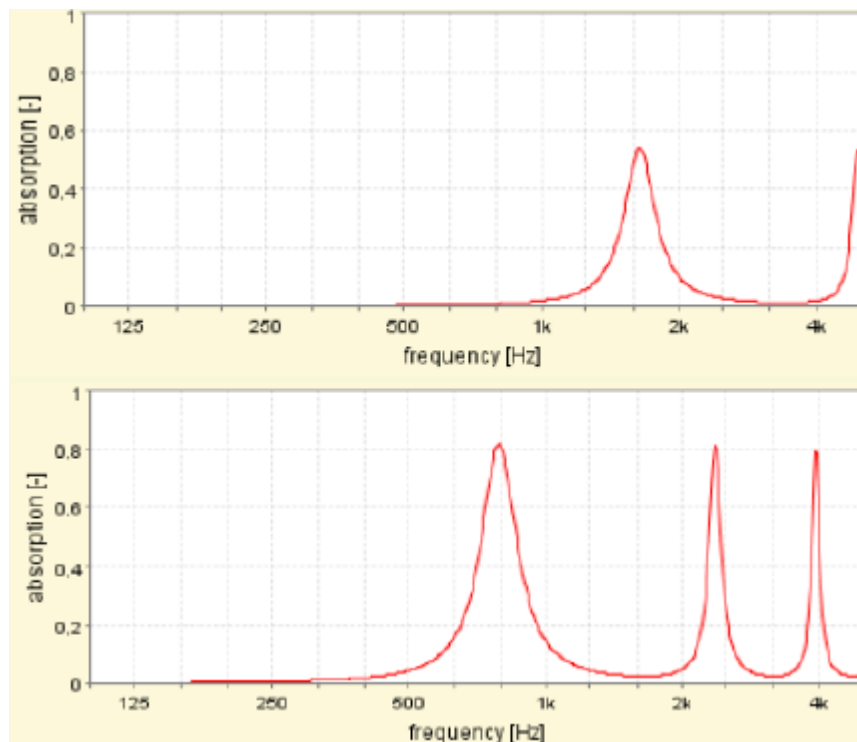


Figure 368: Absorption characteristics of a thin layer (25 mm) noise reducing surface (top) and a 50 mm thick porous asphalt concrete layer.

Li [105] showed that for thin layer noise reducing surfaces ($h = 25 - 35$ mm), the absorption level is strongly related to the void content and the degree of connectivity of the voids (see figure 369).

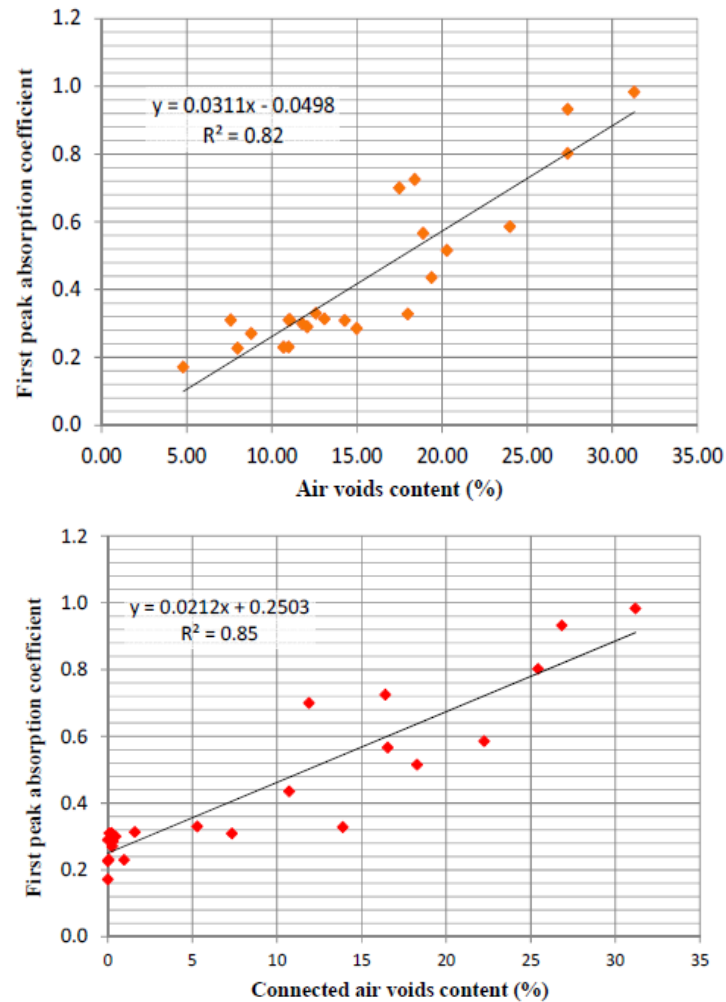


Figure 369: Absorption coefficient of the first peak of the noise absorption characteristics of thin layer noise reducing surfaces in relation to the void content and degree of connectivity of the voids.

Mechanical impedance is defined as being a measure of the ability of a structure to resist motion when subjected to a given force. It is calculated from the ratio of the driving force (F) acting on the system to the resulting displacement velocity of the system (v).

$$Z = F / v$$

Where Z is the mechanical impedance.

One of the systems that is used to measure the mechanical impedance is shown in figure 370. In this system the load is generated by a hit of the hammer on the device standing on the pavement surface. This device contains a load cell and an accelerometer which measure the vertical acceleration due to the impact load. These values are used to determine the displacement velocity.



Figure 370: Method to determine the mechanical impedance.

It will be no surprise that the mechanical impedance and the stiffness of a material are related to each other. This will be described in some detail later on.

The effect of a low mechanical impedance can be explained as walking on the carpet which is placed on the wooden floor compared to walking on the wooden floor. Walking on the much softer carpet produces far less noise.

The significant noise reducing effect a low mechanical impedance material can have, has led to the introduction of Porous Elastic Rubber Surfaces (PERS). PERS is made of rubber granulates from recycled tires and polyurethane is used as a binder; using rubber particles as aggregates makes the pavement surface much softer and make it behave like the carpet mentioned above. Experimental pavement surfaces have been produced with PERS tiles having a size of 1 * 1 * 0.03 or 0.04 m. The void content is > 20 % and the initial noise reduction is around 6.9 dB(A). Figure 371 shows some pictures of the construction of a PERS wearing course in the Netherlands. It will be obvious that the joints between the tiles will open and close because of temperature changes and that these joints are also the reason for noise production when tires are passing them. A much better option therefore is to lay PER surfaces by means of the Roll Pave system that was developed by the Dutch contractor Dura-Vermeer. This system is shown in figure 372.



Figure 371: Construction of a PERS wearing course in the Netherlands.



Figure 372: Roll Pave system as developed by Dura-Vermeer.

Using the Roll Pave system layers were placed consisting of rubber and quartz granulates and a polyurethane binder. The thickness was 30 mm and the void content 30%. Noise reduction values of 6 – 8 dB(A) were achieved. The rolls are coming in lengths of 50 – 60 m and were 3.5 m wide. Unfortunately this very promising development stayed in the development phase and large scale applications, except for a few trial sections, did not occur.

Li [105] did resilient modulus tests on different types of pavement materials amongst which PERS. These results are shown in figure 373.

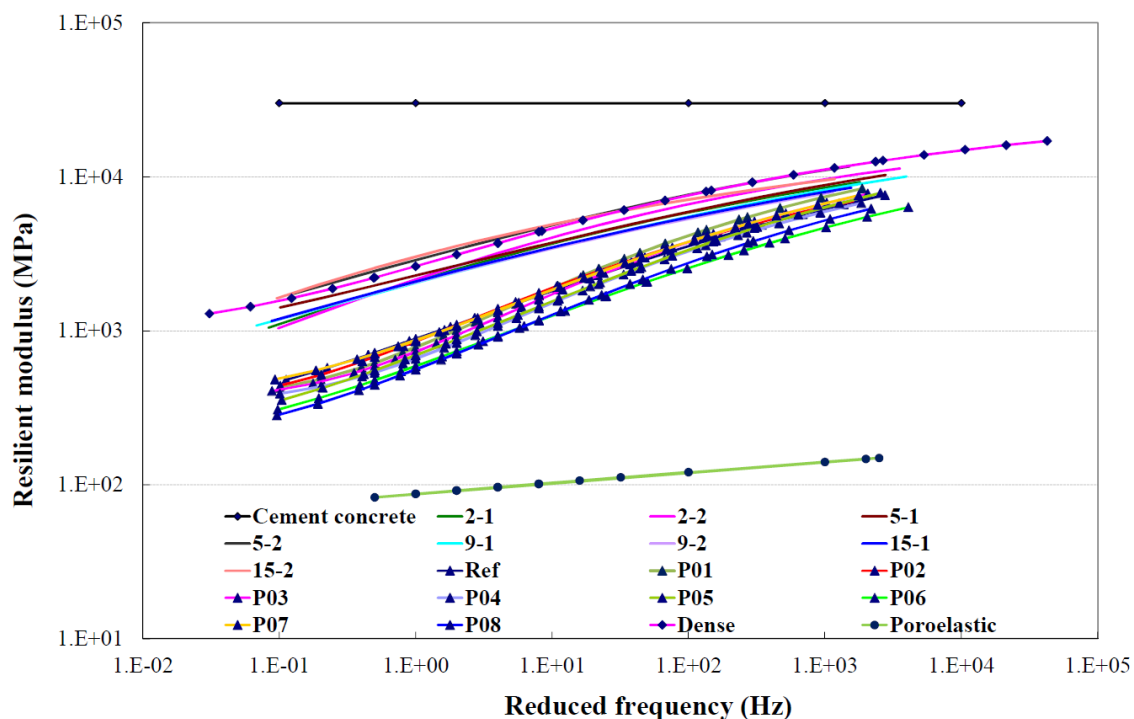


Figure 373: Resilient modulus master curves at 20 °C for cement concrete, different thin noise reducing asphalt layers and PERS.

Figure 373 shows that at a frequency of 10 Hz, the thin noise reducing surface layers have a stiffness which is 10 – 30 times higher than that of PERS. From these data Li also developed a relation between stiffness and mechanical impedance; this is shown in figure 374.

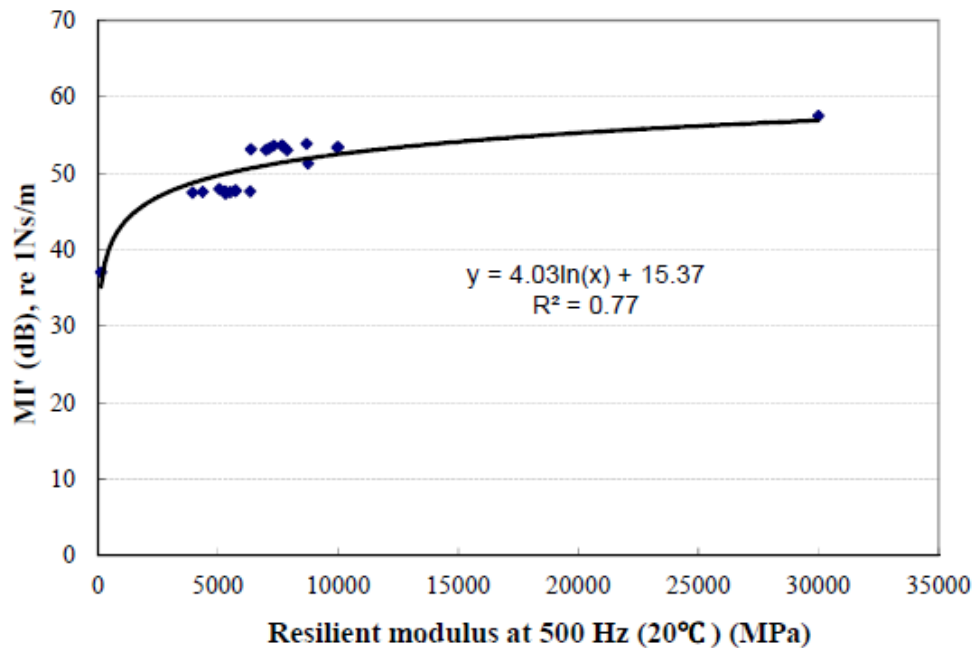


Figure 374: Relation between resilient modulus at 500 Hz and the mechanical impedance.

From figures 373 and 374 it is clear that it is almost impossible to construct a pavement layer with a low mechanical impedance using “normal” road building materials (stone aggregates, sand filler and bitumen). However, there is a saying “never say never” and another saying is “make the impossible possible” and these sayings also apply to developments in binder technology. Dr. Zhao Su e.g. has made some excellent developments in producing highly elastic, low modulus, very adhesive binders by making use of the components shown in figure 375.

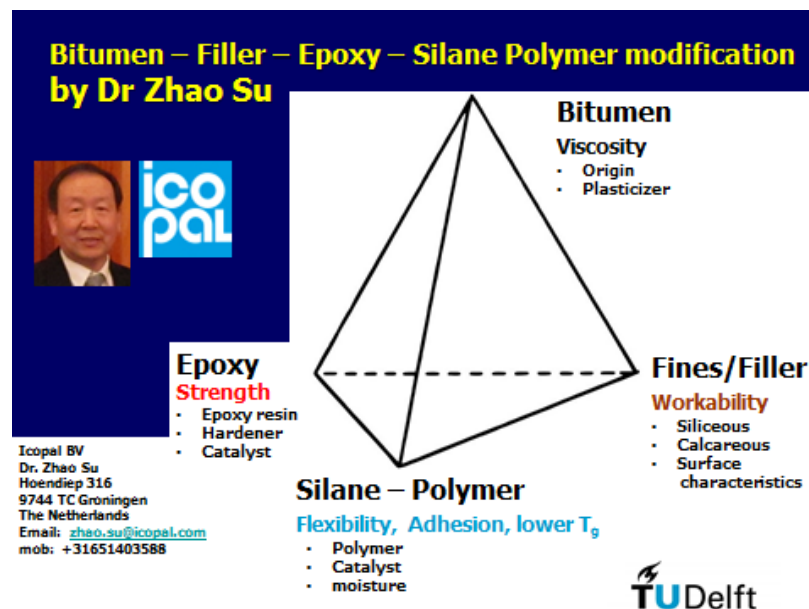


Figure 375: Binder developments made by Dr Zhao Su.

Some of the special features of these bitumen-epoxy-silane-filler mixtures are shown in figure 376.

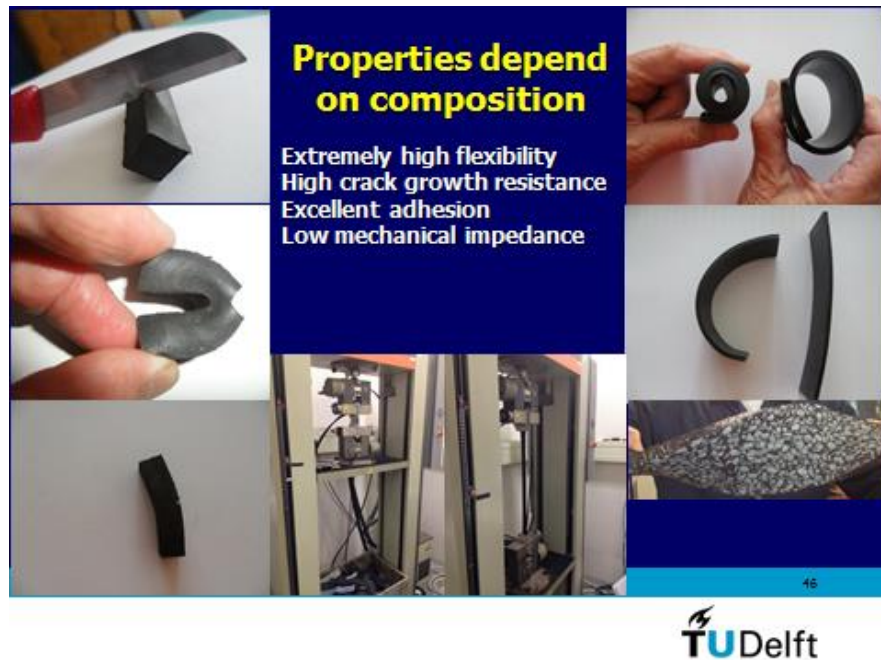


Figure 376: Some features of bitumen-epoxy-silane-filler mixtures.


The left hand upper picture e.g. shows a crack being initiated in the material by means of cutting it. The picture under it shows that the crack doesn't propagate even when subjected to extreme bending. The bottom left picture shows how the beam with the cut came back into its original shape after a few seconds. The center bottom picture consists of two parts. The left hand part shows a sample in a tension testing machine before loading and the right hand picture shows the large deformation that can be taken by the material without cracking. Figure 377 shows how this extremely flexible binder can be used for low noise open graded top layer mixtures.



Figure 377: Bitumen-epoxy-silane-filler binder used in two layer noise reducing system.

Figure 378 shows a picture of a porous asphalt concrete mixture made with this special binder. The very low modulus implies that the material has a low mechanical impedance and it will therefore have a very high noise reducing capacity.

Used as binder for PAC – SC (porous asphalt concrete for Sponge City)



Very flexible/elastic
modulus ≈ 40 MPa
hardly temperature dependent

High resistance to
permanent deformation

February 8, 2018 47



Figure 378: Porous asphalt concrete made with a bitumen-epoxy-silane- filler binder.

For the sake of completeness it should be mentioned that this special product has not yet been used in large scale road paving jobs. It has however been used in smaller projects like e.g. the construction of “silent” joints (e.g. joints between the pavement and a bridge). According to the author, this product should seriously be considered for being used in the construction of very silent and durable road pavements.

Until now we have discussed what noise is, how human beings perceive it and which pavement characteristics affect the production of noise. But how do we measure traffic noise? Two methods will be briefly discussed which are the statistical pass by (SPB) method (figure 379) and the close proximity method (CPM) (figure 380). The SPB method is used to measure the noise generated by actual traffic. The CPM method is excellently suited to measure the noise produced by certain tires on specific surfaces and for measuring the reduction of the noise reducing capacity of pavement surfaces in time.

By means of these measurements it has e.g. been determined that truck tires produce more noise than person car tires and that the tires on the drive axle of a truck are more noisy than those on the steer and trailer axles. It has also been shown that temperature and speed have a significant influence.

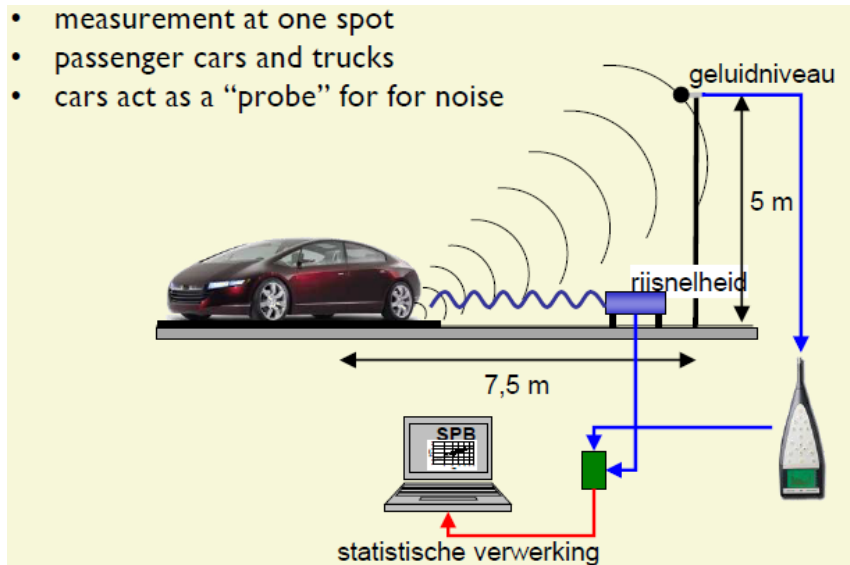


Figure 379: SPB method (statistische verwerking = statistical treatment, rijsnelheid = traffic speed, geluidniveau = noise level)

- Measurement along road with different tyres
- Measures only rolling noise



Figure 380: CPM method and CPM trailers. The top picture shows the inside of the trailer, note the microphones on the left hand side of the tire.

Having all this information available, the question is what can we do with it as pavement engineers. How can we use all this information to design and produce low noise pavement

surfaces? In order to be able to do this we need models that relate noise levels to pavement surface characteristics. Models which are capable to do this are developed by Sandberg [115] and are given hereafter.

$$CRNL_c = 0.5 L_{80} - 0.25 L_5 - a (2 - T) - b \ln (\Omega h) + 67$$

Where:

$CRNL_c$ = combined pass by road noise level for cars [dB],

L_{80} = texture level in the octave band with center at 80 mm texture wavelength [dB] in relation to the reference level of 10^{-6} m,

L_5 = as above but for a wavelength of 5 mm,

T = age of the surface [years],

a = constant = 0.8 when $0 < T < 2$; = 0 when $T \geq 2$; = 0 for all surfaces with MPD > 1.0 mm,

Ω = void content [%],

h = layer thickness [mm],

b = constant = 0 when $\Omega h \leq 4.5$; = 4.7 for $4.5 < \Omega h < 20$; = 7 for $\Omega h \geq 20$.

$$CRNL_t = 0.35 L_{80} - 0.175 L_5 - 0.7 a (2 - T) - 0.7 b \ln (\Omega h) + 81 - 0.2 [70 - 20 \log (MPD / 10^{-6})]$$

Where:

$CRNL_t$ = combined pass by road noise level for trucks [dB]

All other variables and constant as mentioned above

Note: although Sandberg explicitly mentions that Ω is in volume percentage [%], this author expects however that Ω should not be introduced as 20% but 0.2. This author assumes this because otherwise $\Omega \cdot h$ would almost always be ≥ 20 . This would make using various "b" values for different $\Omega \cdot h$ values useless.

Sandberg explicitly mentions that the levels obtained by means of these equations only can be used for comparative purposes and they allow to demonstrate the effect of texture and void content on the noise levels. He mentions that the models will aid in predicting the difference between road surfaces. He nevertheless also mentions that the obtained results will be in the range of typical SPB measurements.

The equations nicely show that a relatively thick porous layer with a high void content and a fine texture will produce the lowest noise levels. Layers which are combining these features are double layer porous asphalt layers which will be discussed briefly hereafter.

Two layer porous asphalt concrete consists mostly of a 30 mm top layer made of 2/6 or 4/8 mm aggregates and 6% polymer modified bitumen on top of a 45 mm layer made of 11/16 mm aggregates and 4.5% bitumen. The void content in both layers is > 20%. Figure 381 shows some results of CT scanning of a double layer porous asphalt core.

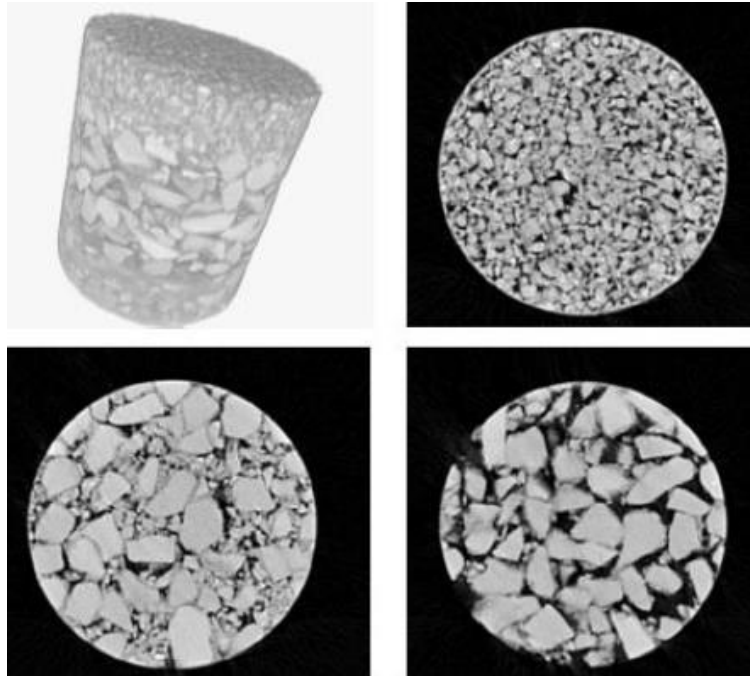


Figure 381: CT scan pictures of a double layer porous asphalt core. Right top is the top layer, right bottom is the bottom layer, left bottom is interface between top and bottom layer.

The interface between the top and bottom layer can be a bit of a problem since in that region the pores of the coarse grained bottom layer might be filled with the grains from the fine grained top layer. Because of this the void content in this region can drop to around 15%.

When different pavement surfaces are compared based on their noise production relative to a standard dense asphalt concrete layer with 0/11 mm aggregates and a void content of 3 – 5%, then we obtain the following ranking.

SMA	- 2 dB(A)
Porous asphalt concrete	- 3 a -5 dB(A)
Double layer porous asphalt concrete	- 6 dB(A)

Figure 382 gives an overview of the noise production of various surface layers. It clearly shows the importance of a fine surface texture (twinlay) and a high porosity (twinlay and drain asphalt) for noise reduction. It also shows the effect of a positive texture (seal coat) on noise production. Seal coats do have a positive texture because the chips are spread on top of a hard surface.

We have already presented the model developed by Sandberg which allowed the noise production of cars and trucks to be predicted from pavement surface characteristics. Also Li [105] has developed such a model for which he used data obtained from test sections in the Netherlands. In her research on noise reducing pavements, the Dutch Ministry of Transport constructed test sections of 9 different noise reducing wearing courses. Four of those sections were semi dense thin layer surfaces, 3 sections were laid with (double layer) porous asphalt, and 2 sections were SMA sections Details of the sections are shown in table 85.

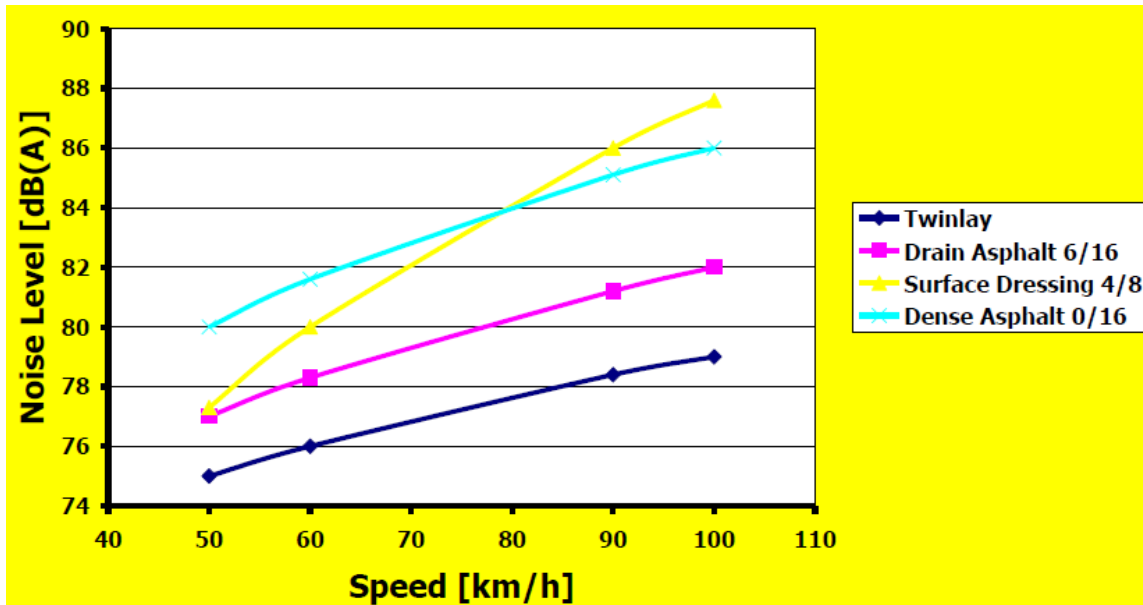


Figure 382: Noise production of wearing courses travelled by trucks.
Note: Drain asphalt = porous asphalt concrete; Twinlay = double layer porous asphalt concrete.

Section number	2	3	4	5	9	15	24	19	20
	TL	TL	TL	TL	PA	PA	PA	SMA	SMA
Max. aggr. size [mm]	4	6	6	8	8	6	8	6	8
Gradation	2/4	2/6	2/6	4/8	4/8	2/6	4/8	0/6	0/8
Binder content by weight [%]	7.2	7.8	7.5	6.6	6.0	6.6	6.0	7.8	7.2
Air voids [mm]	12	8	12	12	>20	>20	>20	4	5
Thickness [mm]	25	25	25	25	25	25	25	20	25

Table 85: Details of the noise reducing wearing course test sections as constructed by the Dutch Ministry of Transport.

Note: TL = thin layer, PA = top layer of the double layer porous asphalt.

Numbers given are the values as designed and NOT the values which were obtained from cores taken after construction.

Each section was laid twice so there were 18 sections in total.

The noise level produced by each section was determined by means of CPX measurements and a total of 10 different car tires was used. The measurements were done at a speed of approximately 80 km/h. Texture measurements and sound absorption measurements were performed as well. Figure 383 gives information about the texture levels and figure 384 shows the measured absorption values. Figure 385 shows the average sound levels produced by 10 tires.

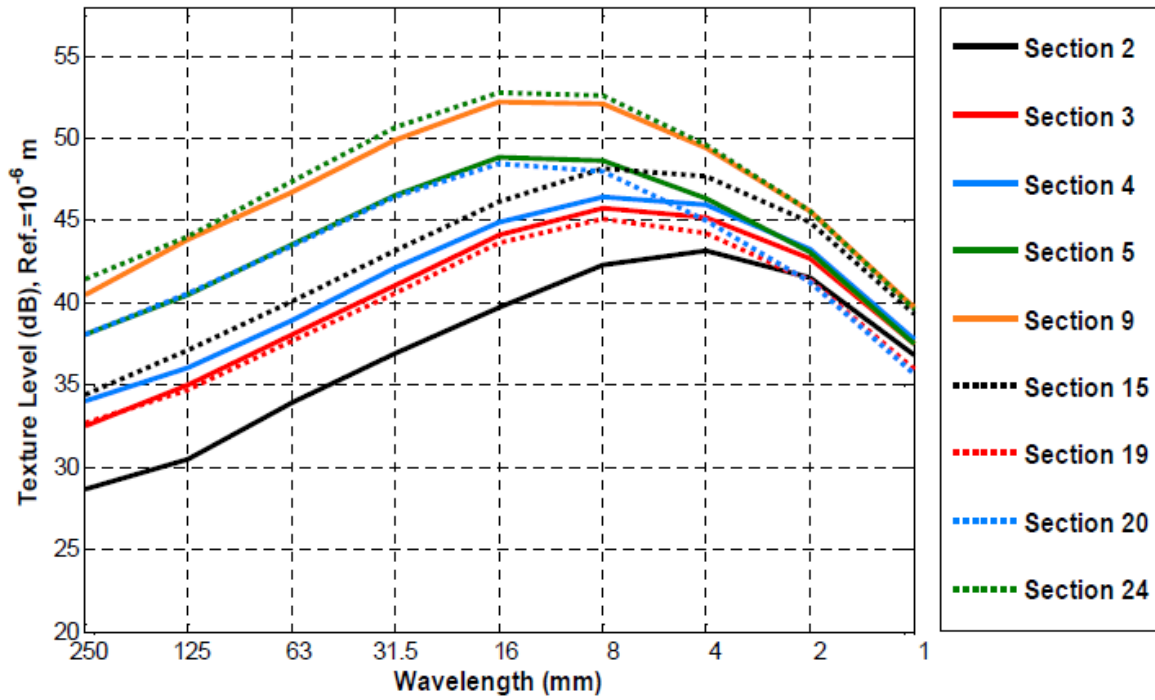


Figure 383: Texture levels of the test sections.

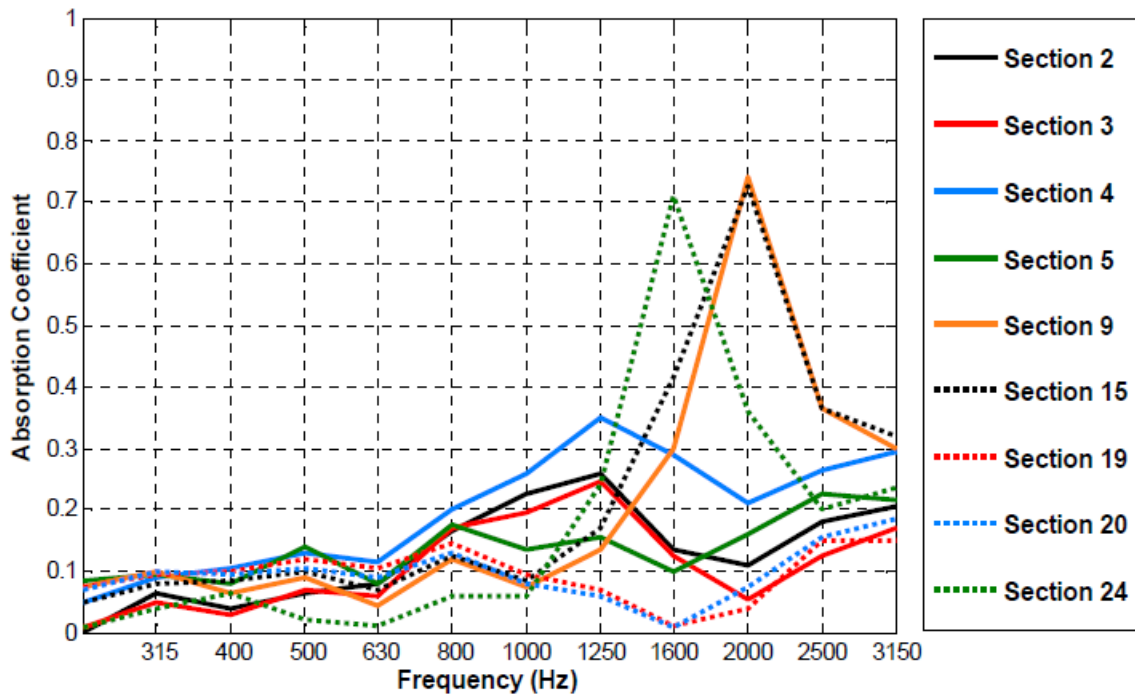


Figure 384: Absorption levels of the test sections.

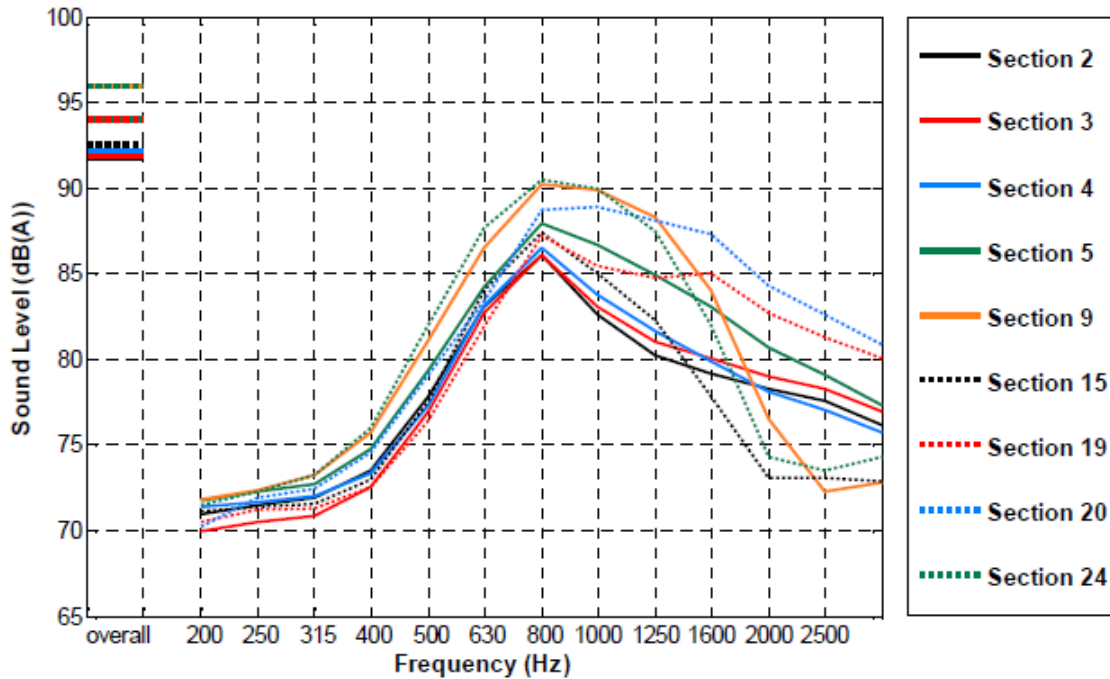


Figure 385: Sound levels measured on the test sections. The sound levels reported are the average values as measured using 10 different car tires.

Based on the data obtained on ALL sections Li [105] developed the following model for the prediction of noise due to car tires from surface layer characteristics.

$$L_{A,eq} = 92.25 + 0.33 MS - 0.06 \Omega - 0.07 h + 2.27 MPD$$

Where:

MS = maximum grain size [mm],

Ω = void content,

h = layer thickness [mm],

MPD = maximum profile depth.

For the THIN noise reducing surfaces ONLY, the equation was:

$$L_{A,eq} = 79.9 + 0.35 TL_{63} - 1.79 A$$

Where:

TL_{63} = texture level at 63 mm wavelength

A = maximum absorption level

Li furthermore showed that TL_{63} could be estimated using:

$$TL_{63} = 19.39 + 2.85 MS + 0.19 \Omega$$

Li's equations show the same trends as those produced by Sandberg being that a small texture depth, a high void content and an as large as possible void content produce the lowest noise producing pavement surface.

Sandberg showed that complying with these requirements will not negatively affect the skid resistance. We have seen however that mixtures with high void contents might suffer from durability issues because of increased moisture sensitivity, increased sensitivity to hardening of the binder and simply because of reduced strength. This later aspect makes porous layers less applicable for situations where high shear stresses may occur (junctions, corners etc).

Finally a few comments need to be made with respect to the construction of porous layers. The mixture should not be too cold when laid because this might result in over-compaction because the required density need to be achieved. Too heavy compaction might result in crushing the aggregates which enhances the moisture sensitivity of the mixture. Furthermore static rollers should be used instead of vibratory rollers because "hammering" the pavement surface by means of vibratory rollers might again result in crushing the aggregates.

Thin layers are always sensitive to a rapid cooling down which makes the time window for compaction rather narrow and can negatively affect the quality of the thin layer mixture. This once again implies that these mixtures should be laid and compacted at the right temperature. It should never be forgotten that laying down porous mixtures, and especially thin layer mixtures, is a kind of a specialty and will only be accomplished correctly when skilled and dedicated paving crews are doing the job. It are not "fool proof" products.

Later on some construction issues and especially the variability due to construction will be discussed in greater detail.

15.8 Road roughness

In the previous sections we have discussed how short wave unevenness influences skid resistance and noise production. In this section we will discuss how longer wavelengths and larger amplitudes affect pavement roughness and riding comfort. Figure 386 gives a nice overview of the wavelength ranges which affect skid resistance, noise and riding comfort.

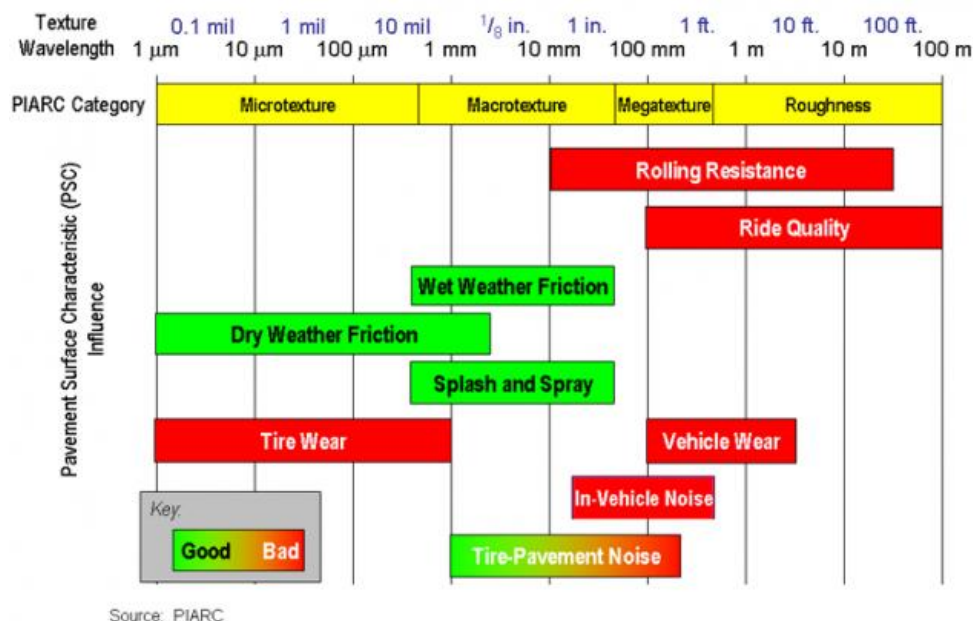


Figure 386: Relation between wave lengths of surface unevenness and functional properties.

As we know, riding comfort is affected by short and long wave roughness. A typical example of short wave roughness are the corrugations which we sometimes observe at traffic light controlled junctions and crossings (see figure 387). Such corrugations are caused by the shear stresses due to accelerating and decelerating vehicles in combination with insufficient stability of one or more of the asphalt layers (predominantly wearing and binder course).



Figure 387: Corrugations, also called washboards, at a traffic light controlled junction.

Corrugations are also a well-known defect type on gravel roads (see figure 388). In this case they are formed due to the high frequency vibration of the tire walls (approximately 30 Hz) and instability of the gravel probably due to a lack of fine materials.

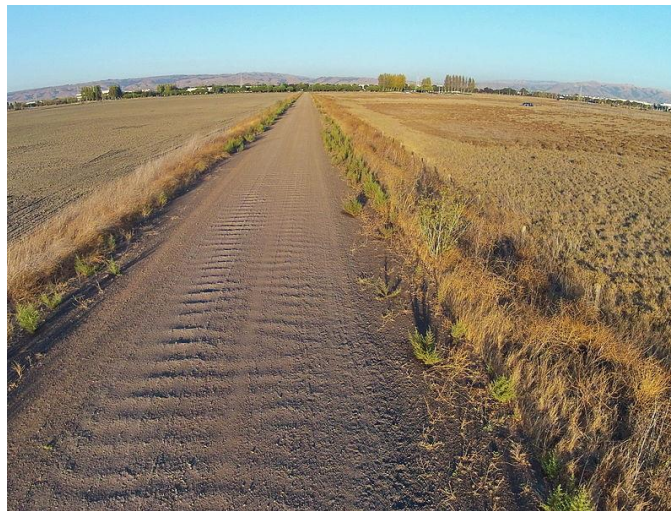


Figure 388: Corrugations in a gravel road.

Long wave unevenness can be caused by a swelling clay subgrade (see figure 389) or uneven settlements in the weak subsoil (see figure 390). It is interesting to notice that these soil related effects (swell and settlement) result in the same type of unevenness.



Figure 389: Unevenness due to an uneven swelling clay subgrade.

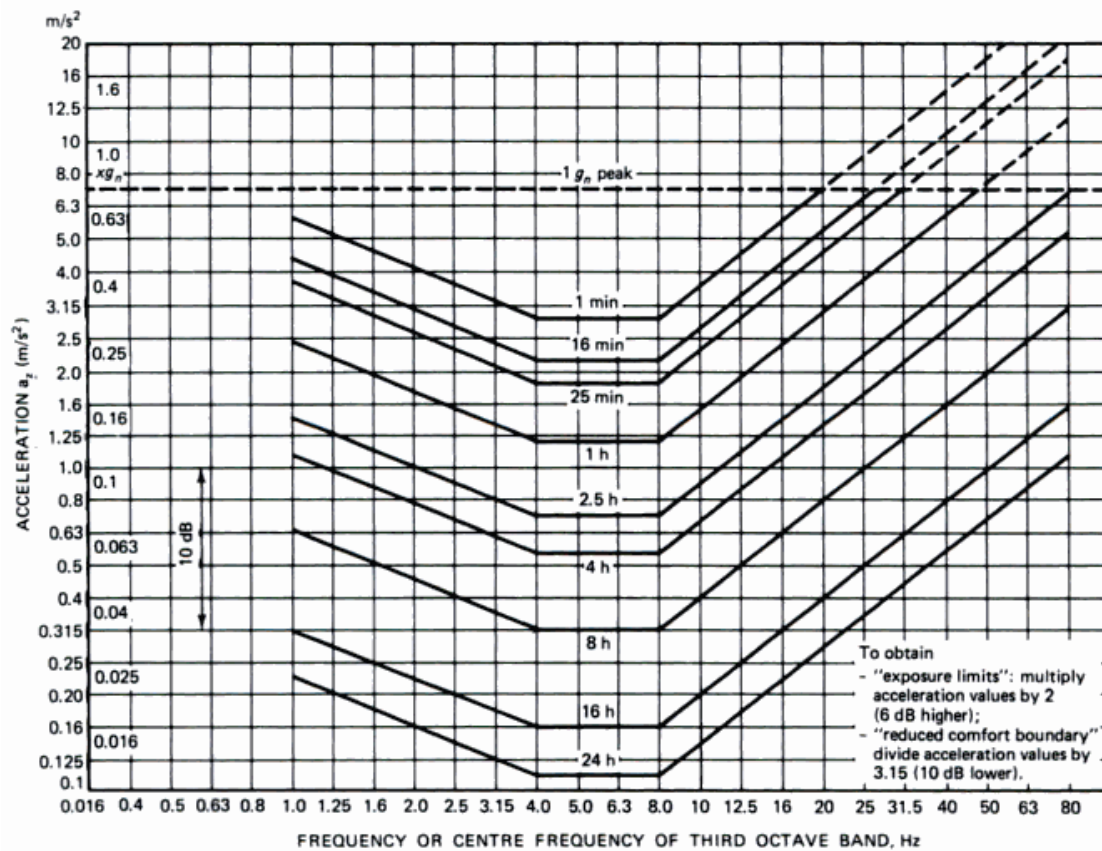


Figure 390: Unevenness due to uneven settlement of the weak subgrade.

There is a rough rule of the thumb that says that the depth of the layers which are causing the unevenness is about half of the wavelength of the unevenness. This implies that corrugations at traffic light controlled junctions is often not due to instability of the top layer but to instability of the binder layer underneath the wearing course.

When driving over rough roads, the driver and her passengers are experiencing vertical and horizontal accelerations of certain magnitudes and frequencies. Human beings are not equally sensitive to each frequency; this is shown in figure 391 where the ISO lines are given for the vertical accelerations and frequency which cause driver fatigue after a certain period of time. The graph shows that we are most sensitive for frequencies between 4 and 8 Hz. This implies that when driving at 72 km/h (20 m/s) and we ignore the effect of the car, we are most sensitive for wavelengths between 18 and 9 m (we recall: v (speed) = f (frequency) * λ (wavelength)). The accelerations we experience depend of course not only on the wavelengths and amplitudes of the pavement roughness and the speed by which we are driving but also on the characteristics of the car.

As we also know, pavement roughness is seldom caused by one single wavelength (in asphalt pavements corrugation in front of traffic lights are an exception), but is composed of a large number wavelengths with various amplitudes. Long waves will have large amplitudes while short



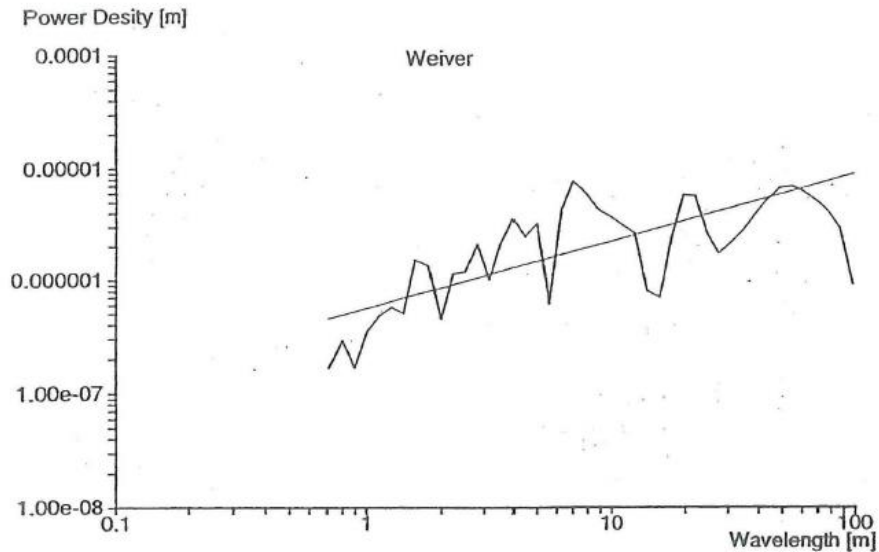


Figure 392: Example of a Power Spectral Density (PSD) curve as determined for a specific pavement (in this case a concrete block pavement).

It is common practice to describe the PSD curve with a straight line following:

$$P(\lambda) = P(\lambda_0) * (\lambda / \lambda_0)^n$$

Where: $P(\lambda)$ = power density at wavelength λ ,
 $P(\lambda_0)$ = power density at reference wavelength λ_0 .
 λ_0 = reference wavelength often taken as 5 m.

In many references the power density is indicated by A so the equation becomes:

$$A(\lambda) = A(\lambda_0) * (\lambda / \lambda_0)^n$$

The question now is how do we measure the road profile? Nowadays high speed profilometers using laser techniques are available for doing this. Figure 393 shows such a high speed measuring device which measures the longitudinal road profile but also the transversal profile by means of the lasers attached to the beam mounted in front of the car. The vehicle shown in figure 393 is also equipped with a laser crack measuring system and high definition cameras allowing the measure in one run and at high speed the entire pavement condition.

These sophisticated pieces of equipment were not available in the "old" days (let say 50 years ago). Remember that when we were discussing the AASHTO empirical design method in the beginning of these notes, we were introducing the present serviceability index (PSI) concept which was a number between 0 and 5 representing the quality of the road as experienced by the road user, with 5 being the highest quality. The psi was determined following:

$$PSI = 5 - 1.91 * \log(1 + SV) - 0.01 * \sqrt{(C + P) - 1.38 RD^2}$$

Where: SV = the variance in the measured slope values of the road profile in 10^{-6} rad^2 ,
C + P = amount of cracking and patching,
RD = rut depth.

Since the PSI is representing the quality of the road as experienced by the road user, it will not be a surprise that the road roughness component in the equation was by far the strongest explaining variable. Therefore also an equation has been developed which predicts the PSI using only the slope variance. This equation is:

$$PSI = 3.27 - 1.37 * (\log SV - 0.78) \text{ with } [SV] = [10^{-6} \text{ rad}^2]$$

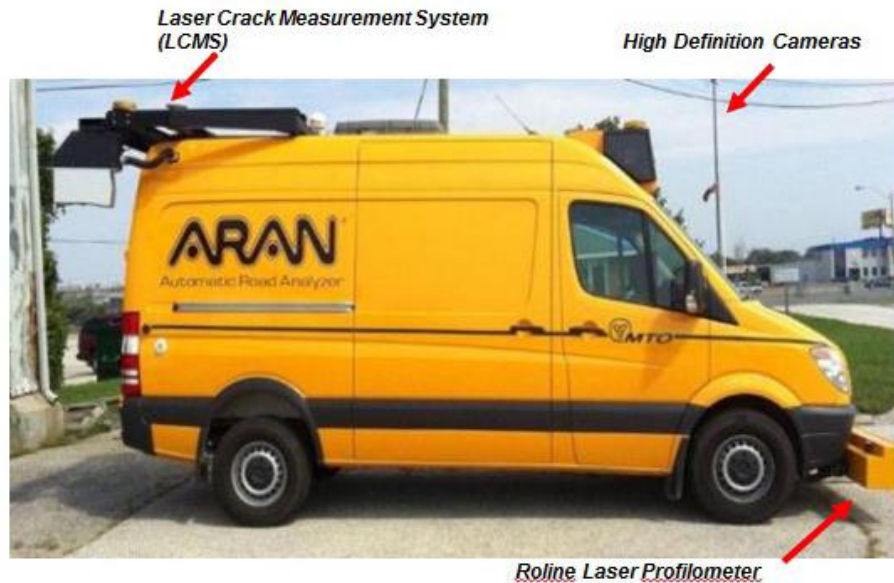


Figure 393: High speed measuring device for road profile measurements and crack detection.

The slope variance SV was measured during the AASHTO road test with the CHLOE profilometer which is shown in figure 394.

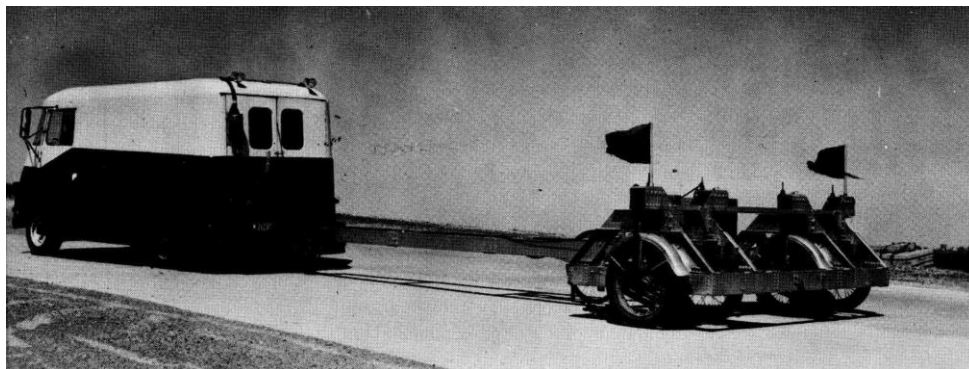


Figure 394: CHLOE profilometer as used during the AASHTO road test.

The principle of the CHLOE profilometer is shown in figure 395, while figure 396 shows an example of the recorded test results and figure 397 shows the chart reader.

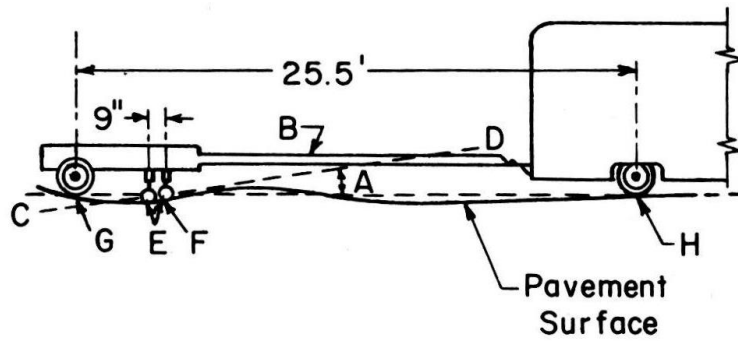


Figure 395: Principle of the CHLOE profilometer.

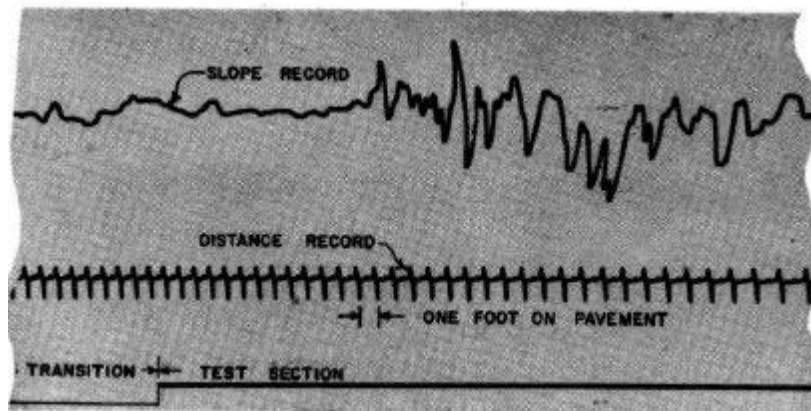


Figure 396: An example of the recorded tests data.

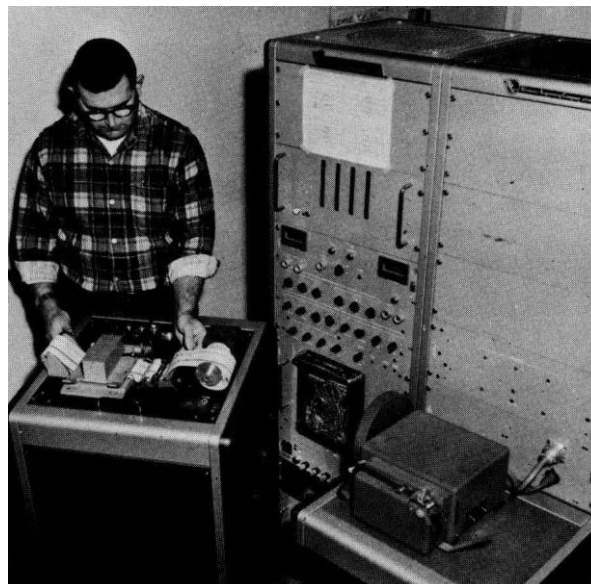


Figure 397: Chart reader.

There should be a relationship between $A(\lambda_o)$ and n on one hand and the SV on the other. This relationship is:

$$SV = 25.046 * n^{-0.574} * A(\lambda_0) - 4.149 \text{ E-7} * n^2 + 5.5734 \text{ E-7} * n - 2.481 \text{ E-7}$$

With: $[SV] = [\text{rad}^2]$ and $[A(\lambda_0)] = [\text{m}]$ and $\lambda_0 = 5 \text{ m}$

The equation was derived based on data given in [118] and is valid for $0.25 \leq n \leq 1.25$.

From Stenschke's data [118] also a relationship between the PSI on one hand and $A(\lambda_0)$ and n on the other was derived which is:

$$PSI = -7.22 + 1.124 * \ln(n) + (0.079 * n - 0.771) * \ln A(\lambda_0)$$

It should be noted that Stenschke calculated the PSI using:

$$PSI = 5.0 - 1.91 * \log(1 + SV)$$

Stenschke claimed that the PSI is mainly controlled by $A(\lambda_0)$ and simplified the equation to:

$$PSI = -7.752 - 0.71 * \ln A(\lambda_0)$$

Since $\ln(X) = 2.303 \log X$ we can also write $PSI = -7.752 - 1.635 \log A(\lambda_0)$

At the high PSI values (around 4.4) the accuracy is ± 0.2 . In the middle range $3.03 < PSI < 3.78$ the accuracy is ± 0.3 and for lower PSI values (< 2) the accuracy is ± 0.4 .

It should be noted that Genschke the PSI using: $PSI = 5.0 - 1.91 * \log(1 + SV)$ when setting up his data base.

Since both the PSD and PSI don't give information on the response of a vehicle when driving over a rough road and because PSI is not a feasible number to represent roughness of very poor roads as one will encounter in developing countries, the World Bank developed the so called International Roughness Index parameter (IRI). This parameter represents the movements of a quarter car vehicle model driving at 80 km/h over the pavement. The quarter car model is shown in figure 398 and figure 399 shows the IRI scale.

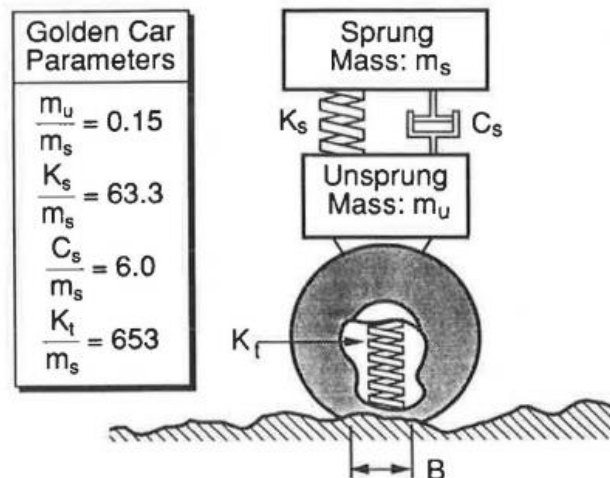


Figure 398: Quarter car model to calculate IRI.

Several relationships have been developed between IRI and PSI and Paterson [3] recommends the following to be used.

$$IRI \approx 5.5 \ln (5 / PSI)$$

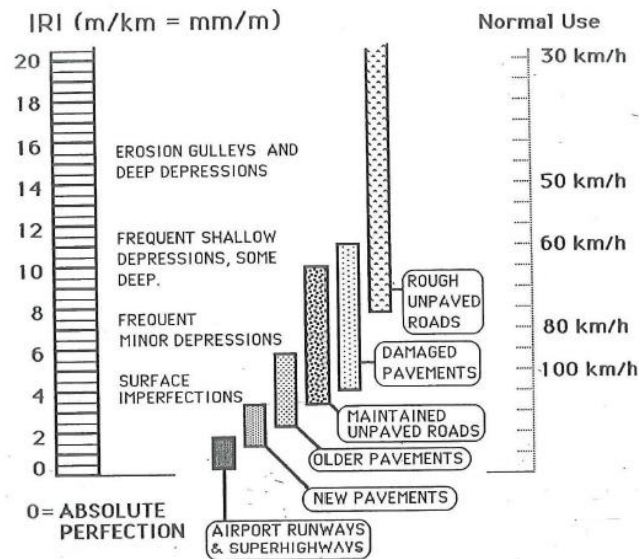


Figure 399: IRI scale

The IRI is a very important parameter in the Highway Design Model that was developed for the World Bank. This model allows to select the most economical structure based on road geometry, pavement thickness, climate construction and maintenance costs as well as vehicle operating costs. It will be no surprise that the IRI level highly affects traffic speed and vehicle operating costs (fuel, tires, maintenance etc). These influences are shown in figures 400 and 401.

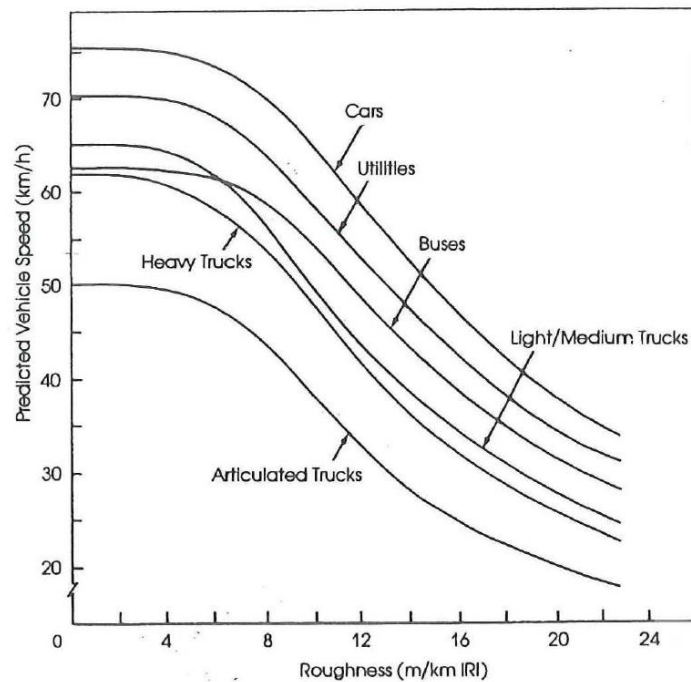


Figure 400: Relationship between IRI and traffic speed.

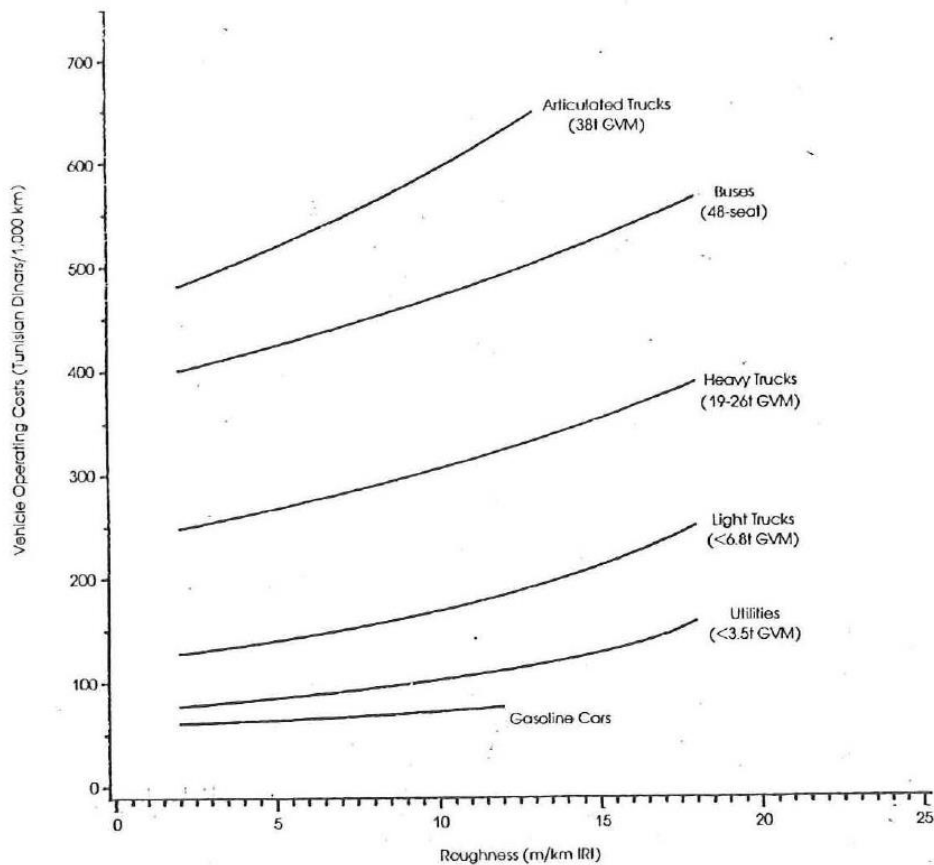


Figure 401: Relationship between IRI and vehicle operating costs.

Pavement roughness of course also influences the dynamic axle loads. Speed and the car characteristics are of course other important parameters affecting dynamic wheel loads. Stenschke [118] e.g. used the half car model shown in figure 402 for analyzing dynamic wheel loads. The model parameters are given in table 86. The values shown in table 86 are valid for a "norm" passenger car and derived from 6 actual passenger cars that were in use in Germany in the 1970's.

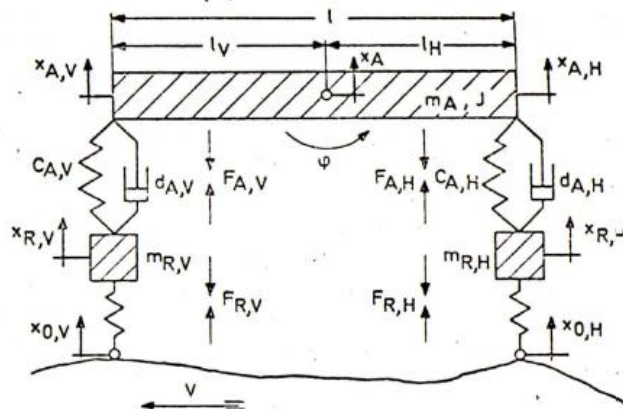


Figure 402: 2D car model used by Stenschke in his simulations.

Table 86 also shows the vehicle parameters as used by Sweere [136] in his analysis on the effects of road roughness on dynamic truck axle loads. Basically Sweere used the same model but changed the vehicle parameters.

Parameter	Stenschke person car	Sweere empty truck	Sweere laden truck
m_A [kg]	903	5500	12447
J [kg * m ²]	1066	9640	28300
$m_{R,V}$ [kg]	63	800	800
$m_{R,H}$ [kg]	77	1300	1300
$c_{A,V}$ [N/mm]	19.6	430	430
$c_{A,H}$ [N/mm]	30.6	700	700
$d_{A,V}$ [Ns/m]	1969	30000	30000
$d_{A,H}$ [Ns/m]	3339	30000	30000
$c_{R,V}$ [N/mm]	280	1500	1500
$c_{R,H}$ [n/mm]	324	4000	4000
l_V [mm]	1283	1020	2240
l_H [mm]	1228	2180	960
Front axle load [kg]		3053	4547
Rear axle load [kg]		4550	10000

Table 86: Values of the parameters by Stenschke in his model and those used by Sweere.

Based on these values Stenschke derived the following equation to estimate the ratio of dynamic axle load ($\Delta P_{dyn,eff}$) over static axle load (P_{stat}):

$$\Delta P_{dyn,eff} / P_{stat} = 0.476 + 0.068 * \log \{A(\lambda_o)\} - 0.23 * n + 0.003 * V$$

Where: $\Delta P_{dyn,eff} = \sqrt{(1/L * \int_0^L \Delta P_{dyn}^2 dl)}$
 $[A(\lambda_o)] = [m]$
 V = vehicle speed [m/s]

When we substitute PSI in the equation instead of $A(\lambda_o)$ (see relation between PSI and $A(\lambda_o)$ given earlier) we obtain:

$$\Delta P_{dyn,eff} / P_{stat} = 0.265 - 0.0416 * PSI - 0.23 * n + 0.003 * V$$

These equations hold for passenger cars and as mentioned earlier Sweere did similar studies for trucks. As input he used the PSD spectra as were measured on several provincial roads in the Netherlands. He arrived to the conclusion that at a speed of 31.5 km/h there was hardly a difference between the dynamic respons of the empty and laden truck. At 63 km/h there was a big difference between the respons of the empty and laden truck. For the "63 km/h laden truck" case and the "31.5 km/h empty and laden truck" cases the respons was mainly determined by the rear axle movements while for the "63 km/h empty" case the respons was mainly determined by the movements of the rear axle and the body of the car.

Based on his analyses Sweere could develop the following equations for the standard deviation (σ) of the axle load at 63 km/h.

$$\begin{aligned} \sigma_{laden} &= 0.302 + 0.057 * SV - 0.0008 * SV^2 \\ \sigma_{empty} &= 0.611 + 0.164 * SV - 0.0036 * SV^2 \end{aligned}$$

Similar results were obtained by Huurman [66] in his research on the performance of concrete block pavements, a pavement type where "roughness" is the most important type of defect together with permanent deformation. For a slightly different truck configuration Huurman arrived to:

$$\log \sigma = -0.5184 + 0.4075 * \log SV$$

Where:

σ = standard deviation of the dynamic axle load (100 kN static) of a two axle truck driving at 63 km/h,

SV = slope variance [rad^2] of the road profile multiplied with 10^6

It will be easy to understand that the characteristics of the car (tire pressure, spring – suspension system, resonance frequency etc) have a very large effect on the dynamic response of a vehicle. A typical frequency response curve is shown in figure 403.

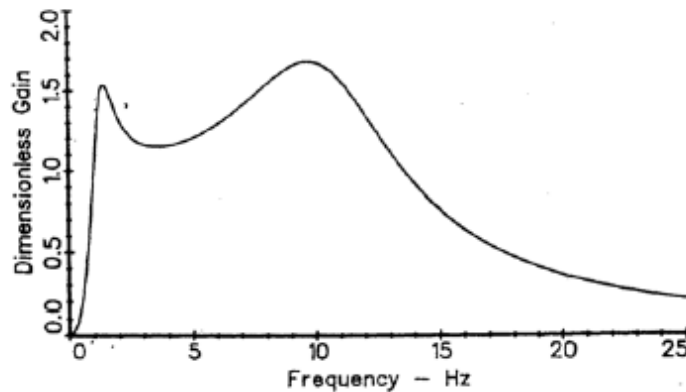


Figure 403: Response of a vehicle to various frequencies.

Figure 403 shows a response peak at around 2 Hz which is due to the vibrations of the body of the vehicle while the peak at around 10 Hz is due to vibrations of the axle. The stiffness of the shock absorber will highly affect the magnitude of the peak values of the dimensionless gain parameter shown in figure 401; a better damping will reduce these peak values. Effects of spring stiffness and shock absorber on the performance of a concrete block pavement have been investigated by Huurman [66]. A block pavement consists of a top layer of concrete blocks (with dimensions length * width * height = 200 * 100 * 80 mm) which are laid on a thin bedding sand layer which rests on a base course. Roughness and permanent deformation are the main defect types observed on those pavements. In interesting aspects of these pavements is that the stiffness of a well designed and constructed block pavement increases with time and number of load repetitions. Huurman investigated what the performance of a well designed and constructed block pavement would be when it would be loaded by trucks with a too high spring stiffness or a too low shock absorber stiffness. The results are shown in figure 404.

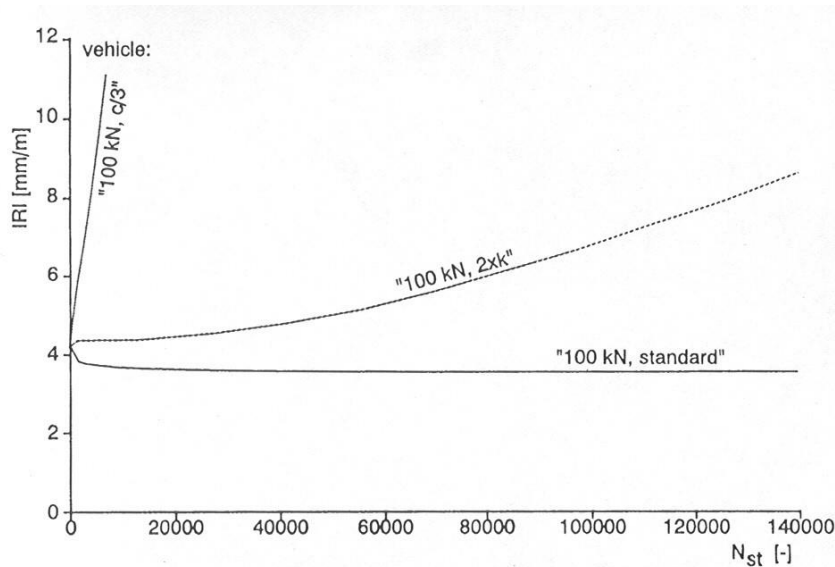


Figure 404: Roughness development of a well designed and constructed block pavement when loaded with well-maintained trucks (100 kN standard) and by trucks with a too stiff spring system (100 kN, 2 * k) or a too low shock absorber stiffness (100 kN, c / 3).

From the material presented in this section on road roughness it has become clear that well maintained roads as well as well-maintained cars and trucks have a very large effect on driving comfort, dynamic axle loads and pavement performance.

We have seen that in the PSI equation pavement damage like cracking and permanent deformation only play a minor role. It is the slope variance that has by far the biggest effect on the PSI. So the question then is to what extent the PSI is affected by surface damage types. An excellent study on this was done by Jain [119] who reanalyzed the AASHTO data and concluded that the change in slope variance is very much controlled by the change in the amount of cracking, patching and permanent deformation following:

$$\text{Arctan} \log(1 + \sqrt{SV_i} - \sqrt{SV_o}) = \text{constant} + [\log(1 + C_i * P_i)]^2$$

Where: SV_o = initial roughness,
 SV_i = roughness at time i,
 C_i = amount of cracking at time i,
 P_i = amount of patching at time i.

The World Bank [3] produced the following model which shows how ride quality is affected by pavement damage:

$$\Delta RI_t = 134 * e^{mt} * SNCK^{-5.0} * \Delta NE_4 + 0.114 * \Delta RDS + 0.0066 * \Delta CRX + 0.003 * H_p * \Delta PAT + 0.16 * \Delta VPOT + m * RI_t * \Delta t$$

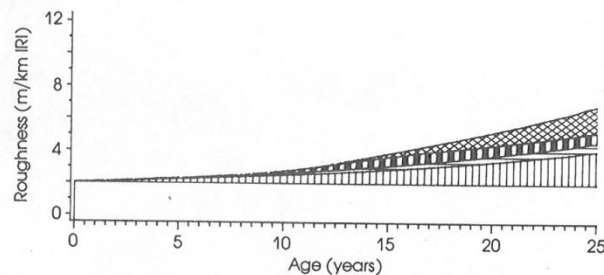
Where:

ΔRI_t = increase in roughness over time period t [m/km IRI],
 RI_t = roughness at time t [m/km IRI],
 ΔRDS = increase in standard deviation of rut depth of both wheel paths [mm],
 ΔCRX = increase in cracked area [%],
 ΔPAT = increase in patched area [%],

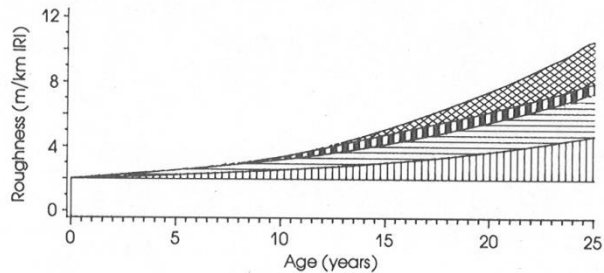
Δt = incremental time period [years],
 ΔNE_4 = incremental number of ESAL's (80 kN) in period Δt [million ESA's/lane],
 $SNCK = 1 + SNC - 0.0000758 * H * CRX$,
 SNC = modified structural number [mm],
 H = thickness of cracked layer [mm],
 CRX = area of cracking [%],
 Mm = environmental coefficient = $0.012 * RG$,
 RG = regional factor = $0.1 * (\text{elevation [1000 ft]} + \text{rainfall [inch/year]} + \text{temperature/freeze cycle zone (1 to 9)})$
 $\Delta VPOT$ = increment in the volume of open potholes [m^2 / lane / km]
 H_p = average rectified potrusion of patch repairs above or below surrounding surface [mm].

The equation shows that many factors influence the development of roughness and that cracking only has a limited influence; environmental factors, age and deformations on the other hand have a significant influence; all this is shown in figure 405.

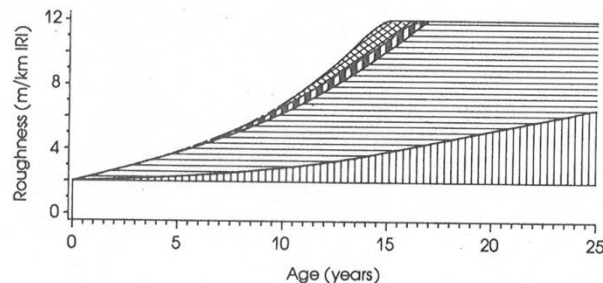
(a) Light Loading, or Overdesigned Pavement



(b) Medium Loading, or Normal Pavement Design



(c) Heavy Loading, or Underdesigned Pavement



[Cross-hatched] Potholing [Vertical lines] Cracking and Patching [Horizontal lines] Deformation [Hatched] Environment-Age.

Note: Surface treatment on granular base pavement, SNC 3, with traffic loading of (a) 0.02, (b) 0.10, and (c) 0.50, million ESA/lane/year, respectively.

Figure 405: Effect of potholing, cracking and patching, deformations, environmental factors and age on roughness development.

16. Thickness design systems

16.1 Introduction

In the last decades many computerized thickness design systems have been developed which calculate e.g. the required asphalt thickness needed to carry the design traffic. Nice examples of such systems are the SPDM system as developed by Shell, KENLAYER as developed by dr Huang and available via his book Pavement Design and Analysis [70], and FPS-21 developed by researchers of the Texas Transportation Institute for the Texas Highway Department. Also the Australian APDS (specially developed for airport pavement design) and the 3DMove package, developed at the University of Nevada at Reno, should be mentioned as well as the suit of programs developed by F(ederal) A(viation) A(uthority). Last but certainly not least the M(echanistic) E(mpirical) P(avement) D(esign) system as developed for AASHTO deserves special attention. Some of these systems are based on multi-layer linear elastic analyses, others do include visco-elastic analyses and some allow finite element analyses to be made.

It is far beyond the scope of these lecture notes to discuss these and all other available design systems in detail and the reader is therefore strongly suggested to surf on the web for pavement design freeware and to try some of these programs to find out which program is the most preferable one for his specific situation.

It will be clear that research institutes and specialized consulting firms will require more advanced software than those users who just want to have an idea about the thickness required for their pavement network.

In general all these programs require input on the expected traffic loads, the expected temperature variations during the year, and the characteristics of the materials used. The required information can be very detailed e.g. in terms of nr. of axles per axle load group, wheel configurations and contact pressures, or can be rather general in terms of expected number of equivalent single wheel loads. Transfer functions for e.g. the fatigue of the asphalt layer can be defined by the user her/(him)self or can be selected from a material library. The required asphalt thickness is either automatically generated or should be selected by the user himself.

Hereafter short introductions to the SPDM system, FPS-21, KENLAYER, 3DMOVE and AASHTO's MEPD will be given. Attention will also be paid to the French and Dutch design system since they include an interesting approach to including probabilistics and risks of failure. Furthermore the South African pavement design catalogue TRH4 [127] (similar systems are still in use in many other countries) will be presented as well as some aspects of the Highway Design Model (HDM) developed for the World Bank .

First of all however we will discuss to what extent we are able to predict pavement performance and if so how detailed such predictions should be.

16.2 How accurate are our pavement performance predictions?

Can we accurately predict pavement performance? No we cannot! This answer will certainly be criticized by researchers who did excellent work in developing design systems like AASHTO's MEPD which claim reliable performance predictions can be made. The reason why this author believes that such accurate predictions cannot be made is because we are dealing with too many unknown variables. Future traffic and climate e.g. are parameters that are hard to predict even if an excellent data is available on how traffic and climate has developed in time. Furthermore even if one does extensive laboratory investigations to determine mixture properties one should realize that the mixtures that are laid in practice do have different properties because lab production and compaction are not simulating what happens in practice. Another important aspect that hinders predicting pavement performance is the high variability in material characteristics that occur in practice. This variation is caused to some extent by the (lack of) workmanship of the contractor

but also because the specifications themselves allow a large amount of variation to occur. The last aspect that needs to be mentioned is the fact that our models are simply not good enough. In most design systems stresses and strains are calculated assuming linear elastic behavior but the question is whether this assumption is still valid when damage starts to initiate. We also calculate the fatigue life of an asphalt layer by using the maximum tensile strain as input in a laboratory determined fatigue relation. So we are simplifying the effects of complex 3D stress/strain conditions into 1D conditions (by only taking into account the maximum tensile strain we ignore the effect of the two other principal stresses and strains) and we are using a lab determined fatigue relationship which is not really simulating what happens in the pavement. A discussion on the effect of simplifying the real 3D stress/strain conditions into 1D conditions on fatigue, as well as the influence of simplifying the wheel load is given in appendix A. Furthermore we have seen that trying to correlate cracking which is visible at the pavement surface to the amount of fatigue cracking expressed by means of Miner's ratio n/N calculated from the maximum tensile strain at the bottom of the asphalt layer (bottom up fatigue) is a tricky thing to do because cracking visible at the pavement surface may, as we have seen, also be due to many other factors than bottom up fatigue. We have even seen that in many cases cracking visible at the pavement surface has very little to do with bottom up fatigue. All this implies that we need calibration factors of significant magnitude to match predictions with observations but even then we are not very successful in making accurate performance predictions. Figure 406 and 407 are examples of how (un)successful we are with our predictions on fatigue cracking.

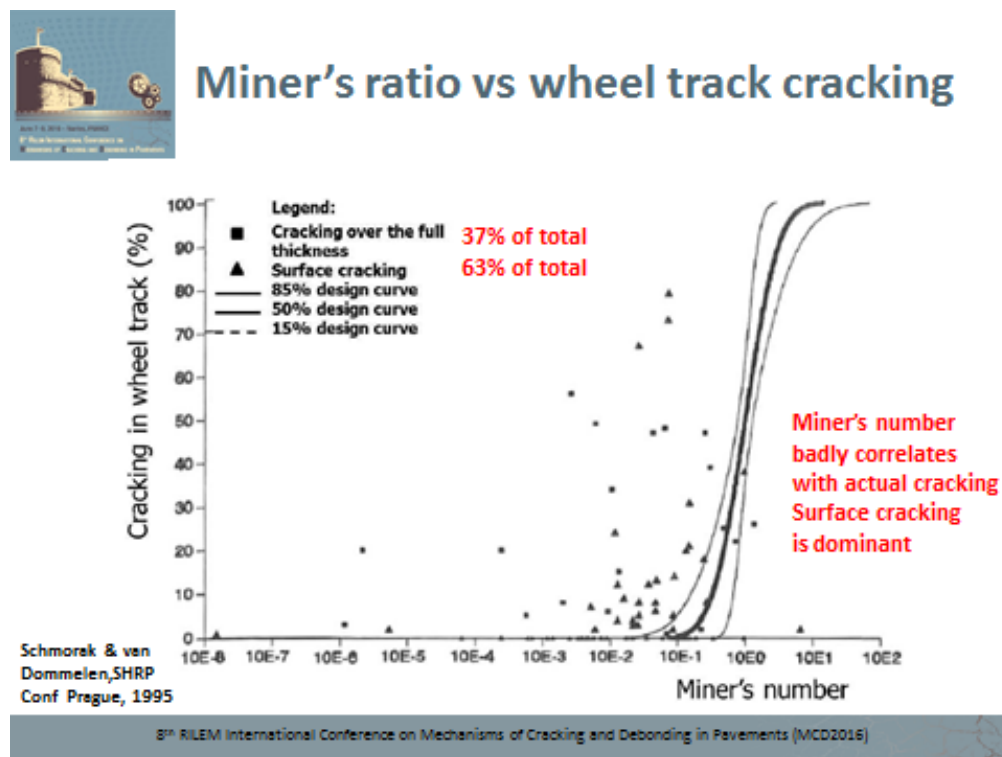


Figure 406: Relation between Miner's number n/N and percentage of wheel path cracking as determined in the SHRP-NL project in the Netherlands.

Prediction vs observation

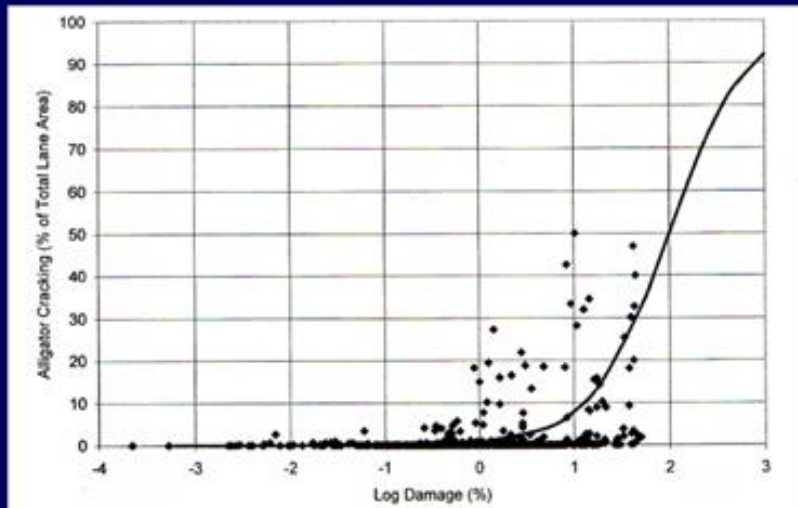


Figure 3.3.20. Bottom-up cracking versus fatigue damage at bottom of HMA layer.

Figure 407: Relation between amount of cracking visible at the pavement surface and the log of Miner's number according to AASHTO's MEPD.

Figure 406 e.g. shows that many pavements showed already extensive cracking before the n/N ratio (ratio of applied number of load repetitions over allowable number of allowable number of repetitions) reached the value of 1. Figure 407 shows that one might between 0 and 20% damage in case $n/N = 1$ and between 0 and 50% damage when $n/N = 10$ ($\log n/N = 1$).

Hereafter just one other example will be given to show that it is very difficult to match predicted performance with observed performance. Groenendijk [23] and Pramesti [38] analyzed the performance of three APT sections that were built at the outside facilities of the Lab for Road and Railroad Research of the Delft University of Technology. Details of the three sections are given in table 87.

Section name	Asphalt thickness [mm]	Asphalt mixture	Load characteristics
I	150 (80+70)	GAC	super single $F = 75$ kN, $p = 950$ kPa
V_A	80	GAC	super single $F = 75$ kN, $p = 950$ kPa
V_B	80	GAC	super single $F = 50$ kN, $p = 700$ kPa

Table 87: Details of the Delft University APT sections.

Figure 408 shows the probability of failure curves based on Miner's ratio n/N and reduction of the asphalt stiffness to 50% of its original value and the percentage of cracking visible at the pavement surface. The number of load repetitions to failure as well as Miner's number was

calculated as follows. First of all, temperature classes were determined and for each temperature class the stiffness of the mixture was determined. Then the tensile strain at the bottom of the asphalt layer was calculated and the allowable number of load repetitions was determined using the fatigue relation that was determined for that temperature using the Beam On Elastic Foundation (BOEF) test (for details of this test see section on fatigue). Miner's number for that temperature class was determined by dividing the actual number of load repetitions that were applied at that temperature by the estimated fatigue life. It should be noted that for each temperature class the tensile strain was calculated using the stiffness modulus valid for the occurring temperature and loading time but ignoring any possible reduction in modulus because of damage development that might have taken place during the load applications. In the analysis lateral wander of the wheel was taken into account as well as variation in fatigue characteristics. The amount of cracking was determined by placing a grid with a size of 100 * 100 mm on top of the pavement surface and counting the number of grid cells which contained a crack. The percentage cracked area was then calculated using:

Percentage cracked area = number of grid cells containing a crack / total number of grid cells.

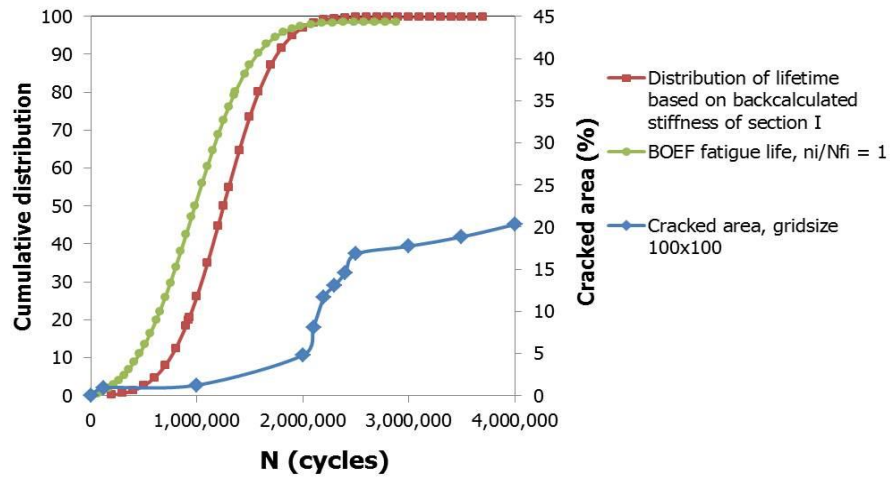
The reduction of the stiffness modulus was determined using the stiffness values that were back calculated from deflection measurements. The probability curve for the lifetime based on stiffness reduction is based on the variation in the back calculated stiffness's in the particular section.

When observing the results shown in figure 408, we again notice that there is a poor agreement between the predicted lifetime and the amount of cracking that was observed at the pavement surface. Furthermore most of the cracking was surface cracking and the question then is "was there any bottom up fatigue?". Let us start with having a view of how the pavement sections looked like at the end of the test.

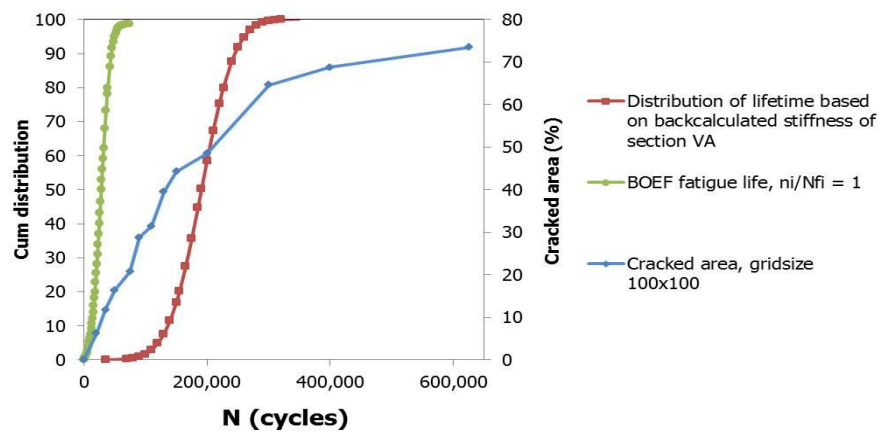
Figure 409 shows the extent of cracking on each of the sections after completion of the test. The blue dots in the pictures indicate the location of the strain gauges that were placed at the bottom of the asphalt layer; DT indicates the strain gauges in the transverse directions while DL indicates the gauges in the longitudinal direction.

Figure 410 shows how the longitudinal and transverse tensile strains measured in section I developed with the number of load repetitions. This figure shows that only 4 gauges out of 8 (DL1, DL3, I-DT-1 and I-DT-4) measured an increase in tensile strain as a function of the number of load repetitions. These strains took such high values that fatigue certainly must have occurred at those locations. The other strain gauges measured a more or less constant value.

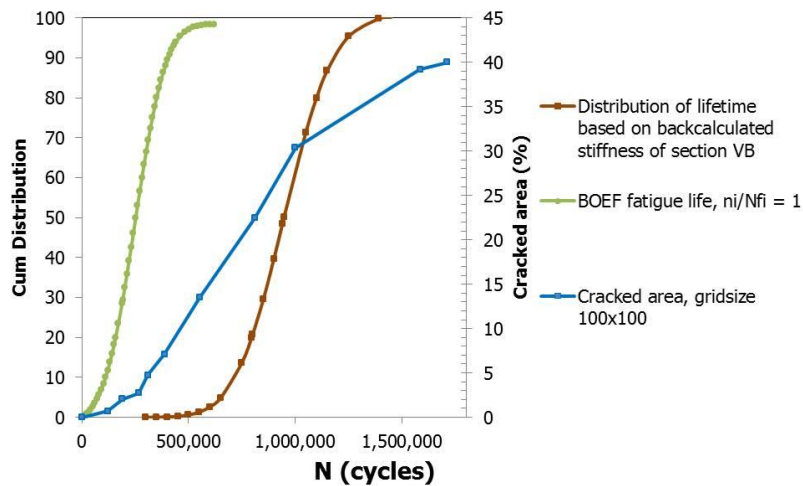
It is interesting to note that although I-DT-4 measured very high strains, hardly any damage at the pavement surface was visible at that location. This again emphasizes the complexity of matching theoretical results with practical observations.



(a)



(b)



(c)

Figure 408: Performance of the three Delft University APT sections [38].
(a) = section I, (b) = section V_A, (c) = section V_B

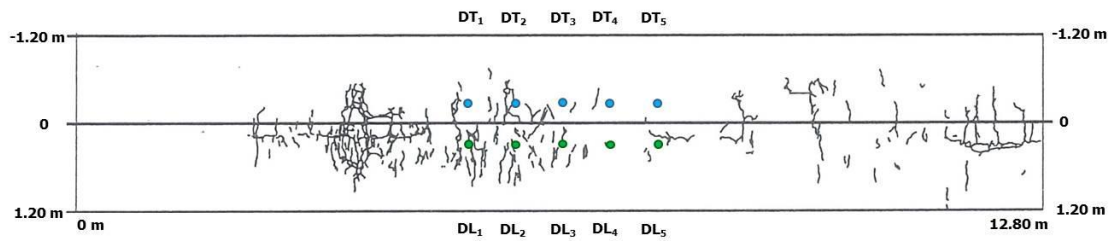


Figure 409a: Crack pattern of section I after 4 Million cycles.

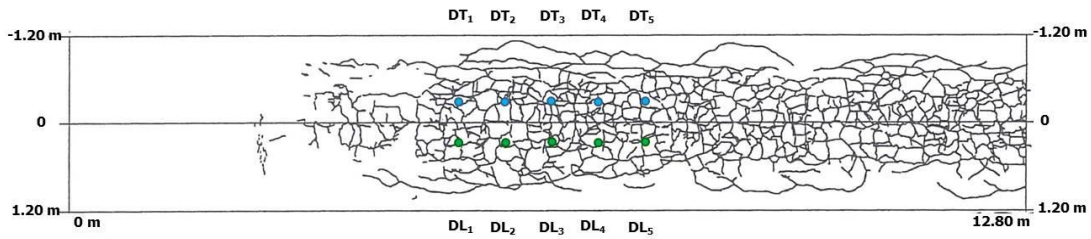


Figure 409b: Crack pattern of section VA after 650 kilocycles.

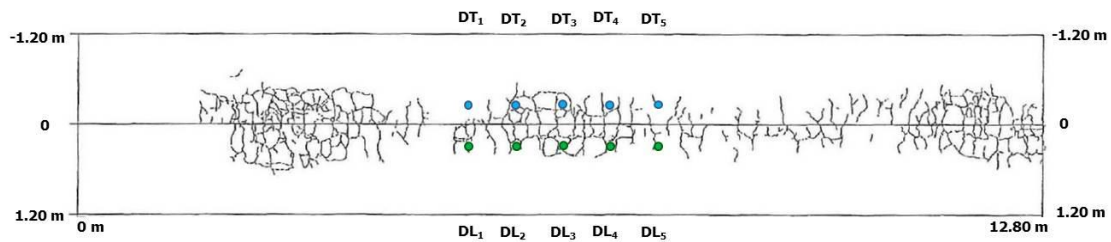
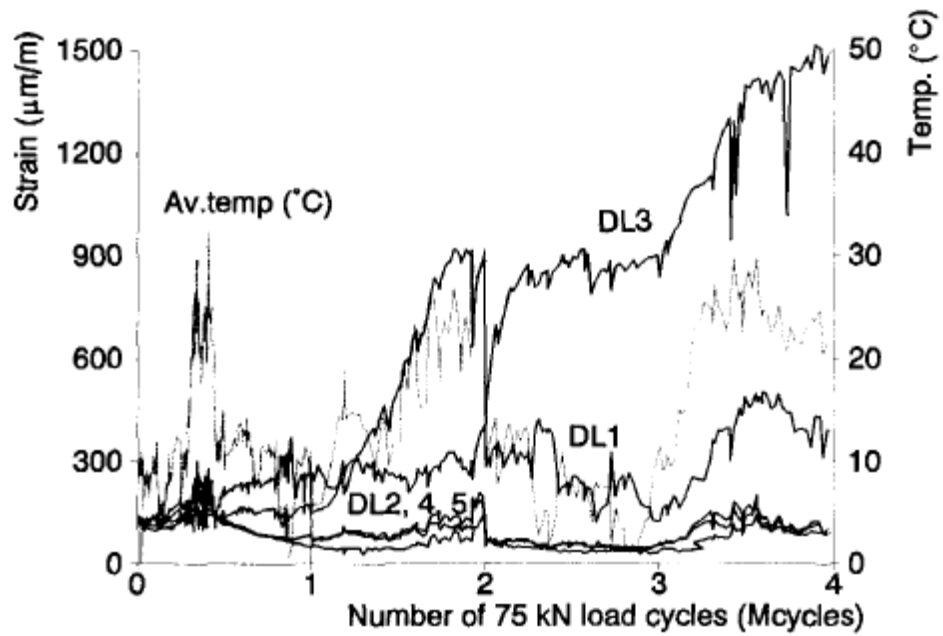
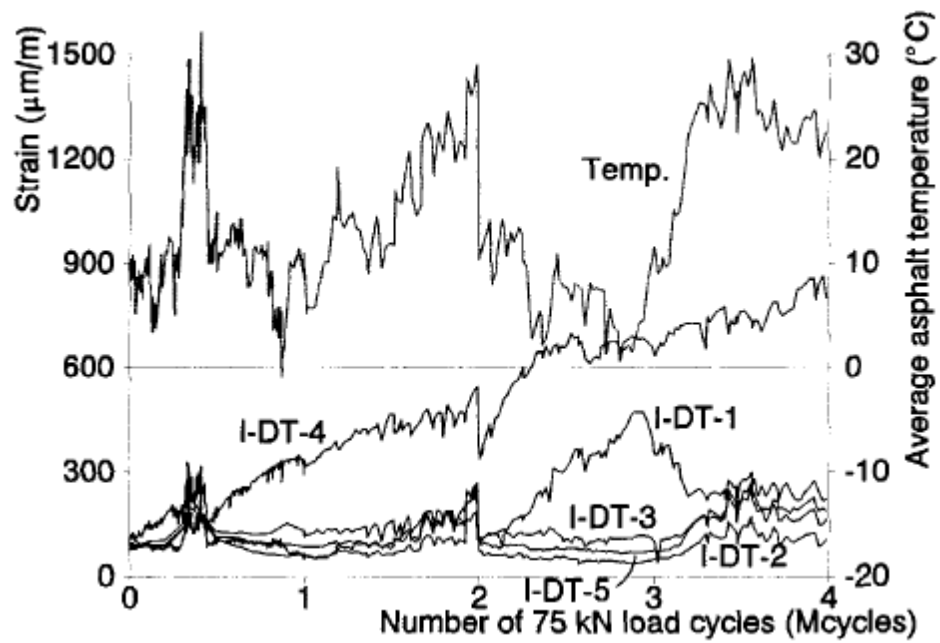


Figure 409c: Crack pattern of section VB after 1722 kilocycles.

In spite of all these complexities, AASHTO's MEPD software allows to make performance predictions like the ones shown in figure 403. As is described in the manuals which come with the design system (e.g. [31]), the designers have to collect values for a lot of input parameters. The input not only implies material characteristics and traffic but also moisture conditions, aging, temperature, temperature distributions over the height of the asphalt pavement, etc. Graphs like those shown in figure 411 give the impression that the amount of rutting (permanent deformation) will be 12 mm after 10 years (120 months) for pavement "AC flex S-1 T-4 Pen" and about 10.5 mm for pavement "AC flex S-1 T-4 PG". This seems a very accurate and precise prediction but this author claims that, because of the reasons mentioned above, the actual rut depths after 12 months will be different than the ones predicted.



(a)



(b)

Figure 410: Increase in longitudinal and transverse strain in section I in relation to the number of load repetitions.

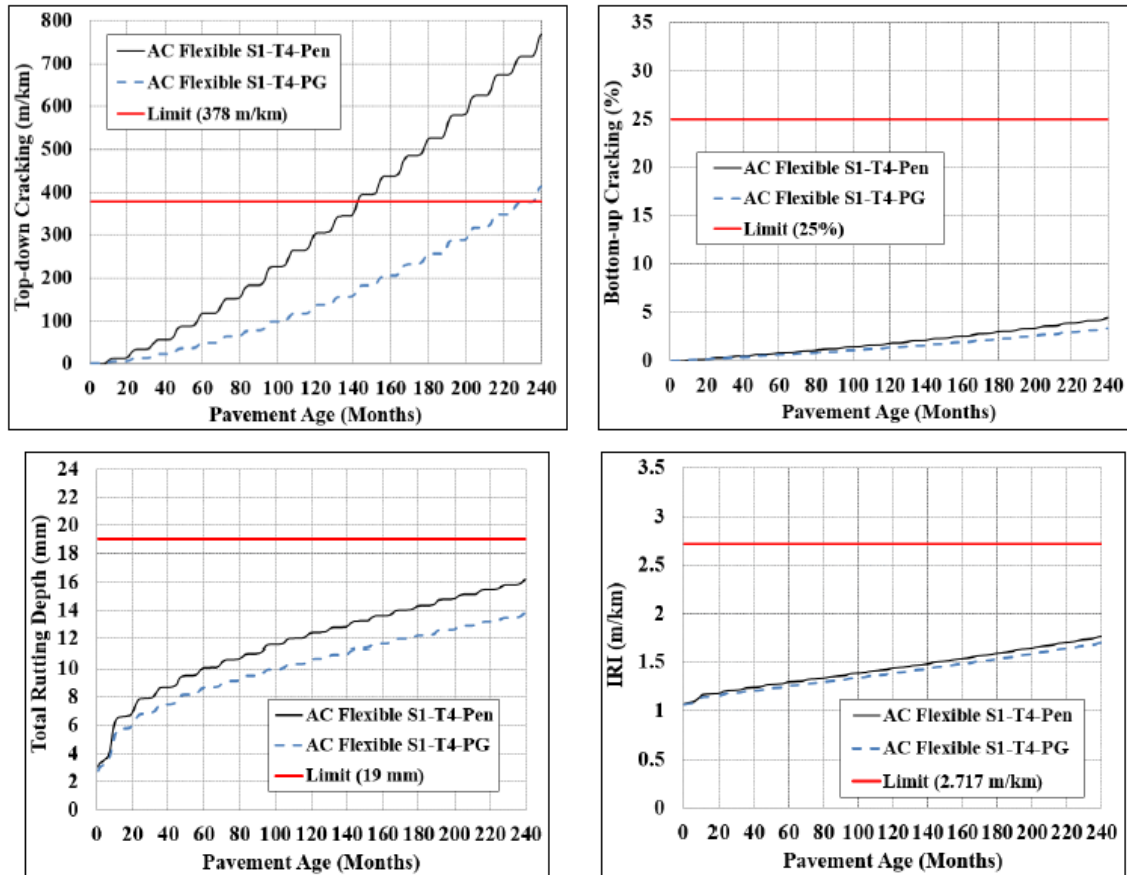


Figure 411: Examples of performance predictions as produced by AASHTO's MEPD software.

To some extent this author rates pictures like these as misleading because from his experience he knows that users of such design systems and especially clients tend to believe that "the computer is telling the truth and nothing but the truth" and don't realize that these predictions are just an estimate which have a certain degree of uncertainty. He therefore strongly prefers a design system that tells the user/client what the **chance** is that a certain amount of permanent deformation would be after a certain a number of years, which would be the most important factors influencing permanent deformation. Then it could be decided which would be the factors that really can be controlled by the contractor and which factors are "uncontrollable by both the designer and the contractor". Traffic, climate, model errors are amongst those "uncontrollable" factors. This information is of vital importance especially when pavements do not perform as expected since then it needs to be determined to what extent this is due to the contractor, the designer or whether it is simply due to factors which are beyond the control of the designer and contractor.

This author is therefore of the opinion that a probabilistic approach to pavement design is essential.

According to this author, the strength of the available design systems is not so much in making performance predictions like those shown in figure 411, but the possibility to make relative comparisons of the lifetime of different structures, to make relative comparisons of the effect of using different materials with e.g. different fatigue characteristics and the possibility of answering "what - if questions". Such questions could involve questions like "what would be the relative improvement in fatigue life if the mixture composition is changed?" and "what would be

the relative decrease in pavement life when specifications are not met?”. The question is whether advanced systems like AASHTO’s MEPD are really needed to answer these questions or whether “simpler” design systems can do such a job. This will be discussed in some detail later on but first we will present some pavement design systems.

16.3 Pavement design systems

The basic principles of how pavement design systems arrive to a prediction of pavement life are shown in figure 412. Depending on the system, the traffic loads are introduced as a number of equivalent axle loads with a standard, fixed wheel configuration and a fixed contact pressure. Other systems allow to input a full axle load spectrum with different axle load configurations and contact pressures. Most systems model the wheel load contact area with a circular area assuming the contact pressure is equal to the tire pressure. Only a few systems allow careful modelling of the contact area and contact pressure depending on the type of tire, tire load and tire pressure.

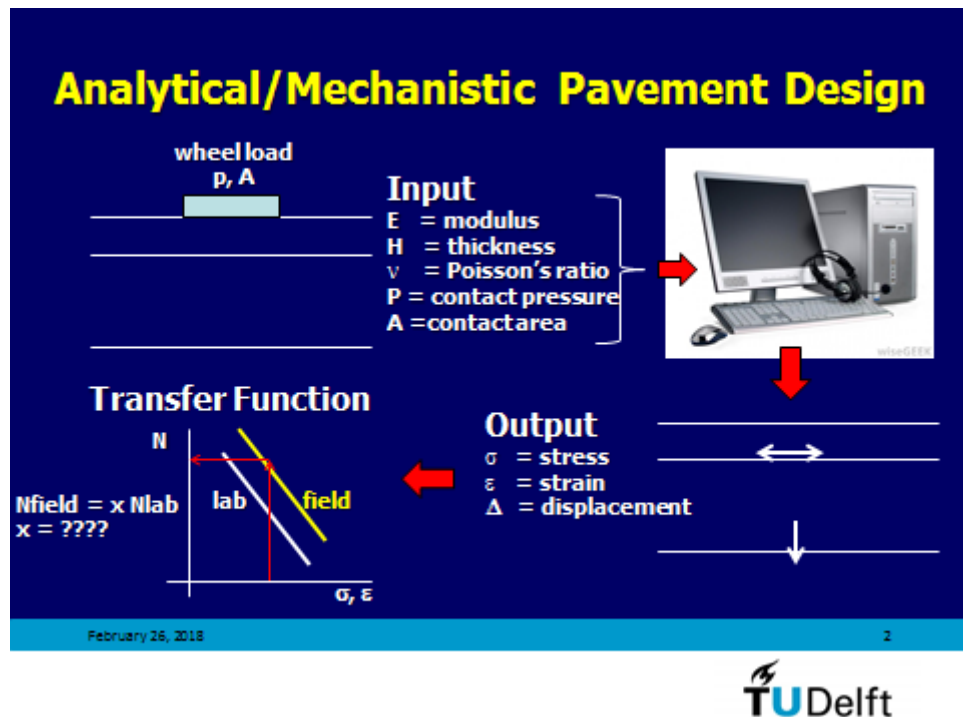


Figure 412: Principle of a mechanistic analysis on fatigue cracking.

In the “simple” design systems, material characteristics are input as single representative values while other systems allow to define “periods” during which the material characteristics (modulus and fatigue characteristics) take particular values. Such periods could be seasonal periods including freeze and thaw periods.

Some systems model the stiffness of granular materials and soils with an “elastic modulus” while other systems take into account the stress dependent nature of such materials.

Most systems are based on elastic layer theory while a few systems allow the asphalt layers to be modelled as visco-elastic materials.

Furthermore some systems do calculate the lifetime of a pavement given the input values for traffic, material characteristics, layer thicknesses etc, while other systems include an iteration procedure which results in the required thickness of e.g. the asphalt layer given the projected amount of traffic. Some systems allow performance predictions to be made like those shown in

figure 411 and a few systems take into account probabilistics implying that the input values show a certain amount of variation.

One must keep in mind that in a number of countries the AASHTO empirical design method, which was discussed in the beginning of these lecture notes, is still used. In other countries the Highway Design Model as developed by the World Bank for use in developing countries needs to be used for projects sponsored by the Bank.

Finally it should be mentioned that a number of countries are using catalogue type of design systems.

All in all it is clear that there is a wide variety of models available and the user should inform her/himself well before picking the one which suits her/his requirements.

In the remainder of this section the following design systems will be discussed briefly.

- SHELL SPDM,
- FPS21,
- KENLAYER,
- AASHTO MEPD,
- 3DMOVE,
- French design system,
- Dutch design system,
- Catalogue system used in South Africa,
- Highway Design Model developed for the World Bank.

16.3.1 SHELL pavement design software

The Shell pavement design software, the principles of which are discussed in [28] and [29], allows the user to determine the required asphalt thickness given the traffic load, the mean monthly air temperature, the stiffness of the subgrade and the stiffness and thickness of the base layer. Furthermore the volumetric composition of the asphalt mixture can be used as input as well as the pen and Tr&b of the bitumen used. The user can select his own fatigue criterion for the asphalt layer and his own subgrade strain criterion or he can use the relationships developed by Shell. The load configuration is fixed. It is an 80 kN axle load and the analysis takes into account a dual wheel configuration having a 20 kN load on each wheel. The contact pressure is assumed to be 600 kPa. The center to center spacing of the two wheels is 320 mm. The total traffic load is expressed in terms of 80 kN equivalent axle loads which is calculated following:

$$N_{eq} = \sum_{i=1}^k (n_i * L_i / 80)^4$$

Where:

- N_{eq} = number of equivalent 80 kN axle loads,
 k = number of axle load classes,
 L_i = magnitude of the axle load in class i ,
 n_i = number of axle loads in class i .

Table 88 is an example of the output produced by the design system. The result is printed in the lower left box "Asphalt Stiffness and Layer Thickness". The input that is provided by the user is printed in the boxes "Traffic & Design Life" and "Climate". As one will observe, the required asphalt thickness for this particular example is 0,084 m and is dictated by the subgrade strain criterion.

The program also gives a so called iteration report (table 89), which shows how many calculations were done to arrive to the end result and which intermediate results were obtained.

The program, which runs on 36 bits pc's, is extremely user friendly and allows, in spite of its limitations, to make quick analyses on e.g. the effect of asphalt mixture composition, type of

bitumen used and variations therein on pavement life. To the opinion of the author, the biggest limitation of the program is that it uses a fixed load configuration. Although the program was developed in the second half of the 1980's he still considers it as a nice, quick, and handy tool for rapid analyses of the lifetime of pavement structures.

Calculated: 19 Mar 2007 17:57:42

Print Date: 19/03/2007

Page: 1

Table 88: Output of the SPDM software.



SPDM 3.0 - Thickness Design Iteration Report

ct4860

Asphalt Thickness designed at 0,084 m
(Determined by the Subgrade Strain Criterion)

Case	Thickness (m)	Strain ($\mu\text{m/m}$)				Life (x 1 million), 80 kN s.a.			
		Asphalt		Subgrade		Asphalt		Subgrade	
		Under a wheel	Between wheels	Under a wheel	Between wheels	Under a wheel	Between wheels	Under a wheel	Between wheels
1,00	0,200	77,82	80,68	-177,00	-188,20	516,62	431,32	208,75	163,32
2,00	0,250	56,62	59,56	-132,70	-139,90	2458,62	1908,83	660,73	534,86
3,00	0,056	250,50	214,80	-511,30	-564,50	1,76	3,80	3,00	2,02
4,00	0,089	188,10	179,00	-391,20	-430,40	6,95	8,91	8,75	5,97
5,00	0,084	197,10	185,90	-407,60	-449,20	5,59	7,49	7,42	5,03
Design:		200,42	200,42	-446,82	-446,82	5,14	5,14	5,14	5,14

Calculated: 19 Mar 2007 17:57:42

Print Date: 19/03/2007

Page: 1

Table 89: Iteration report.

16.3.2 FPS21

FPS21 [123] is the required method for designing flexible pavements in Texas especially for the higher volume highways (> 10000 ADT, 5 million equivalent 80 kN axles). The program can be downloaded from the website of the Texas Department of Transportation. Also downloadable is a pdf of the user's manual [123].

FPS21 provides a methodology for selecting a complete pavement design strategy such as the selection of an initial structure as well as future overlays. It calculates the initial costs as well as future costs for routine maintenance and overlays. It also calculates the user costs due to traffic delay when not all lanes are available for traffic due to maintenance.

The system calculates the stresses, strains and deflections of the specified structure and lifetime is calculated in terms of fatigue of the asphalt layer and permanent deformation of the subgrade. In order to do so, the user can input his own transfer functions for asphalt fatigue and subgrade deformation. The program also takes into account the loss in present serviceability as a function of the structure selected and the amount of traffic. The serviceability loss is based on the AASHTO serviceability concepts but instead of being based on SN (structural number) it is based on deflection; details on this will not be given here.

The program also uses a confidence level approach to take into account variations in layer thickness and properties as well as uncertainties in the expected amount of traffic. A certain confidence level is obtained by using a certain multiplier on the expected amount of traffic. It will be clear that the higher the desired confidence level, the higher the value of this multiplier.

The system allows structures consisting of 6 layers to be analyzed. The user can define his own structures or can make use of fixed design options.

Tables 90 and 91 and figures 413 and 414 provide information on input and output of the FPS21 system.

The author likes this design system because it selects structures not only based on asphalt fatigue and subgrade deformation but also on serviceability and because it takes into account construction and maintenance costs and user delay costs.

Another good thing of the program is that it allows to input a single tire load or a dual tire load or a falling weight deflectometer load.

The system allows the design of so called perpetual or long life pavements (> 30 years) assuming that asphalt fatigue will not occur if the tensile strain at the bottom of the asphalt layer is $\leq 70 \mu\text{m/m}$ and the vertical compressive strain at the top of the subgrade is $\leq 200 \mu\text{m/m}$.

16.3.3 KENLAYER

The KENLAYER program is developed by Huang and comes as a cd with his book "Pavement Analysis and Design" [70]. It is a rather powerful program allowing linear elastic multi-layer analyses to be done but granular layers and subgrades can also be modelled as stress dependent materials. Furthermore asphaltic materials can be modelled as linear visco-elastic materials. When using the visco-elastic option, the creep compliance curve of the asphalt mixture at a particular reference temperature should be defined as well as the shift factor. From this information the master curves for the mixture stiffness at other temperatures are determined. The design period can be divided in a user selected number of "sub"-periods (maximum 12) which differ from each other in terms of layer moduli etc. The user can set his own fatigue criteria for asphalt and own vertical strain criteria for the subgrade. User selected load groups can be identified (single axles, dual and triple axles, single and dual wheel loads or multiple wheel loads). For further details the reader is referred to reference [70], which is the 2nd edition of the book, and also to the first edition which was published in 1993. In the first edition a description of the input parameters as well as illustrative examples of the program were given. In the 2nd edition this info can be found on the cd.

Table 92 shows the input and output of a visco-elastic analysis of a three layer system. A short explanation of the input and output will be given hereafter.

The third line of page 1 shows that there are four periods; this implies that a year is divided in four periods. On page 2 of the input one can see the temperature for each period being 49.7,

59.5, 81.6, and 70.1 °F. On page one the layer thicknesses are given being 6 inch for the top layer and 8 inch for the base course. The moduli for the base layer and subgrade for each period are also given taking values of 3E4 psi and 1.5E4 psi respectively. Of course different modulus values can be used for each of the periods but in this example the modulus values were kept constant.

The top layer is taken as a visco-elastic layer and creep compliance values for a set of 11 creep times is also part of the input. Also the temperature at which these compliance values are determined is input (70 °F in this case) as well as the shift factor (0.133).

On page 2 the creep compliance values are given which are calculated by the program for each of the four temperatures that were specified. Also on page 2 we see the number of load repetitions per period. It should be noted that the program allows to specify several types of load groups together with their number of applications.

Then we see the damage coefficients for bottom tension of layer 1 and compression of layer 3. These are the coefficients by means of which the fatigue relation for the top layer and the compressive vertical strain relation for layer 3 are described. These relations are written as:

$$N_{\text{asphalt fatigue}} = f_1 \varepsilon_{\text{tensile asphalt}}^{-f_2} E_{\text{asphalt}}^{-f_3}$$

$$N_{\text{subgrade}} = f_4 \varepsilon_{\text{vertical subgrade}}^{-f_5}$$

At the bottom of page 2 and on page 3 we can find per period a.o. the horizontal tensile strain at the bottom of the top layer and the vertical compressive strain at the top of layer 3 as well as the allowable number of load repetitions N which is calculated based on these tensile and compressive strains. Also the damage ratio is given which is the ratio of the applied number of load repetitions divided by the allowable number of load repetitions.

At the bottom of page 3 we see the sums of the damage ratios (= damage ratio period 1 + damage ratio period 2 + etc) and the pavement life in years is calculated by taking the inverse of the maximum damage ratio.

It should be reminded that this is just an example. The program can take into account several load groups and the modulus of unbound granular layers can be modelled as being stress dependent following:

$$M_R = k_1 \theta^{k_2}$$

Where:

M_R = resilient modulus of the unbound layer,

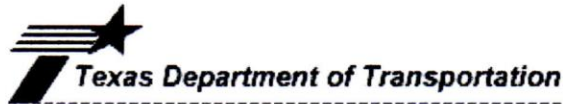
k_1, k_2 = material coefficients.

For soils a different type of model is used; for more information about this model the reader is referred to Huang's book.

The following comment should be made with respect to the mathematical stability of the program. KENLAYER program (like some other programs) has difficulties in analyzing stresses and strains at the interfaces. It is therefore recommended to select the analysis point 1 mm above or below the interface. It is recalled that BISAR doesn't suffer from this instability.

Is the program easy to use? Well, one gets used to everything but it is not as user friendly as the SHELL program and FPS21. The reader will agree that the input and output as shown in table 92 is difficult to read and understand for e.g. uninformed clients who are only interested in what the pavement life is going to be and which criterion is the decisive one.

However, the strong points of the program are that it allows granular materials and subgrade soils to be modelled as stress dependent materials and asphalt mixtures as visco-elastic ones.



TEXAS DEPARTMENT OF TRANSPORTATION

FPS21-1.3

FLEXIBLE PAVEMENT SYSTEM

Release:7-1-2015

PAVEMENT DESIGN TYPE # 4 -- ACP + ASPH STAB BASE + FLEX BASE OVER SUBGRADE

PROB	DIST.-18	COUNTY- 71	CONT.	SECT.	JOB	HIGHWAY	DATE	PAGE
006	Dallas	ELLIS	1234	2	123	SH 69	2/27/2018	1

COMMENTS ABOUT THIS PROBLEM

FDR design of IH 35
Use cement stabilized subbase
Traffic 2 million

BASIC DESIGN CRITERIA

LENGTH OF THE ANALYSIS PERIOD (YEARS)	20.0
MINIMUM TIME TO FIRST OVERLAY (YEARS)	10.0
MINIMUM TIME BETWEEN OVERLAYS (YEARS)	5.0
DESIGN CONFIDENCE LEVEL (80.0%)	A
SERVICEABILITY INDEX OF THE INITIAL STRUCTURE	4.5
FINAL SERVICEABILITY INDEX P2	2.0
SERVICEABILITY INDEX P1 AFTER AN OVERLAY	4.0
DISTRICT TEMPERATURE CONSTANT	31.0
SUBGRADE ELASTIC MODULUS by COUNTY (ksi)	16.00
INTEREST RATE OR TIME VALUE OF MONEY (PERCENT)	1.0

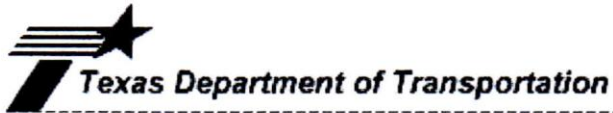
PROGRAM CONTROLS AND CONSTRAINTS

NUMBER OF SUMMARY OUTPUT PAGES DESIRED (8 DESIGNS/PAGE)	3
MAX FUNDS AVAILABLE PER SQ.YD. FOR INITIAL DESIGN (DOLLARS)	99.00
MAXIMUM ALLOWED THICKNESS OF INITIAL CONSTRUCTION (INCHES)	69.0
ACCUMULATED MAX DEPTH OF ALL OVERLAYS (INCHES) (EXCLUDING LEVEL-UP)	10.0

TRAFFIC DATA

ADT AT BEGINNING OF ANALYSIS PERIOD (VEHICLES/DAY)	20000.
ADT AT END OF TWENTY YEARS (VEHICLES/DAY)	30000.
ONE-DIRECTION 20YEAR 18 kip ESAL (millions)	6.000
AVERAGE APPROACH SPEED TO THE OVERLAY ZONE(MPH)	70.0
AVERAGE SPEED THROUGH OVERLAY ZONE (OVERLAY DIRECTION) (MPH)	45.0
AVERAGE SPEED THROUGH OVERLAY ZONE (NON-OVERLAY DIRECTION) (MPH)	50.0
PROPORTION OF ADT ARRIVING EACH HOUR OF CONSTRUCTION (PERCENT)	6.0
PERCENT TRUCKS IN ADT	6.7

Table 90: Input for FPS21.



TEXAS DEPARTMENT OF TRANSPORTATION
FLEXIBLE PAVEMENT SYSTEM

FPS21-1.3

Release:7-1-2015

PAVEMENT DESIGN TYPE # 4 -- ACP + ASPH STAB BASE + FLEX BASE OVER SUBGRADE

PROB	DIST.-18	COUNTY- 71	CONT.	SECT.	JOB	HIGHWAY	DATE	PAGE
006	Dallas	ELLIS	1234	2	123	SH 69	2/27/2018	2

INPUT DATA CONTINUED

CONSTRUCTION AND MAINTENANCE DATA

MINIMUM OVERLAY THICKNESS (INCHES)	1.5
OVERLAY CONSTRUCTION TIME (HOURS/DAY)	12.0
ASPHALTIC CONCRETE COMPACTED DENSITY (TONS/C.Y.)	1.90
ASPHALTIC CONCRETE PRODUCTION RATE (TONS/HOUR)	200.0
WIDTH OF EACH LANE (FEET)	12.0
FIRST YEAR COST OF ROUTINE MAINTENANCE (DOLLARS/LANE-MILE)	0.00
ANNUAL INCREMENTAL INCREASE IN MAINTENANCE COST (DOLLARS/LANE-MILE)	0.00

DETOUR DESIGN FOR OVERLAYS

TRAFFIC MODEL USED DURING OVERLAYING	3
TOTAL NUMBER OF LANES OF THE FACILITY	4
NUMBER OF OPEN LANES IN RESTRICTED ZONE (OVERLAY DIRECTION)	1
NUMBER OF OPEN LANES IN RESTRICTED ZONE (NON-OVERLAY DIRECTION)	2
DISTANCE TRAFFIC IS SLOWED (OVERLAY DIRECTION) (MILES)	0.60
DISTANCE TRAFFIC IS SLOWED (NON-OVERLAY DIRECTION) (MILES)	0.60
DETOUR DISTANCE AROUND THE OVERLAY ZONE (MILES)	0.00

PAVING MATERIALS INFORMATION

LAYER CODE	MATERIALS NAME	COST PER CY	E MODULUS	POISSON RATIO	MIN. DEPTH	MAX. DEPTH	SALVAGE PCT.
1	A ASPH CONC PVMT	115.00	500000.	0.35	2.00	2.00	30.00
2	B ASPH STAB BASE	100.00	400000.	0.35	4.00	10.00	90.00
3	C FLEXIBLE BASE	37.00	48000.	0.33	6.00	12.00	75.00
4	D SUBGRADE(200)	2.00	16000.	0.40	200.00	200.00	90.00

Table 90: Input for FPS21 continued.



TEXAS DEPARTMENT OF TRANSPORTATION

FPS21-1.3

FLEXIBLE PAVEMENT SYSTEM

Release:7-1-2015

PAVEMENT DESIGN TYPE # 4 -- ACP + ASPH STAB BASE + FLEX BASE OVER SUBGRADE

PROB	DIST.-18	COUNTY- 71	CONT.	SECT.	JOB	HIGHWAY	DATE	PAGE
006	Dallas	ELLIS	1234	2	123	SH 69	2/27/2018	3

C. LEVEL A SUMMARY OF THE BEST DESIGN STRATEGIES IN ORDER OF INCREASING TOTAL COST

	1	2	3
MATERIAL ARRANGEMENT	ABC	ABC	ABC
INIT. CONST. COST	25.06	24.69	23.67
OVERLAY CONST. COST	0.00	0.00	5.29
USER COST	0.00	0.00	0.02
ROUTINE MAINT. COST	0.00	0.00	0.00
SALVAGE VALUE	-14.58	-14.19	-14.73
TOTAL COST	10.47	10.51	14.24
NUMBER OF LAYERS	3	3	3
LAYER DEPTH (INCHES)			
D(1)	2.00	2.00	2.00
D(2)	4.50	4.00	4.00
D(3)	6.00	7.00	6.00
NO.OF PERF.PERIODS	1	1	2
PERF. TIME (YEARS)			
T(1)	22.	20.	19.
T(2)			37.
OVERLAY POLICY(INCH)			
(INCLUDING LEVEL-UP)			
O(1)			2.0

THE TOTAL NUMBER OF FEASIBLE DESIGNS CONSIDERED WAS

169

Table 91: Output of FPS21.

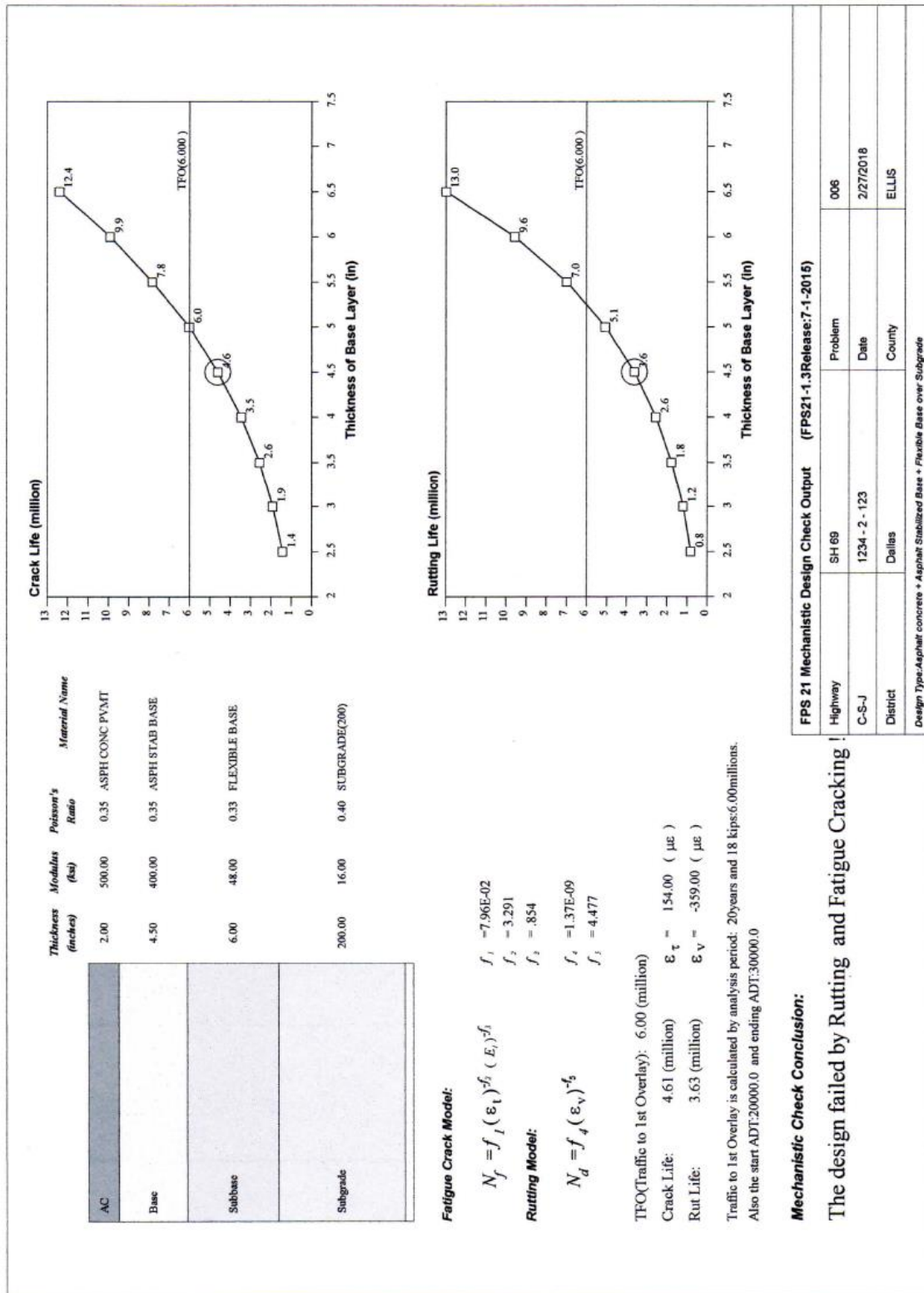


Figure 413: Output of FPS21.

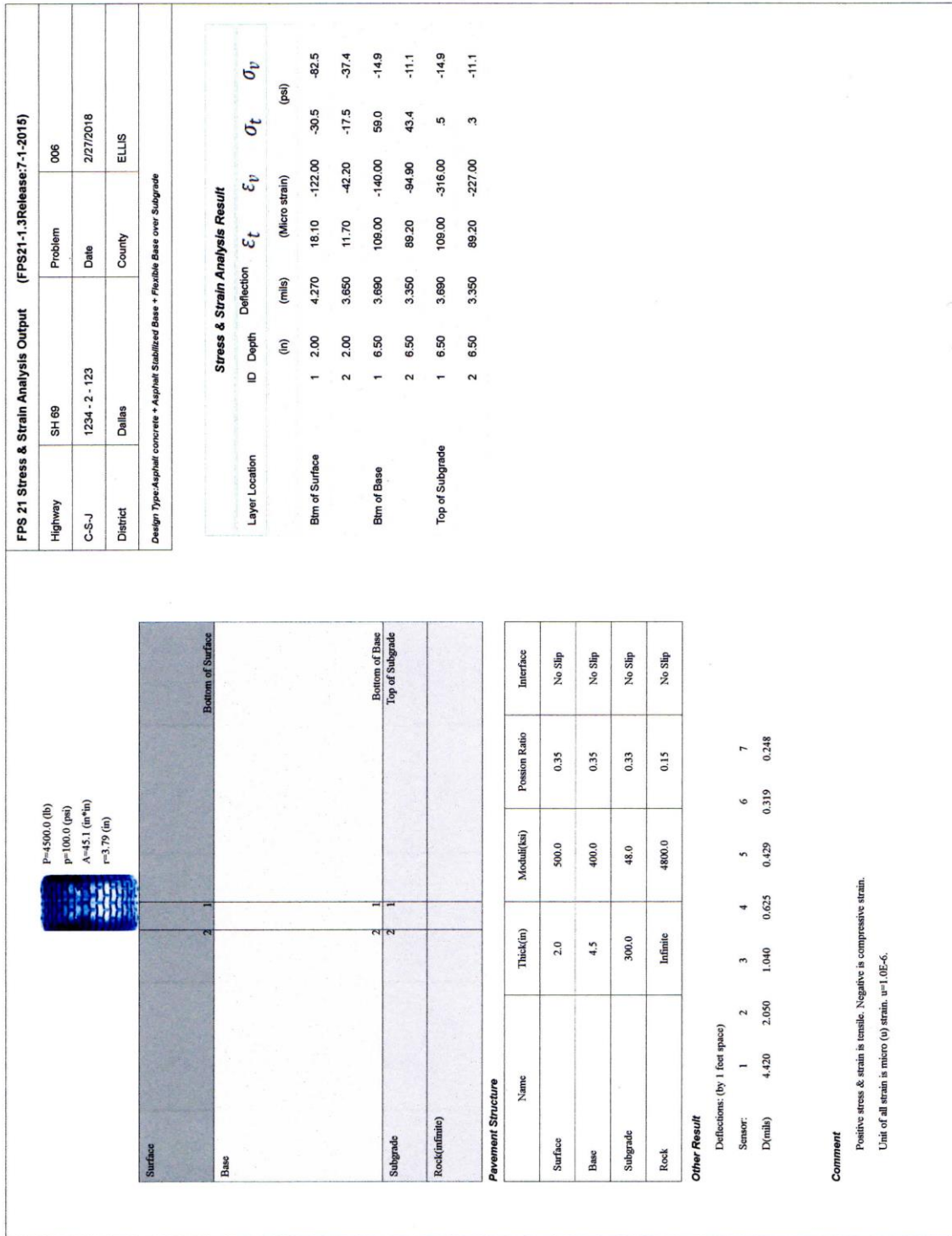


Figure 414: Output of FPS21.

```

INPUT FILE NAME -F:\KENPAVE\lay4.DAT

NUMBER OF PROBLEMS TO BE SOLVED = 1

TITLE -EX. 4: VISCOELASTIC THREE LAYER SYSTEM WITH 4 PERIODS AND 1 LOAD G.

MATL = 3 FOR VISCOELASTIC LAYERED SYSTEM
NDAMA=2, SO DAMAGE ANALYSIS WITH DETAILED PRINTOUT WILL BE PERFORMED
NUMBER OF PERIODS PER YEAR (NPY) = 4
NUMBER OF LOAD GROUPS (NLG) = 1
TOLERANCE FOR INTEGRATION (DEL) -- = 0.001
NUMBER OF LAYERS (NL)----- = 3
NUMBER OF Z COORDINATES (NZ)----- = 1
LIMIT OF INTEGRATION CYCLES (ICL)- = 80
COMPUTING CODE (NSTD)----- = 9
SYSTEM OF UNITS (NUNIT)----- = 0

Length and displacement in in., stress and modulus in psi
unit weight in pcf, and temperature in F

THICKNESSES OF LAYERS (TH) ARE : 6 8
POISSON'S RATIOS OF LAYERS (PR) ARE : 0.5 0.5 0.5
ALL INTERFACES ARE FULLY BONDED

FOR PERIOD NO. 1 LAYER NO. AND MODULUS ARE : 1 0.000E+00 2 3.000E+04
3 1.500E+04

FOR PERIOD NO. 2 LAYER NO. AND MODULUS ARE : 1 0.000E+00 2 3.000E+04
3 1.500E+04

FOR PERIOD NO. 3 LAYER NO. AND MODULUS ARE : 1 0.000E+00 2 3.000E+04
3 1.500E+04

FOR PERIOD NO. 4 LAYER NO. AND MODULUS ARE : 1 0.000E+00 2 3.000E+04
3 1.500E+04

LOAD GROUP NO. 1 HAS 1 CONTACT AREA
CONTACT RADIUS (CR)----- = 6
CONTACT PRESSURE (CP)----- = 80
RADIAL COORDINATES OF 1 POINT(S) (RC) ARE : 0

DURATION OF MOVING LOAD (DUR) = 0.1
NUMBER OF VISCOELASTIC LAYER (NVL) = 1
LAYER NUMBERS WHICH ARE VISCOELASTIC (LNV) = 1
CREEP TIMES (TYME) ARE: 0.001 0.003 0.01 0.03 0.1 0.3 1 3 10 30 100

FOR LAYER 1 TIME TEMPERATURE SHIFT FACTOR (BETA) = 0.113
REFERENCE TEMPERATURE (TEMREF) = 70

CREEP COMPLIANCES (CREEP) AT REFERENCE TEMP. (TEMREF) OF 70 ARE:
3.700E-07 5.200E-07 8.600E-07 1.450E-06 2.500E-06 4.000E-06 6.200E-06
8.600E-06 1.200E-05 1.600E-05 1.900E-05

LAYER NO. 1 DIRICHLET SERIES AT REFERENCE TEMPERATURE (TEMREF) OF 70 ARE:
-6.594E-07 3.123E-07 -2.196E-06 -4.217E-06 -4.040E-06 -8.178E-06 1.927E-05

```

Table 92: Input and output of KENLAYER in case of a visco-elastic analysis.

page 2

COMPUTED COMPLIANCES (CREEP) AT REFERENCE TEMP.(TEMREF) OF 70 ARE:

3.704E-07 5.120E-07 8.772E-07 1.434E-06 2.506E-06 4.019E-06 6.152E-06
8.667E-06 1.192E-05 1.606E-05 1.898E-05

FOR PERIOD NO. 1 LAYER NO. AND TEMPERATURE ARE: 1 49.7

CREEP COMPLIANCES (CREEP) OF LAYER 1 AT TEMPERATURE (TEMP) OF 49.7 ARE:

2.916E-07 2.924E-07 2.954E-07 3.037E-07 3.322E-07 4.097E-07 6.389E-07
1.067E-06 1.810E-06 3.057E-06 4.839E-06

FOR PERIOD NO. 2 LAYER NO. AND TEMPERATURE ARE: 1 59.5

CREEP COMPLIANCES (CREEP) OF LAYER 1 AT TEMPERATURE (TEMP) OF 59.5 ARE:

2.965E-07 3.072E-07 3.435E-07 4.405E-07 7.159E-07 1.192E-06 2.033E-06
3.403E-06 5.279E-06 7.685E-06 1.057E-05

FOR PERIOD NO. 3 LAYER NO. AND TEMPERATURE ARE: 1 81.6

CREEP COMPLIANCES (CREEP) OF LAYER 1 AT TEMPERATURE (TEMP) OF 81.6 ARE:

1.216E-06 1.977E-06 3.468E-06 5.170E-06 7.792E-06 1.041E-05 1.461E-05
1.820E-05 1.926E-05 1.927E-05 1.927E-05

FOR PERIOD NO. 4 LAYER NO. AND TEMPERATURE ARE: 1 70.1

CREEP COMPLIANCES (CREEP) OF LAYER 1 AT TEMPERATURE (TEMP) OF 70.1 ARE:

3.725E-07 5.171E-07 8.881E-07 1.451E-06 2.538E-06 4.057E-06 6.209E-06
8.726E-06 1.201E-05 1.615E-05 1.900E-05

NUMBER OF LAYERS FOR BOTTOM TENSION (NLBT)---- = 1

NUMBER OF LAYERS FOR TOP COMPRESSION (NLTC)--- = 1

LAYER NO. FOR BOTTOM TENSION (LNBT) ARE: 1

LAYER NO. FOR TOP COMPRESSION (LNTC) ARE: 3

LOAD REPETITIONS (TNLR) IN PERIOD 1 FOR EACH LOAD GROUP ARE : 45630

LOAD REPETITIONS (TNLR) IN PERIOD 2 FOR EACH LOAD GROUP ARE : 45630

LOAD REPETITIONS (TNLR) IN PERIOD 3 FOR EACH LOAD GROUP ARE : 45630

LOAD REPETITIONS (TNLR) IN PERIOD 4 FOR EACH LOAD GROUP ARE : 45630

DAMAGE COEF.'S (FT) FOR BOTTOM TENSION OF LAYER 1 ARE: 0.0796 3.291 0.854

DAMAGE COEFFICIENTS (FT) FOR TOP COMPRESSION OF LAYER 3 ARE: 1.365E-09 4.477

DAMAGE ANALYSIS OF PERIOD NO. 1 LOAD GROUP NO. 1

RADIAL COORDINATE	VERTICAL COORDINATE	VERTICAL DISPLACEMENT	VERTICAL STRESS (STRAIN)	RADIAL STRESS (STRAIN)	TANGENTIAL STRESS (STRAIN)	SHEAR STRESS (STRAIN)
0.00000	6.00000	0.00844	4.847	-319.147	-319.147	0.000
(STRAIN)			9.811E-05	-4.906E-05	-4.906E-05	.000E+00
0.00000	14.00010	0.00758	2.843	0.955	0.955	0.000
(STRAIN)			1.259E-04	-6.293E-05	-6.293E-05	.000E+00

AT BOTTOM OF LAYER 1 TENSILE STRAIN = -4.906E-05

ALLOWABLE LOAD REPETITIONS = 3.279E+07 DAMAGE RATIO = 1.391E-03

AT TOP OF LAYER 3 COMPRESSIVE STRAIN = 1.259E-04

ALLOWABLE LOAD REPETITIONS = 3.945E+08 DAMAGE RATIO = 1.157E-04

Table 92 (continued): Input and output of KENLAYER in case of a visco-elastic analysis.

DAMAGE ANALYSIS OF PERIOD NO. 2 LOAD GROUP NO. 1

RADIAL COORDINATE	VERTICAL COORDINATE	VERTICAL DISPLACEMENT	VERTICAL STRESS (STRAIN)	RADIAL STRESS (STRAIN)	TANGENTIAL STRESS (STRAIN)	SHEAR STRESS (STRAIN)
0.00000	6.00000	0.00929	5.967	-296.902	-296.902	0.000
(STRAIN)			1.258E-04	-6.289E-05	-6.289E-05	.000E+00
0.00000	14.00010	0.00822	3.336	1.033	1.033	0.000
(STRAIN)			1.535E-04	-7.676E-05	-7.676E-05	.000E+00

AT BOTTOM OF LAYER 1 TENSILE STRAIN = -6.289E-05
ALLOWABLE LOAD REPETITIONS = 1.896E+07 DAMAGE RATIO = 2.406E-03

AT TOP OF LAYER 3 COMPRESSIVE STRAIN = 1.535E-04
ALLOWABLE LOAD REPETITIONS = 1.621E+08 DAMAGE RATIO = 2.815E-04

DAMAGE ANALYSIS OF PERIOD NO. 3 LOAD GROUP NO. 1

RADIAL COORDINATE	VERTICAL COORDINATE	VERTICAL DISPLACEMENT	VERTICAL STRESS (STRAIN)	RADIAL STRESS (STRAIN)	TANGENTIAL STRESS (STRAIN)	SHEAR STRESS (STRAIN)
0.00000	6.00000	0.01786	25.010	-110.379	-110.379	0.000
(STRAIN)			6.510E-04	-3.255E-04	-3.255E-04	.000E+00
0.00000	14.00010	0.01355	9.148	1.306	1.306	0.000
(STRAIN)			5.228E-04	-2.614E-04	-2.614E-04	.000E+00

AT BOTTOM OF LAYER 1 TENSILE STRAIN = -3.255E-04
ALLOWABLE LOAD REPETITIONS = 6.863E+05 DAMAGE RATIO = 6.649E-02

AT TOP OF LAYER 3 COMPRESSIVE STRAIN = 5.228E-04
ALLOWABLE LOAD REPETITIONS = 6.719E+05 DAMAGE RATIO = 6.791E-02

DAMAGE ANALYSIS OF PERIOD NO. 4 LOAD GROUP NO. 1

RADIAL COORDINATE	VERTICAL COORDINATE	VERTICAL DISPLACEMENT	VERTICAL STRESS (STRAIN)	RADIAL STRESS (STRAIN)	TANGENTIAL STRESS (STRAIN)	SHEAR STRESS (STRAIN)
0.00000	6.00000	0.01291	12.203	-211.861	-211.861	0.000
(STRAIN)			2.899E-04	-1.449E-04	-1.449E-04	.000E+00
0.00000	14.00010	0.01072	5.649	1.255	1.255	0.000
(STRAIN)			2.930E-04	-1.465E-04	-1.465E-04	.000E+00

AT BOTTOM OF LAYER 1 TENSILE STRAIN = -1.449E-04
ALLOWABLE LOAD REPETITIONS = 3.206E+06 DAMAGE RATIO = 1.423E-02

AT TOP OF LAYER 3 COMPRESSIVE STRAIN = 2.930E-04
ALLOWABLE LOAD REPETITIONS = 8.980E+06 DAMAGE RATIO = 5.081E-03

* SUMMARY OF DAMAGE ANALYSIS *

AT BOTTOM OF LAYER 1 SUM OF DAMAGE RATIO = 8.452E-02
AT TOP OF LAYER 3 SUM OF DAMAGE RATIO = 7.339E-02

MAXIMUM DAMAGE RATIO = 8.452E-02 DESIGN LIFE IN YEARS = 11.83

Table 92 (continued): Input and output of KENLAYER in case of a visco-elastic analysis.

16.3.4 AASHTO MEPD

Sadek [124] in his thesis has given an excellent summary of the main features of AASHTO's MEPD system. The text hereafter is to a very large extent taken from his thesis.

The mechanistic empirical pavement design (MEPD) software has been developed under the National Cooperative Highway Research Program (NCHRP) Project 1-37A by Applied Research Associates, Inc. Arizona State University (2009). Details about the flexible pavement design part can be found in [125].

The user starts with preparing a large amount of input which includes details of the structure, material characteristics, traffic loading and climatic conditions. Then the software calculates the damage and main distresses over the design period and finally the design is verified against the performance criteria which are set. This criteria include:

- amount of longitudinal cracking in [ft/mile] which is believed to be top-down cracking,
- amount of bottom up alligator cracking in [%],
- total amount of rutting [inch],
- roughness in terms of International Roughness Index (IRI) in [inch/mile].

The system recognizes three levels for obtaining the input.

At Level 1 the input is obtained through laboratory tests to obtain the material parameters and axle load surveys to determine the axle load spectrum, axle configurations etc.

At Level 2 the input is obtained via correlations between e.g. asphalt mixture composition and mixture stiffness and CBR of the subgrade and resilient modulus. In previous sections of these lecture notes we have already discussed quite a few the models for asphalt concrete, granular materials and soils which allow such predictions to be made. We also have presented some of the moisture models which allow moisture conditions to be predicted.

At Level 3 national or regional default values are used as input.

Most of the time the input is obtained via a mixture of the level 1, 2 and 3 approach.

In order to take into account the effect of climatic conditions on pavement performance, temperatures and moisture profiles in the pavement structure and subgrade and temperature gradient over the asphalt concrete thickness are all modelled using the Enhanced Integrated Climatic Model (EICM) software which is incorporated in the MEPD software. EICM is a one-dimensional coupled heat and moisture flow program that simulates changes in the behavior of asphalt concrete, granular materials and soils in conjunction with climatic conditions. The climatic conditions can be selected by the user by simply selecting a climatic file for a particular weather station in the existing database.

Detailed traffic data can be introduced; these data comprise:

- design life in years,
- number of lanes per design direction,
- percentage of trucks in the design direction,
- percentage of trucks in the design lane,
- operational speed,
- traffic growth,
- axle load groups (single, dual, tridem and quads),
- wheel configuration and tire pressure used in the axle load groups.

The amount of longitudinal cracking, which is assumed to be top down cracking, is calculated using:

$$\text{Longitudinal top down cracking [ft/mile]} = 10560 / (1 + e^{(7.0 - 3.5 \log (FD * 100))})$$

This equation implies that if $n/N = 1$ (so $\log (FD * 100) = 2$), the amount of longitudinal cracking = 5280 ft/mile = 1000 m/km

The amount of alligator cracking, which is assumed to be bottom up cracking, is calculated using:

$$\text{Bottom up alligator cracking [\% of the total lane area]} = 100 / (1 + e^A)$$

$$A = (-2.40874 - 39.748 * (1 + ha)^{-2.856}) * (-2 + \log FD)$$

ha = asphalt thickness

If we assume $n/N = 1$ which implies $\log (FD * 100) = 2$ and $ha = 4$ inch then the percentage of cracking equals 50%. When $n/N = 0.3$ ($\log (FD * 100) = 1.477$) the percentage of cracking equals 18.7%.

N in Miner's ratio is calculated from the tensile strain at the pavement surface and at 0.5 inch below the surface (top down cracking), and the tensile strain at the bottom of the asphalt layer (bottom up alligator cracking). The horizontal analysis locations are shown in figure 415. The figure shows that the program calculates the stresses, strains and displacements in a large number of locations.

For both the bottom up and top down cracking, the same fatigue relationship is used which is:

$$N = 0.00432 * k_1' * c * (1 / \epsilon_t)^{3.9492} * (1/E^*)^{1.281}$$

Where:

$$E^* = \text{complex modulus [psi] (see section on asphalt mix stiffness for equations)}$$

$$k_1' = \text{for top down cracking} = 1 / (0.01 + 12 / (1 + \Omega))$$

$$\Omega = e^{15.676 - 2.8186 * ha}$$

$$ha = \text{thickness asphalt layer [inch]}$$

$$k_1^1 = \text{for bottom up cracking} = 1 / (0.000398 + 0.003602 / (1 + \xi))$$

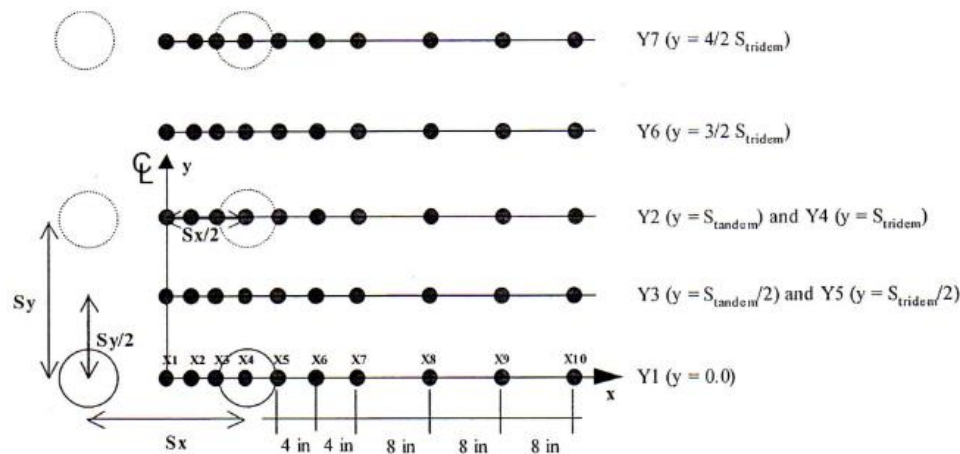
$$\xi = e^{11.02 - 3.49 * ha}$$

$$c = 10^{4.84 * \alpha}$$

$$\alpha = [Vb / (Vb + Va)] - 0.69$$

$$Vb = \text{volume percentage of bitumen}$$

$$Va = \text{void percentage}$$



Computed Responses

- Single
 - Response 1 = Y1
- Tandem
 - Response 1 = Y1 + Y2
 - Response 2 = 2 * Y3
- Tridem
 - Response 1 = Y1 + 2 * Y4
 - Response 2 = 2 * Y5 + Y6
- Quad
 - Response 1 = Y1 + 2 * Y4 + Y7
 - Response 2 = 2 * Y5 + 2 * Y6

Figure 415: Horizontal analysis locations in AASHTO's MEPD system.

Please note that the slope of the fatigue relation (3.942) is taken as a constant value while we have seen in the section on fatigue that this cannot be the case. Other systems allow the user to input his own fatigue relationship. Furthermore this author is of the opinion that the MEPD surface cracking model is a very poor one. As has been shown in the section on top down cracking, modelling of this defect type can only be done if the contact pressure distribution is carefully modelled and if hardening effects etc are taken into account. This author does therefore not recommend to use this surface cracking model.

Permanent deformation in the total asphalt thickness δ_{AC} is calculated using:

$$\delta_{AC} = \sum_{i=1}^m h_i \varepsilon_i$$

Where:

- m = number of asphalt sublayers,
- h_i = thickness of sublayer i [inch],
- ε_i = permanent deformation in sublayer i.

$$\varepsilon_i = \varepsilon_{vi} * (\beta_1 * k_1 * 10^{-\beta_2 * 3.35412} * T^{\beta_3 * 1.5606} * N^{\beta_4 * 0.4491})$$

Where:

$\beta_1, \beta_2, \beta_3, \beta_4$ = calibration factors which Sadek took as 0.7,
 T = temperature in the sublayer [$^{\circ}\text{F}$],
 T = $T_{\text{air}} * (1 + 1 / X) + 34 / X + 6$
 X = depth + 4 [inch]
depth = distance to the pavement surface
 N = number of 18 kip equivalent single axles,
 ε_{vi} = vertical compressive strain at mid depth of the sublayer,
 k_1 = $(c_1 + c_2 * ha) * 0.328196^{ha}$
 c_1 = $-0.1039 * ha^2 + 2.4868 * ha - 17.342$
 c_2 = $0.0172 * ha^2 - 0.17331 * ha + 27.428$

The permanent strain in the base and subbase sublayers as well as in the subgrade is calculated using:

$$\varepsilon_i = \varepsilon_{vi} * 1.35 * [0.5 * (0.15 * e^y + 20 * e^z)] * e^{-p/N}$$

Where:

$y = \rho^{\beta}$
 $z = (\rho / 10^9)^{\beta}$
 $\rho = 10^9 * [-4.89285 / (1 - (10^9)^{\beta})]$
 $\beta = 1.673$ for base and subbase layers and 1.35 for the subgrade.

The reader will agree with this author that the equations presented are “impressive” and that the physical meaning of some equations is difficult to understand. With respect to fatigue cracking large multiplication factors should obviously be applied on the calculated n/N ratio in order to get a match with the observed amount of cracking, a match which, according to figure 407, is still not too good in spite of the enormous effort researchers have done to develop the MEPD system.

16.3.5 3D-MOVE

The 3D-MOVE system [126], developed at the Western Regional Superpave Center, University of Nevada at Reno, uses a continuum-based finite-layer approach for making the pavement response computations. The 3D-MOVE analysis model can account for important pavement response factors such as the moving traffic-induced complex 3D contact stress distributions (normal and shear) of any shape, vehicle speed, and viscoelastic material characterization for the pavement layers. This approach treats each pavement layer as a continuum and uses the Fourier transform technique; therefore, it can handle complex surface loadings such as multiple loads and non-uniform tire pavement contact stress distribution. Since the tire imprint can be of any shape, this approach is suitable to analyze tire imprints, including those generated by wide-base tires. The finite-layer method is much more computationally efficient than the moving load models based on the finite element method. This is because pavements are horizontally layered and pavement responses are customarily required only at a few selected locations and for such problems the finite layer approach of 3D-MOVE analysis is ideally suited. Since rate-dependent material properties (viscoelastic) can be accommodated by the approach, it is an ideal tool to model the behavior of asphalt concrete (AC) layer and also to study pavement response as a function of vehicle speed. Frequency-domain solutions are adopted in 3D-MOVE analysis, which enables the direct use of the frequency sweep test data of HMA mixture in the analysis.

Many attempts that included field calibrations (e.g., Penn State University test track, Mn/Road and UNR Off-road Vehicle study) that compared a variety of independently-measured pavement responses (stresses, strains, and displacements) with those computed have been reported in the

literature. These verification studies have validated the applicability and versatility of the approach. The 3D-MOVE analysis (ver. 2.1) includes pavement performance models, which allow many important pavement distress modes to be investigated. One set of models that is incorporated are the models described in the previous paragraph on AASHTO MEPD.

The opening screen of the 3D-MOVE program is shown in figure 416. Figure 417 shows that complex contact pressure distributions can be introduced, while figure 418 shows that a full dynamic analysis of the pavement response due to a moving truck can be analyzed.

Unfortunately the author has limited experience with the 3D-MOVE package but that limited experience showed him that the package is a very versatile one allowing many types of analyses to be made ranging from linear elastic ones to visco-elastic ones and from simple stress/strain calculations to performance predictions. It is also, the only package, as far as he knows, that allows non uniform contact pressure distributions to be taken into account which is considered to be a great benefit when analyzing surface damage. It is a pity however that the stress dependent nature of unbound materials and soils cannot be taken into account.

Being such a versatile program also implies that it is not that easy to use especially if one wants more advanced analyses to be done. With increasing complexity also the computation time increases and when doing advanced analyses, the computation time can be hours. The computation time needed to run the SHELL SPDM software is less than a second.

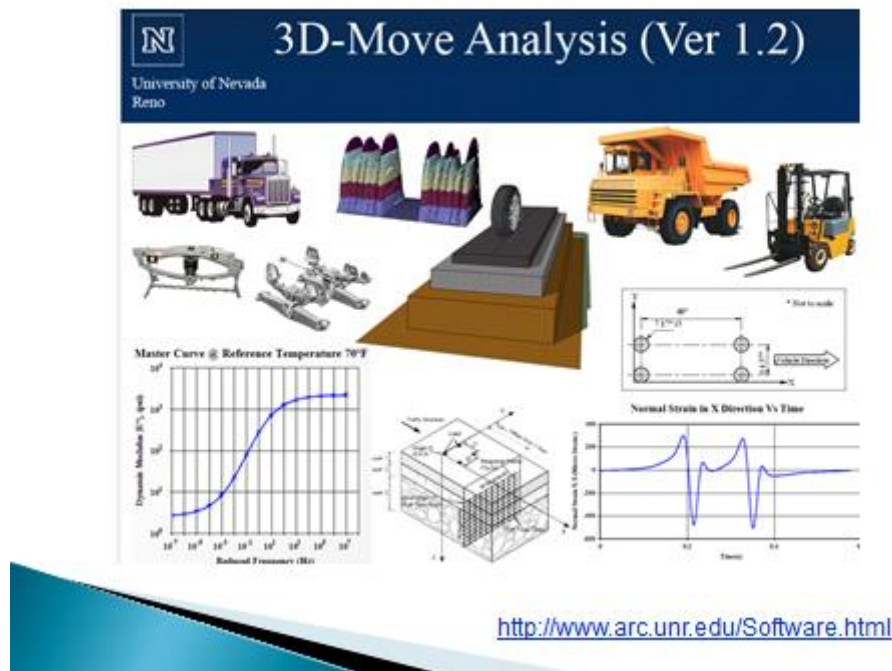
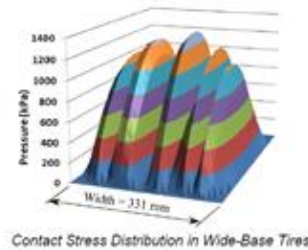
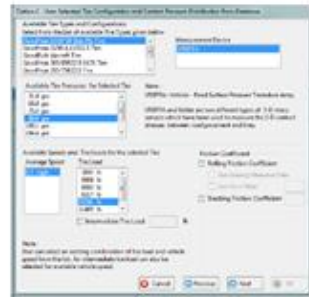


Figure 416: Opening screen of the 3D-MOVE package.
Note: picture is made available by dr X. Liu of the Delft University of Technology.

Selected Features of 3D-Move Analysis

- Type 3: User-Selected Tire configuration and Contact Pressure Distribution from Database (Uniform Pressure Distribution):



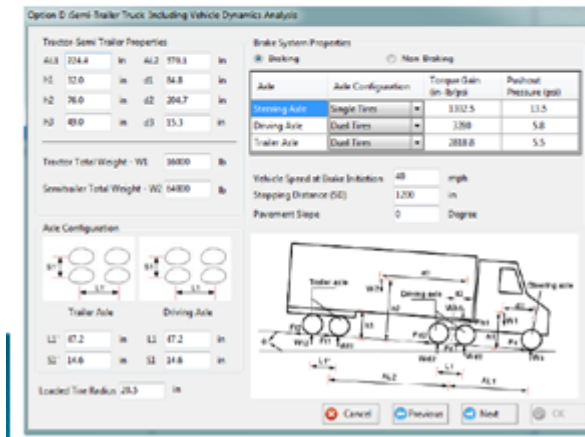
In this case, VRPTA (de Beer and Fisher (1997)) and Kistler MODULUS (Sime and Ashmore (1999)) databases which have reported measured contact pressure distributions for many single tires are used. A variety of tire types that include single and wide base tires under a tire pressure range of 220 – 1000 kPa and a tire load range of 26 – 106 kN are considered in both databases. The user can specify the axle configuration, which can vary from a single axle, single tire to a tridem axle, dual tire configuration. For a specified axle configuration and tire load, a contact pressure distribution can be generated from the available databases.

Figure 417: 3D-MOVE allows the effect of complex contact pressures to be analyzed.

Note: picture is made available by dr X. Liu of the Delft University of Technology.

Selected Features of 3D-Move Analysis

- Type 4: Semi-Trailer Truck Including Vehicle Dynamics (Uniform/Non-Uniform Contact Pressure Distribution):



Under this option, the load distribution on the various tires of the 18-wheel tractor-semitrailer during normal highway traffic and during braking is initially computed. Braking causes the vehicle to decelerate and the loads to transfer to the front of the vehicle. The resulting axle load can be higher or lower than the initial static load, depending on the location of the axle. Once the load distribution among the axles of the semitrailer is evaluated, the contact pressure distribution can be assigned (Uniform or Non-Uniform).

Figure 418: 3D-MOVE allows stress/strain analyses to be made using a moving semi-trailer truck as input.

Note: picture is made available by dr X. Liu of the Delft University of Technology.

16.3.6 French design system

In this section an introduction to the French design system [138] will be given. This introduction is more detailed than the introductions given to the other systems because the system includes, in an effective way, probabilistic concepts.

The pavement types shown in figure 419 are included in the system.

It is interesting to see that also inverted pavement structures are involved. This is a pavement type which, as we will see later on, is very often used in South Africa.

In the design systems we have discussed so far, pavement life is based on calculating stresses and strains and using these values as input in transfer/fatigue functions. In the French design system however the design number of load repetitions is used as input in a fatigue relation and the allowable strain or stress is calculated. So instead of taking the stress or strain as independent variable and the number of load repetitions as the dependent variable, the French system takes the number of load repetitions as the independent variable and the stress or strain as the dependent one.

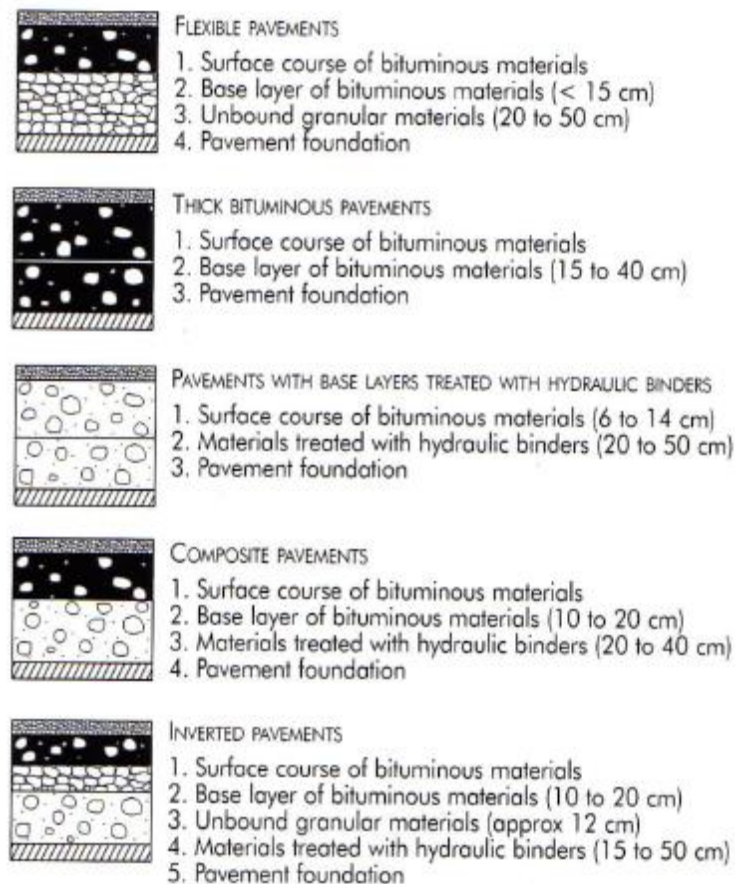


Figure 419: Pavement types included in the French design system.

Reliability concepts and traffic

A probabilistic approach is adopted in determining the allowable stress or strain. This principle is shown in figure 420.

The standard deviation δ is calculated from the scatter (standard deviation) in the fatigue results and the variation in the tensile strain due to a variation in the pavement thickness following:

$$\delta = [SN^2 + (c^2 / b^2) Sh^2]^{0.5}.$$

Where:

- δ = standard deviation,
- SN = standard deviation in fatigue test results,
- c = coefficient that links the variation in strain (or stress) in the pavement to the random variation in thickness, Δh , following $\log \varepsilon = \log \varepsilon_0 - c * \Delta h$,
- b = slope of the fatigue relation following $\varepsilon / \varepsilon_6 = (N / 10^6)^b$,
- ε_6 = strain level which can be taken 10^6 times until fatigue occurs.

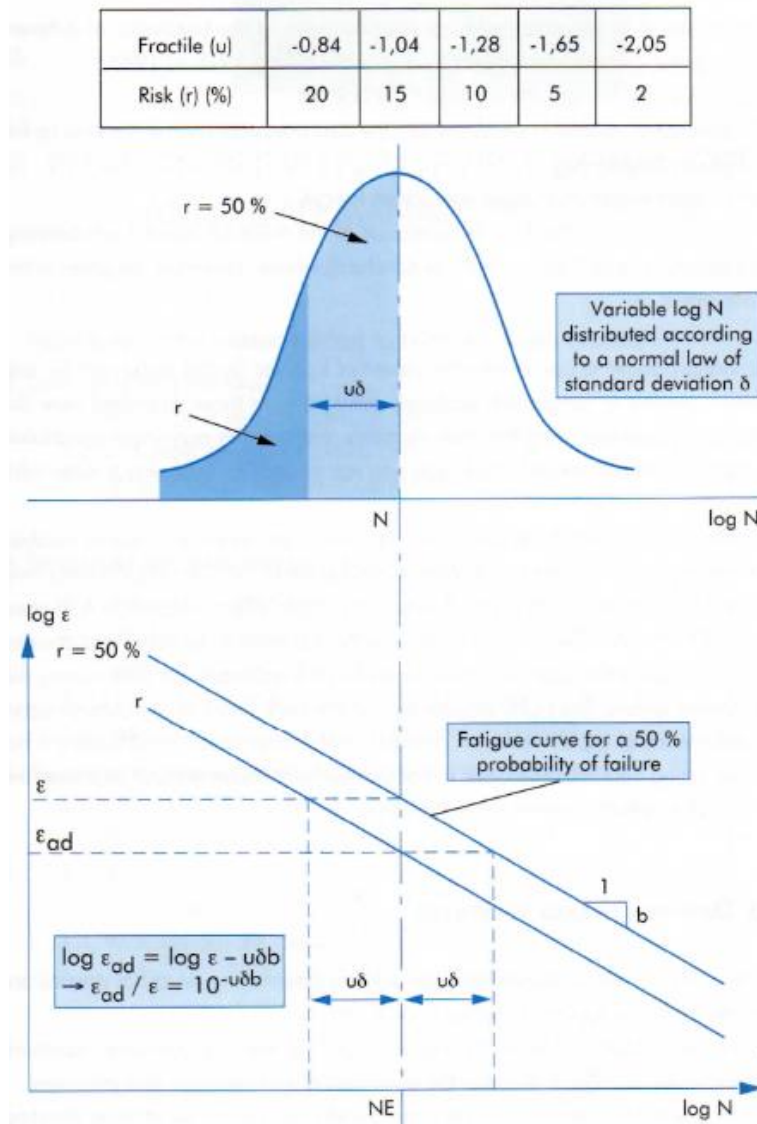


Figure 420: Principle of the probabilistic approach. Determination of the working strain for a cumulative amount of traffic equal to NE and given risk r.

We have seen in the chapter on fatigue of asphalt concrete that the constant (k_1) in the fatigue relation $\log N = \log k_1 - n \log \varepsilon$ is controlled to a large extent by the stiffness modulus of the mixture. In the French design system it is claimed that over a fairly broad range of temperatures

$\varepsilon_6(\theta) * E(\theta)^{0.5}$ takes a constant value.

The parameter $\varepsilon_6(\theta)$ is the tensile strain that can be taken 1 million times at temperature θ and $E(\theta)$ is the stiffness modulus at temperature θ .

Fatigue tests on asphalt mixtures are done on 2 point bending beam specimens at 10 °C and 25 Hz.

Modulus testing is done at 10 Hz and various temperatures.

The equivalent temperature in the pavement is selected as 15 °C and the loading frequency due to traffic loads is selected as 10 Hz. It is stated in the method that *"It is usually considered for base layers that the stress frequency characteristic is approximately 10 Hz and that frequency adjustment between 10 Hz and 25 Hz for ε_6 can be ignored for average temperatures"*.

For a 50% probability of survival which equals a risk of 50%, $u = 0$ and $k_r = 1$.

The standard deviation of asphalt concrete layers that has to be taken into account is shown table 93.

h_{asphalt} [cm]	≤ 10	$10 < h_a < 15$	≥ 15
S_h [cm]	1	$1 + 0.3$	2.5

Table 93: Standard deviation of the asphalt layer thickness.

For layers made with a hydraulic binder (e.g. cement stabilized layer) $S_h = 3$ cm.

In the French design system, traffic is categorized by means of the number of heavy trucks. A heavy truck (PL) is defined as a vehicle with a payload of 5 metric tons or more. Then the amount of heavy traffic is further categorized in traffic classes being the annual daily mean (ADM) of heavy trucks in the design lane during the first year after opening of the road to traffic.

The pavement design is based on the number of equivalent 130 kN axles (NE) which have a dual wheel configuration on either side of the axle. The dual wheels have a center to center distance of 0.375 m. The contact radius of each wheel print equals 0.125 m and the contact pressure is 0.662 MPa.

NE is calculated using:

$$NE = N * CAM$$

Where:

N = number of heavy trucks (PL's) during the design period

CAM = mean coefficient of "aggressiveness" of the PL compared to the reference axle of 130 kN

CAM is calculated in the following way. First the damage (A) of a given axle (P) relative to the standard axle of 130 kN is calculated following:

$$A = K * (P / 130)^\alpha$$

Values for K and α are given in table 94.

	α	Single axle (K)	Tandem axle (K)	Triple axle (K)
Flexible and bituminous pavements	5	1	0.75	1.1
Semi-rigid pavements	12	1	12	113

Table 94: Values for K and α

CAM is then calculated following:

$$\text{CAM} = (1 / \text{NPL}) * [\sum_{j=1}^n K_j n_{ij} (P_i/130)^\alpha]$$

Where:

NPL = number of heavy vehicles,

K_j = coefficient corresponding to axle type (single, tandem, triple),

n_{ij} = number of axles of type j in axle load class P_i

An example of how CAM is calculated is given in table 95.

Load classes (kN)	Mid-class (kN)	Single elementary axles			Tandem elementary axles			Tridem elementary axles		
		Aggressive-ness of midclass A	Number of axles N1	A x N1	Aggressive-ness of mid-class A	Number of axles N2	A x N2	Aggressive-ness of midclass A	Number of axles N3	A x N3
10-30	20	1.8 E-10	210	3.78 E-8	2 E-9	107	2 E-7	2 E-8	48	9 E-9
30-40	35	1.45 E-7	160	2.32 E-5	1.5 E-6	78	0.0001	1.5 E-5	34	0.0005
40-50	45	3 E-6	100	0.0003	4.2 E-5	66	0.0027	3.1 E-4	28	0.009
50-60	55	3.3 E-5	290	0.001	3.6 E-4	60	0.02	3.4 E-3	22	0.07
60-70	65	0.00025	280	0.07	0.003	50	0.15	0.028	16	0.45
70-80	75	0.0014	216	0.3	0.02	28	0.56	0.16	14	0.45
80-90	85	0.006	210	1.26	0.08	24	1.92	0.68	4	2.72
90-100	95	0.023	180	4.14	0.3	8	1.8	2.6	2	5.2
100-110	105	0.08	68	5.44	1	6	6	9	0	0
110-120	115	0.23	50	11.5	2.76	5	13.8			
120-130	125	0.62	40	24.8	7.4	2	14.8			
130-140	135	1.57	25	39.25	18.8	1	18.8			
140-150	145	3.7	9	33.3	18.8	1	44.4			
150-160	155	8.25	7	57.75	99	0	0			
160-170	165	17.5	5	87.39						
170-180	175	35.4	2	70.82						
180-190	185	69	1	68.98						
190-200	195	130	1	129.75						
200-210	205	236	0	0						
TOTAL			N1= 1 854	535		N2= 436	102		N3= 168	11

Table 95: Example of CAM calculation.

In the example CAM equals:

$$\text{CAM} = (A * N1 + A * N2 + A * N3) / (N1 + N2 + N3) = (535 + 102 + 11) / (1854 + 436 + 168) = 0.8$$

As mentioned before, pavements are designed taking probabilistic concepts into account. The allowed probability of failure is related to the traffic class and is shown in table 96.

Traffic class	T0	T1	T2	T3
Annual daily mean heavy traffic loads (ADM) on the heaviest loaded lane	750 - 2000	300 - 750	150 - 300	50 - 150
Flexible pavements	2%	2.5%	12%	25%
Semi rigid pavements	2.5%	5%	7.5%	12%

Table 96: Acceptable probability of failure in relation to pavement type and traffic class.

Note : heavy traffic load is a vehicle with a payload ≥ 5 tons

When designing the thickness of the total asphalt thickness the tensile strain at the bottom of the bituminous base layer should stay below a certain working value. This working strain $\varepsilon_{t,ad}$ is calculated in the following way.

$$\varepsilon_{t,ad} = \varepsilon(NE, \theta_{eq}, f) * k_r * k_c * k_s$$

Where:

$\varepsilon(NE, \theta_{eq}, f)$ = the tensile strain at which fatigue failure would occur in a fatigue test after NE cycles with a probability of 50%, at an equivalent temperature θ_{eq} and a frequency equal to "f",

k_r = coefficient which adjust the working strain value to the risk level chosen,
 $k_r = 10^{-u\delta b}$

Where:

u = constant determined from the normal distribution table related to risk r,

b = slope of the fatigue relationship on log – log basis,

δ = standard deviation of log N.

$$\delta = [SN^2 + (c^2 / b^2) * S_h^2]^{0.5}$$

c = coefficient linking the variation in tensile strain to the variation in pavement thickness;
for commonly used structures $c = 0.02 \text{ cm}^{-1}$.

The parameter k_c is a parameter which brings the results of the calculations in line with practical experience. One could say that this parameter is a calibration parameter matching predictions with observations. Values for k_c are given in table 97.

Material	k_c
Road base asphalt concrete GB	1.3
Bituminous concrete BB	1.1
High modulus asphalt concrete EME	1
Cement bound graded aggregates	1.4
Other materials treated with a hydraulic binder	1.5

Table 97: Values for k_c for different types of material.

The parameter k_s is taking care for lack of uniformity in the bearing capacity of the subgrade; values for k_s are given in table 98.

Modulus	$E < 50 \text{ MPa}$	$50 \leq E < 120 \text{ MPa}$	$E \geq 120 \text{ MPa}$
k_s	1 / 1.2	1 / 1.1	1

Table 98: Values for k_s

Asphalt mixtures

Some information of bituminous road base mixtures as used in the French design system will be given hereafter.

Three classes of bituminous road base mixtures are defined. They are shown in table 99.

Class	Richness modulus	Binder content by mass	Gradation	Maximum void content	Minimum stiffness modulus [MPa] (15 °C, 10 Hz)	Minimum ε_6 (10 °C, 25 Hz)
1	2	3.4%	0 / 20 mm	$\leq 13\%$	7000	$70 * 10^{-6}$
2	2.5	4.2%	0 / 14 mm	$\leq 11\%$	9000	$80 * 10^{-6}$
3	2.8	4.5%	0 / 14 mm	$\leq 10\%$	9000	$90 * 10^{-6}$

Table 99: Classes for bituminous road bases.

Note: binder content for a specific mass of the aggregates of 2.65 g/cm^3

In general the bitumen grade is 35/50 or even 50/70; pure and modified bitumens are allowed. The thickness in which the layers have to be built is 8 – 12 cm for the 0/14 mixtures and 10 – 15 cm for the 0/20 mixtures. It is stated that the larger thicknesses make it more difficult to obtain satisfactory evenness. This author likes to comment that to his opinion the thicknesses in which the asphaltic base course layers have to be constructed is rather thick and that the allowed void contents are rather high.

The richness modulus is a measure for the bitumen film thickness around the aggregate particles. It is calculated as follows.

$$\% \text{ of bitumen by mass} = \Gamma * K * \Lambda^{1/5}$$

Where:

$$\Gamma = 2.65 / \gamma_G$$

γ_G = apparent density of the aggregates,

K = richness modulus,

$$\Lambda = 0.25 * G + 2.3 * S + 12 * sa + 135 * f$$

G = mass % retrieved on sieve 6.3 mm,

S = mass % through sieve 6.3 mm but on sieve 300 μm ,

sa = mass % through sieve 300 μm but on sieve 75 μm ,

f = mass % through sieve 75 μm .

The richness modulus is introduced to avoid that mixtures are produced with a too thin film thickness.

Table 100 gives some indicative values for the stiffness and fatigue properties of the bituminous road base mixtures.

Temperature [°C]	-10	0	10	20	30	40		1/b	SN
Modulus class 1 [MPa]	18000	14000	9000	5000	2000	800	Class 1	- 5	0.4
Modulus class 2 and 3 [MPa]	23000	18800	12300	6300	2700	1000	Class 2 and 3	- 5	0.3

Table 100: Indicative values for the stiffness modulus and fatigue characteristics of bituminous road bases.

In the design manual it is stated that *"the thickness of the asphalt wearing course is not decided on the results of computations but essentially according to technological requirements and empirical considerations regarding reflective cracks"*. The following thicknesses are recommended:

- 6 cm for traffic categories T2 and under,
- 8 cm for T1,
- 10 – 14 cm for T0, depending on the materials used in the base layer and the conditions of construction.

The wearing course is defined as the surface course + the binder course. The binder course can have a thickness of 50 mm in case 0/8 mm aggregate size is used to 80 mm in case 0/14 mm aggregate is used. An overview of the characteristics of some wearing course mixtures is given in table 101.

Mixture	Grading [mm]	Minimum richness modulus	Average layer thickness [cm]	E [MPa] 15 °C and 10 Hz	ε_6 [μm/m] 10 °C and 25 Hz	b	SN
Semi-course Asphalt concrete BBSG	0/10 0/14	3.5 3.3	6 – 7 7 – 9	5400	100	- 0.2	0.25
Thin asphalt Concrete BBM	0/10 0/14	3.6 3.3	3 – 4 3.5 – 5	5400	100	- 0.2	0.25
Porous asphalt Concrete BBDr	0/10 and 0/14 also 0/6.3		4 3	3000	100		
Chipped asphalt Concrete BBC	0/6.3 0/10	3.8 3.6	3 6	5000	100	- 0.2	0.25
High modulus Asphalt concrete BBME class 1	0/10 0/14		6 – 7 7 – 9	9000	110	- 0.2	0.25
BBME class 2	0/10 0/14		6 – 7 7 - 9	12000	100	- 0.2	0.25

Table 101: Some characteristics of some wearing coarse mixtures.

Subgrade, capping layer and granular layers

The quality of the subgrade and top of the layer on which the pavement is built (the pavement formation class) is divided in classes as shown in table 102.

Modulus [MPa]	20	50	120	200
Class of planed surface	AR1	AR2	AR3	AR4
Pavement formation class	PF1	PF2	PF3	PF4

Table 102: Long term bearing classes for the planed surface of the earthworks and pavement formation classes (PF).

By using a capping layer on top of the subgrade one can “increase” the planed surface class from e.g AR1 to pavement formation class PF2, PF3 or PF4. Two options are possible being the application of a stabilized layer or a granular layer on top of the subgrade. The classification of capping layer materials treated with hydraulic binders like cement, lime etc is also done in classes using figure 421.

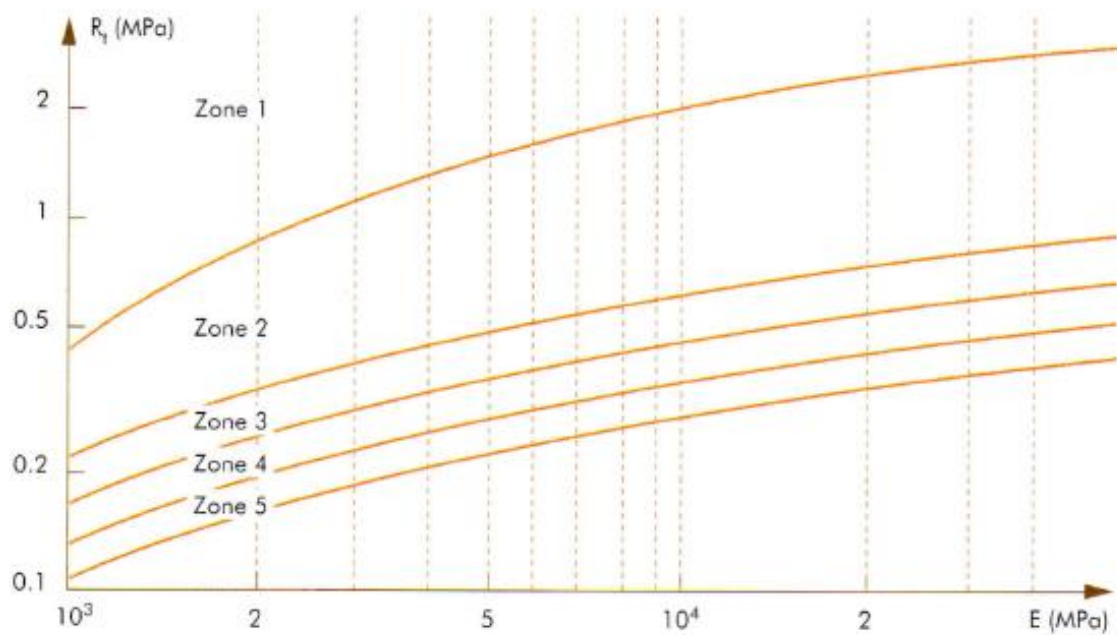


Figure 421: Classification of stabilized capping layers.

In this figure R_t is the direct tensile strength and E is the secant modulus at 30% of the failure load determined after 90 days. Instead of doing a direct tension test to determine the tensile strength also an indirect tension test can be done which results in f_t . R_t can then be estimated using:

$$R_t = 0.8 * f_t$$

Materials complying to zone 1 – 5 can be obtained by mix in plant methods while mix in place technology can only achieve materials in zone 2 – 5.

Table 103 shows which pavement formation classes are obtained by using a stabilized capping layer.

Class of planed surface	Zone 3	Zone 4	Zone 5	Pavement formation class obtained
AR1		30	35	PF2
AR1	30	35	50***	PF3
AR1	40	45***	55***	PF4
AR2	25	30	35	PF3
AR2	30	35	45***	PF4

*** to obtain the require degree of compaction at the bottom of the layer, the layer normally needs to be constructed in 2 layers

Table 103: Upgrading of subgrade class to pavement formation class.

Poisson's ratio is set at 0.25 for stabilized layers.layer

The granular layer on top of the stabilized capping has a fixed modulus of 480 MPa.

The upgrade to a certain pavement formation class by means of a granular capping layer can be determined using figure 422. As one notices, there are three dashed vertical lines. The area left of the 50 MPa line indicates the PF1 formation, between 50 and 120 MPa the PF2 formation, and between 120 and 180 MPa the PF3 formation level is indicated.

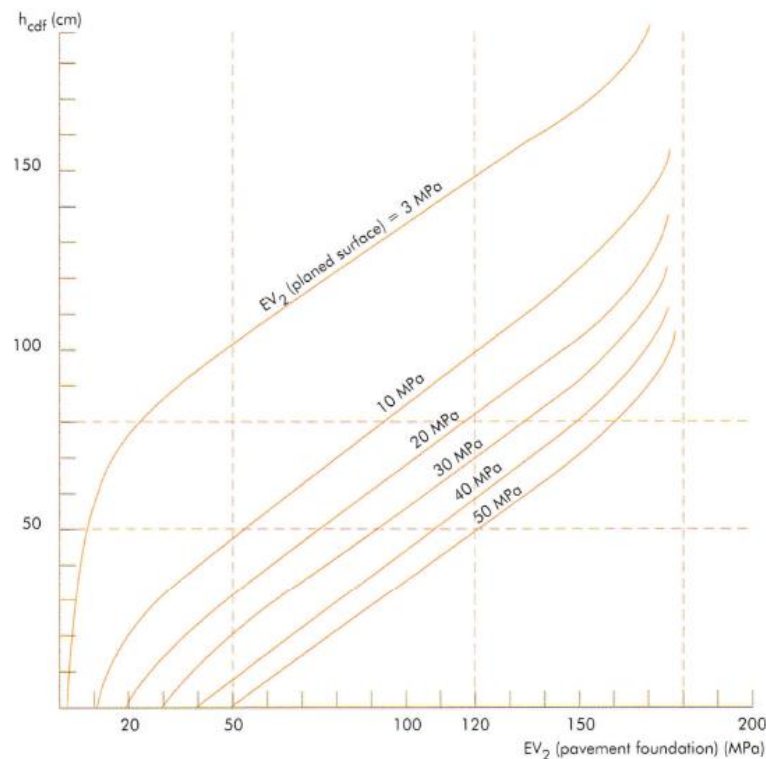


Figure 422: Modulus on top of the capping layer (EV_2 pavement foundation) as a function of the modulus of the subgrade (EV_2 planned surface) and the thickness of the capping layer (h_{cdf}).

The manual specifies two subgrade strain criteria. The first one applies to pavements subjected to medium and heavy traffic ($T \geq T_3$) being:

$$\varepsilon_{z,ad} = 0.012 NE^{-0.222}$$

For low traffic pavements ($T < T_3$) the subgrade strain relationship is:

$$\varepsilon_{z,ad} = 0.016 NE^{-0.222}$$

The granular base layer (thickness 25 cm) has a modulus of 3 times the modulus of the pavement foundation with a maximum of 380 MPa.

Cement treated layers and layers stabilized with a hydraulic binder

The fatigue behavior of cement treated layers is often described by means of the following equation.

$$\sigma / f_f = 1 + \beta \log N$$

Although this is a semi logarithmic equation, it can be replaced by a log – log relationship which is valid for a particular range in log N. If e.g. one is only interested in the fatigue behavior in the range of 10^5 to 10^7 load repetitions, then the relation can be written as:

$$\sigma = \sigma_6 * (N / 10^6)^b$$

Where σ_6 is the stress level which can be allowed 10^6 times.

The relation between b and β is given below.

$$b = -0.5 * \log[(1 + 5\beta) / (1 + 7\beta)]$$

The allowable tensile stress (σ_{ad}) in the stabilized layer at a certain confidence level is calculated in the same way as the allowable tensile strain in the asphalt layer so:

$$\sigma_{ad} = \sigma_6 * (NE / 10^6)^b * k_r * k_c * k_s$$

Where NE is the number of equivalent 130 kN axles.

Table 104 show for two types of stabilized materials, the characteristics which can be used for design.

Material	E [MPa]	σ_6 [MPa]	-1/b	SN	Minimum tensile strength after 360 days [MPa]
Aggregate and cement mix	23000	0.75	15	1	1.15
Aggregate and granulated slag	15000	0.6	12.5	1	0.9

Table 104: Characteristics of two types of stabilized materials.

The procedure to calculate σ_{ad} is illustrated with an example.

Assume that the number of equivalent axle loads for which the design has to be made equals $NE = 6.47 * 10^6$

Assume: $E_{formation\ level} = 50$ MPa so $k_s = 1/1.5$ (see table 98)

Assume: the layer is a slag stabilized layer so $k_c = 1.5$ (see table 97)

We calculate k_r assuming a risk level of 10% then $u = -1.285$

Table 104 shows that $b = -1/12.5$

As mentioned earlier $c = 0.02$

Table 104 shows $SN = 1$

Just below table 93 it is given that $S_h = 3$ cm for these types of layers

Then: $\delta = [SN^2 + (c^2 / b^2) * S_h^2]^{0.5} = 1.25$

Since $k_r = 10^{-u\delta b}$ we obtain $k_r = 0.744$

Table 104 shows that $\sigma_6 = 0.6$ MPa so we obtain for σ_{ad} :

$$\sigma_{ad} = 0.6 * (6.47 * 10^6 / 10^6)^{-1/12.5} * 0.744 * 1.5 * (1/1.1) = 0.52 \text{ MPa}$$

As has been mentioned earlier, reflection cracking will occur if a cemented layer is placed directly under the asphalt top layers. In order to keep this reflective cracking under control the manual specifies that the total thickness of the asphalt layers should be 50% of the total pavement thickness (asphalt + base layer treated with a hydraulic binder).

Furthermore it should be mentioned that the design of a composite pavement (asphalt on top of base treated with a hydraulic binder) is done in two phases. In the first phase all layers are assumed to be perfectly bonded to each other. This implies that tension will only occur at the bottom of the (hydraulically bound) base layer. After fatigue has occurred in that layer (after N1 load applications) the base layer is assumed to have a modulus of 20% of its initial value (the value used in the first phase analysis) and full slip is assumed between the asphalt and the base. In this case fatigue of the asphalt layer will occur (after N2 load applications). The total pavement life is then $N1 + N2$

16.3.7 Dutch design method

In this section the Dutch design method [139] will be discussed as it used for the main highways in the Netherlands. The Dutch design method needs to be given attention since it has an interesting approach to risk of failure of the pavement. A computer program called OIA is developed for this purpose. OIA stands for "Ontwerpinstrument Asphaltverhardingen" which can be translated as "Design Tool for Asphalt Pavements".

Like in the French method, the total asphalt thickness can be divided in a number of sub-layers each having their own characteristics. OIA uses characteristic values for the design parameters in combination with partial safety factors. All this will be explained in more detail later on.

Traffic

The total number of axle loads to be expected is calculated using:

$$n_{total} = V * a * W * F_t * G * t * F_v$$

Where:

- Nn_{total} = total nr of truck axles with a load heavier than 20 kN,
- V = number of trucks per working day per direction,
- a = average number of axles per truck (= 3.5),
- W = number of working days per year (= 270),
- F_t = correction factor for the number of lanes per direction,
- G = grow factor,
- t = design period (= 20 years or as specified),
- F_v = correction factor related to speed of truck traffic.

$F_t = 1$ for one lane per direction, = 0.95 lanes per direction, = 0.9 for 3 or more lanes per direction.

$F_v = 1.76$ when the speed is 20 km/h, = 1.33 when the speed is 40 km/h, = 1.12 when the speed is 60 km/h, and = 1.0 when the speed is 80 km/h and higher.

The characteristic number of truck axles is calculated following:

$$n_{\text{char}} = F_h * n_{\text{total}}$$

The factor F_h represents the uncertainty in the traffic predictions. F_h varies between 1.2 and 2 depending on how the axle loads are estimated. When they are based on axle load measurements on a nearby road section then $F_h = 1.4$ and when it is based on estimations than $F_h = 2.0$. When it is based on the standard provided by the Ministry of Transport for main roads then $F_h = 1.75$.

The ministry of transport has three standard axle load distributions which are given in table 105.

Axle load class [kN]	Lightly loaded roads	Medium loaded roads	Heavily loaded roads
20 – 40	27%	23.3%	15.6%
40 – 60	32.5%	30.7%	27.1%
60 – 80	19.5%	21.1%	28.1%
80 – 100	11.9%	12.6%	14.6%
100 – 120	6.6%	8.16%	8.75%
120 – 140	1.95%	3.19%	4.6%
140 – 160	0.45%	0.79%	1.04%
160 – 180	0.08%	0.11%	0.13%
180 – 200	0.02%	0.05%	0.08%
200 – 220	0%	0%	0%

Table 105: Axle load distributions as defined by the Dutch Ministry of Transport. For the design of pavements for main roads the "heavily loaded roads" distribution needs to be used.

In OIA the following distribution of the wheel/tire spectrum is assumed:
39% single wheels, 38% dual wheels, 23% single wheels with wide base tires

Truck traffic intensity is classified in 4 classes.

A: < 50 trucks per day per direction,

B: 51 – 2500 trucks per day per direction,

C: > 2500 trucks per day per direction,

IB: heavily loaded areas like crossings with slow moving (< 15 km/h) and standing heavy truck traffic with an intensity of more than 250 trucks per day per direction.

The contact area of the tire loads are assumed to be circular. The radius of the contact area and the contact pressure are calculated in the following way.

$$A = \beta * 1000 * F_n / \sigma_n$$

Where:

A = contact area [mm²],

F_n = wheel load = axle load / number of wheels on axle [kN],

σ_n = tire pressure [MPa]

$\beta = 1 + 0.59454 B_{eq} - 0.10182 B_{eq}^2$

$B_{eq} = (F_a / F_n) - 1$

F_a = actual wheel load [kN].

As we have seen in the chapter on axle and wheel loads, the actual wheel load F_a is quite often not equal to F_n !

The actual contact pressure σ_a is calculated using:

$$\sigma_a = F_a / A$$

The actual radius of the contact area r_a is calculated using:

$$r_a = \sqrt{(A / \pi)}$$

In the analyses, lateral wander is taken into account. How this is done is described in chapter 14.2.

Base materials

The Ministry of Transport only allows the base materials shown in table 106 to be used.

Type	Material	Minimum total asphalt thickness [mm]	Thickness [mm]	Characteristic modulus value [MPa], Poisson's ratio	Truck traffic intensity
Unbound	Crushed masonry	120	≥ 200	150 / 0.35	All
Slightly bound	Mixture of crushed masonry and crushed concrete aggregates	120	≥ 200	400 / 0.35	All
Slightly bound	Self-binding mixture of crushed masonry and concrete aggregates	120	≥ 200	600 / 0.35	All
Slightly bound	Crushed concrete aggregate	120	≥ 200	600 / 0.35	All
Slightly bound	Phosphorous slag mixture	120	≥ 200	1000 / 0.35	All
Cement bound	RAP mixed with cement	120	≥ 200	1200 / 0.20	A
Cement bound	RAP mixed with cement	140	≥ 200	1200 / 0.20	B, C, IB
Cement bound	RAP mixed with emulsion and cement	120	≥ 200	1200 / 0.20	A
Cement bound	RAP mixed with emulsion and cement	140	≥ 200	1200 / 0.20	B, C, IB

Table 106: Type of materials allowed by the Dutch Ministry of Transport to be used in base courses and some characteristic values.

The Dutch Ministry of Transport doesn't allow base courses made of blast furnace slags, sand-cement stabilized base courses, and other cemented layers resulting in a high stiffness and strength. This is because slag bases have shown stability problems (which were discussed earlier) and strong cement treated base courses resulted in significant reflection cracking (large crack spacing but wide cracks).

When designing the pavements, it is not allowed to use modulus values which are higher than those given in table 106. The values are conservative values and can be taken as characteristic values which have a reliability of 85%. The modulus values given in table 106 can only be applied for the top 300 mm of the base layer. If the base layer has a larger thickness then a modulus value of 150 MPa has to be used for the part beyond 300 mm.

Subgrade

Table 107 gives some values for the characteristic stiffness of some subgrade materials.

Material	E [MPa]
Weak clay	30
Stiff clay	50
Sand	100
Well graded sand	120
Loamy fine sand	150

Table 107: Characteristic stiffness values of some subgrade materials as proposed by the Dutch Ministry of Transport.

The values given in table 107 are conservative values and can be taken as characteristic values which have a reliability of 85%. Poisson's ratio is taken as 0.35 for all materials.

The subgrade strain criterion used is:

$$\log N_{\text{subgrade}} = 17.289 - 4 \log \varepsilon_{v, \text{subgrade}}$$

Where $\varepsilon_{v, \text{subgrade}}$ is the vertical compressive strain at the top of the subgrade in [$\mu\text{m}/\text{m}$]. N_{subgrade} is the allowable number of load repetitions with a reliability level of 85%.

Asphalt mixtures

The characteristic stiffness modulus of the asphalt concrete mixtures is calculated following:

$$\ln(E_a) = C_1 - 0.0184 * T_f - 0.001098 * T_f^2$$

Where:

- E_a = characteristic asphalt mixture stiffness [MPa],
- T_f = fictitious temperature [$^{\circ}\text{C}$],
- C_1 = $\ln(E_{20\text{C}, 8\text{Hz}} - \Delta E_{20\text{C}, 8\text{Hz}}) + 0.80734$
- $E_{20\text{C}, 8\text{Hz}}$ = average mixture stiffness at 20 $^{\circ}\text{C}$ and 8 Hz [MPa],
- $\Delta E_{20\text{C}, 8\text{Hz}}$ = reduction to "translate" average stiffness to characteristic stiffness [MPa].

The characteristic asphalt stiffness is the 85% reliable stiffness value.

The magnitude of the reduction factor depends on the number of specimens used for determining the stiffness, the number of times the stiffness determination has been performed and the standard deviation of the stiffness values measured. An example of the reduction factors is given in table 108. In [139] it is described on which basis and assumptions this table has been developed. It takes into account the variation that occurs when different laboratories are testing the same mixture using the same equipment and following the same procedure. Also variations are taken into account due to possible differences in e.g. preparation of the same mixture and finally variations due to the variability of the material itself is taken into account.

The fictitious temperature T_f is calculated from the real asphalt temperature T and the real loading frequency f following:

$$1 / (T_f + 273) = 1 / (T + 273) - (1 / 11242) * \log (8 \text{ Hz} / f)$$

In the design program a fixed asphalt temperature of 20 $^{\circ}\text{C}$ is used. The loading frequency is calculated following:

$$\log(f) = -0.6 - 0.5 h_a + 0.94 * \log(V)$$

Where:

f = loading frequency [Hz],
 h_a = thickness of the asphalt layer [m],
V = speed truck traffic [km/h].

Nr of times the stiffness investigation has been performed	σ < 300	σ 300 - 500	σ 500 - 700	σ 700 - 900	σ > 900
1	1282	1286	1291	1301	1314
2	1259	1262	1267	1273	1281
3	1251	1254	1258	1264	1271
4	1247	1250	1254	1260	1267
5	1244	1247	1251	1257	1264

Table 108: Reduction factor [MPa] to be applied on the average stiffness in relation to the standard deviation of the measured stiffness (σ , [MPa]) and the number of times the investigation has been performed. The table is valid for the case when the stiffness is determined as part of a fatigue investigation in which 18 beams are tested.

Poisson's ratio is taken as 0.35

The characteristic fatigue relationship is determined in the following way. Fatigue tests have to be performed on 18 beams and a fatigue relation has to be developed following:

$\ln(N) = A + p \ln(\epsilon)$ and r^2 has to be determined.

The tests have to be performed at 20 °C and 30 Hz. Then the value of $\ln(N(x_{av} - 1))$ at a strain level of $x_{av} - 1$ where x_{av} is the average value for $\ln(\epsilon)$ as determined from all tests.

Then the value of $\ln(N(x_{av}-1))$ is reduced with the correction value which is to be taken from table 109 in order to determine the characteristics fatigue life $\ln(N_{charac}(x_{av} - 1))$.

sx	<0,55	0,55-0,60	0,60-0,65	0,65-0,70	0,70-0,75	0,75-0,80	0,80-0,85	0,85-0,90	0,90-0,95	>0,95
< 0,15	1,941718	1,779265	1,627710	1,484403	1,347582	1,215071	1,083639	0,950687	0,812597	0,663317
0,15-0,20	1,923467	1,763477	1,615891	1,475601	1,342227	1,211456	1,081184	0,950274	0,813184	0,663841
0,20-0,25	1,913779	1,754947	1,607984	1,470020	1,337873	1,208447	1,080813	0,950021	0,813901	0,664531
0,25-0,30	1,915090	1,754602	1,606864	1,468535	1,336497	1,207992	1,080661	0,951271	0,814694	0,665382
0,30-0,35	1,925903	1,762427	1,612311	1,472291	1,339099	1,210005	1,082306	0,952694	0,816691	0,666383
0,35-0,40	1,944778	1,777407	1,624065	1,481208	1,345764	1,215159	1,086205	0,955938	0,819130	0,667526
0,40-0,45	1,970084	1,798509	1,641279	1,494944	1,356514	1,223244	1,092212	0,960282	0,821744	0,668800
0,45-0,50	2,000681	1,824609	1,663208	1,512953	1,370919	1,234392	1,100565	0,966036	0,825811	0,670191
0,50-0,55	2,035614	1,854953	1,689143	1,534719	1,388657	1,248372	1,111084	0,973343	0,830123	0,671949
0,55-0,60	2,074245	1,888862	1,718555	1,559726	1,409434	1,264990	1,123681	0,982203	0,835721	0,674213
0,60-0,65	2,116076	1,925875	1,750915	1,587586	1,432837	1,283987	1,138289	0,992565	0,841896	0,676626
0,65-0,70	2,160805	1,965606	1,785907	1,617908	1,458576	1,305118	1,154789	1,004363	0,849034	0,679175
0,70-0,75	2,208093	2,007793	1,823210	1,650479	1,486415	1,328186	1,172975	1,017520	0,857088	0,681847
> 0,75	2,257695	2,052193	1,862590	1,685013	1,516108	1,352986	1,192716	1,031956	0,865929	0,684871

Table 109: Reduction of $\ln(N(x_{av} - 1))$ and $\ln(N(x_{ax} + 1))$ in relation to the number of times the fatigue analysis was repeated (k), the standard deviation sx of the applied values for $\ln(\epsilon)$ and the correlation coefficient r^2 .

The same procedure is used to determine $\ln(N(x_{av} + 1))$ and $\ln(N_{charac}(x_{av} + 1))$. Also $\ln(N(x_{av}))$ is determined based on the average value of $\ln(\varepsilon)$ as used in the test. The characteristic value $\ln(N_{charac}(x_{av}))$ is determined by subtracting the values shown in table 110 from $\ln(N(x_{av}))$.

sx	<0,55	0,55-0,60	0,60-0,65	0,65-0,70	0,70-0,75	0,75-0,80	0,80-0,85	0,85-0,90	0,90-0,95	>0,95
< 0,15	0,608163	0,603160	0,598809	0,594993	0,591864	0,589430	0,587230	0,585231	0,583409	0,581742
0,15-0,20	0,636426	0,625667	0,617013	0,609349	0,603292	0,597822	0,592839	0,589143	0,585699	0,582486
0,20-0,25	0,674480	0,656818	0,641918	0,629407	0,618719	0,609246	0,601554	0,594384	0,588660	0,583469
0,25-0,30	0,721540	0,695645	0,673593	0,654731	0,638447	0,624288	0,612121	0,601683	0,592216	0,584682
0,30-0,35	0,775920	0,741151	0,711132	0,685142	0,662435	0,642546	0,625182	0,610088	0,597151	0,586116
0,35-0,40	0,836227	0,792192	0,753795	0,720078	0,690303	0,664056	0,640794	0,620530	0,602870	0,587760
0,40-0,45	0,901167	0,847775	0,800721	0,758967	0,721725	0,688438	0,658686	0,632439	0,609133	0,589599
0,45-0,50	0,969762	0,906969	0,851189	0,801218	0,756207	0,715544	0,678838	0,645915	0,616845	0,591619
0,50-0,55	1,041202	0,969086	0,904556	0,846315	0,793359	0,745067	0,701009	0,660962	0,625068	0,594037
0,55-0,60	1,114893	1,033528	0,960321	0,893781	0,832845	0,776749	0,725026	0,677507	0,634548	0,596973
0,60-0,65	1,190362	1,099854	1,018019	0,943240	0,874290	0,810318	0,750755	0,695450	0,644715	0,600106
0,65-0,70	1,267294	1,167701	1,077332	0,994339	0,917408	0,845527	0,778042	0,714687	0,655833	0,603423
0,70-0,75	1,345382	1,236809	1,137966	1,046853	0,961966	0,882175	0,806686	0,735119	0,667840	0,606906
> 0,75	1,424408	1,306957	1,199702	1,100533	1,007739	0,920065	0,836548	0,756649	0,680613	0,610755

Table 110: Reduction of $\ln(N(x_{av}))$ in relation to the number of times the fatigue analysis was repeated (k), the standard deviation sx of the applied values for $\ln(\varepsilon)$ and the correlation coefficient r^2 .

Then the characteristic fatigue line is determined from $\ln(N(x_{av} - 1))$, $\ln(N(x_{av}))$ and $\ln(N(x_{av} + 1))$ following:

$$\ln(N_{charac}) = a \ln^2(\varepsilon) + b \ln(\varepsilon) + c$$

For design purposes a mixture stiffness dependent characteristic fatigue relation has to be determined following:

$$\ln(N_{charac}) = C_1 + C_5 \{ \ln(\varepsilon) + C_2 * \ln^2(S) + C_3 * \ln(S) + C_4 \}^2$$

Where:

$$C_1 = -(b^2 - 4ac)/4a,$$

$$C_2 = -0.064449,$$

$$C_3 = 1.404363,$$

$$C_4 = b/2a - C_2 * \ln^2(S_{20C, 30 Hz}) - C_3 * \ln(S_{20C, 30 Hz})$$

$$C_5 = a$$

a,b,c = coefficients of the fatigue relation mentioned above.

If only stiffness values at 20 °C and 8 Hz are available then $S_{20C, 30Hz}$ can be obtained by:

$$S_{20C, 30 Hz} = 1.2393 * S_{20C, 8 Hz}$$

In this way characteristic fatigue lines like those shown in figure 423 are obtained.

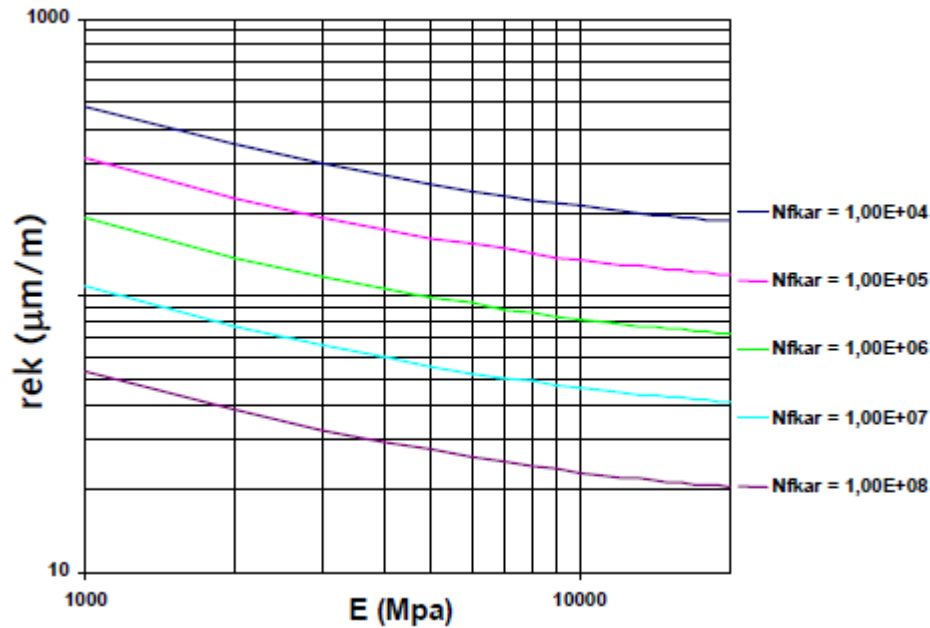


Figure 423: Example of characteristic fatigue lines.

Note: "rek" = tensile strain

In order to match the lab fatigue behavior to the fatigue behavior in practice a shift factor (SF) needs to be applied which is calculated following:

$$SF = 1 + 0.0000419 * V_b^{1.06} * Pen^{2.45}$$

Where:

V_b = mass percentage bitumen (e.g. 5),

Pen = penetration of the bitumen (e.g. 40).

The maximum value for SF is 4.

Values for the design parameters

Using the characteristic values in the design analyses would imply that one stacks "safety on safety" and this would result in an unrealistic high safety factor for the entire structure. In order to overcome this the characteristic values for the parameters mentioned below are divided by a so called partial factor.

- layer thicknesses,
- layer stiffnesses,
- fatigue resistance,
- resistance to permanent deformation,
- tensile strength,
- strain at break

The characteristic value for the truck traffic intensity is multiplied by a partial factor. The value for each of these partial factors is given in table 111.

Parameter	85%	75%	70%	50%
Thickness layer 1j	0.971	0.966	0.964	0.953
Stiffness layer 1	0.868	0.849	0.843	0.82
Fatigue res layer 1	0.925	0.790	0.744	0.592
Thickness layer 2	0.924	0.922	0.922	0.919
Stiffness layer 2	0.906	0.863	0.846	0.775
Tensile strength self binding base course*	1	1	1	1
Crushing strength bound base course*	1	1	1	1
Strain at break at bottom bound base course*	1	1	1	1
Thickness layer 3	0.918	0.918	0.918	0.917
Stiffness layer 3	0.743	0.734	0.730	0.717
Stiffness layer 4	0.829	0.821	0.818	0.808
Truck traffic intensity	0.852	0.768	0.737	0.633

Note: * not applicable/not to be used for/in designs for the Dutch Ministry of Transport

Table 111: Partial factors.

Damage analysis

As is done in all other design programs, Miner's ratio is calculated. Based on Miner's number (n/N) the "structural damage" is calculated using the information given in table 112.

Structural damage [%]	Miner's number n/N
5	0.32
10	0.43
15	0.54
20	0.64
25	0.74

Table 112: Relation between structural damage and Miner's number (n/N).

It should be noted that the maximum amount of structural damage in projects of the Dutch Ministry of Transport is 15%.

From the above it is clear that much attention is placed on the quality of the asphalt structure. This is because in the Netherlands pavements with rather thick asphalt layers are built. This is done because the authorities want to overcome as much as possible the need for regular maintenance which normally takes quite a bit of time to be performed. By doing so the authorities want to reduce hinder to traffic due to maintenance works as much as possible. Keep in mind that the Netherlands is a small country, but it is densely populated, has the highest road density (km roads/km²) in Europe and the roads are heavily loaded both in terms of numbers and axle loads.

16.3.8 South African design catalogue TRH4

At the time the author was preparing these notes a large effort was undertaken in South Africa to develop a design system like AASHTO's MEPD. This effort was undertaken to replace the design catalogue TRH4 [125] which has been in use for many years and is still being used.

The catalogue is an empirical design system which is based on performance observations of existing roads, results of accelerated full scale testing of in situ pavements and specially constructed test sections, extensive material testing (especially on soils and granular materials) and analysis using multi-layer linear elastic programs like the South African program MePADS.

Although being based on practical experience is an advantage of such catalogue systems, the disadvantage is that do not allow to analyze the beneficial effects application of new materials can have, changes in axle load patterns, wheel loads and contact pressure distributions etc. Nevertheless a catalogue system is a very handy tool to get a quick first estimate of the required thickness of the pavement.

The catalogue is shown in figure 424. It should be kept in mind that it is developed for South African conditions which not only means that it is valid for South African climatic and traffic conditions but also for South African types of materials. South Africa is blessed by having an abundance of high quality aggregates from which high quality base and subbase courses can be built. Furthermore the use of a cement treated subbase is typical for South African pavements. This cement treated layer act as a capping layer bridging weaker spots in the subgrade but also acts as a working platform on which the granular base course is placed. Because of the capping layer, the granular base course can be compacted to very density levels and because of the deeper lying stiff cemented subbase, horizontal compressive stresses occur in the granular base due to the traffic loads. These horizontal stresses provide such a confinement that the modulus of the granular layer can take fairly high values.

The basic assumption is that the subgrade CBR is 15%. If this is not the case then an improved subgrade should be applied; table 113 shows how this has to be achieved.

Subgrade CBR Class	SG4	SG3	SG2	SG1
Design CBR of subgrade	< 3	3 - 7	7 - 15	> 15
Add selected layers: Upper Lower	Not applicable	150 mm G7 150 mm G9*	150 mm G7 -	- -
Treatment of in situ subgrade	Special treatment required	Rip and re-compact to 150 mm G10	Rip and re-compact to 150 mm G9	Rip and re-compact to 150 mm G7

* If the in situ subgrade is expected to be very wet, or in wet regions an additional 150 mm layer of G9 should be used.

Table 113: Measures needed to upgrade existing subgrade to platform with CBR = 15%.

There are four road categories, category A being the most important one and category D the least important. This is also reflected in the design reliability. For the different road categories the design reliability is 95% for A, 90% for B, 80% for C and 50% for D. Very important are the specifications to which the different materials should comply; these are given in table 114. The required structure depends on the design reliability and the traffic class. As one will notice these traffic classes are rather wide implicitly indicating that pavement life predictions cannot be very accurate and precise.

As mentioned before similar catalogues are used in other countries. An example is the catalogue which is used in Tanzania which is highly comparable to TRH4.

16.3.9 Highway Design Model (HDM)

The Highway Design Model [3] is developed for the World Bank to be used for pavement design and rehabilitation purposes in developing countries. It has to be used in cases where road authorities want their projects to be sponsored by the Bank. The model is extremely useful in finding solutions with the overall highest benefit (lowest costs). The costs do not only imply construction and maintenance costs but also vehicle operating costs. In this section we will certainly not present and discuss the entire model. We will only focus on the models which are developed for thickness design and performance predictions. The models presented are part of the HDM III model; it should be noted that later versions are already available.

GRANULAR BASES

(DRY REGIONS)

DATE 1996

PAVEMENT CLASS AND DESIGN BEARING CAPACITY (80 KN AXLES/LANE)											Foundation
ROAD CAT.	ES1 < 3000	ES2 0,3-1,0x10 ⁴	ES3 1,0-3,0x10 ⁴	ES4 3,0-10x10 ⁴	ES5 0,1-0,3x10 ⁶	ES6 0,3-1,0x10 ⁶	ES7 1,0-3,0x10 ⁶	ES8 3,0-10x10 ⁶	ES9 10-30x10 ⁶	ES10 30-100x10 ⁶	
A							150 G5 150 G2 40A	150 G2 250 C3 40A	150 G1 250 C3 50A	150 G1 300 C3 50A	
B						150 G4 150 C4 S	150 G3 150 G3 S*/30A 40A	150 G2 200 C4 30A			
C				100 G5 125 C4 S	125 G4 125 C4 S	125 G4 125 C4 S	150 G3 150 G3 S				
D	100 G5 100 G7 S1	100 G5 125 G7 S1	100 G4 125 G7 S1	100 G4 125 G6 S1	125 G4 125 G6 S	125 G4 150 G6 S					
										150 G9 G10	

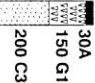
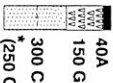
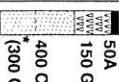

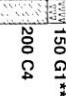
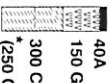
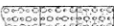
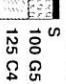
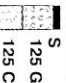

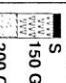


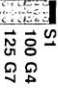
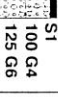
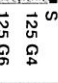
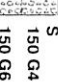
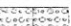
Symbol A denotes AG, AC, OR AS. A0, AP may be recommended as a surfacing measure for improved skid resistance when wet or to reduce water spray.

S denotes Double Surface Treatment (seal or combinations of seal and slurry)

S1 denotes Single Surface Treatment

* If seal is used, increase C4 and G5 subbase thickness to 200mm.

Figure 424: TRH4 catalogue.

GRANULAR BASES											(WET REGIONS)	DATE 1996
PAVEMENT CLASS AND DESIGN BEARING CAPACITY (80 kN AXLES/LANE)												
ROAD CAT.	ES1 < 3000	ES2 0,3-1,0x10 ⁴	ES3 1,0-3,0x10 ⁴	ES4 3,0-10x10 ⁴	ES5 0,1-0,3x10 ⁶	ES6 0,3-1,0x10 ⁶	ES7 1,0-3,0x10 ⁶	ES8 3,0-10x10 ⁶	ES9 10-30x10 ⁶	ES10 30-100x10 ⁶	Foundation	
A							 30A 150 G1** 200 C3	 40A 150 G1 300 C3 *(250 C3)	 50A 150 G1 400 C3 *(300 C3)			
B						 S 150 G2 150 C4 200 G5	 S/30A 150 G1** 200 C4	 40A 150 G1 300 C4 *(250 C4)			 150 G7 150 G9 G10	
C				 S 100 G5 125 C4	 S 125 G5 125 C4	 S 125 G2 150 C4	 S 150 G2** 200 C4					
D	 S1 100 G5 100 G7	 S1 100 G5 125 G7	 S1 100 G4 125 G7	 S1 100 G4 125 G6 100 C4	 S 125 G4 125 G6 100 G5 125 C4	 S 150 G4 150 G6 150 G5 150 C4					 150 G9 G10	

Symbol A denotes AG, AC, OR AS. A0, AP may be recommended as a surfacing measure for improved skid resistance when wet or to reduce water spray.
 S denotes Double Surface Treatment (seal or combinations of seal and slurry)
 S1 denotes Single Surface Treatment

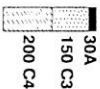
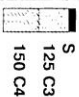
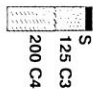
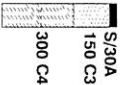
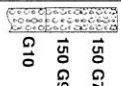



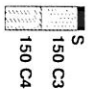


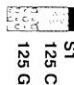
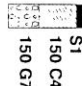
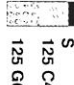
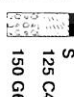

* If water is prevented from entering the base, the subbase thickness may be reduced to the values indicated in brackets.
 ** Base thickness may be reduced by 25 mm if cemented subbase thickness is increased by 50 mm.

Figure 424: TRH4 catalogue (continued).

HOT-MIX ASPHALT BASES											
PAVEMENT CLASS AND DESIGN BEARING CAPACITY (80 kN AXLES/LANE)											
ROAD CAT.	ES1 < 3000	ES2 $0.3-1.0 \times 10^4$	ES3 $1.0-3.0 \times 10^4$	ES4 $3.0-10 \times 10^4$	ES5 $0.1-0.3 \times 10^6$	ES6 $0.3-1.0 \times 10^6$	ES7 $1.0-3.0 \times 10^6$	ES8 $3.0-10 \times 10^6$	ES9 $10-30 \times 10^6$	ES10 $30-100 \times 10^6$	Foundation
A											
B											
C											
D											

Symbol A denotes AG, AC, OR AS. A0, AP may be recommended as a surfacing measure for improved skid resistance when wet or to reduce water spray.
 Symbol BC does not include LAMBS (BC1 Table 13)
 S denotes Double Surface Treatment (seal or combinations of seal and slurry)
 S1 denotes Single Surface Treatment

Figure 424: TRH4 catalogue (continued).

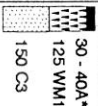
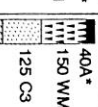
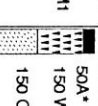
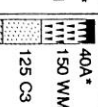
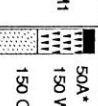
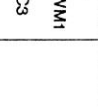
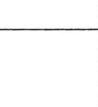
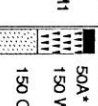
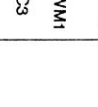
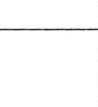
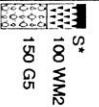
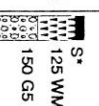
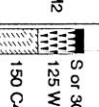
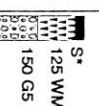
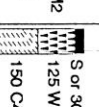
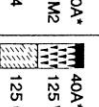
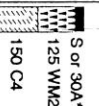
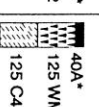
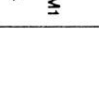
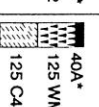
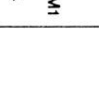
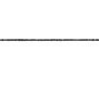
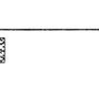
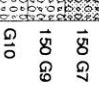

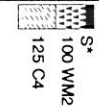
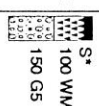

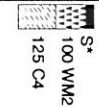
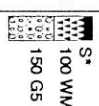

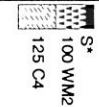
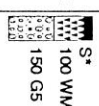

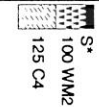
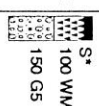

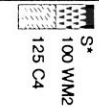
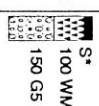
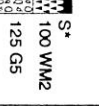

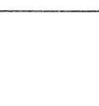
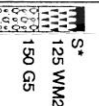
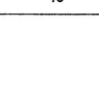
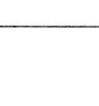
CEMENTED BASES											DATE 1996
PAVEMENT CLASS AND DESIGN BEARING CAPACITY (80 kN AXLES/LANE)											
ROAD CAT.	ES1 < 3000	ES2 $0,3-1,0 \cdot 10^4$	ES3 $1,0-3,0 \cdot 10^4$	ES4 $3,0-10 \cdot 10^4$	ES5 $0,1-0,3 \cdot 10^6$	ES6 $0,3-1,0 \cdot 10^6$	ES7 $1,0-3,0 \cdot 10^6$	ES8 $3,0-10 \cdot 10^6$	ES9 $10-30 \cdot 10^6$	ES10 $30-100 \cdot 10^6$	Foundation
A							 30A 150 C3 200 C4				
B						 S 125 C3 150 C4	 S 125 C3 200 C4	 S/30A 150 C3* 300 C4		 150 G7 150 G9 G10	
C				 S 100 C4 100 G6	 S 200 C3 125 C4 125 G6	 S 125 C3 125 C4	 S 150 C3 150 C4				
D	 S1 100 C4 100 G8	 S1 100 C4 125 G8	 S1 125 C4 125 G7	 S1 150 C4 150 G7	 S 125 C4 125 G6	 S 125 C4 150 G6					 150 G9 G10

Symbol A denotes AG, AC, OR AS. AO, AP may be recommended as a surfacing measure for improved skid resistance when wet or to reduce water spray.
 S denotes Double Surface Treatment (seal or combinations of seal and slurry)
 S1 denotes Single Surface Treatment
 * Crushing of cemented base may occur

Figure 424: TRH4 catalogue (continued).

WATERBOUND MACADAM BASES

DATE 1996

PAVEMENT CLASS AND DESIGN BEARING CAPACITY (80 kN AXLES/LANE)											
ROAD CAT.	ES1 < 3000	ES2 $0.3 \cdot 10^4$	ES3 $1.0 \cdot 3.0 \cdot 10^4$	ES4 $3.0 \cdot 10^4$	ES5 $0.1 \cdot 0.3 \cdot 10^6$	ES6 $0.3 \cdot 1.0 \cdot 10^6$	ES7 $1.0 \cdot 3.0 \cdot 10^6$	ES8 $3.0 \cdot 10^6$	ES9 $10 \cdot 30 \cdot 10^6$	ES10 $30 \cdot 100 \cdot 10^6$	Foundation
A #							 30-40A*  125 WM1  150 C3	 40A*  125 WM1  125 C3  125 C4	 50A*  150 WM1  150 C3		
B					 S*  100 WM2  150 G5	 S*  125 WM2  150 G5	 S or 30A*  125 WM2  150 C4	 40A*  125 WM1  125 C4  125 C4	 150 G7 150 G9 G10		
C				 S*  100 WM2  100 C4	 S*  100 WM2  125 C4	 S*  100 WM2  150 G5	 S*  125 WM2  100 C4	 S*  125 WM2  150 G5			
D				 S*  100 WM2  125 G5			 S*  125 WM2  150 G5				

* Symbol A denotes AG, AC, or AS. Symbol S denotes S2 or S4. See Table 13 for Material Symbols.
 For selected layers see Section 8.4.2; For future maintenance see Section 9.5.




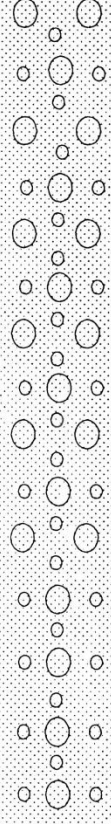
A0, AP permitted as a surfacing measure for skid resistance or reduction of water spraying.

For Category A pavements constructed without a paver, an asphalt leveling course of 25 mm to 30 mm is normally needed to improve on the riding quality.

WATERBOND

Figure 424: TRH4 catalogue (continued).

Material symbols and abbreviated specifications used in the Catalogue designs

SYMBOL	CODE	MATERIAL	ABBREVIATED SPECIFICATIONS
	G1	Graded crushed stone	Dense - graded unweathered crushed stone; Maximum size 37,5 mm; 86 - 88 % apparent relative density; Soil fines PI < 4
	G2	Graded crushed stone	Dense - graded crushed stone; Maximum size 37,5 mm; 100 - 102 % Mod. AASHTO or 85 % bulk relative density; Soil fines PI < 6
	G3	Graded crushed stone	Dense - graded stone and soil binder; Maximum size 37,5 mm; 98 - 100 % Mod. AASHTO ; Soil fines PI < 6
	G4	Crushed or natural gravel	Minimum CBR = 80 % @ 98 % Mod. AASHTO; Maximum size 37,5 mm; 98 - 100 % Mod. AASHTO; PI < 6; Maximum Swell 0,2 % @ 100 % Mod. AASHTO. For calcrete PI ≤ 8
	G5	Natural gravel	Minimum CBR = 45 % @ 95 % Mod. AASHTO; Maximum size 63 mm or 2/3 of layer thickness; Density as per prescribed layer usage; PI < 10; Maximum swell 0,5 % @ 100 % Mod. AASHTO. *
	G6	Natural gravel	Minimum CBR = 25 % @ 95 % Mod. AASHTO; Maximum size 63 mm or 2/3 of layer thickness; Density as per prescribed layer usage; PI < 12; Maximum swell 1,0 % @ 100 % Mod. AASHTO. *
	G7	Gravel / Soil	Minimum CBR = 15 % @ 93 % Mod. AASHTO; Maximum size 2/3 of layer thickness; Density as per prescribed layer usage; PI < 12 or 3GM** + 10; Maximum swell 1,5 % @ 100 % Mod. AASHTO. ***
	G8	Gravel / Soil	Minimum CBR = 10 % @ 93 % Mod. AASHTO; Maximum size 2/3 of layer thickness; Density as per prescribed layer usage; PI < 12 or 3GM** + 10; Maximum swell 1,5 % @ 100 % Mod. AASHTO. ***
	G9	Gravel / Soil	Minimum CBR = 7 % @ 93 % Mod. AASHTO; Maximum size 2/3 of layer thickness; Density as per prescribed layer usage; PI < 12 or 3GM** + 10; Maximum swell 1,5 % @ 100 % Mod. AASHTO. ***
	G10	Gravel / Soil	Minimum CBR = 3 % @ 93 % Mod. AASHTO; Maximum size 2/3 of layer thickness; Density as per prescribed layer usage;

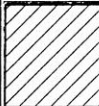

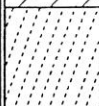
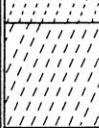
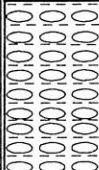



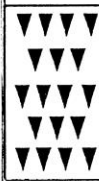
* For calcrete PI ≤ 15 on condition that the Linear Shrinkage (LS) does not exceed 6 %.

** GM = Grading Modulus (TRH14, 1985) =
$$\frac{300 - [\rho_{2,00mm} + \rho_{0,425mm} + \rho_{0,075mm}]}{100}$$
 where $\rho_{2,00}$ etc., denote the percentage passing through the sieve size .

*** For calcrete PI ≤ 17 on condition that the Linear Shrinkage (LS) does not exceed 7 %.

Table 114: Abbreviated specifications for the materials used in the TRH4 design catalogue.

Material symbols and abbreviated specifications used in the Catalogue designs

SYMBOL	CODE	MATERIAL	ABBREVIATED SPECIFICATIONS
	C1	Cemented crushed stone or gravel	UCS**** : 6 to 12 MPa at 100 % Mod. AASHTO; Specification at least G2 before treatment; Dense-graded ; Maximum aggregate 37, 5 mm
	C2	Cemented crushed stone or gravel	UCS : 3,5 to 6 MPa at 100 % Mod. AASHTO; Minimum ITS ***** = 400 kPa at 95 % to 97 % Mod. AASHTO compaction; Specification at least G2 or G4 before treatment; Dense-graded; Maximum aggregate 37, 5 mm; Max. fines loss = 5 %*****
	C3	Cemented natural gravel	UCS : 1 to 3,5 MPa at 100 % Mod. AASHTO; Minimum ITS***** = 250 kPa at 95 % to 97 % Mod. AASHTO compaction; Maximum aggregate 63 mm; 5 % Maximum PI = 6 after stabilization; Max. fines loss = 20 %
	C4	Cemented natural gravel	UCS : 0,75 to 1,5 MPa at 100 % Mod. AASHTO; Minimum ITS***** = 200 kPa at 95 % to 97 % Mod. AASHTO compaction; Maximum aggregate 63 mm; 5 % Maximum PI = 6 after stabilization; Max. fines loss = 30 %
	BEM	Bitumen emulsion Modified gravel	Residual bitumen: 0,6 % to 1, 5 % (SABITA, manual 14, 1993); Minimum CBR = 45 and Minimum UCS = 500 KPa @ 95 % Mod. AASHTO. Compaction: 100-102 % Mod. AASHTO. Residual bitumen 1,5 % to 5,0 % (SABITA, manual 14, 1993); Minimum ITS***** = 100 KPa; Minimum resilient modulus 1000 kPa. Compaction: 100-102% Mod. AASHTO.
	BES	Bitumen emulsion Stabilized gravel	
	BC1	Hot - mix asphalt	LAMBS; Max. size 53 mm (SABITA, manual 13, 1993) Continuously graded; Max. size 37,5 mm Continuously graded; Max. size 26,5 mm Semi-gap graded; Max. size 37,5 mm
	BC2	Hot - mix asphalt	
	BC3	Hot - mix asphalt	
	BS	Hot - mix asphalt	
	AG	Asphalt surfacing	Gap graded (TRH 8, 1987) Continuously graded (TRH 8, 1987) Semi -gap graded (TRH 8, 1987) Open graded (TRH 8, 1987) Porous (Drainage) asphalt (SABITA, manual 17, 1994)
	AC	Asphalt surfacing	
	AS	Asphalt surfacing	
	AO	Asphalt surfacing	
	AP	Asphalt surfacing	
	S1	Surface treatment	Single seal (TRH 3, 1996) Multiple seal (TRH 3, 1996) See TRH 3, 1996 See TRH 3, 1996 Fine grading Medium grading Coarse grading Rejuvenator Diluted emulsion
	S2	Surface treatment	
	S3	Sand seal	
	S4	Cape seal	
	S5	Slurry	
	S6	Slurry	
	S7	Slurry	
	S8	Surface renewal	
	S9	Surface renewal	
	WM1	Waterbound macadam	Max. size 75 mm; Max.PI of fines = 6; 88 % to 90 % apparent relative density
	WM2	Waterbound macadam	
	PM	Penetration macadam	
	DR	Dumprock	

**** UCS: Unconfined Compressive Strength (TMH 1, 1979, Method A14)

***** ITS: Indirect Tensile Strength (SABITA Manual 14, 1993)

***** Durability (TMH 1, 1979, Method A19)

Table 114: Abbreviated specifications for the materials used in the THR4 design catalogue (continued).

The pavement models are empirical and based on pavement performance studies done in a.o. Brasil and Kenia.

The bearing capacity of the pavement is expressed by means of the modified structural number (SNC) which is calculated as:

$$SNC = 0.04 \sum a_i * h_i + SN_{SG}$$

Where: SNC = modified structural number,
 a_i = strength coefficient of the material used in layer I,
 h_i = thickness of layer i [mm], where $\sum h_i \leq 700$ mm
 SN_{SG} = $3.51 * \log CBR - 0.85 * \log^2 CBR - 1.43$
 CBR = in situ CBR of the subgrade [%].

Values for the strength coefficient are given in table 115. Please note that the strength coefficients for asphalt concrete are related to the resilient modulus determined with the indirect tension test at 30 °C. The loading time at which the measurement are done is unfortunately not specified.

The strength coefficients can also be determined following:

$$a_i = 0.14 * \sqrt[3]{(E_i * (1 - \mu_i^2) / 175.5)}$$

Where: E_i and μ_i are the modulus and Poisson's ratio of layer i. The strength coefficient is calculated relative to a material with $a = 0.14$, $\mu = 0.35$ and $E = 200$ MPa.

For existing pavements, SNC can be determined by means of falling weight deflection measurements ($F = 50$ kN, plate diameter = 300 mm) [127] using:

$$\log SNC = 1.82472 + 0.03344 \log h_1 + 0.11832 \log BCI - 0.16207 \log BDI + 0.12659 \log d_o - 0.57878 \log d_{900} + 0.19996 \log d_{1800} - 0.19829 \log SCI_{300}$$

Where: d_i = deflection at i mm from loading center [μ m],
 SCI_{300} = $d_o - d_{300}$ [μ m],
 BDI = $d_{300} - d_{600}$ [μ m],
 BCI = $d_{600} - d_{900}$ [μ m],
 h_1 = thickness top layer [mm].

In [127] it is also reported that the tensile strain at the bottom of the asphalt layer due to a 50 kN falling weight load can be calculated using:

$$\log \varepsilon_a = 4.241 - 3.24 \log SNC + 0.211 \log h_1$$

Where: ε_a is the tensile strain at the bottom of the asphalt layer in [μ m/m] and h_1 is the thickness of the asphalt layer [mm].

The same report also shows that the vertical compressive strain at the top of the subgrade ε_{vo} in [μ m/m] can be estimated following:

$$\log \varepsilon_{vo} = 6.42702 - 2.33291 * \log SNC - 0.71998 \log H$$

Where: H is the total thickness of asphalt layer + base + subbase [mm].

It should be noted that this equation is valid for pavements where the stiffness of the layers increases from bottom to top. This is not always the case because sometimes one might experience a weaker layer in between two stiffer layers.

Pavement layer	Strength coefficient a_1	
Surface course	0.20 to 0.40	
Surface treatments	0.20	
Asphalt mixtures (cold or hot premix of low stability)	0.20	
Asphalt concrete (hot premix of high stability) ¹	0.30	
$MR_{30} = 1,500$ MPa	0.40	
$MR_{30} = 2,500$ MPa	0.45	
$MR_{30} = 4,000$ MPa or greater		
Base course	For maximum axle loading:	
Granular materials ²	< 80 kN	> 80 kN
CBR = 30% ³	0.07	0.
CBR = 50%	0.10	0.
CBR = 70%	0.12	0.10
CBR = 90%	0.13	0.12
CBR = 110%	0.14	0.14
Cemented materials ⁴		
UCS = 0.7 MPa		0.10
UCS = 2.0 MPa		0.15
UCS = 3.5 MPa		0.20
UCS = 5.0 MPa		0.24
Bituminous materials ⁵		0.32
Subbase and selected subgrade layers (to total pavement depth of 700 mm)		
Granular materials ⁶		
CBR = 5%		0.06
CBR = 15%		0.09
CBR = 25%		0.10
CBR = 50%		0.12
CBR = 100%		0.14
Cemented materials		
UCS > 0.7 MPa		0.14

1/ Applicable only when thickness > 30 mm. MR_{30} = resilient modulus by indirect tensile test at 30° C.

2/ $a_1 = (29.14 \text{ CBR} - 0.1977 \text{ CBR}^2 + 0.00045 \text{ CBR}^3) 10^{-4}$; the coefficient a_1 may be increased by 60 percent if CBR > 70 and the subbase is cement- or lime-treated. Note: $a_1 = 0$ for CBR < 60 when maximum axle loading exceeds 80 kN.

3/ CBR = California Bearing Ratio (in percent) determined at the equilibrium in situ conditions of moisture content and density.

4/ $a_1 = 0.075 + 0.039 \text{ UCS} - 0.00088 \text{ UCS}^2$; where UCS = unconfined compressive strength in MPa at 14 days. "Cemented" implies development of tensile strength through portland cement- or lime-treatment, or the use of certain flyash, slag, lateritic or ferricrete materials that are self-cementing over time.

5/ Dense-graded bitumen-treated base of high stiffness, e.g., $MR_{20} = 4000$ MPa, resilient modulus by indirect tensile test at 20°C.

6/ $a_1 = 0.01 + 0.065 \log_{10} \text{ CBR}$.

Source: Adaptation of Hodges and others (1975), GEIPOT (1982) and NITRR (1978).

Table 115: Strength coefficients for different types of materials.

In [3] the equations shown in table 116 are given which allow the pavement life to initiation of cracking to be calculated. Also equations for the prediction of initiation of wide cracking are given; these are shown in table 117.

	TIME to initiation
Asphalt pavements	$TYN = 4.21 * \exp(0.139 * SNC - 17.1 * YE_4 / SNC^2)$
Surface treatment pavements	$TYN = 13.2 * \exp[-20.7 * (1 + CQ) * YE_4 / SNC^2]$
	CUMMULATIVE TRAFFIC to initiation
Asphalt pavements	$TEN = 0.0362 * SNC^{2.65} * e^{-0.14355 * SY}$ or $TEN = 0.0342 * EHM^{2.86} * e^{-0.198 * EY}$
Surface treatment pavements	$TEN = 0.0072 * SNC^{3.97} * e^{0.39 * CQ}$

TYN = number of years to initiation of narrow cracking; TEN = cumulative amount of 80 kN equivalent single axles to crack initiation; SNC = modified structural number [mm]; YE_4 = annual traffic loading [million ESA's / lane / year], $SY = SNC^4 / (1000 * YE_4)$ provided $SY \leq 8$; EHM = maximum tensile strain at the bottom of the asphalt layer [in 10^{-3} m/m]; $EY = 1 / (EHM^4 * 1000 * YE_4)$ provided that $EY \leq 6$; CQ = construction quality seal coat = 1 if construction was faulty (poor binder distribution, early stripping, contaminated aggregates etc), otherwise = 0.

Table 116: Pavement life to crack initiation equations.

Pavement type	TYW [years]
Asphalt concrete	$2.46 + 0.93 TYN$
Surface treatment	$2.66 + 0.88 TYN$ $1.16 TYN$ The best prediction is given by the maximum of these two equations
Asphalt overlays	$2.04 + 0.98 TYN$
Reseals	$1.85 + 1.0 TYN$
Open graded cold mix asphalt	$0.26 + 1.44 TYN$

Table 117: Models to predict time to initiation of wide cracking (TYW).

The permanent deformation model given in [3] is described below.

$$\text{Mean rut depth: } RDM = AGER^{0.166} * SNC^{-0.502} * COMP^{-2.30} * NE_4^{ERM}$$

$$\text{Standard deviation rut depth: } RDS = 2.063 RDM^{0.532} * SNC^{-0.422} * COMP^{-1.664} * NE_4^{ERS}$$

$$ERM = 0.0902 + 0.0384 * DEF - 0.009 * RH + 0.00158 * MMP * CRX$$

$$ERS = -0.009 * RH + 0.00116 * MMP * CRX$$

Where: RDM = mean rut depth [mm],
RDS = standard deviation rut depth [mm],
AGER = age of pavement since latest overlay or construction [years],
COMP = compaction index of the pavement = ratio of achieved compaction of the granular layers over the specified compaction level; COMP cannot be greater than 1,
 NE_4 = cumulative 80 kN equivalent axles computed with damage power 4,
SNC = modified structural number [mm],
DEF = mean of Benkelman beam peak deflection under an 80 kN single axle load of both wheel paths [mm],
RH = rehabilitation state (= 0 for new pavements and 1 otherwise),
MMP = mean monthly precipitation [m/month],
CRX = cracked area [%].

Finally the roughness progression model should be mentioned which is:

$$RI(t) = [RI_0 + 725 * (1 + SNC)^{-4.99} * NE_4(t)] * e^{0.0153 * t}$$

Where: RI_0 and $RI(t)$ = roughness at time $t = 0$ and $t = t$ in m/km IRI
 $NE_4(t)$ = cumulative equivalent 18 kip axles until time t in million ESA/lane
 t = age of pavement since overlay or construction.

Also models for the prediction of raveling and potholes are given but these will not be reported here.

The careful reader certainly will have observed the similarities between the models presented here and those of the empirical AASHTO model which were presented in the beginning of these notes. The advantage of the HDM model however is that pavement performance is not only described in terms of riding quality but also in terms of cracking and permanent deformation.

The interesting thing about the (complex) HDM models is that interactions are taken into account. This is clearly visible in the rutting model which shows that rutting is affected by cracking and precipitation. The effect of precipitation however is only "activated" when there is cracking implying when moisture can enter the pavement.

17. Do we build what we have designed?

In the previous chapters and sections we have spent a lot of attention on how we can determine values for the input parameters. We have also discussed the numerous methods which are available to estimate values for the input parameters from e.g. mixture composition data etc. We have also seen that some design methods allow detailed predictions to be made of the performance of the pavement as designed but the question is of course "do we actually build what we have designed?". If this is not the case then our predictions certainly may not come true. In this section we will pay attention to some construction related factors which cause that we don't get what we designed.

Let us start with a simple real life example. The author has been involved in the asphalt mixture design for runways and taxiways at a large international airport. When the optimal mixture composition finally was decided upon and construction was about to start, the contractor came with the message that because of all kind of delivery problems he could not get in time enough of the specified aggregate type therefore requested to be allowed to use a different type of aggregate which complied to specifications on hardness, texture etc but which had a lower density than the aggregate which was used for the design analysis. Since at the mixing plant, the constituents of asphalt mixtures are added and mixed by weight, using an aggregate with a different specific weight implies that the composition by volume will be different from the volumetric composition of the mixture that was analyzed during the design process. Although the client was aware of this he didn't think that an analysis on the effects of using a different aggregate type was necessary although such an analysis could have been easily made by means of e.g. the BANDS program which would allow a relative comparison of the characteristics of both mixtures to be made. In any way, the client did not get the pavement that was designed.

Furthermore we have to realize that e.g. gradations are always specified with a certain gradation band while in mixture studies we normally don't take this variation in gradation into account. The effect of these "accepted" variations in composition on the fatigue characteristics of a particular mixture are shown in tables 118 and 119 and in figure 425.

		Min.	Desired	Max.
Aggregate on sieve				
C31.5	(% m/m)	0	0	1
2 mm	(% m/m)	52	57	62
63 μ m	(% m/m)	93	94	95
Binder content m_b	(% m/m)	4	-	5
	at 100% aggregate)			
Voids	(% V/V)	-	-	7
Penetration 25°C	(0.1 mm)	45	-	60
Penetration index	(-)	-1	-	+1

Table 118: Example of variability in mixture composition as allowed in specifications.

Mat.	Composition				Binder		
	m_b (%m/m)	V_e (%V/V)	V_b (%V/V)	V_a (%V/V)	pen (0.1mm)	P (-)	
(A)	4.5	83.9	11.1	5.0	50	0	Medium
(B)	4.0	83.3	9.7	7.0	45	1	Poor
(C)	5.0	84.6	12.4	3.0	45	1	Good
(D)	4.0	83.3	9.7	7.0	60	-1	Poor
(E)	5.0	84.6	12.4	3.0	60	-1	Good

Table 119: Example of effect of allowed composition variations by mass on variations in composition by volume.

Table 118 e.g. shows a part of the specifications which were valid for base course mixtures in the Netherlands. Please note that these specifications are specs by mass. We know that the mechanical characteristics are not controlled by the mass composition but by the composition by volume. Therefore 5 mixtures were composed by volume (see table 119) which all comply with the specs by mass shown in table 118. Using nomographs the fatigue characteristics of mixtures A to E were estimated and they are pictured in figure 425. It is interesting to note that the specifications allow a difference in fatigue life with a factor of about 4.6 to occur!

One might say "this is an interesting theoretical analysis but do such variations occur in practice?". Let us therefore have a look in various sources of variation that do occur when producing and laying an asphalt mixture.

Mohajeri [129] in his thesis measured the temperature of the asphalt mixture during production and laying. Figure 426 shows the double drum mixer on which the measurements were made. In the double drum mixer, the virgin aggregates are preheated in the inner drum and when they reach the end of the drum they are discharged into the outer drum where also Reclaimed Asphalt Pavement (RAP) material, virgin bitumen and filler (fines) are added. The mixture that was analyzed was a mixture in which 50% RAP was used; the RAP was at ambient temperature. In order to arrive to the preferred mixing temperature of around 180 °C, the virgin aggregates should be pre-heated to rather high temperatures in the inner drum. Depending on the moisture content of the RAP which is added in the outer drum where the actual mixing takes place, this temperature can be as high as 500 °C.

Figure 427 shows the temperature distribution of the mixture when being discharged. One will agree that the temperature is not very homogeneous and hot spots due to the super-heated aggregates can easily be recognized.

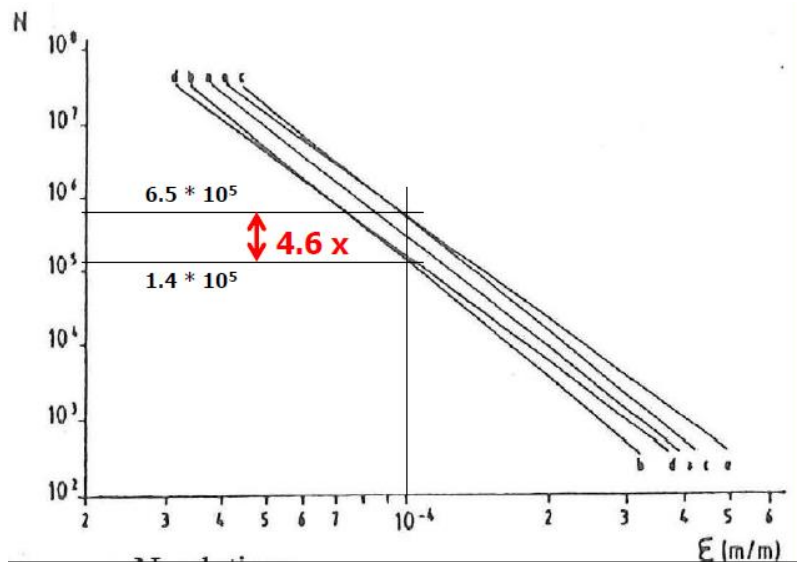


Figure 425: Effect of allowed variations in composition by volume on fatigue characteristics.



Figure 426: Double drum mixer.

Figure 428 shows the variation in temperature during a 30 minutes (1800 seconds) production period. The picture nicely shows the variation in production temperature. This variation in temperature might of course decrease somewhat when the mixture is stored in a silo before being transported to the site.

Based on these findings it was concluded that preheating the RAP to 130 °C in a parallel drum would most probably increase the temperature homogeneity. Preheating of RAP would certainly lead to much lower preheating temperatures of the virgin aggregates.

Mohajeri also did temperature measurements on a construction site and arrived to pictures like those shown in figure 429 and 430.

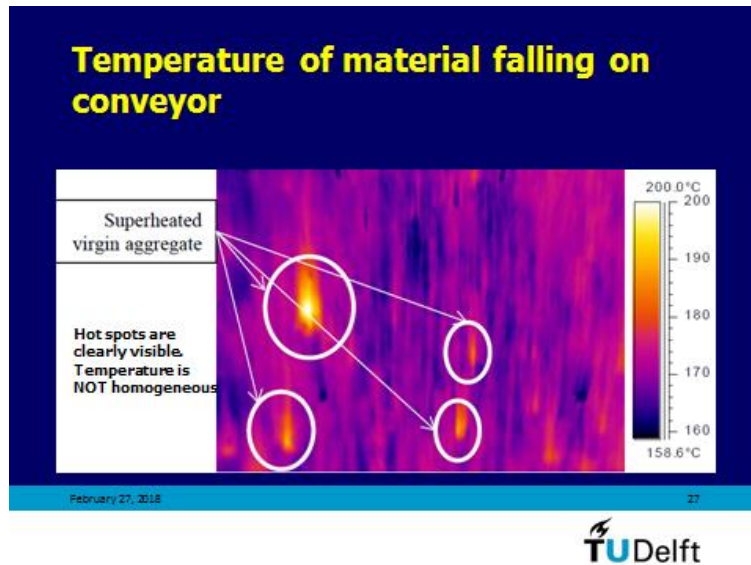


Figure 427: Temperature distribution of the asphalt mixture when being discharged from the outer drum of the double drum mixer.

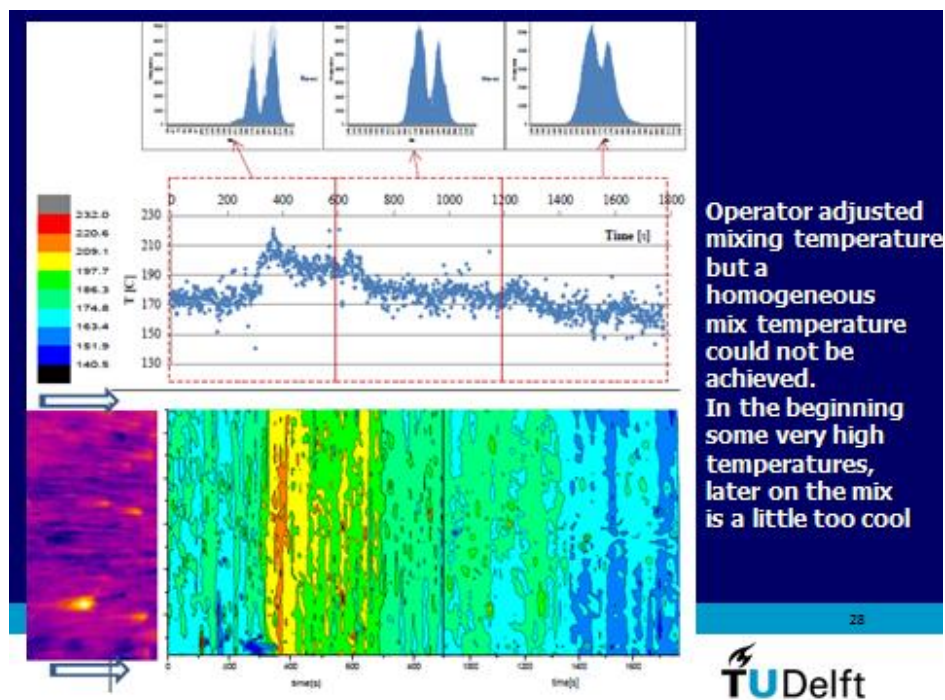


Figure 428: Variation in temperature during a 30 minute production cycle.



Figure 429: Temperature measurements on site.

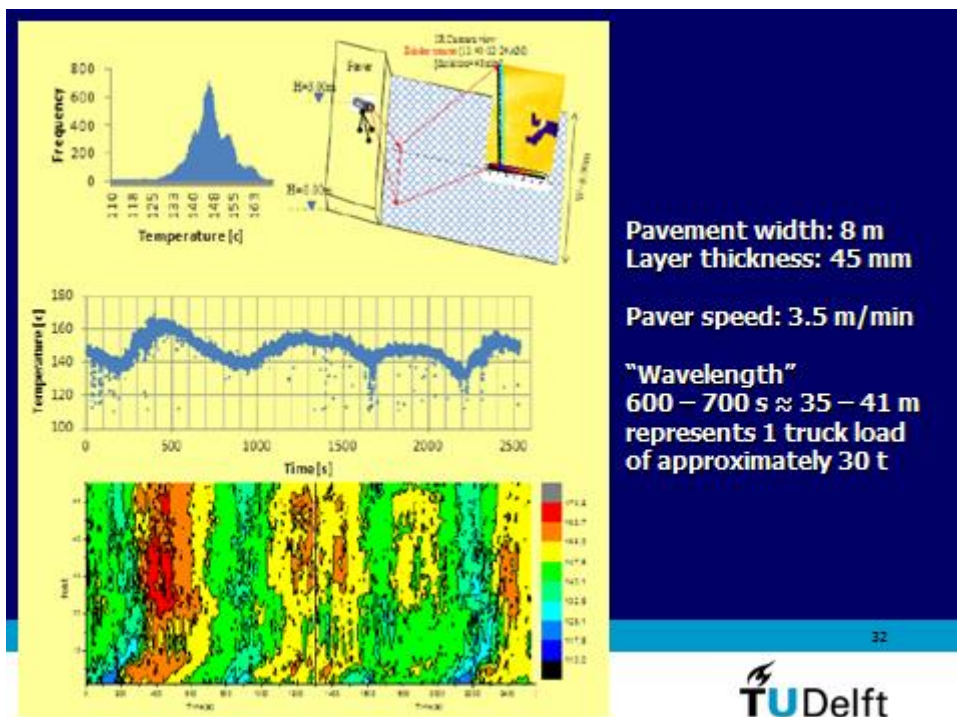
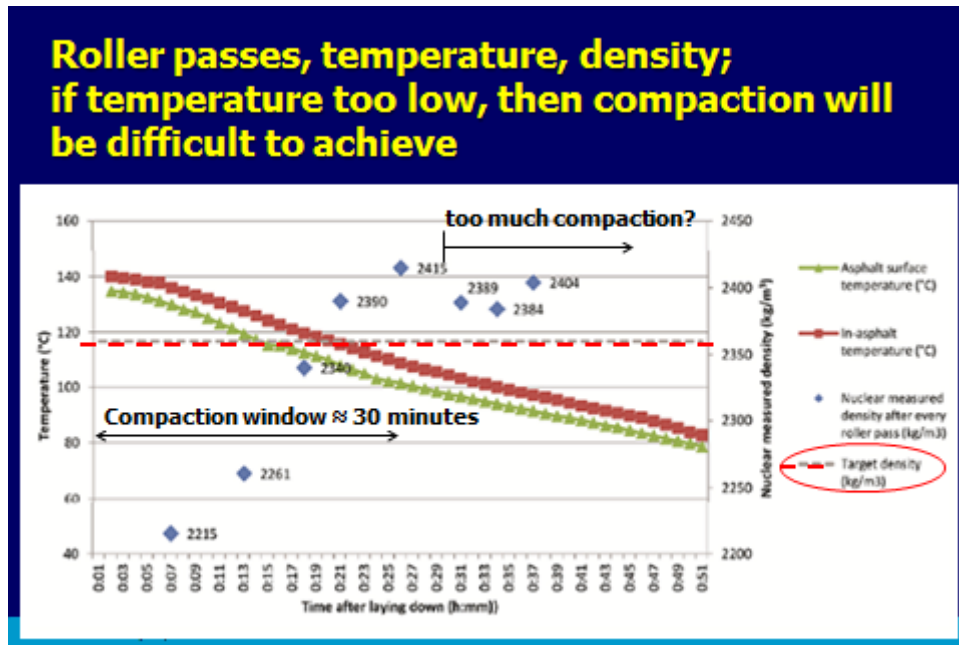


Figure 430: Temperature of the asphalt mat.

Figure 430 clearly shows that the temperature distribution of the asphalt mat as laid is far from homogeneous and it is not unreasonable to assume that this variation in temperature will also have an effect on the mechanical characteristics. Please note that the "wavy" temperature profile (blue line in the middle of figure 430) coincided with the individual truck loads. Figure 429, upper left hand corner, shows that insulated trucks were used to reduce loss of temperature of the mixture when being transported from plant to site but in spite of that a temperature band (variation) of approximately 20 °C occurred.

Compaction of the asphalt mixture is essential to give the mixture its required quality. Sufficient compaction can be achieved when the temperature of the mixture is high enough. Compaction at too low temperatures ($< 90\text{ }^{\circ}\text{C}$) doesn't make sense and might even damage the mixture. Figure 431 gives an example of how compaction developed on a specific site. The picture shows that the maximum density was reached after 5 roller passes. The last 3 passes done at an asphalt temperature of around $100\text{ }^{\circ}\text{C}$ were not effective anymore. The additional passes seemed even to have resulted in a slight decrease in density.



TU Delft

Figure 431: Compaction progress on a specific site [130].

The laying down and compaction of the asphalt mixture should be a well-balanced process. The paving machine should preferably proceed at a not too high speed without stopping and enough rollers should be there to complete compaction within the compaction temperature window. Figure 432 gives some details about the output rate of rollers.

Figure 433 shows the output rate of a paver in a specific project. The picture nicely shows that a constant paver speed is sometimes hard to achieve in practice because of a multitude of reasons. It will be clear however that stopping times of 30 and 45 minutes are not good for the quality of the mixture because the roller cannot compact the asphalt which is placed close to the standing paver.

Roller output rates

- Speed $2.6 < v < 5.1$ km/h
- 4.8 passes on normal sections
- 7.9 passes on special sections (joints, curves etc)
- Output: 996 – 1826 m²/h depending on road geometry
- Pavement geometry has effect on output rates!
- Output rates are variable

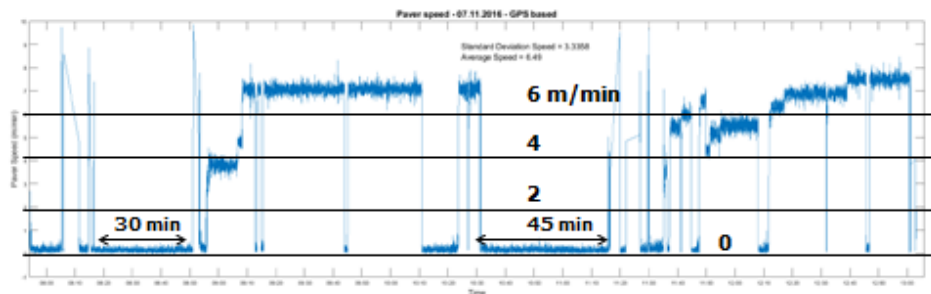
February 28, 2018

33



Figure 432: Output rate of rollers.

**Paver speed; average = 6.49 m/min
standard deviation = 3.34 m/min**



**Normally, speed of asphalt finisher = 3.5 – 4.9 m/min
a standing finisher implies that logistics need to be improved
some asphalt mix cannot be compacted well because of cooling down**

**Variable speed of finisher implies variable compaction
by vibrating beam**



Figure 433: Example of the output rate of a paver on a specific project [130].

Some important remarks with respect to paver speeds are made in figure 434! The most important one being that the vibrating beam at the end of the paver should NOT be switched off! It provides most of the compaction! Not using the vibration beam will allow higher paver speeds and higher production rates (this is being done in a number of countries). A higher paver speed demands however a higher rolling capacity which unfortunately is not always fulfilled.

**Highest paver speed I ever noticed was
14 m/min!**

**You can do this by switching of the
vibrating beam.**

**This is stupid because the beam gives ca
80 - 90 % of the compaction!**

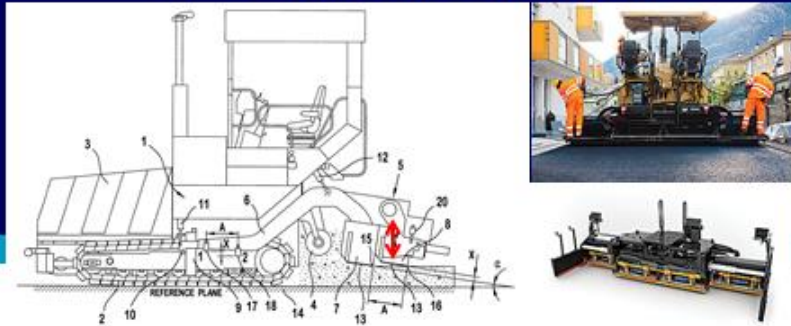


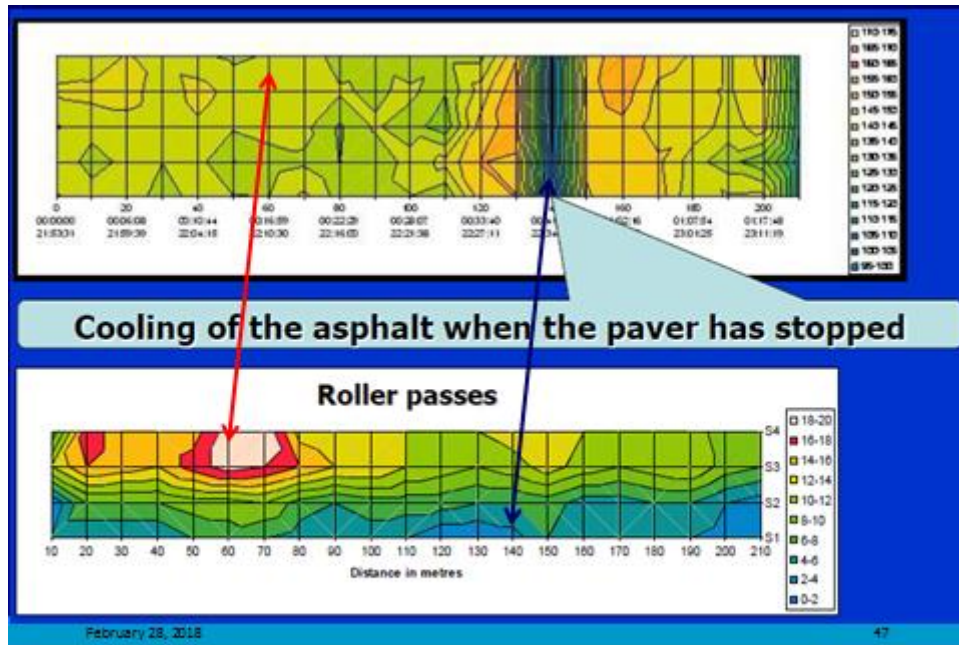
Figure 434: Importance of using the vibrating beam (red arrow) at the back of the paver. From the information given above we can conclude that we can optimize the production and laying process by taking into account the following factors.

- plant production rate,
- production rate of the paver,
- roller production rate,
- number and size of trucks,
- travel distance.

The goal should be an as homogeneously as possible laying and compaction process (homogeneous temperature, homogeneous paver speeds, no stopping times, homogeneous compaction). This implies that one has to optimize logistics!

The last example which shows that one might not always get the pavement that was designed is the following. Figure 435 shows the temperature profile and the number of roller passes as was measured in one of the ASPARI projects [130]. As one will observe, the roller passes were rather unevenly distributed over the pavement and at one location low temperatures were measured because the paver was standing idle there for some time.

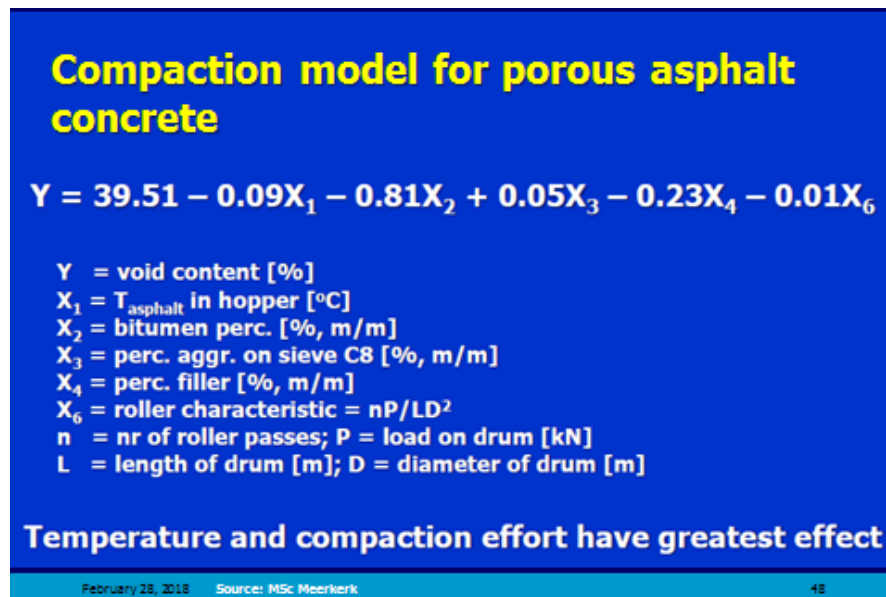
When using the compaction model that was developed by Meerkerk [131] (see figure 436) for PAC and using the relationships he developed to determine the stiffness and the strength of the mixture in relation to the void content, figure 437 could be developed which shows how variable the quality of the pavement will be as a result of the applied roller passes and the mixture temperature. Figure 437 nicely shows that within a distance of 100 m, large variations in stiffness modulus and tensile strength would occur which will certainly affect pavement performance. Unfortunately no condition data are available to substantiate this.



Source: S.R. Miller, Twente University

TU Delft

Figure 435: Temperature profile and roller passes as measured on a particular project.



TU Delft

Figure 436: Compaction model for PAC.

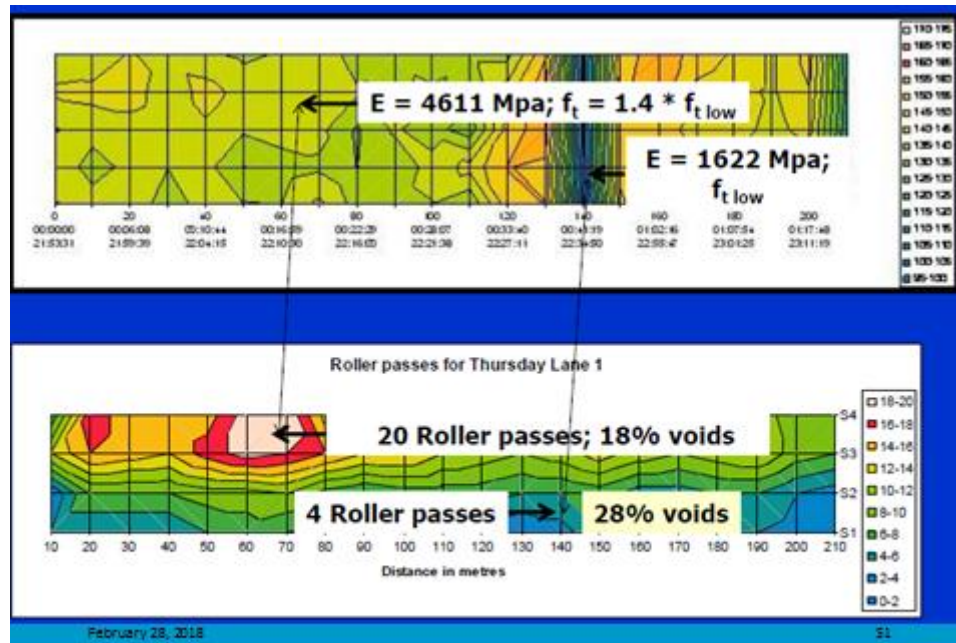


Figure 437: Variation in tensile strength and stiffness modulus as a result of the applied roller passes and temperature distribution.

All in all these examples show that there is a good chance that the asphalt mixture as laid is not the same as the one which was assumed when designing the pavement. Similar “stories” can e.g. be given about the variability of granular bases simply because of the fact that the gradation is certainly not a fixed parameter but will show a fairly large amount of variation from one site to the other simply because the specifications allow such variations to occur and because segregation might occur when dumping and spreading the material on site.

Unfortunately the variability which occurs during production, transportation, laying and compaction cannot be taken into account in the design process because it is “unpredictable”. The magnitude of these variations can only be measured afterwards during e.g. the quality control process.

Next to the fact that due to production, transportation, laying and compaction differences may occur between the mixture that was assumed in the design and the mixture that is actually laid one furthermore has to understand that differences between lab produced mixtures and mixtures placed in the field differ from each other simply due to the differences in lab production and compaction techniques and the ones that are used in the field. This author therefore strongly recommends to do the testing on samples taken from short test sections placed next to the asphalt plant which are made using plant produced material and constructed with real pavers and rollers when mixture characteristics are needed for design purposes and performance predictions. When relative comparisons need to be made between mixtures one can, according to his opinion, rely on laboratory produced and compacted material.

One should however keep in mind that when a particular mixture is tested a second time by the same laboratory or when it is tested at two or more laboratories one will not get the same answers as those one obtained after doing the first series of tests.

We started this section with the question “Do we build what we have designed?”. From the discussions we must come to the conclusion that because of a large number of reasons, the

pavement structure as built might not have the thicknesses and material characteristics which we assumed in our design analyses; we have to live with the fact that fairly large variations in characteristics may occur. This implies that pavement life and performance predictions can never be accurate and precise. Therefore we should make probabilistic analyses in order to determine what the chance will be that the pavement will stay in an acceptable condition. The principles of making such analyses will be discussed in the next chapter.

18 Measuring material properties; how many tests do we need?

There is a Dutch saying which goes "meten is weten". This could be translated in English as "measuring is knowing" but I am not sure whether this is a correct English saying. Anyway, we assume we can obtain knowledge about material characteristics by doing measurements. The question however is "how many measurements should we do to obtain a reliable number?". This is an important question since, as mentioned earlier, we are dealing with (highly) variable materials. In [2] an approach is described which can be used to estimate e.g. the reliability of the mean value which is calculated from a limited number data points. This procedure is in an abbreviated form presented hereafter.

One can calculate a statistical quantity R , called the limit of accuracy, which represents the probable range the true mean differs from the average obtained by " n " tests at a given degree of confidence. The larger the n is, the smaller value will be obtained for R which means that the mean value calculated from the data obtained from the tests will differ less from the true mean value. The mathematical expression is:

$$R = K_{\alpha} (\sigma / \sqrt{n})$$

Where:

- K_{α} = standardised normal deviate which is a function of the desired confidence level $100*(1-\alpha)$,
- n = number of observations,
- σ = standard deviation of the random variable (parameter) considered.

If the confidence level is chosen and if a proper estimate for σ is obtained, R is inversely proportional to the square root of the number of tests. Figure 438 shows the basic shape of the relation between n and R .

As shown in figure 438, 3 zones can be discriminated. In zone I a small increase in the number of tests reduces the value of R tremendously and the accuracy of the predictions will increase drastically. In other words, a small increase in the budget to increase the number of data points is really value for money.

In zone III, R hardly reduces with increasing number of tests. This means that in this case very little extra value is obtained from an increased measurement budget.

The optimal number of tests can be found in zone II.

The main problem in calculating R is the assessment of the standard deviation σ . It is very difficult to give a single value for σ but some guidelines with respect to the coefficient of variation (CV) can be given.

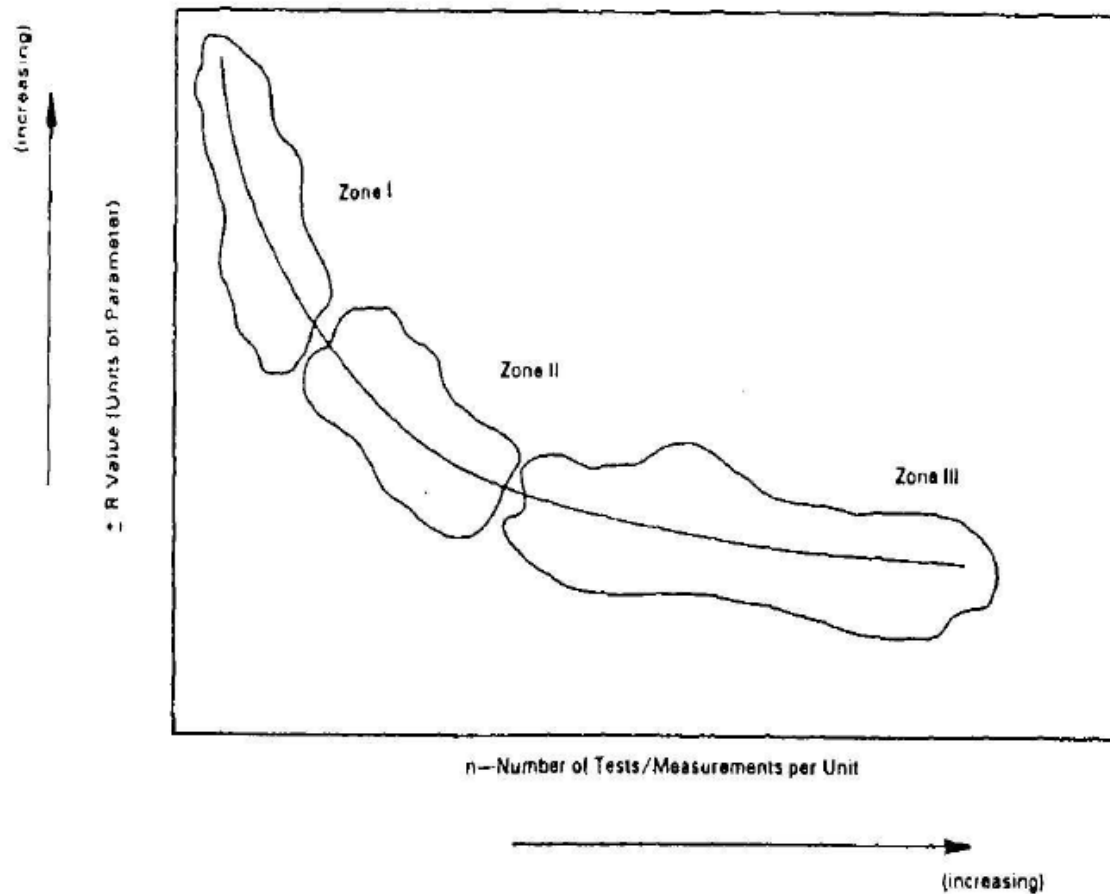


Figure 438: Typical limit of accuracy curve for all variables showing general zones.

Typical values for CV (standard deviation / mean) are given below:

- CV = 0.15, low variation,
- = 0.30, high variation,
- = 0.45, extremely high variation.

To the author's experience, CV is normally somewhere between 0.15 and 0.30 when doing material tests. This could be the CV for the tensile strength obtained from tension tests but also the CV in log N when doing fatigue tests.

By using these CV values and adopting confidence levels of 95% ($\alpha = 0.05$) and 85% ($\alpha = 0.15$), figure 439 has been constructed.

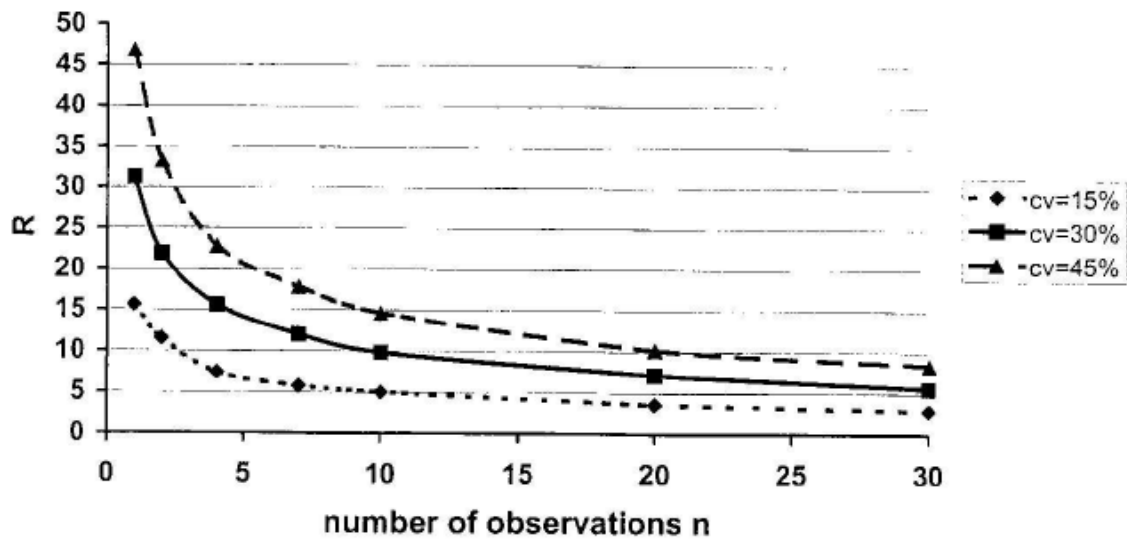


Figure 439a: Graph to estimate the number of observations required at a confidence level of 85%.

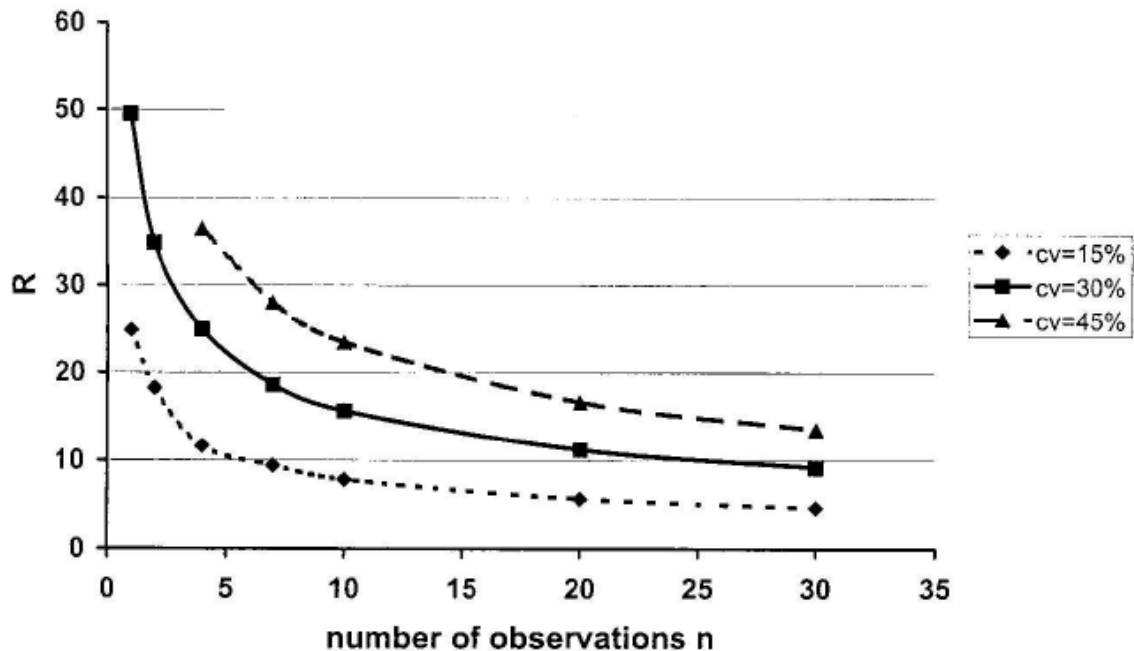


Figure 439b: Graph to estimate the number of observations required at a confidence level of 95%.

The use of the procedure is illustrated by means of the following example. The indirect tensile strength of a stabilized material needs to be determined and the question is how many tests are needed such that the average values differs less than 10% from the true mean. The required confidence level is 95%. From experience we know that the CV of the indirect tensile strength can be taken as 20%. By interpolation the position of the line for CV = 20% is estimated in figure 439b. Using this line and the R value of 10%, the number of tests to be performed is equal to 10! This is a much higher number of tests than we usually perform!

Quite often we only take 3 tests which implies that at a confidence level of 85% and a CV = 20%, the average value calculated from these tests will differ about 10% from the true mean value (use figure 439a to determine this).

All in all this gives "food for thought" when setting up test programs for materials with highly variable properties like road materials.

19 Probabilistic approach to pavement design

We have already discussed applying probabilistic concepts to some extent when presenting the French and Dutch design systems. In this chapter we will deal with this important aspect in much greater detail. Let us start with discussing how variation in stresses and strains in the pavement develop.

In the section on stresses and strains in pavements, charts have been presented for two layer systems which allow the tensile stress at the bottom of the top layer be estimated from the ratio E_1 / E_2 and the ratio h / a where "h" is the thickness of the top layer and "a" the radius of the loaded area. Since E_1 , E_2 , h and a are not fixed values but show a certain amount of variation, also the stress at the bottom of the top layer will show a certain amount of variation. This is schematically shown in figure 440. Failure occurs when the applied stress is larger than the strength of the material but also strength is not a fixed value and will show a certain amount of variation. Failure will occur when the stress is larger than the strength of the material and we can define the probability of failure knowing the distribution of the occurring tensile stress and the strength distribution. This is schematically shown in figure 441.

Based on the strength and stress distribution we can define a difference density function following:

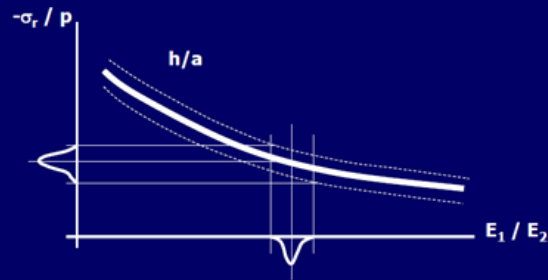
$$D = \text{strength} - \text{stress}$$

$$\mu_D = \mu_S - \mu$$

$$\sigma_D = \sqrt{(\sigma_S^2 + \sigma^2)}$$

Where: μ_S and σ_S are mean and standard deviation of the strength and μ and σ are the mean and standard deviation of the applied stress.

Can we accurately predict stresses and strains?



March 1, 2018

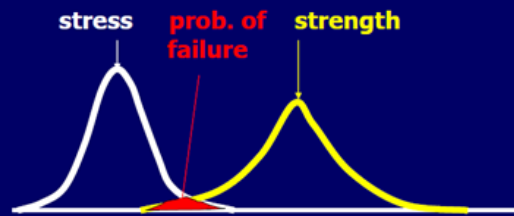
11

TU Delft

Figure 440: Variation in the tensile stress σ_r at the bottom of the top layer of a two layer system as a function of the variation in E_1 / E_2 and h / a .

Note: p = contact pressure.

Stress, strength, failure



March 1, 2018

5

TU Delft

Figure 441: Probability of failure.

The difference density function is shown in figure 442.

The reliability, which is the probability that the structure will not fail (also called probability of survival) is calculated following:

$$R = \int_{-\mu_D/\sigma_D}^{\infty} e^{-\beta} dz / \sqrt{2\pi}$$

Where: $\beta = z^2$ and $z = (D - \mu_D) / \sigma_D$

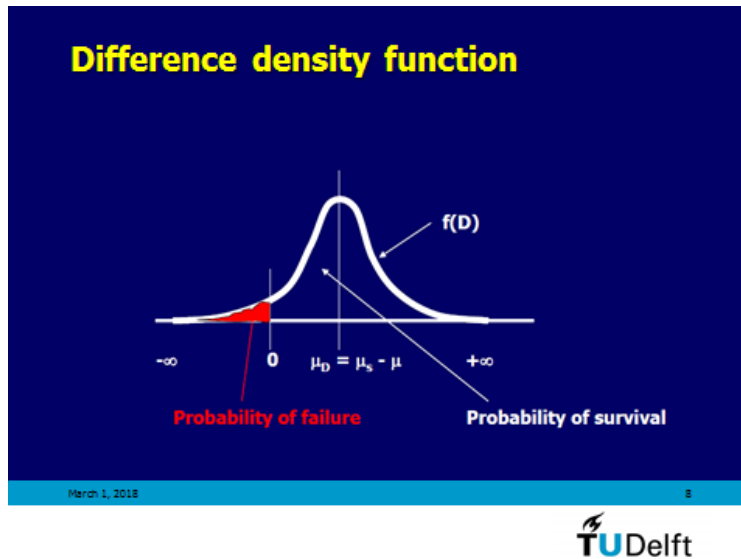


Figure 442: Difference density function.

Let us illustrate this with an example. Assume that the strength and stress characteristics are as follows:

Strength: $\mu_S = 6 \text{ MPa}$ and $\sigma_S = 1 \text{ MPa}$
 Stress: $\mu = 4 \text{ MPa}$ and $\sigma = 0.5 \text{ MPa}$

Then: $Z_0 = -\mu_D / \sigma_D = (\mu_S - \mu) / \sqrt{(\sigma_S^2 + \sigma^2)} = -1.788$

From the normal distribution tables we determine that the area between -1.788 and ∞ equals 0.96. Therefore $R = 96\%$ and the probability of failure = $1 - R = 4\%$.

Let us now consider the fatigue life of an asphalt layer. If we assume that all material characteristics take a constant value, then the tensile strain at the bottom of the asphalt layer due to a fixed load will also take a constant value and will show no variation. When there is also no variation in the fatigue characteristics we can model pavement performance as shown in figure 441. The entire pavement will be in good condition and will show no cracks until the fatigue life is reached and after that moment the pavement will be entirely cracked. Until the number of load repetitions to failure is not reached, the probability of survival equals 1; after the number of load repetitions have been reached the probability of survival = 0.

In reality however all material characteristics (moduli, layer thickness and fatigue resistance) will show some variability so the tensile strain at the bottom of the asphalt layer will show variability. This variability in tensile strain together with the variability in fatigue life results in a probability of survival curve as shown in figure 444. This is the approach which is followed in the French design system.

Figure 444 shows that the variability in fatigue life is controlled by the variation in the tensile strain, the variation in the fatigue characteristics and the slope of the fatigue relation. The steeper the fatigue relationship the bigger the effect of a variation in tensile strain is on the variation in fatigue life. Figure 444 also shows that the location of the probability of survival of the number of load repetitions on the log N axis strongly depends on $\log k_1$ in the fatigue relation (remember: $\log N = \log k_1 - n \log \epsilon$) and as we have shown $\log k_1$ strongly depends on the type of test which is used for the fatigue relationship. This brings in another uncertainty in predicting probability of survival of the pavement in relation to the number of load repetitions.

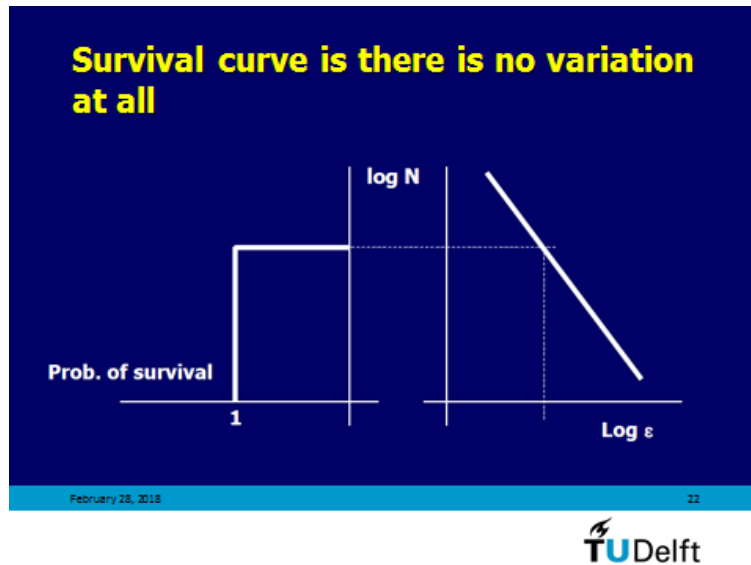


Figure 443: Probability of survival in terms of fatigue life if no variations occur.

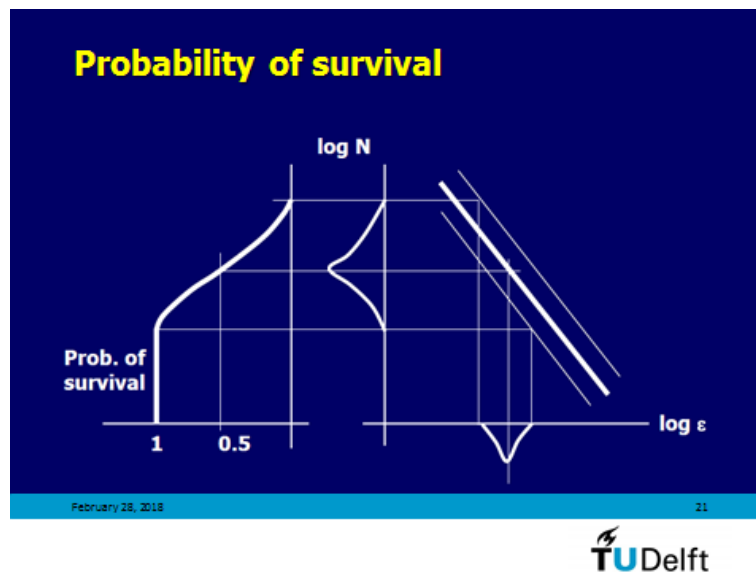


Figure 444: Variation in pavement (fatigue) life due to variations in the tensile strain and variation in the fatigue characteristics.

The question now is how can we incorporate variability in our design analyses? One way to do this is by means of Monte Carlo simulations. Such simulations imply that a large number of calculations are done using each time new values for the input parameters. In such a way a distribution of possible pavement lives can be obtained. For a successful simulation one needs to know the mean value of each parameter and its standard deviation. Also the type of distribution, e.g. normal distribution or a log-normal distribution, should be known. By taking into account the distribution function, a value for each parameter is selected by the pre-processor and in this way a distribution of the lifetime of the pavement can be calculated by repeating the pavement life analyses over and over each time by using different input values.

One should keep in mind that Monte Carlo simulations can take a considerable amount of computation time.

A program which is doing such simulations is the PerRoad 4.4 program which can be downloaded via <http://www.asphaltroads.org/perpetual-pavement/about-perpetual-pavements/>

The program takes the following into account:

- Seasonal pavement layer moduli and annual coefficient of variation (COV).
- Seasonal resilient moduli of unbound materials and annual COV.
- Thickness of the bound layers and COV.
- Thickness of the unbound layers and COV.
- Traffic load spectrum.
- Location for pavement response analysis.
- Magnitude of limiting pavement responses (e.g. the asphalt strain should not be higher than a particular value)
- Transfer functions for pavement responses exceeding the user-specified level for accumulating damage.

The program doesn't take into account the variation in fatigue characteristics although we have just discussed that these have a great effect on the probability of survival curve of the pavement life. PerRoad 4.4 actually only gives the fatigue pavement life in relation to the variation in tensile strain that is calculated.

There are easier ways to determine the variability of pavement life such as approximation of the variances by means of the partial derivative method [132]. This is a relative easy to use and accurate method to determine the variance of rather complex functions. The method is described briefly hereafter.

The method implies that we can calculate the variance V of function $g(x_1, x_2, x_3, \dots, x_j)$ following:

$$V[g(x_1, x_2, \dots, x_j)] \approx \sum_{i=1}^j (\partial g / \partial x_i)^2 * S_{x_i}^2$$

Where: $S_{x_i}^2$ = variance = (standard deviation)² of variable x_i

For example: if: $g(x) = A_0 * x_1 + A_1 * x_1^2 * x_2$, and x_1 and x_2 are random independent variables then:
 $V(x) = (A_0 + 2 * A_1 * x_1 * x_2)^2 * S_{x_1}^2 + (A_1 * x_1^2)^2 * S_{x_2}^2$

If we apply this on the fatigue relationship

$$\log N = \log k_1 - n \log \varepsilon$$

$$\text{we obtain: } V(\log N) = S_{\log N}^2 = S_{\log k_1}^2 + (\log \varepsilon)^2 * S_n^2 + n^2 * S_{\log \varepsilon}^2$$

If we assume that $\log k_1$ and n are constants (which they are not as we have seen before, they are variables which depend on other parameters) then

$$\text{we obtain: } S_{\log N}^2 = n^2 * S_{\log \varepsilon}^2$$

If we assume n is a constant then we obtain: $S_{\log N}^2 = S_{\log k_1}^2 + n^2 * S_{\log \varepsilon}^2$ and this is exactly what we see in figure 444. It is recalled that in many equations that predict the fatigue resistance (SHELL, AASHTO MEPD, French design method) n is indeed taken as a constant.

In order to avoid a Monte Carlo simulation to be used for predicting the variance in the tensile strain we need to predict the tensile strain in another way. If we can derive an equation that

gives us the tensile strain as a function of a number of parameters we then can use the partial derivative method to calculate the variance in the tensile strain.

We have seen that the tensile strain at the bottom of the asphalt layer due to a 50 kN load (radius = 150 mm) can be estimated using:

$$\log \varepsilon_a = 4.241 - 3.24 \log \text{SNC} + 0.211 \log h_1$$

Using the partial derivative method we can calculate:

$$V_{\log \varepsilon} = S^2_{\log \varepsilon} = (-3.24)^2 * V_{\log \text{SNC}} + (0.211)^2 * V_{\log h_1}$$

Since $\log \text{SNC} = \log (a_1 * h_1 + a_2 * h_2 + a_3 * h_3 + \text{SN}_{\text{SG}})$ we can calculate:

$$V_{\log \text{SNC}} = \left\{ \frac{a_1}{(Z * \ln 10)} \right\}^2 * V_{h_1} + \left\{ \frac{a_2}{(Z * \ln 10)} \right\}^2 * V_{h_2} + \left\{ \frac{a_3}{(Z * \ln 10)} \right\}^2 * V_{h_3} + \left\{ \frac{h_1}{(Z * \ln 10)} \right\}^2 * V_{a_1} + \left\{ \frac{h_2}{(Z * \ln 10)} \right\}^2 * V_{a_2} + \left\{ \frac{h_3}{(Z * \ln 10)} \right\}^2 * V_{a_3} + \left\{ \frac{1}{(Z * \ln 10)} \right\}^2 * V_{\text{SN}_{\text{SG}}}$$

$$\text{Where: } Z = a_1 * h_1 + a_2 * h_2 + a_3 * h_3 + \text{SN}_{\text{SG}}$$

Since $\text{SN}_{\text{SG}} = 3.51 * \log \text{CBR} - 0.85 * (\log \text{CBR})^2 - 1.43$ we can calculate

$$V_{\text{SN}_{\text{SG}}} = \left\{ \frac{3.51}{(\text{CBR} * \ln 10)} \right\}^2 * V_{\text{CBR}} + \left\{ -1.7 * \log \text{CBR} * \left(\frac{1}{(\text{CBR} * \ln 10)} \right) \right\}^2 * V_{\text{CBR}}$$

$$V_{\log h_1} = 1 / (h_1 * \ln 10)$$

We have to realize that the variation in the predicted strain is not only due to a variation in $\log \text{SNC}$ and a variation in $\log h_1$. We also have to take into account the variation due to the error in the strain prediction model. We know there is scatter in the relation between $\log \varepsilon_a$ on one hand and $\log \text{SNC}$ and $\log h_1$ on the other. We should take these model errors into account in our strain predictions but quite often we tend to ignore these model errors.

Bouwmeester [133] showed that the maximum error in the log of the tensile strain predicted with the SNC based equation is 4.33 % while the minimum error is -4.29 %. This implies a standard deviation of the error in the predicted log of the tensile strain of $(4.33 + 4.29) / 6 = 1.44$ %

He also reported an equation for the tensile strain at the bottom of the asphalt layer in a 4 layer pavement system which is:

$$\log \varepsilon = \log \left[da \cdot \left(\frac{S_{\text{mix}}}{E_o^*} \right)^{1/3} \cdot \frac{1}{S_{\text{mix}}} \cdot \left(\frac{1}{da} \right)^{c_1} \cdot c_2 \cdot \frac{P}{50} \right]$$

$$E_o^* = E_{o,z} + (E_f - E_{o,z}) \cdot \left(1 - \frac{c_3}{df + c_3} \right)^{c_4}$$

$$E_{o,z} = E_o + (E_z - E_o) \cdot \left(1 - \frac{c_3}{dz + c_3} \right)^{c_4}$$

Where:

- ε = tensile strain at the bottom of the asphalt layer [m/m],
 da = thickness of the asphalt layer [mm],
 df = thickness of the unbound base [mm],
 dz = thickness of the unbound subbase (which is mostly sand in the Netherlands) [mm],
 E_a = stiffness modulus of the asphalt mixture [MPa],
 E_f = stiffness modulus of the base course [MPa],
 E_z = stiffness modulus of the subbase [MPa],
 E_o = stiffness modulus of the subgrade [MPa],
 P = single wheel load [kN],
 $c_1 = 2.56$; $c_2 = 779.88$; $c_3 = 19.61 \cdot 10^6$; $c_4 = 0.09$

The equations have been derived for the ranges of the different parameters shown in table 120.

Variable	h_a [mm]	E_a [MPa]	h_b [mm]	E_b [MPa]	h_{SB} [mm]	E_{SB} [MPa]	E_{SG} [MPa]	P [kN]
Minimum value	150	3000	200	400	250	40	20	50
Maximum value	350	8000	700	1000	1000	300	100	50

Table 120: Range of the values of the variables predicting the tensile strain in the asphalt layer.

The variance in the tensile strain was then calculated as:

$$\begin{aligned}
 V[\log \varepsilon] = & \left(\left(\frac{1}{da} + \frac{-c_1 \cdot da^{-c_1-1}}{\left(\frac{1}{da} \right)^{c_1}} \right) \cdot \frac{1}{\ln 10} \right)^2 \cdot V[da] + \left(\left(\frac{1}{3} \cdot \left(\frac{E_o^*}{S_{mix}} \right) \cdot \frac{1}{E_o^*} - \frac{1}{E_a} \right) \cdot \frac{1}{\ln 10} \right)^2 \cdot V[S_{mix}] + \\
 & - \frac{1}{3} \cdot \frac{1}{E_o^*} \cdot V[E_o^*] + \left(\frac{1}{P} \right)^2 \cdot V[P]
 \end{aligned}$$

With:

$$\begin{aligned}
 V[E_{o,z}] = & \left(\frac{\partial E_{o,z}}{\partial E_o} \right)^2 \cdot V[E_o] + \left(\frac{\partial E_{o,z}}{\partial E_z} \right)^2 \cdot V[E_z] + \left(\frac{\partial E_{o,z}}{\partial dz} \right)^2 \cdot V[dz] = \\
 = & \left(1 - \left(1 - \frac{c_3}{dz + c_3} \right)^{c_4} \right)^2 \cdot V[E_o] + \left(\left(1 - \frac{c_3}{dz + c_3} \right)^{c_4} \right)^2 \cdot V[E_z] + \\
 & \left((E_z - E_o) \cdot c_4 \cdot \left(1 - \frac{c_3}{dz + c_3} \right)^{c_4-1} \cdot \frac{c_3}{(dz + c_3)^2} \right)^2 \cdot V[dz]
 \end{aligned}$$

En:

$$\begin{aligned}
 V[E_o^*] = & \left(1 - \left(1 - \frac{c_3}{df + c_3} \right)^{c_4} \right)^2 \cdot V[E_{o,z}] + \left(\left(1 - \frac{c_3}{df + c_3} \right)^{c_4} \right)^2 \cdot V[E_f] + \\
 & + \left((E_f - E_{o,z}) \cdot c_4 \cdot \left(1 - \frac{c_3}{df + c_3} \right)^{c_4-1} \cdot \frac{c_3}{(df + c_3)^2} \right)^2 \cdot V[df]
 \end{aligned}$$

Although the equation to predict the maximum tensile strain is much more elaborated than the one based on SNC. The maximum error in the predicted log value is 3.5 % while the minimum error is - 3.42 %. This leads to a standard deviation in the predicted log of the tensile strain of $(3.5 + 3.42) / 6 = 1.153$ % which is slightly better than the error related to the SNC based equation.

All these equations look impressive, they are not that difficult to derive. *One only should work carefully and avoid making typing errors (in both I am not that good ;-) so please check the original source.*

In the previous sections we have presented equations to predict the stiffness of the bitumen and asphalt mixture as well as equations to predict "log k_1 " and "n". The partial derivative method can also be used to predict the variance in these parameters when knowing e.g. the variance in the penetration and softening point as well as the variation in the mixture composition. The equation for calculating the variance in log k_1 as presented in [133] is given below.

$$\log k_1 = 6,589 - 3,72 \cdot n + \frac{3209}{S_{mix}} + 2,2332 \cdot \log V_b + 0,149 \cdot \frac{V_b}{V_a} + 0,928 \cdot PI - 0,0721 \cdot T_{r\&k}$$

So we can calculate $V[\log k_1]$ as:

$$V[\log k_1] = [-3,72]^2 \cdot V[n] + \left[-\frac{3209}{S_{mix}^2} \right]^2 \cdot V[S_{mix}] + \left[\frac{2,2332}{V_b \cdot \ln 10} + 0,149 \cdot \left(\frac{1}{100 - V_g - V_b} + \frac{V_b}{(100 - V_g - V_b)^2} \right) \right]^2 \cdot V[V_b] +$$

$$\left[\frac{0,149 \cdot V_b}{(100 - V_g - V_b)^2} \right]^2 \cdot V[V_g] + [0,928]^2 \cdot V[PI] + [-0,0721]^2 \cdot V[T_{r\&k}]$$

It should be noted that in none of the equations for calculating the variances possible dependency of variables of each other is not taken into account. Dependency of variables on each other is certainly the case in the log k_1 equation because S_{mix} is related to PI, softening point $T_{R\&K}$, V_b and V_a . The same is true for parameter "n". This dependency can of course be taken into account, it only makes the equations more complicated and for reasons of simplicity it was decided not to show these more complex equations.

Determining the variances by means of the partial derivative method has the big advantage that the contribution of the variance of each of the parameters to the total variance can easily be determined. This allows a ranking of the importance of the variables on e.g. fatigue life to be made. This then could be very helpful in determining whether all the variables the values of which have been specified in contract documents should carry an equal weight or if some variables are of prime importance or of less importance.

When discussing the AASHTO MEPD method we mentioned that designs could be made on three levels, level 1 being the most advanced level since then all input is determined by means of testing. It has also been mentioned that this will be impossible in many cases because of the costs and time involved. Therefore input is very often generated via the level 2 approach which implies that input parameters are determined via nomographs, regression equations etc. One should however be aware of the fact that all these nomographs and equations carry a model error. We have already mentioned this when discussing the variability in tensile strain due to variation in log SNC and log h_1 . On average they might do a pretty good job but the predicted values might be not close to reality. Typical examples of how big model errors can be are shown

in figures 447 and 448. As one can observe from figure 447, the difference between the S_{mixture} values determined by means of the SHELL equations and the measured values can be as high as ± 1.5 %.

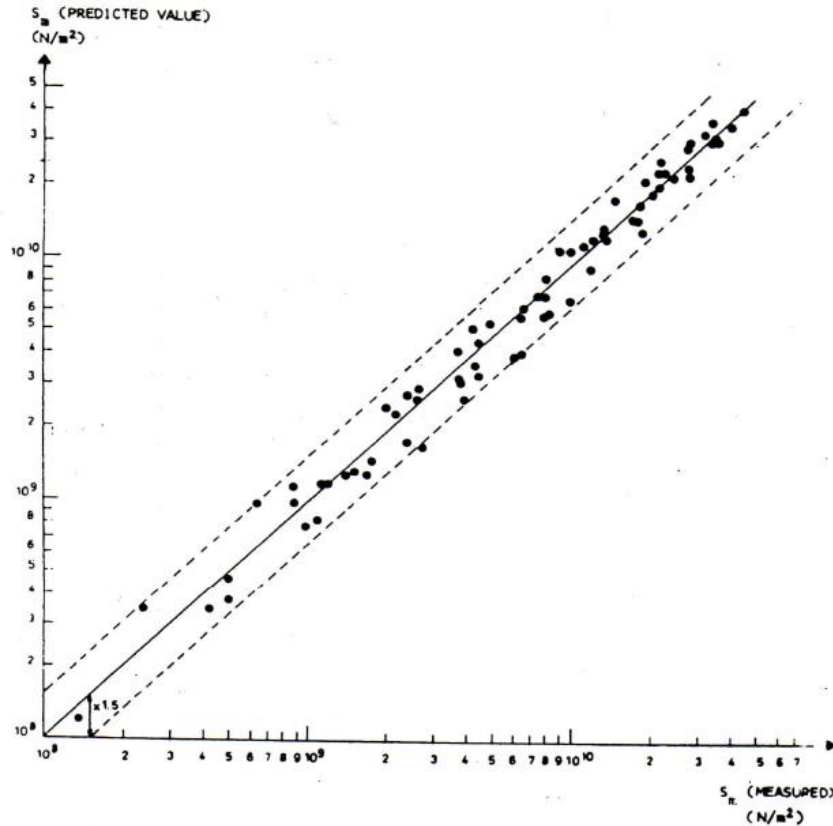


Figure 447: Relation between measured mixture stiffness values and mixture stiffness values as determined by means of the SHELL equations.

Figure 448 shows that the difference between the predicted $\log k_1$ and the measured one can be as high as $\pm 10\%$. Although this doesn't seem too much one has to keep in mind that a 10% difference on a log scale means a quite bigger difference on the linear scale.

All this implies that the total variance in e.g. predicted pavement life might be largely affected by the variance caused by the model errors. Bouwmeester [133] in his work concluded that the predictions on the probability of failure in terms of fatigue life of a pavement were highly affected by the variance of $\log k_1$ and the model error in the equation used to predict $\log k_1$.

This finding has of course consequences on the value we should give to performance predictions. It indicates in any way that we better measure parameters rather than estimating them in case of important projects and in case performance has to be guaranteed over a long period of time.

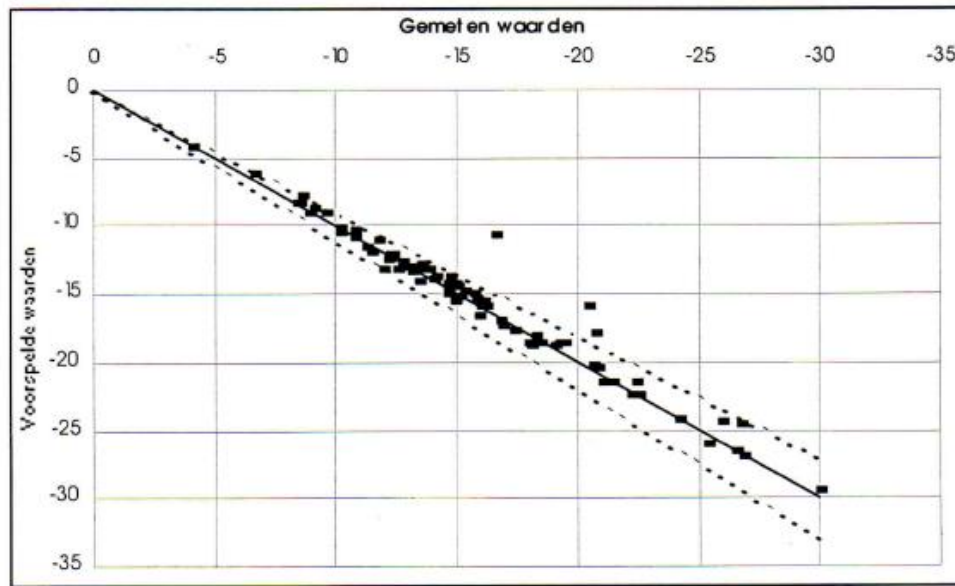


Figure 448: Comparison of the measured log k_1 values (horizontal axis) and the ones predicted with the equation (vertical axis).

20. Relation between contract type, type of specifications and pavement design

It is not the intention to give here an extensive expose on how road building contracts are being formulated. The main purpose of this chapter is to inform the reader about the different types of contracts that exists and the different types of specifications that come with them. We will discuss:

- Traditional contracts which use recipe based specifications.
- Design and construct (DC) contracts where performance related specifications are used.
- Design, build, finance and maintain (DBFM) contracts which are using performance based specifications.

As we will see the role of the client and contractor in a traditional contract is significantly different from the role they play in the DC and DBFM contracts. Also the distribution of the risks in a DBFM contract differs significantly from how the risks are divided in a traditional contract. This has also an effect on how specifications are formulated and quality control is performed.

In general one would expect that a close relation exists between the performance the client wants from the pavement, the thickness design, the specifications set for the structure in terms of materials and layer thicknesses in order to obtain the performance that was expected by the client. It seems a bit odd if there would be little to no relation between the performance expectations, the specifications, and the design and the quality control. It is remarkable to note that in pavement engineering such a logical relation is not always the case. Especially when one is dealing with so called recipe type specifications, the relation between the desired performance and the specifications that are set in order to make sure that one will get the desired performance, is rather weak to say it mildly. Recipe type of specifications strongly rely on the experience of the client and contractor since they know from experience that if a pavement is built according to the specifications it will perform according to the expectations. Past experience

is of course not very helpful when new materials such as polymer modified mixtures, warm asphalt mixtures, crushed masonry and concrete come available and when rapid growth in traffic both in volume and weight is occurring. Therefore other types of specifications have been developed in time which are the so called performance related specifications and the performance based specifications. It should be noted that the type of specifications to be used for a particular project strongly depends on the available testing technology. It doesn't make sense e.g. to set specifications for the asphalt mixture stiffness (which is a performance related parameter) when equipment needed to measure mixture stiffness is hardly or not available. The possibilities to use new types of contracts and specifications strongly depends on the knowledge and testing infrastructure available at the client's and contractor's side. Changing e.g. from a recipe type specification regime to a performance related regime involves large investments in equipment and training of personnel. Therefore one should make a detailed evaluation of the pros and cons of the different contract types before making a decision on which way to go.

20.1 Traditional contracts and recipe type specifications

Recipe type specifications are the "oldest" type of specifications used in road engineering. They perfectly fit in the traditional type of contracts where the client describes in detail "what he wants" and the contractor "does as he is told". With this type of contract the client is responsible for the design and quality control and he is in fact taking most of the risks. In the traditional contracts, the contract is awarded to the contractor who gives the lowest price. Most of the time the warrantee period is limited and can be as short as 1 – 1.5 year (which, according to this author, is ridiculously low); in the Netherlands the warrantee period was 3 years for a long time.

Recipe based specifications for asphalt mixtures include specifications on their gradation and properties of the bitumen used. Furthermore requirements are set on the bitumen and void content, the percentage of voids in the aggregate skeleton as well on the degree of compaction. Also requirements on the quality of the aggregates and particle shape are set.

When the Marshall method is used for the mixture design, then the mechanical properties are defined in terms of Marshall stability, Marshall flow and Marshall quotient. The Marshall test and design procedure will not be described here. The interested reader is referred to e.g. [134].

With respect to unbound materials and soils, recipe specifications specify gradation, degree of compaction and plasticity characteristics of the fine fraction. Furthermore levels are set for the required CBR values in relation to degree of compaction and moisture content.

For cement and lime treated materials requirements are usually set for the unconfined compressive strength or indirect tensile strength.

Next to the requirements set to the materials used in the various layers, also requirements with respect to layer thickness, road surface evenness and skid resistance are defined.

The simple tests that are used in recipe type specifications do not provide information on the stiffness modulus, resistance to permanent deformation and fatigue resistance of the materials. At best one can derive those parameters using relationships between e.g. the volumetric composition of asphalt mixtures on one hand and mechanistic characteristics (stiffness and fatigue etc) on the other. This implies that a mechanistic pavement design based on stresses, strains and transfer functions can only be made using a level 2 design approach if only the material properties as specified in recipe type specs are available.

All this implies that the "distance" between what is designed and built and the pavement performance which is implicitly expected is rather large. One could say that the relation between recipe specs and pavement performance can be compared with the quality of cakes from a bakery namely "having all the ingredients of the cake at the right quality and quantity doesn't necessarily mean that you get a good cake".

20.2 Performance related specifications and contracts

In the Netherlands a new policy with respect to contracting was developed some twenty years ago because of a number of reasons some of which are listed below.

- The vision that the "market should do what the market can do". This vision was inspired on the idea that in many markets the client doesn't interfere with the construction of the product. In case of a car, the client makes his choice based on his preferences for color, design, comfort, accessories, mileage etc and is not involved in the selection of the materials the car is built of and with the construction process.
- The vision that a reduction in technical staff, so a reduction in costs, could be realized at the client's side when tasks (such as design and material selection) which were traditionally done by the client were moved to the contractor.
- The wish that the contractor should take a larger share in the risk.
- The vision that the client should not place emphasis whether all the "ingredients" are used in the right amount (recipe specification) but whether the end result, the performance of the road is to the satisfaction of the client.

This resulted in the so called DC (design – construct) contracts in which the client specified a structural lifetime of 20 years and a lifetime of the wearing course of at least 7 years. The contractor was made responsible for the material selection and the design of the structure which implied he had to collect information on e.g. fatigue and permanent deformation resistance of the asphalt mixtures as well as on the stiffness characteristics. These parameters are not performance parameters but they are parameters which are related to performance.

In order to make sure that he "gets what he wants" the client in this case is checking the performance related parameters. In the Netherlands a rather advanced protocol has been developed for doing so. This protocol involves deflection testing and coring; the protocol is described in appendix D. By means of the protocol it is determined whether the moduli of the asphalt layer, base and subgrade as well as the layer thickness comply with a reliability of 95% with the values used in the design. The values should be reached over at least 95% of the section considered. If the layer thicknesses and/or on stiffness moduli do not pass this test, an equivalent asphalt thickness shortage is calculated on which a penalty is based. If the total equivalent asphalt layer thickness shortage is more than 20 mm then an independent body has to perform an additional evaluation and most probably additional repair work has to be performed. It should be noticed that in case additional asphalt thickness has to be added to the pavement, then this additional asphalt has to be laid below the wearing course. This implies removal of the existing wearing course, placing of the additional asphalt thickness and placement of a new wearing course. It will be clear that such repair work can become rather costly. For the sake of completeness it is recalled that the shortage of asphalt thickness is the sum of:

- real shortage of asphalt thickness
- equivalent shortage in asphalt thickness due to a too thin base course,
- equivalent shortage in asphalt thickness due to too low layer moduli.

The penalty might vary per project; an indicative value is Euro 0.5 / m² per mm asphalt shortage. So if the total asphalt shortage is 10 mm and the size of the project is 10,000 m², the penalty will be Euro 50,000.

A short example will illustrate the effect of the protocol. If e.g. the design asphalt thickness is 195 mm and the area considered is 10,000 m², then a penalty of Euro 10,000 has to be paid in the following cases (table 121):

Average thickness [mm]	Standard deviation [mm]
199	10
204	12
208	14

Table 121: Average thickness and standard deviation resulting in a penalty of Euro 10,000.

No penalty has to be paid for the combinations of average thickness and standard deviation shown in table 122.

Average layer thickness [mm]	Standard deviation [mm]
201	10
206	12
211	14

Table 122: Combinations of average thickness and standard deviation which do not result in a penalty.

It should be mentioned that DC contracts were made possible by the fact that the Netherlands decided to follow the so called "fundamental route" in setting the specifications according to the rules layed out by the European Union. In order to promote freedom of trade, the EU concluded that a harmonization of norms would be essential in order to avoid that national norms were forming barriers against this freedom of trade principle. As part of this harmonization also European norms for asphalt mixtures have been developed.

These norms allow mixtures to be specified in an empirical way (composition, Marshall test results etc) and in a fundamental way. The fundamental way involves specifying mixtures in terms of:

- mixture stiffness in 6 classes,
- fatigue resistance in 8 classes,
- rutting resistance in 7 classes,
- water resistivity in 2 classes.

The EU norms specify several types of tests to determine these characteristics. The Netherlands has chosen for the 4 point bending test for stiffness and fatigue, the triaxial test for rutting resistance and the indirect tensile test for water resistivity.

In the Netherlands each contractor has to specify all mixtures produced by him according to the EC marking system which implies that a code is attached to each mix telling the client what type of mixture he is dealing with, and in which class the characteristics mentioned above are classified. It will be obvious that this is important "design information".

Figure 449 gives the stiffness classification and figure 450 shows the principle of the fatigue classification. Figure 451 gives an example of a mixture classification.

Class	Stiffness modulus E [MPa]
A	$E \geq 14000$
B	$9000 \leq E < 14000$
C	$5500 \leq E < 9000$
D	$3600 \leq E < 5500$
E	$1500 \leq E < 3600$
F	$E < 1500$

Figure 449: Stiffness classification of asphalt mixtures

With respect to the fatigue classification it is noted that no specification for the slope of the fatigue relation is developed. This is a bit remarkable because we have seen that the slope is a true material property and is telling a lot about the behavior of the mixture, while the intercept of the fatigue relation (represented by the ϵ_6 value) is not! Furthermore not specifying the slope could imply that rather brittle mixtures (characterized with a steep slope) can be accepted while such crack sensitive mixtures are not always desire-able.

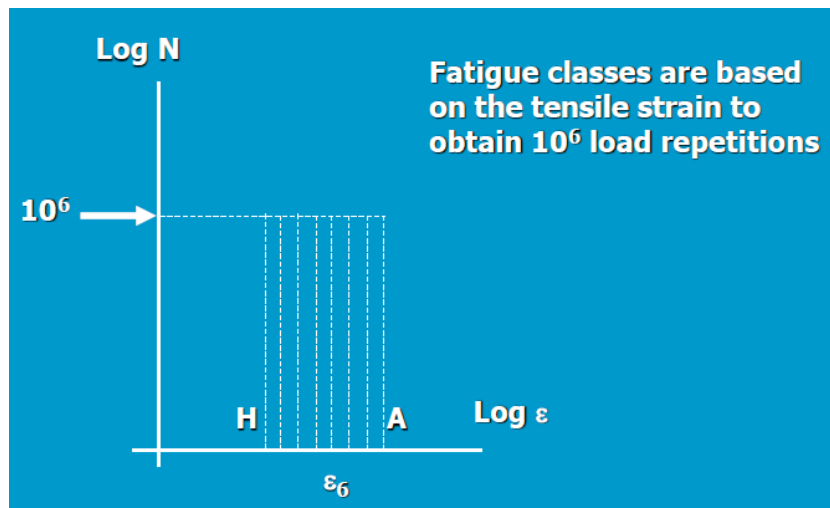


Figure 450: Principle of the fatigue resistance classification.

Note: Classification is done based on the ϵ_6 value which is the strain value at which fatigue failure occurs after 10^6 load repetitions.

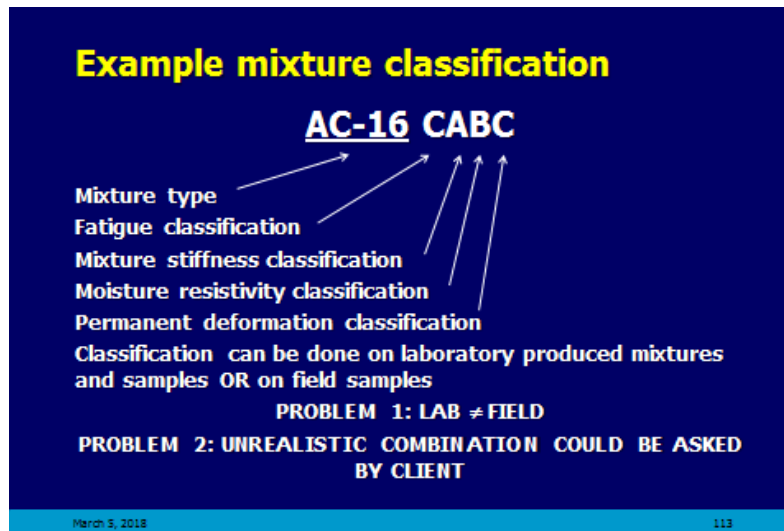


Figure 451: Example of a mixture classification.

Figure 451 also indicates two possible problems with the system. The first one is the fact that when the classification is based on tests on lab produced specimens (which is allowed according to the regulations), this classification might not comply with the classification which would be obtained when testing was done on samples taken from the field. The second problem is that the client, who can use the system to specify his wishes, is specifying an unrealistic combination or a combination which is (very) hard to produce (the client might e.g. ask for a mixture that has AND a high stiffness, AND a high permanent deformation resistance, AND a high fatigue resistance).

The question now is whether “embracing” a DC contract and performance related specifications did solve all potential contractual disputes. The answer is that it didn’t; some of the problems encountered were the following.

- The contractor was focusing on reaching the 7 year minimum life of the wearing course and was “hoping” that he did achieve the 20 year structural life.
- The combination of giving the contract to the lowest bid and applying a bonus – malus regulation in case of early or a too late completion of the work did not always result in an optimal result. The bonus – malus results in an as quick as possible execution of the work which is not always leading to the best result.
- The client had difficulties in defining desired performance.
- There was too often a disappointed client.
- Too many arbitration and court cases.

It became clear that in order to have successful DC contracts, both the client and the contractor must be ready and prepared to work under such a contract. Furthermore it is clear that both the client and the contractor must have enough technical expertise to work with performance related specifications.

20.3 Design, build, finance and maintain contracts

The ultimate type of contracts are the design – build – finance - and maintain (DBFM) contracts in which the contractor is made responsible for the performance of the road for a considerable amount of time. Such contracts are used for building toll roads where the concessionaire is responsible for the performance of the toll road. In such contracts the client is setting minimum

allowable levels for skid resistance, driving comfort, structural performance etc and the contractor/concessionaire is completely free to determine which actions need to be undertaken to comply with the client's demands.

Hereafter some details will be given about a particular DBFM contract in which the author was involved.

The project was a 30 km stretch on a very busy west – east motorway in the Netherlands. It involved widening of the road from 2 * 2 lanes to 2 * 3 lanes, the construction of a few new viaducts and the reconstruction of some existing ones, the lighting system and some other works. The area to be paved was 600,000 m² and the types of wearing courses to be used were double layer porous asphalt concrete over 80% of the area, 15% single layer porous asphalt concrete and 5% dense asphalt concrete. The contract covered a period of 30 years and the service to the road user was the key performance indicator. Also environmental issues played an important role.

Pricing of the project was done in the following way. First of all there was the bid of the consortium; on top of that a fictitious amount of money was placed which was determined by how well the consortium would take care for a number of aspects that were very important to the client. If the consortium complied completely to the wishes of the client, the amount of money added to the bid would be zero. Furthermore the bid was increased by the amount of money the consortium calculated for taking care of some risks.

The ceiling price was Euro 350,000,000.

The aspects which were very important to the client are listed hereafter. Between brackets the maximum amount of money is given which would fictitiously be added to the bid if the answers/proposals given by the consortium were not to the satisfaction of the client. A part would be added if the client was partly satisfied.

- A: Optimum collaboration (15 million).
- B: Minimum traffic disruption during the construction phase (50 million).
- C: Minimum traffic disruption during the operational phase (20 million).
- D: Minimum traffic disruption on the secondary road network during the construction and operational phase (20 million).
- E: Minimization of environmental hinder (15 million).

The overview shows that if the consortium did not comply at all with the wishes of the client, a fictitious amount of 120 million Euro's would be added to his bid.

From the overview it is also clear that "service to the road user" is a key issue in these contracts. This can be seen from the fact that traffic related aspects amounted 75% of the total amount of money that could fictitiously be added to the bid.

The aspect optimum collaboration that was taking into account covered a.o. how fast and accurate information to the public would be given about hinder because of the ongoing and planned works, cooperation with provincial and city authorities involved, cooperation with utility companies like power supply etc..

The aspect minimum traffic disruption of the secondary network was dealing e.g. with measures to be taken to minimize overflow of the secondary network because of temporarily detours necessary because of partly closure of the main road due to the ongoing work.

The aspect minimization of environmental hinder involved traffic noise reducing measures, measures to reduce noise due to construction works like pile driving, and methods and materials to reduce the CO₂ footprint and energy consumption etc.

The risks that needed to be quantified were a.o. delays because of works that needed to be done by other parties like cables and utility works, delays related to getting permits, risks involved with

the fact that the pavement condition of the sections to be reconstructed would be less than quantified and qualified by the client/owner, change in traffic flows etc. For each topic a maximum amount of money to cover the risk was allowed. Also a certain maximum compensation for some risks was defined.

In the contract the number of times and the duration of lane closures because of maintenance is defined. In case lane closures were needed for applying unforeseen emergency maintenance, The following penalties did apply (table 123)

Day / Hr	0 - 5	5 - 8	8 - 22	22 - 24
Mo – Fr	12,500	25,000	25,000	12,500
Sa - Su	12,500	12,500	25,000	25,000

Table 123: Penalty in Euro's per 15 minute per lane in case of lane not being available for traffic.

Table 124 shows the bids, quantified risks and quantified preferences (aspects very important to client) and the total price (EMAP = economical most advantageous proposal).

	Consortium A	Consortium B	Consortium C
Bid	231,649,399	253,059,908	221,016,948
Listed risks	1,500,000	450,000	450,000
Preferences	56,430,929	47,688,006	28,955,052
EMAP	289,580,317	301,197,914	250,422,000

Table 124: Overview of the bids, quantified risks and preferences as proposed by three different consortiums.

From table 124 it will be clear that consortium C was awarded the contract. Consortium C not only had the lowest bid but was also complying the best to the aspects which were important for the client. The fictitious amount of money added to his bid due to not completely fulfilling the client's wishes was the lowest.

As one will have noticed, nowhere in the entire description the words "mechanical characteristics of the asphalt mixtures", "mixture composition", etc appear. This is all left to the consortium/contractor. Although not explicitly mentioned, these items as well as construction techniques are very important aspects in realizing the best solutions for client's wishes B, C and E. A long life pavement structure which needs a minimum of maintenance and which can be placed in the shortest possible time using the most environmentally friendly techniques is highly to be preferred and this requires a proper design and material selection. So the design and material aspects might not be that visible in these contracts, they play a very important role in arriving to the best solution.

In conclusion we can state that with this type of DBFM contract the following is achieved.

- The benefits the client is looking for are defined and quantified in a transparent way.
- To realize these benefits a high quality in design, material selection and construction is required.
- With DBFM contracts, contractors become much more quality conscious because they carry a high risk.
- Contractors see the need for and the benefits of research driven solutions.

21. Closure

An attempt has been made to provide students a reader which can serve as an introduction to the design of flexible pavements. From the wide variety of topics discussed it will be clear that designing a pavement is much more than using a computer program that calculates a "pavement life". It will also be clear that making accurate pavement performance predictions is an impossible task because of the assumptions and simplifications made and because we are dealing with highly variable materials. Perhaps the weakest point in our performance predictions is the quality of the transfer functions we are using. It has been shown several times that correlating predicted fatigue behavior to observed fatigue behavior is still a very hard thing to do and we need calibration/match factors of significant magnitude to match theory with practice. I strongly believe that understanding the causes and reasons for those calibration factors and developing tools to reduce their magnitude should be a research topic for the coming decade. I hope these lecture notes have shown the importance of such research.

As I mentioned in the preface, this reader is far from complete because a large number of topics have remained untouched. I might cover some of them in a next version if I feel the need to rewrite these notes once again.

For now I am wishing you all the best and enjoy your career in the fascinating world of designing, building and maintaining pavements.

References

1. Highway Research Board; *The AASHO Road Test*, Special Report 61. Washington D.C., 1962.
2. AASHTO; *AASHTO guide for design of pavement structures 1986*. Washington D.C., 1986.
3. Paterson, W.D.O.; *Road deterioration and maintenance effects*. John Hopkins University Press. Baltimore, 1987.
4. Boussinesq, M.J.; *Application des potentials à l'étude de l'équilibre et du mouvement des solides élastiques*. Gauthier-Villars. Paris, 1885.
5. Burmister, D.M.; *Theory of stresses and displacements in layered systems and application to the design of airport runways*. Proc. 23rd Annual Meeting Highway Research Board. Washington D.C., 1943.
6. Ahlvin, R.G.; Ulery, H.H.; *Tabulated values for determining the complete pattern of stresses, strains and deflections beneath a uniform circular load on a homogeneous half space*. Highway Research Board Bulletin 342. Washington D.C., 1962.
7. Jones, A.; *Tables of stresses in three layer elastic systems*. Highway Research Board Bulletin 342. Washington D.C., 1962.
8. Peattie, K.R.; *Stress and strain factors for three layer elastic systems*. Highway Research Board Bulletin 342. Washington D.C., 1962.
9. Meier, H.; Eisenmann, J.; Koroneos, E.; *Beanspruchung der Strasse unter Verkehrslast*. Heft 76, Forschungsarbeiten aus dem Strassenwesen. Kirschbaum Verlag. Bonn, 1968.
10. Proceedings 1st International Conference on the Structural Design of Asphalt Pavements. Ann Arbor, 1962
11. Proceedings 2nd International Conference on the Structural Design of Asphalt Pavements. Ann Arbor, 1967
12. Proceedings 3rd International Conference on the Structural Design of Asphalt Pavements. London, 1972
13. Kroezen, M.F.J.M.; *Odemark's theory with respect to the design of road pavements (in Dutch)*. Report 7-71-1, Loab for Road and Railway Research, Delft University of Technology, Delft, 1971.
14. Vesic, A.B.; *Prepared discussion*. Proc. 1st Int. Conference Struct. Design of Asphalt Pavements pp 283 – 290, Ann Arbor, 1967.
15. Harste, E.; *Neue dänische Bemessungsdiagramme im Asphaltstraßen bau*. Bitumen 5/1972
16. Verstraeten, J.; *Stresses and displacements in elastic layered systems*. Proc. 2nd Int. Conference on the Structural Design of Asphalt Pavements. Ann Arbor, 1967.
17. Gerrard, C.M.; Wardle, L.J.; *Stresses, strains and displacements in three-layer elastic systems under various traffic loads*. Australian Road Research Board. Special Report No 4. Vermont, 1976.
18. Kumapley, N.K.; Molenaar, A.A.A.; *Axle load survey report*. Report to the Commission of the European Communities. Accra, 1996.
19. Houben, L.J.M.; Braam, C.R.; Van Leest, A.J.; Stet, M.J.A.; Frénay, J.W.; Bouquet, G. Chr.; *Backgrounds of the VENCON2.0 software for the structural design of plain and continuously reinforced concrete pavements*. Proc. 6th Int. DUT Workshop on Fundamental Modeling of Design and Performance of Concrete Pavements. Old Turnhout, 2006.
20. Al-Ashwal, Y. M.; *Evaluating the performance of highways in Yemen through overlay design for Sanaa – Hodeidah Road*. MSc Thesis TRE 085; International Institute for Infrastructural, Hydraulic and Environmental Engineering. Delft, 2000.
21. Houben, L.J.M.; *Damaging effect of axle loads*. Proc. Sino-Netherlands seminar on Road Maintenance Technology. Hainan, 2005.

22. De Beer, M.; *Reconsideration of the tyre-pavement input parameters for the structural design of flexible pavements*. Proc. 10th Int. Conference on Asphalt Pavements (CD). Quebec, 2006.
23. Groenendijk, J.; *Accelerated testing and surface cracking of asphaltic concrete pavements*. PhD Dissertation Delft University of Technology. Delft, 1998.
24. Park, D.W.; Fernando, E.; Leidy, J.; *Evaluation of predicted pavement response using measured tire contact stresses*. CD Annual Meeting Transportation Research Board. Washington DC, 2005.
25. Myers, L.A.; *Development and propagation of surface-initiated longitudinal wheel path cracks in flexible pavements*. PhD Dissertation University of Florida. 2000.
26. Blab, R.; *Analytische Methoden zur Modellierung der Verformungseigenschaften Flexibeler Fahrbahnaufbauten*. Mitteilungen nr. 11. Institut für Strassenbau und Strassenerhaltung, Technische Universität Wien. Vienna, 2001.
27. Van Gurp, C.A.P.M.; *Characterization of seasonal influences on asphalt pavements with the use of falling weight deflectometers*. PhD Dissertation Delft University of Technology. Delft, 1995.
28. Shell International Petroleum Compny Ltd; *Shell pavement design manual*. London, 1978.
29. Claessen, A.I.M.; Edwards, J.M.; Sommer, P., Ugé, P.; *Asphalt pavement design – the Shell method*. Proc. 4th Int. Conference on the Structural Design of Asphalt Pavements. Ann Arbor, 1977.
30. Saxton, K.E., Rawls, W.J., Romberger, J.S., Papendick, R.I.; *Estimating generalized soil-water characteristics from texture*. Soils Science of America Journal, Vol. 50, No 4. Madison, 1986.
31. ARA, Inc., ERES Division; *Guide for Mechanistic-Empirical Design of New and Rehabilitated Pavement structures, Part 2. Design Inputs*. NCRHP I-37A. Washington DC, 2004
32. Côté, J., Konrad, J.M.; *Assessment of hydraulic characteristics of unsaturated base course materials – a practical method for pavement engineers*. Proc. Int. Workshop on Pavement Engineering from a Geotechnical Perspective (CD). Quebec, 2004.
33. Whiteoak, D.; *The Shell bitumen handbook*. Shell Bitumen UK. Chertsey, 1990.
34. Francken, L., Vanelstraete, A.; *PRADO, design of bituminous mixtures* (in Dutch). Belgian Road Research Centre. Brussels, 1997.
35. Christensen Jr, D.W.; Pellinen, T.; Bonnaquist, R.F.; *Hirsch Model for Estimating the Modulus of Asphalt Concrete*. Journal of the Association of Asphalt Paving Technologists. Lexington, 2003.
36. Antes, P.W., Van Dommelen, A.E.; Houben, L.J.M.; Molenaar, A.A.A., Parajuli, U.; *Stress dependent behavior of asphalt mixtures at high temperatures*. Journal of the Association of Asphalt Paving Technologists. Lexington, 2003.
37. Hagos, E.T.; *The effect of aging on the binder properties of porous asphalt concrete*. PhD thesis Delft University of Technology. Delft, 2008.
38. Pramesti, F.P.; *Laboratory and field asphalt fatigue performance, matching theory with practice*. PhD thesis Delft University of Technology. Delft, 2015.
39. Molenaar, A.A.A.; *Structural performance and design of flexible pavements and asphalt concrete overlays*. PhD thesis. Delft University of Technology. Delft, 1983.
40. Sayegh, G.; *Visco-elastic properties of bituminous mixtures*. 2nd Int. Conf. on Structural Design of Asphalt Pavements. Ann Arbor, 1967.
41. Li, N.; *Asphalt mixture fatigue testing. Influence of test type and specimen size*. PhD thesis. Delft University of Technology. Delft, 2013.
42. Bodin, D.; *Size effect regarding fatigue evaluation of asphalt mixtures*. 2nd European Asphalt Technology Association Meeting, 2006.
43. Van Dijk, W.; Visser W.; *The energy approach to fatigue for pavement design*. Proc. Association of Asphalt Paving Technologists (AAPT), 1977.

44. Gerritsen, A.H.; van Gurp, C.A.P.M.; van der Heide, J.P.J.; Molenaar, A.A.A.; Pronk, A.C.; *Prediction and prevention of surface cracking in asphaltic pavements*. Proc. 6th Int. Conf. Structural Design of Asphalt Pavements. Ann Arbor, 1987.
45. Van Dijk, W.; *Practical fatigue characterization of bituminous mixes*. Proc. Association Asphalt Paving Technologists (AAPT). 1975.
46. Schapery, R.A.; *A theory of crack growth in visco-elastic media*. Report MM 2764-73-1, Mechanics and Materials Research Centre, Texas A&M University. 1973
47. Schapery, R.A.; *A theory of crack initiation and growth in visco-elastic media; I: Theoretical development, II: Approximate methods of analysis, III: Analysis of continuous growth*. Int. Journal of Fracture, Sijthoff and Noordhoff Int. Publishers, Vol. 11, No. 1. Vol. 11, No. 3. Vol. 11, No. 4. 1975.
48. Schapery, R.A.; *A method for predicting crack growth in non-homogeneous media*. Int. Journal of Fracture, Sijthoff and Noordhoff Int. Publishers. Vol. 13, No. 3. 1978.
49. Shook, J.F.; Finn, F.N.; Witczak, M.W.; Monismith, C.L.; *Thickness design of asphalt pavements – the Asphalt Institute Method*. Proc. 5th Int. Conference on the Structural Design of Asphalt Pavements. Delft, 1982.
50. Francken, L; Clauwaert C.; *Characterization and structural assessment of bound materials for flexible road structures*. Proc. 6th Int. Conference on the Structural Design of Asphalt Pavements. Ann Arbor, 1987.
51. Medani, T.O., Molenaar, A.A.A.; *A simplified procedure for the estimation of fatigue and crack growth characteristics of asphalt mixes*. Int. Journal of Road Materials and Pavement Design, vol. 1 issue 4. 2000.
52. Van Gooswilligen, G.; de Hilster, E. Robertus, C.; *Changing needs and requirements for bitumen and asphalts*. Proc. 6th Conference on Asphalt Pavements for Southern Africa. Cape Town, 1994.
53. Qiu, J.; *Self healing of asphalt mixtures; towards a better understanding of the mechanism*. PhD thesis Delft University of Technology. Delft, 2012.
54. Van Lent, D.Q.; *Interfacial interactions and mass transfer at the interfacial region of bituminous hydrocarbon mixtures*. PhD thesis Delft University of Technology. Delft, 2014.
55. Hefer, A.W.; Bashin, A.; Little, D.; *Bitumen surface energy characterization using a contact angle approach*. Journal of Materials in Civil Engineering, Nov – Dec 2006.
56. Van Lent, D.; Li, N.; *Application of the CSME fatigue analysis approach of the Texas A&M University – Model introduction and surface free energy measurements report*. Report 7-10-213-1 Road and Railway Research Laboratory, Delft University of Technology. Delft, 2010.
57. Little, D.; Jones, D.; *Chemical and mechanical processes of moisture damage in hot-mix asphalt pavements*. Moisture Sensitivity of Asphalt Pavements: a National Seminar by the Transportation Research Board. San Diego, 2003.
58. Mo, L.; *Damage development in the adhesive zone and mortar of porous asphalt concrete*. PhD thesis Delft University of Technology. Delft, 2010.
59. Rowe, G.M.; King, G.N.; Anderson, M.; *The influence of binder rheology on the cracking of asphalt mixes*. Presentation at the 4th Int. Conf. on Asphalt Materials. Guangzhou, 2013.
60. Wang, J.; *Characterization of failure and permanent deformation behaviour of asphalt concrete*. PhD thesis Delft University of Technology. Delft, 2015.
61. Muraya, P.M.; *Permanent deformation of asphalt mixtures*. PhD Dissertation Delft University of Technology. Delft, 2007.
62. Molenaar, A.A.A.; *Cohesive and non-cohesive soils and unbound granular material for bases and sub-bases in roads*. Lecture notes CT4850, Part I. Delft University of Technology. Delft, 2005.

63. Kenis, W.J.; *Predictive design procedures, VESYS user manual*. Federal Highway Administration Report No. FHWA-RD-77-154. 1977.
64. Bolk, H.J.N.A.; van der Heide, J.P.J.; van Zantvliet, M.C.; *Basic research into the effect of filler on the mechanical properties of dense asphaltic concrete*. Proc. AAPT, Vol. 51. Kansas City, 1982.
65. Yau, A.; Von Quintus, H.L.; *Study of LTPP laboratory resilient modulus test data and response characteristics*. Federal Highway Administration Report FHWA-RD-02-051. 2002.
66. Huurman, M.; *Permanent deformation in concrete block pavements*. PhD Disseration. Delft University of Technology. Delft, 1997.
67. Van Niekerk A.A.; *Mechanical behavior and performance of granular bases and subbases*. PhD Disseration. Delft University of Technology. Delft, 2002.
68. Huurman, M.; Genene, L.B.; *Repeated load CBR and cyclic load triaxial compression test correlations to determine resilient modulus of subbase sand for mechanistic pavement design*. MSc Thesis. Delft University of Technology. Delft, 2006.
69. Theyse, H.L.; De Beer, M.; Rust, F.C.; *Overview of the South African mechanistic pavement design analysis method*. Paper presented at the 1996 Annual Meeting of the Transportation Research Board (nr. 961294). Washington DC, 1996.
70. Huang, Y.H.; *Pavement analysis and design*. Pearson Education Inc., Pearson Prentice Hall. 2012.
71. Opiyo, T.O.; *A mechanistic approach to laterite based pavements*. MSc Thesis. International Institute for Infrastructural, Hydraulic and Environmental Engineering. Delft, 1995.
72. Barker, W.R.; Brabston, W.N.; Chou, Y.T.; *A general system for the structural design of flexible pavements*. Proc. 4th Int. Conference Structural Design of Asphalt Pavements. Ann Arbor, 1977.
73. CROW; *Design and overlay design for pavements with thin asphalt surfacings (in Dutch)*. Publication 157. Ede, 2002.
74. Alemgena, A.A.; *Characterization of unbound granular materials for pavements*. PhD thesis Delft University of Technology. Delft, 2011.
75. Descornet, G.H.D.; *Repeated compression tests on granular materials*. Proceedings 9th Int. Conf. on Soil Mechanics and Foundation Engineering. Tokyo, 1977.
76. Van Niekerk, Alemgena, A.A.; *Estimation of maximum strains in road bases and pavement performance prediction*. MSc Thesis TRE 127. International Institute for Infrastructural, Hydraulic and Environmental Engineering. Delft, 2002.
77. Felix, T.F.; Molenaar, A.A.A.; Galjaard, P.J.; *In situ evaluation of base course materials*. Report 7-92-209-28-M Laboratory for Road and Railroad Research. Delft University of Technology. Delft, 1992.
78. Carpenter, S.H.; Croveti, M.R.; Smith, K.L.; Rmeili, R.; Wilson, T.; *Soil and base stabilization and associated drainage considerations; Vol I, Pavement design and construction considerations*. Report FHWA-SA-93-004. 1992
79. Carpenter, S.H.; Croveti, M.R.; Smith, K.L.; Rmeili, R.; Wilson, T.; *Soil and base stabilization and associated drainage considerations; Vol II, Mixture design considerations*. Report FHWA –SA-93-005. 1992
80. Van der Spreng, J.G.; *Tensile and compressive characteristics of sand – cement*. MSc Thesis. Delft University of Technology. Delft, 1975.
81. Little, D.N.; Shafee Yusuf, F.A.M.; *Example problem illustrating the application of the National Lime Association mixture design and testing protocol (MDTP) to ascertain engineering properties of lime treated subgrades for mechanistic pavement design/analyses*. Paper presented at TRB. Washington DC, 2001.
82. Getahun, A.S.; *Stabilization of expansive soils for pavement subgrade: a case study on Ethiopian clay*. MSc Thesis TRE 126 IHE. Delft, 2001.

83. Beyene, B.D.; *Stabilization of Ethiopian expansive soil for pavement structures*. MSc Thesis TRE 126 IHE. Delft, 2002.
84. Little, D.N.; *Evaluation of structural properties of lime stabilized soils and aggregates. Vol 1: Summary of findings*. National Lime Association, 1999. (<http://www.lime.org/SOIL.PDF>).
85. Pu, B.; *Analysis of the performance of pavements with a cement treated base*. MSc Thesis Delft University of Technology. Delft, 2007.
86. Xuan, D.; *Cement treated recycled crushed concrete and masonry aggregates for pavements*. PhD Thesis Delft University of Technology. Delft, 2012.
87. Van Rutten, J.; *Mixed granulates in base courses; prediction of mechanical properties from easy to determine material characteristics*. MSc thesis Delft University of Technology. Delft, 2002.
88. Akbarnejad, S.; *Development of an evaluation protocol for self-cementing secondary road base materials*. PhD thesis Delft University of Technology. Delft, 2013.
89. Houben, L.J.M.; *Personal communication about the computer program developed by Houben for determining the development of crack spacing and crack width in time*. Contact l.j.m.houben@tudelft.nl for details.
90. De Bondt A.H.; *Anti-reflective cracking design of (reinforced) asphaltic overlays*. PhD thesis Delft University of Technology. Delft, 1999.
91. Zhou, F; Hu, S.; Hu, X.; Scullion, T.; *Mechanistic empirical asphalt overlay thickness design and analysis system*. Report FHWA/Tx-09/0-5123-3. Texas Transportation Institute, Texas A&M University, 2009. URL: <http://tti.tamu.edu/documents/0-5123-3.pdf>
92. Lytton, R.L.; *Use of geotextiles for reinforcement and strain relief in asphalt concrete*. Geotextiles and Geomembranes, Vol. 8, No. 3. 1989.
93. Jacobs, M.M.J.; de Bondt, A.H.; Molenaar, A.A.A.; Hopman, P.C.. *Crack growth in asphalt pavements (in Dutch)*. Proceedings Wegbouwkundige Werkdagen. CROW, 1992.
94. Dauzats, M.; Linder, R., *A method for the evaluation of the structural condition of pavements with thick bituminous road bases*. Proc. 5th Int. Conf. on the Structural Design of Asphalt Pavements. Delft, 1982.
95. Schmorak, N.; van Dommelen, A.; *Analysis of the structural behaviour of asphalt concrete pavements in SHRP-NL test sections* in Road Safety in Europe and Strategic Highway Research Program (SHRP). Prague, 1995.
96. Jacobs, M.M.J.; *Crack growth in asphaltic mixes*. PhD thesis Delft University of Technology. Delft, 1995.
97. Bode G.; *Forces and movements under rolling truck tires (in German)*. Automobiltechnisches Zeitschrift ATZ, Vol.64, No.10. 1962.
98. Miradi, M.; *Knowledge discovery and pavement performance; intelligent data mining*. PhD thesis Delft University of Technology. Delft, 2009.
99. Huurman, M.; Mo, L.; Woldekidan, M.; Khedoe, R.; Moraal, J.; *Overview of the LOT meso mechanical research into porous asphalt paving*. Proc 7th Int. RILEM Symposium Advanced Testing and Characterization of Bituminous Materials. Rhodes, 2009.
100. Huurman, M.; Mo, L.; Woldekidan, M.; *Unraveling porous asphalt concrete. Towards a mechanistic material design tool*. Int. Journal Road Materials and Pavement Design, ICAM 2009, Vol. 10, Special Issue 2009.
101. Mohan, S.A.; *Winter damage of porous asphalt*. MSc thesis Delft University of Technology. Delft, 2010.
102. Milne, T.I.; *Towards a performance related seal design method for bitumen and modified road seal binders*. PhD thesis University of Stellenbosch. Stellenbosch, 2004.
103. Gerber, J.A.K.; *Numerical modelling of performance and failure criteria for surfacing seals*. PhD thesis University of Stellenbosch. Stellenbosch, 2016.

104. Terrel, R.L.; Al-Swailmi, A.; *Water sensitivity of asphalt – aggregate mixes; test selection*. Report SHRP-A-403, 1994.
105. Li, M.; *Tyre-road noise, surface characteristics and material properties*. PhD thesis Delft University of Technology. Delft, 2013.
106. Kringos, N.; *Modelling of combined physical-mechanical moisture induced damage in asphaltic mixes*. PhD thesis Delft University of Technology. Delft, 2007.
107. Varveri, A.; *Moisture damage susceptibility of asphalt mixtures – Experimental characterization and modelling* -. PhD thesis Delft University of Technology. Delft, 2017.
108. Kane, M.; Scharnigg, K.; *Report on different parameters influencing skid resistance, rolling resistance and noise emissions. Deliverable D10*. TYROSAFE program, EC 7th framework programme. 2009 <http://tyrosafe.fehrl.org>
109. Andriejauskas, T.; Vorobjovas, V.; Mielonas, V.; *Evaluation of skid resistance characteristics and measurement methods*. 9th Int. Conf. Environmental Engineering. Vilnius. 2014. [Leidykla.vgtu.lt/conferences/ENVIRO.../141 Andriejauskas.pdf](http://Leidykla.vgtu.lt/conferences/ENVIRO.../141_Andriejauskas.pdf)
110. Erichson, E.; Ulvik, A.; Wolden, K.; Neeb, P.R.; *Aggregates in Norway, properties defining the quality of sand, gravel and hard rock for use as aggregate for building purposes*. Geological Survey of Norway. Trondheim. 2004. Citeseerx.ist.psu.edu/viewdoc/download?doi=10.1.1...type...
111. EAPA. *Asphalt surface courses; skid resistance*. <http://www.eapa.org/userfiles/2/DAV/Skid%Resistance.pdf>
112. Hosking, J.R.; Szatkowski, W.S.; *The effect of traffic and aggregates on the skidding resistance of bituminous surfacings*. TRL Report LR 504. Transport Research Laboratory. 1972.
113. Roe, P.G.; Hartshorne, S.A.; *The polished stone value of aggregates and in service skidding resistance*. TRL report 322. Transport Research Laboratory. 1999.
114. Design manual for roads and bridges HD 28/04; Skid Resistance. www.ukroads.org/.../HD%2028-04%20Skid%Resistance.pdf
115. Sandberg, U.; Ejsmont, J.; *Tyre/road noise reference book*. Kisa, Sweden. 2002.
116. Xiao, Y.; *Towards a performance evaluation method for durable and sustainable thin surfacings*. PhD thesis Delft University of Technology. Delft, 2013.
117. Lanoye, R.; de Bree, H.E.; Lauriks, W.; Vermeir, G.; *A practical device to determine the reflection coefficient of acoustic materials in-situ based on a Microflown microphone sensor*. Int. Conf. on Noise and Vibration Engineering. Leuven, 2004.
118. Stenschke, R.; *Dependency of riding comfort and dynamic axle loads on road roughness (in German)*. PhD thesis, Technical University of Berlin. Berlin, 1977.
119. Jain, S.P., McCullough, B.F.; Hudson, W.R.; *Flexible pavement design system – second generation, incorporating fatigue and stochastic concepts*. Research Report 123-10, Center for Highway Research, University of Texas at Austin. Austin, 1971.
120. Erkens, S.M.J.G.; *Asphalt Concrete Response - Determination, Modeling and Prediction*. PhD thesis, Delft University of Technology. Delft, 2002.
121. Medani, T.O., *Design principles of surfacings on orthotropic steel bridge decks*. PhD thesis, Delft University of Technology. Delft, 2006.
122. Texas Department of Transportation; *Pavement manual, revised 2017*. <ftp://ftp.dot.state.tx.us/pub/txdot-info/cst/>
123. Liu, W.; Scullion, T.; *Flexible pavement design system FPS21, User's Manual*. Texas Department of Transportation and Texas Transportation Institute. Austin, 2011. <http://manualzz.com/doc/6611714/flexible-pavement-design-system-fps21--user-s-manual>
124. Sadek, H.; *Mechanistic-based characterization of fatigue resistance of alternative mix designs*. PhD thesis University of Liverpool. Liverpool, 2015.
125. ARA, INC., ERES Consultants Division; *Guide for mechanistic-empirical design of new and rehabilitated pavement structures. Part 3 Design Analysis. Chapter 3 Design of new and reconstructed flexible pavements*. 2004

126. www.arc.unr.edu/software.html
127. Department of Transport; *Structural design of flexible pavements for interurban and rural roads TRH4*. Pretoria, 1996.
128. Van Gurp, C.A.P.M.; Wennink, P.M.; *Pavement design for rural roads (in Dutch)*. KOAC.WMD consultants. Apeldoorn, 1996
129. Mohajeri, M.; *Hot mix asphalt recycling; practices and principles*. PhD thesis Delft University of Technology. Delft, 2015.
130. ASPARI, see <https://www.utwente.nl/en/et/aspari/> other sites are also available such as aspari.nl/index.php?page=news-2
131. Meerkerk, A.J.J.; *Variation in quality of new porous asphalt concrete (in Dutch)*. MSc thesis Delft University of Technology. Delft, 2004.
132. Haugen, E.B.; *Probabilistic approaches to design*. John Wiley and Sons Inc. 1968
133. Bouwmeester, D.; *Probabilistic design of asphalt pavements – design based on fatigue cracking- (in Dutch)*. MSc thesis, Delft University of Technology. Delft, 2001.
134. Asphalt Institute; *MS-4 The asphalt handbook 7th edition*
135. Emery, S.J.; *The prediction of moisture content in untreated pavement layers and an application to design in Southern Africa*. CSRI Research Report 644. Pretoria, 1988.
136. Sweere, G.T.H.; *Vehicle simulation on the hybrid computational device AD4-IBM1800 (in Dutch)*. Report WB-18 (7-80-115-11) Road and Railway Research Laboratory, Delft University of Technology. Delft, 1980.
137. Van den bergh, W.; *The effect of ageing on the fatigue and healing properties of bituminous mortars*. PhD thesis Delft University of Technology. Delft, 2011.
138. LCPC, SETRA; *French design manual*. 1997
139. Department of Large Projects and Maintenance Dutch Ministry of Transport; *Specifications design asphalt pavements (in Dutch)*. Delft, 2014.

APPENDIX A

Factors influencing accuracy of fatigue performance predictions

A1. Introduction

As we mentioned before, fatigue analyses are usually done by calculating the maximum tensile strain at the bottom of the asphalt layer, using that value as input in a laboratory determined fatigue relationship, and applying some correction or calibration factors to arrive to the number of load repetitions to failure. This process is schematically shown in figure A1.

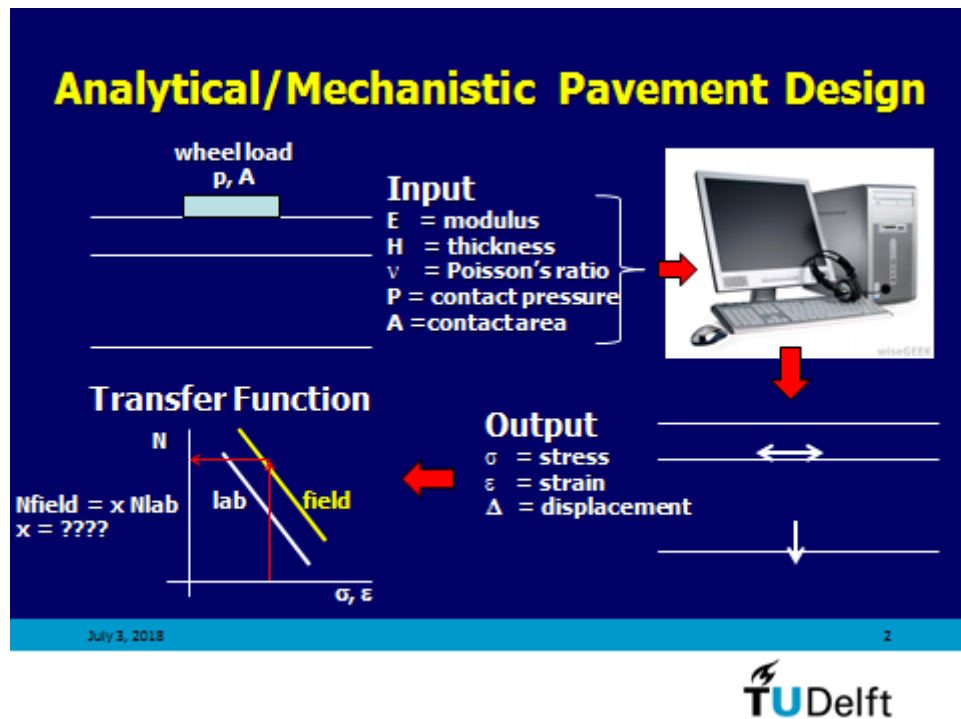


Figure A1: Principles of mechanistic empirical design methods.

As we have shown, we are making simplifications and assumptions in the design process which can significantly affect the result. The the most important influence factors are:

- simplification of the wheel load,
- simplification of the 3D stress/strain situation to a 1D situation,
- the applicability of the used fatigue relationship,
- the definition of failure.

A2 Effect of simplifying the wheel load

We have seen in the section on wheel loads and contact pressures, that the contact pressure distribution is complex and by far not homogeneously distributed over the contact area and certainly not equal to the tire pressure as we often assume. Furthermore the contact area is not

circular but rectangular. A method developed by Fernando e.a [24] has been presented which “takes care” for the differences between reality and what we assume; this resulted in an equivalent contact pressure p_e and an equivalent radius of the contact area r_e . The effects of taking into p_e and r_e were analyzed by means of an example problem the details of which are shown in figure A2. The tire was assumed to be the super single tire as used by Groenendijk [23] in his research. The fatigue life based on the maximum horizontal strain at the bottom of the asphalt layer in case of using r_e and p_e appeared to 74% of the fatigue life assuming a contact pressure equal to the tire pressure of 700 kPa and a radius of the loaded area of 150 mm. This result cannot be generalized because it depends on the type of tire, fatigue relationship applied etc.

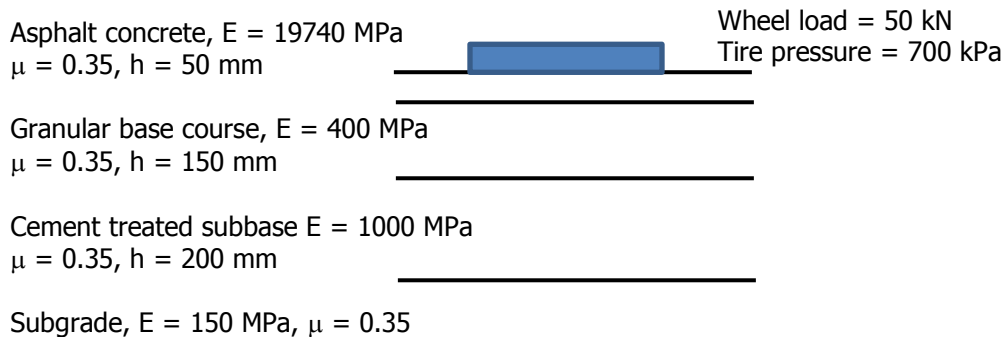


Figure A2: Pavement design example.

Note: the asphalt stiffness is for a fine dense asphalt concrete at 10 Hz and 5 °C. Data are taken from Li [41].

All in all this small example is a warning that assuming a circular contact area with a contact pressure equal to the tire pressure might result in an overprediction of pavement life! Fernando [24] however also showed that the effect of not taken into account the real contact pressure distribution on the tensile strain at the bottom of the asphalt layer “disappears” for thicker asphalt layers ($> 100 \text{ mm}$).

A3 Effect of simplifying 3D stress/strain conditions into 1D conditions.

As mentioned above, the standard procedure is to use the maximum tensile strain at the bottom of the asphalt layer as input in the fatigue relation.

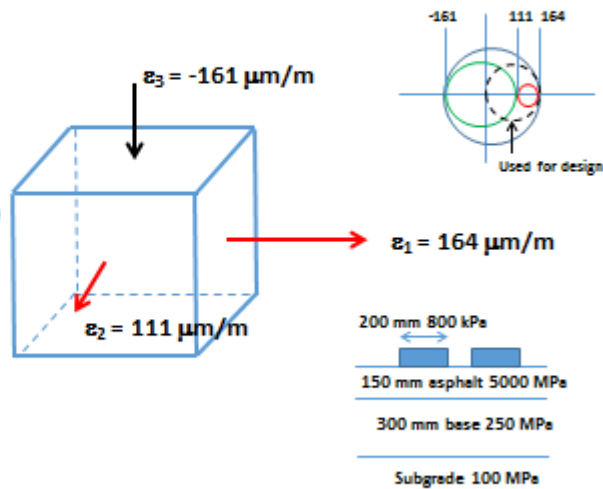
This principle does however imply that we ignore the effect of the other two principal strains. An example of this is given in figure A3. It seems very likely that we overestimate the fatigue life by ignoring what happens in the other two directions. In order to be able to determine this we need to know when and how materials fail under 3D stress conditions. So let us have a closer look into fatigue test results in relation to their yield surface (failure line).

When we perform a compression test we arrive to a stress – strain relation as shown in figure A4. A similar curve will be obtained when we perform a tension test.



Fatigue life based on maximum tensile strain?

We take into account the major principal (tensile) strain. What are we doing with the intermediate and minor principal strain? Are we ignoring them?



8th RILEM International Conference on Mechanisms of Cracking and Debonding in Pavements (MCD2016)

Figure A3: 3D strain conditions at the bottom of the asphalt layer.

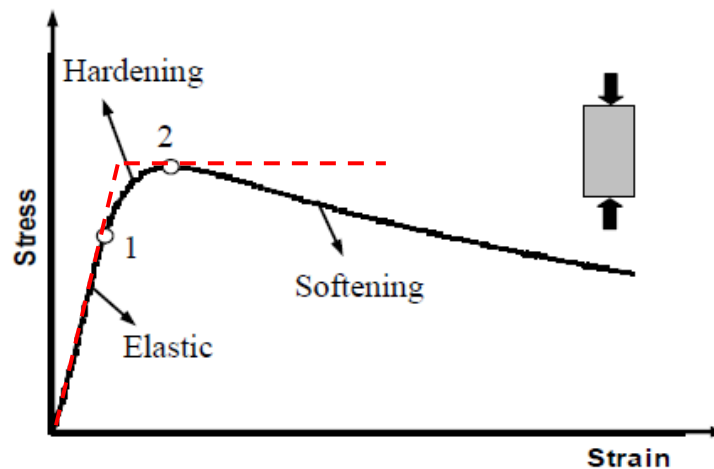


Figure A4: Response of asphalt concrete when subjected to a compression test and simplified elasto-plastic model (red dashed line).

Note: the simplified elasto-plastic model is the basis for the Mohr-Coulomb surface which will be discussed later on.

Since asphalt concrete is an elasto-visco-plastic material, the shape of the curve is dependent on the test temperature and strain rate. A yield surface characterizes the combination of stresses and strains which result in failure. When the stress conditions are below the yield surface, the material will fail at the first load application. Desai has formulated how the yield surface depends on the stress conditions and material characteristics. He showed that the yield surface can be written as follows:

$$f = \frac{J_2}{P_a^2} - \frac{\left[-\alpha \left(\frac{I_1 - R}{P_a} \right)^n + \gamma \left(\frac{I_1 - R}{P_a} \right)^2 \right]}{\sqrt{(1 - \beta \cos(3\theta))}} = 0$$

Where:

- σ_i = ith principal stress,
- I_1 = first stress invariant,
- J_2 = second stress invariant,
- p = isotropic stress,
- θ = lode angle,
- P_a = atmospheric pressure = 0.1 MPa,
- $\alpha, \beta, \gamma, n, R$ = model parameters.

$$I_1 = \sigma_1 + \sigma_2 + \sigma_3$$

$$J_2 = \frac{1}{6} \left[(\sigma_1 - \sigma_2)^2 + (\sigma_2 - \sigma_3)^2 + (\sigma_1 - \sigma_3)^2 \right]$$

The model is shown in figure A5.

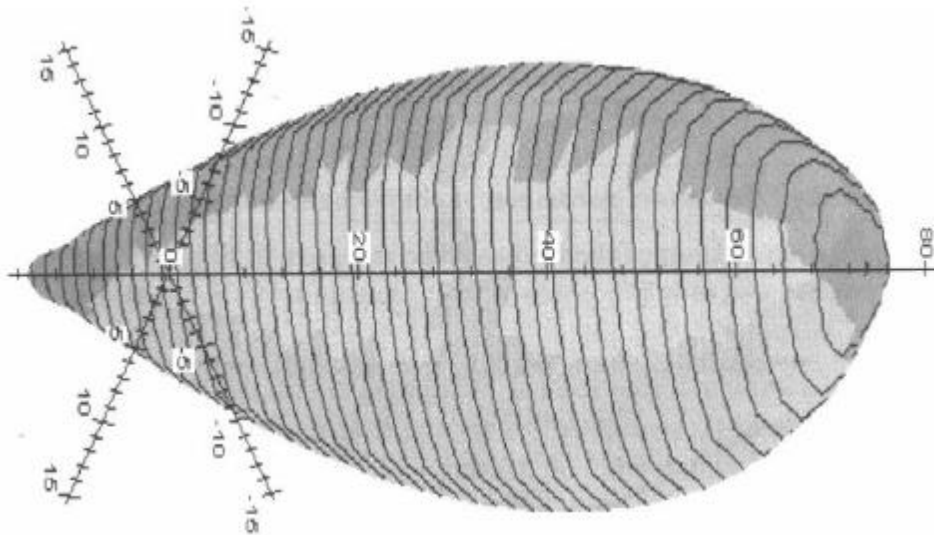


Figure A5: Desai's response surface.

Desai's response surface exhibits a spindle shape in the $I_1, \sqrt{J_2}$, lode angle θ plane (see figure A5). The size, shape and position of the yield surface are controlled by the model parameters α, β, γ, n and R which are related to the properties of the material and can be directly determined by means of laboratory tests.

At peak stress the parameter $\alpha = 0$.

The parameter β determines the shape of the model on the octahedral plane. For $\beta = 0$ it is a circle and with increasing β it becomes triangular. In order to simplify the model β is often taken as $\beta = 0$ and in that case the model reduces to:

$$f = \frac{J_2}{P_a^2} - \left[-\alpha \left(\frac{I_1 - R}{P_a} \right)^n + \gamma \left(\frac{I_1 - R}{P_a} \right)^2 \right] = 0$$

For a uniaxial test, like the compression and tension test, we can write:

$$\sigma_1 = \sigma, \sigma_2 = \sigma_3 = 0 \Rightarrow$$

$$I_1 = \sigma_1 + \sigma_2 + \sigma_3 = \sigma$$

and

$$J_2 = \frac{1}{6} \left[(\sigma_1 - \sigma_2)^2 + (\sigma_2 - \sigma_3)^2 + (\sigma_1 - \sigma_3)^2 \right] = \frac{1}{3} \sigma^2$$

When we substitute this in Desai's equation we obtain:

$$\frac{\sigma^2}{3P_a^2} = \left[-\alpha \left(\frac{\sigma - R}{P_a} \right)^n + \gamma \left(\frac{\sigma - R}{P_a} \right)^2 \right]$$

When $\alpha = 0$, we can write:

$$J_2 = \gamma (I_1 - R)^2$$

The question now is how this information can be used for fatigue analyses. Well, this is in fact very simple. It will be easy to understand that the farther the stress conditions are away from the yield surface, the more load repetitions the material can take so we might be able to develop a relationship between the distance to the yield surface on one hand and the number of load repetitions on the other.

The flow surface can be defined by doing uni-axial tension and compression tests. In that case I_1 and J_2 can be written as follows.

$$\text{Tension test:} \quad I_1 = f_t \quad J_2 = f_t^2 / 3 \quad f_t = \text{tensile strength}$$

$$\text{Compression test:} \quad I_1 = f_c \quad J_2 = f_c^2 / 3 \quad f_c = \text{compressive strength}$$

It should be noted that flow surfaces based on strain can be formulated along the same lines; the σ parameters in the equations should then be replaced by ε parameters.

When defining I_1 and J_2 based on the strains occurring in a tension or compression test one need to take into account the strains that occur perpendicular to the line of loading (see figure A6).

In the tension and compression test we have a principal strain in the direction of the load (vertical deformation) and two horizontal principal strains which are equal to each other. Both

horizontal strains have the sign which is opposite to the sign of the vertical strain. Taking all this into account, I_1 and J_2 in terms of principal strains become:

$$I_1 = \varepsilon_v + 2 \varepsilon_h \quad \text{and} \quad J_2 = (\varepsilon_v - \varepsilon_h)^2 / 3$$

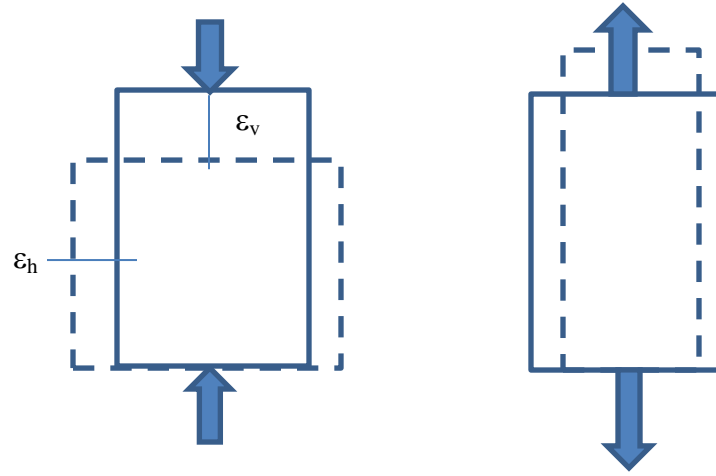


Figure A6: Deformations in a compression (left) and a tension (right) test. Also a deformation perpendicular to the paper exists; this one is equal to the horizontal deformation indicated in the figure.

Figure A7 shows a number of yield surfaces, formulated following the equations given above, as determined by means of the UTC test for the fine graded dense asphalt concrete which we use for the example problem [41]. The data points indicating different strain levels are the conditions at which UTC fatigue tests were performed.

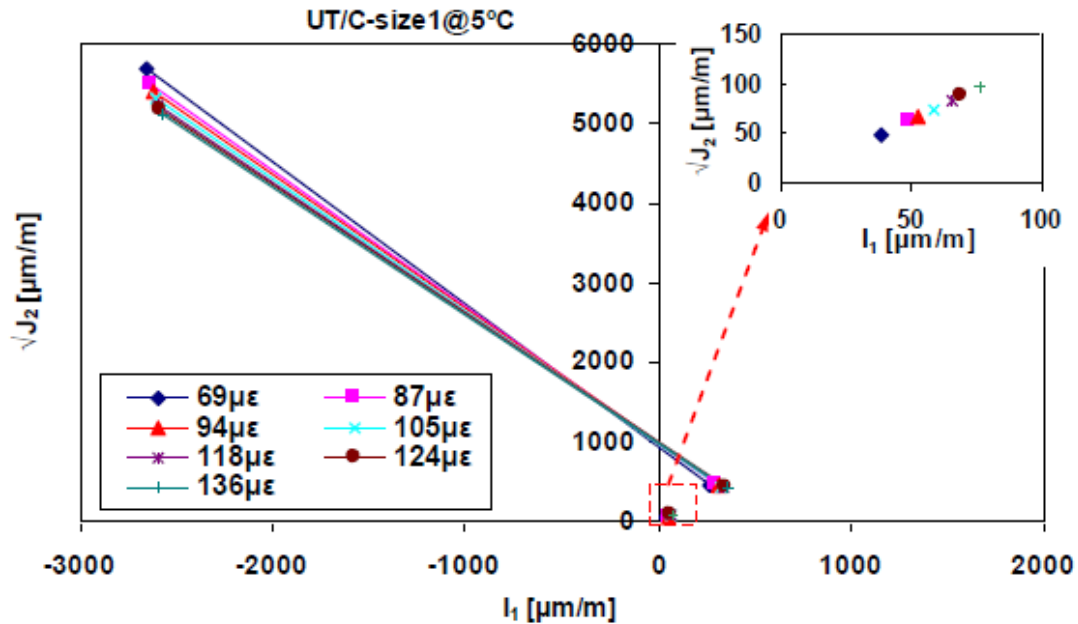


Figure 386. Strain based yield surfaces for the fine graded dense asphalt concrete as determined at different strain rates at 5 °C. [41].

Figure A7 shows that in this case the influence of the strain rate on the relation between I_1 and $\sqrt{J_2}$ can be neglected. We can write:

$$\sqrt{J_2} = -1.64 * I_1 + 897$$

Although all the fatigue test results shown in figure A7 were performed at the same frequency, differences in strain rate occur since the strain rate equals the peak strain/pulse duration implying that test performed at a higher strain level were also performed at a higher strain rate. As mentioned above, the position of the yield surface is, in this case, hardly affected by the strain rate. Please note that the test performed at the highest tensile strain ($136 \mu\text{m/m}$), resulting in lowest number of load applications to failure, is closest to the yield surface (see picture in upper right corner) and that the test performed at the lowest strain ($69 \mu\text{m/m}$), resulting in the highest number of load repetitions to failure, is farthest away from the yield surface. It is therefore reasonable to assume that a relationship can be developed between the distance of the strain point to the yield surface and the number of load repetitions to failure. The procedure that was used in [41] to develop such a relationship is schematically shown in figure A8. The distance to the yield surface is defined by means of the parameter R_Δ , which is defined as:

$$R_\Delta = \Delta_i / \Delta_{\text{tot}}$$

Li [41] not only performed UTC tests but also 4 PB tests and when these results are also presented in a R_Δ vs N diagram, figure A9 is obtained. Please note that figure A9 is not given in the usual log – log representation but in a linear – linear way. The figure shows some interesting information.

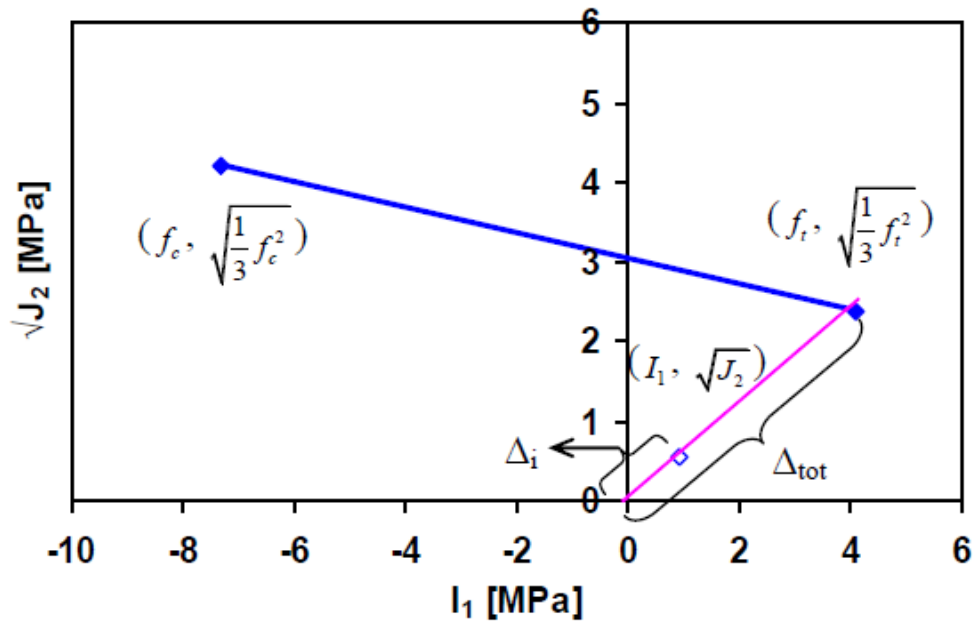


Figure A8: Formulation of the yield surface and definition of R_Δ [41].

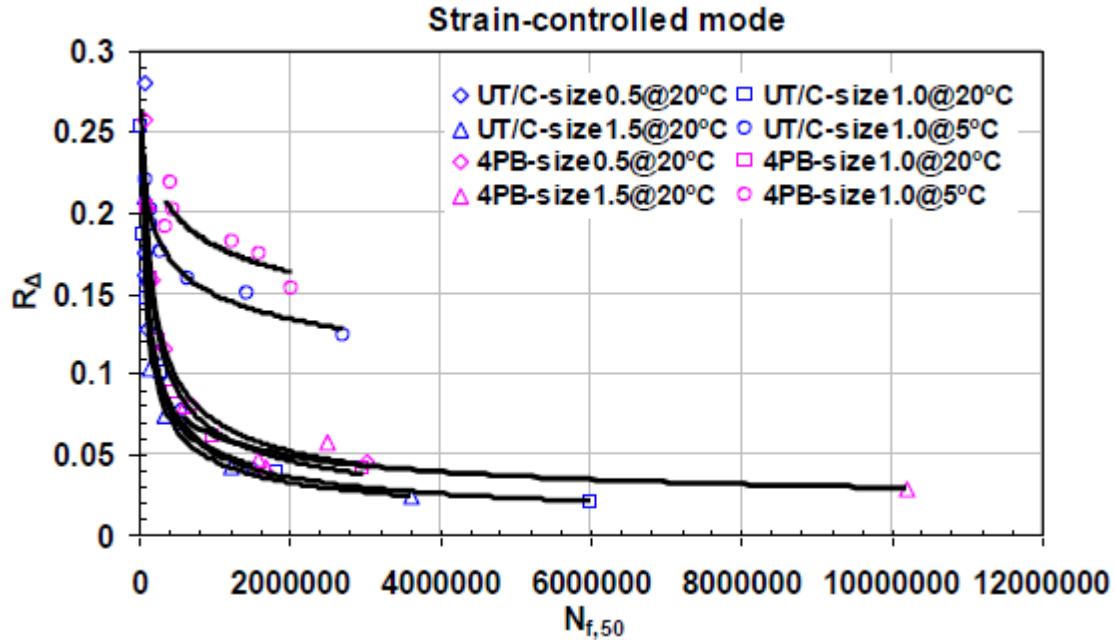


Figure A9: R_{Δ} vs N fatigue diagrams for a fine graded dense asphalt concrete as determined by means of UTC and 4PB fatigue tests [41].

Note: size 0.5, 1 and 1.5 refer to the dimensions of the specimens; for details see section of fatigue.

It seems that the differences between the 4PB and UTC tests are rather small in the R_{Δ} - N diagram. There also seems to be a threshold value for R_{Δ} below which no fatigue occurs. Such a threshold is called the "endurance limit". For 20 °C this endurance limit is approximately $R \approx 0.025$. For 5 °C it is estimated to be approximately $R \approx 0.13$. This implies that the endurance limit is dependent on the stiffness of the mixture. It is interesting to note that the influence of the test method and specimen size is not visible in the 20 °C results.

For this particular fine graded dense asphalt concrete mixture the fatigue relation based on the strain controlled UTC tests could be written as:

$$N = 5.22 R_{\Delta}^{-6.37}$$

Having available fatigue relationships of the R_{Δ} type allows us to take into account the 3D strain conditions in the pavement. From tension and compression tests the flow surface is determined and from the stresses and strains in a particular point in the pavement we can determine the values of I_1 and J_2 . Then we can determine the R_{Δ} vs N relationship. This is a major step forward since in the traditional fatigue analysis only the maximum strain is used as input and the influence of the other two principal strains is neglected. Let us see how this works out when using the results shown in figure A3.

Figure A3 shows that the 3 principal strains are: $\varepsilon_1 = 164 \mu\text{m/m}$, $\varepsilon_2 = 111 \mu\text{m/m}$ and $\varepsilon_3 = -161 \mu\text{m/m}$. In case we take ALL three principal strains into account, we obtain: $I_1 = 114$ and $\sqrt{J_2} = 174.4$. In case we ONLY take the maximum tensile strain into account (which we usually do) then $I_1 = 164$ and $\sqrt{J_2} = 94.7$.

We have seen earlier that we can write the yield surface as:

$$\sqrt{J_2} = -1.64 * I_1 + 897$$

This implies that at $I_1 = 114$ (the 3D case taking into account all three principal strains) the $\sqrt{J_2}$ value at which failure would occur would be 710. The actual $\sqrt{J_2} = 174.4$ so the ratio actual / failure $\sqrt{J_2}$ value would be 0.25. In case of the 1D case (only taking into account the maximum tensile strain) this ratio would be 0.15. All this implies that only taking into account the maximum tensile strain and ignoring the effect of the other two principal strains will lead to an overestimation of the fatigue life. If the ratio's are used as R values and used as input in the fatigue relation mentioned above one would notice a significant difference in fatigue lives when ignoring or taking into account the 3D strain conditions.

As mentioned before, beam bending, UTC, and IT tests are not the ideal fatigue tests; rolling wheel tests and BOEF type tests are to be preferred. A comparison between the BOEF and 4PB R_Δ - N relationships as determined for a gravel asphalt concrete base course is given in figure A10 (please note that this mixture is from reference [38] and is different from the mixture we used in the example problem). It should be noted that in this case the I_1 , J_2 and R_Δ values are based on the principal *stresses*. The figure clearly shows that a much longer fatigue life will be predicted when using R_Δ - N relationships which are based on the BOEF test.

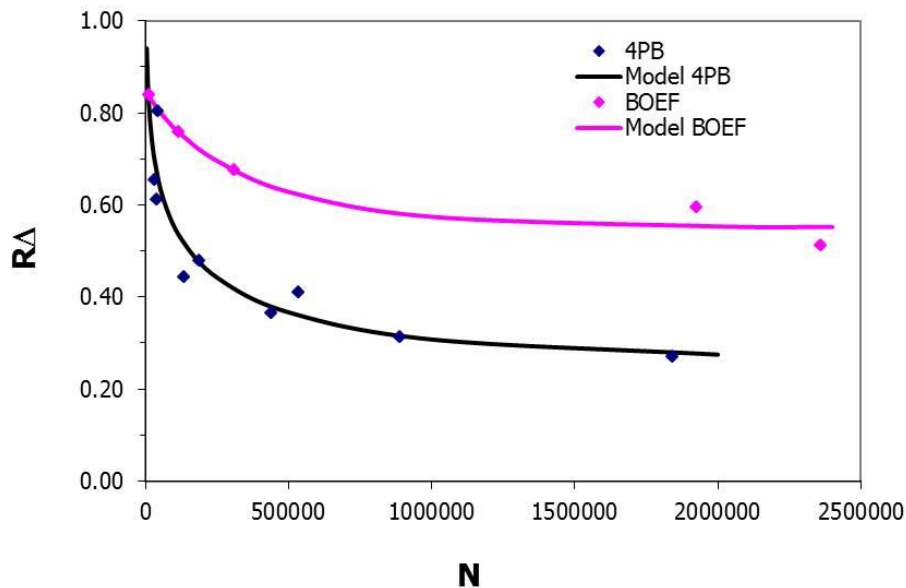


Figure A10: Stress based R_Δ - N relationships as determined by means of the BOEF and 4PB test on a gravel asphalt concrete base course [38].

Although the R_Δ - N approach is the desired approach, it has the disadvantage that next to fatigue tests, tension and compression tests are needed to determine the yield surface. "Tension and compression tests" are easily used words and the principle of these tests is indeed simple but reality is that they are not that easy to perform. High requirements need to be set to the equipment (stiffness of the test frame, signal and temperature control etc) as well to e.g. friction reduction when a compression test is performed. Fortunately Li [41] has done extensive work to estimate the tensile and compressive strength from mixture parameters. This will be discussed in the next section.

Before we will discuss how the tensile and compressive strength can be estimated, we will pay attention to how fatigue results can be represented using the well-known Mohr-Coulomb flow surface. As we have discussed earlier, the stress field in any point of the pavement can be represented by means of the three principal stress σ_1 , σ_2 and σ_3 which then can be used to

construct Mohr's circles (see figure A11). From the principal stresses we can easily calculate α and if the cohesion C is known we should be able to calculate the number of load repetitions to failure using:

$$N = (\alpha / C)^b$$

The cohesion and angle of internal friction of a particular asphalt mixture can easily be determined by means of tension and compression tests. Since the tensile and compressive strength are temperature and loading rate dependent, also C and ϕ will show this dependency although ϕ is hardly affected and almost takes a constant value. The cohesion C can also easily be determined from the tensile strength of the material and the angle of internal friction. This is in the derivation given hereafter (see also figure A12).

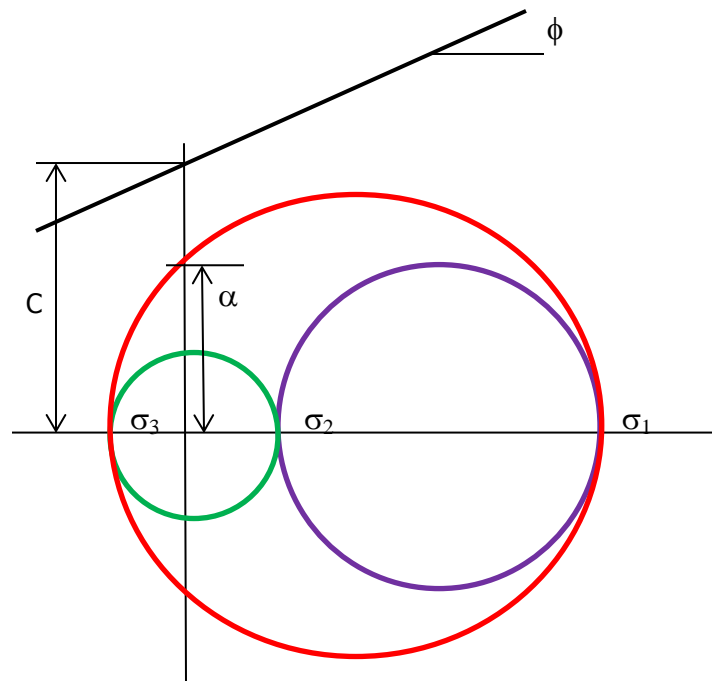


Figure A11: Mohr's circles connecting the three principal stresses.

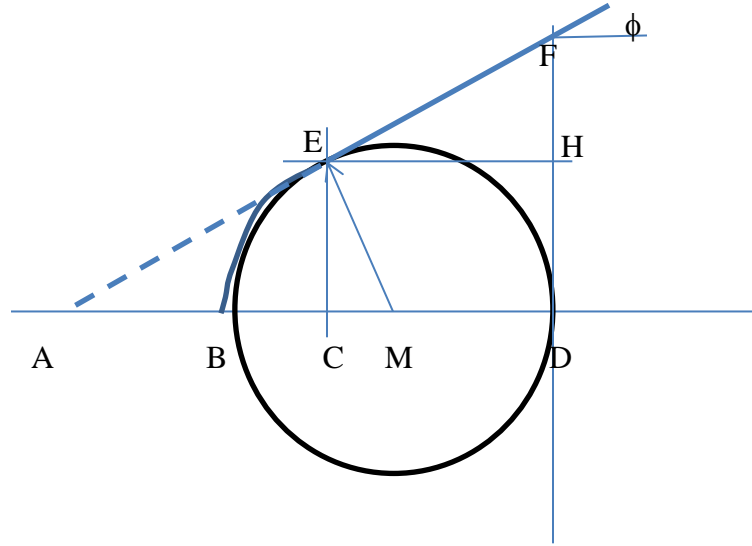


Figure A12: Relation between ϕ and C .

Let $BD = \text{tensile strength} = f_t$

Then we can calculate the cohesion C from

$$C = FH + HD = FH + CE = EH * \tan \phi + EM * \cos \phi$$

Since $EM = 0.5 * BD = 0.5 * f_t$ and $EH = CM + MD = EM * \sin \phi + 0.5 * f_t = 0.5 * f_t * \sin \phi + 0.5 * f_t = 0.5 * f_t * (\sin \phi + 1)$

C becomes $C = [0.5 * f_t * (\sin \phi + 1)] * \tan \phi + 0.5 * f_t * \cos \phi$

$$C = 0.5 * f_t * (1 + \sin \phi) / \cos \phi$$

Tension and compression tests are needed to determine the compressive strength f_c and tensile strength f_t . If these values are known ϕ can easily be determined from the ratio f_c / f_t following:

$$\phi = 26 \ln (f_c / f_t) \text{ where } [\phi] = [^\circ]$$

A4. Estimation of the tensile and compressive strength from mixture composition data

In order to be able to get a proper estimate of the tensile and compressive strength without the need to do extensive testing, Li [41] used the test results of several researchers to develop equations which allow such estimates to be made. Some details about the mixtures are given in table A1.

Gradation	E [MPa]	V _a [%]	V _b [%]	C _c
DAC 0/8	5200	3.0	14.9	3.25
EME 0/14	5700	3.4	12.2	0.73
PAC 0/16	2500	20.0	8.2	12.25
DAC 0/16	6900	2.7	12.9	20.48
SMA 0/11	2800	5.2	14.5	0.95
ACRe 0/4	3543	2.6	19.3	0.99
GAC	4700	4.4	8.9	1.60

Table A1: Mixtures involved in Li's analysis [41].

Note: DAC = dense asphalt concrete, EME = enrobe module elevee, PAC = porous asphalt concrete, SMA = stone mastic asphalt, ACRe = very fine dense asphalt concrete, GAC = gravel asphalt concrete, E = modulus at 20 °C and strain rate of 0.1%/s, V_a = void content, V_b = volume percentage bitumen, C_c = D30/(D10*D60), D_x = sieve size through which x % of the aggregates are passing.

The model to predict the tensile and compressive strength is based on the assumption that at high temperatures and long loading times the strength is at its lowest and that at very low temperatures and short loading times the strength reaches a maximum value. It is further more assumed that the change from minimum to maximum strength follows a S-shaped curve. This curve can be written as:

$$P = P_h + (P_l - P_h) S$$

Where: P = compressive or tensile strength at a given temperature and strain rate,
P_h = the highest strength,
P_l = the lowest strength,
S = parameter describing the shape of the S curve,
S = $\exp(-(u_r / u_o)^\gamma)$,
u_r = reduced time derivative value,
u_o = reference value of time derivative value u,
γ = model parameter.

Li showed that P_l, P_h, u_o, and γ could be estimated by means of the information given in table A2.

Strength	P _l	P _h	u _o	γ
compressive	0	$= 1.755 E^{0.402} (V_b / (V_b + V_a))^{0.623}$	7.87E-02	0.322
tensile	0	$= 0.555 E^{0.308} (V_b / (V_b + V_a))^{0.849}$	5.44E-02	0.565

Table A2. Parameters of the equation to predict the tensile and compressive strength.

Note: [E] and [P] = [MPa]; E determined at 20 °C and strain rate of 0.1 %/s

Figure A13 shows how the predicted stress values corresponded with the measured values. In general the predictive equation did a pretty good job in estimating the compressive and tensile strength.

One will notice that in order to be able to use these equations one should know the elastic (stiffness) modulus of the asphalt mixture. Collecting such data doesn't mean an extension of the test program since stiffness data are needed anyhow for thickness design analyses.

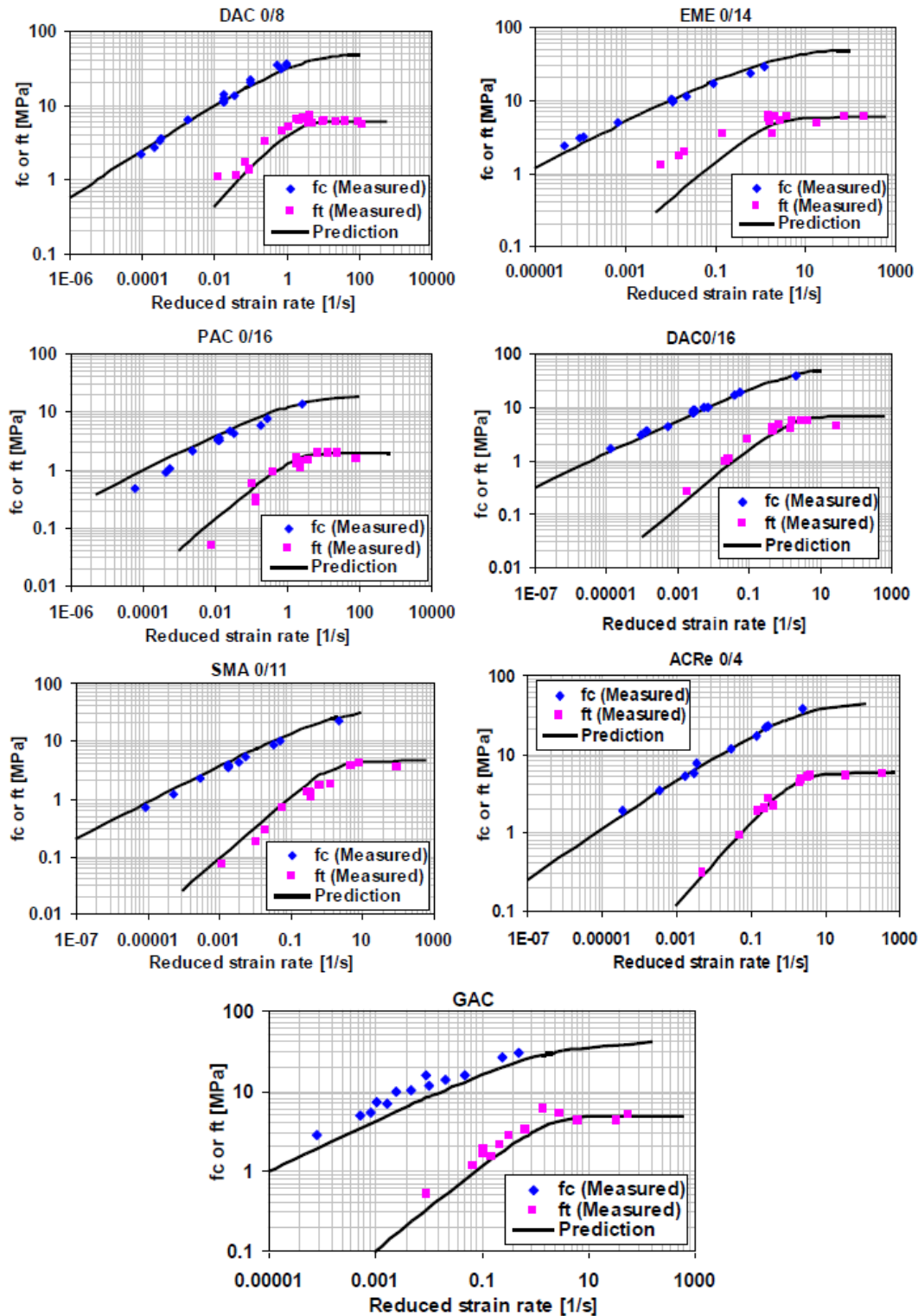


Figure A13: Comparison between measured and predicted tensile and compressive strength values [41].

Appendix B

Quality control procedure for flexible pavements in case of innovative contracts as used in the Netherlands for main roads

B1. Purpose of the procedure

This procedure is meant for contracts where the contractor has the freedom to design the structure himself. The procedure describes how the quality of the pavement will be checked in terms of the layer thickness, and stiffness modulus of the pavement layers. By means of the procedure it will be determined whether the layer thicknesses and moduli are in agreement with those that were used by the contractor when making his design.

B2. Measurements

The procedure prescribes deflection measurements and measurement of the pavement temperature during the falling weight deflection tests. The deflection tests need to be performed between 6 and 12 months after completion of construction.

The falling weight deflectometer tests need to be performed with a device which is calibrated according to a prescribed procedure. The geophones need to be placed at the following distances from the loading center: 0, 300, 600, 900, 1200 and 1800 mm.

The deflection measurements can be done by the contractor or by a party selected by the contractor.

B2.1 Performing the measurements

The deflection measurements should be performed between the wheel paths of the lane that needs to be investigated. The distance between the measurement locations should be between 10 and 50 m. At each location the test should be repeated 4 times with a nominal load of 50 kN. At each measurement location, the temperature should be measured at a depth of 100 mm below the pavement surface. During the tests the temperature should be between 15 °C and 25 °C.

B3. Evaluation of the measurements

B3.1 Evaluation of the data per measurement location

At each location, the deflection profile is determined 4 times. In the evaluation, the first profile is not taken into account. Profiles 2, 3 and 4 are normalized to a load level of 50 kN and after that the average per geophone location is calculated. The deflections are not corrected for temperature effects.

B3.2 Defining sub-sections

The coefficient of variation of the maximum deflection should not be higher than 15%; if this is not the case sub-sections should be defined. In each sub-section the coefficient of variation should be lower than 15%. The minimum number of measurement locations per sub-section is 12.

In case no sub-sections can be defined which comply to the above mentioned requirements, then the sub-sections should be defined in such a way that the EVV (exceeding variation value) takes a minimum value. Also in this case the minimum measurement locations per sub-section should be 12. The EVV is calculated as follows:

$$EW = \sum^n (CV_i - 15\%) * L_i$$

Where:

CV_i = coefficient of variation of the maximum deflection of sub-section i where CV is higher than 15%,

n = number of section with a CV > 15%,

L_i = length of sub-section i with a CV > 15%.

The sub-sections are determined using the deflection measurements between the wheel paths. They also apply however for the wheel path closest to the edge of the pavement.

B3.3 Calculation of the average normalized deflection profile per sub-section

For each sub-section the average is determined of the average normalized deflection profiles that were determined for each measurement location (see 3.1). For each sub-section the average is determined of the pavement temperature that was measured at each measurement location.

B4. Layer thickness

The thickness of the asphalt layer and (if possible) the base layer has to be determined by means of coring. The minimum number of cores to be taken is 10. Coring needs to be done by a third party which is selected by the client.

The cores need to be sent to a certified laboratory for layer thickness measurements.

If no cores can be taken from the base layer, its thickness should be determined from the available production control data which should be collected by the contractor.

It should be proven that over a length of less than 5% of the section, the layer thicknesses as determined in this way do not deviate 20 mm or more from the thicknesses assumed in the design analyses. This should be proven with a reliability of 95% and this should be done with the statistical method described in appendix I.

If the layer thicknesses do not comply with this requirement the "lack of asphalt thickness parameter (LOAT) should be calculated following the procedure described in appendix B1.

B5. Assessment of the layer moduli

The layer moduli are back calculated from the measured deflection profiles and layer thicknesses. The pavement model that needs to be used is a three-layer system consisting of subgrade, base course and asphalt layer.

In case there is more than one base layer, then only the top base layer is taken into account. The base layers below this top base layer are taken into by calculating an equivalent stiffness of the subgrade. The equivalent subgrade stiffness applies for all layers, inclusive of the subgrade, below the asphalt layer and the top layer of the base course. This equivalent stiffness should be such that the deflection profile calculated using this value matches as good as possible with the measured deflection profile.

This equivalent stiffness should be reported by the contractor in his design documents.

The stiffness of the subgrade is defined as the equivalent subgrade stiffness mentioned above.

The stiffness modulus of the asphalt layer as used in the design analysis is corrected for the loading frequency and temperature during the deflection test. This is done using the stiffness vs temperature relationship which was used in the design analysis and which was determined in the laboratory. This relationship shows the stiffness vs temperature at a given load frequency. First of fictitious temperature is calculated following:

$$1 / (T_{\text{fictitious}} + 273) = 1 / (T + 273) - \log (f_{\text{char}} / f) / 11242$$

Where:

$T_{\text{fictitious}}$ = fictitious temperature at which the stiffness will be determined [$^{\circ}\text{C}$],
 T = asphalt temperature at the time of the deflection measurements [$^{\circ}\text{C}$],
 f_{char} = frequency at which the stiffness temperature relationship is determined in the laboratory [Hz],
 f = loading frequency of the falling weight deflectometer test = 20 Hz.

If different stiffness characteristics are used for each of the individual layers of the total asphalt thickness then this correction has to be applied for each of those layers. Then the effective stiffness of the entire asphalt thickness should be calculated following the procedure described in appendix B2.

B6. Back calculation of the layer stiffness

Back calculation of the layer moduli should be done with a linear elastic multi-layer program using a three layer system (see above). The following considerations should be taken into account.

- All asphalt layers should be taken together as one layer.
- If there is more than one base layer, these should be treated as mentioned above.
- Full friction is assumed between the layers.
- The layer thickness to be used is the average thickness determined from the cores (see above).
- The values to be used for Poisson's ratio should be equal to those used in the design.
- It is not allowed to apply weighing factors on the deflections.
- The deflection measured at each of the geophone positions must be taken into account.

When back calculating the layer moduli, the RMS should be minimized. The RMS is calculated following:

$$\text{RMS} = \sqrt{\frac{1}{n} \sum_{i=1}^n (\delta_i \text{ calculated} - \delta_i \text{ measured})^2}$$

The fit of the calculated deflection profile with the measured one should be calculated and reported. The fit is calculated following:

$$\text{FIT} = \left[\frac{1}{n} \sum_{i=1}^n \text{abs}\left\{ \frac{(\delta_i \text{ calculated} - \delta_i \text{ measured})}{\delta_i \text{ measured}} \right\} * 100\% \right] / n$$

Where:

$\delta_i \text{ calculated}$ = calculated deflection at position i [μm],
 $\delta_i \text{ measured}$ = measured deflection at position i [μm],
 n = number of geophone positions per deflection profile.

B7. Comparison of back calculated moduli with moduli assumed in the design process

B7.1 Subgrade modulus

The back calculated subgrade modulus should be at least equal to the (effective) modulus mentioned in section 5. If this is not the case then the lack in stiffness can be compensated by a higher stiffness of one of the other layers. For this a fictitious base modulus is calculated following the procedure described in appendix B3. The back calculated base modulus should then be equal to this fictitious stiffness.

B7.2 Asphalt and base layer modulus

From the back calculated asphalt and base layer modulus, shift factors are calculated following:

Shift factor asphalt stiffness = back calculated stiffness / stiffness assumed in design,

Shift factor base stiffness = back calculated stiffness / stiffness assumed in the design

In the equation of the base layer shift factor, the base layer stiffness "assumed in the design" is corrected (when needed) for a too low subgrade modulus (see 7.1).

Both shift factors should have a value between 0.67 and 1.5. The product of both shift factors should be at least 1 so:

Shift factor asphalt stiffness * shift factor base stiffness ≥ 1.0

If the results can not comply with the requirements mentioned then the base layer stiffness should be set equal to the design stiffness (if needed corrected for lack of subgrade stiffness) and the asphalt modulus should then be recalculated. The then obtained shift factor for the asphalt stiffness should then be ≥ 1 . If not an effective lack of asphalt thickness due to lack of layer stiffness is calculated following the procedure mentioned in appendix B4.

Appendix B1: Check on layer thickness

The layer thickness values as determined by means of coring should be checked against the thickness values assumed in the design. With a reliability of 95% it should be shown that the layer thickness values over 5% of the considered section do not deviate more than 20 mm from the design thickness. This is determined in the following way.

First the parameter Q_u is calculated following:

$Q_u = \{(\text{layer thickness as designed} - 20 \text{ mm}) - \text{average layer thickness determined from the cores}\} / \text{standard deviation of the layer thickness determined from the cores.}$

Then parameter Z is calculated following:

$$Z = Q_u + 1.65 * \sqrt{\{ (1 / \text{number of cores}) + [Q_u^2 / (2 * \text{number of cores})] \}}$$

Z is then used to determine the percentage of the measurements that not comply with the requirements. It is therefore used together with the normal distribution table to determine the risk of non-compliance. This risk should be equal or less than 5% implying that Z should not be higher than -1.65.

Figure B1 is a graphical representation of the procedure.

If this is not the case then a $Q_{u_{\text{required}}}$ needs to be calculated in an iterative way following:

$$Q_{u_{\text{required}}} = -1.65 * \{ 1 + \sqrt{[1 / \text{nr of cores} + Q_{u_{\text{required}}}^2 / (2 * \text{nr of cores})]} \}$$

Or figure B1 can be used ($Q_{u_{\text{required}}}$ follows from the intersection of the 5% dotted line with line that indicates the number of cores.

Then the required asphalt thickness (RAT) is determined from:

$$\text{RAT} = (\text{design asphalt thickness} - 20 \text{ mm}) - Q_{u_{\text{required}}} * \text{standard deviation asphalt thickness}$$

The shortage, or lack, in asphalt thickness (SAT) is then calculated using:

$$\text{SAT} = \text{RAT} - \text{average asphalt thickness as determined from the cores.}$$

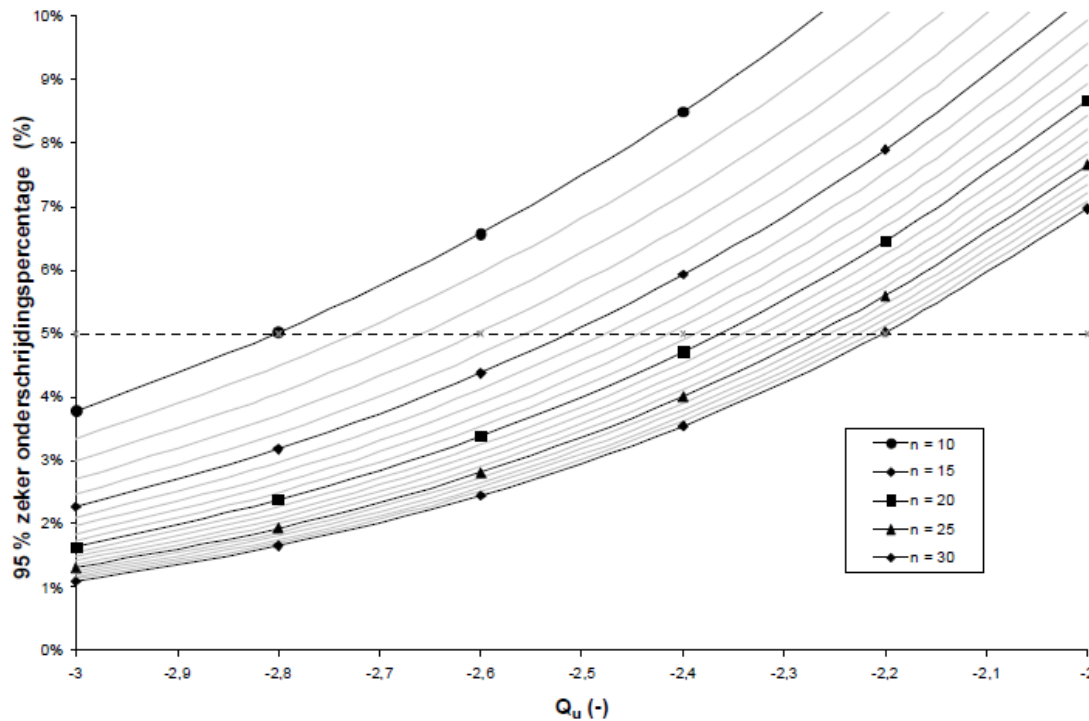


Figure B1: Relation between risk percentage, number of cores and Q_u .

If the thickness of the base course deviates more than 20% over 5% of the section then RBT (required base thickness) is calculated in the same way as the RAT so:

$$\text{RBT} = (\text{design base thickness} - 20 \text{ mm}) - Q_{u_{\text{required}}} * \text{standard deviation base thickness}$$

The RBT is then “translated” into an equivalent asphalt thickness shortage (SAT) by using figure B2. In this figure the base and subgrade stiffness as described in section B5 are used as input.

Appendix B2: Check on layer stiffness

If the stiffness of the layers doesn't comply with the requirements mentioned in section B7, an equivalent asphalt thickness due to insufficient layer moduli is calculated. This is done in the following way. The starting point is the shift factor for the asphalt stiffness which is calculated using the stiffness of the asphalt layer which back calculated by setting the base layer stiffness at the level used in the design (or the base modulus corrected for lack of subgrade stiffness as described in section B7.1). The equivalent asphalt thickness is calculated using:

$$\text{Equivalent SAT due to insufficient modulus} = \text{asphalt thickness as designed} * \alpha$$

$$\alpha = (1 - \sqrt[3]{(\text{shift factor asphalt stiffness})} / \sqrt[3]{(\text{shift factor asphalt stiffness})})$$

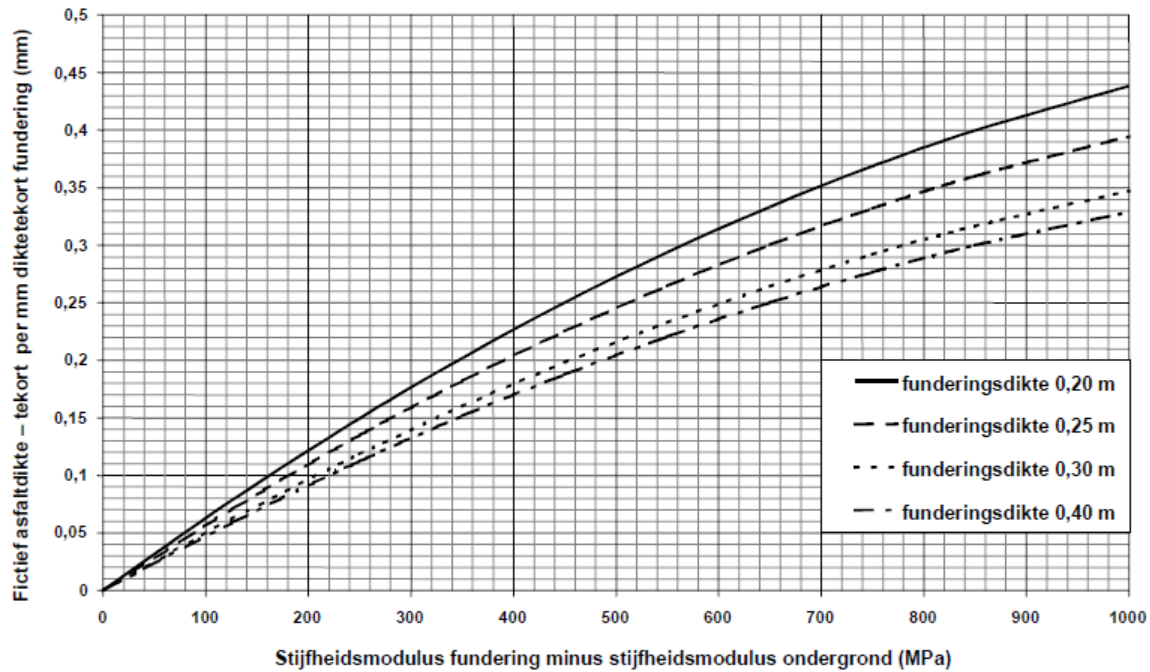


Figure B2: Determination of the equivalent shortage in asphalt thickness due to a shortage in base thickness.

Note: horizontal axis gives stiffness modulus of the base course minus the subgrade stiffness [MPa]
The vertical axis gives the fictitious shortage in asphalt thickness due to a shortage in base layer thickness.
Legend gives base layer thicknesses of 0.2, 0.25, 0.3 and 0.4m

Appendix B3: Increase of base layer stiffness due to insufficient subgrade stiffness

The back calculated subgrade modulus has to be compared with the base stiffness assumed in the design process. If the back calculated value is too low, then the stiffness of the base layer as used in the design needs to be increased. The additional stiffness needed for the base layer can be calculated using:

$$\Delta E_{fund} = E_{fund} \cdot \left(0,976 \cdot \left(\frac{E_{asf}}{E_{fund}} \right)^{0,108} + 1,00 \cdot h_{asf}^{0,418} - 0,000266 \cdot \left(\frac{E_{fund}}{E_{ond}} \right)^{1,71} - 1,05 \cdot h_{fund}^{0,426} - 0,393 \right) \cdot \frac{\Delta E_{ond}}{E_{ond}}$$

Where:

- ΔE_{fund} = required additional stiffness of the base compared to the design value [MPa],
- ΔE_{ond} = deficit in subgrade stiffness compared to the value used in the design [MPa],
- E_{asf} = stiffness of the asphalt layer as used in the design [MPa],
- E_{fund} = stiffness of the base layer as used in the design [MPa],
- E_{ond} = stiffness of the subgrade as used in the design [MPa],
- h_{asf} = total asphalt thickness according to the design [m],
- h_{fund} = thickness of the base layer according to the design [m].

Appendix B4: Calculation of the composite layer stiffness

In case the total asphalt thickness is composed of n layers each with a different E_i and layer thickness h_i then a composite stiffness modulus is calculated (E_{eq}) which is valid for the total

asphalt thickness h_t ($h_t = \sum h_i$) resulting in the same bending stiffness. The first step in this calculation is the determination of the distance of neutral axis z_t of the entire package to the bottom of the entire package. This is done following:

$$z_t = \frac{\sum_{i=1}^n E_i \cdot z_i \cdot h_i}{\sum_{i=1}^n E_i \cdot h_i}$$

Where:

- E_i = modulus of layer i [MPa],
- h_i = thickness of layer i [m],
- z_i = distance of bottom of total asphalt thickness to the middle of layer i [m],
- n = number of layers,
- z_t = distance of bottom of total asphalt thickness to neutral axis of composite layer [m].

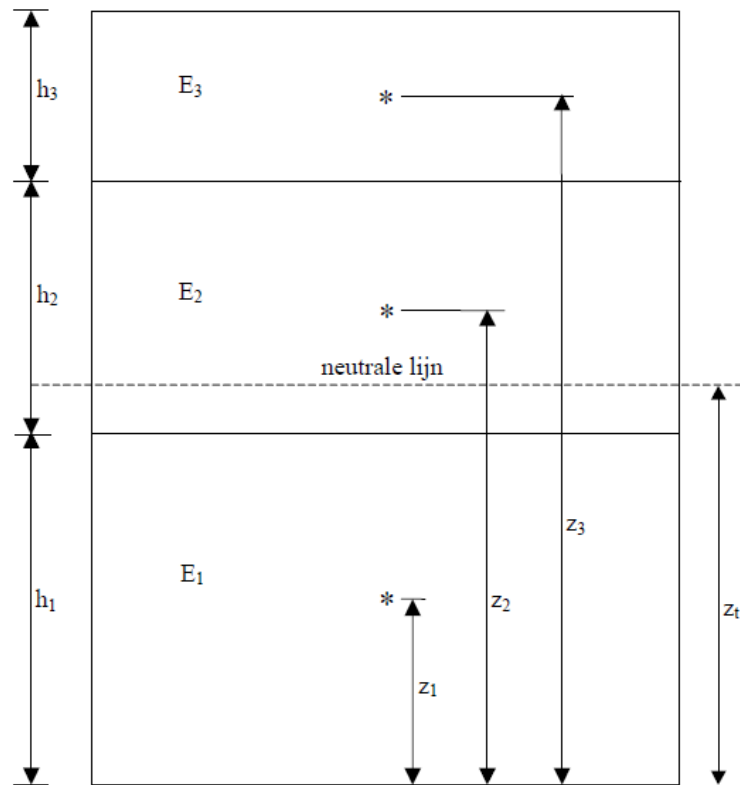


Figure B3: Calculation of the composite layer stiffness E_{eq} .

Then the bending stiffness of the composite system (EI) is calculated using:

$$EI = E_1 \cdot \left\{ \frac{1}{12} \cdot h_t^3 + h_t \cdot \left(z_t - \frac{1}{2} \cdot h_t \right)^2 + \sum_{i=2}^n \left(\frac{E_i - E_1}{E_1} \cdot \left(\frac{1}{12} \cdot h_i^3 + h_i \cdot (z_i - z_t)^2 \right) \right) \right\}$$

Where:

- EI = bending stiffness of composite layer [MPa * m⁴ / m]

E_1 = modulus of the lowest layer [MPa],
All other variables as defined above.

Then the composite stiffness E_{eq} is calculated using:

$$E_{eq} = 12 * EI / h_t^3$$